Cardiff University

School of Chemistry

Tuning the Photophysics of Ir(III) and Pt(II) Complexes by Synthetic Modification of Quinoxaline Ligands

Thesis submitted for the degree of Doctor of Philosophy by:

Sophie Ann Fitzgerald

March 2023

Cardiff University

School of Chemistry

Abstract

Doctor of Philosophy

Tuning the Photophysics of Ir(III) and Pt(II) Complexes by Synthetic Modification of Quinoxaline Ligands

By Sophie Ann Fitzgerald

The work presented in this thesis focuses on the development and analysis of organic ligands primarily derived from 2-phenylquinoxaline, and their resultant Ir(III) and Pt(II) phosphorescent complexes. Through efficacious ligand design, their desirable photophysical properties offer potential applications in a multitude of areas including OLED development and biological imaging.

Chapter 2 explores the impact of altering the nature and position of electron-donating and electron-withdrawing substituents at the cyclometallating ligand to form a series of Ir(III) complexes. Fine tunability of the emission wavelength within the yellow to deep-red regions of the visible range was achieved.

Chapter 3 investigates long-range electron-withdrawing substituents at varying positions on the phenyl ring of the cyclometallated ligand system, and their resultant impact on the electronic and structural properties of a series of neutral square planar Pt(II) complexes. Comparisons were made with Ir(III) analogues and the complexes were also investigated as photosensitisers for TTA-UC.

Chapter 4 describes the development of deep-red emitting Ir(III) complexes with 2-thienyl quinoxaline type ligands. Absorption and emission properties were monitored, where both subtle and prominent tunability was observed.

Chapter 5 focused on the utilisation of pendant naphthalimide units at the extremities of Ir(III) complexes to initiate triplet-triplet energy transfer mechanisms for the development of long-lived phosphorescent species.

Chapter 6 explored the synthesis of a novel pyrene-based quinoxaline ligand system and its resultant Ir(III) complex – monitoring the impact on spectroscopic properties upon direct cyclometallation to a pyrene unit.

Contents

Acknowledgements

Table of Figures

Table of Tables

Table of Schemes

List of Abbreviations

Experimental Techniques

(FT)IR – (Fourier transform) infrared

$[M]^+$ – Molecular ion peak

$\{^1H\}$ – Proton decoupled

abs – Absorption

ATR – Attenuated total reflectance

br – Broad

CI – Chemical ionisation

DFT – Density Functional Theory

δ – Chemical shift

EI+ – Electron impact

em – Emission

eq – Equivalents

ES+ – Electrospray inoisation

ex – Excitation

HRMS – High-resolution mass spectrometry

K – Kelvin

LRMS – Low-resolution mass spectrometry

LT – Low temperature

m/z – Mass/charge

MO – Molecular Orbital

NBO – Natural Bond Orbital

NIR – Near-infrared

NMR – Nuclear Magnetic Resonance

OD – Optical density

PMT – Photomultiplier tube

ppm – Parts per million

QTAIM – Quantum Theory of Atoms in Molecules

RT – Room temperature

sh – Shoulder

TA – Transient absorption

TD-DFT – Time-Dependent Density Functional Theory

TLC – Thin-layer chromatography

UV(-vis) – Ultraviolet(-visible)

XRD – X-ray Diffraction

Δ – Heat energy

ε – Molar extinction coefficient

λ – Wavelength

d – Doublet

m – Multiplet

q – Quartet

s – Singlet

t – Triplet

μs – Microseconds

h – Hours

ms – Milliseconds

ns – Nanoseconds

s – Seconds

Solvents and Chemicals

$(CD_3)_2CO$ – Deuterated acetone

2,2'-bpy – 2,2'-bipyridine

4,6-dfppy – 2-(2,4-difluorophenyl)pyridine

6tFmppy – 2-(4-(trifluoromethyl)phenyl)pyridine

acac – Acetylacetonate

AcOH – Acetic acid

AgCl – Silver(I) chloride

aq – Aqueous

BODIPY – 4,4-difluoro-4-bora-3a,4a-diaza-s-indacene

$CHCl_3$ / $CDCl_3$ – Chloroform / Deuterated chloroform

DCM – Dichloromethane

DDB – Dioxane dibromide

DMAP – 4-Dimethylaminopyridine

DMSO / DMSO-d_6 – Dimethylsulfoxide / Deuterated DMSO

DPA – 9,10-diphenylanthracene

dpm – Dipivolylmethanoate

Et_2O – Diethyl ether

EtOH – Ethanol

H_2O_2 – Hydrogen peroxide

H_2SO_4 – Sulphuric acid

HCl – Hydrochloric acid

KNO_3 – Potassium nitrate

KOH – Potassium hydroxide

M – Molar

MeCN / CD_3CN – Acetonitrile / Deuterated acetonitrile

MeOH – Methanol

$NaHCO_3$ – Sodium bicarbonate

NaOH – Sodium hydroxide

NBS – N-Bromosuccinimide

NH_4PF_6 – Ammonium hexafluorophosphate

NI – 1,8-naphthalimide

phen –1,10-phenanthroline

ppq – 2,4-diphenylquinoline

ppy – 2-phenylpyridine

pq – 2-phenylquinoline

pqx – 2-phenylquinoxaline

sat – Saturated

SiO_2 – Silica

THF – Tetrahydrofuran

thpy – 2-(2'-thienyl)pyridyl)

TMS – Tetramethylsilane

TPBP – 5,10,15,20-tetraphenyltetrabenzoporphyrin

TPPy – 1,3,6,8-tetraphenylpyrene

tptpy – 4′-terphenyl-2,2′:6′,2″-terpyridine

tpy – 6′,2″-terpyridine

Photophysics

$^1(X)$ – Singlet excited state of X

$^3(X)$ – Triplet excited state of X

AIE – Aggregation induced emission

EDG – Electron-donating group

EWG – Electron-withdrawing group

FRET – Förster resonance energy transfer

HOMO – Highest occupied molecular orbital

IL – Intra-ligand

ISC – Intersystem crossing

k_{nr} – Non-radiative decay rate constant

k_r – Radiative decay rate constant

LC – Ligand-centred

LUMO – Lowest occupied molecular orbital

MC – Metal centred

MLCT – Metal-to-ligand charge transfer

MMLCT – Metal-metal-to-ligand charge transfer

PET – Photoinduced electron transfer

PL – Photoluminescence

S_0 – Singlet electronic ground state

S_1 – First (lowest-lying) singlet electronic excited state

S_n – Singlet electronic excited state

SOC – Spin-orbit coupling

T_1 – First (lowest-lying) triplet electronic excited state

TADF – Thermally activated delayed fluorescence

TITC – Twisted internal charge transfer

TTA – Triplet-triplet annihilation

TTA-UC – Triplet-triplet annihilation upconversion

TTET – Triplet-triplet energy transfer

τ_{obs} – Observed luminescence lifetime

Φ_P – Phosphorescence quantum yield

Φ_{PL} – Photoluminescence quantum yield

Φ_{UC} – Upconversion quantum yield

Φ_Δ – Singlet oxygen quantum yield

Applications

EQE – External Quantum Efficiency

FBA – Fluorescent Brightening Agent

OLED – Organic Light Emitting Diode

PDT – Photodynamic Therapy

POLED – Polymer organic light emitting diode

WOLED – White organic light emitting diode

Chapter 1: Introduction

1.1: Introduction

The work presented in this thesis focuses on the design, synthesis, and characterisation of organic ligands and their corresponding Ir(III) and Pt(II) complexes. With potential applications in the development of photoactive materials, the photophysical attributes of these species are explored in detail. This introductory chapter aims to set the scene for the forthcoming studies by discussing the fundamental concepts that this research is based on. Relevant studies will be used to elucidate key principles and how they can lead to applications in areas such as OLED fabrication, solar cell technology and biological imaging.

1.2: Photoluminescence

1.2.1: Principles of Photoluminescence

Luminescence is described as the emission of light from an electronically excited state,[1] specifically without the requirement of heat energy.[2] *Photoluminescence* occurs by absorption of light energy to generate this excited state, which is subsequently deactivated through the release of a photon.[3] Depending on the nature of the excited state, photoluminescence can be categorised into two classes; fluorescence and phosphorescence. An electron can either retain its spin orientation to generate a singlet excited state (S_1) or experience a change in spin quantum number to give rise to a triplet excited state (T_1). Radiative (*i.e.* emissive) deactivation from a singlet excited state gives rise to fluorescence, whilst phosphorescence occurs from a paramagnetic triplet state.[4] These processes are illustrated in **Figure 1.1** by a *Jablonski energy level diagram* (named after physicist Aleksander Jabłoński). Simplistically, transitions tend to arise from the highest-occupied molecular orbital (HOMO) to the lowest unoccupied molecular orbital (LUMO), where the energy difference between the two orbitals dictates the optical properties of the species.
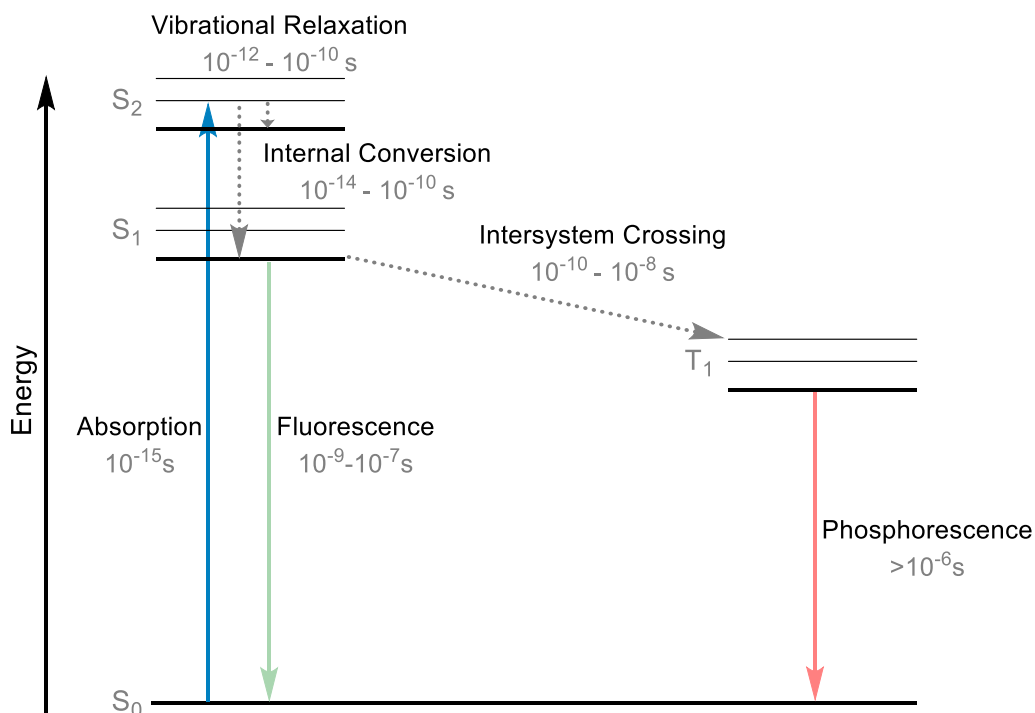
Figure 1.1: *Jablonski diagram indicating the radiative (solid) and non-radiative (dashed) transitions involved in the process of photoluminescence, along with their corresponding average timescales.[1,5] Ground state vibrational levels not included.*

Firstly, *absorption* of energy in the form of photons (hv) activates the transition from the singlet ground state to a singlet excited state of higher energy ($S_0 \rightarrow S_n$). This process is extremely rapid (10^{-15} s) and generally requires light within the region of the UV (200 – 380 nm) or visible (380 – 780 nm) range of the electromagnetic spectrum for organic compounds (**Figure 1.2**).[6] Relaxation to the lowest lying electronic state (S_1) usually occurs through rapid *internal conversion* (IC) ($<10^{-10}$ s), so any deactivation happens directly from the S_1 state. Additionally, thermal relaxation between vibrational levels within electronically excited states usually takes place at room temperature (*vibrational relaxation*, 10^{-12}-10^{-10}s). Both IC and vibrational relaxation are *non-radiative* decay processes since they account for energy loss without emission of a photon and therefore compete with *radiative* pathways. The most probable transition from an excited state is generally that which is fastest.[7]

Fluorescence ($S_1{\rightarrow}S_0$) is a *radiative* transition that results in the emission of a photon and takes place at a comparatively long timescale (>10^{-9} s). Another form of non-radiative decay is *intersystem crossing* (ISC), where energy is transferred to the lowest-lying triplet excited state ($S_1{\rightarrow}T_1$). Radiative decay from this excited state results in a phenomenon known as *phosphorescence*, an extremely long-lived process (>10^{-6} s). If a peak in the absorption or emission spectrum experiences a change in position to longer wavelengths, it is referred to as a *bathochromic* or *red shift*. If the peak position repositions to a shorter wavelength, it is termed a *hypsochromic* or *blue shift*.
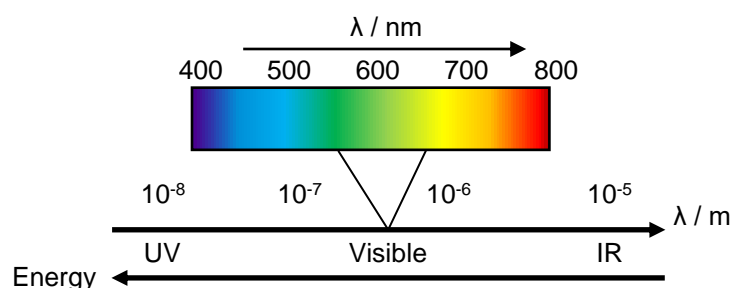
Figure 1.2: *Illustration of the narrow optical range of the electromagnetic spectrum – the region of interest for studying photophysical properties.*

Radiative transitions can be quantified by the *Planck relation* (**Equation 1.1**), where an inverse relationship between photonic energy (E) and wavelength (λ) is recognised. Therefore, longer wavelengths of light are associated with a lower energy process.

$$E = hv = \frac{hc}{\lambda}$$

Equation 1.1

- **h**: Planck's constant (6.626 × 10^{-34} J s^{-1})
- ***v***: Frequency (Hz)
- **c**: speed of light (3 × 10^8 m s^{-1})

The probability of absorption taking place is related to the similarity between vibrational levels in the ground and excited states, where the most likely transition is that which presents no change in nuclear motion. Therefore, the almost instantaneous nature of absorption leads to a vertical transition between vibrational states. This concept is known as the *Franck-Condon Principle* and

is illustrated in **Figure 1.3**,[8,9] where excitation occurs from the lowest-lying vibrational level in the ground state ($v = 0$).
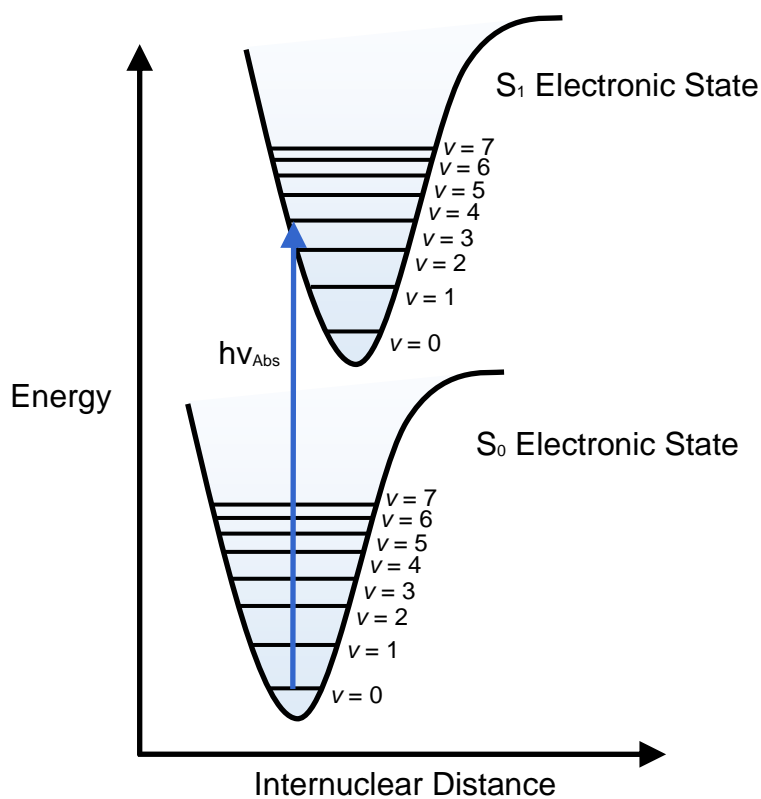
Figure 1.3: Energy level diagram demonstrating the Franck-Condon Principle. Vibrational energy levels (v = n) are also labelled.

1.2.2: Selection Rules for Electronic Transitions

The *Beer-Lambert Law* (**Equation 1.2**) quantifies the excitation process of a sample in solution. Absorbance (A) is dependent on the *molar extinction coefficient* (ε) – an intrinsic property of the sample that is indicative of absorption intensity at a particular wavelength of light.

$$A = \varepsilon \, c \, L$$

Equation 1.2

The magnitude of ε reflects how likely absorption is to take place. In general, the probability of electronic transitions is governed by spectroscopic *selection rules*,[10] which include the:

- *Laporte selection rule* (Δl = ± 1), where transitions between atomic orbitals with the same angular momentum quantum numbers (*l*) such as d→d are formally *forbidden* in molecules containing an inversion centre. Additionally, a change in parity must be recognised.
- *Spin selection rule* (ΔS = 0), where changes in spin orientation (spin quantum number, *S*) between states such as $T_1 \rightarrow S_1$ is formally *forbidden*.

The latter rule is responsible for the disparities in timescales between fluorescence and phosphorescence, in consequence of the "spin-allowed" and "spin-forbidden" nature of these transitions, respectively. Relaxation of these rules increases the probability of a forbidden process occurring and will be discussed in a later section.

1.2.3: Lifetimes

The *luminescence lifetime* (τ) is defined as the average time a luminescent species remains in its excited state before subsequent relaxation back to the ground state.[1,5] This intrinsic property can be related to the probability of radiative or non-radiative decay pathways in the form of their first-order rate constants (k_r and k_{nr} respectively), where the radiative lifetime is the reciprocal of the sum of rate constants (**Equation 1.3**).

$$\tau = \frac{1}{(k_r + k_{nr})}$$

Equation 1.3

Rate constants are calculated for particular deactivation pathways and directly impact the magnitude of the observed lifetime. Fluorescence generally lies within the range of nanoseconds whilst phosphorescence can extend into the realm of microseconds to seconds, due to the *spin-forbidden* nature of this pathway.[11] Although long-lived species are regularly sought after, excited state lifetimes also determine the time in which a species can interact with its local environment whilst in its excited state. This makes a species more prone to particular deactivation mechanisms, which will be discussed in a later section.

1.2.4: Quantum Yields

The *photoluminescence quantum yield* (Φ_{PL}) is described as the ratio of the number of photons emitted to the number of photons absorbed.[12,13] This parameter relates to the efficiency of deactivation of the excited state *via* radiative decay pathways relative to the non-radiative pathways, and values approaching unity can arise when k_r dominates over k_{nr}. Therefore, it can be described with reference to the rates of relaxation processes according to **Equation 1.4**.[1]

$$\Phi_{PL} = \frac{k_r}{(k_r + k_{nr})}$$

<div align="right">*Equation 1.4*</div>

This value can be experimentally determined by a *relative method* wherein a standard with a known quantum yield (Φ_R) is used as a reference to determine the corresponding value of a sample (Φ_S) (**Equation 1.5**). Integrated emission spectra (F_S and F_R) and relative absorbances at a fixed excitation wavelength (A_s and A_R) should be measured under the same conditions.[14] A correction factor for the refractive indices of the solvents (η) must also be included if the species are in different solutions.

$$\Phi_S = \Phi_R \left(\frac{F_S}{F_R}\right)\left(\frac{A_R}{A_S}\right)\left(\frac{\eta^2_S}{\eta^2_R}\right)$$

<div align="right">*Equation 1.5*</div>

Once the experimental values for Φ and τ have been determined, k_r can be calculated (**Equation 1.6**). From this, it is possible to calculate k_{nr} using **Equation 1.4**.

$$k_r = \frac{\Phi}{\tau}$$

<div align="right">*Equation 1.6*</div>

1.2.5: Stokes Shifts

The energy of emitted photons is generally lower than that of absorbed photons, so longer emission wavelengths are seen relative to the corresponding absorption peak. This phenomenon is referred to as the *Stokes shift*, which is

quantified by measuring the difference between the peak maxima for the absorption and emission profiles and is illustrated in **Figure 1.4**.[15] This is a consequence of energy loss *via* non-radiative decay pathways such as vibrational relaxation, ISC and IC and is substantiated by *Kasha's rule* which states that emission occurs predominantly from the lowest-lying excited electronic state of a particular multiplicity (S_1 for fluorophores).[16] Therefore, the emission wavelength is independent of the excitation wavelength used.
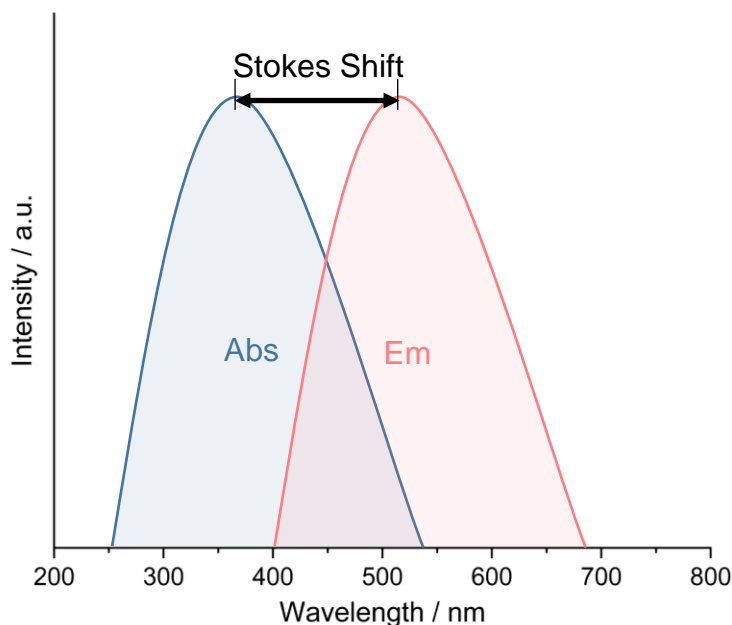
Figure 1.4: *Illustration of the Stokes shift observed between absorption (blue) and emission (red) spectra.*

Electrons usually occupy a higher vibrational level within the ground state upon deactivation. Since the spacing between vibrational levels is comparable within the ground and excited states (a consequence of the Franck-Condon principle), the emission profile appears to be a 'mirror image' of the corresponding absorption spectrum. Here, any vibronic features present in the absorption bands are reflected in the corresponding emission profile – this effect is often referred to as the *mirror image rule*.[1] In accordance with *Kasha's rule*, the emission spectrum is only a mirror image of the $S_0 \rightarrow S_1$ transition since deactivation occurs exclusively from the S_1 level. Species that deviate from the mirror image rule generally undergo a transformation upon excitation. One example is pyrene – a highly planar compound that forms an excited state dimer (termed *excimer*) at high concentrations in solution, initiating a change in the electronic properties relative to that of the ground state.[17]

1.2.6: Quenching Pathways

Quenching is the name given to any process which results in the diminution of emission intensity. The most common types are *static* and *dynamic* quenching.[12]

Dynamic quenching occurs after excitation whilst an emissive species is in its excited state, where subsequent interaction with a quencher (Q) causes energy to be dissipated by means of transfer to the quencher. This has a direct impact on the luminescence lifetime of the compound and can be rationalised through the original *Stern-Volmer relationship* (**Equation 1.7**). This relationship describes the kinetics of the deactivation process for single exponential decay of the luminescent species, where τ_0/Φ_0 and τ/Φ are the luminescence lifetimes and quantum yields in the absence and presence of quencher, respectively. The rate constant k_q corresponds to that of the quenching process.[18]

$$\frac{\Phi_0}{\Phi} = \frac{\tau_0}{\tau} = 1 + k_q \tau_0 [Q]$$

Equation 1.7

One example of a dynamic quencher is molecular oxygen, which deactivates the triplet excited state of a luminescent species by excitation of triplet ground state oxygen to form highly reactive singlet oxygen ($^3O_2 \rightarrow {}^1O_2$). The long-lived nature of triplet excited states makes them prone to dynamic quenching mechanisms.[19] Although seemingly unfavourable, $^1O_2$ generation has applications in areas such as photodynamic therapy.[20,21] This form of quenching leads to diminished lifetimes and is dependent on the quencher concentration, [Q], whilst absorption (*i.e.* ground state) properties are unaffected.

Static quenching occurs when the luminescent species forms a non-emissive complex with a quencher whilst in its ground state. This can be rationalised through the classical model of the *Stern-Volmer relationship* (**Equation 1.8**), which is independent of the lifetime. The ratio of emission intensity in the absence of quencher (I_0) to that of in the presence of quencher (I) increases linearly with respect to [Q]. K_a represents the association constant for the initial complexation.[22]

$$\frac{I_0}{I} = 1 + K_a[Q]$$

Equation 1.8

1.2.7: Spectroscopic Measurements and Instrumentation

Steady-state emission data can be recorded using a fixed excitation wavelength (λ_{ex}), which can be derived from the corresponding absorption spectrum. Light at this wavelength is applied continuously to the sample. By scanning through emission wavelengths within a suitable range, emission intensity is measured as a function of emission wavelength (λ_{em}) to generate a luminescence spectrum. An excitation spectrum is essentially the reverse of this, where a fixed λ_{em} is used whilst scanning across a range of λ_{ex} and the resultant profile relates to the probability of excitation at different wavelengths of incident light.[23] Therefore, it is expected to closely resemble the absorption spectrum.

These measurements are recorded using a *spectrofluorometer*, where monochromators are used to separate light into its constituent wavelengths by an internal diffraction grating. This diffracted light is then filtered to match the desired wavelengths (λ_{ex} and λ_{em}) by use of optical filters, preventing any unwanted wavelengths of light entering the excitation or emission beams. The intrinsic property of a Stokes shift is beneficial since the emission scan range can be selected at longer wavelengths than that of the excitation, prohibiting its detection in the emission profile. A simplified schematic is shown in **Figure 1.5**,[24] where a suitable light source (typically a xenon arc) is used to generate the excitation light. Finally, emitted photons are detected by a photomultiplier tube (PMT), allowing the data to be processed. Increasing the slit width of the monochromators generally results in greater sensitivity at the expense of a poorer resolution and selectivity.
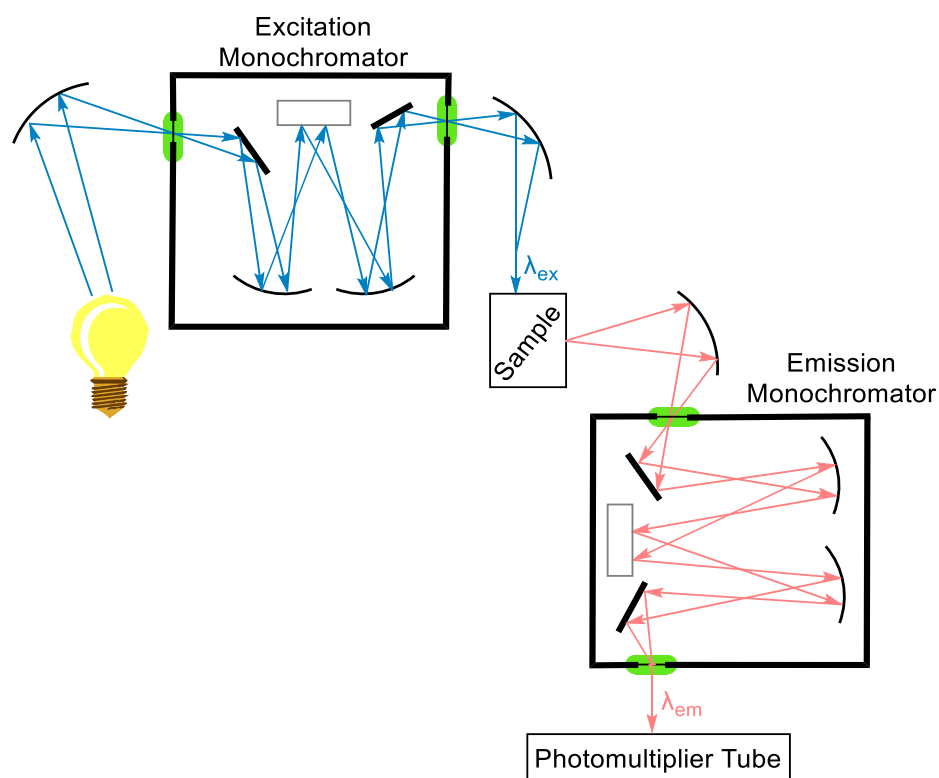
Figure 1.5: *Illustration of the spectrofluorometer for the collection of steady-state emission spectra.*[24] *Mirrors are represented by curved lines, diffraction gratings by grey squares and slits are highlighted in green.*

Time-resolved measurements are also recorded with a spectrofluorometer to generate an exponential decay profile, where the decay in fluorescence intensity is measured as a function of time (*I(t)*). This is described by **Equation 1.9** for a single exponential decay, where I_0 is the intensity directly after excitation (*i.e.* when t = 0).[5]

$$I(t) = I_0 e^{-\left(\frac{t}{\tau}\right)}$$

Equation 1.9

The most common method of time-resolved measurements is *time-correlated single photon counting* (TCSPC), where a pulsed laser light source is used. A strong excitation source is not usually required and the most important factors are pulse width and repetition rate, where the former must generally be shorter than the decay time of the sample and determines the resolution, whilst the latter impacts the speed at which data can be collected.[24]

1.3: Luminescent Species

1.3.1: Organic Fluorophores

A *luminophore* is a species or a component that exhibits luminescence upon excitation.[25] Organic luminophores tend to emit light from a singlet excited state and are therefore assigned as *fluorophores*. Here, absorption tends to be dominated by $\pi \rightarrow \pi^*$ transitions and the energy required is dependent upon the amount of double bonds conjugated together.[26] In general, extending the π-conjugated system results in a reduced HOMO-LUMO energy gap,[27] where low-energy light can be used to initiate excitation whilst enhancing absorption at longer wavelengths.[28] Therefore, many organic fluorophores are predicated on polyaromatic hydrocarbons (PAHs) such as those presented in **Figure 1.6**,[29] where the effect of added conjugation on emission properties is exemplified.

	Naphthalene	Anthracene	Phenanthrene	Pyrene	Perylene
λ_{em} / nm	327	400	368	376	467
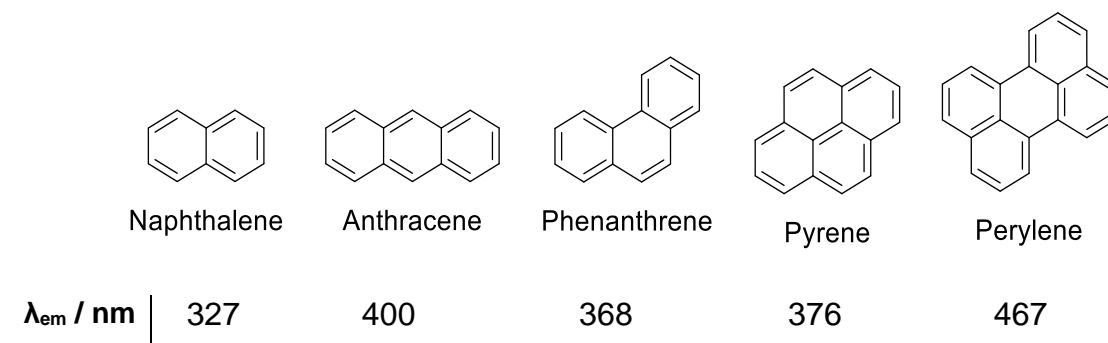
Figure 1.6: Examples of some PAHs, where fluorescence (in MeOH) is dominated by their highly delocalised π-systems.[29]

Although PAHs have excellent charge-transporting capabilities, aggregation-induced quenching can weaken their luminescence due to their planarity. Therefore, these molecules are often used as a delocalised framework between *electron-donating* and *electron-withdrawing* substituents (EDG and EWG respectively), which enhance electronic properties by permitting mechanisms such as *intramolecular charge transfer* (ICT).[30] If non-bonding electrons are available, symmetry-forbidden $n \rightarrow \pi^*$ transitions can occur to generate a peak of reduced intensity in alignment with the selection rules. The transitions mentioned are by far the most studied in the field of organic photochemistry.
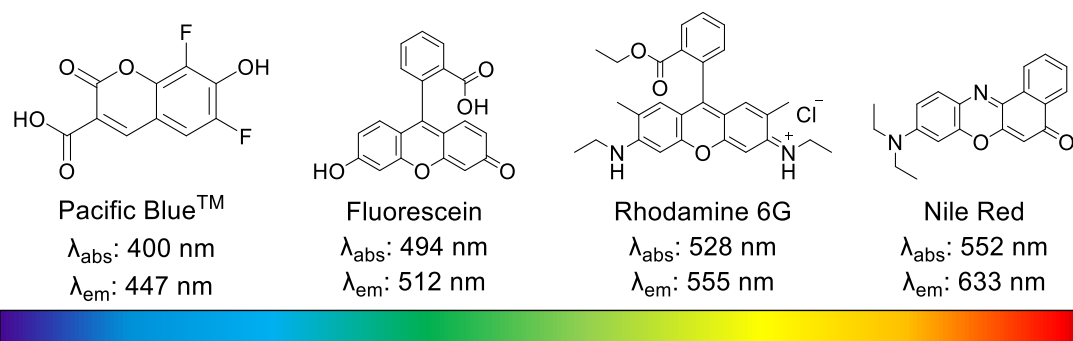
Figure 1.7: *Examples of common fluorescent dyes and their corresponding λ$_{abs}$ and λ$_{em}$. From left to right: Pacific Blue^{TM},[31] Fluoroscein,[32] Rhodamine 6G[33] in dilute aqueous solutions, and Nile Red[34] in DMSO.*

Examples of some common synthetic dyes are shown in **Figure 1.7**, where λ$_{abs}$ and λ$_{em}$ can be specifically tailored across the entire visible range by modulation of the HOMO-LUMO energy gap.[31–34] In general, most organic fluorophores have small Stokes shifts and narrow absorption and emission bands, making them susceptible to self-quenching.[1] However, the photostability of these common fluorophores have been vastly improved by synthetic modification, making them more viable in biological imaging applications by improved signal-to-noise ratios.[35] D-π-A organic dyes adopt many of the concepts previously discussed, where an electron-donor and electron-acceptor are conjoined by a delocalised π-system. These have applications in the development of optoelectronic materials such as dye-sensitised solar cells (DSSCs)[36] and organic light emitting diodes (OLEDs).[37] Examples of modified dyes are presented in **Figure 1.8**, where pronounced photophysical properties such as extended Stokes shifts have enabled their use in specific applications.

DQF-570
λ_{abs}: 570 nm
λ_{em}: 646 nm
Φ_F: 0.31
Stokes shift: 76 nm

a

DSSC Dye 2
λ_{abs}: 459 nm
λ_{em}: 663 nm

b

OLED Dyad 1
λ_{abs}: 390 nm
λ_{em}: 502 nm
Φ_F: 0.18
Stokes shift: 112 nm

c

Stokes shift: 204 nm
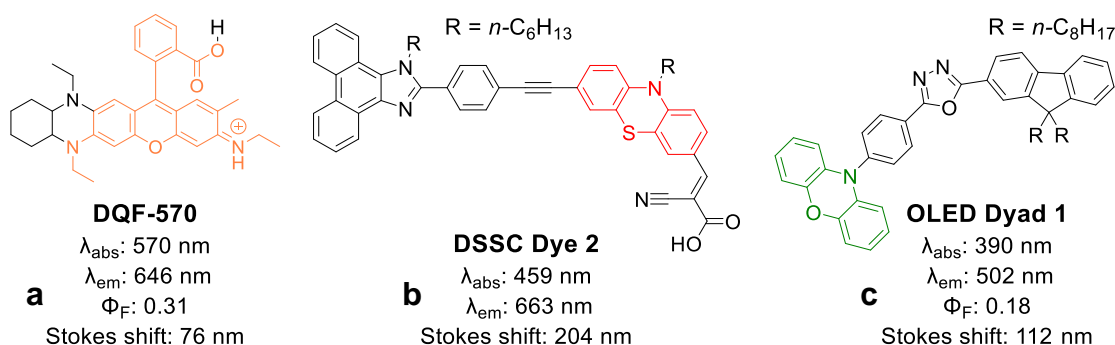
Figure 1.8: *Some functionalised organic dyes for various applications; **a** (EtOH, based on Rhodamine 6G)[35] for biological imaging, **b** (THF, based on phenothiazine)[36] for DSSC development and **c** (toluene, based on phenoxazine)[37] for OLED development.*

1.3.2: Photoactive Transition Metal Complexes

Phosphorescence is seldom observed under ambient conditions for organic compounds, since the radiative rate constant associated with $T_1 \rightarrow S_0$ is often too low to compete with the non-radiative pathways once in the triplet manifold.[38] This is due to the spin-forbidden nature of the transition, but relaxation of the spectroscopic selection rules can enable formally forbidden pathways. One such example involves *spin-orbit coupling* (SOC), a perturbation interaction that promotes efficient mixing of singlet and triplet states through rapid ISC.[39] SOC constants (ζ) can be calculated for atoms, quantifying the magnitude in which they experience this effect and is proportional to the effective nuclear charge to the order of four (Z^4).[40] Therefore, this effect becomes significant in the presence of a heavy atom and is commonly referred to as the *heavy atom effect*, allowing the emission properties of luminescent late-transition metal complexes to be dominated by phosphorescence.

Complexes based on the platinum group metals (Ru, Rh, Pd, Os, Ir and Pt) have been explored as phosphorescent species for decades. A molecular orbital (MO) diagram is shown in **Figure 1.9**,[41] where an Ir^{3+} octahedral complex with a $5d^6$ electronic configuration is used as an example and is the main type of system explored within this thesis. A variety of electronic transitions can occur between these states, where the nature of the HOMO and LUMO are critical for the resultant photophysical properties of the complex.
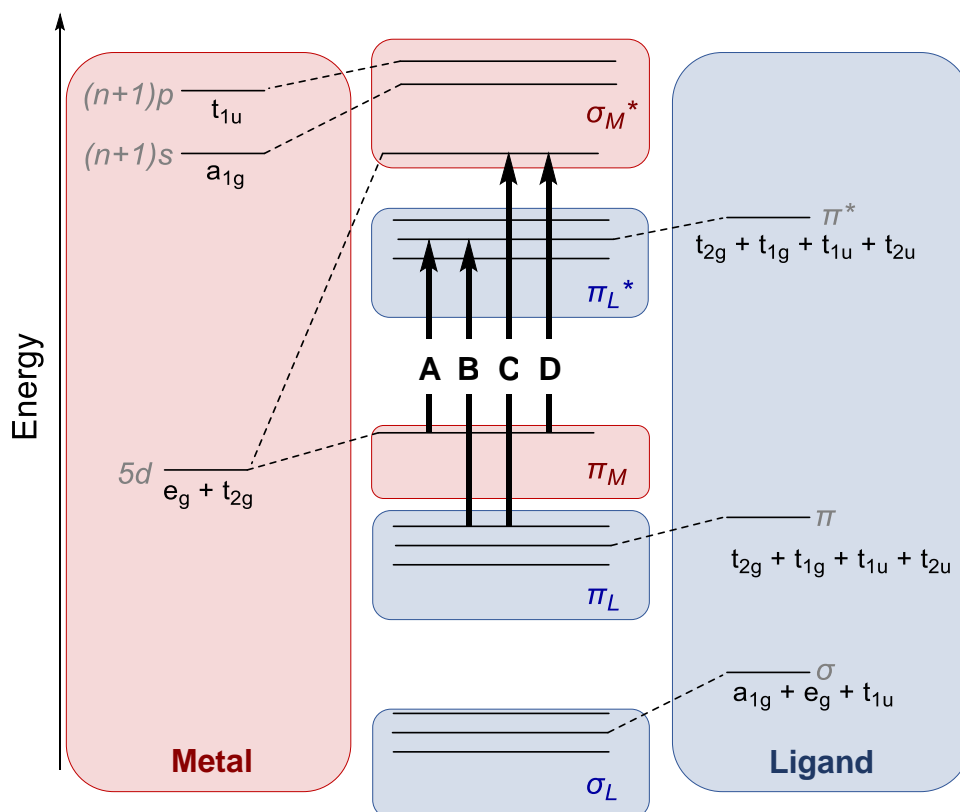
Figure 1.9: *MO diagram for an octahedral third-row transition metal complex with a $5d^6$ electron configuration (Ir^{3+}), displaying the various possible transitions associated with the observed luminescence; (**A**): MLCT; (**B**): ILCT or LLCT, depending on if the transfer occurs within one or between two ligand(s); (**C**): LMCT; (**D**): MC ($d_\pi \rightarrow d_\sigma*$).*[41]

5d atomic orbitals lose their degeneracy upon complexation, splitting into two MOs localised over the metal centre. Transitions from a low-lying d_π level (HOMO) to an unoccupied, ligand-centred $\pi*$ orbital (LUMO) is known as a *metal-to-ligand charge transfer* (MLCT) (**A**) and is usually the targeted emission pathway for these species. There are two main types of ligand-centred (LC) processes; $\pi \rightarrow \pi*$ transitions within the same ligand are referred to as *intra-ligand charge transfer* (ILCT), whereas transfer to a different ligand is known as *ligand-to-ligand charge transfer* (LLCT) (**B**). If the HOMO is a π orbital on the ligand and the LUMO is a low-lying $\sigma*$ orbital at the metal centre, a *ligand-to-metal charge transfer* (LMCT) arises (**C**). Finally, movement of electrons between the d-orbitals localised at the metal gives rise to *metal-centred* (MC or d-d) transitions (**D**).

Phosphorescence can occur through radiative relaxation from ^{3}MLCT or ^{3}LC excited states. These are generated *via* deactivation of their respective singlet

excited states though rapid ISC, mediated by efficient SOC through the heavy metal atom. Phosphorescence quantum yields (Φ_P) in octahedral complexes can be maximised by reducing the impact of radiationless pathways such as deactivation from a ^{3}MC excited state. Stabilisation of this state can result in competition with the emissive ^{3}MLCT level, diminishing phosphorescence.[42] One strategy to prevent this is to use a strong-field σ-donor cyclometallating ligand, which destabilises the ^{3}MC state by enhanced ligand-field splitting energy (LFSE) whilst promoting MLCT/LC excited state mixing.[43,44] Another approach involves using strong-field π-accepting ligands with extended conjugation to stabilise the π* orbital so that electron transfer becomes more feasible *via* MLCT, thus enhancing metal-ligand interaction whilst making the MC state less accessible.[45] These are illustrated in **Figure 1.10**.
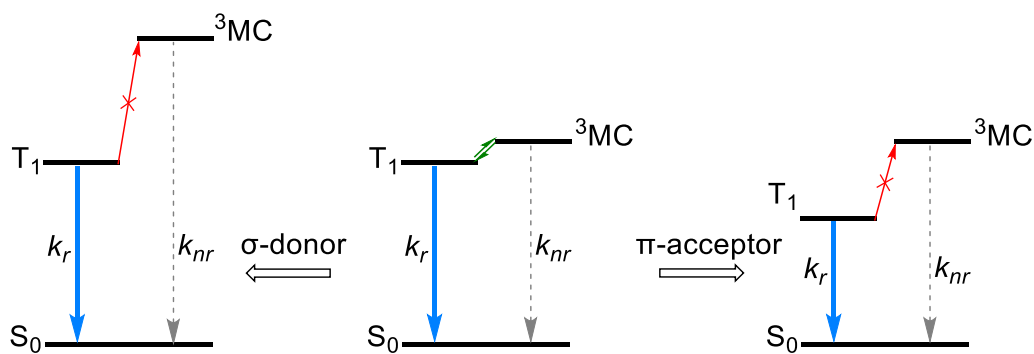
Figure 1.10: *Energy level diagram showing that the nature of the ligand can disrupt the thermal equilibrium between the triplet emissive (T_1) and deactivating ^{3}MC state.*[44]

Modifying the relative energies of the HOMO and LUMO offers scope for significant colour tunability, where the energy difference between them is responsible for the λ_{em}. However, maintaining desirable photophysical properties whilst targeting a specific optical range remains as a challenge. Efficient, deep-blue phosphorescence is desirable for the development of lighting solutions and OLEDs. Achieving this type of emission is difficult due to the requirement of a large HOMO-LUMO energy gap, where significant destabilisation of the T_1 emissive state can result in thermal population of the ^{3}MC state.[46] In contrast, the efficiency of deep-red phosphorescence suffers from the consequences of the *energy gap law*, which states that an inverse relationship exists between the energy of emission and k_{nr}.[47] Φ_P and τ are

diminished in both instances, but synthetic alterations and judicious ligand design can lead to significant enhancements of these properties.[48,49]

1.3.3: Luminescent d[6] Transition Metal Complexes

The emission properties of **[Ru(bpy)₃]²⁺** were first reported in 1959 alongside recognition of its chemical and thermal stability.[50] This was one of the earliest reports on systems displaying MLCT emission and is still widely used as a standard for quantum yield determination in the form of **[Ru(bpy)₃](PF₆)₂**.[51] Later investigated as a photosensitiser,[52] this complex generated a surge in the development of Ru(II) complexes with polypyridyl ligands (**Figure 1.11**),[53,54] which remain as a subject of exploration in the field of ¹O₂ generation for photodynamic therapy (PDT) applications.[55,56]

[Ru(bpy)₃](PF₆)₂

λ_{abs}: 450 nm

λ_{em}: 621 nm

τ: 153 (850) ns

Φ: 0.018

[Ru(dip)₃](PF₆)₂

λ_{abs}: 464 nm

λ_{em}: 613 nm

τ: (6.3) μs

Φ: 0.20

[Ru(phen)₂(dppz-7,8(OMe)₂)](PF₆)₂

λ_{abs}: 420 nm

λ_{em}: 620 nm

τ: 325 (645) nm

Φ: 2.8 × 10⁻³
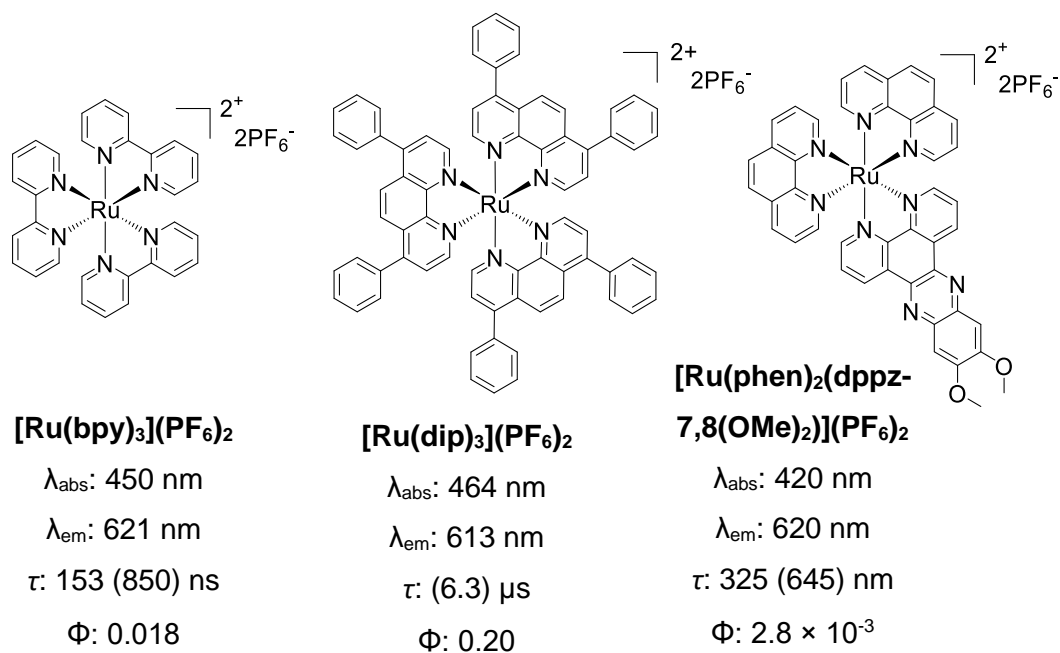
Figure 1.11: Ru(II) species and their photophysical properties in MeCN.[51,53,54,56]
Values in parentheses are in degassed solvent; λ_{abs} is the signal at λ_{max}.

Isoelectronic Os(II) complexes can be considered as a third-row equivalent to Ru(II) species, with enhanced SOC from the heavier osmium atom.[57,58] These generally have destabilised ³MC excited states relative to their Ru(II) equivalents, rendering them less accessible by thermal activation. This was clearly depicted in a study by Beley *et al.* where **[Ru(tpy)₂]²⁺** showed no observable emission at room temperature, whilst **[Os(tpy)₂]²⁺** displayed a

relatively long-lived, deep-red emission. Upon arylation of the **tpy** ligand to form **tptpy**, the energy of the MLCT state was lowered and the Ru(II) complex presented very weak, short-lived emission (**Figure 1.12**).[58]

[Os(tpy)₂](PF₆)₂

λ_{abs}: 477, 657 nm

λ_{em}: 718 nm

Φ: 0.014

τ: 269 ns

[Ru(tpy)₂](PF₆)₂

λ_{abs}: 476 nm

NO EMISSION

[Os(tptpy)₂](PF₆)₂

λ_{abs}: 502, 692 nm

λ_{em}: 751 nm

Φ: 0.028

τ: 266 ns

[Ru(tptpy)₂](PF₆)₂

λ_{abs}: 501 nm

λ_{em}: 650 nm

Φ: 7.4 × 10⁻⁴

τ: 3.8 ns
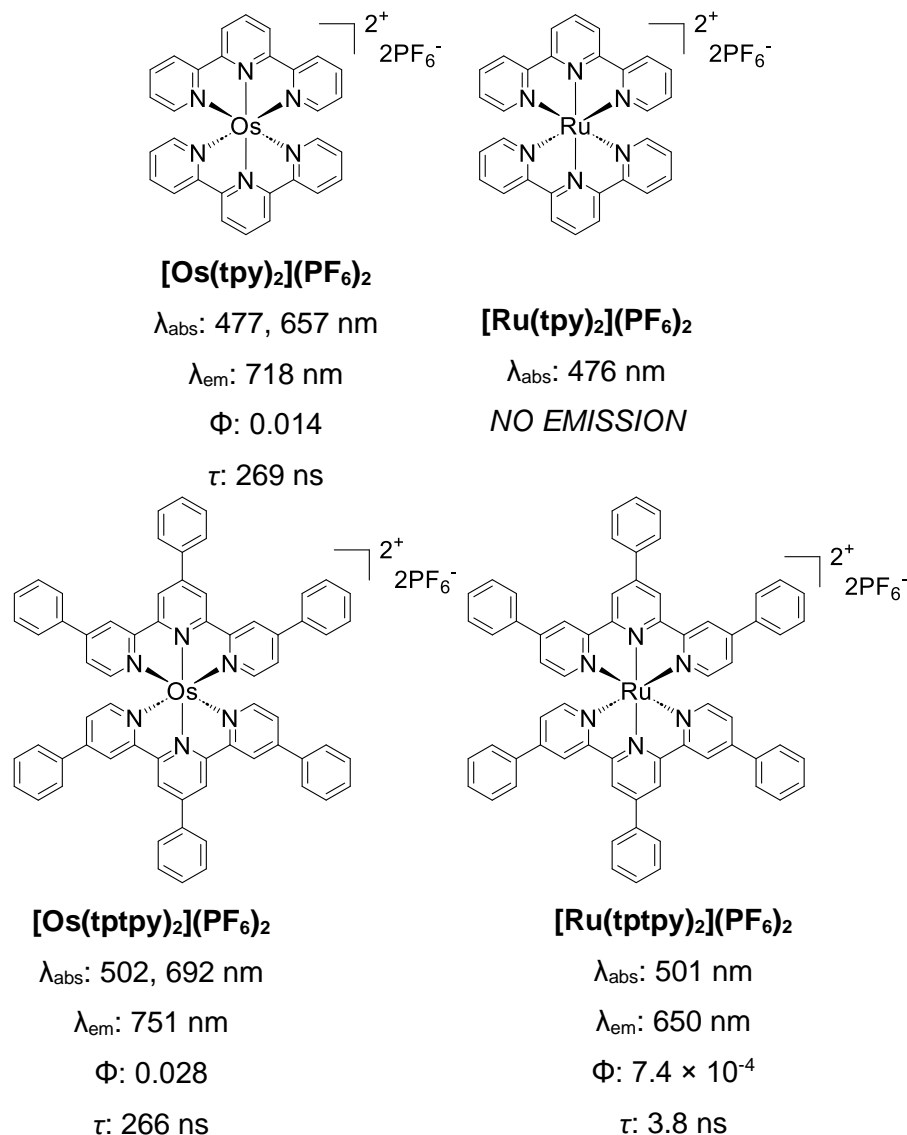
Figure 1.12: Comparison of the excited state properties of [Os(tpy)₂](PF₆)₂ and [Os(tptpy)₂](PF₆)₂ and their equivalent Ru^{II} variants, measured in MeCN, tpy = 2,2';6',2''-terpyridine, tptpy = 4,4',4''-triphenyl-2,2':6',2''-terpyridine.[57]

Re(I) complexes are also capable of possessing strong MLCT character and are most commonly explored as tricarbonyl species with the general formula **[Re(CO)₃(N^N)X]**, where X is a monodentate ancillary ligand. The N^N ligand is often utilised as the point of modification for photophysical behaviour, whilst X is frequently used to impart chemical alterations for specific applications. One recent study by Gazda *et al.* suggested that incorporating electron-donating

carbazole (**cbz**) or pyrrolidine (**pyrr**) moieties into a methylated phenanthroline N^N ligand significantly altered the HOMO and LUMO energy levels and subsequent ground and excited state properties (**Figure 1.13**). The LUMO energy decreased drastically upon attachment of **cbz**, whereas an increase was seen when **pyrr** was incorporated. The emissive state was deemed to be [3]IL for the **pyrr**-substiuted species, whereas the emissive character of the **cbz**-containing complex was more representative of the model complex by displaying predominantly [3]MLCT character. [59]
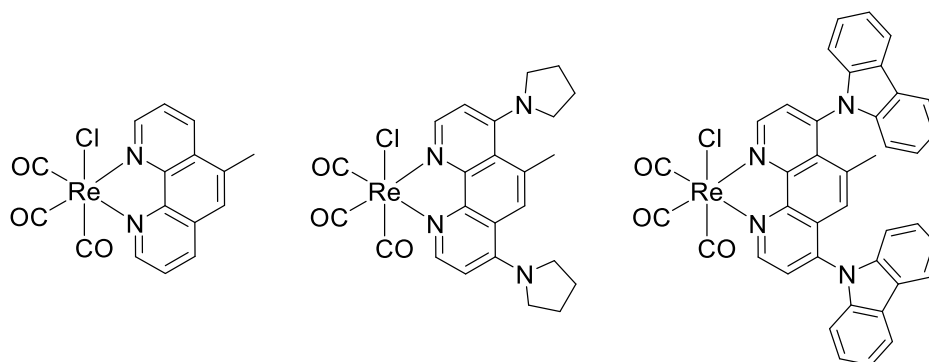
| **[ReCl(CO)₃(CH₃phen)]** | **[ReCl(CO)₃(pyrr₂- CH₃phen)]** | **[ReCl(CO)₃(cbz₂-** |

λ_{abs}: 401 nm λ_{abs}: 408 nm   **CH₃phen)]**

λ_{em}: 611 nm λ_{em}: 565 nm λ_{abs}: 423 nm

Φ: 0.42 Φ: 0.56 λ_{em}: 651 nm

τ: 214 ns τ: 235 ns Φ: 0.36

τ: 102 ns

Figure 1.13: *Phosphorescent Re(I) complexes studied by Gazda et al. in CHCl₃.*[59]

The large SOC constant of iridium (ζ = 3909 cm^{-1})[60] has resulted in the exploration of Ir(III) complexes being favoured over other d[6] platinum-group metals such as Os(II) (ζ = 3381 cm^{-1})[61] and Ru(II) (ζ = 1042 cm^{-1}).[60] Additionally, the Ir(III) centre possesses a smaller atomic radius, thereby enhancing stability in conjunction with MLCT character *via* strong metal-ligand interactions.[61] Rh(III) analogues have been investigated, but the luminescent properties are generally inferior due to; (i) reduced SOC and k_r associated with phosphorescence, (ii) destabilised MLCT states, resulting in exclusively [3]LC-type emission, and (iii) weaker LFSE experienced by the second-row transition metals, granting accessibility of the MC state.[62] Recent studies have employed quinoxaline ligands as strong σ-donors in a Rh(III) species, destabilising the [3]MC state to

promote emission from a low-lying ^{3}LC level.[63] However, the analogous Ir(III) species offers significant enhancement of Φ values (**Figure.1.14**).[64]

[Rh(dpqx)$_2$(acac)]

λ_{abs}: 455 nm

λ_{em}: 612 nm

Φ: 0.11

[Ir(dpqx)$_2$(acac)]

λ_{abs}: 480 nm

λ_{em}: 670 nm

Φ: 0.50
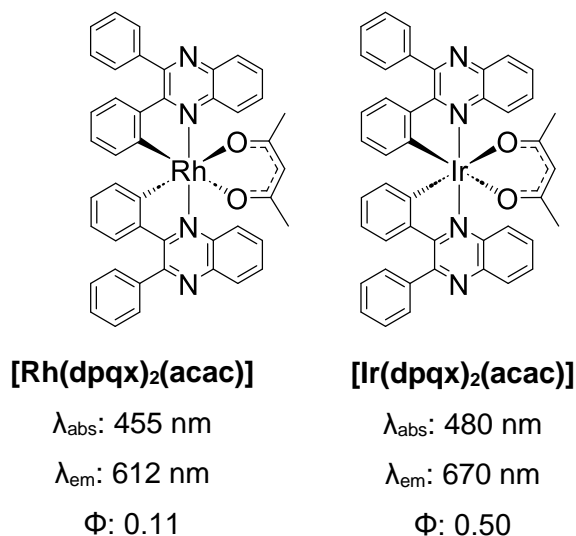
Figure.1.14: Photophysical properties of analogous Rh(III)[61] and Ir(III)[62] species in degassed DCM; dpqx = 2,3-diphenylquinoxaline.

Therefore, Ir(III) complexes with strong σ-donating ligands are most widely studied for optoelectronic applications, where the ^{3}MC state is usually far more destabilised than the emissive T$_1$ state to generate highly efficient phosphorescence.[44] This is often demonstrated by high triplet quantum yields relative to other d^6 analogues, due to the efficient mixing of singlet and triplet states.[65] Other advantages include vast colour tunability spanning the entirety of the visible range, enhanced chemical stability and more synthetic control over the excited state properties *via* the ligands.[66]

1.3.4: Other Luminescent Transition Metal Complexes

First-row transition metal complexes have been explored due to their low cost and high abundances (**Figure 1.15**). In 2006, a series of highly luminescent Cu(I) complexes with a d^{10} electronic configuration were reported, displaying intense green emission with an efficiency comparable to Ru(II) systems.[67] The lack of reported earth-abundant metal complexes with reduced electron counts (d < 10) is due to lowered LFSE and subsequent deactivation by low-lying ^{3}MC states. However, Heinze *et al.* reported a six-coordinate Cr(III) (3d^3) species, **[Cr(ddpd)$_2$](PF$_6$)$_3$**, exhibiting long-lived NIR phosphorescence at room temperature, with the highest quantum yield value (12.1%) to date for a Cr(III)

complex.[68] This was achieved by increasing LFSE through employing a ligand with a large bite angle and strong σ-donor ability. A ground-breaking study in 2017 also suggested that **[Fe(btz)₃](PF₆)₃** could offer potential for future iron-based photoluminescent materials, where emission occurred from an LMCT state.[69]

[Cu(dpep)(POP)](BF₄)[a]	**[Cr(ddpd)₂](PF₆)₃**[b]	**[Fe(btz)₃](PF₆)₃**[b]
λ_{abs}: 400 nm	λ_{abs}: 435 nm	λ_{abs}: 528, 558 nm
λ_{em}: 544 nm	λ_{em}: 775 nm*	λ_{em}: 600 nm
Φ: 6 × 10⁻³ (0.26)	Φ: (0.12)	Φ: 3 × 10⁻⁴
τ: 0.3 (17.6) μs	τ: (899) μs	τ: ~100 ps
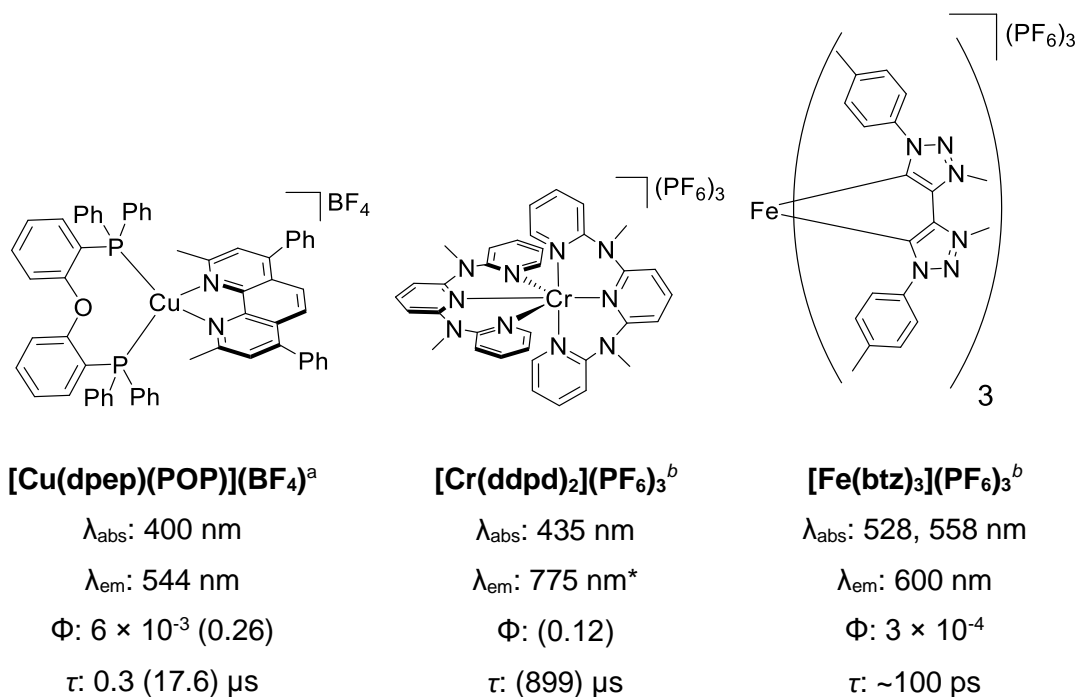
Figure 1.15: Examples of some photoactive first-row transition metal complexes and their corresponding photophysical properties; ᵃin DCM; ᵇin MeCN. Values in parentheses are in degassed solutions.[67–69] * maximum intensity peak. (dpep = 9-diphenethyl-1,10-phenanthroline, ddpd = N,N'-dimethyl-N,N'-dipyridine-2-ylpyridine-2,6-diamine, btz = 3,3'-dimethyl1,1'-bis(p-tolyl)-4,4'-bis(1,2,3-triazol-5-ylidene)).

Heavier d¹⁰ metal complexes based upon Ag(I) and Au(I) have also been studied. Luminescent properties of Ag(I) complexes are generally associated with either ³LC phosphorescence, LLCT or LMCT character. These are frequently explored for their aggregation properties, where the photophysics is reliant upon interactions between the Ag atoms through cluster-centred emission.[70] One example is displayed in **Figure 1.16**, where a series of Ag(I) complexes containing *nido*-carborane ligands were developed as luminophores that exhibit thermally activated delayed fluorescence (TADF), a promising quality for OLED progress.[71] The photophysical characteristics of the complexes were dependent on the nature of the phen-type ligand and resultant structural rigidity, where photoluminescent quantum yields (Φ_PL) approached

unity for **Ag(dbp)(P₂-nCB)** by maximising k_r. In comparison, removal of the alkyl chains to generate **Ag(phen)(P₂-nCB)** showed a dramatic decrease in Φ (36%).

Ag(dbp)(P₂-nCB)

λ_{abs}: 385 nm[a]

λ_{em}: 585 nm,[a] 526 nm[b]

Φ: 100%[b]

τ: 1.4 µs[b]

Au2Naph

λ_{abs}: 370 nm[c]

λ_{em}: 482 nm[d]

Φ: 0.11[d]

τ: 120 µs[d]
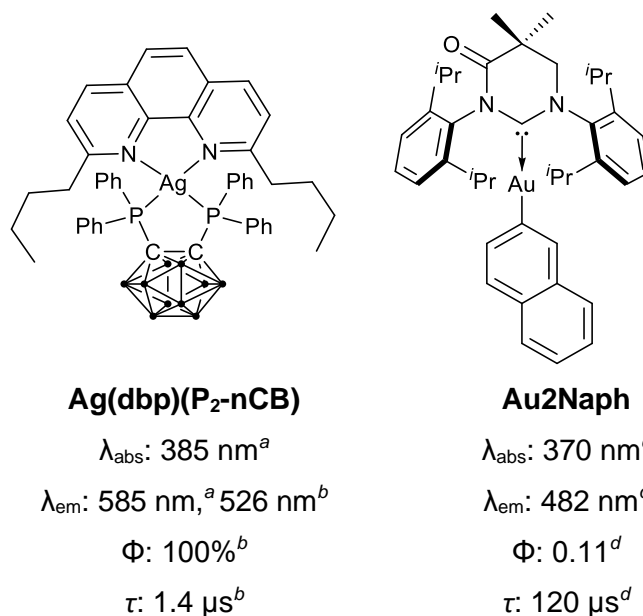
Figure 1.16: *Recent examples of Ag(I)[71] and Au(I)[72] luminophores; [a]in DCM; [b]as a powder; [c]in cyclohexane; [d]in N₂-saturated MeTHF. P₂-nCB = bis(diphenylphosphine)-nido-carborane, dbp = 2,9-di-n-butyl-1,10-phenanthroline.*

A series of two-coordinate Au(I) complexes bearing one *N*-heterocyclic carbene ligand and one aryl ligand were also synthesised, with phosphorescence being observed predominantly from the aryl-based triplet state (^{3}LC) and emission properties were dependent on the nature of the aryl ligand. **Au2Naph** (**Figure 1.16**) achieved Φ_{PL} of 0.84 in polymer film samples, making it a promising candidate for the development of photonic materials.[72]

Further examples of alternative transition metal-based complexes are presented in **Figure 1.17**. Air-stable, luminescent W(VI) complexes incorporating polydentate Schiff-type ligands were reported by Yeung *et al.* in 2016, where phosphorescence from a ^{3}IL state yielded promising results for applications in photocatalysis.[73] The absence of MC states along with the relative abundance and cost-effective nature of tungsten were suggested to be advantageous over the precious metals previously discussed.

Pd(II) and Pt(II) d^8 complexes with square planar coordination geometries offer distinctive features for solid-state phosphorescence through intermolecular interactions and will be explored in more detail for Pt(II) in **Chapter 3**. **Pd-B-1**

(**Figure 1.17**) was reported by Chow as a blue-green phosphorescent Pd(II) species, where red emission (λ_{em} = 599 nm) can be achieved upon fusing a phenyl ring into the pyridyl backbone. These were suggested to be promising potential OLED sensitisers, with high colour purity and external quantum efficiencies (EQE) up to 14.32%, accompanied by long operational lifetimes.[74]

In 2013, To *et al.* described the formation of Au(III) complexes displaying strong emissive properties at room temperature by incorporation of a fluorene component on the backbone of the phenyl rings in tridentate C^N^C ligands (**Figure 1.17**). These exhibited high Φ_{PL} of up to 58% with extended lifetimes exceeding 200 μs in solution, unprecedented for Au(III) species at the time. The emission properties were correlated with metal-perturbed ^{3}IL transitions.[75]

[WO$_2$(Ph-Salpn)]	**Pd-B-1**	**[Au(C^N^C)(PA)]**
λ_{abs} = 400 nm	λ_{abs} = 387 nm	λ_{abs} = 429 nm
λ_{em} = 600 nm	λ_{em} = 466, 495 nm	λ_{em} = 539, 579 nm
Φ = 0.028	Φ = 0.47	Φ = 0.55
τ = 96.9 μs	τ = 106 μs	τ = 233 μs
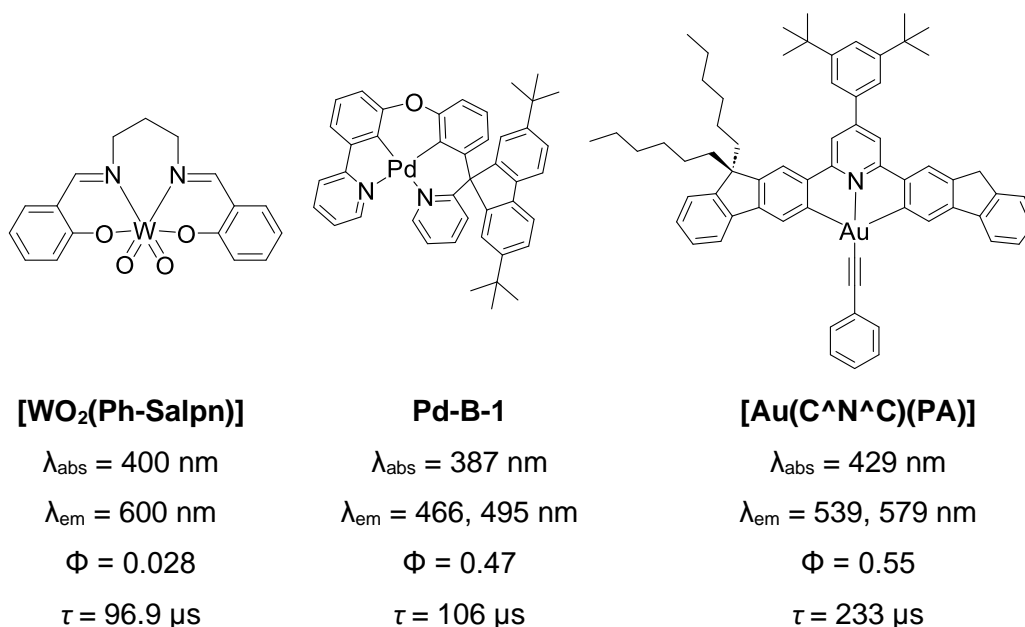
Figure 1.17: *Examples of luminescent W(VI),[73] Pd(II)[74] and Au(III)[75] complexes, along with their corresponding photophysical properties in degassed DCM solutions. PA = phenylacetylene.*

1.3.5: Applications of Transition Metal Phosphors

The unique photophysical properties of transition metal complexes render them useful for specific applications. The versatility of these applications is broad, so a few examples will be discussed in the following section, with more detail in subsequent chapters of this thesis.

1.3.5.1: OLED Development

Since the pioneering work of Tang and VanSlyke in 1987,[76] organic light emitting diodes (OLEDs) have been developed and manufactured as digital displays for electronic devices. The general structure of a multi-layered OLED system is shown in **Figure 1.18**.[77]

Cathode
Electron Transport
EMISSIVE LAYER
Hole Transport Layer
Hole Injection Layer
Anode
Glass Substrate
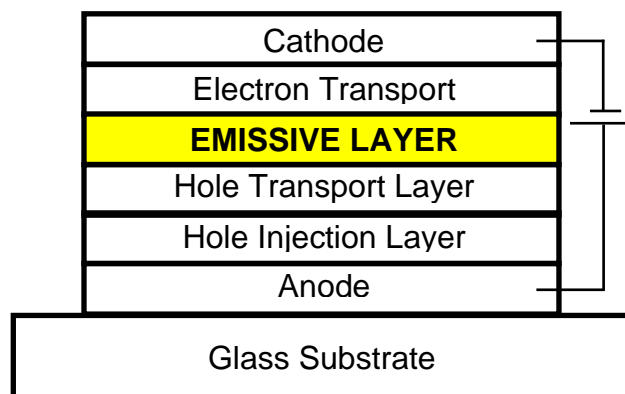
Figure 1.18: Simplified schematic of a multi-layer OLED system.[77]

Transition metal complexes have permitted the development of PhOLEDs, where the emissive layer (EML) comprises of organic molecules as hosts and efficient phosphors as guest materials.[78] These offer significant advantages such as high efficiency, pronounced resolution and energy-saving features that are particularly attractive for solid-state lighting solutions.[79] In 2001, Adachi *et al.* paved the way for future research on OLED production, where an internal electroluminescence efficiency approaching unity was measured using **Ir(ppy)$_2$(acac)** co-deposited with **TAZ** (3-phenyl-4-(1-naphthyl)-5-phenyl-1,2,4-triazole) in the EML.[80] As a result, cyclometallated Ir(III) complexes have since become one of the most widely studied dopants for the development of highly efficient OLED devices with full colour displays. Some examples of efficient blue,[81] green[82] and red[83] species, specifically designed for this purpose, are presented in **Figure 1.19**. Other metals have been explored as dopants in OLED development such as Re(I),[84] Pt(II)[85] and Os(II).[86]
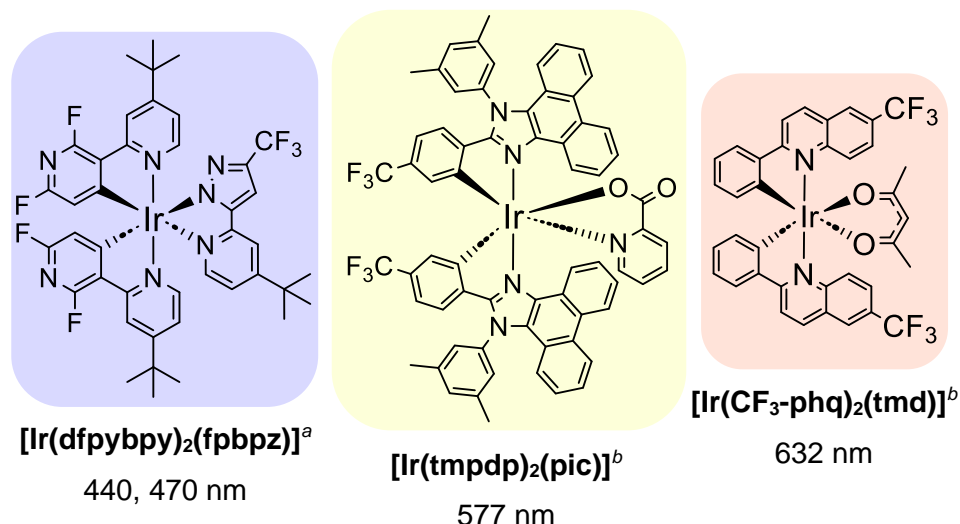
Figure 1.19: *Examples of efficient blue,[81] green[82] and red[83] bis-cyclometallated Ir(III) complexes that have been explored as dopants in OLEDs. λ_{em} values are indicated below each structure. [a]2-MeTHF; [b]DCM.*

White OLEDs (WOLEDs) have been of considerable interest over recent years as appealing energy efficient lighting solutions. White emission can be achieved by carefully combining two or more emissive species of complementary colours, either through separate emissive layers or by blending them into a single one.[87]

1.3.5.2: Biological Imaging Agents

Transition metal based luminophores offer unique properties that are desirable in fluorescence microscopy studies for cell imaging, overcoming limitations presented by organic fluorophores. These unique properties include high photostability, enhanced chemical stability, long luminescence lifetimes and large Stokes shifts (advantageous in eliminating signal from indigenous chromophores).[88] The Ir(III) complex in **Figure 1.20** presented a high affinity for DNA through intercalation, specifically staining the nuclei of cells whilst possessing low cytotoxicity.[89] The Re(I) complex shown specifically targeted mitochondria, where the selectivity was attributed to the resultant glutathione adduct (displayed in **Figure 1.20**) formed upon accumulation within mitochondrion. With observable emission at 551 nm, this was the first [3]MLCT-type biological probe of its kind.[90]
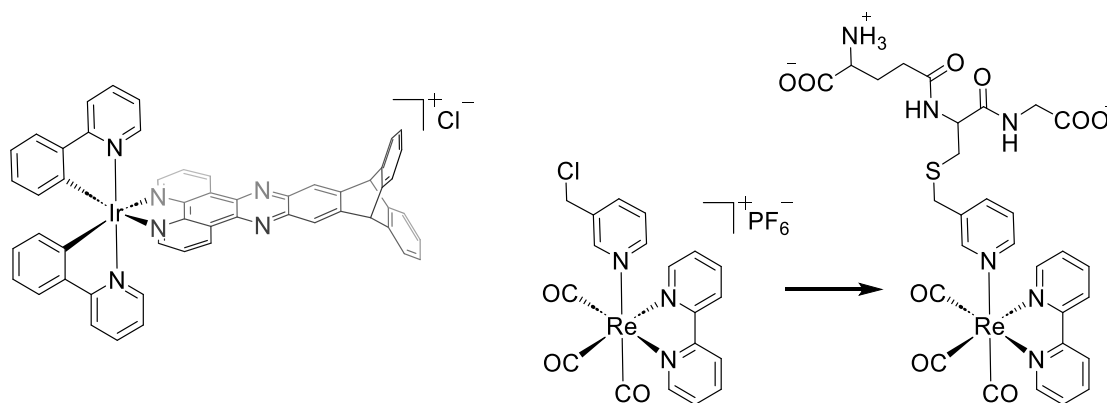
Figure 1.20: Ir(III)[89] and Re(I)[90] species for biological imaging applications.

1.3.5.3: Oxygen Photosensitisers

Dual-type probes can be used to initiate cytotoxicity whilst being photochemically active, behaving therapeutically as well as diagnostically. Transition metal complexes have been explored as photosensitisers for PDT applications, where generation of highly reactive $^1O_2$ through energy transfer processes can impart cytotoxicity to cancerous cells upon illumination. Two examples are shown in **Figure 1.21**, where the Ir(III) complex acted as a lysosome-specific imaging species as well as a photosensitiser in acidic media. Enhanced phototoxicity against cancer cells was achieved with high selectivity through lysosomal damage and subsequent cell apoptosis, whilst being able to be monitored due to its phosphorescent nature.[91] Similarly, a Ru(II) porphyrin-type compound (**RuP**) has been studied for bladder cancer treatment, where $^1O_2$ is generated most efficiently through blue light absorption.[92]
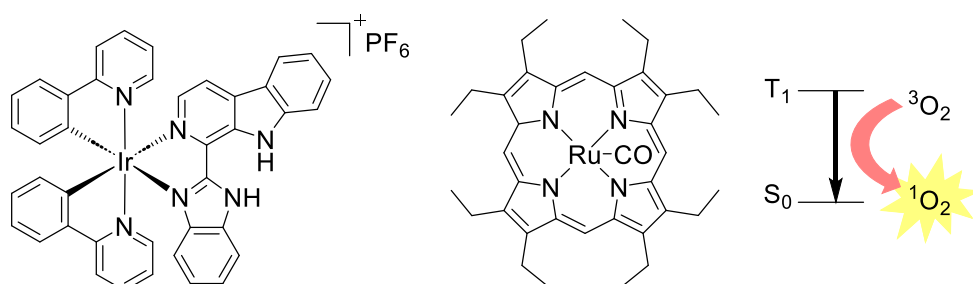
Figure 1.21: Ir(III)[91] and Ru(II)[92] species as photosensitisers for photodynamic therapy applications, where $^1O_2$ is generated by energy transfer from T_1.

1.4: Quinoxalines

The work presented in this thesis focuses on ligand systems derived from 2-phenylquinoxaline as alternatives to the commonly explored 2-phenylpyridine chromophores. Quinoxalines constitute of a heterocyclic pyrazine moiety fused with a benzene ring and are therefore classed as benzodiazines (**Figure 1.22**).
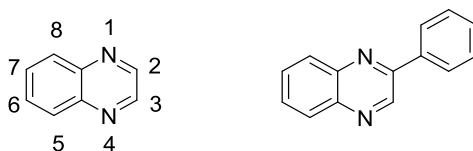
Figure 1.22: Structure of quinoxaline (left) and 2-phenylquinoxaline (right).

1.4.1: Applications

The chemical and biological properties of quinoxalines enable their exploration in medicinal chemistry as anticancer,[93] antibacterial[94] and antiviral agents,[95] where synthetic versatility permits the incorporation of a variety of substituents into the backbone. This also offers advantages in modifying electronic behaviour to generate compounds containing π-conjugated systems with a strong electron-withdrawing effect. Therefore, they have been explored in the development of D-π-A systems as organic sensitisers in solar cell development, where quinoxalines greatly improve the electron delocalisation and subsequent photovoltaic properties by acting as an electron-acceptor. [96,97]

Some examples of quinoxalines for optoelectronic applications are shown in **Figure 1.23**. Early work by Wang *et al.* explored the synthesis of [3,4-*b*]quinoxaline compounds exhibiting ICT character, where *N,N*-dialkylamino groups were used as EDGs. Fluorescence quantum yields (Φ_F) approached unity in DCM solutions at room temperature, offering potential as highly efficient green organic dopants for optoelectronic applications.[98] In 2017, Wang *et al.* reported deep-red to NIR quinoxaline-based organic chromophores (**TPA-QCN**) where the planar π-conjugated system significantly narrowed the band gap, promoting TADF and offering advantages in OLED manufacturing with organic-type dopants.[99] Incorporation of a bulky substituent prevents intermolecular interactions that could promote non-radiative decay pathways, whilst altering

the nature of the donor and acceptor moieties allows colour tunability throughout the visible range. This concept has been exploited recently in the search for highly efficient low-cost organic dopants such as **Q-DMAC**.[100]

Q1[a]

λ_{abs} = 467 nm

λ_{em} = 538 nm

Φ = 0.95

TPA-QCN[b]

λ_{abs} = 448 nm

λ_{em} = 584 nm

Φ = 0.65 (0.85)

τ = 5.1 (5.3) ns

Q-DMAC

λ_{abs} = 400 nm[b]

λ_{em} = 522 nm[b]

Φ = 0.38[c]

τ = 20.4 ns[d]
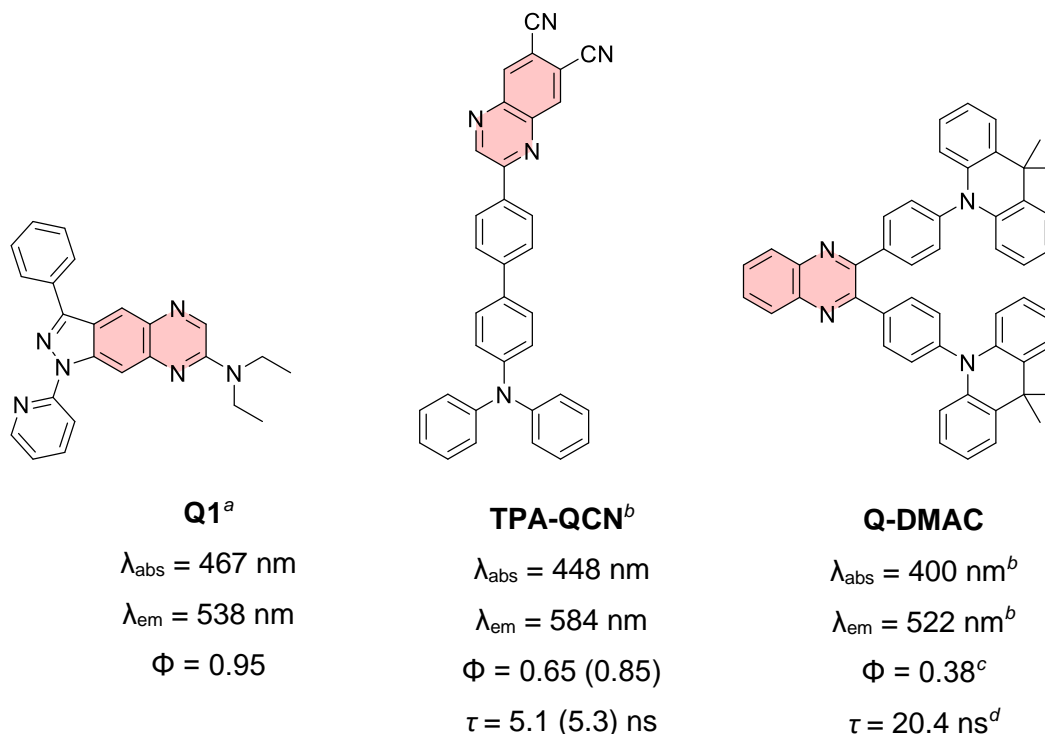
Figure 1.23: *Examples of quinoxaline chromophores used in optoelectronic applications;* [98–100] *[a]DCM; [b]toluene, values in parentheses are in N$_2$-saturated solutions; [c]film; [d]prompt fluorescence.*

1.4.2: Ligand Systems for Phosphorescent Species

Quinolines have been explored as an advancement of cyclometallating phenylpyridine ligands, where extension of π-conjugation imparts significant changes to the electronic behaviour.[101] Quinoxalines offer unique advantages in the development of deep-red emissive complexes, where low-energy absorption and emission features are promoted by means of lowering the LUMO energy. This was exemplified by Tao *et al.*, where subtle modification from quinoline to quinoxaline in the *N*-coordinating fragment of the C^N ligands in a *bis*-cyclometallated Ir complex led to significant bathochromic shifts of 45 nm and 61 nm in the λ_{abs} and λ_{em}, respectively (**Figure 1.24**).[61]

[Ir(pbq-g)₂(Bphen)]PF₆

λ_{abs} = 485 nm

λ_{em} = 694 nm

Φ = 0.03

τ = 1.86 µs

[Ir(mpbqx-g)₂(Bphen)]PF₆

λ_{abs} = 530 nm

λ_{em} = 755 nm

Φ = 0.002

τ = 0.35 µs
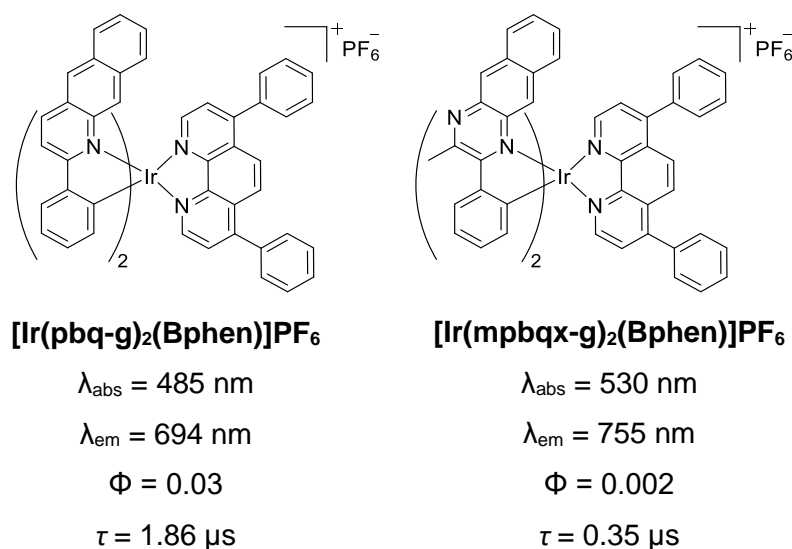
Figure 1.24: *Cationic **[Ir(C^N)₂(N^N)]PF₆** complexes reported by Tao, measurements were recorded in MeCN.*[61]

As previously stated, limitations arise with regard to the phosphorescence efficiencies and lifetimes of orange-to-red emitters as a result of pronounced non-radiative decay pathways by means of the energy gap law.[102] Attempts to overcome these issues have been prosperous, offering feasibility in optoelectronic applications. Some examples of these are shown in **Figure 1.25** and are discussed below.

Hwang presented a series of *ortho*-metallated phosphors containing 2,3-diphenylquinoxalines as C^N ligands displaying saturated red emission with high Φ_{PL}, suitable for efficient light-emitting devices. Tunability within the red region was established by fluorination within a spectral range of 622 – 649 nm, with emission emanating from a mixture of ³IL and ³MLCT states.[103] In 2017, Jing expanded on these systems, where photophysical properties were altered by adjusting the position and extent of fluorination. Desirable electroluminescent properties were achieved as a result, offering specific applications in OLED fabrication.[104] Recent studies have explored congeneric Rh(III) species as an alternative to iridium. However, these were expectedly less efficient than Ir(III) analogues (Φ_{PL} < 1.7%, τ < 0.9 µs) in solution.[105]
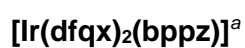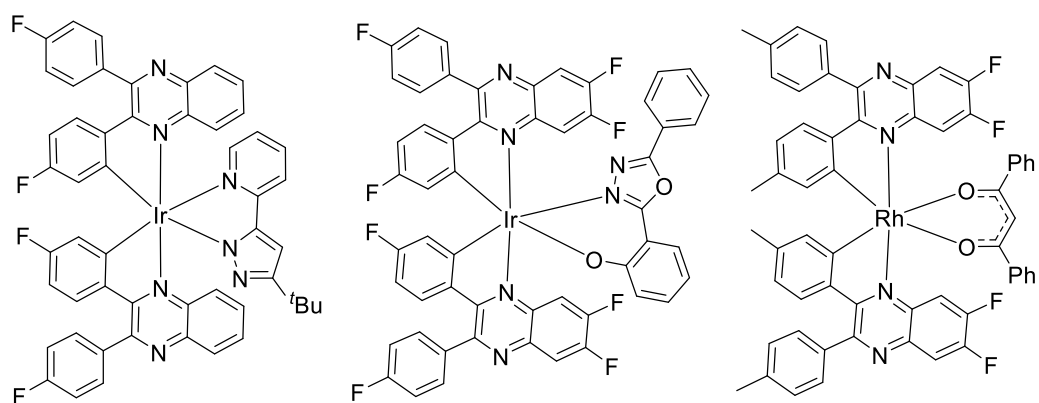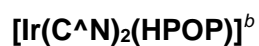
[Ir(dfqx)₂(bppz)][a]

Hwang, 2005

λ_{abs} = 469 nm

λ_{em} = 649 nm

Φ = 0.62

τ = 1.9 µs

[Ir(C^N)₂(HPOP)][b]

Hwang, 2017

λ_{abs} = 391 nm

λ_{em} = 639 nm

Φ = 0.406

τ = 1.98 µs

[Rh(C^N)₂(phacac)][c]

Wei, 2021

λ_{abs} = 460 nm

λ_{em} = 614 nm

Φ = 0.017
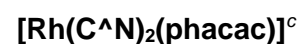
τ = 0.76 µs

Figure 1.25: *Examples of some neutral, efficient, deep red organometallic phosphors for OLED applications. Photophysical properties were measured in degassed DCM solutions; [a]**dfqx** = 2,3-bis(4-fluorophenyl)quinoxaline, **bppz** = 2-(5-(tert-butyl)-2λ^2-pyrazol-3-yl)pyridine;[103] [b]**C^N** = 6,7-difluoro-2,3-bis(4-fluorophenyl)quinoxaline), **HPOP** = 2-(5-phenyl-1,3,4-oxadiazol-2-yl)phenol;[104] [c]**C^N** = 6,7-difluoro-2,3-di-p-tolylquinoxaline, **phacac** = 1,3-diphenylpropane-1,3-dionate.[105]*

1.5: Conclusions

This introductory chapter explored the chemical and photophysical properties of late transition metal complexes and how they compared with organic luminophores. Complexes based on iridium are particularly promising for applications in areas such as OLED development, biological imaging, and photodynamic therapy. Literature findings have demonstrated that iridium and platinum are desirable candidates for generating MLCT-based, deep-red phosphorescence. Therefore, the premise of this thesis is to develop systems incorporating these heavy atoms to generate highly efficient emission from an excited electronic state possessing significant MLCT character. Through careful ligand design, the aim is to alleviate the impact of common issues that arise with deep-red emitters (owing to the energy gap law), such as shorter lifetimes and reduced phosphorescence quantum yields. Other features such as colour tunability will also be explored throughout, offering a method for fine-tunability of the emission wavelength, which is particularly important in the field of optoelectronics.

1.6: References

1   J. R. Lakowicz, *Principles of fluorescence spectroscopy*, Springer, New York, 3rd edn., 2006.

2   P. B. O'Hara, C. Engelson and W. St. Peter, *J. Chem. Educ.*, 2005, **82**, 49–52.

3   N. W. Barnett and P. S. Francis, in *Encyclopedia of Analytical Science: Second Edition*, Elsevier, 2005, pp. 305–315.

4   G. N. Lewis and M. Kasha, *J. Am. Chem. Soc.*, 1944, **66**, 2100–2116.

5   A. Jain, C. Blum and V. Subramaniam, in *Advances in Biomedical Engineering*, Elsevier, Amsterdam, 2009, pp. 147–176.

6   M. Zygmunt and M. Balcerzak, in *Analytical Spectroscopy Library*, Elsevier, 2000, vol. 10, pp. 26–38.

7   B. P. Kafle, *Chemical Analysis and Material Characterization by Spectrophotometry*, 2020, 269–296.

8   J. Franck and E. G. Dymond, *Trans. Faraday Soc.*, 1926, **21**, 536–542.

9   E. Condon, *Phys. Rev.*, 1926, **28**, 1182.

10   D. C. Harris and M. D. Bertolucci, *Symmetry and Spectroscopy: An Introduction to Vibrational and Electronic Spectroscopy*, Dover Publications Inc., New York, 1978.

11   L. B. McGown and K. Nithipahkom, *Appl. Spectrosc. Rev.*, 2007, **35**, 353–393.

12   M. A. Omary and H. H. Patterson, in *Encyclopedia of Spectroscopy and Spectrometry*, Academic Press, Oxford, 2017, pp. 636–653.

13   K. L. Wong, J. C. G. Bünzli and P. A. Tanner, *J. Lumin.*, 2020, **224**, 117256.

14   P. Klán and J. Wirz, *Photochemistry of Organic Compounds: From Concepts to Practice*, John Wiley and Sons, 2009, vol. 6.

15   J. R. Albani, in *Structure and Dynamics of Macromolecules: Absorption and Fluorescence Studies*, Elsevier, Amsterdam, 2004, pp. 55–98.

16   M. Kasha, *Discuss. Faraday Soc.*, 1950, **9**, 14–19.

17   J. B. Birks and L. G. Christophorou, *Spectrochim. Acta*, 1963, **19**, 401–410.

18   D. Genovese, M. Cingolani, E. Rampazzo, L. Prodi and N. Zaccheroni, *Chem. Soc. Rev.*, 2021, **50**, 8414–8427.

19   A. A. Abdel-Shafi, M. D. Ward and R. Schmidt, *Dalton Trans.*, 2007, 2517–2527.

20   M. Üçüncü, E. Karakuş, E. Kurulgan Demirci, M. Sayar, S. Dartar and M. Emrullahoglu, *Org. Lett.*, 2017, **19**, 2522–2525.

21   N. Mehraban and H. S. Freeman, *Materials 2015, Vol. 8, Pages 4421-4456*, 2015, **8**, 4421–4456.

22   E. Ciotta, P. Prosposito and R. Pizzoferrato, *J. Lumin.*, 2019, **206**, 518–522.

23   M. E. Díaz-García and R. Badía-Laíño, in *Encyclopedia of Analytical Science*, Academic Press, Amsterdam, 3rd edn., 2019, pp. 309–319.

24   N. V. Tkachenko, *Optical Spectroscopy: Methods and Instrumentations*, Elsevier Science, Amsterdam, 2006.

25   S. E. Braslavsky, *Pure Appl. Chem.*, 2007, **79**, 293–465.

26   D. R. Arnold, N. C. Baird, J. R. Bolton, J. C. D. Brand, P. W. M. Jacobs, P. de Mayo and W. R. Ware, *Photochemistry: An Introduction*, Academic Press, New York, 1974.

27   J. P. Clayden, N. Greeves and S. Warren, *Organic Chemistry*, Oxford University Press, New York, 2nd edn., 2012.

28   G. R. Chatwal and Madhu. Arora, *Organic photochemistry*, Himalaya Pub. House, New Delhi, 2007.

29   R. Weinberger and L. J. C. Love, *Spectrochim. Acta A Mol. Biomol. Spectrosc.*, 1984, **40**, 49–55.

30   M. Tonga, *J. Photochem. Photobiol. A: Chem.*, 2021, **412**, 113247.

31   W. C. Sun, K. R. Gee and R. P. Haugland, *Bioorg. Med. Chem. Lett.*, 1998, **8**, 3107–3110.

32   S. Sehrawat, R. K. Yadav and A. Pratap Singh, *Mater. Today: Proc.*, 2022, **61**, 1093–1099.

33   M. Chapman and W. B. Euler, *J. Fluoresc.*, 2018, **28**, 1431–1437.

34   V. Martinez and M. Henary, *Eur. J. Chem.*, 2016, **22**, 13764–13782.

35   T. B. Ren, W. Xu, W. Zhang, X. X. Zhang, Z. Y. Wang, Z. Xiang, L. Yuan and X. B. Zhang, *J. Am. Chem. Soc.*, 2018, **140**, 7716–7722.

36   N. Duvva, Y. K. Eom, G. Reddy, K. S. Schanze and L. Giribabu, *ACS Appl. Energy Mater.*, 2020, **3**, 6758–6767.

37   S. Thurakkal, K. S. Sanju, A. Soman, K. N. N. Unni, J. Joseph and D. Ramaiah, *New J. Chem.*, 2018, **42**, 5456–5464.

38   B. Minaev, H. Ågren and F. De Angelis, *Chem. Phys.*, 2009, **358**, 245–257.

39   D. Magero, T. Mestiri, K. Alimi and M. E. Casida, *Computational studies of ruthenium and iridium complexes for energy sciences and progress on greener alternatives*, Elsevier, 2022.

40   L. F. Gildea and J. A. G. Williams, *Iridium and platinum complexes for OLEDs*, Woodhead Publishing, 2013.

41   M. L. P. Reddy and K. S. Bejoymohandas, *J. Photochem. Photobiol. C: Photochem. Rev.*, 2016, **29**, 29–47.

42   T. Sajoto, P. I. Djurovich, A. B. Tamayo, J. Oxgaard, W. A. Goddard and M. E. Thompson, *J. Am. Chem. Soc.*, 2009, **131**, 9813–9822.

43   M. E. Thompson, P. E. Djurovich, S. Barlow and S. Marder, in *Comprehensive Organometallic Chemistry III*, Elsevier, 2007, vol. 12, pp. 101–194.

44   H. Na, L. M. Cañada, Z. Wen, J. I-Chia Wu and T. S. Teets, *Chem. Sci.*, 2019, **10**, 6254–6260.

45   C. Otero, A. Carreño, R. Polanco, F. M. Llancalahuen, R. Arratia-Pérez, M. Gacitúa and J. A. Fuentes, *Front. Chem.*, 2019, **7**, 454.

46   G. Godefroid, L. Yuqi, S. Yanling, S. Juanjuan, Q. Xiaochun, S. Xiaohong and W. Zhijian, *J. Mater. Chem. C*, 2014, **2**, 8364–8372.

47   J. V. Caspar and T. J. Meyer, *J. Phys. Chem.*, 1983, **87**, 952–957.

48   P. N. Lai, C. H. Brysacz, M. K. Alam, N. A. Ayoub, T. G. Gray, J. Bao and T. S. Teets, *J. Am. Chem. Soc.*, 2018, **140**, 10198–10207.

49   J. H. Kim, S. Y. Kim, S. Jang, S. Yi, D. W. Cho, H. J. Son and S. O. Kang, *Inorg. Chem.*, 2019, **58**, 16112–16125.

50   J. P. Paris and W. W. Brandt, *J. Am. Chem. Soc.*, 1959, **81**, 5001–5002.

51   K. Suzuki, A. Kobayashi, S. Kaneko, K. Takehira, T. Yoshihara, H. Ishida, Y. Shiina, S. Oishi and S. Tobita, *Phys. Chem. Chem. Phys.*, 2009, **11**, 9850–9860.

52   J. N. Demas and A. W. Adamson, *J. Am. Chem. Soc.*, 1971, **93**, 1800–1801.

53   W. R. Browne, P. Passaniti, M. T. Gandolfi, R. Ballardini, W. Henry, A. Guckian, N. O'Boyle, J. J. McGarvey and J. G. Vos, *Inorganica Chim. Acta*, 2007, **360**, 1183–1190.

54   E. Babu, P. M. Mareeswaran, M. M. Krishnan, V. Sathish, P. Thanasekaran and S. Rajagopal, *Inorg. Chem. Commun.*, 2018, **98**, 7–10.

55   D. García-Fresnadillo, Y. Georgiadou, G. Orellana, A. M. Braun and E. Oliveros, *Helv. Chim. Acta*, 1996, **79**, 1222–1238.

56   J. Hess, H. Huang, A. Kaiser, V. Pierroz, O. Blacque, H. Chao and G. Gasser, *Eur. J. Chem.*, 2017, **23**, 9888–9896.

57   J. P. Sauvage, J. P. Collin, J. C. Chambron, S. Guillerez, C. Coudret, V. Balzani, F. Barigelletti, L. De Cola and L. Flamigni, *Chem. Rev.*, 1994, **94**, 993–1019.

58   M. Beley, J. P. Collin, J. P. Sauvage, H. Sugihara, F. Heisel and A. Miehé, *J. Chem. Soc., Dalton Trans.*, 1991, 3157–3159.

59   J. Palion-Gazda, B. Machura, A. Szłapa-Kula, A. M. Maroń, J. E. Nycz, P. Ledwon, E. Schab-Balcerzak, M. Siwy, J. Grzelak and S. Maćkowski, *Dyes Pigments*, 2022, **200**, 110113.

60   S. Kanti Seth, P. Gupta and P. Purkayastha, *New J. Chem.*, 2017, **41**, 6540–6545.

61   R. Tao, J. Qiao, G. Zhang, L. Duan, L. Wang and Y. Qiu, *J. Phys. Chem.*, 2012, **116**, 11658–11664.

62   L. F. Gildea, A. S. Batsanov and J. A. G. Williams, *Dalton Trans.*, 2013, **42**, 10388–10393.

63   F. Wei, S. L. Lai, S. Zhao, M. Ng, M. Y. Chan, V. W. W. Yam and K. M. C. Wong, *J. Am. Chem. Soc.*, 2019, **141**, 12863–12871.

64   US 2005/0191527 A1, 2005.

65   Md. K. Nazeeruddin, R. Humphry-Baker, D. Berner, S. Rivier, L. Zuppiroli and M. Graetzel, *J. Am. Chem. Soc*, 2003, **125**, 8790–8797.

66   V. W. W. Yam and K. M. C. Wong, *Chem. Commun.*, 2011, **47**, 11579–11592.

67   N. Armaroli, G. Accorsi, M. Holler, O. Moudam, J. F. Nierengarten, Z. Zhou, R. T. Wegh and R. Welter, *Adv. Mater.*, 2006, **18**, 1313–1316.

68   S. Otto, M. Grabolle, C. Förster, C. Kreitner, U. Resch-Genger and K. Heinze, *Angew. Chem., Int. Ed. Engl.*, 2015, **54**, 11572–11576.

69   P. Chábera, Y. Liu, O. Prakash, E. Thyrhaug, A. el Nahhas, A. Honarfar, S. Essén, L. A. Fredin, T. C. B. Harlang, K. S. Kjær, K. Handrup, F. Ericson, H. Tatsuno, K. Morgan, J. Schnadt, L. Häggström, T. Ericsson, A. Sobkowiak, S. Lidin, P. Huang, S. Styring, J. Uhlig, J. Bendix, R.

Lomoth, V. Sundström, P. Persson and K. Wärnmark, *Nature 2017 543:7647*, 2017, **543**, 695–699.

70   A. Barbieri, G. Accorsi and N. Armaroli, *Chem. Commun.*, 2008, 2185–2193.

71   M. Z. Shafikov, A. F. Suleymanova, R. Czerwieniec and H. Yersin, *Inorg. Chem.*, 2017, **56**, 13274–13285.

72   T. Li, P. I. Djurovich and M. E. Thompson, *Inorganica Chim. Acta*, 2021, **517**, 120188.

73   K. T. Yeung, W. P. To, C. Sun, G. Cheng, C. Ma, G. S. M. Tong, C. Yang and C. M. Che, *Angew. Chem., Int. Ed.*, 2017, **56**, 133–137.

74   P. K. Chow, G. Cheng, G. S. M. Tong, C. Ma, W. M. Kwok, W. H. Ang, C. Y. S. Chung, C. Yang, F. Wang and C. M. Che, *Chem. Sci.*, 2016, **7**, 6083.

75   W. P. To, K. T. Chan, G. S. M. Tong, C. Ma, W. M. Kwok, X. Guan, K. H. Low and C. M. Che, *Angew. Chem., Int. Ed.*, 2013, **52**, 6648–6652.

76   C. W. Tang and S. A. Vanslyke, *Appl. Phys. Lett.*, 1987, **51**, 913.

77   N. Thejo Kalyani and S. J. Dhoble, *Renew. Sustain. Energy Rev.*, 2012, **16**, 2696–2723.

78   C. Fan and C. Yang, *Chem. Soc. Rev.*, 2014, **43**, 6439–6469.

79   X. Yang, G. Zhou and W. Y. Wong, *Chem. Soc. Rev.*, 2015, **44**, 8484–8575.

80   C. Adachi, M. A. Baldo, M. E. Thompson and S. R. Forrest, *J. Appl. Phys.*, 2001, **90**, 5048.

81   C. H. Yang, M. Mauro, F. Polo, S. Watanabe, I. Muenster, R. Fröhlich and L. De Cola, *Chem. Mater.*, 2012, **24**, 3684–3695.

82   J. Jayabharathi, V. Thanikachalam and R. Sathishkumar, *New J. Chem.*, 2015, **39**, 235–245.

83   Y. Ding, D. Liu, J. Li, H. Li, H. Ma, D. Li and R. Niu, *Dyes Pigments*, 2020, **179**, 108405.

84   G. W. Zhao, J. H. Zhao, Y. X. Hu, D. Y. Zhang and X. Li, *Synth. Met.*, 2016, **212**, 131–141.

85   C. M. Che, C. C. Kwok, S. W. Lai, A. F. Rausch, W. J. Finkenzeller, N. Zhu and H. Yersin, *Eur. J. Chem.*, 2010, **16**, 233–247.

86   J. L. Liao, Y. Chi, Y. De Su, H. X. Huang, C. H. Chang, S. H. Liu, G. H. Lee and P. T. Chou, *J. Mater. Chem. C*, 2014, **2**, 6269–6282.

87   J. Liang, L. Ying, F. Huang and Y. Cao, *J. Mater. Chem. C*, 2016, **4**, 10993–11006.

88   C. Caporale and M. Massi, *Coord. Chem. Rev.*, 2018, **363**, 71–91.

89   S. S. Bhat, N. Shivalingegowda, V. K. Revankar, N. K. Lokanath, M. S. Kugaji, V. Kumbar and K. Bhat, *J. Inorg. Biochem.*, 2017, **177**, 127–137.

90   A. J. Amoroso, R. J. Arthur, M. P. Coogan, J. B. Court, V. Fernández-Moreira, A. J. Hayes, D. Lloyd, C. Millet and S. J. A. Pope, *New J. Chem.*, 2008, **32**, 1097–1102.

91   L. He, Y. Li, C. P. Tan, R. R. Ye, M. H. Chen, J. J. Cao, L. N. Ji and Z. W. Mao, *Chem. Sci.*, 2015, **6**, 5409–5418.

92   V. Bogoeva, M. Siksjø, K. G. Sæterbø, T. B. Melø, A. Bjørkøy, M. Lindgren and O. A. Gederaas, *Photodiagnosis Photodyn. Ther.*, 2016, **14**, 9–17.

93   A. M. S. El Newahie, Y. M. Nissan, N. S. M. Ismail, D. A. Abou El Ella, S. M. Khojah and K. A. M. Abouzid, *Molecules*, 2019, **24**, 1175.

94   R. Xia, T. Guo, M. Chen, S. Su, J. He, X. Tang, S. Jiang and W. Xue, *New J. Chem.*, 2019, **43**, 16461–16467.

95   H. S. A. El-Zahabi, *Arch. Pharm. (Weinheim)*, 2017, **350**, 1700028.

96   X. Li, Y. Hu, I. Sanchez-Molina, Y. Zhou, F. Yu, S. A. Haque, W. Wu, J. Hua, H. Tian and N. Robertson, *J. Mater. Chem. A*, 2015, **3**, 21733–21743.

97   J. Shi, Z. Chai, J. Su, J. Chen, R. Tang, K. Fan, L. Zhang, H. Han, J. Qin, T. Peng, Q. Li and Z. Li, *Dyes Pigments*, 2013, **98**, 405–413.

98   P. Wang, Z. Xie, O. Wong, C. S. Lee, N. Wong, L. Hung and S. Lee, *Chem. Commun.*, 2002, **2**, 1404–1405.

99   C. Li, R. Duan, B. Liang, G. Han, S. Wang, K. Ye, Y. Liu, Y. Yi and Y. Wang, *Angew. Chem., Int. Ed.*, 2017, **56**, 11525–11529.

100   T. Huang, D. Liu, J. Jiang and W. Jiang, *Eur. J. Chem.*, 2019, **25**, 10926–10937.

101   Y. Zhou, W. Li, L. Yu, Y. Liu, X. Wang and M. Zhou, *Dalton Trans.*, 2014, **44**, 1858–1865.

102   D. Schneidenbach, S. Ammermann, M. Debeaux, A. Freund, M. Zöllner, C. Daniliuc, P. G. Jones, W. Kowalsky and H. H. Johannes, *Inorg. Chem.*, 2010, **49**, 397–406.

103   F. M. Hwang, H. Y. Chen, P. S. Chen, C. S. Liu, Y. Chi, C. F. Shu, F. I. Wu, P. T. Chou, S. M. Peng and G. H. Lee, *Inorg. Chem.*, 2005, **44**, 1344–1353.

104   Y. M. Jing and Y. X. Zheng, *RSC Adv.*, 2017, **7**, 37021–37031.

105   F. Wei, Z. Qian, S. L. Lai, S. Zhao, M. Y. Chan and K. M. C. Wong, *Energy Fuels*, 2021, **35**, 19123–19131.

Chapter 2: Polysubstituted 2-Phenylquinoxaline Ligands for Colour-Tunable Phosphorescent Iridium(III) Complexes

Chapter 2

2.1: Introduction

Cationic *bis*-cyclometallated Ir(III) complexes have become a prevalent area of research over the years, but achieving efficient emission at specific wavelengths of light remains as a challenge. This chapter offers scope into fine-tunability within the yellow, orange, and deep-red regions of the visible range.

2.1.1: Importance of Ligand Design in Colour Tunability

Transition metal complexes are fundamental in the development of electroluminescent technology as a result of their desirable photophysical attributes. The presence of d-electrons alongside variable oxidation states, coordination modes, and molecular geometries allow a certain degree of control over excited state properties,[1] offering limitless possibilities for colour-tunability. As previously discussed, iridium metal centres are desirable due to enhanced LFSE, where ^{3}MC quenching states become less accessible.[2]

The nature of the emissive state and subsequent properties of the metal complex can be directly altered by rational design of the ligands in the coordination sphere.[3] This has been reported for homoleptic complexes containing C^N ligands based on phenylpyridine (**ppy**), where **Ir(ppy)₃** displays an λ_{em} of 497 – 530 nm in DCM solutions.[4] However, attention has been directed to heteroleptic, *bis*-cyclometallated iridium complexes in recent years, where incorporation of a chelating ancillary ligand generally requires less harsh reaction conditions and offers significant control over the subsequent luminescent and chemical properties.[5] Functionalisation exclusively at the ancillary ligand has been explored as a facile approach to inducing specific excited state properties, where luminescence has been observed across a wide range of colours.[6] This is synthetically advantageous, since the energy-demanding dimerisation step often suffers from steric and electronic limitations.

However, it has since been reported that the photophysical properties of complexes of this type are dominated by the nature of the cyclometallating (C^N) ligands.[7] Therefore, judicious C^N ligand design offers excellent scope and versatility with reference to emission colour tunability. An early example of this was reported in 2001, when Lamansky developed a series of *bis*-

cyclometallated Ir(III) complexes exhibiting extraordinary colour-tunability (**Figure 2.1**).[8,9] Here, alteration of the C^N ligand in a **Ir(C^N)₂(acac)** species heavily influenced the emission wavelength, offering diversification of emission colours across a large range of 100 nm.

| 612 nm | 597 nm | 586 nm | 550 nm | 512 nm |
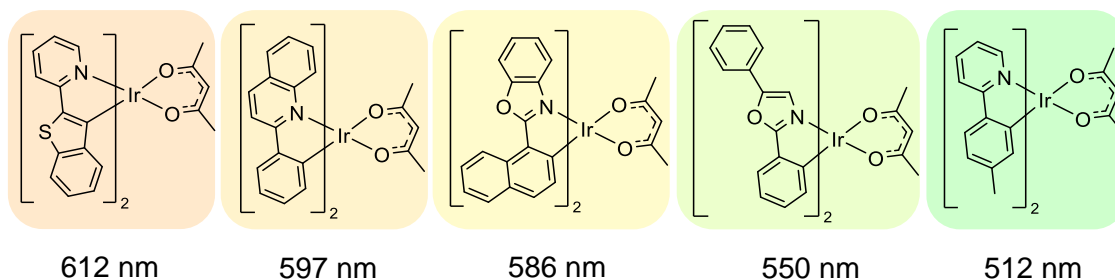
Figure 2.1: Neutral Ir(III) complexes developed by Lamansky.[8,9] λ_em maxima (in 2,4-methyl THF) are displayed below each structure.

Control can also be achieved within a specific region of the visible range. Sun *et al.* investigated the effects of fluorination at the phenyl moiety in **ppy** ligands,[10] where previous work has shown that highly efficient phosphorescence can occur from these structural motifs.[11] In doing so, discrete tunability was achieved, where a bathochromic shift of 21 nm in emission maxima occurred upon incorporation of an additional fluorine atom and by altering the positions of these substituents. This was accompanied by an enhancement in Φ_{PL} (**Figure 2.2**). Interestingly, absorption peak positions were almost identical in both specie, suggesting that fluorination did not impact the ground state whilst offering a route to explicitly altering the energy of the excited state.

(F₂,₄ppy)₂Ir(tfmptz)   **(F₄,₃,₅ppy)₂Ir(tfmptz)**

λ_abs: 400 nm Φ_P: 20.1   λ_abs: 402 nm Φ_P: 24.3

λ_em: 481 nm   τ_obs: 2.48 µs   λ_em: 502 nm   τ_obs: 3.23 µs
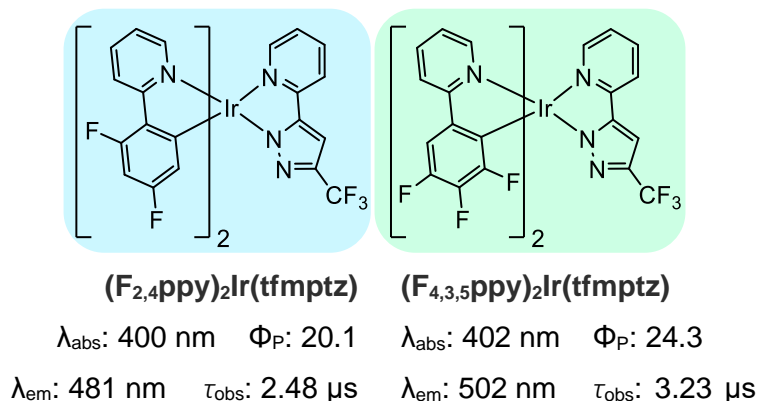
Figure 2.2: Structures and photophysical data (in DCM) of Ir(III) complexes by Sun.[10]

More recently, Chen *et al.* investigated the effects of fluorination at various regions of the cyclometallating ligands in **ppy**-based systems, where the N^N ligand was 2,2'-bipyridine throughout (**Figure 2.3**).[12] Emission was measured between 514 – 575 nm in DCM solutions, and the most blue-shifted complex (**1f**) exhibited the greatest quantum yield (Φ_P = 0.51) and longest observed lifetime (τ_{obs} = 1.29 µs), consistent with the energy gap law. Resultantly, fluorine was considered to be a desirable electron-withdrawing group for excited state tunability. Stability of the ^{3}MLCT state can be modified by altering the extent of σ-donation from the carbon atom to the iridium centre, which is impacted by the electronic nature of the substituents.[13] Increased electron density at the C^N carbon atom will generally promote a bathochromic shift in λ_{em} by stabilising the excited state.[14]

1a: 575 nm   **1c**: 542 nm   **1e**: 524 nm

1b: 567 nm   **1d**: 534 nm   **1f**: 514 nm
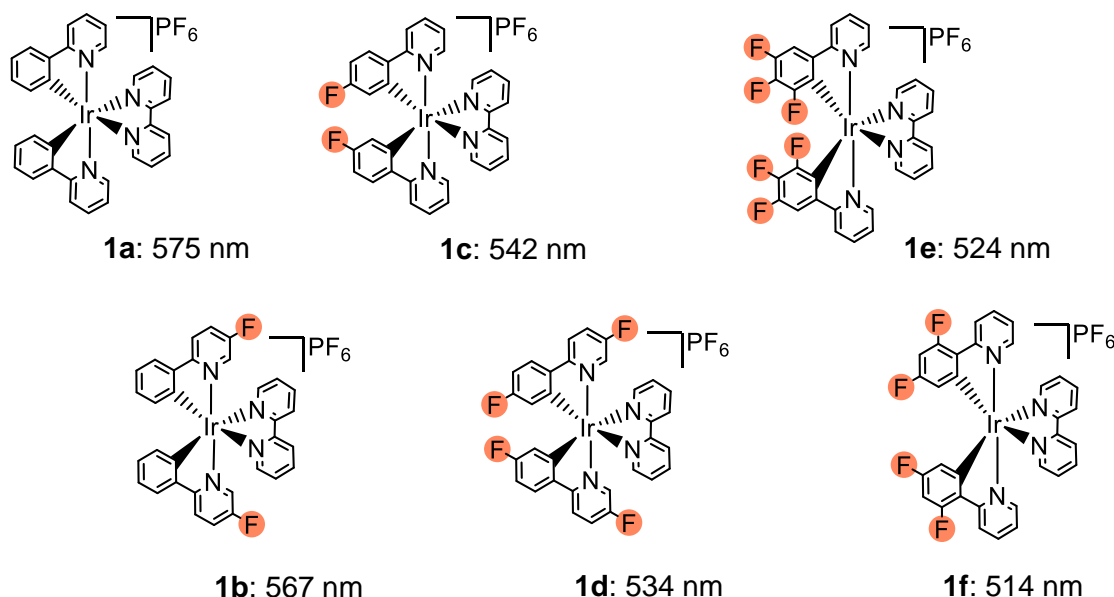
Figure 2.3: Fluorinated ppy-type complexes synthesised and examined by Chen et al. (2019), and their corresponding λ_{em} (DCM, λ_{ex} = 400 nm).[12]

The opposite effect has been achieved by incorporating a weak EDG (such as a methyl substituent) into the **ppy**-type C^N ligand, resulting in red-shifted emission.[15] Therefore, a combinative approach has been adopted in this study as a method of fine-tuning the emission properties. The extent of π-conjugation in the C^N ligand also influences the excited state, since extension of this system at the heterocyclic component has prompted a bathochromic shift in emission whilst displaying high quantum yields.[16–19] Therefore, the properties of these types of iridium species can be predicted by efficacious ligand design.

2.1.2: Applications in OLED Development

Producing compounds with very specific emission wavelengths in conjunction with characteristically high phosphorescent quantum yields is of vital importance in the advancement of OLED technology and the development of high-quality RGB (red-green-blue) displays. Therefore, the compounds discussed in **Section 2.1.1** have been widely studied as dopants in the development of PhOLEDs and have promoted the expansion of interest in this area since the early 2000s.[20–23] Highly efficient orange-to-red emissive phosphors have been sought after for this purpose,[18,24] with more recent traction in the development of WOLEDs.[25] Two-element white light can be generated using a combination of specific complementary wavelengths of emission, such as orange and blue emitters.[26] However, obtaining highly efficient long-wavelength species of this nature remains as a challenge due to the energy gap law, which promotes depopulation of the excited state through non-radiative processes.[27]

Ir(BCF₃-pq)₂(acac)[a]   **Ir(Cl-MDPQ)₂Ir(acac)**[b]   **Ir(piqCN)₂Ir(acac)**[c]

λ_{em}: 614 nm λ_{em}: 662 nm λ_{em}: 696 nm
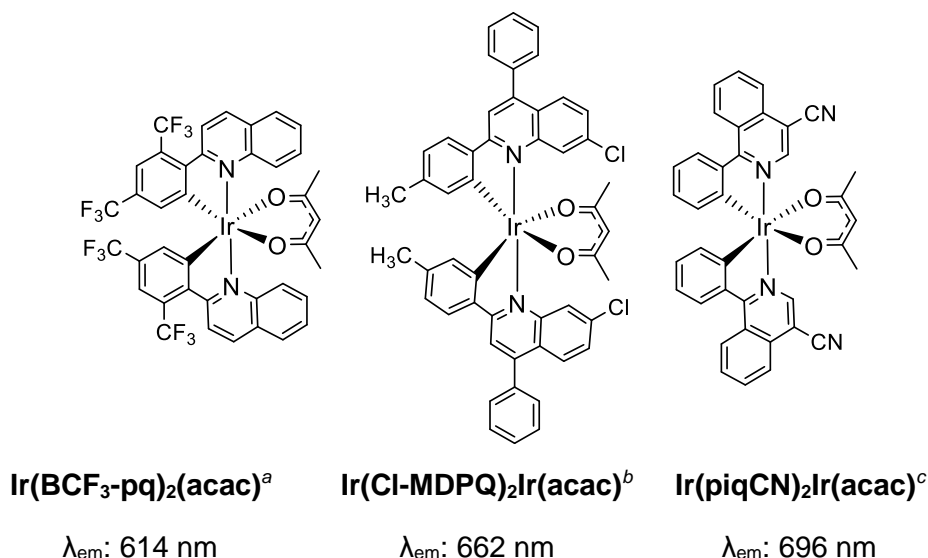
Figure 2.4: Examples of red-emissive phosphors designed for OLED fabrication.
[a]Chen (2018);[13] [b]Dahule (2011);[28] [c]Chen (2020).[29] All spectroscopic measurements were performed in 10⁻⁴M degassed THF solutions.

Selected examples of red phosphors for use in OLED development are displayed in **Figure 2.4**.[13,28,29] Here, disparities in emission properties are a direct result of the nature of the C^N ligand, since the ancillary ligand remains constant throughout. All possess additional π-conjugation on the backbone of

the pyridine ring, inflicting a bathochromic shift in λ_{em}. **Ir(BCF$_3$-pq)$_2$(acac)** and **Ir(piqCN)$_2$Ir(acac)** were reasonably efficient for red-emissive compounds (Φ_{PL} = 40% in 10^{-4}M degassed THF, and Φ_{PL} = 16% in 10^{-4}M aerated THF, respectively).

Quinoxaline-based compounds have also been investigated for use in OLED applications (**Figure 2.5**).[30] In 2017, Wang reported that pyrazine rings incorporated into an extended π-system gives rise to interesting photophysical properties, a direct result of the structural rigidity and electron-withdrawing capability of such systems.[31] These organic compounds displayed tunability from yellow to red, but transition metal complexes offer significant advantages in this field due to their phosphorescent nature. Early work in 2008 showed that the HOMO-LUMO energy gap can be controlled in a previously reported[32] **Ir(2,3-dpqz)$_2$(acac)** system (2,3-dpqz = diphenylquinoxaline), where a more saturated red emission and improved electroluminescence efficiency were achieved upon fluorination of the phenyl rings, with a subtle enhancement upon methylation of the quinoxaline fragment.[33] This was exemplified by a hypsochromic shift in emission wavelength. Further work showed that fluorination at the 6-position led to even further tunability in red OLEDs, where saturated red emission was achieved by reducing the energy of the LUMO.[34]

Ir(2,3-dpqx)$_2$(acac)   **Ir(2,3-dpqx-F$_2$)$_2$(acac)**   **Ir(6-Me-2,3-dpqx-F$_2$)$_2$(acac)**

Complex	λ_{abs} / nm	λ_{em} / nm
Ir(2,3-dpqx)$_2$(acac)[a]	370, 475, 635	675
Ir(2,3-dpqx-F$_2$)$_2$(acac)[b]	378, 388, 465, 543	632
Ir(6-Me-2,3-dpqx-F$_2$)$_2$(acac)[b]	372, 465, 543	630
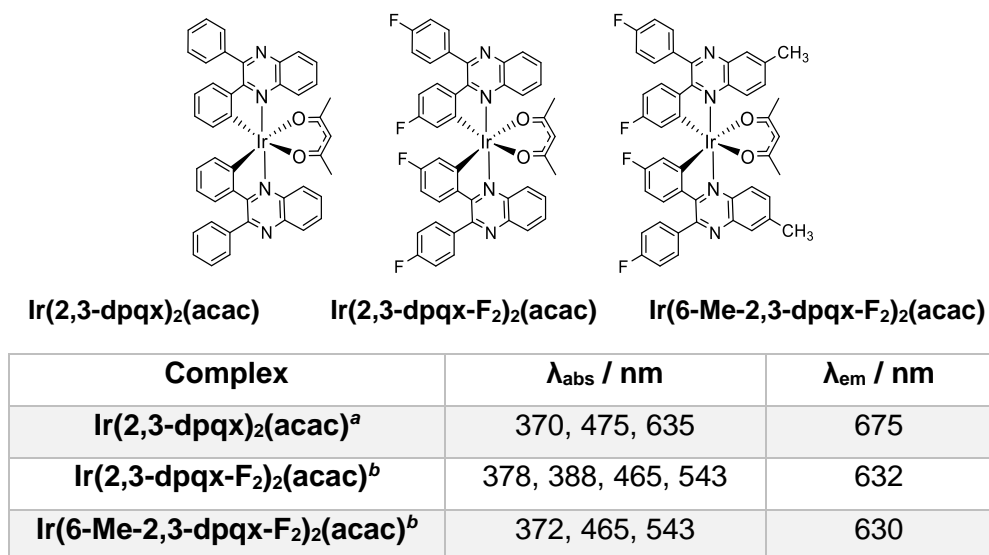
Figure 2.5: *Structures and selected photophysical properties (in DCM) of 2,3-diphenylquinoxaline-based Ir(III) complexes as red-emissive species. [a]Gao;[32] [b]Ha.[33]*

2.2: Aims

This chapter explores the synthesis and characterisation of a series of 2-phenylquinoxaline based compounds, and their use as ligands in cationic *bis*-cyclometallated iridium complexes. Methyl and fluorine substituents were employed as weakly electron-donating and electon-withdrawing substituents, respectively, and were incorporated into the two separate components of the ligands. The resultant photophysical properties of all compounds were investigated to study the influence of substitution on electronic behaviour in the resultant complexes. Computational studies were performed to complement the experimental observations. This study was a collaborative effort, where **Ir-2b** was synthesised and characterised by Christopher Elgar, and **Ir-2e** by Natalia Sawicka. More information can be found in the published work relating to this chapter.[35]

2.3: Results and Discussion

2.3.1: Synthesis and Characterisation of Ligands

In total, ten structural variants based upon 2-phenyl quinoxaline were successfully synthesised. These compounds contained various substitution patterns, where weakly electron-donating (methyl) and electron-withdrawing (fluorine) groups were employed at alternating positions to impart subtle changes to the electronic behaviour of each molecule.
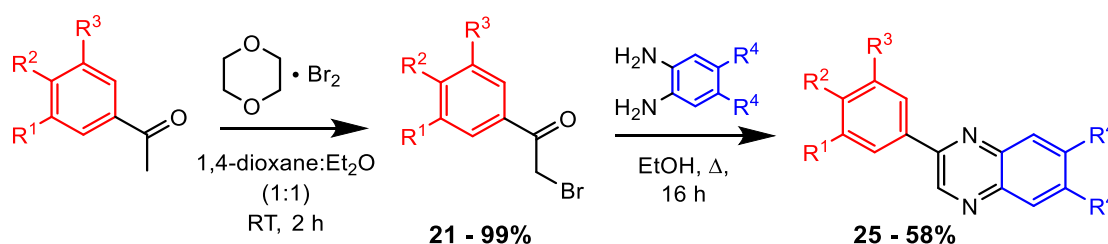
Scheme 2.1: *General synthetic approach for the preparation of* **L**[1-10]**H**.

The general synthesis of these compounds (**Scheme 2.1**) comprised of two stages; firstly, bromination of the acetophenone precursors took place to generate a range of α-bromoacetyl species. The brominating agent was dioxane dibromide (DDB),[36,37] a highly selective and environmentally friendly alternative to other brominating species including elemental bromine and NBS, which generally require more forceful conditions such as the use of catalyst to promote electrophilicity.[38,39] These can also generate the undesired dibrominated species *in situ*.[40] Previous theoretical studies have indicated that the enhanced electrophilicity in DDB is due to slight polarisation of the Br_2.[41] Resultantly, the mono-brominated precursors were mostly generated in high yields (up to 99%) at room temperature over a relatively short time (<2h). The reactions were monitored by TLC and the presence of an indicative singlet at ~4.5 ppm in the ^{1}H NMR spectra confirmed the formation of the compounds.

The second step in the synthesis resulted in formation of **L**[1-10]**H** (**Figure 2.6**) *via* a condensation reaction of the brominated species with either 1,2-phenylenediamine or its di-substituted variants. These reactions were performed in ethanol at reflux and the experimental yields were moderate (41 – 58%). Other reports have demonstrated that improved yields are achievable

through use of a catalyst and harsher conditions,[42,43] but the relatively eco-friendly approach reported here was deemed sufficient for the purposes of this study. Advantageously, all precursors displayed enhanced solubility in ethanol, whereas the pure products precipitated out of solution – offering a facile approach to obtaining the compounds. Of the ten compounds, only two (**L⁵H** and **L⁶H**)[44,45] have been previously reported in the literature. Therefore, eight novel products were isolated and fully characterised in this study.
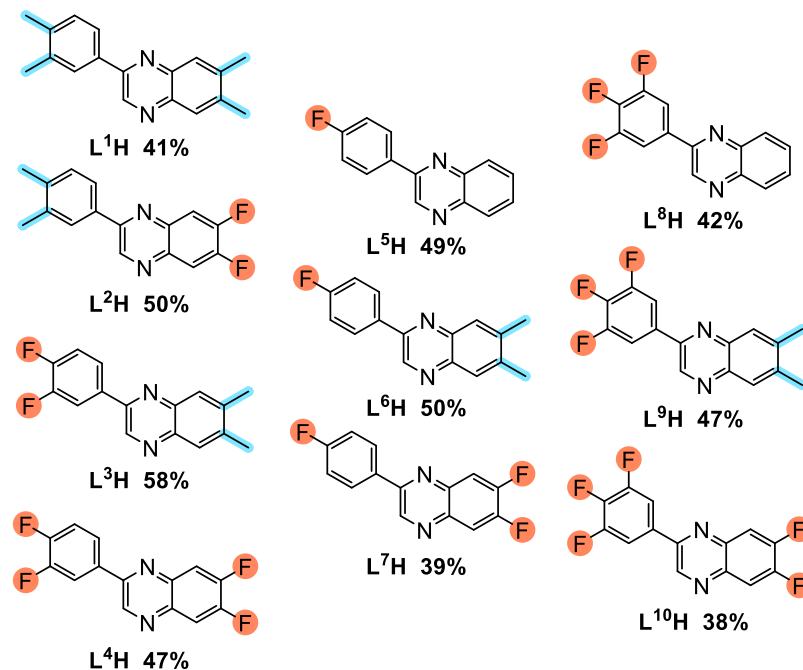
Figure 2.6: *Structures and experimental yields of* ***L¹⁻¹⁰H***.

L¹⁻¹⁰H were analysed by ¹H and ¹⁹F{¹H} (where applicable) NMR spectroscopies, with the novel species being further characterised by ¹³C{¹H} and IR spectroscopies along with HRMS.

The ¹H NMR spectra of **L²H** and **L³H** are shown in **Figure 2.7**, where all proton environments have been assigned. An indicative singlet at ~9.20 ppm was seen for **L¹⁻¹⁰H**, corresponding to the proton on the pyrazine sub-unit of the quinoxaline moiety, as it experienced significant deshielding by the heterocyclic system. For **L¹⁻³H**, **L⁶H** and **L⁹H**, aliphatic protons displayed peaks between 2.36 – 2.53 ppm. In the cases of **L¹H**, **L³H** and **L⁹H**, a single signal was seen at 2.52 ppm, which corresponded to two overlapping singlets from the methyl groups on the quinoxaline (**Figure 2.7**, top). Although these protons were chemically inequivalent (due to the asymmetric nature of the molecules), their chemical environments were indistinguishable, so the peaks were coincident.

In contrast, methylation at the phenyl ring resulted in two distinct singlets (**Figure 2.7**, bottom), due to pronounced differences in chemical environment.

The presence of NMR-active ^{19}F nuclei gave rise to characteristic splitting patterns with J_{HF} couplings. This is exemplified in **Figure 2.7**, where additional splitting alongside a change in chemical shift value was seen due to the presence of a fluorine atom in close proximity to the protons.
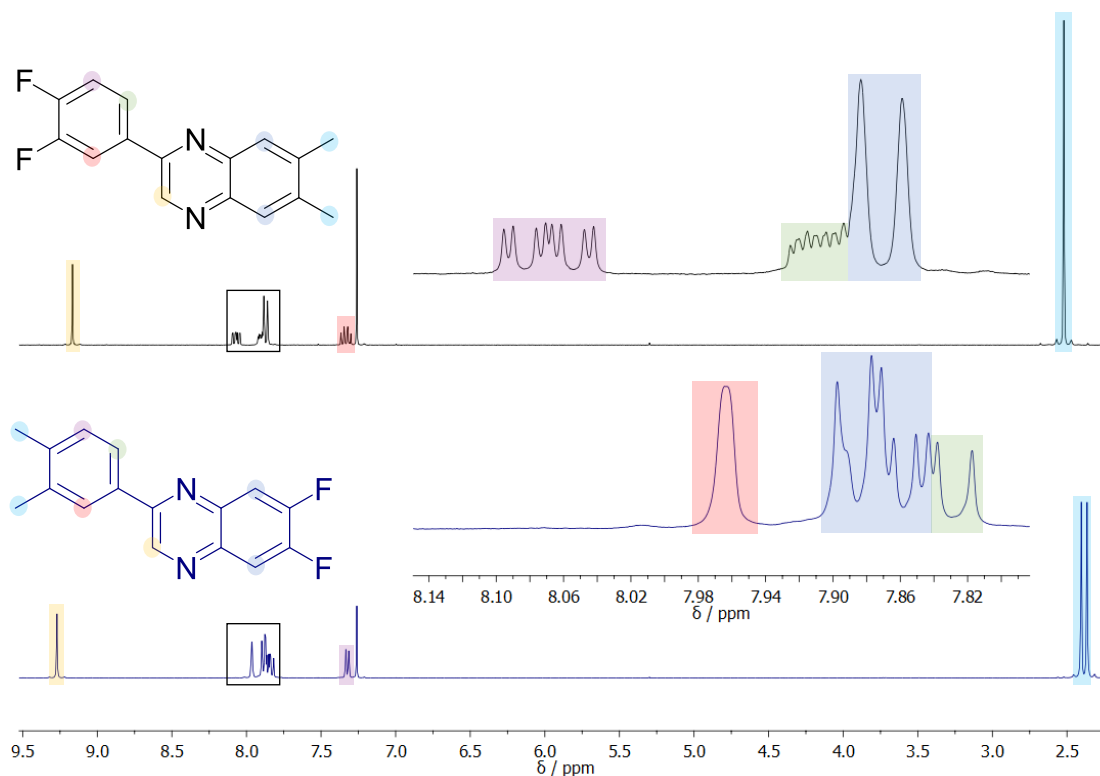
*Figure 2.7: ^{1}H NMR spectra of **L³H** (black) and **L²H** (blue), CDCl₃, 400 MHz.*

^{13}C{^{1}H} NMR data of the trifluorophenyl compounds **L⁸⁻¹⁰H** provided insight into C-F couplings. The characteristic peak positions and J_{CF} couplings on the phenyl ring were assigned (**Table 2.1**). $^1J_{CF}$ couplings were expectedly within the range of 250.6 – 256.9 Hz and $^2J_{CF}$ values were measured at 10.1 – 17.3 Hz.

A distinct doublet of triplets (dt) represented the carbon positioned *para-* to the quinoxaline unit; this was due to the equivalence of the two fluorine atoms positioned on the adjacent carbons. Doublets of doublets of doublets (ddd) were seen for the other two fluorinated carbon atoms at ~152 ppm, where these were chemically equivalent due to free rotation of the phenyl ring, coupling with three inequivalent fluorine atoms. The rest of the phenyl ring displayed longer range

interactions, where $^2J_{CF} \approx 17.1$ Hz and $^3J_{CF} = 5.5 - 7.5$ Hz. Interaction with fluorine at the *para*-position relative to the carbon results in a long-range observable coupling, where $^4J_{p\text{-}CF} \approx 4.5$ Hz. These values were consistent with the literature on polyfluorinated rings.[46]

Compound	δ_C / ppm		
	X = H (*L⁸H*)	X = CH₃ (*L⁹H*)	X = F (*L¹⁰H*)
	151.9 *(ddd)* $^1J_{CF} = 250.9$ Hz $^2J_{CF} = 10.2$ Hz $^3J_{CF} = 4.0$ Hz	151.9 *(ddd)* $^1J_{CF} = 250.6$ Hz $^2J_{CF} = 10.1$ Hz $^3J_{CF} = 3.8$ Hz	152.0 *(ddd)* $^1J_{CF} = 251.3$ Hz $^2J_{CF} = 10.2$ Hz $^3J_{CF} = 4.0$ Hz
	141.4 *(dt)* $^1J_{CF} = 256.7$ Hz $^2J_{CF} = 15.4$ Hz	141.1 *(dt)* $^1J_{CF} = 255.1$ Hz $^2J_{CF} = 15.1$ Hz	141.5 *(dt)* $^1J_{CF} = 256.9$ Hz $^2J_{CF} = 15.4$ Hz
	111.8 *(dd)* $^2J_{CF} = 17.1$ Hz $^3J_{CF} = 5.5$ Hz	111.5 *(dd)* $^2J_{CF} = 17.3$ Hz $^3J_{CF} = 5.5$ Hz	111.7 (dd) $^2J_{CF} = 17.1$ Hz $^3J_{CF} = 5.6$ Hz
	132.9 *(td)* $^3J_{CF} = 7.5$ Hz $^4J_{p\text{-}CF} = 4.5$ Hz	133.3 *(td)* $^3J_{CF} = 7.2$ Hz $^4J_{p\text{-}CF} = 4.1$ Hz	132.2 (td) $^3J_{CF} = 7.5$ Hz $^4J_{p\text{-}CF} = 4.5$ Hz

*Table 2.1: Selected $^{13}C\{^1H\}$ NMR chemical shifts and coupling constants obtained for the trifluorophenyl ligands, **L⁸⁻¹⁰H**; CDCl₃, 500 MHz.*

L¹⁰H displayed an additional two C-F couplings due to fluorination at the quinoxaline. These are tabulated in **Table 2.2** and similar peak positions and J_{CF} couplings were seen for **L²H**, **L⁴H** and **L⁷H**.

	Position	
δ$_C$ / ppm	153.2 *(dd)* $^1J_{CF}$ = 255.6 Hz $^2J_{CF}$ = 13.6 Hz	115.3 *(dd)* $^2J_{CF}$ = 17.3 Hz $^3J_{CF}$ = 1.8 Hz
	152.8 *(dd)* $^1J_{CF}$ = 257.3 Hz $^2J_{CF}$ = 15.4 Hz	115.1 *(dd)* $^2J_{CF}$ = 17.4 Hz $^3J_{CF}$ = 1.9 Hz

Table 2.2: *$^{13}C\{^1H\}$ NMR chemical shifts and J-couplings for **L^{10}H**, corresponding to carbon atoms on the fused benzene component of the quinoxaline; CDCl$_3$, 500 MHz.*

$^{19}F\{^1H\}$ NMR spectroscopy was carried out on the fluorinated compounds (**L^{2-} ^{10}H**) and some examples are shown in **Table 2.3**. By comparison of **L^{2}H** And **L^{3}H**, it was clear that fluorination directly on the quinoxaline resulted in a downfield shift of 5 – 6 ppm, indicating that these atoms were more deshielded than those on the phenyl ring. Doublets were seen for the difluorinated species with $^3J_{FF}$ couplings between 20– 22 Hz, consistent with literature.[47] The mono-fluorinated phenyl ring variants (**L$^{5-7}$H**) generated downfield-shifted singlet peaks – for example, **L^{6}H** displayed a singlet around ~25 ppm lower relative to its di-substituted analogue, **L^{3}H**. Likewise, **L^{8}H** presented an upfield chemical shift whilst displaying a triplet peak as a result of coupling with two equivalent fluorine atoms.

Compound	δ$_F$ / ppm
L^{2}H	−129.8 (d, $^3J_{FF}$ = 20.8 Hz) −130.9 (d, $^3J_{FF}$ = 20.8 Hz)
L^{3}H	−135.8 (d, $^3J_{FF}$ = 21.9 Hz) −136.4 (d, $^3J_{FF}$ = 21.3 Hz)
L^{6}H	-111.2 (s)
L^{9}H	-132.9 (d, $^3J_{FF}$ = 20.5 Hz) -158.2 (t, $^3J_{FF}$ = 20.5 Hz)

Table 2.3: *$^{19}F\{^1H\}$ NMR data for **L^{2}H, L^{3}H, L^{6}H** and **L^{9}H**, CDCl$_3$, 376 MHz.*

All NMR spectroscopy data was supported by HRMS and IR spectroscopy, where the obtained data were consistent with the theorised structures.

2.3.2: Synthesis and Characterisation of Complexes
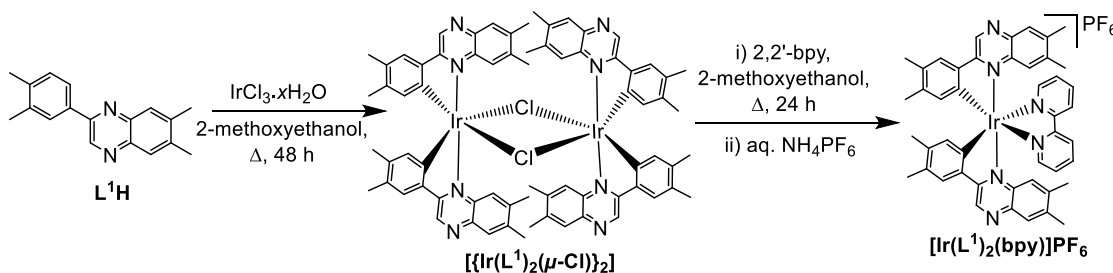
Scheme 2.2: *General synthetic approach for the preparation of **[Ir(L^1)$_2$(bpy)]PF$_6$**.*[48]

L$^{1-10}$H were subsequently studied as cyclometallating ligands on iridium, following the preparative procedure reported by Nonoyama.[48] The chloro-bridged dimeric species **[{Ir(L^n)$_2$(μ-Cl)}$_2$]** formed upon heating stoichiometric quantities of free ligand and IrCl$_3$.xH$_2$O in 2-methoxyethanol and water (3:1 v/v) for 48 hours. These were cleaved into monometallic, cationic Ir(III) complexes with the general formula **[Ir(L^n)$_2$(bpy)]$^+$** using 2,2'-bipyridine as the N^N-coordinating ancillary ligand. The splitting reaction was performed in either 2-methoxyethanol or chloroform, depending on the solubility of the dimer. This procedure is illustrated in **Scheme 2.2**, where the preparation of **[Ir(L^1)$_2$(bpy)]PF$_6$** is shown as an example.

The iridium complexes initially formed alongside a chloride counterion, but an anionic exchange was performed to isolate the compounds as PF$_6$ salts using a saturated aqueous NH$_4$PF$_6$ solution. This form was considered to be favourable since the hexafluorophosphate anion has a low coordination tendency,[49] desirable photophysical properties[50] and enhanced solubility in polar organic solvents. The change in solubility allowed some of the PF$_6$ forms of the complexes to precipitate out of aqueous solution, due to a higher degree of lipophilicity as a result of low charge density on the anion.

Purification was required for all complexes. Column chromatography was initially performed, where silica gel was used as the stationary phase in all instances. The mobile phase was either DCM:MeOH (9:1) or acetone followed by a solvent mixture of MeCN:H$_2$O:KNO$_3$ (*sat., aq.*) in a ratio of 14:2:1, where all products eluted as distinguishable red bands. The compounds were further purified by recrystallisation with DCM and Et$_2$O to give the pure samples as red or beige solids, where eight of the ten complexes were successfully isolated.

Despite multiple efforts at purification, **Ir-2c** and **Ir-2d** were not attainable. All structures are shown in **Figure 2.8**, and the isolated compounds were fully characterised by ^1H, $^{19}F\{^1H\}$, $^{13}C\{^1H\}$ NMR and IR spectroscopies along with HRMS. The synthetic yields ranged from low to moderate, with comparatively low product generation for the methylated quinoxaline species (**Ir-2a**, **Ir-2f** and **Ir-2i**) in relation to their fluorinated or unsubstituted counterparts.
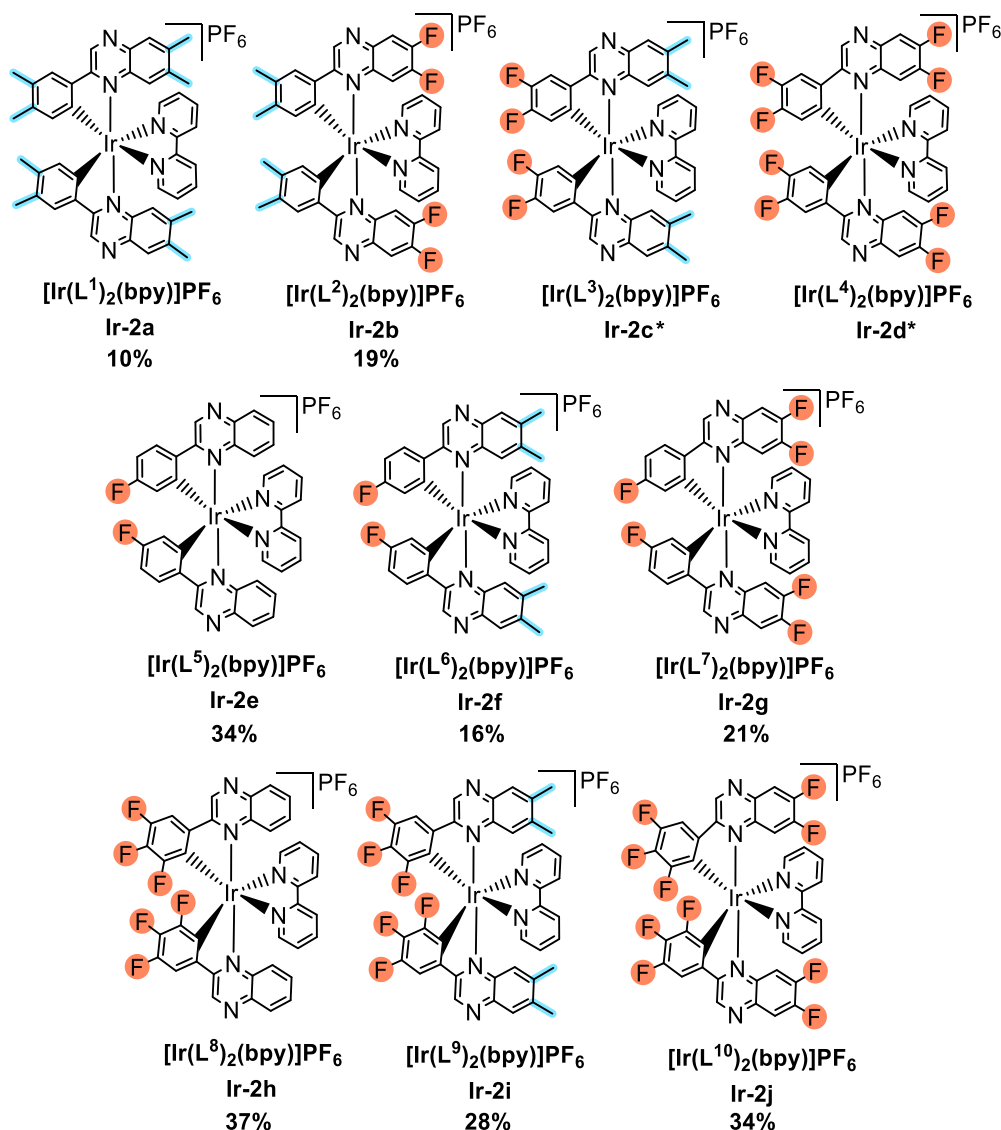
Figure 2.8: *Structures of the bis-cyclometallated cationic iridium complexes formed in this study. Experimental yields are provided below each complex. *Spectroscopically pure samples of **Ir-2c** and **Ir-2d** were unobtainable.*

^1H NMR data was collected for all complexes. 7 unique proton environments were seen in **L^{1}H** and 13 were detected in the corresponding complex **Ir-2a**, including 5 singlet resonances within the aromatic region. The overlaid aromatic

regions for **L¹H** and **Ir-2a** are displayed in **Figure 2.9**, where the integrations and peak positions shown relate to the complex.
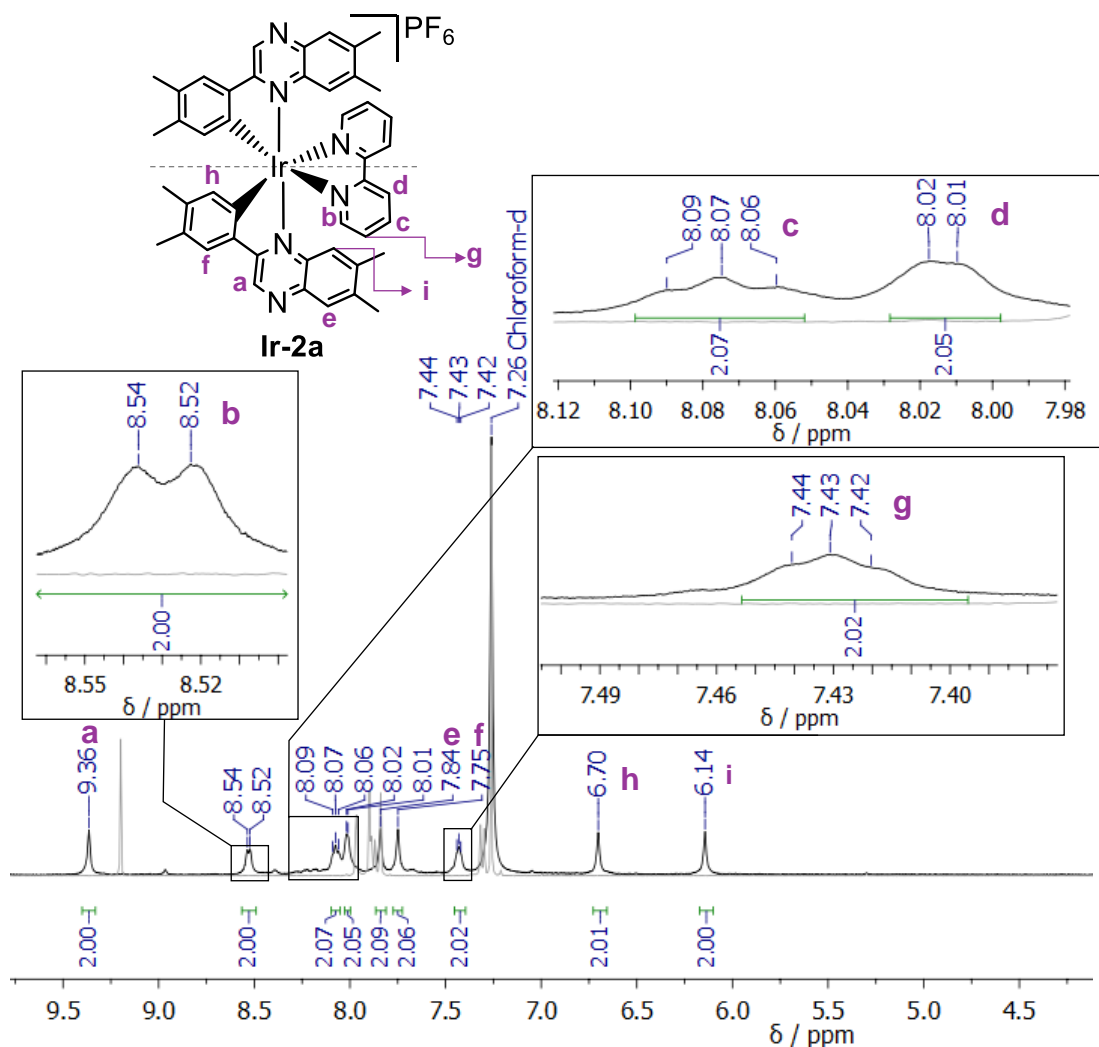
*Figure 2.9: Overlapped aromatic regions of **L¹H** (grey) (CDCl₃, 400 MHz) and the corresponding Ir(III) complex **Ir-2a** (black) (CDCl₃, 500 MHz) in the ¹H NMR spectra.*

All complexes possessed C₂ symmetry, represented by the dotted line in **Figure 2.9**, which is why 13 unique environments were observed in the spectrum for **Ir-2a** for a total of 42 protons in the chemical structure. The spectra for all isolated complexes indicated that only one isomer had formed and that only one coordination mode was present, consistent with previous reports on **[Ir(ppy)₂(bpy)⁺]**.[51] The proton at position **i** exhibited the lowest aromatic chemical shift value at 6.14 ppm, whereas the analogous position on **L¹H** was ~2 ppm higher. This significant upfield shift was a result of the proton becoming drastically shielded upon coordination due to the fixed orientation of the ligand, where the proton interacts directly with the π-system on the adjacent bpy ligand.

Additionally, the two singlets observed at close proximity in **L^{1}H** (δ_H = 7.84 and 7.90 ppm) relating to the protons on the benzene component of the quinoxaline, become much more chemically distinct upon complexation to form **Ir-2a** (δ_H = 7.85 and 6.14 ppm). This interaction can be seen in the X-ray crystal structure, which will be discussed in **Section 2.2.3**. A similar observation was made for the signal at 6.70 ppm in **Ir-2a**, which represented the proton adjacent to the site of cyclometallation (**h**). Here, the proton interacts with the aromatic system on the adjacent C^N ligand, promoting an upfield chemical shift value from 7.31 ppm in **L^{1}H** to 6.70 ppm in **Ir-2a**. This peak was present as a doublet in the free ligand, but upon deprotonation and subsequent cyclometallation at the adjacent position, it became a singlet. This was supported by the absence of this peak in the trifluorophenyl complexes (**Ir-2h**, **Ir-2i**, **Ir-2j**) and the presence of a similar peak in **Ir-2b** (δ_H = 6.12 ppm), supporting the suggested coordination mode.

As previously discussed, methylation at the quinoxaline resulted in two singlets with similar chemical shift values in the free ligands. In **L^{1}H**, these overlapped to produce one discernible peak correlating to 6 protons at 2.52 ppm. Upon cyclometallation, four unique singlets were seen in the aliphatic region between 1.75 – 2.33 ppm, where the methyl resonances became more chemically distinct, accompanied by an upfield chemical shift (**Figure 2.10**). The chemical shift range for the methyl peaks expanded from 2.36 – 2.53 ppm to 1.67 – 2.33 ppm upon complexation. This suggested that the protons within the methyl substituents experienced a considerable change in chemical environment upon complexation, primarily due to shielding effects. For example, the signals differ by 0.01 ppm in **L^{6}H**, but by 0.55 ppm in the corresponding complex, **Ir-2e**.

Compound	δ$_H$ / ppm (Ligand)	δ$_H$ / ppm (Complex)
L^{1}H	2.36, 2.40, 2.52 (6H, overlapping)	1.75, 1.95, 2.27, 2.33[b]
L^{2}H	2.37, 2.40	1.99, 2.29[b]
L^{3}H	2.52 (6H, overlapping)	*Not isolated*
L^{6}H	2.52, 2.53[a]	1.76, 2.31[c]
L^{9}H	2.52 (6H, overlapping)[b]	1.67, 2.17
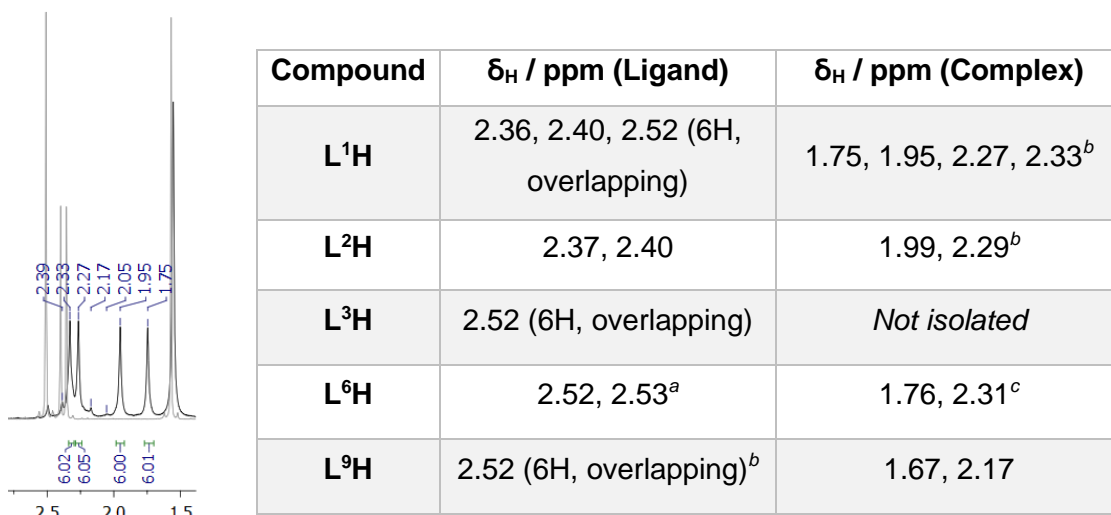
*Figure 2.10: (Left) Overlapped aliphatic regions of the ^{1}H NMR spectra of **L^{1}H** (grey) (CDCl$_3$, 400 MHz) and **Ir-2a** (black) (CDCl$_3$, 500 MHz). (Right) Methyl group resonances for the relevant free ligands and complexes. 400 MHz, CDCl$_3$, unless otherwise stated; ^{a}(CD$_3$)$_2$CO; ^{b}500 MHz; ^{c}CD$_3$CN.*

Some C-F couplings for the fluorinated complexes were observable in the measured ^{13}C{^{1}H} NMR spectra and were comparable to signals exhibited by the free ligands. For example, the doublet at 164.6 ppm in **L^{7}H** ($^1J_{CF}$ = 251.6 Hz) was consistent with a doublet seen at 165.3 ppm in **Ir-2g** ($^1J_{CF}$ = 257.5 Hz).

^{19}F{^{1}H} NMR spectra were obtained for all complexes, where an overall downfield shift was seen relative to the free ligands for the fluorinated systems. This deshielding effect was caused by the withdrawal of electron density from the ligand upon complexation. The resonances for the trifluorinated phenyl compounds were manifested as a doublet and a triplet in the free ligands (**L$^{8-10}$H**). These developed into three doublets of doublets upon coordination as a result of restricted rotation at the phenyl ring, inducing the chemical inequivalence of these fluorine atoms. The relevant ^{19}F{^{1}H} NMR data of the free ligands alongside their corresponding complexes are shown in **Table 2.4**. A doublet was also seen at ~ −73 ppm for all complexes, consistent with a PF$_6$ counterion, where a $^1J_{PF}$ coupling constant of between 706 – 712 Hz was measured. This, alongside experimental observations such as precipitation, suggested that all complexes were present as PF$_6$ salts and that the counterion exchange was successful. This was verified by IR spectroscopy, where strong

P-F stretching vibrations were present within the expected range of 830 – 851 cm^{-1} for all complexes.[52]

Compound	δ_F / ppm	
	Free Ligand	**Complex**
L^2	−129.9 (d) $^3J_{FF}$ = 21.1 Hz −131.0 (d) $^3J_{FF}$ = 21.1 Hz	−123.8 (d) $^3J_{FF}$ = 20.9 Hz −128.6 (d) $^3J_{FF}$ = 19.9 Hz
L^3	−135.8 (d) $^3J_{FF}$ = 21.7 Hz −136.4 (d) $^3J_{FF}$ = 21.9 Hz	*Not isolated*
L^4	−128.6 (d) $^3J_{FF}$ = 21.0 Hz −129.3 (d) $^3J_{FF}$ = 20.9 Hz −134.3 (d) $^3J_{FF}$ = 21.3 Hz −135.8 (d) $^3J_{FF}$ = 21.2 Hz	*Not isolated*
L^5	−110.5 (s)	−107.5 (s)^a
L^6	−111.2 (s)	−104.9 (s)
L^7	-109.8 (s) −129.2 (d) $^3J_{FF}$ = 21.1 Hz −130.1 (d) $^3J_{FF}$ = 21.1 Hz	-106.5 (s)^a −128.6 (d) $^3J_{FF}$ = 21.5 Hz −133.1 (d) $^3J_{FF}$ = 21.5 Hz
L^8	−132.62 (d) $^3J_{FF}$ = 20.5 Hz −157.48 (t) $^3J_{FF}$ = 20.5 Hz	−127.1 (dd) $^3J_{FF}$ = 21.8, $^4J_{FF}$ = 5.6 Hz^a −142.2 (dd) $^3J_{FF}$ = 18.9, $^4J_{FF}$ = 5.7 Hz −156.1 (dd) $^3J_{FF}$ = 21.8, $^3J_{FF}$ = 19.1 Hz
L^9	−132.9 (d) $^3J_{FF}$ = 20.5 Hz −158.2 (t) $^3J_{FF}$ = 20.6 Hz	−127.3 (dd) $^3J_{FF}$ = 22.0, $^4J_{FF}$ = 5.5 Hz^a −142.6 (dd) $^3J_{FF}$ = 18.9, $^4J_{FF}$ = 5.4 Hz −157.0 (dd) $^3J_{FF}$ = 21.8, $^3J_{FF}$ = 18.7 Hz
L^{10}	−128.07 (d) $^3J_{FF}$ = 20.8 Hz −128.51 (d) $^3J_{FF}$ = 20.8 Hz −132.27 (d) $^3J_{FF}$ = 20.4 Hz −156.74 (t) $^3J_{FF}$ = 20.5 Hz	−126.93 (dd) $^3J_{FF}$ = 22.3, $^4J_{FF}$ = 5.7 Hz^b −127.86 (d) $^3J_{FF}$ = 21.7 Hz −131.44 (d) $^3J_{FF}$ = 21.7 Hz −141.70 (dd) $^3J_{FF}$ = 19.2, $^4J_{FF}$ = 5.7 Hz −154.97 (dd) $^3J_{FF}$ = 22.2, $^3J_{FF}$ = 19.4 Hz

Table 2.4: *$^{19}F\{^1H\}$ NMR data for all free ligands and complexes, where necessary (376 MHz, CDCl$_3$, unless stated otherwise).^{a}CD$_3$CN; ^{b}(CD$_3$)$_2$CO.*

Electrospray ionisation (ES+) was the adopted technique for obtaining HRMS data for all complexes, where a [M]$^+$ molecular ion peak was generated. In all instances, the *m/z* peaks for all isolated complexes were consistent with the calculated theoretical masses and molecular formulae of the target compounds, where the PF$_6$ counterion had been omitted as the sample was measured in the gas phase. The HRMS data for **Ir-2f** and **Ir-2i** are shown in **Figure 2.11**.

Characteristic isotopic distribution patterns were seen for all complexes and can be attributed to the iridium atom, as iridium exists in two abundant isotopic forms; ^{191}Ir and ^{193}Ir. The peak corresponding to the heavier isotope, ^{193}Ir, is of greater intensity, due to its higher relative abundance.
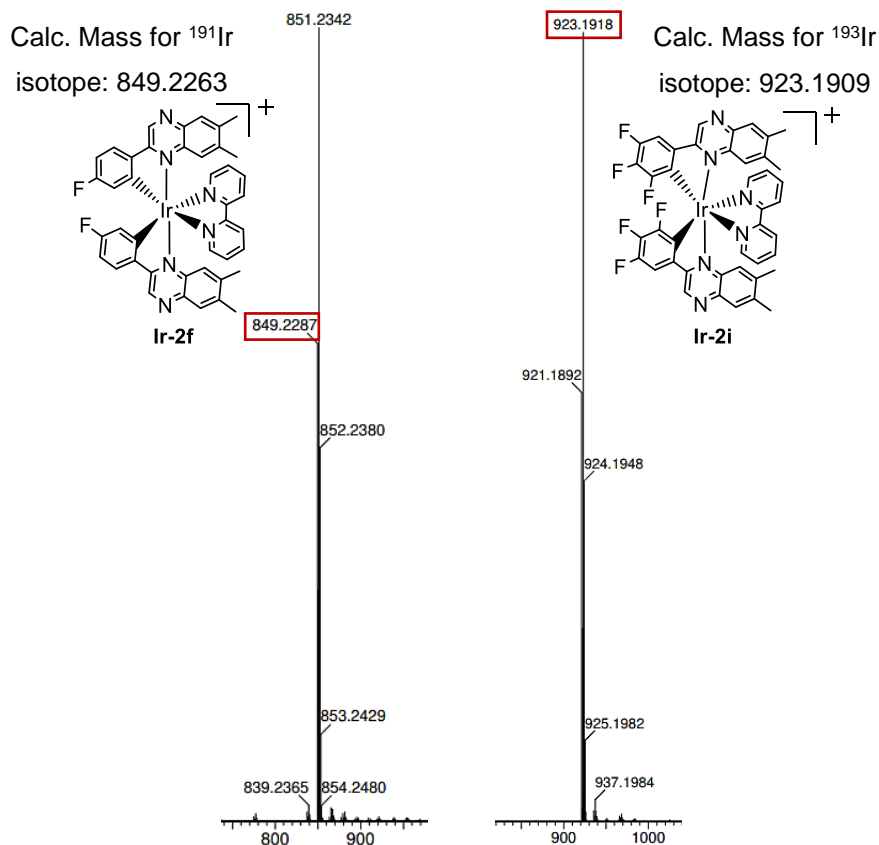
Figure 2.11: HRMS (ES+) of selected Ir complexes, displaying the characteristic isotopic pattern of the iridium atom. The peaks corresponding to the calculated masses are highlighted.

Ir-2c was not isolated, but crude ^{1}H NMR data provided insight into why this may have been the case. In other methylated quinoxaline complexes, the C$_2$ symmetry gave rise to two singlet resonances in the aliphatic region in the ^{1}H NMR spectra. However, four methyl signals (all distinct from the free ligand) were observed for **Ir-2c** and are shown in **Figure 2.12**. Although these peaks fell within the expected range of 2.31 and 1.76 (identical to **Ir-2f**), there were twice as many peaks as predicted from the chemical structure. Therefore, it was concluded that the product had been formed, but the sample contained a mixture of species. This was hypothesised to be a result of the formation of structural (or geometric) isomers and was supported by LRMS, where a *m/z* parent ion was seen at 887.21 – consistent with the molecular mass of the

proposed compound. The characteristic isotope pattern was also consistent with the formation of an iridium complex, where a lower intensity peak was seen at m/z = 885.21, corresponding to the [191]Ir isotope (**Figure 2.11**). Additionally, ^{19}F{^{1}H} NMR data collected for **Ir-2c** displayed multiple sets of resonances with peak positions that differed to the free ligand. Four sets of two doublets were observed between −127 and −143 ppm and an overall upfield shift was seen relative to the free ligand, as anticipated. Although various coordination species were present, the J-coupling values were consistent throughout, where doublets possessed $^3J_{HF}$ values of 20.7 – 23.2 Hz. Additionally, only one peak was seen for the PF$_6$ counterion and fell within the expected region at −73.0 ppm ($^1J_{PF}$ = 713 Hz). Similar observations were noted in attempts to isolate **Ir-2d**.
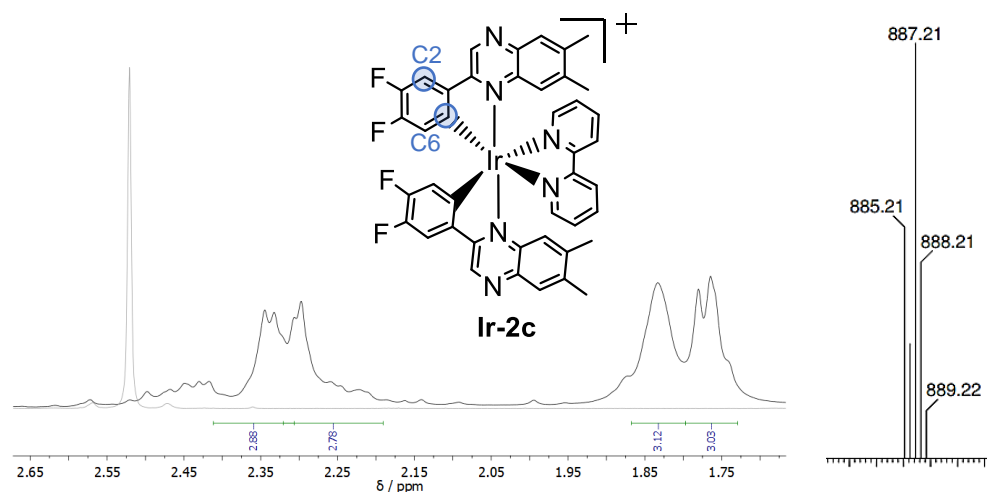
Figure 2.12: *(Left) Aliphatic region of overlapped ^1H NMR spectra of **L^{3}H** (grey, 400 MHz) and **Ir-2c** (black, 500 MHz) recorded in CDCl$_3$. (Right) LRMS (ES+) of **Ir-2c**.*

It was concluded that **Ir-2c** and **Ir-2d** were formed but were unable to be isolated due to various isomeric forms being present in the samples. TLC analysis showed that red-emissive species were present in both cases but were not able to be purified through chromatographic techniques due to co-elution. The mixture of products was ascribed to the two possible sites of *ortho*-metallation on the phenyl ring of **L^{3}H** and **L^{4}H** at the C2 and C6 positions (represented in **Figure 2.12**). Both positions were favourable in obtaining the dimeric species, as a five-membered chelate intermediate can be generated during cyclometallation in both instances, with little to no steric interference. **Ir-2a** and **Ir-2b** were formed without these issues arising, as only one structural variant

was detected. This was suggested to be the result of the methyl groups imparting steric bulk around these positions, whereas the small fluorine atoms failed to induce a preference.

2.3.3: X-Ray Crystallography

Single crystal X-ray diffraction (XRD) data was collected for **Ir-2a**, **Ir-2b**, **Ir-2e** and **Ir-2f**, where all data was congruent with the theorised structures of the complexes. Crystals of **Ir-2a**, **Ir-2b** and **Ir-2e** were grown *via* vapour diffusion techniques, where a saturated DCM or $CHCl_3$ solution of the complex was used with Et_2O as the antisolvent. Red cut shard-shaped, dark red, rod-shaped, and red plate-shaped single crystals were formed for **Ir-2a**, **Ir-2b** and **Ir-2e**, respectively. Orange block crystals of **Ir-2f** were grown by slow evaporation from MeCN. Subsequent single crystal X-ray diffraction data was collected by Dr. Peter N Horton of the UK National Crystallography Service at the University of Southampton, and the crystal structures of **Ir-2a** and **Ir-2f** are shown in **Figure 2.13**. The cationic complexes were accompanied by a PF_6 anion for achieving net neutrality, visible in all resolved structures.
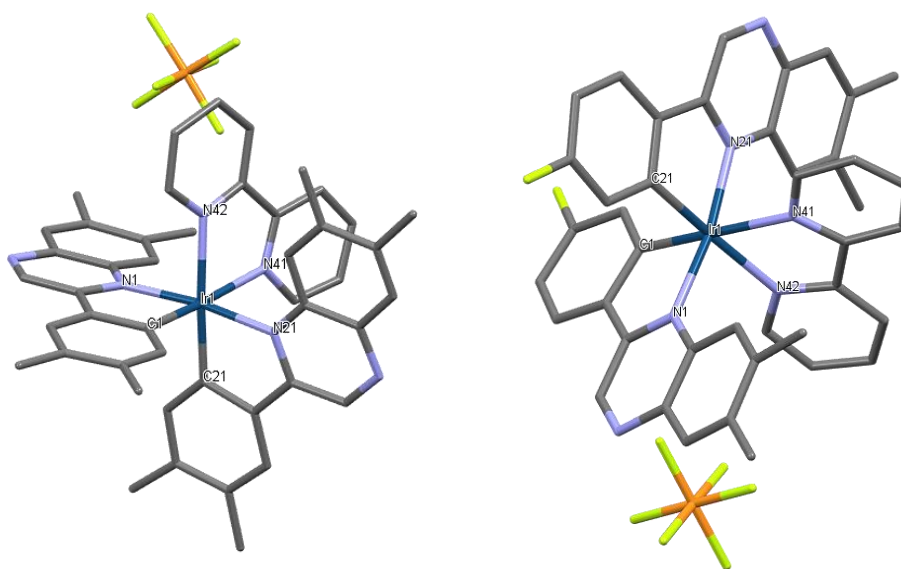
*Figure 2.13: X-ray single-crystal structures of **Ir-2a** and **Ir-2f**.*

Selected bond angles and lengths are shown in **Table 2.5** and are consistent with analogous Ir(III) systems.[27,53,54] The data showed that all complexes exhibited a distorted octahedral geometry with a N-Ir-N bond angle of 171-174°, and the cyclometallating ligands expectedly displayed *trans*-N,N and *cis*-C,C configurations relative to one another.[55,56] Ir-C bond lengths were shorter than

that of Ir-N, owing to a pronounced *trans influence* from the phenyl ring and a high degree of covalency. From these representations, the rationale behind the previous assignment of the upfield aromatic protons at positions **h** and **i** (δ_H = 6.70 and 6.14 ppm, respectively) for **Ir-2a** (**Figure 2.9**) is clearly depicted. These protons are highly shielded due to their close proximity to the π-system on the adjacent ligand and are positioned towards the centre of the complex.

Bond	Length / Å			
	Ir-2a	Ir-2b	Ir-2e	Ir-2f
Ir(1)-N(1)	2.100(8)	2.079(3)	2.068(4)	2.0890(18)
Ir(1)-N(21)	2.090(8)	2.080(3)	2.073(4)	2.093(2)
Ir(1)-N(41)	2.176(8)	2.161(3)	2.191(4)	2.1653(19)
Ir(1)-N(42)	2.148(8)	2.167(3)	2.159(4)	2.1412(19)
Ir(1)-C(1)	2.023(9)	1.992(3)	1.992(5)	2.006(2)
Ir(1)-C(21)	1.974(9)	2.017(3)	2.009(4)	2.009(2)

Bonds	Angle / °			
	Ir-2a	Ir-2b	Ir-2e	Ir-2f
N(1)-Ir(1)-N(41)	105.5(3)	102.99(10)	106.77(15)	105.77(7)
N(1)-Ir(1)-N(42)	84.8(3)	83.70(10)	85.55(14)	85.44(7)
N(21)-Ir(1)-N(1)	171.9(3)	173.30(10)	171.30(15)	171.01(7)
N(21)-Ir(1)-N(41)	81.2(3)	80.83(10)	79.61(15)	81.15(7)
N(21)-Ir(1)-N(42)	101.5(3)	102.66(11)	102.02(15)	102.00(8)
N(42)-Ir(1)-N(41)	75.3(3)	75.93(10)	75.04(15)	76.03(7)
C(1)-Ir(1)-N(1)	79.4(4)	79.50(12)	79.77(16)	79.54(8)
C(1)-Ir(1)-N(21)	94.6(4)	97.76(12)	95.04(17)	94.32(8)
C(1)-Ir(1)-N(41)	171.3(3)	169.35(11)	168.05(16)	171.33(8)
C(1)-Ir(1)-N(42)	98.3(3)	94.19(11)	95.87(16)	97.86(8)
C(21)-Ir(1)-N(1)	94.1(3)	94.65(12)	93.25(16)	93.10(9)
C(21)-Ir(1)-N(21)	80.5(3)	79.37(13)	79.96(17)	80.13(9)
C(21)-Ir(1)-N(41)	96.0(3)	96.31(12)	96.60(17)	97.53(8)
C(21)-Ir(1)-N(42)	170.5(3)	171.41(12)	170.75(15)	172.69(8)
C(21)-Ir(1)-C(1)	90.8(3)	93.78(13)	92.93(17)	88.91(9)

*Table 2.5: Selected bond lengths (above) and angles (below) for the crystal structures of **Ir-2a**, **Ir-2b**, **Ir-2e** and **Ir-2f**.*

As expected, cyclometallation occurred at the C6 position for **Ir-2a** and **Ir-2b**, minimising steric repulsion from the methyl substituents. This supported the previous discussion of isomer formation for **Ir-2c** and **Ir-2d** since fluorine has a Van der Waals atomic radius (1.47 Å) comparable to H (1.20 Å) and therefore would not impose significant steric influence.[57]

Additionally, one of the methyl substituents at the quinoxaline for **Ir-2a** were situated at a position directly adjacent to the plane of the bipyridine ancillary ligand. Distances of 4.319 Å from C17 to the centroid in the C41-N41 ring, and 3.945 Å from C37 to the centroid in the C46-N42 ring were measured, illustrating the enhanced electronic shielding imparted on the methyl group closest to the metal centre (**Figure 2.14**). The C-Ir-C bond angles are 130.48° and 126.78°, representing the geometry and fixed orientations of these ligands.
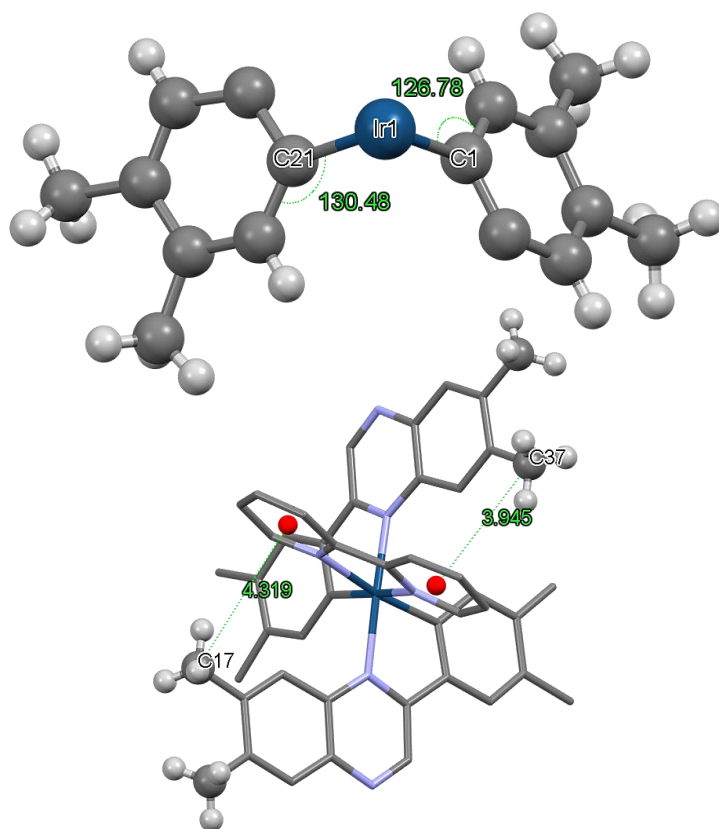
Figure 2.14: C-Ir-C bond angle (above) and interaction of the methyl substituents with the adjacent π-system on the bipyridine ligand (below) for Ir-2a.

2.3.4: Photophysical Properties

UV-vis absorption spectroscopy data was collected for all isolated compounds. The absorption profiles of the free ligands **L$^{1-10}$H** were measured in *ca.* 10^{-5} M aerated acetonitrile solutions at room temperature and are shown in **Figure 2.15**. The organic chromophores absorbed light within the UV range and all absorption bands were below 375 nm – indicative of π→π* transitions due to their high molar extinction coefficients. Theoretically, n→π* transitions were also possible due to the presence of heteroatoms, however, the inherently low ε values associated with these transitions (due to their symmetry-forbidden nature) were not reflected in these instances. At least two identifiable transitions were present in each case, suggested to be representative of the various aromatic units within each compound.
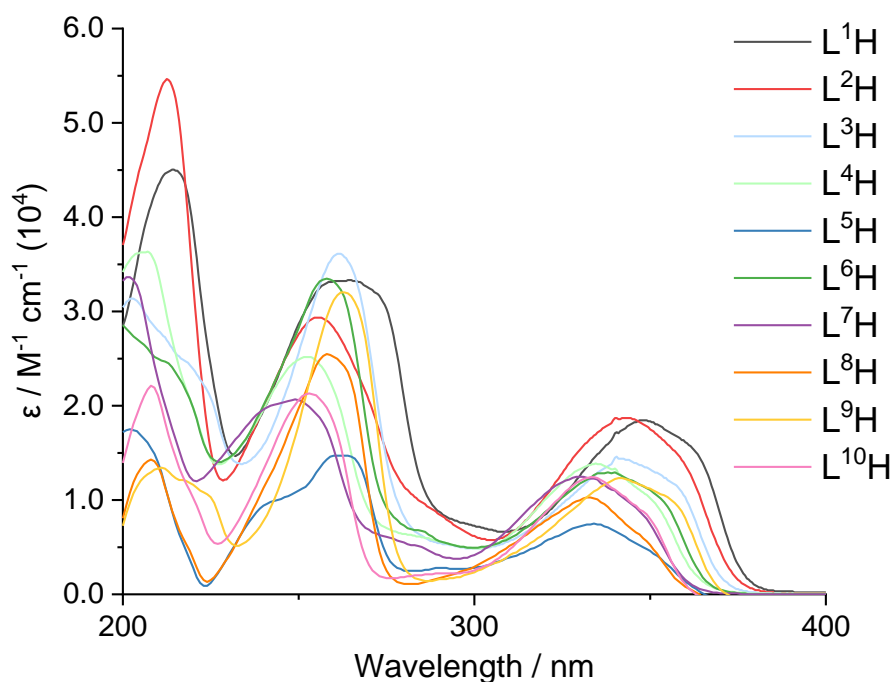
Figure 2.15: *UV-vis absorption spectra of the free ligands **L$^{1-10}$H** (MeCN, RT). Concentrations (in 10^{-5} M) of; 0.95 (**L^{1}H**), 0.92 (**L^{2}H**), 0.88 (**L^{3}H**), 1.11 (**L^{4}H**), 1.00 (**L^{5}H**), 1.01 (**L^{6}H**), 1.03 (**L^{7}H**), 0.99 (**L^{8}H**), 0.99 (**L^{9}H**), 0.99 (**L^{10}H**).*

The nature and position of the substituents on each ligand had a significant impact on the electronic behaviour and resultant absorption properties. Methylation at the phenyl ring imposed a bathochromic shift in absorption wavelength for the lowest energy band along with an enhancement in molar absorptivity, where λ$_{max}$ peaks were seen at 349 and 343 nm for **L^{1}H** and **L^{2}H**, respectively. Adversely, the extent of fluorination on the phenyl ring resulted in

little influence on these absorption features, where **L⁵H** and **L⁸H** both displayed λ_{max} values at 333 nm. The shortest λ_{max} was seen for **L⁷H** at 329 nm, indicating that fluorination at the quinoxaline promoted a small bathochromic shift in λ_{abs}, with less of an impact on absorption features in comparison to methylation. Interestingly, **L⁹H** exhibited a small bathochromic shift compared with **L⁶H**, suggesting that the amount of fluorination becomes more impactful upon methylation of the quinoxaline.

Steady state luminescence spectroscopy measurements were performed for the free ligands in the same solutions. Emission maxima were found within the visible range between 394 – 407 nm, and the normalised emission profiles are shown in **Figure 2.16**.
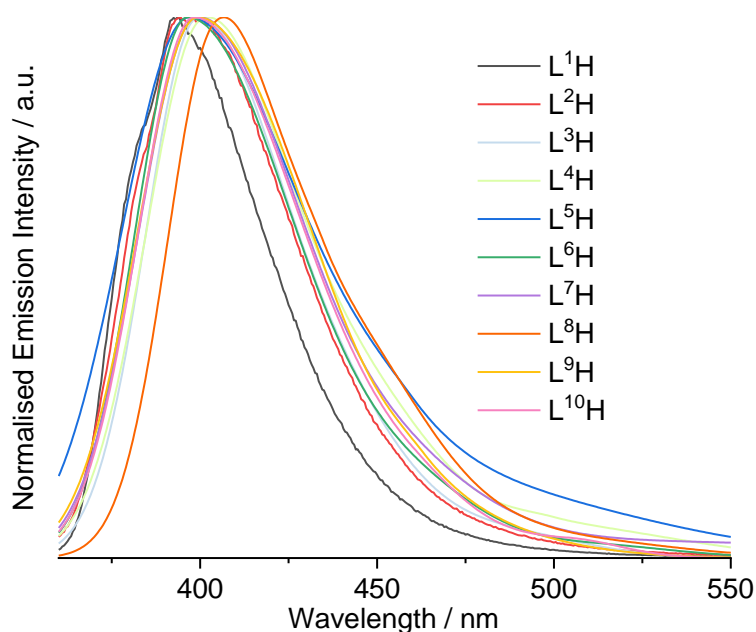
*Figure 2.16: Normalised emission spectra of **L¹⁻¹⁰H** in aerated MeCN solutions (ca. 10⁻⁵ M, RT, λ_{ex} = 350 nm). Emission for **L³⁻¹⁰H** was weak and MeCN scattering dominated – therefore, non-linear curve fitting using the fityk program was applied to determine λ_{max}.[84]*

Absorption and emission data for **L¹⁻¹⁰H** is tabulated in **Table 2.6**, summarising the key photophysical features of the organic compounds. Although emission was weak, luminescence lifetimes were measured within the nanosecond domain and were indicative of a fluorescence decay pathway.

Ligand	λ_{abs} / nm ($\varepsilon \times 10^4$ / M^{-1} cm^{-1})	λ_{em} / nm[a]
L^1H	214 (4.5), 265 (3.3), 349 (1.8)	394
L^2H	213 (5.5), 256 (2.9), 343 (1.9)	398
L^3H	203 (3.1), 262 (3.6), 343 (0.1)	401
L^4H	207 (3.6), 253 (2.5), 335 (1.4)	403
L^5H	202 (1.8), 262 (1.5), 334 (0.8)	398
L^6H	213 (2.4), 258 (3.3), 340 (1.3)	397
L^7H	202 (3.7), 249 (2.1), 331 (1.2)	400
L^8H	208 (1.4), 258 (2.5), 333 (1.0)	407
L^9H	211 (1.3), 263 (3.2), 342 (1.2)	401
$L^{10}H$	208 (2.2), 253 (2.1), 334 (1.2)	399

Table 2.6: Absorption and emission properties of $L^{1-10}H$, measured in aerated MeCN (ca. 10^{-5} M, RT). [a] λ_{ex} = 350 nm.

Photophysical measurements were also carried out for the resultant complexes (**Ir-2a** – **Ir-2j**). These were once again measured in *ca.* 10^{-5} M aerated acetonitrile solutions under ambient conditions and the absorption profiles of all isolated complexes are presented in **Figure 2.17**, where three distinct regions were recognised. Firstly, high energy absorption bands were seen between 230 – 320 nm and were indicative of ligand-centred (^{1}LC) π→π* transitions, where the high molar absorption coefficients were consistent with a spin-allowed process. Additionally, the high intensities of these bands reflected those observed in the free ligand spectra between 220 – 280 nm, where perturbations occur upon complexation.

The peaks at 320 – 400 nm were also assigned as π→π* transitions (consistent with the benchmark complex **[Ir(ppy)₂(bpy)]⁺**) but with enhanced aromatic character from the quinoxaline.[12] An additional low energy feature between 439 – 518 nm arose upon coordination – these were relatively low in intensity with epsilon values of up to ~7000 M^{-1} cm^{-1}, and were assigned as an MLCT contribution. This is a commonly observed facet in these kinds of systems and the broad nature of this peak has been ascribed to the two contributions that are within it, including a formally spin-allowed ^{1}MLCT transition of higher intensity, and a weak, spin-forbidden contribution to a ^{3}MLCT excited state. The

accessibility of the latter state is influenced by the iridium atom itself, which promotes ISC through efficient spin-orbit coupling as a result of its large spin-orbit coupling constant (ξ = 3909 cm^{-1}).[58] This is a consequence of the considerable atomic size of the iridium atom, where the heavy atom effect reinforces the relaxation of this process and increasing the probability of this transition enables a phosphorescent decay pathway. Interestingly, this signal appeared to be most sensitive to the structural variations within the C^N ligands, as the position and shape varied drastically between each complex. Methylation at the phenyl ring promoted a significant bathochromic shift in λ_{abs} for the assigned MLCT band, as seen in **Ir-2a** and **Ir-2b**, whereas a blue-shift is detected upon fluorination at the phenyl ring. Conversely, fluorination at the quinoxaline resulted in a slight red-shift in this feature relative to the methylated variants. This trend was consistent with previous spectroscopic analyses on similar systems.[59]
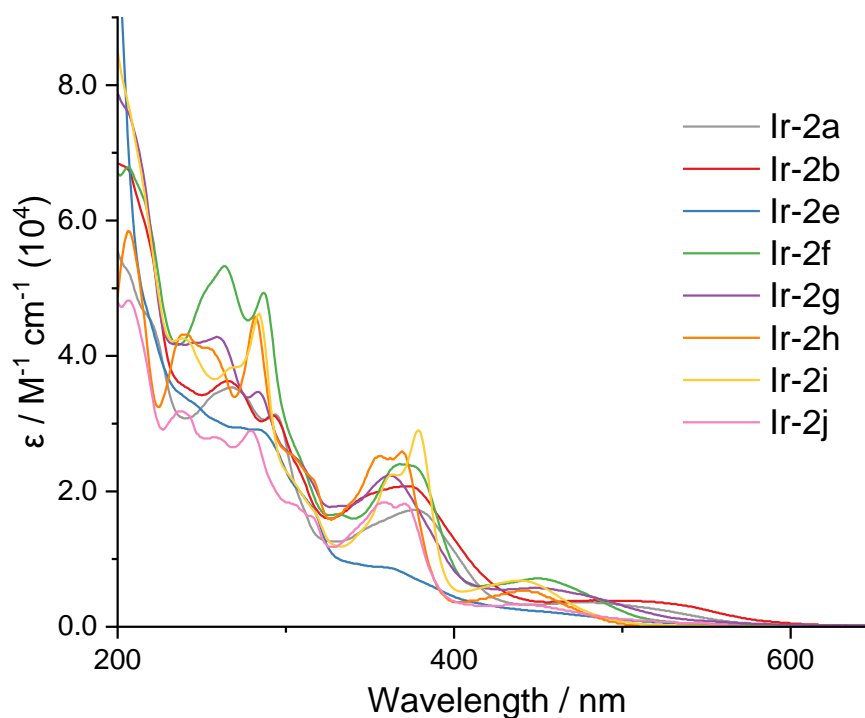
Figure 2.17: *UV-vis absorption spectra of all the Ir(III) complexes (MeCN, RT). Concentrations (in 10^{-5} M) of; 0.94 (**Ir-2a**), 1.06 (**Ir-2f**), 0.99 (**Ir-2b, Ir-2e, Ir-2g, Ir-2h, Ir-2i, Ir-2j**).*

The absorption spectra of **L^{10}H** and its corresponding iridium complex (**Ir-2j**) are directly compared in **Figure 2.18**. The low energy signal at >430 nm was only observable for **Ir-2j** and its absence in the corresponding free ligand profile reinforces the postulation that this is of MLCT character. Here, the two contributions within this signal are discernible, where the 'tail' feature suggested the presence of a spin-forbidden triplet excited state. Incorporation of the metal also impacts the ligand-centred transitions, where a clear bathochromic shift of ~38 nm is induced.
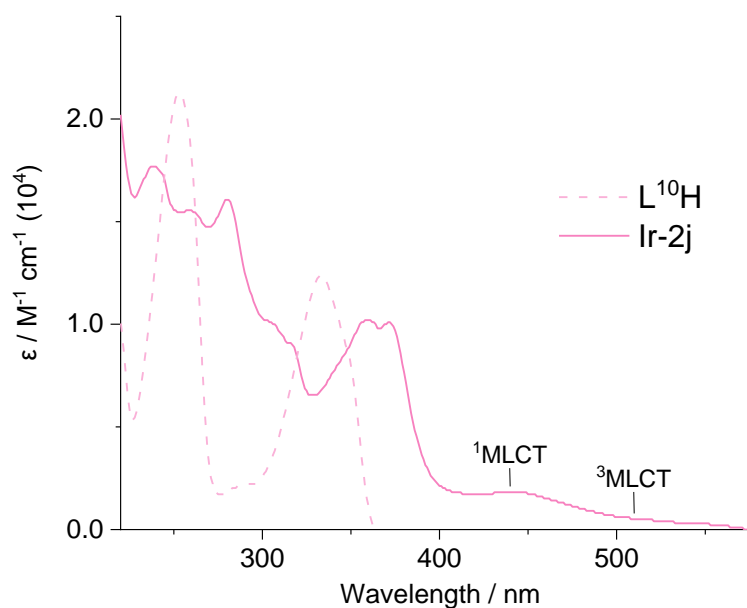
Figure 2.18: *Comparison of UV-vis absorption spectra of **L^{10}H** and **Ir-2j**, both in aerated MeCN (ca. 10^{-5} M, RT). The assigned MLCT contributions have been assigned.*

Steady state emission data was also collected for all iridium complexes in acetonitrile solutions (**Figure 2.19**). An λ_{ex} of 450 nm was applied invariably to gain access to the lowest energy transitions observed in the corresponding absorption profiles, previously assigned as MLCT states. Emission properties were reliant upon the position and electronic character of the substituents incorporated into the phenylquinoxaline ligands, suggesting that they had a profound effect on the nature of the excited states. The complexes gave rise to broad emission profiles within the range of 579 – 655 nm, allowing tunability throughout the yellow, orange, and red regions of the visible range in accordance with previous studies on similar structural motifs.[60] Notably, trifluorinated phenyl donors in Ir(III) systems are limited in the literature, where they have been mostly incorporated into ppy-type ligand systems. [61,62]
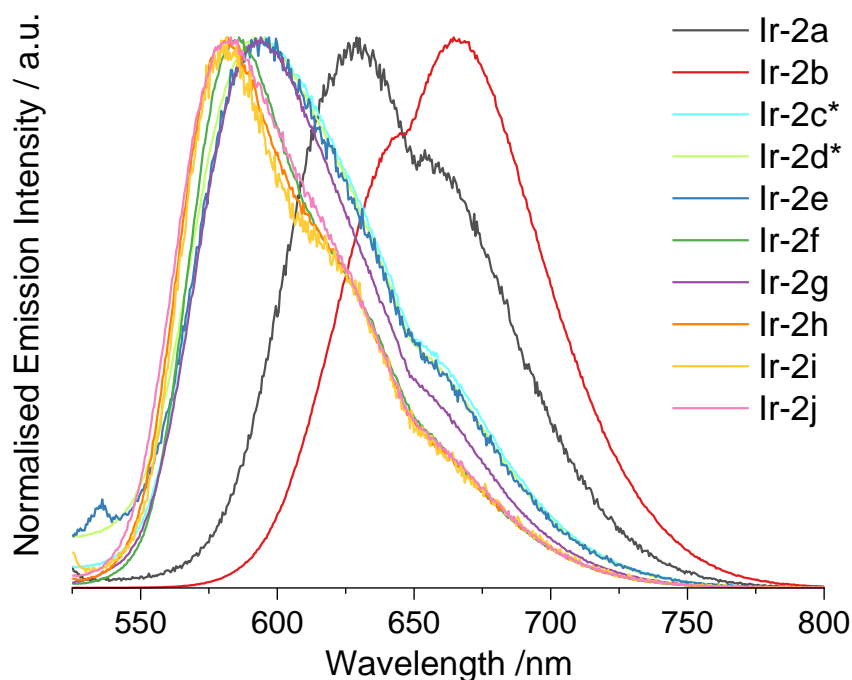
Figure 2.19: *Normalised emission spectra for all iridium complexes in aerated MeCN solutions (10^{-5} M, RT), $\lambda_{ex}= 450 – 490$ nm. ***Ir-2c** and **Ir-2d** were crude.*

Consistent with trends seen in the absorption profiles, the complexes with methylated quinoxaline ligands displayed a bathochromic shift in emission where **Ir-2b** exhibited the longest λ_{em} at 655 nm, succeeded by **Ir-2a** with an λ_{em} of 628 nm. Fluorinated analogues **Ir-2c** – **Ir-2j** displayed peak maxima at wavelengths shorter than 595 nm, demonstrating an overall hypsochromic shift in λ_{em} relative to the methylated variants. Generally, substitution at the phenyl ring prompted a significant shift in λ_{em}, whereas fine tunability was achieved by altering the nature of the substituents at the quinoxaline. This offered scope for excellent colour-tunability, where simple modifications at different sites on the phenylquinoxaline ligand scaffold induced both subtle and significant changes to the photophysical behaviour, whilst maintaining low-energy emission.

The characteristic luminescence profiles for each complex were attributed to the nature of the excited state where emission originated. **Ir-2a** and **Ir-2b** presented broader and more featureless peaks than the bands at shorter wavelengths, suggesting phosphorescence primarily from a ^{3}MLCT excited state. Vibronic features and sharper bands in the hypsochromically-shfited complex spectra proposed a more significant contribution from the ligand-centred $^3\pi$-π^* excited state.[63] This was suggested to be a result of reduced σ-donation from the

carbon atom due to the presence of EWGs (*i.e.* fluorination) at the phenyl ring, destabilising the ^{3}MLCT state.[13] This was supported by computational studies, which will be discussed in **Section 2.3.5**.
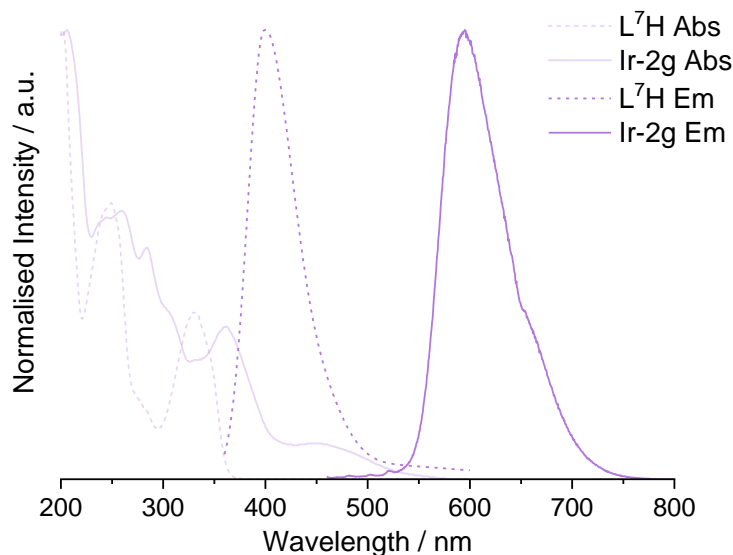
Figure 2.20: *Normalised absorption and emission spectra of **L^{7}H** (dotted) and **Ir-2g** (solid) measured in aerated MeCN solutions (10^{-5} M, RT).*

The absorption and emission spectra of **L^{7}H** and the corresponding complex, **Ir-2g**, are presented in **Figure 2.20**. The magnitude of Stokes' shift increased drastically from 69 to 145 nm upon complexation. This was expected, since an enhancement of SOC and subsequent crossing into the triplet state results in an energy stabilisation effect by minimised electronic repulsion of the unpaired electrons, thereby increasing the wavelength of emission.[64]

Low temperature (77 K) emission data was collected for **Ir-2a** and **Ir-2f** (3:1 EtOH/MeOH, glass) (**Figure 2.21**). At reduced temperatures, the ligand-centred contribution becomes more significant, resulting in an apparent blue-shift in emission and accessibility of the ^{3}MLCT state becomes significantly reduced.
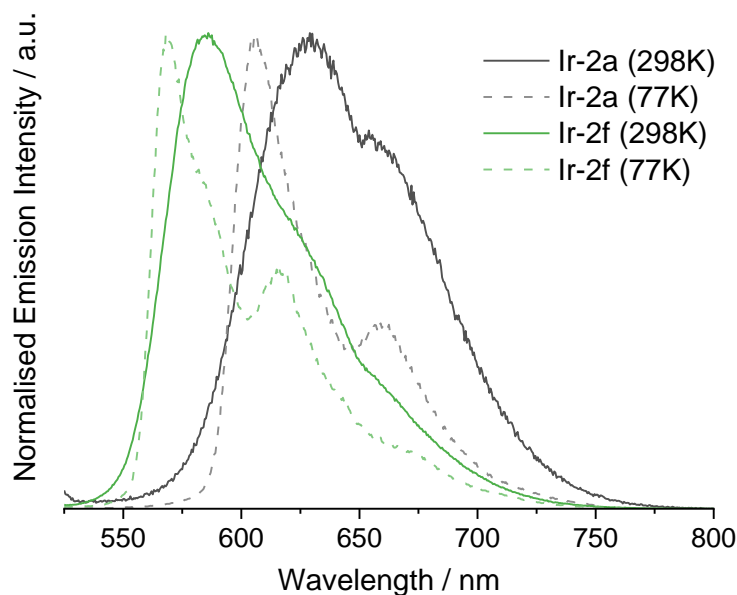
Figure 2.21: *Normalised emission spectra for **Ir-2a** and **Ir-2f** at RT (298 K, MeCN, λ_{ex}= 450 nm) and low temperature (77 K, 3:1 (v/v) EtOH:MeOH, glass, λ_{ex}= 400 nm).*

The photophysical properties of the complexes are summarised in **Table 2.7**. Time-resolved luminescence experiments were measured relative to the unique λ_{em} for each complex and revealed luminescence lifetimes (τ_{obs}) within the sub-microsecond domain between 215 – 747 ns in oxygenated solutions. Degassed samples of the complexes were also measured by Haleema A. Otaif and Dr Joseph Beames at Cardiff University. As anticipated, deoxygenated samples displayed a significant enhancement of lifetimes,[65] where all complexes were measured within microsecond domain in the range of 659 ns – 6.518 μs. The disparities between these values were alluded to the presence of $^3O_2$, where collisional quenching and energy transfer from the emissive triplet state to molecular oxygen diminished the observed lifetimes.[66] Φ_P values of up to 11% were achieved in aerated solutions, comparatively high for red-emissive species of this nature.[13,29] This offers potential in biological applications,[67] where high quantum yields in oxygenated solutions are favourable. These attributes were indicative of a phosphorescent decay pathway for all species, where the dominant emissive state was suggested to be of ^{3}MLCT character with some contribution from ^{3}LC states.

The photophysical properties of **[Ir(ppy)₂(bpy)]PF₆** are comparable to the complexes **Ir-2a** – **Ir-2i**, making it a suitable standard for reference, where emission is centred at 602 nm, with Φ_P = 9.3% and τ_{obs} = 275 ns in acetonitrile

solution.[58] It has been concluded that emission from **[Ir(ppy)₂(bpy)]PF₆** occurs from a mixture of low-lying ^{3}LLCT and ^{3}MLCT states,[68] supporting the previous assignment of mixed ^{3}MLCT/^{3}LC phosphorescence.

Complex	λ_{abs} / nm ($\varepsilon \times 10^4$ / M⁻¹ cm⁻¹)	λ_{em}/ nm[a]	Φ_P[b]	τ_{obs}/ ns[c]	τ_{obs}/ ns[d]	$\Delta\lambda$ / nm[e]
Ir-2a	219 (4.5), 267 (3.5), 294 (3.1), 378 (1.7), 486 sh (3.5)	628	0.03	253 (2691)	1886	143
Ir-2b	206 (6.8), 266 (3.6), 292 (3.1), 373 (2.1), 518 sh (0.4)	655	0.01	215 (2362)	659	137
Ir-2c*	-	595	-	352 (-)	-	-
Ir-2d*	-	594	-	510 (-)	-	-
Ir-2e	249 (3.2), 288 (2.9), 359 (0.9), 460 sh (0.2)	590	0.04	430 (1795)	3416	130
Ir-2f	206 (6.8), 263 (5.3), 287 (4.9), 372 (2.4), 452 sh (0.7)	585	0.08	446 (3636)	4872	135
Ir-2g	259 (4.3), 284 (3.5), 362 (2.2), 451 sh (0.6)	594	0.09	571 (4210)	1387	145
Ir-2h	207 (5.8), 240 (4.3), 282 (4.6), 356 (2.5), 370 (2.6), 444 sh (0.5)	579	0.08	747 (4818)	5322	137
Ir-2i	240 (4.3), 284 (4.6), 362 (2.2), 379 (2.9), 440 sh (0.7)	584	0.10	612 (5184)	6518	145
Ir-2j	206 (4.8), 239 (3.2), 280 (2.9), 360 (1.8), 371 (1.8), 441 sh (0.3)	583	0.11	535 (4306)	1446	143

Table 2.7: Photophysical data for the complexes in aerated MeCN (10^{-5} M, RT). [a]λ_{ex}= 450 nm; [b][Ru(bpy)₃](PF₆)₂ in MeCN (Φ = 0.016)[69] used as standard for quantum yield determination, λ_{ex}= 450 nm; [c]λ_{ex}= 295nm or 355 nm, values in parentheses at 77 K in MeCN glass; [d]Degassed, λ_{ex}= 295nm or 355 nm; [e]Stokes' shift.

Methylation at the phenyl ring afforded red-shifted emission bands when compared with the benchmark complex **[Ir(ppy)₂(bpy)]PF₆** (as seen in **Ir-2a** and **Ir-2b**), alongside a reduction in Φ_P and τ_{obs} values. This was consistent with the energy gap law, which states that the rate of non-radiative decay processes (k_{nr}) increases rapidly as the gap between the ground and excited electronic states decreases.[27,70] This disposition can be directly monitored by calculated k_r and k_{nr} rate constants, shown in **Table 2.8**. Overall, the radiative decay rate (k_r) is lowest for the most red-shifted complex **Ir-2b**, supported by perturbation theory

analysis which concludes that k_r is proportional to the square of the energy of emission in a phosphorescent system.[3] However, the overall trend is less obvious since k_r is also dependent on the nature and relative energies of the excited states. The trend for methylation at the quinoxaline was less significant, where only subtle deviations in emission maxima were measured when compared with the unsubstituted quinoxalines. For example, λ_{em} was shorter by 5 nm for **Ir-2f** when compared with **Ir-2e**, whereas λ_{em} was 5 nm longer for **Ir-2i** when compared with **Ir-2h**.

	$k_r / s^{-1} (10^5)$	$k_{nr} / s^{-1} (10^5)$
Ir-2a	1.19	0.38
Ir-2b	0.47	0.46
Ir-2e	0.93	0.22
Ir-2f	1.79	0.21
Ir-2g	1.58	0.16
Ir-2h	1.07	0.12
Ir-2i	1.63	0.15
Ir-2j	2.06	0.17

Table 2.8: Calculated radiative and non-radiative decay rate constants for the complexes.

2.3.5: Density Functional Theory

Computational studies for this chapter were performed by Haleema A. Otaif and Dr Joseph Beames at Cardiff University. The B3LYP functional with a 6-31G* basis set was applied in all cases to obtain the optimised ground state structures, where a SDD effective core potential (ECP) basis set was used for the iridium atom. Time dependent DFT (TD-DFT) calculations were performed with use of the CAM-B3LYP functional on the optimised structures, and acetonitrile solvent correction was implemented in accordance with the spectroscopic measurements.

Firstly, the XRD structures (**Section 2.3.3**) were overlaid with computationally optimised structures (**Figure 2.22**) for **Ir-2a** and **Ir-2b**. The geometries of the calculated minimum energy structures obtained through DFT analysis are in excellent agreement with the crystallographic data.

Figure 2.22: *Overlaid X-ray crystallographic structure (blue) and computationally optimised structure (brown) obtained by DFT analysis (B3LYP/ 6-31G*(SDD)) for **Ir-2a** (left) and **Ir-2b** (right).*

Previous theoretical studies on **[Ir(ppy)₂(bpy)]⁺** state that the HOMO is localised over the d_π (t_{2g}) orbitals on the metal centre and the π-orbitals on the phenyl ring of the ppy ligand, whilst the LUMO typically resides almost entirely on the N^N ancillary ligand.[71–74] Therefore, the rationale behind the ligand design for the complexes discussed in this study is based upon altering the energy of the HOMO, whilst ensuring that the ancillary ligand remains constant.

Molecular orbital (MO) decomposition calculations were performed on each isolated complex, where the major contributions towards the MOs of the complex were established. These are illustrated in **Figure 2.23** by the calculated Kohn-Sham frontier molecular orbitals, where **Ir-2h** is displayed as an example, and are quantified for all complexes in **Table 2.9**. The data showed that the relative contributions remained reasonably consistent throughout the series, where the HOMO comprised of almost equal contributions from the iridium centre (32 – 35%) and the C^N ligands (31 – 63%) with negligible contribution from the N^N ligand (2%). These contributions are indicative of a T_1 emissive state possessing mixed MLCT and ILCT character, respectively, and is consistent with the benchmark complex.[72]
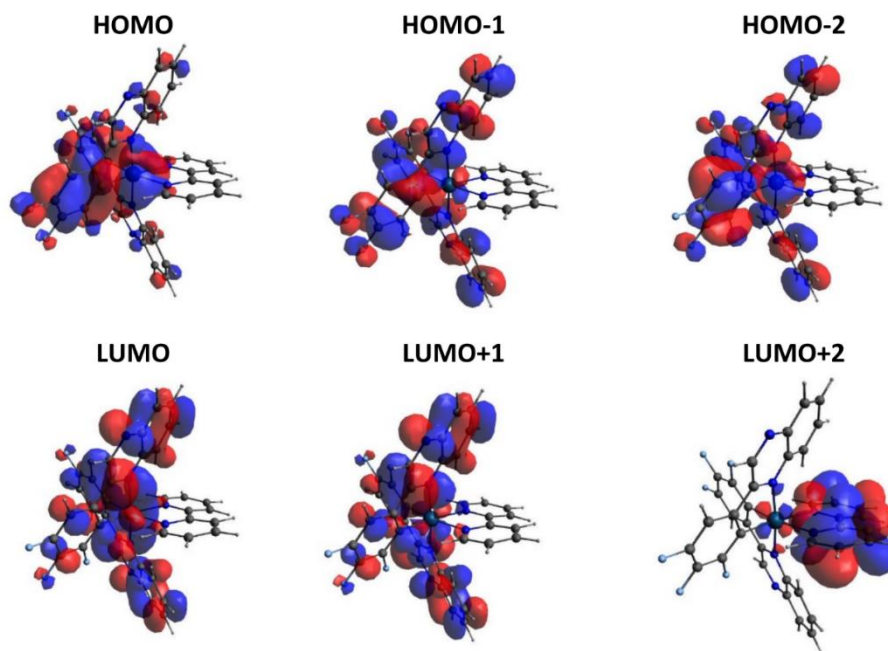
Figure 2.23: *Selected calculated Kohn-Sham frontier molecular orbitals for **Ir-2h**, illustrating the relative contributions displayed in **Table 2.9**.*

In contrast to **[Ir(ppy)₂(bpy)]⁺**, the LUMO resides exclusively on the heterocyclic moieties of the C^N ligands, leading to low-lying excited states (attributed to the absorption bands at λ_{max} in the UV-vis spectra). Slight discrepancies in contributions to the LUMO and LUMO+1 resulted in the observed *pseudo-*degeneracy of these unoccupied states. The bipyridine ligand is almost exclusively contributing to the LUMO+2 (>95%) in all cases rather than the LUMO, as seen in **[Ir(ppy)₂(bpy)]⁺**.[73] This suggested that the emissive state possesses more LC (C^N) character, with minimal contribution from the bipyridine ligand due to inaccessibility of higher-energy states upon excitation. Experimental data for the complexes exemplified this by the presence of highly structured emission profiles and enhanced k_r values.[73]

Complex	Ir 5d		(Lⁿ)1				(Lⁿ)2				bpy
	HOMO -1	HOMO	LUMO	LUMO +1	HOMO	HOMO - 1	LUMO	LUMO + 1	HOMO	HOMO -1	LUMO + 2
Ir-2a	4	32	50	44	33	47	44	50	33	47	95
Ir-2b	4	32	63	31	33	47	31	64	33	47	96
Ir-2e	8	35	48	48	32	46	47	48	32	46	96
Ir-2f	5	32	50	45	33	47	45	50	33	47	96
Ir-2g	6	33	41	54	32	47	54	41	32	47	96
Ir-2h	4	34	48	47	32	48	47	48	32	48	97
Ir-2i	2	32	48	47	33	49	46	47	33	49	97
Ir-2j	2	33	47	48	33	49	48	48	33	49	96

Table 2.9: *Calculated relative contributions to the frontier molecular orbitals of the complexes. (Lⁿ)1 and (Lⁿ)2 are representative of the two independent C^N ligands.*

TD-DFT calculations were carried out to complement the experimental data in investigating the effect of substitution at the ligands on the optical and electronic properties of the subsequent complexes (**Table 2.10**). Calculated peak positions were congruent with spectroscopic measurements and supported previous assignments. For example, the calculated λ_{abs} values relating to the $S_0 \rightarrow T_1$ transitions in all complexes were consistent with the tail ends of the weak broadened features in the corresponding UV-vis spectra, previously assigned as a ^{3}MLCT feature.

HOMO-LUMO energy gaps were calculated to evaluate the electronic behaviour of the complexes. It was established that substitution at the phenyl ring rendered greater influence on the stability of the HOMO and LUMO compared to substitution at the quinoxaline, consistent with the trends seen in the spectroscopic measurements discussed in **Section 2.3.4**. For instance, **Ir-2b** depicted the smallest energy gap in the computational studies, due to destabilisation of the HOMO upon methylation (donation of electron density) of the phenyl ring and stabilisation of the LUMO upon fluorination (withdrawal of electron density) at the quinoxaline. This was compliant with the experimental data, where the bathochromic shift in emission and reduced lifetime was

rationalised by the energy gap law, suggesting that the MOs at the phenyl ring contributed greatly to the HOMO. Similarly, fluorination at the phenyl unit was predicted to result in energy stabilisation of the HOMO, thus increasing the energy gap, and was represented experimentally by blue-shifted emission in **Ir-2e** − **Ir-2j**. Hence, a combined approach strengthened the initial inferences made, where tunability prospects arose from substituents altering the energies of the relative frontier orbitals.

Complex	$S_0 \rightarrow S_1$	$S_0 \rightarrow T_n$	λ_{abs}[a]	$T_n \rightarrow S_0$	λ_{em}[b]
Ir-2a	409	544	378, 485	622	628
Ir-2b	419	563	373, 518	640	655
Ir-2e	385	502	359, 460	586	590
Ir-2f	383	496	372, 450	585	585
Ir-2g	390	510	362, 449	589	594
Ir-2h	377	493	370, 442	582	579
Ir-2i	375	486	379, 439	583	584
Ir-2j	381	501	372, 440	585	583

Table 2.10: Computationally calculated values for the absorption and emission peak positions of the isolated iridium complexes. All values are in nm; [a]Experimentally obtained absorption profile maxima for the longest wavelength positions. [b]Experimental values for the emission peak maxima, reported in Section 2.3.4.

Predicted λ_{em} values were calculated from the DFT-optimised excited state geometries (**Table 2.10**). The calculated trends were in remarkably close agreement with the experimental observations, where the longest λ_{em} was seen for **Ir-2b** and the shortest for **Ir-2h**. Overall, the $T_1 \rightarrow S_0$ values closely resembled the peak maxima in the emission spectra.

Overall, TD-DFT calculations suggested a mixed MLCT/ILCT/LLCT emissive state, where ILCT and LLCT localised on the C^N ligands had a significant impact on the photophysical properties, in agreement with the experimental studies.

2.3.6: Transient Absorption Spectroscopy and Kinetics

Nanosecond transient absorption (TA) spectroscopy studies were carried to examine triplet state dynamics of all isolated complexes. These measurements were carried out by Haleema A. Otaif and Dr Joseph Beames at Cardiff University. Samples were once again recorded in aerated acetonitrile solutions with a pump wavelength of 355 nm. All eight complexes displayed similar spectral features, where overall bleaching of the ground state ^{1}MLCT band can be seen between λ = 330 – 400 nm, represented by a negative signal for the change in optical density (ΔOD). These are shown in **Figure 2.24**.
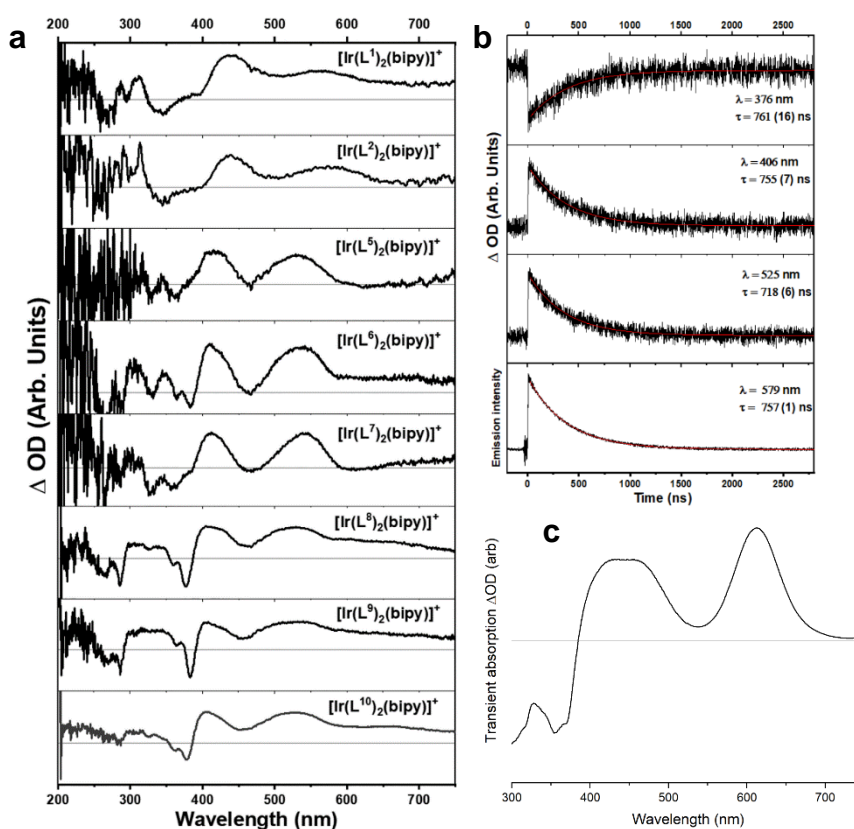
*Figure 2.24: a: Transient absorption spectra of all complexes in aerated MeCN (λ_{ex} = 355 nm), where the grey line represents ΔOD = 0. b: Kinetic traces of the major features in the TA spectrum of **Ir-2h**, where λ and τ values are displayed. c: Simulated TA spectrum for **Ir-2h** from the experimental absorption data.*

Two high-intensity components were present in each case between λ = 410 – 435 and 550 – 670 nm and can be assigned as $T_1 \rightarrow T_n$ absorption transitions. The latter peaks were most pronounced for the fluorinated variants, whereas these features were broadened for **Ir-2a** and **Ir-2b**. **Ir-2b** displayed the longest

wavelength peak maxima, whilst the fluorinated variants exhibited peaks at shorter wavelengths, consistent with the experimental absorption and emission data.

A simulated TA spectrum of **Ir-2h** was generated from the experimental absorption data by TD-DFT calculations. This was compared with the experimental TA spectrum, where it was found that these were directly comparable – indicating that the UV-vis and transient absorption spectra were in superb agreement with each other.

Kinetic traces were collected for the major features present in the TA spectra of the complexes, where a mono-exponential decay was seen for all samples. All features present for each complex displayed comparable lifetimes within hundreds of nanoseconds. Therefore, all were attributed to the same activation pathways that generate a triplet charge-transfer excited state, where phosphorescent decay was consistent with the magnitude of these values.

2.4: Conclusions

In conclusion, a series of ten red-emissive *bis*-cyclometallated iridium(III) complexes were formed, where the cyclometallating ligands were based upon 2-phenylquinoxaline. Simple synthetic modifications incorporated into these ligands allowed significant control over the electronic and photophysical behaviour of the resultant complexes, where excellent scope for tunability of phosphorescence was achieved within the yellow, orange, and deep-red regions of the visible range between 579 – 655 nm.

Spectroscopic techniques combined with theoretical studies provided insight into the excited state properties of these complexes, where emission was discovered to occur from a mixed ILCT/LLCT/MLCT excited state. Previous studies have shown that the LUMO typically resides on the ancillary ligand in **[Ir(ppy)$_2$(bpy)]$^+$** type systems, where emission tunability can be implemented through synthetic alterations within the N^N component.[73] However, it was discovered that the ancillary ligand in these systems imparted little influence on the excited state properties, due to the HOMO residing on the iridium centre and phenyl constituent of the C^N ligand and the LUMO consisting of contributions exclusively from the quinoxaline moiety. Therefore, colour-tunability was achieved by alteration of the relative energies of these states by judicious C^N ligand design, specifically through incorporation of weakly electron-withdrawing or electron-donating substituents at different positions.

This tunability offers advantages in applications such as the development of OLED devices but also in biological applications, where quantum yields up to 11% were recorded in oxygenated solutions.

2.5: Experimental

2.5.1: General Considerations

All commercially available reagents were used without further purification, and all reactions employed vacuum line and Schlenk techniques. ^{1}H, ^{13}C{^{1}H} and ^{19}F{^{1}H} NMR spectra were recorded on NMR-FT Bruker 500, 400 and 300 MHz spectrometers in the appropriate solvents (CDCl$_3$, (CD$_3$)$_2$CO, CD$_3$CN or DMSO-d_6), where chemical shift (δ) positions (ppm) were determined relative to TMS and residual solvent peaks[75] through digital locking. Most high-resolution mass spectra were obtained by the staff at Cardiff University using a Waters Xevo G2-XS QTof spectrometer, with some being carried out at the EPSRC National Mass Spectrometry Facility (on a Waters GCT Premier spectrometer) at Swansea University. IR spectra were recorded on a Shimadzu IRAffinty-1 FTIR spectrometer. UV-vis spectroscopy studies were performed on 10^{-5} M MeCN solutions using a Shimadzu UV-1800 spectrophotometer. The 10^{-5} M samples were prepared by dilution of 10^{-3} M bulk stock solutions. Upon sonication in an ultrasonic bath, the samples were inspected to ensure that solute was fully dissolved. Luminescence data was acquired for dilute MeCN solutions of the samples using a JobinYvon-Horiba Fluorolog spectrometer fitted with a JY TBX picosecond single-photon detection module, unless otherwise specified. Steady-state emission spectra were uncorrected (unless otherwise specified), and the excitation spectra were instrument corrected. Time-resolved measurements were recorded using a Nano-LED pulsed laser source configured for 295 or 355 nm output, operating at 1 MHz. Time-resolved measurements were recorded using the JobinYvon-Horiba FluoroHub single photon counting module and the data was resolved using the DAS6 deconvolution software. Low temperature measurements at 77 K were performed in acetonitrile using an Oxford Instruments Optistat DN2 variable temperature liquid nitrogen cryostat. Further information and detail on the experimental considerations for the transient absorption measurements and computational calculations can be found in the published work related to this study.[35]

2.5.2: X-Ray Crystallography

Crystals were grown *via* evaporation techniques from concentrated solutions of DCM or MeCN. Suitable crystals were mounted on a MITIGEN holder in perfluoroether oil on a Rigaku 007HF diffractometer equipped with HF Varimax confocal mirrors and an AFC11 goniometer and HyPix 6000HE detector for **Ir-2a**, or a Rigaku FRE+ diffractometer equipped with VHF Varimax confocal mirrors and an AFC12 goniometer and HyPix 6000 detector for **Ir-2b**, **Ir-2e** and **Ir-2f**.[76] The crystals were kept at 100(2) K, using an Oxford Cryosystems low-temperature device. Using Olex2,[77] the structures were solved with the ShelXT[78] structure solution program, using the Intrinsic Phasing Solution method. The models were refined with version 2018/3 of ShelXL[79] by use of Least Squares minimisation. All non-H atoms were refined anisotropically and idealised hydrogen atom positions were calculated using the riding hydrogen model.

2.5.3: Preparation of Organic Ligands and Precursors

Synthesis of dioxane dibromide *(DDB)* [36,37]

Bromine (37.2 g, 12.0 mL, 232.8 mmol) was added dropwise to 1,4-dioxane (30.8 g, 29.9 mL, 349.2 mmol) whilst stirring under air, where a low temperature was maintained (<5°C). The resultant solution was stirred for 2h at room temperature, where the product precipitated out of solution. The mixture was filtered under suction and washed with cold 1,4-dioxane to give the product as a yellow solid (40.31 g, 69.8%). The reagent was stored at low temperature (<0°C) and used in subsequent reactions without further purification.

Synthesis of 2-bromo-(3,4-dimethylphenyl)ethan-1-one

A simple bromination reaction took place, where DDB (1.84 g, 7.43 mmol) in a solution of 1,4-dioxane and diethyl ether (1:1, 40 mL) was added dropwise to 3,4-dimethylacetophenone (1.00 g, 1.00 mL, 6.75 mmol) in the same solvent mixture whilst stirring under air at room temperature for 2h. The solution was added to water and extracted with diethyl ether. The combined organic layers were dried over $MgSO_4$, and the solvent was removed *in vacuo*. A minimum amount of hexane was added, and the resultant suspension was filtered under

suction to give the product as an off-white solid (1.36 g, 89.2%). ^{1}H NMR (400 MHz, CDCl$_3$) δ_H = 7.79 (s, 1H), 7.74 (d, $^3J_{HH}$ = 7.9 Hz, 1H), 7.27 (d, $^3J_{HH}$ = 7.9 Hz, 1H), 4.46 (s, 2H), 2.36 (2 overlapping s, 6H) ppm. The data was consistent with literature findings.[80,81]

Synthesis of 2-bromo-(3,4-difluorophenyl)ethan-1-one

Prepared similarly from 3,4-difluoroacetophenone (1.00 g, 0.80 mL, 6.41 mmol) and DDB (1.75g, 7.05 mmol) to give the product as an off-white solid (311 mg, 20.7%). ^{1}H NMR (400 MHz, CDCl$_3$) δ_H = 7.84 (ddd, $^3J_{HF}$ = 10.1, $^3J_{HH}$ = 7.6, $^4J_{HF}$ = 2.2 Hz, 1H), 7.80 – 7.74 (m, 1H), 7.33 – 7.27 (m, 1H) 4.38 (s, 2H) ppm. ^{19}F{^{1}H} NMR (376 MHz, CDCl$_3$) δ_F = -127.67 (d, $^3J_{FF}$ = 20.9 Hz), -135.10 (d, $^3J_{FF}$ = 20.9 Hz) ppm. The data was consistent with literature findings.[82]

Synthesis of 2-bromo-(4-fluorophenyl)ethan-1-one

Prepared similarly from 4'-fluoroacetophenone (3.00 g, 2.63 mL, 21.7 mmol) and DDB (5.92 g, 24.0 mmol) to give the product as white crystals (2.51 g, 53.3%). ^{1}H NMR (300 MHz, CDCl$_3$) δ_H = 8.08 – 7.89 (m, 2H), 7.22 – 7.08 (m, 2H), 4.42 (s, 2H) ppm. The data was consistent with literature findings.[83]

Synthesis of 2-bromo-(3,4,5-trifluorophenyl)ethan-1-one

Prepared similarly from 3,4,5-trifluoroacetophenone (1.00 g, 0.751 mL, 5.74 mmol) and DDB (1.57 g, 6.32 mmol) to give the product as a yellow oil (1.45 g, 99.8%). ^{1}H NMR (400 MHz, CDCl$_3$) δ_H = 7.62 (dd, $^3J_{HF}$ = 7.8 $^4J_{HF}$ = 6.5 Hz, 2H), 4.37 (s, 2H) ppm. ^{19}F{^{1}H} NMR (376 MHz, CDCl$_3$) δ_F = -131.62 (d, $^3J_{FF}$ = 20.2 Hz), -150.69 (t, $^3J_{HF}$ = 20.2 Hz) ppm. ^{13}C{^{1}H} NMR (101 MHz, CDCl$_3$) δ_C = 188.2, 151.4 (ddd, $^1J_{CF}$ = 253.5, $^2J_{CF}$ = 10.4, $^3J_{CF}$ = 3.4 Hz), 143.7 (dt, $^1J_{CF}$ = 261.6, $^2J_{CF}$ = 15.4 Hz), 129.6 (dd, $^2J_{CF}$ = 10.2, $^3J_{CF}$ = 5.9 Hz), 114.0– 113.4 (m), 29.7 ppm. The data was consistent with literature findings.[61]

Synthesis of 2-(3,4-dimethylphenyl)-6,7-dimethylquinoxaline (L^{1}H)

2-bromo-(3,4-dimethylphenyl)ethan-1-one (799   mg, 3.52 mmol) and 4,5-dimethyl-1,2-phenylenediamine (528 mg, 3.87 mmol) were heated to reflux in ethanol (10mL) for 24 h under an inert nitrogen atmosphere. The formation of a precipitate took place upon cooling the mixture to room temperature, and the resultant suspension was filtered under reduced pressure. This was washed with a small amount of cold ethanol and hexane to give the product as an orange

solid (374 mg, 40.5%). ^{1}H NMR (400 MHz, CDCl$_3$) δ_H = 9.20 (s, 1H), 7.97 (d, $^4J_{HH}$ = 0.9 Hz, 1H), 7.90 (s, 1H), 7.88 (dd, $^3J_{HH}$ = 7.8, $^4J_{HH}$ = 1.7 Hz, 1H), 7.84 (s, 1H), 7.31 (d, $^3J_{HH}$ = 7.8 Hz, 1H), 2.51 (2 overlapping s, 6H), 2.40 (s, 3H), 2.36 (s, 3H) ppm. ^{13}C{^{1}H} NMR (101 MHz, CDCl$_3$) δ_C = 142.7, 140.8, 139.0, 137.6, 134.9, 130.5, 128.7, 128.6, 128.3, 124.9, 20.5, 20.5, 20.1, 19.9 ppm. HRMS (EI+) m/z calc'd 262.1470 for C$_{18}$H$_{18}$N$_2$; found 262.1465 [M]$^+$. UV−vis (MeCN) λ_{max} ($\varepsilon \times 10^4$ / L mol^{-1} cm^{-1}): 214 (4.5), 265 (3.3), 349 (1.8) nm. FTIR (solid, cm^{-1}) (ATR) v_{max}: 2972, 2945, 2907, 1628, 1605, 1570, 1528, 1483, 1447, 1362, 1317, 1283, 1234, 1209, 1121, 1053, 1022, 1003, 991, 964, 943, 885, 862, 837, 794, 737, 716, 637, 623, 546, 488, 442, 428.

Synthesis of 2-(3,4-dimethylphenyl)-6,7-difluoroquinoxaline (*L^{2}H*)

Prepared similarly from 2-bromo-(3,4-difluorophenyl)ethan-1-one (998 mg, 4.40 mmol) and 4,5-difluoro-1,2-phenylenediamine (760 mg, 5.27 mmol) to give the product as an off-white solid (593 mg, 50.0%). ^{1}H NMR (400 MHz, CDCl$_3$) δ_H = 9.27 (s, 1H), 7.96 (d, $^4J_{HH}$ = 0.6 Hz, 1H), 7.91 − 7.86 (m, 2H), 7.86 − 7.81 (m, 1H), 7.32 (d, $^3J_{HH}$ = 7.9 Hz, 1H), 2.40 (s, 3H), 2.37 (s, 3H) ppm. ^{13}C{^{1}H} NMR (101 MHz, CDCl$_3$) δ_C = 152.4 (d, $^3J_{CF}$ = 3.1 Hz), 152.8 (d, $^1J_{CF}$ = 256.0, $^2J_{CF}$ = 16.1 Hz), 152.0 (d, $^1J_{CF}$ = 254.9, $^2J_{CF}$ = 16.1 Hz), 143.6 (d, $^3J_{CF}$ = 3.2 Hz), 139.8, 138.7 (dd, $^2J_{CF}$ = 10.7, $^3J_{CF}$ = 1.0 Hz), 137.9, 133.9, 130.7, 128.7, 125.0, 115.2 (dd, $^2J_{CF}$ = 17.2, $^3J_{CF}$ = 1.6 Hz), 115.0 (dd, $^2J_{CF}$ = 17.2 Hz, $^3J_{CF}$ = 1.6 Hz), 20.1, 20.0 ppm. ^{19}F{^{1}H} NMR (376 MHz, CDCl$_3$) δ_F = −129.8 (d, $^3J_{FF}$ = 20.8 Hz), −130.9 (d, $^3J_{FF}$ = 20.8 Hz) ppm. HRMS (EI+): m/z calc'd 270.0969 for C$_{16}$H$_{12}$F$_2$N$_2$; found 270.0970 [M]$^+$. UV−vis (MeCN) λ_{max} ($\varepsilon \times 10^4$ / L mol^{-1} cm^{-1}): 213 (5.5), 256 (2.9), 343 (1.9) nm. FTIR (solid, cm^{-1}) (ATR) v_{max}: 3067, 2978, 2922, 1636, 1609, 1545, 1493, 1449, 1433, 1385, 1350, 1315, 1283, 1225, 1167, 1165, 1128, 1051, 1016, 988, 968, 926, 880, 862, 835, 752, 731, 710, 650, 613, 602, 546, 492, 463, 440.

Synthesis of 2-(3,4-difluorophenyl)-6,7-dimethylquinoxaline (*L^{3}H*)

Prepared similarly from 2-bromo-(3,4-difluorophenyl)ethan-1-one (311 mg, 1.32 mmol) and 4,5-dimethyl-1,2-phenylenediamine (216 mg, 1.59 mmol) to give the product as a pale yellow solid (209 mg, 58.3%). ^{1}H NMR (400 MHz, CDCl$_3$) δ_H = 9.16 (s, 1H), 8.07 (ddd, $^3J_{HF}$ = 11.4, $^3J_{HH}$ = 7.7, $^4J_{HF}$ = 2.2 Hz, 1H), 7.93 − 7.89 (m, 1H), 7.89 (s, 1H), 7.86 (s, 1H), 7.38 − 7.29 (m, 1H), 2.52 (2 overlapping s,

6H) ppm. $^{13}C\{^1H\}$ NMR (101 MHz, CDCl$_3$) δ_C = 141.7, 141.4, 141.2, 140.9, 128.7, 128.3, 123.7 − 123.4 (m), 118.0 (d, $^2J_{CF}$ = 17.4 Hz), 116.7 (d, $^2J_{CF}$ = 18.9 Hz), 20.6, 20.6 ppm. $^{19}F\{^1H\}$ NMR (376 MHz, CDCl$_3$) δ_F = −135.8 (d, $^3J_{FF}$ = 21.9 Hz), −136.4 (d, $^3J_{FF}$ = 21.3 Hz) ppm. HRMS (EI+): *m/z* calc'd 270.0969 for C$_{16}$H$_{12}$F$_2$N$_2$; found 270.0969 [M]$^+$. UV−vis (MeCN) λ_{max} ($\varepsilon \times 10^4$ / L mol^{-1} cm^{-1}): 203 (3.1), 262 (3.6), 343 (1.4) nm. FTIR (solid, cm^{-1}) (ATR) v_{max}: 3040, 2978, 2355, 1616, 1604, 1520, 1518, 1487, 1472, 1442, 1369, 1364, 1323, 1290, 1273, 1254, 1213, 1188, 1165, 1113, 1049, 1007, 1003, 976, 939, 897, 876, 829, 773, 710, 638, 583, 492, 457, 434.

Synthesis of 2-(3,4-difluorophenyl)-6,7-difluoroquinoxaline (*L⁴H*)

Prepared similarly from 2-bromo-(3,4-difluorophenyl)ethan-1-one (679 mg, 2.89 mmol) and 4,5-difluoro-1,2-phenylenediamine (500 mg, 3.47 mmol) to give the product as an off-white solid (448 mg, 46.5%). ^1H NMR (400 MHz, CDCl$_3$) δ_H = 9.25 (s, 1H), 8.08 (ddd, $^3J_{HF}$ = 11.2, $^3J_{HH}$ = 7.6, $^4J_{HF}$ = 2.2 Hz, 1H), 7.95 − 7.90 (m, 1H), 7.89 (dd, $^3J_{HF}$ = 8.2, $^4J_{HF}$ = 2.1 Hz, 1H), 7.86 (dd, $^3J_{HF}$ = 8.2, $^4J_{HF}$ = 2.0 Hz, 1H), 7.39 – 7.32 (m, 1H) ppm. $^{13}C\{^1H\}$ NMR (101 MHz, CDCl$_3$) δ_C = 153.1 (dd, $^1J_{CF}$ = 256.8, $^2J_{CF}$ = 15.4 Hz), 152.6 (dd, $^1J_{CF}$ = 257.0, $^2J_{CF}$ = 15.8 Hz), 152.2 (dd, $^1J_{CF}$ = 253.4, $^2J_{CF}$ = 12.6 Hz), 151.2 (dd, $^1J_{CF}$ = 250.9, $^2J_{CF}$ = 14.2 Hz), 149.9, 142.7 (d, $^3J_{CF}$ = 3.3 Hz), 139.9 – 139.0 (m), 139.3 – 138.9 (m), 133.4, 124.0 – 123.6 (m), 118.3 (d, $^2J_{CF}$ = 17.7 Hz), 116.8 (d, $^2J_{CF}$ = 19.0 Hz), 115.3 (dd, $^2J_{CF}$ = 17.3 Hz, $^3J_{CF}$ = 1.8 Hz), 115.1 (dd, $^2J_{CF}$ = 17.3 Hz, $^3J_{CF}$ = 1.9 Hz) ppm. $^{19}F\{^1H\}$ NMR (376 MHz, CDCl$_3$) δ_F = −128.6 (d, $^3J_{FF}$ = 20.9 Hz), −129.3 (d, $^3J_{FF}$ = 21.1 Hz), −134.3 (d, $^3J_{FF}$ = 21.2 Hz), −135.8 (d, $^3J_{FF}$ = 21.2 Hz) ppm. HRMS (EI+): *m/z* calc'd 278.0467 for C$_{14}$H$_6$F$_4$N$_2$; found 278.0470 [M]$^+$. UV−vis (MeCN) λ_{max} ($\varepsilon \times 10^4$ / L mol^{-1} cm^{-1}): 207 (3.6), 253 (2.5), 335 (1.4) nm. FTIR (solid, cm^{-1}) (ATR) v_{max}: 3042, 1636, 1609, 1508, 1476, 1445, 1410, 1350, 1300, 1281, 1273, 1233, 1223, 1188, 1124, 968, 901, 889, 818, 779, 731, 706, 660, 611, 581, 494, 492, 451, 399.

Synthesis of 2-(4-fluorophenyl) quinoxaline (*L⁵H*)

Prepared similarly from 2-bromo-(4-fluorophenyl)ethan-1-one (929 mg, 4.28 mmol) and 1,2-phenylenediamine (500 mg, 4.62 mmol) to give the crude product. Column chromatography (SiO$_2$, DCM) was undertaken, where the product eluted as the second yellow band with a 3:1 DCM/hexane mobile phase

to give the pure product as a yellow crystalline solid (470 mg, 49.0%). ^{1}H NMR (400 MHz, CDCl$_3$) δ_H = 9.27 (s, 1H), 8.22 − 8.15 (m, 2H), 8.15 − 8.08 (m, 2H), 7.81 − 7.67 (m, 2H), 7.28 − 7.20 (m, 2H) ppm. ^{13}C{^{1}H} NMR (101 MHz, CDCl$_3$) δ_C = 143.1, 130.6, 129.8, 129.7, 129.6, 129.3, 116.5, 116.3 ppm. ^{19}F{^{1}H} NMR (376 MHz, CDCl$_3$) δ_F = -110.5 (s) ppm. UV−vis (MeCN) λ_{max} ($\varepsilon \times 10^4$ / L mol^{-1} cm^{-1}): 202 (1.8), 262 (1.5), 334 (0.8) nm. The data was consistent with literature findings.[44]

Synthesis of 2-(4-fluorophenyl)-6,7-dimethylquinoxaline *(L^{6}H)*

Prepared similarly from 2-bromo-(4-fluorophenyl)ethan-1-one (1.00 g, 4.61 mmol) and 4,5-dimethyl-1,2-phenylenediamine (753 mg, 5.53 mmol) to give the product as a yellow solid (580 mg, 50.0%). ^{1}H NMR (400 MHz, d_6-acetone) δ_H = 9.38 (s, 1H), 8.42 − 8.36 (m, 2H), 7.87 (s, 1H), 7.85 (s, 1H), 7.39 − 7.33 (m, 2H), 2.53 (s, 3H), 2.52 (s, 3H) ppm. ^{13}C{^{1}H} NMR (101 MHz, CDCl$_3$) δ_C = 164.2 (d, $^1J_{CF}$ = 250.2 Hz), 150.1, 142.1, 141.3, 141.2, 140.6, 140.4, 133.4 (d, $^3J_{CF}$ = 3.0 Hz), 129.5, 128.7, 128.3, 116.3 ($^2J_{CF}$ = 21.8 Hz), 20.6, 20.5 ppm. ^{19}F{^{1}H} NMR (376 MHz, CDCl$_3$) δ_F = −111.2 (s). HRMS (EI+): *m/z* calc'd 252.1063 for C$_{16}$H$_{13}$FN$_2$; found 252.1063 [M]$^+$. UV−vis (MeCN) λ_{max} ($\varepsilon \times 10^4$ / L mol^{-1} cm^{-1}): 213 (2.4), 258 (3.3), 340 (1.3) nm. FTIR (solid, cm^{-1}) (ATR) v_{max}: 1653, 1624, 1599, 1535, 1514, 1487, 1441, 1375, 1329, 1315, 1283, 1211, 1161, 1107, 1047, 1020, 1005, 1001, 951, 935, 887, 868, 843, 814, 795, 739, 729, 723, 675, 638, 628, 611, 594, 552, 513, 488, 457, 434, 419. The data was consistent with literature findings.[45]

Synthesis of 6,7-difluoro-2-(4-fluorophenyl)quinoxaline *(L^{7}H)*

Prepared similarly from 2-bromo-(4-fluorophenyl)ethan-1-one (1.00 g, 4.61 mmol) and 4,5-difluoro-1,2-phenylenediamine (797 mg, 5.53 mmol) to give the product as an off-white solid (462 mg, 38.5%). ^{1}H NMR (400 MHz, CDCl$_3$) δ_H = 9.27 (s, 1H), 8.25 − 8.14 (m, 2H), 7.92 − 7.82 (m, 2H), 7.29 − 7.23 (m, 2H) ppm. ^{13}C{^{1}H} NMR (101 MHz, CDCl$_3$) δ_C = 164.6 (d, $^1J_{CF}$ = 251.6 Hz), 152.8 (d, $^1J_{CF}$ = 256.6 Hz), 152.4 (d, $^1J_{CF}$ = 256.4 Hz), 143.1 (d, $^3J_{CF}$ = 3.1 Hz), 139.8, 139.7, 138.9, 138.8, 132.5, 116.5 (d, $^2J_{CF}$ = 21.9 Hz), 115.2 (dd, $^2J_{CF}$ = 21.2, $^3J_{CF}$ = 1.8 Hz), 115.0 (dd, $^2J_{CF}$ = 21.3, $^3J_{CF}$ = 1.9 Hz) ppm. ^{19}F{^{1}H} NMR (376 MHz, CDCl$_3$) δ_F = −109.8 (s), −129.2 (d, $^3J_{FF}$ = 21.1 Hz), −130.1 (d, $^3J_{FF}$ = 21.1 Hz) ppm. HRMS (EI+): *m/z* calc'd 261.0640 for C$_{14}$H$_7$F$_3$N$_2$; found 261.0641 [M]$^+$. UV−vis

(MeCN) λ_{max} ($\varepsilon \times 10^4$ / L mol^{-1} cm^{-1}): 202 (3.4), 249 (2.1), 331 (1.2) nm. FTIR (solid, cm^{-1}) (ATR) ν_{max}: 3042, 1632, 1603, 1501, 1441, 1440, 1350, 1310, 1300, 1285, 1223, 1204, 1175, 1155, 1132, 1103, 1040, 1011, 955, 924, 885, 876, 868, 831, 787, 756, 731, 718, 650, 642, 608, 579, 509, 488, 451, 442.

Synthesis of 2-(3,4,5-fluorophenyl)quinoxaline (L^{8}H)

Prepared similarly from 2-bromo-(3,4,5-trifluorophenyl)ethan-1-one (1.146 g, 4.53 mmol) and 1,2-phenylenediamine (588 mg, 5.44 mmol) to give the product as pale yellow crystals (500 mg, 42.4%). ^{1}H NMR (500 MHz, CDCl$_3$) δ_H = 9.24 (s, 1H), 8.16 − 8.10 (m, 2H), 7.92 − 7.85 (m, 2H), 7.84 − 7.77 (m, 2H) ppm. ^{13}C{^{1}H} NMR (126 MHz, CDCl$_3$) δ_C = 151.9 (ddd, $^1J_{CF}$ = 250.9, $^2J_{CF}$ = 10.2, $^3J_{CF}$ = 4.0 Hz), 148.4 (dd, $^4J_{CF}$ = 4.7, $^5J_{CF}$ = 2.5 Hz), 142.2, 142.1, 142.1, 141.4 (dt, $^1J_{CF}$ = 256.7, $^2J_{CF}$ = 15.4 Hz), 132.9 (td, $^3J_{CF}$ = 7.5, $^4J_{CF}$ = 4.5 Hz), 131.0, 130.5, 129.8, 129.4, 111.8 (dd, $^2J_{CF}$ = 17.1, $^3J_{CF}$ = 5.5 Hz) ppm. ^{19}F{^{1}H} NMR (376 MHz, CDCl$_3$) δ_F = −132.6 (d, $^3J_{FF}$ = 20.4 Hz), −157.5 (t, $^3J_{FF}$ = 20.4 Hz) ppm. HRMS (ES+): m/z calc'd 261.0640 for C$_{14}$H$_7$F$_3$N$_2$; found 261.0647 [M + H]$^+$. UV−vis (MeCN) λ_{max} ($\varepsilon \times 10^4$ / L mol^{-1} cm^{-1}): 208 (1.4), 258 (2.5), 333 (1.0) nm. FTIR (solid, cm^{-1}) (ATR) ν_{max}: 2082, 1532, 1494, 1437, 1420, 1366, 1325, 1248, 1207, 1131, 1055, 1042, 978, 918, 891, 880, 775, 772, 749, 707, 694, 638, 618, 578, 530, 452, 444, 431.

Synthesis of 6,7-dimethyl-2-(3,4,5-fluorophenyl)quinoxaline (L^{9}H)

Prepared similarly from 2-bromo-(3,4,5-trifluorophenyl)ethan-1-one (947 mg, 3.74 mmol) and 4,5-dimethyl-1,2-phenylenediamine (612 mg, 4.49 mmol) to give the product as an off-white solid (508 mg, 47.1%). ^{1}H NMR (500 MHz, CDCl$_3$) δ_H = 9.13 (s, 1H), 7.88 − 7.81 (m, 4H), 2.52 (2 overlapping s, 6H) ppm. ^{13}C{^{1}H} NMR (126 MHz, CDCl$_3$) δ_C = 151.9 (ddd, $^1J_{CF}$ = 250.6, $^2J_{CF}$ = 10.1, $^3J_{CF}$ = 3.8 Hz), 147.6, 141.7, 141.3, 141.3, 141.1, 141.1 (dt, $^1J_{CF}$ = 255.1, $^2J_{CF}$ = 15.1 Hz), 133.3 (td, $^3J_{CF}$ = 7.2, $^4J_{CF}$ = 4.1 Hz), 128.7, 128.3, 111.5 (dd, $^2J_{CF}$ = 17.3, $^3J_{CF}$ = 5.5 Hz), 20.6 (overlapping) ppm. ^{19}F{^{1}H} NMR (376 MHz, CDCl$_3$) δ_F = −132.9 (d, $^3J_{FF}$ = 20.5 Hz), −158.2 (t, $^3J_{FF}$ = 20.5 Hz) ppm. HRMS (ES+): m/z calc'd 289.0953 for C$_{14}$H$_7$F$_3$N$_2$; found 289.0951 [M + H]$^+$. UV−vis (MeCN) λ_{max} ($\varepsilon \times 10^4$ / L mol^{-1} cm^{-1}): 211 (1.3), 263 (3.2), 342 (1.2) nm. FTIR (solid, cm^{-1}) (ATR) ν_{max}: 2091, 1624, 1604, 1528, 1488, 1449, 1444, 1400, 1361, 1332, 1256, 1243, 1203, 1165, 1058, 1046, 1039, 1022, 1002, 979, 893, 887, 875, 764, 737,

705, 697, 643, 638, 558, 492, 463, 463, 458, 442, 434, 420.

Synthesis of 6,7-difluoro-2-(3,4,5-fluorophenyl)quinoxaline *(L^{10}H)*

Prepared similarly from 2-bromo-(3,4,5-trifluorophenyl)ethan-1-one (1.453 g, 5.74 mmol) and 4,5-difluoro-1,2-phenylenediamine (993 mg, 6.89 mmol) to give the product as a pale yellow solid (551 mg, 37.9%). ^{1}H NMR (500 MHz, CDCl$_3$) δ_H = 9.20 (s, 1H), 7.90 − 7.80 (m, 4H) ppm. ^{13}C{^{1}H} NMR (126 MHz, CDCl$_3$) δ_C = 153.2 (dd, $^1J_{CF}$ = 255.6, $^2J_{CF}$ = 13.6 Hz), 152.8 (dd, $^1J_{CF}$ = 257.3, $^2J_{CF}$ = 15.4 Hz), 152.0 (ddd, $^1J_{CF}$ = 251.3, $^2J_{CF}$ = 10.2, $^3J_{CF}$ = 4.0 Hz), 148.6, 141.5 (dt, $^1J_{CF}$ = 256.9, $^2J_{CF}$ = 15.4 Hz), 142.3 (d, $^4J_{CF}$ = 3.2 Hz), 139.6 (d, $^2J_{CF}$ = 10.4 Hz), 139.4 (d, $^2J_{CF}$ = 10.4 Hz), 132.2 (td, $^3J_{CF}$ = 7.5, $^4J_{CF}$ = 4.5 Hz), 115.3 (dd, $^2J_{CF}$ = 17.3, $^3J_{CF}$ = 1.8 Hz), 115.1 (dd, $^2J_{CF}$ = 17.4, $^3J_{CF}$ = 1.9 Hz), 111.7 (dd, $^2J_{CF}$ = 17.1, $^3J_{CF}$ = 5.6 Hz) ppm. ^{19}F{^{1}H} NMR (376 MHz, CDCl$_3$) δ_F = −128.1 (d, $^3J_{FF}$ = 20.9 Hz), −128.5 (d, $^3J_{FF}$ = 20.9 Hz), −132.3 (d, $^3J_{FF}$ = 20.4 Hz), −156.7 (t, $^3J_{FF}$ = 20.4 Hz) ppm. HRMS (ES+): *m/z* calc'd 297.0451 for C$_{14}$H$_7$F$_3$N$_2$; found 297.0454 [M + H]$^+$. UV−vis (MeCN) λ_{max} (ε × 10^4 / L mol^{-1} cm^{-1}): 208 (2.2), 253 (2.1), 334 (1.2) nm. FTIR (solid, cm^{-1}) (ATR) v_{max}: 2985, 1629, 1606, 1536, 1503, 1484, 1457, 1412, 1379, 1370, 1354, 1259, 1232, 1218, 1211, 1197, 1187, 1167, 1059, 1044, 985, 944, 937, 886, 877, 868, 843, 776, 746, 710, 692, 678, 639, 630, 611, 587, 532, 512, 496, 463, 446, 435.

2.5.4: Preparation of Inorganic Complexes

General synthetic route to the dimers, [(Ir(L^n)$_2$(μ-Cl))$_2$]

The chloride-bridged dimer intermediates were synthesised according to the Nonyama route,[48] where IrCl$_3$.xH$_2$O (1.0 eq.) and **L^{n}H** (>2.0 eq.) were dissolved in 2-methoxyethanol and distilled water (3:1, ~20 mL) and the mixture was heated to reflux under an inert nitrogen atmosphere whilst stirring for 48 h. The reaction mixture was then cooled to room temperature, where the crude product precipitated out of solution upon addition of distilled water (~ 30 mL). The solids were collected by filtration under reduced pressure and washed with water (>10 mL). The crude product was dissolved in dichloromethane and filtered under suction to remove any insoluble side-products, the solvent was removed *in vacuo* to give the products as brown or orange solids (23.8 − 91.1%), which were used in subsequent steps without further purification or characterisation.

Synthesis of [Ir(L^1)$_2$(bpy)][PF$_6$] *(Ir-2a)*

[(Ir(L^1)$_2$(μ-Cl))$_2$] (179 mg, 0.119 mmol) and 2,2'-bipyridine (41.0 mg, 0.262 mmol) were dissolved in 2-methoxyethanol (20 mL) and the solution was heated to reflux for 24 h under an inert nitrogen atmosphere. Upon cooling, the saturated aqueous NH$_4$PF$_6$ solution was added to the reaction mixture, where the product precipitated out of solution as the PF$_6$ salt. The product was purified by column chromatography (SiO$_2$, DCM/MeOH), collecting the first red band that eluted with 95:5 DCM/MeOH. The solvent was removed *in vacuo*, and then product was dissolved in a minimum amount of DCM and recrystallized with Et$_2$O. The product was filtered under reduced pressure and dried in an oven overnight to give the pure product as a red solid (23.5 mg, 9.7%). ^{1}H NMR (500 MHz, CDCl$_3$) δ_H = 9.36 (s, 2H), 8.53 (d, $^3J_{HH}$ = 8.1 Hz, 2H), 8.07 (dd, $^3J_{HH}$ = 8.2, $^4J_{HH}$ = 6.9 Hz), 8.04 − 7.99 (m, 2H), 7.84 (s, 2H), 7.75 (s, 2H), 7.40 − 7.45 (m, 2H), 6.70 (s, 2H), 6.14 (s, 2H), 2.33 (s, 6H), 2.27 (s, 6H), 1.95 (s, 6H), 1.75 (s, 6H) ppm. ^{13}C{^{1}H} NMR (126 MHz, CDCl$_3$) δ_C = 162.3, 156.0, 149.0, 148.0, 143.4, 142.0, 141.6, 141.0, 141.0, 140.7, 140.5, 139.8, 135.3, 132.0, 130.0, 128.8, 128.0, 125.7, 123.1, 20.5, 20.4, 19.9, 19.8 ppm. HRMS (EI+) *m/z* calc'd 871.3100 for C$_{46}$H$_{42}$N$_6$^{193}Ir; found 871.3391 [M − PF$_6$]$^+$. UV−vis (MeCN) λ_{max} (ε × 10^4 / L mol^{-1} cm^{-1}): 219 (4.5), 267 (3.5), 294 (3.1), 378 (1.7), 486 (0.4) nm. FTIR (solid, cm^{-1}) (ATR) v_{max}: 1597, 1518, 1449, 1342, 1314, 1281, 1215, 1148, 1074, 1005, 839, 768, 662, 640, 556, 442, 426, 417, 403.

Synthesis of [Ir(L^2)$_2$(bpy)][PF$_6$] *(Ir-2b)*

Prepared similarly from **[(Ir(L^2)$_2$(μ-Cl))$_2$]** (40.0 mg, 0.026 mmol) and 2,2'-bipyridine (9.0 mg, 0.057 mmol) to give the product as a red solid (10.2 mg, 19.0%). ^{1}H NMR (500 MHz, CDCl$_3$) δ_H = 9.46 (s, 2H), 8.52 (d, $^3J_{HH}$ = 8.1 Hz, 2H), 8.15 − 8.11 (m, 4H), 8.00 − 7.98 (m, 2H), 7.92 (s, 2H), 7.84 (dd, $^3J_{HF}$ = 9.3, $^3J_{HF}$ = 8.3 Hz, 2H), 7.54 (ddd, $^3J_{HH}$ = 7.6, 5.5, $^4J_{HH}$ = 1.2 Hz, 2H), 6.73 (dd, $^3J_{HF}$ = 11.8, $^4J_{HF}$ = 7.5 Hz, 2H), 6.12 (s, 2H), 2.29 (s, 6H), 1.99 (s, 6H) ppm. ^{13}C{^{1}H} NMR (101 MHz, (CD$_3$)$_2$CO) δ_C = 156.7, 150.7, 149.7, 145.1, 143.6, 141.8, 141.4, 136.1, 133.0, 130.3, 130.1, 126.0, 111.6, 20.1, 19.5 ppm. ^{19}F{^{1}H} NMR (376 MHz, CDCl$_3$) δ_F = −73.0 (d, $^1J_{PF}$ = 712.7 Hz), −124.7 (d, $^3J_{FF}$ = 22.1 Hz), −128.6 (d, $^3J_{FF}$ = 21.0 Hz) ppm. HRMS (EI+): *m/z* calc'd 885.2074 for C$_{42}$H$_{30}$N$_6$F$_4$^{193}Ir; found 885.2098 [M − PF$_6$]$^+$. UV−vis (MeCN) λ_{max} (ε × 10^4 / L

mol^{-1} cm^{-1}): 206 (6.8), 266 (3.6), 292 (3.1), 373 (2.1), 518 (0.4) nm.

Synthesis of [Ir(L^5)$_2$(bpy)][PF$_6$] *(Ir-2e)*

Prepared similarly from **[(Ir(L^5)$_2$(μ-Cl))$_2$]** (100 mg, 0.074 mmol) and 2,2'-bipyridine (29.0 mg, 0.163 mmol) to give the product as a red solid (47.3 mg, 34.0%). ^{1}H NMR (500 MHz, CD$_3$CN) δ_H = 9.61 (s, 2H), 8.38 (dd, $^3J_{HH}$ = 8.4, $^4J_{HH}$ = 5.6 Hz, 2H), 8.16 (d, $^3J_{HH}$ = 8.1, Hz, 2H), 8.11 (ddd, $^3J_{HH}$ = 5.5, $^4J_{HH}$ = 1.5, $^5J_{HH}$ = 0.7 Hz, 2H), 8.03 (dd, $^3J_{HH}$ = 8.4, $^4J_{HH}$ = 1.4 Hz, 2H), 8.00 (ddd, $^3J_{HH}$ = 8.2, 7.7, $^4J_{HH}$ = 1.6 Hz, 2H), 7.62 (ddd, $^3J_{HH}$ = 8.3, 6.9, $^4J_{HH}$ = 1.3 Hz, 2H), 7.53 (ddd, $^3J_{HH}$ = 7.6, 5.5, $^4J_{HH}$ = 1.3 Hz, 2H), 7.16 (ddd, $^3J_{HH}$ = 8.6, 6.9, $^4J_{HH}$ = 1.5 Hz, 2H), 7.06 (d, $^3J_{HF}$ = 9.0 Hz, 2H), 7.07 – 7.03 (m, 2H), 6.27 (dd, $^3J_{HF}$ = 9.6, $^4J_{HH}$ = 2.5 Hz, 2H) ppm. ^{13}C{^{1}H} NMR (126 MHz, CD$_3$CN) δ_C = 165.1 (d, $^1J_{CF}$ = 256.6 Hz), 163.7, 156.3, 155.9 (d, $^3J_{CF}$ = 7.0 Hz), 149.9, 144.8, 143.2, 141.6, 141.1, 132.7, 131.8 (d, $^3J_{CF}$ = 10.0 Hz), 131.5, 130.8, 129.9, 125.3, 124.3, 121.4 (d, $^2J_{CF}$ = 18.8 Hz), 112.1 (d, $^2J_{CF}$ = 23.7 Hz) ppm. ^{19}F{^{1}H} NMR (376 MHz, CDCl$_3$) δ_F = −72.9 (d, $^1J_{PF}$ = 712.9 Hz), − 110.6 (s) ppm. HRMS (EI+): *m/z* calc'd 793.1636 for C$_{38}$H$_{24}$N$_6$F$_2$^{193}Ir; found 793.1649 [M − PF$_6$]$^+$. UV−vis (MeCN) λ_{max} (ε × 10^4 / L mol^{-1} cm^{-1}): 249 (3.2), 288 (2.9), 359 (0.9), 460 sh (0.2) nm.

Synthesis of [Ir(L^6)$_2$(bpy)][PF$_6$] *(Ir-2f)*

Prepared similarly from **[(Ir(L^6)$_2$(μ-Cl))$_2$]** (320 mg, 0.219 mmol) and 2,2'-bipyridine (75.3 mg, 0.482 mmol) to give the product as an orange solid (26.5 mg, 16.5%). ^{1}H NMR (400 MHz, CD$_3$CN) δ_H = 9.50 (s, 2H), 8.32 (dd, $^3J_{HH}$ = 8.7, $^4J_{HF}$ = 5.6 Hz, 2H), 8.25 (d, $^3J_{HH}$ = 8.2 Hz, 2H), 8.15 (d, $^3J_{HH}$ = 5.7 Hz, 2H), 8.04 (*app.* td, $^3J_{HH}$ = 7.8, $^4J_{HH}$ = 1.6 Hz, 2H), 7.79 (s, 2H), 7.56 (ddd, $^3J_{HH}$ = 6.3, $^4J_{HH}$ = 1.7, $^5J_{HH}$ = 0.5 Hz, 2H), 7.02 (*app.* td, $^3J_{HF}$ = 9.0, $^4J_{HF}$ = 2.4 Hz, 2H), 6.78 (s, 2H), 6.18 (dd, $^3J_{HF}$ = 9.5, $^4J_{HH}$ = 2.3 Hz, 2H), 2.31 (s, 6H), 1.76 (s, 6H) ppm. ^{13}C{^{1}H} NMR (101 MHz, CD$_3$CN) δ_C = 159.6, 156.4, 150.2, 147.3, 144.3, 143.7, 141.9 (d, $^2J_{CF}$ = 24.0 Hz), 141.2 (d, $^2J_{CF}$ = 21.9 Hz), 131.1, 130.5, 129.8, 125.4, 123.9, 20.2, 19.6 ppm. ^{19}F{^{1}H} NMR (376 MHz, CDCl$_3$) δ_F = −73.6 (d, $^1J_{PF}$ = 712.2 Hz), −104.9 (s) ppm. HRMS (EI+): *m/z* calc'd 849.2263 for C$_{42}$H$_{32}$N$_6$F$_2$^{191}Ir; found 849.2287 [M − PF$_6$]$^+$. UV−vis (MeCN) λ_{max} (ε × 10^4 / L mol^{-1} cm^{-1}): 206 (6.8), 263 (5.3), 287 (4.9), 372 (2.4), 452 (0.7) nm. FTIR (solid, cm^{-1}) (ATR) v_{max}: 1587, 1566, 1526, 1445, 1341, 1258, 1196, 1123, 1065, 851, 810, 775, 735, 656, 557, 459, 446, 409.

Synthesis of [Ir(L⁷)₂(bpy)][PF₆] *(Ir-2g)*

[(Ir(L⁷)₂(*μ*-Cl))₂] (92.9 mg, 0.062 mmol) and 2,2'-bipyridine (21.4 mg, 0.137 mmol) were dissolved in chloroform (10mL) and the solution was heated to reflux for 24 h under an inert nitrogen atmosphere. The reaction mixture was cooled to room temperature and the solvent was removed *in vacuo*. The crude solid was then purified by column chromatography (MeCN:H₂O:KNO₃ (*aq. sat.*) (14:2:1), SiO₂), where the red band was collected. The solvent was removed *in vacuo* and the product was left to dry in a heated oven at ~60°C for 16 h. The product was dissolved in acetonitrile, and the insoluble salts were filtered off under suction. A saturated aqueous solution of NH₄PF₆ was added to the filtrate and stirred for 15 min to ensure that all of the complex existed purely as a PF₆ salt. The solvent was removed *in vacuo*, and then washed with distilled water to remove excess insoluble inorganic salts. The crude product was recrystallised from dichloromethane and diethyl ether to give the pure product as a red solid (26.5 mg, 20.8%). ^{1}H NMR (500 MHz, CD₃CN) δ_H = 9.59 (s, 2H), 8.38 (dd, $^3J_{HH}$ = 8.8, $^4J_{HH}$ = 5.6 Hz, 2H), 8.28 (d, $^3J_{HH}$ = 8.1 Hz, 2H), 8.11 − 8.05 (m, 4H), 7.94 (dd, $^3J_{HF}$ = 10.3, $^4J_{HF}$ = 8.4 Hz, 2H), 7.57 (dd, $^3J_{HH}$ = 7.1, 6.0 Hz, 2H), 7.07 (*app.* td, $^3J_{HF}$ = 8.9, $^4J_{HH}$ = 2.5 Hz 2H), 6.80 (dd, $^3J_{HF}$ = 12.4, $^4J_{HF}$ = 7.8 Hz, 2H), 6.29 (dd, $^3J_{HF}$ = 9.5, $^4J_{HH}$ = 2.5 Hz, 2H) ppm. ^{13}C{^{1}H} NMR (126 MHz, CD₃CN) δ_C = 165.3 (d, $^1J_{CF}$ = 257.5 Hz), 163.9, 163.9, 156.3, 155.7, 155.6, 149.9, 145.2 (d, $^3J_{CF}$ = 3.1 Hz), 141.3, 140.5, 140.4, 139.3 (d, $^3J_{CF}$ = 10.2 Hz), 132.1 ($^3J_{CF}$ = 10.2 Hz), 130.1, 126.0, 121.4 (d, $^2J_{CF}$ = 19.0 Hz), 112.3 (d, $^2J_{CF}$ = 23.7 Hz), 111.7 (d, $^2J_{CF}$ = 22.7 Hz) ppm. ^{19}F{^{1}H} NMR (376 MHz, CD₃CN) δ_F = −72.9 (d, $^1J_{PF}$ = 709.4 Hz), −106.5 (s), −128.6 (d, $^3J_{FF}$ = 21.6 Hz), −133.1 (d, $^3J_{FF}$ = 21.5 Hz) ppm. HRMS (ES+): *m/z* calc'd 867.1283 for C₃₈H₂₀N₆F₆^{193}Ir; found 867.1292 [M − PF₆]⁺. UV−vis (MeCN) λ_{max} (ε × 10^4 / L mol⁻¹ cm⁻¹): 259 (4.3), 284 (3.5), 362 (2.2), 451 (0.6) nm. FTIR (solid, cm⁻¹) (ATR) v_{max}: 1588, 1570, 1534, 1509, 1448, 1353, 1262, 1232, 1202, 1165, 1126, 1065, 1031, 835, 817, 765, 738, 669, 628, 556, 447, 418.

Synthesis of [Ir(L⁸)₂(bpy)][PF₆] *(Ir-2h)*

Prepared similarly from **[(Ir(L⁸)₂(*μ*-Cl))₂]** (216 mg, 0.145 mmol) and 2,2'-bipyridine (49.8 mg, 0.319 mmol) to give the product as a red solid (55.9 mg, 19.0%). ^{1}H NMR (500 MHz, (CD₃)₂CO) δ_H = 9.87 (s, 2H), 8.65 (dd, $^3J_{HH}$ = 5.6,

$^4J_{HH}$ = 0.8 Hz, 2H), 8.58 (ddd, $^3J_{HF}$ = 10.8, $^4J_{HF}$ = 6.6, $^5J_{HF}$ = 1.6 Hz, 2H), 8.46 (d, $^3J_{HH}$ = 8.1 Hz, 2H), 8.22 (*app.* td, $^3J_{HH}$ = 7.9, $^4J_{HH}$ = 1.5 Hz, 2H), 8.05 (dd, $^3J_{HH}$ = 8.3, $^4J_{HH}$ = 1.1 Hz, 2H), 7.81 (ddd, $^3J_{HH}$ = 7.6, 5.6, $^4J_{HH}$ = 1.3 Hz, 2H), 7.71 (ddd, $^3J_{HH}$ = 8.3, 6.5, $^4J_{HH}$ = 1.7 Hz, 2H), 7.32 − 7.25 (m, 4H) ppm. $^{13}C\{^1H\}$ NMR (126 MHz, (CD$_3$)$_2$CO) δ_C = 156.5, 149.9, 144.6, 143.9, 143.6, 142.9, 142.4, 142.0, 132.8, 131.5, 131.3, 130.5, 125.5, 124.8, 114.3 (dd, $^2J_{CF}$ = 19.2, $^3J_{CF}$ = 3.4 Hz) ppm. $^{19}F\{^1H\}$ NMR (376 MHz, CD$_3$CN) δ_F = −73.0 (d, $^1J_{PF}$ = 706.0 Hz), −127.1 (dd, $^3J_{FF}$ = 21.9, $^4J_{FF}$ = 5.6 Hz), −142.2 (dd, $^3J_{FF}$ = 18.9, $^4J_{FF}$ = 5.6 Hz), −156.1 ($^3J_{FF}$ = 21.9, $^4J_{FF}$ = 19.0 Hz) ppm. HRMS (ES+): *m/z* calc'd 867.1283 for C$_{38}$H$_{20}$N$_6$F$_6$^{193}Ir; found 867.1296 [M − PF$_6$]$^+$. UV−vis (MeCN) λ_{max} (ϵ × 10^4 / L mol^{-1} cm^{-1}): 207 (5.8), 240 (4.3), 282 (4.6), 356 (2.5), 370 (2.6), 444 (0.5) nm. FTIR (solid, cm^{-1}) (ATR) v_{max}: 1705, 1628, 1604, 1539, 1478, 1469, 1417, 1368, 1298, 1200, 1141, 1137, 1045, 832, 677, 737, 674, 639, 556.

Synthesis of [Ir(L^9)$_2$(bpy)][PF$_6$] *(Ir-2i)*

Prepared similarly from **[(Ir(L^9)$_2$(μ-Cl))$_2$]** (67.0 mg, 0.042mmol) and 2,2'-bipyridine (14.3 mg, 0.092 mmol) to give the product as an orange solid (14.8 mg, 16.6%). ^1H NMR (500 MHz, CD$_3$CN) δ_H = 9.43 (s, 2H), 8.35 (dd, $^3J_{HH}$ = 5.6, $^4J_{HH}$ = 0.8 Hz, 2H), 8.21 (ddd, $^3J_{HF}$ = 10.8, $^4J_{HF}$ = 6.6, $^5J_{HF}$ = 1.6 Hz, 2H), 8.16 (d, $^3J_{HH}$ = 8.0 Hz, 2H), 8.05 (*app.* td $^3J_{HH}$ = 7.9, $^4J_{HH}$ = 1.5 Hz, 2H), 7.75 (s, 2H), 7.62 (ddd, $^3J_{HH}$ = 7.6, 5.6, $^4J_{HH}$ = 1.3 Hz, 2H), 6.82 (s, 2H), 2.30 (s, 6H), 1.79 (s, 6H) ppm. $^{13}C\{^1H\}$ NMR (126 MHz, CD$_3$CN) δ_C = 161.6, 158.9 − 156.1 (m), 156.4, 150.0, 144.6, 143.4, 142.7, 141.9, 141.7, 141.1, 130.1 (d, $^3J_{CF}$ = 3.2 Hz), 127.8, 127.6, 125.6, 124.2, 113.3 (dd, $^2J_{CF}$ = 18.8, $^3J_{CF}$ = 3.2 Hz), 20.1, 19.6 ppm. $^{19}F\{^1H\}$ NMR (376 MHz, CD$_3$CN) δ_F = −72.9 (d, $^1J_{PF}$ = 706.1 Hz), −127.3 (dd, $^3J_{FF}$ = 22.0, $^4J_{FF}$ = 5.5 Hz), −142.7 (dd, $^3J_{FF}$ = 18.9, $^4J_{FF}$ = 5.5 Hz), −157.0 (dd, $^3J_{FF}$ = 21.9, 19.0 Hz) ppm. HRMS (ES+): *m/z* calc'd 923.1909 for C$_{42}$H$_{28}$N$_6$F$_6$^{193}Ir; found 923.1918 [M − PF$_6$]$^+$. UV−vis (MeCN) λ_{max} (ϵ × 10^4 / L mol^{-1} cm^{-1}): 240 (4.3), 284 (4.6), 362 (2.2), 379 (2.9), 440 (0.7) nm. FTIR (solid, cm^{-1}) (ATR) v_{max}: 1559, 1533, 1481, 1466, 1437, 1369, 1297, 1163, 1045, 1026, 911, 855, 850, 796, 780, 738, 704, 672, 556, 520, 484, 453.

Synthesis of [Ir(L^{10})$_2$(bpy)][PF$_6$] *(Ir-2j)*

Prepared similarly from **[(Ir(L^{10})$_2$(μ-Cl))$_2$]** (69.0 mg, 0.042mmol) and 2,2'-bipyridine (14.5 mg, 0.093 mmol) to give the product as an orange solid (17.4

mg, 19.0%). ^{1}H NMR (500 MHz, (CD$_3$)$_2$CO) δ_H = 9.90 (s, 2H), 8.69 (dd, $^3J_{HH}$ = 5.7, $^4J_{HH}$ = 0.8 Hz, 2H), 8.64 − 8.56 (m, 4H), 8.34 − 8.29 (m, 2H), 8.05 (dd, $^3J_{HF}$ = 10.2, $^4J_{HF}$ = 8.4 Hz, 2H), 7.86 (ddd, $^3J_{HH}$ = 7.6, 5.6, $^4J_{HH}$ = 1.3 Hz, 2H), 7.10 ($^3J_{HF}$ = 12.3, $^4J_{HF}$ = 7.8 Hz, 2H) ppm. ^{13}C{^{1}H} NMR (126 MHz, (CD$_3$)$_2$CO) δ_C = 163.5, 156.7, 153.7 (dd, $^1J_{CF}$ = 259.7, $^2J_{CF}$ = 19.1 Hz), 150.1, 145.2 (d, $^3J_{CF}$ = 3.2 Hz), 142.3, 140.5 (d, $^2J_{CF}$ = 11.8 Hz), 140.3 (d, $^2J_{CF}$ = 11.1 Hz), 130.7, 126.4, 117.7 (dd, $^2J_{CF}$ = 17.8, $^3J_{CF}$ = 1.4 Hz), 114.8 (d, $^2J_{CF}$ = 22.3 Hz), 112.4 (d, $^2J_{CF}$ = 22.5 Hz) ppm. ^{19}F{^{1}H} NMR (376 MHz, (CD$_3$)$_2$CO) δ_F = −72.6 (d, $^1J_{PF}$ = 707.4 Hz), −126.9 (dd, $^3J_{FF}$ = 22.3, $^4J_{FF}$ = 5.7 Hz), −127.9 (d, $^3J_{FF}$ = 21.7 Hz), −131.4 (d, $^3J_{FF}$ = 21.7 Hz), −141.7 (dd, $^3J_{FF}$ = 19.2, $^4J_{FF}$ = 5.7 Hz), -155.0 (dd, $^3J_{FF}$ = 22.9, $^3J_{FF}$ = 18.7 Hz) ppm. HRMS (ES+): m/z calc'd 939.0906 for C$_{38}$H$_{16}$N$_6$F$_{10}$^{193}Ir; found 939.0911 [M − PF$_6$]$^+$. UV−vis (MeCN) λ_{max} ($\varepsilon \times 10^4$ / L mol^{-1} cm^{-1}): 206 (4.8), 239 (3.2), 280 (2.9), 360 (1.8), 371 (1.8), 441 (0.3) nm. FTIR (solid, cm^{-1}) (ATR) v_{max}: 2945, 1732, 1541, 1495, 1470, 1443, 1404, 1373, 1250, 1234, 1202, 1165, 1045, 1007, 837, 766, 673, 625, 557, 442, 419.

2.6: References

1   V. W. W. Yam, A. K. W. Chan and E. Y. H. Hong, *Nat. Rev. Chem.*, 2020, **4**, 528–541.

2   M. S. Lowry and S. Bernhard, *Eur. J. Chem.*, 2006, **12**, 7970–7977.

3   Y. You and S. Y. Park, *Dalton Trans.*, 2009, 1267–1282.

4   G. Zhou, Q. Wang, C. L. Ho, W. Y. Wong, D. Ma, L. Wang and Z. Lin, *Chem. Asian J.*, 2008, **3**, 1830–1841.

5   J. Li, P. I. Djurovich, B. D. Alleyne, M. Yousufuddin, N. N. Ho, J. C. Thomas, J. C. Peters, R. Bau and M. E. Thompson, *Inorg. Chem.*, 2005, **44**, 1713–1727.

6   Y. You and S. Y. Park, *J. Am. Chem. Soc.*, 2005, **127**, 12438–12439.

7   Z. Feng, Y. Sun, X. Yang and G. Zhou, *Chem. Rec.*, 2019, **19**, 1710–1728.

8   S. Lamansky, P. Djurovich, D. Murphy, F. Abdel-Razzaq, R. Kwong, I. Tsyba, M. Bortz, B. Mui, R. Bau and M. E. Thompson, *Inorg. Chem.*, 2001, **40**, 1704–1711.

9   S. Lamansky, P. Djurovich, D. Murphy, F. Abdel-Razzaq, H.-E. Lee, C. Adachi, P. E. Burrows, S. R. Forrest and M. E. Thompson, *J. Am. Chem. Soc.*, 2001, **123**, 4304–4312.

10   P. Sun, K. Wang, B. Zhao, T. Yang, H. Xu, Y. Miao, H. Wang and B. Xu, *Tetrahedron*, 2016, **72**, 8335–8341.

11   S. Tao, S. L. Lai, C. Wu, T. W. Ng, M. Y. Chan, W. Zhao and X. Zhang, *Org. Electron.*, 2011, **12**, 2061–2064.

12   Y. Chen, C. Liu and L. Wang, *Tetrahedron*, 2019, **75**, 130686.

13   Z. Chen, L. Wang, C. L. Ho, S. Chen, S. Suramitr, A. Plucksacholatarn, N. Zhu, S. Hannongbua and W. Y. Wong, *Adv. Opt. Mater.*, 2018, **6**, 1800824.

14   X. Xu, Y. Zhao, J. Dang, X. Yang, G. Zhou, D. Ma, L. Wang, W. Y. Wong, Z. Wu and X. Zhao, *Eur. J. Inorg. Chem.*, 2012, **2012**, 2278–2288.

15   C. Liu, X. Rao, X. Lv, J. Qiu and Z. Jin, *Dyes Pigments*, 2014, **109**, 13–20.

16   Y. J. Su, H. L. Huang, C. Le Li, C. H. Chien, Y. T. Tao, P. T. Chou, S. Datta and R. S. Liu, *Adv. Mater.*, 2003, **15**, 884–888.

17   G. Li, P. Li, X. Zhuang, K. Ye, Y. Liu and Y. Wang, *ACS Appl. Mater. Interfaces*, 2017, **9**, 11749–11758.

18   Y. Ding, D. Liu, J. Li, H. Li, H. Ma, D. Li and R. Niu, *Dyes Pigments*, 2020, **179**, 108405.

19   K. R. J. Thomas, M. Velusamy, J. T. Lin, C. H. Chien, Y. T. Tao, Y. S. Wen, Y. H. Hu and P. T. Chou, *Inorg. Chem.*, 2005, **44**, 5677–5685.

20   J. Lin, N. Y. Chau, J. L. Liao, W. Y. Wong, C. Y. Lu, Z. T. Sie, C. H. Chang, M. A. Fox, P. J. Low, G. H. Lee and Y. Chi, *Organometallics*, 2016, **35**, 1813–1824.

21   G. Zhou, W.-Y. Wong and X. Yang, *Chem. Asian J.*, 2011, **6**, 1706–1727.

22   T.-Y. Li, J. Wu, Z.-G. Wu, Y.-X. Zheng, J.-L. Zuo and Y. Pan, *Coord. Chem. Rev.*, 2018, **374**, 55–92.

23   H. J. Bolink, E. Coronado, S. Garcia Santamaria, M. Sessolo, N. Evans, C. Klein, E. Baranoff, K. Kalyanasundaram, M. Graetzel and Md. K. Nazeeruddin, *Chem. Commun.*, 2007, **0**, 3276.

24   S. Okada, K. Okinaka, H. Iwawaki, M. Furugori, M. Hashimoto, T. Mukaide, J. Kamatani, S. Igawa, A. Tsuboyama, T. Takiguchi and K. Ueno, *Dalton Trans.*, 2005, 1583–1590.

25   X. Liu, S. Wang, B. Yao, B. Zhang, C. L. Ho, W. Y. Wong, Y. Cheng and Z. Xie, *Org. Electron.*, 2015, **21**, 1–8.

26   C. L. Ho, W. Y. Wong, Q. Wang, D. Ma, L. Wang and Z. Lin, *Adv. Funct. Mater.*, 2008, **18**, 928–937.

27   A. B. Tamayo, S. Garon, T. Sajoto, P. I. Djurovich, I. M. Tsyba, R. Bau and M. E. Thompson, *Inorg. Chem.*, 2005, **44**, 8723–8732.

28   H. K. Dahule, S. J. Dhoble, J. S. Ahn and R. Pode, *J. Phys. Chem. Solids*, 2011, **72**, 1524–1528.

29   Z. Chen, H. Zhang, D. Wen, W. Wu, Q. Zeng, S. Chen and W. Y. Wong, *Chem. Sci.*, 2020, **11**, 2342–2349.

30   X. Mao, F. Xie, X. Wang, Q. Wang, Z. Qiu, M. R. J. Elsegood, J. Bai, X. Feng, C. Redshaw, Y. Huo, J. Y. Hu and Q. Chen, *Chin. J. Chem.*, 2021, **39**, 2154–2162.

31   S. Wang, Z. Cheng, X. Song, X. Yan, K. Ye, Y. Liu, G. Yang and Y. Wang, *ACS Appl. Mater. Interfaces*, 2017, **9**, 9892–9901.

32   J. Gao, H. You, J. Fang, D. Ma, L. Wang, X. Jing and F. Wang, *Synth. Met.*, 2005, **155**, 168–171.

33   Y. Ha, J. H. Seo and Y. K. Kim, *Synth. Met.*, 2008, **158**, 548–552.

34   S. Y. Ahn, H. S. Lee, J. Seo, Y. K. Kim and Y. Ha, *Thin Solid Films*, 2009, **517**, 4111–4114.

35   S. A. Fitzgerald, H. Y. Otaif, C. E. Elgar, N. Sawicka, P. N. Horton, S. J. Coles, J. M. Beames and S. J. A. Pope, *Inorg. Chem.*, 2021, **60**, 15467–15484.

36   S. K. Chaudhuri, S. Roy and S. Bhar, *Beilstein J. Org. Chem.*, 2012, **8**, 323–329.

37   J. D. Billimoria and N. F. Maclagan, *J. Chem. Soc.*, 1954, **11**, 3257–3262.

38   S. K. Juneja, D. Choudhary, S. Paul and R. Gupta, *Synth. Commun.*, 2006, **36**, 2877–2881.

39   S. K. Guha, B. Wu, B. S. Kim, W. Baik and S. Koo, *Tetrahedron Lett.*, 2006, **47**, 291–293.

40   D. Vražic, M. Jereb, K. K. Laali and S. Stavber, *Molecules*, 2013, **18**, 74–96.

41   A. Vektariene, G. Vektaris, J. Svoboda, A. Vektariene, G. Vektaris and J. Svoboda, in *12th International Electronic Conference on Synthetic Organic Chemistry*, Molecular Diversity Preservation International, 2008, pp. 1–9.

42   B. Das, K. Venkateswarlu, K. Suneel and A. Majhi, *Tetrahedron Lett.*, 2007, **48**, 5371–5374.

43   Q. Guo, J. Chen, G. Shen, G. Lu, X. Yang, Y. Tang, Y. Zhu, S. Wu and B. Fan, *J. Org. Chem.*, 2022, **87**, 540–546.

44   P. Y. Lin, R. S. Hou, H. M. Wang, I. J. Kang and L. C. Chen, *J. Chin. Chem. Soc.*, 2009, **56**, 683–687.

45   L. J. Martin, A. L. Marzinzik, S. V. Ley and I. R. Baxendale, *Org. Lett.*, 2011, **13**, 320–323.

46   V. Wray, L. Ernst and E. Lustig, *J. Magn. Reson. (1969)*, 1977, **27**, 1–21.

47   N. Castillo, C. F. Matta and R. J. Boyd, *J. Chem. Inf. Model.*, 2005, **45**, 354–359.

48   M. Nonoyama, *Bull. Chem. Soc. Jpn.*, 1974, **47**, 767–768.

49   H. G. Mayfield and W. E. Bull, *J. Chem. Soc. A*, 1971, 2279–2281.

50   J. N. Gayton, S. Autry, R. C. Fortenberry, N. I. Hammer and J. H. Delcamp, *Molecules*, 2018, **23**, 3051.

51   K. A. King and R. J. Watts, *J. Am. Chem. Soc.*, 1987, **109**, 1589–1590.

52   D. Lin-Vien, N. B. Colthup, W. G. Fateley and J. G. Grasselli, *The Handbook of Infrared and Raman Characteristic Frequencies of Organic Molecules*, 1991, 263–276.

53   D. Zeng, X. A. Yuan, J. C. Liu, L. Li, L. P. Wang, M. F. Qin, S. S. Bao, J. Ma and L. M. Zheng, *ACS Omega*, 2019, **4**, 16543–16550.

54   E. E. Langdon-Jones, A. J. Hallett, J. D. Routledge, D. A. Crole, B. D. Ward, J. A. Platts and S. J. A. Pope, *Inorg. Chem.*, 2013, **52**, 448–456.

55   Y. C. Zhu, L. Zhou, H. Y. Li, Q. L. Xu, M. Y. Teng, Y. X. Zheng, J. L. Zuo, H. J. Zhang and X. Z. You, *Adv. Mater.*, 2011, **23**, 4041–4046.

56   S. Ikawa, S. Yagi, T. Maeda, H. Nakazumi, H. Fujiwara and Y. Sakurai, *Dyes Pigments*, 2012, **95**, 695–705.

57   A. Bondi, *J. Phys. Chem.*, 1964, **68**, 441–451.

58   S. Ladouceur and E. Zysman-Colman, *Eur. J. Inorg. Chem.*, 2013, 2985–3007.

59   T. M. Stonelake, K. A. Phillips, H. Y. Otaif, Z. C. Edwardson, P. N. Horton, S. J. Coles, J. M. Beames and S. J. A. Pope, *Inorg. Chem.*, 2020, **59**, 2266–2277.

60   F. M. Hwang, H. Y. Chen, P. S. Chen, C. S. Liu, Y. Chi, C. F. Shu, F. I. Wu, P. T. Chou, S. M. Peng and G. H. Lee, *Inorg. Chem.*, 2005, **44**, 1344–1353.

61   P. Si, H. F. Zhe, A. H. Zhou, X. Q. Liu, M. Y. Teng, M. Z. Rong, Y. F. Wang, Q. Wang, Z. L. Wang and J. Zhang, *New J. Chem.*, 2021, **45**, 18796–18804.

62   C. C. Wang, Y. M. Jing, T. Y. Li, Q. L. Xu, S. Zhang, W. N. Li, Y. X. Zheng, J. L. Zuo, X. Z. You and X. Q. Wang, *Eur. J. Inorg. Chem.*, 2013, **2013**, 5683–5693.

63   A. Tsuboyama, H. Iwawaki, M. Furugori, T. Mukaide, J. Kamatani, S. Igawa, T. Moriyama, S. Miura, T. Takiguchi, S. Okada, M. Hoshino and K. Ueno, *J. Am. Chem. Soc.*, 2003, **125**, 12971–12979.

64   C. Caporale and M. Massi, *Coord. Chem. Rev.*, 2018, **363**, 71–91.

65   K. K. W. Lo, D. C. M. Ng and C. K. Chung, *Organometallics*, 2001, **20**, 4999–5001.

66   I. S. Kritchenkov, A. I. Solomatina, D. O. Kozina, V. V. Porsev, V. V. Sokolov, M. V. Shirmanova, M. M. Lukina, A. D. Komarova, V. I. Shcheslavskiy, T. N. Belyaeva, I. K. Litvinov, A. V. Salova, E. S. Kornilova, D. V. Kachkin and S. P. Tunik, *Molecules*, 2021, **26**, 2898.

67   F. S. M. Canisares, A. M. G. Mutti, E. F. Santana, V. C. Oliveira, D. G. S. M. Cavalcante, A. E. Job, A. M. Pires and S. A. M. Lima, *Photochem. Photobiol. Sci.*, 2022, **21**, 1077–1090.

68   S. H. Wu, J. W. Ling, S. H. Lai, M. J. Huang, C. H. Cheng and I. C. Chen, *J. Phys. Chem. A*, 2010, **114**, 10339–10344.

69   K. Suzuki, A. Kobayashi, S. Kaneko, K. Takehira, T. Yoshihara, H. Ishida, Y. Shiina, S. Oishi and S. Tobita, *Phys. Chem. Chem. Phys.*, 2009, **11**, 9850–9860.

70   P. Douglas, H. D. Burrows and R. C. Evans, in *Applied Photochemistry*, 2013, pp. 71–73.

71   K. J. Suhr, L. D. Bastatas, Y. Shen, L. A. Mitchell, G. A. Frazier, D. W. Taylor, J. D. Slinker and B. J. Holliday, *Dalton Trans.*, 2016, **45**, 17807–17823.

72   R. D. Costa, E. Ortí, H. J. Bolink, S. Graber, S. Schaffner, M. Neuburger, C. E. Housecroft and E. C. Constable, *Adv. Funct. Mater.*, 2009, **19**, 3456–3463.

73   R. D. Costa, E. Ortí, H. J. Bolink, F. Monti, G. Accorsi and N. Armaroli, *Angew. Chem. Int. Ed.*, 2012, **51**, 8178–8211.

74   M. Santander-Nelli, B. Boza, F. Salas, D. Zambrano, L. Rosales and P. Dreyse, *Molecules*, 2022, **27**, 2623.

75   G. R. Fulmer, A. J. M. Miller, N. H. Sherden, H. E. Gottlieb, A. Nudelman, B. M. Stoltz, J. E. Bercaw and K. I. Goldberg, *Organometallics*, 2010, **29**, 2176–2179.

76   S. J. Coles and P. A. Gale, *Chem. Sci.*, 2012, **3**, 683–689.

77   O. V. Dolomanov, L. J. Bourhis, R. J. Gildea, J. A. K. Howard and H. Puschmann, *J. Appl. Crystallogr.*, 2009, **42**, 339–341.

78   G. M. Sheldrick, *Acta Crystallogr. A*, 2015, **71**, 3–8.

79   G. M. Sheldrick, *Acta Crystallogr. C*, 2015, **71**, 3–8.

80   B. Macchia, M. Macchia, C. Manera, E. Martinotti, S. Nencetti, E. Orlandini, A. Rossello and R. Scatizzi, *Eur. J. Med. Chem.*, 1995, **30**, 869–880.

81   A. M. Patel, D. J. Patel and K. S. Pandya, *Der Chem. Sin.*, 2014, **5**, 24–29.

82   Q. Xu, K. Bao, M. Sun, J. Xu, Y. Wang, H. Tian, D. Zuo, Q. Guan, Y. Wu and W. Zhang, *Sci. Rep.*, 2017, **7**, 1–12.

83   A. K. MacHarla, R. Chozhiyath Nappunni, M. R. Marri, S. Peraka and N. Nama, *Tetrahedron Lett.*, 2012, **53**, 191–195.

84   M. Wojdyr, *J. Appl. Cryst.*, 2010, **43**, 1126–1128.

Chapter 3: Neutral Pt(II) Complexes as Efficient Photosensitisers for Triplet-Triplet Annihilation Upconversion

Chapter 3

3.1: Introduction

Square planar platinum complexes have gained traction as phosphors for luminescent applications in recent times. These compounds offer unique properties by virtue of potential aggregation features along with other intermolecular interactions that can facilitate photophysical pathways. However, further research is required to overcome issues such as reduced solubility, whilst enhancing absorption at longer wavelengths.

3.1.1: Properties and Applications of Platinum Compounds

Pt(II) species have specific chemical properties which are responsible for their vast range of potential applications. Such properties include the ability to form stable structures based upon square planar geometries, attributed to the d^8 electron configuration and rearrangement of d-orbital energies.

In 1978, *cis*-platin gained regulatory approval for use as a highly-effective chemotherapy medication for a variety of cancers, initiating a surge in the development of Pt(II) species as antitumour agents.[1] More recently, related complexes have been explored in the field of photoluminescence. As discussed previously for Ir(III) species, Pt(II) compounds can also act as phosphorescent emitters where the heavy platinum atom induces strong spin-orbit coupling, enhancing the mixing of singlet and triplet excited states. As a result, these compounds offer advantages in applications such as bioimaging,[2] OLEDs,[3–5] photocatalysis,[6] and as singlet oxygen sensitisers,[7] where a variety of ligand motifs have been implemented with varying chelation modes.

In contrast to octahedral analogues, square planar complexes offer possibilities for aggregation features due to the absence of ligands along the z-axis. These features can give rise to unique photophysical properties, where emission can originate from a mixed metal-metal-to-ligand charge transfer (^{3}MMLCT) excited state, a result of non-covalent metallophilic Pt---Pt interactions formed by aggregation-induced emission (AIE).[8] This interaction occurs when the sum of Van der Waals radii of the two metal atoms is larger than the metal-metal distance. The filled dz^2 orbital lies outside the plane of the molecule at the axial position, allowing it to interact with the equivalent frontier orbitals on adjacent

monomers in the form of a $dz^2 \rightarrow dz^2$ interaction to produce filled d_σ and $d_\sigma*$ molecular orbitals, where the latter becomes the new HOMO. Che reported that this is the result of relativistic effects, wherein metal-metal Pauli repulsion is induced by significant mixing of the $(n+1)s$ and nd orbitals of the metal centre, but is suppressed by hybridisation of the $(n+1)p$ and nd orbitals in closed-shell organometallic complexes, thereby making this interaction favourable.[9] By controlling the distance between the two Pt atoms in a binuclear species, tunability of the photophysical properties can be achieved, where a bathochromic shift in emission wavelength has been demonstrated upon decreasing this spacing. This has been correlated with the nature of the emissive state, which consists of mixed ^{3}LC/^{3}MLCT character for a monomeric species and a lower-energy ^{3}MMLCT state when a Pt-Pt interaction was permitted.[10] This phenomenon is illustrated in **Figure 3.1**.[11]
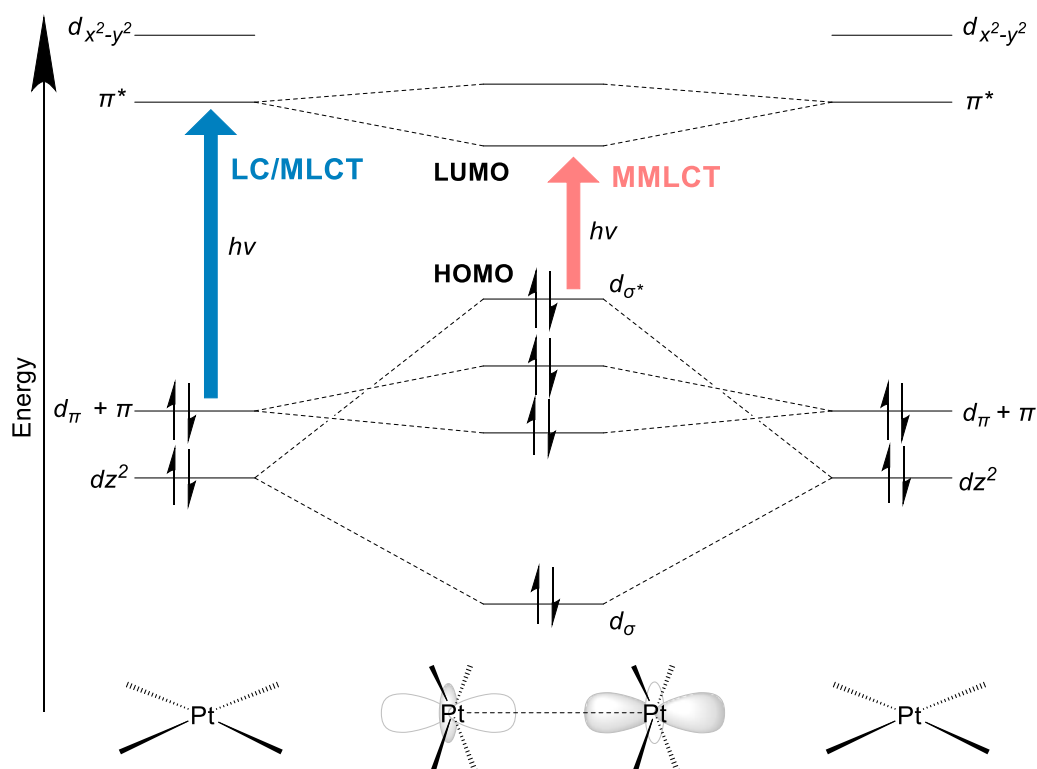
Figure 3.1: MO diagram depicting the energy levels of the monomeric Pt(II) species and the subsequent rearrangement upon aggregation.[11]

Compounds based upon **[Pt(C^N)(O^O)]** are often explored, where the O^O ligand is acetylacetonate (**acac**) or another functionalised β-diketonate. An early study by Brooks *et al.* investigated these types of species (**Figure 3.2**) where

the benchmark complex, **[Pt(ppy)(acac)]**, displayed emission at 486 nm in degassed 2-methyl THF solutions, with τ_{obs} = 2.6 µs and Φ_P = 15%.[12] Here, the ligands surrounding the metal greatly influenced the nature of the electronic and photophysical properties of the subsequent complexes. Computational studies showed that the energy of the LUMO was dominated by the C^N ligand, whilst the HOMO consisted of contributions from the Pt atom, acac and C^N ligand collectively.

[Pt(ppy)(acac)]   [Pt(ppy)(dpm)]

[Pt(4,6dfppy)(acac)]   [Pt(6*t*Fmppy)(dpm)]
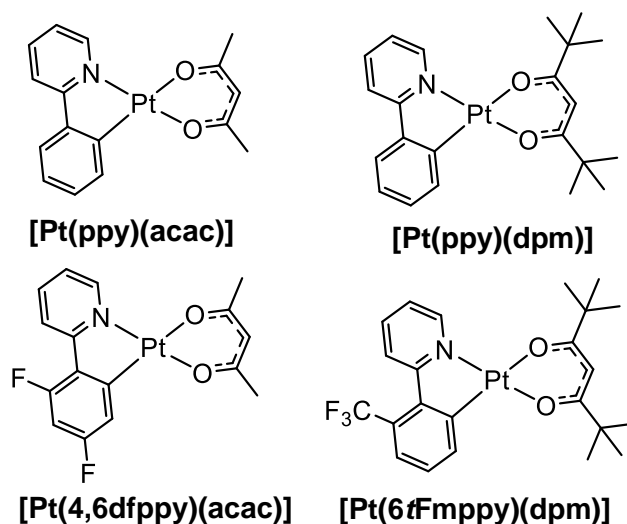
Figure 3.2: Structures of monocyclometallated phosphorescent Pt(II) complexes developed by Brooks in 2002.[12]

Functionalisation of the β-diketonate ligand offers a route to desirable properties such as enhanced solubilities and reduced self-quenching mechanisms, without directly changing the C^N ligand.[13,14] However, studies have shown that the photophysical properties can differ greatly when certain O^O ligands are used, due to perturbation of the excited state and energy back-flow.[15] For example, Tronnier *et al.* reported that tunable stacking behaviour was attainable through functionalised O^O ancillary ligands by means of steric repulsion, but no emission was seen in the case for when O^O = **hfacac** (hexafluoroacetylaceonate) (**Figure 3.3**).[16]

NO EMISSION λ_{em}: 530 nm
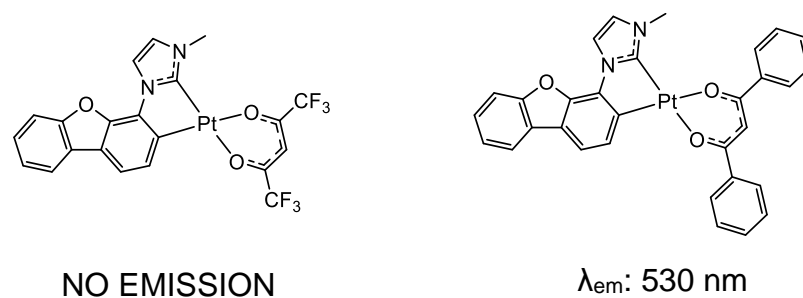
Figure 3.3: *Pt(II) complexes bearing chelating NHC bidenzofuranyl ligands, where the ancillary ligand was altered. Emission measured in PMMA films (2 wt%).*[16]

However, substitution at the cyclometallated ligand has offered a route towards more varied properties. Studies conducted by Xing *et al.* showed that fluorination or phenylation at different positions of the phenyl ring in **[Pt(ppy)(acac)]** resulted in complexes spanning a range of emission wavelengths with different oxygen sensitivities and photostabilities.[17,18]

λ_{abs}: 404 nm λ_{abs}: 414 nm λ_{abs}: 398 nm
λ_{em}: 586 nm λ_{em}: 588 nm λ_{em}: 581 nm
τ_{obs}: 7.08 µs τ_{obs}: 2.85 µs τ_{obs}: 8.89 µs
Φ_P: 0.09 Φ_P: 0.06 Φ_P: 0.12
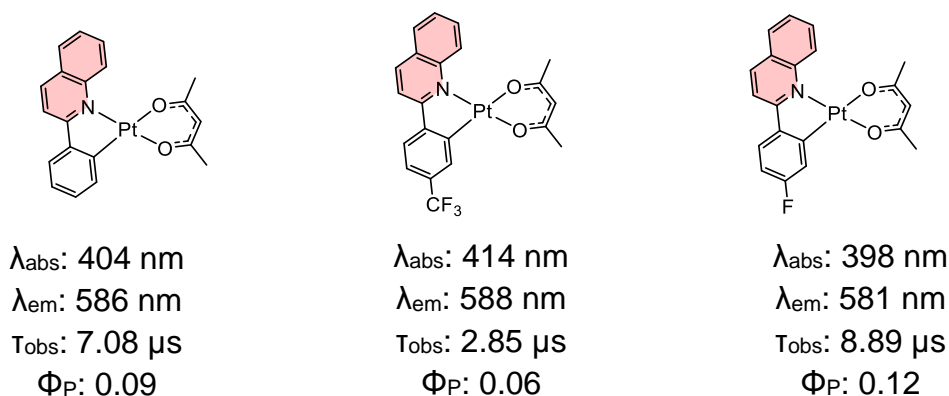
Figure 3.4: *Pt(II) complexes containing 2-phenylquinoline ligands by Liu in 2014, where all measurements were recorded in degassed DCM solutions.*[19]

In addition to Pt-Pt interactions, planar C^N ligands with extended π-conjugated systems offer possibilities for interplanar π-π contacts, where the introduction of nitrogen into an aromatic system increases the tendency to stack and take part in such interactions.[20] In 2014, Liu *et al.* reported the first example of Pt(II) complexes containing 2-phenylquinoline ligands for oxygen sensing applications.[19] These compounds displayed red-shifted phosphorescence between 578 – 599 nm relative to **[Pt(ppy)(acac)]**, where a bathochromic shift of ~100 nm was seen alongside an enhancement in τ_{obs}, whilst exhibiting remarkable sensitivity to oxygen. Subtle tunability in emission properties was also achievable by functionalisation of the phenyl ring at the 4-position (**Figure 3.4**).

Quinoxalines have also been incorporated into Pt(II) complexes for use as potential anti-cancer agents,[21,22] but are relatively unexplored within the area of photoluminescent Pt(II) chemistry. One of the few studies, reported by Culham in 2013, investigated pyrazine-based C^N ligands on Pt(II) in the development of efficient red phosphors.[23] However, the use of **dpm** (dipivaloylmethane) as an ancillary ligand to promote solubility, prevented any observable aggregation features and thus ^{3}MMLCT emission (**Figure 3.5**).

λ$_{abs}$: 455, *488* nm
λ$_{em}$: 668 nm
T$_{obs}$: 3.7 (0.7) µs
Φ$_P$: 14%

λ$_{abs}$: 511 nm
λ$_{em}$: 639, *686* nm
T$_{obs}$: 3.8 (0.7) µs
Φ$_P$: 13%
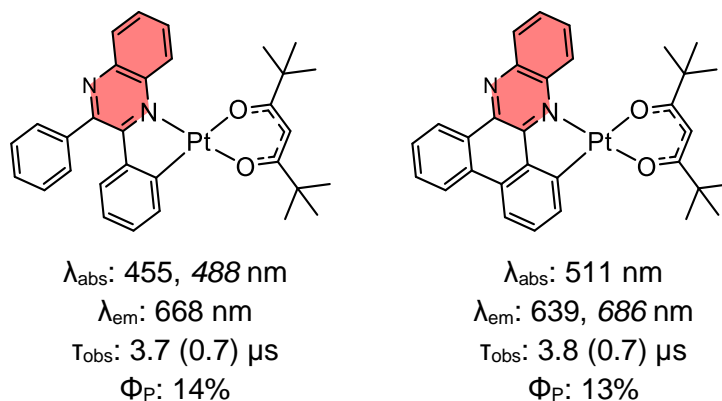
Figure 3.5: *Pt(II) complexes reported by Culham in 2013. Spectroscopic data was recorded in degassed DCM solutions at RT, except for the values in parentheses, which were in aerated solutions. Italicised values are shoulder peaks.*

3.1.2: Triplet-Triplet Annihilation Upconversion (TTA-UC)

In general, energy upconversion is an *anti*-Stokes process involving the absorption of low-energy light and generation of higher-energy photons, where λ$_{em}$ is shorter than λ$_{ex}$. The utilisation of longer excitation wavelengths offers significant advantages in areas such as biosensing, where NIR excitation results in reduced autofluorescence and deep penetration of tissue.[24] Upconversion components are regularly explored in solar cell technology[25,26] and photocatalysis,[27] where high efficiency can be achieved through the harvesting of low-energy light.

TTA-UC is a specific type of upconversion process where energy is exchanged from the triplet state of the sensitiser (through ISC) to the triplet state of the acceptor or *annihilator* molecule (usually a highly efficient organic chromophore) through triplet-triplet energy transfer (TTET). For this process to occur, the triplet state of the acceptor must lie below that of the sensitiser, where the process becomes more favourable upon increasing this energy gap.

Population of the acceptor triplet state permits triplet-triplet annihilation (TTA) to occur between two of the acceptor molecules, where the singlet state becomes populated in one, and deactivation back to the ground state occurs in the other.[28] This process is represented schematically in **Figure 3.6**. TTA-UC offers advantages over other energy upconversion methods due to high Φ_{UC} values, tunable excitation and emission wavelengths and low excitation power (akin to the energy of sunlight).[29]
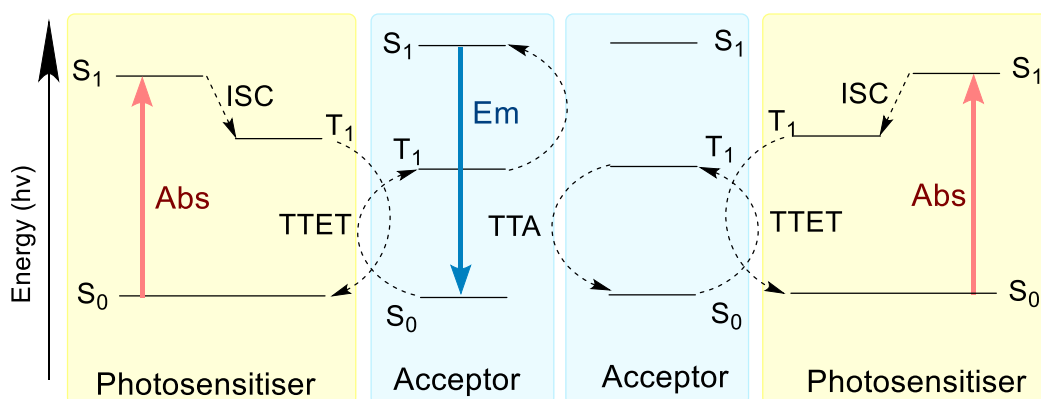
Figure 3.6: Jablonski diagram for the TTA-UC process, where the dotted lines represent non-radiative decay pathways.

Transition metal complexes are useful as sensitisers since they tend to have longer excitation wavelengths with large molar extinction coefficients. They also possess relatively long triplet lifetimes compared to organic chromophores, which facilitates diffusional quenching and interaction with the acceptor whilst in its triplet state.

Some examples of transition metal-based photosensitisers are displayed in **Figure 3.7**. Pt has repeatedly been investigated in the form of porphyrin-type complexes due to enhanced SOC facilitating efficient ISC (near unity), in addition to high photostabilities.[28] One such complex includes **Pt(TPBP)** (**1**), which displays high λ_{abs} with triplet state lifetimes of 41.5 µs and a maximum Φ_{UC} of 65% in conjunction with perylene as an acceptor.[30] However, the lack of flexibility with regard to tuning the T_1 excited states comes as a disadvantage, so cyclometallated Pt(II) complexes (with tunable T_1 states) have also been investigated as triplet photosensitisers.[29] For example, chromophore-functionalised acetylide ligands incorporated into the structure demonstrated Φ_{UC} of up to 19.5% by enhanced triplet lifetimes (localised on the tridentate

ligand) and intense absorption within the visible range (**2**).[31] Other examples include Pt(II) complexes with Schiff-base type ligands (**3**),[32,33] and *bis*(aryleneethynylene) *bis*(trialkylphosphine) complexes (**4**).[34] Examples also exist with Pd(II)[35] (**5**), Ir(III)[36](**6**), and Re(I)[37] (**7**).
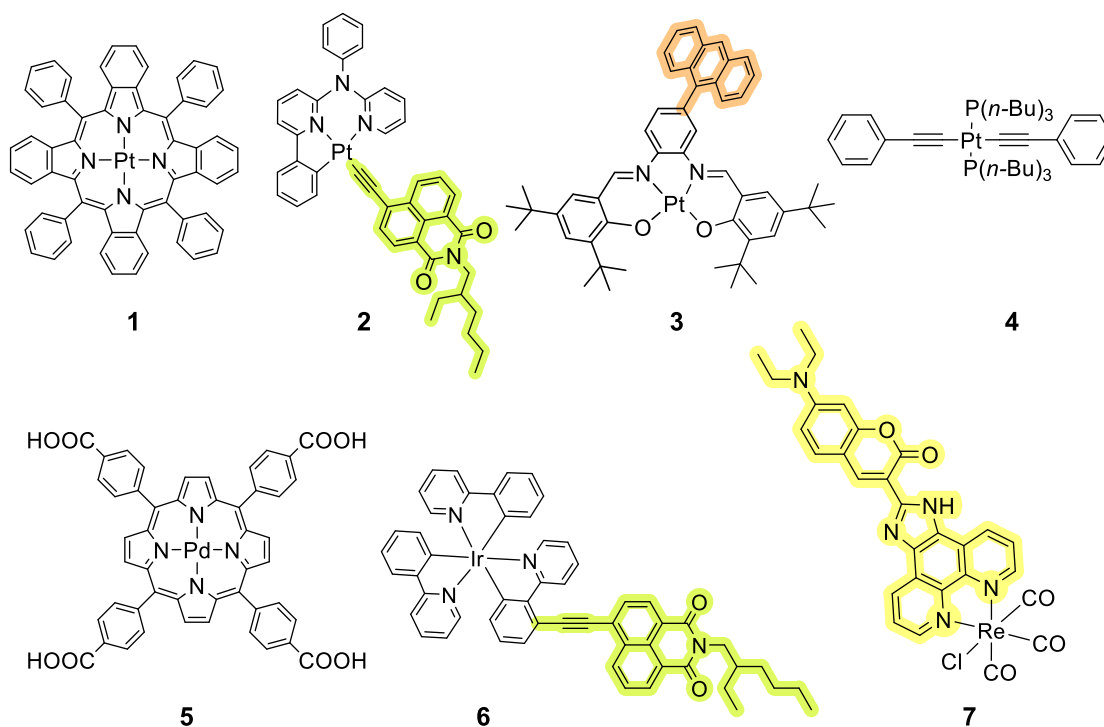
Figure 3.7: *Examples of transition metal-based photosensitisers reported in the literature. Chromophores based upon naphthalimide (green), anthracene (orange) and phenanthroline/imidazole (yellow) have been incorporated into the backbone of common structural motifs.*

The acceptor unit must display high fluorescence quantum yields, as this directly impacts the overall efficiency of emission. The singlet state of the annihilator must lie above that of the sensitiser and the triplet state must lie below that of the sensitiser, whilst the combined energy of the triplet states of two excited forms of the annihilators must be greater than or equal to the singlet state of the acceptor, so that the population of the singlet state remains energetically feasible.[38] Typical examples of acceptor species are based upon polycyclic aromatic hydrocarbons such as anthracene (**DPA**),[39] tetracene (**Rubrene**),[40] pyrene (**TPPy**),[41] and heterocyclic components such as **BODIPY** (**Figure 3.8**).[42]
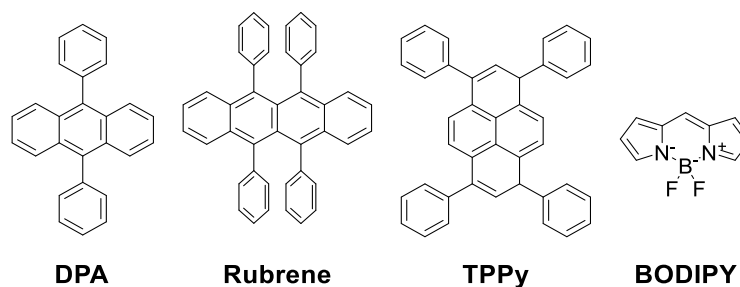
Figure 3.8: *Some commonly used acceptor species for TTA-UC.*

3.1.3: Electronic Nature of the -OCF$_3$ and -CF$_3$ Groups

Fluorination has a profound impact on the subsequent electronics of delocalised systems, where the development of highly fluorinated aromatic compounds has led to a plethora of research in drug development and biological applications.[43] This has promoted a rise in the generation of commercially available materials incorporating unique functionalities such as trifluoromethyl (CF$_3$) and trifluoromethoxy (OCF$_3$) groups, by means of specialised methods.[44–46] These exhibit long-range electron-withdrawing capabilities, whilst NMR-active ^{19}F nuclei permit their use as biological tags in drug mechanistic studies.[47] The high electronegativity of fluorine atoms greatly influences the electronics of the system whilst enhancing lipophilicity.[48] Direct attachment of the OCF$_3$ group to aromatic systems imparts a unique hyperconjugative effect, where the CF$_3$ fragment lies orthogonal to the plane of the ring system.[49]

These properties have been explored in transition metal chemistry, where Ionkin reported ppy-type ligands containing CF$_3$ groups on Pt(II).[20] The CF$_3$ groups displayed directionality outwards from the coordination sphere with very little distortion from square planar geometry and close π-π contacts. The electronic effects have also been recognised, where CF$_3$ being used as a strong acceptor at the 5-position of ppy in **[Pt(ppy)(acac)]** afforded a red-shift in emission wavelength whilst significantly improving Φ_{PL} and oxidation potentials, rendering them extremely useful as oxygen sensors.[50] However, very few examples exist for the OCF$_3$ functionality within this field.[51]

3.2: Aims

The previous chapter focused on the formation of positively charged *bis*-cyclometallated Ir(III) complexes, where properties were explored for potential use in photoluminescent applications. The work presented in this chapter describes the investigation of neutral Pt(II) species, where one bidentate cyclometallated ligand based upon 2-phenylquinoxaline was incorporated into the structure. These ligands contained long-range electron-withdrawing substituents in the form of OCF_3 or CF_3 at different positions on the phenyl ring, where the subsequent structural and electronic properties were monitored through spectroscopic and computational analysis and were directly compared with the analogous Ir(III) species for the relatively unexplored OCF_3-substituted ligands. Characterisation of the Pt(II) species in solution demonstrated that they were viable candidates for photosensitisers in TTA-UC experiments, where Φ_{UC} values were measured up to 14.1%. Further detail can be found in the published findings of this work.[52]

3.3: Results and Discussion

3.3.1: Synthesis and Characterisation of Ligands

In this study, a series of six chromophores were successfully synthesised and investigated as potential C^N ligands. These were once again based upon 2-phenyl quinoxaline, and the synthetic procedures were comparable to those reported in previous chapters (**Scheme 3.1**).[53]

L^1H: R = o-OCF$_3$ **39%**
L^2H: R = m-OCF$_3$ **24%**
L^3H: R = p-OCF$_3$ **26%**
L^4H: R = m-CF$_3$ **11%**
L^5H: R = p-CF$_3$ **25%**
L^6H: R = o-CF$_3$ **41%**

87 - 97%
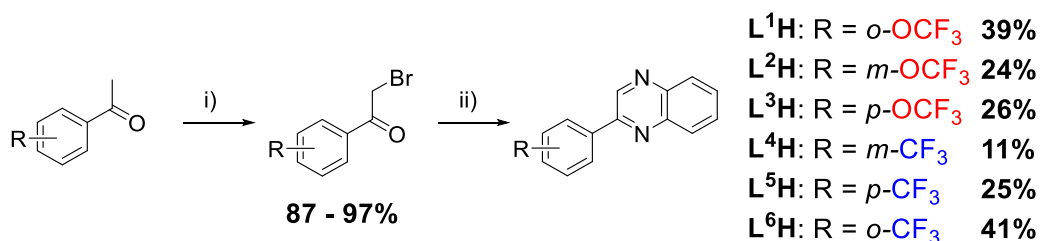
Scheme 3.1: General synthetic approach for the preparation of $L^{1-6}H$. i) Dioxane dibromide, 1,4-dioxane/Et$_2$O (1:1), RT, 2h; ii) 1,2-phenylenediamine, EtOH, 24h.

Trifluoromethoxy (OCF$_3$) and trifluoromethyl (CF$_3$) substituents were studied as long-range EWGs, where it was theorised that the electronic properties of the resultant organometallic species were directly impacted by the nature and position of these groups. These were introduced to the phenyl ring at positions *ortho*-, *meta*- and *para*- to the quinoxaline moiety in the final ligands. Affixing trifluoromethyl ethers directly onto aromatic systems is generally considered to be challenging,[54] so commercially available precursors already incorporating the desired functionalities were employed for convenience. In doing so, the electronic behaviours were able to be explored through a straightforward synthetic approach. Additionally, these highly polarised substituents were deemed to be beneficial for promoting solubility of the resultant square planar Pt(II) species, as they have been proven to increase lipophilicity more so than common fluorine-containing groups.[48,55] Although L^1H and L^2H were the only organic compounds that were previously unreported in the literature, research based around the free ligands has largely focused on their use in medicinal chemistry and drug discovery.[43,56] Therefore, the novelty of these structural motifs in organometallic chemistry and photophysical applications must be acknowledged.

Overall, the brominated compounds were obtained in excellent yields up to 97%, rendering this step extremely efficient. In contrast, the quinoxalines were formed in low-to-moderate yields with an observed trend of *ortho > para > meta*, suggesting that the electrophilicity of the acetyl carbonyl is diminished in the *meta* variant.

Column chromatography was required for isolation of all free ligands since the enhanced lipophilicity prevented the ease of precipitation from organic solvents. This involved DCM as the mobile phase and silica gel as the stationary phase, where all six compounds, **L$^{1-6}$H**, were isolated in high purity. These were analysed by ^{1}H, ^{19}F{^{1}H} NMR and IR spectroscopies to explore the unique electronic and vibrational characteristics of each compound. The two novel species, **L^{1}H** and **L^{2}H** were further characterised by HRMS and ^{13}C{^{1}H} NMR.
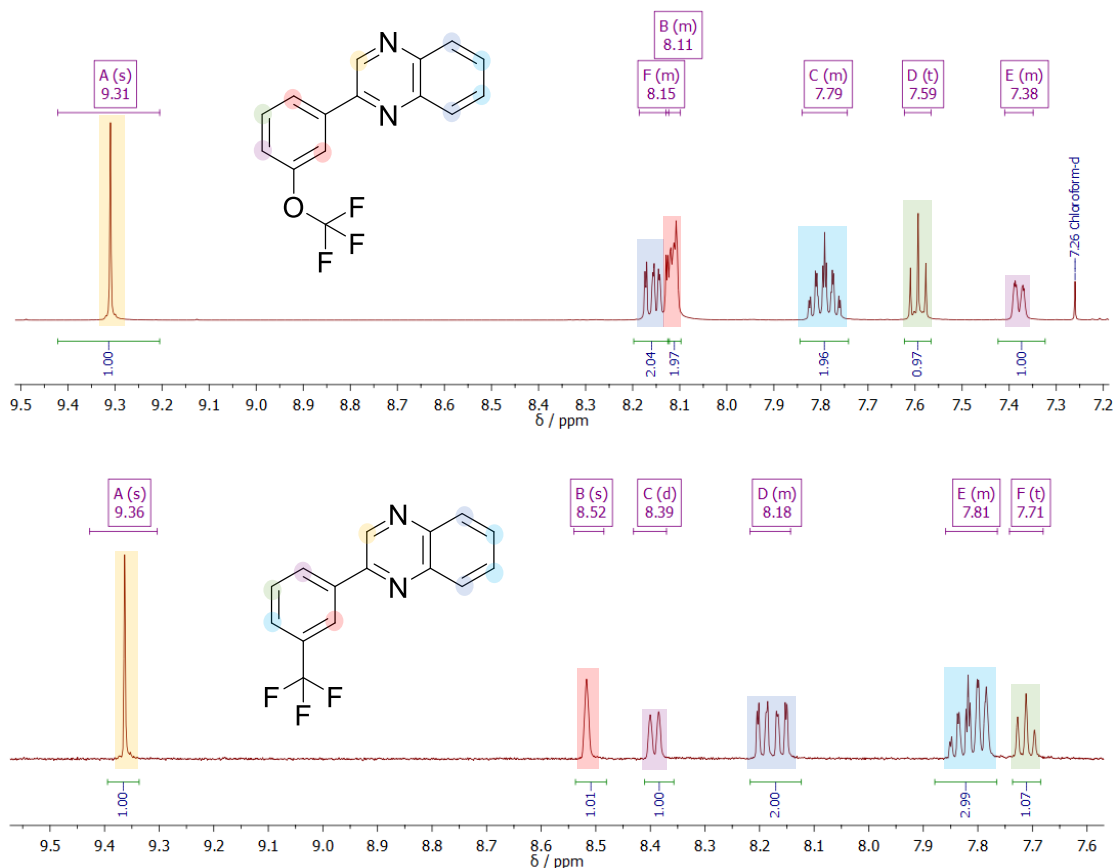
Figure 3.9: *^{1}H NMR spectra of **L^{2}H** (top) and **L^{4}H** (bottom) (CDCl$_3$, 500 MHz).*

The ^{1}H NMR spectra were consistent with the formation of the pyrazine ring, where an indicative singlet was observed between 8.99 – 9.36 ppm. Two examples are displayed in **Figure 3.9**, where the spectra for the two *meta-*

substituted compounds, **L²H** and **L⁴H**, are presented. An overall downfield shift was seen for the resonances in **L⁴H** when compared with **L²H**, suggesting that the protons experienced a greater degree of deshielding by the CF$_3$ substituent. This was attributed to the reduced distance between the fluorine atoms and aromatic system, further exemplified by the chemical inequivalence seen for the positions directly adjacent to the EWG in **L⁴H**.
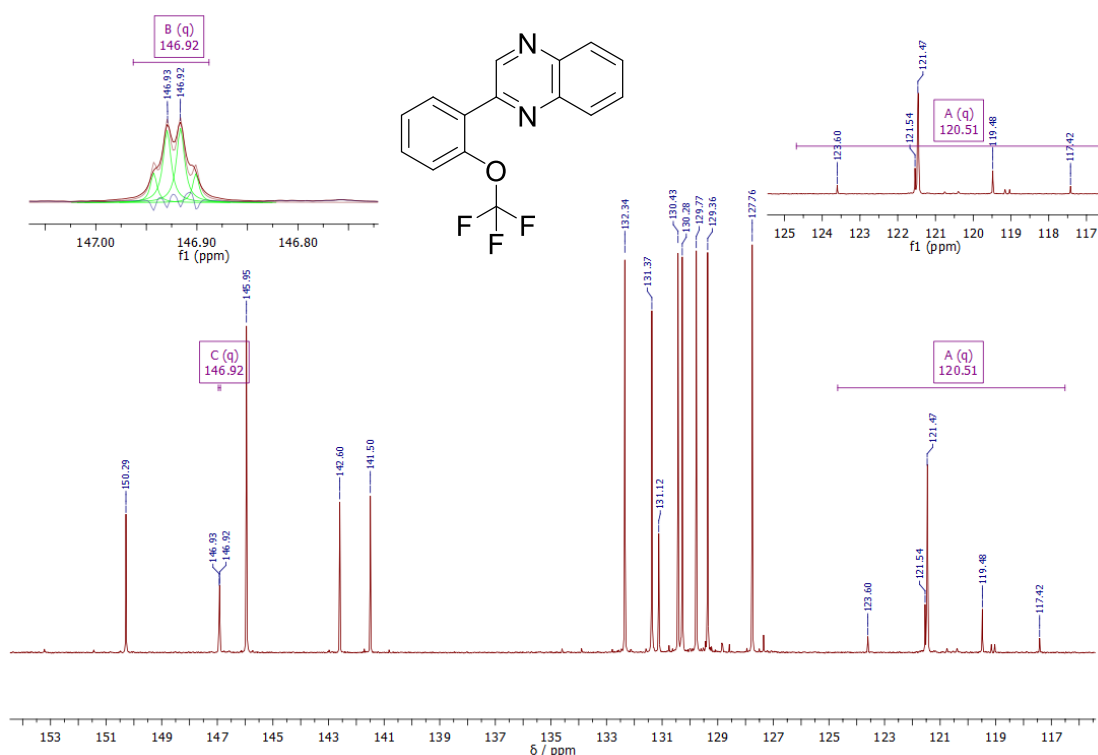
Figure 3.10: $^{13}C\{^1H\}$ *NMR spectrum for **L¹H** (CDCl$_3$, 500 MHz).*

$^{13}C\{^1H\}$ spectroscopy provided insight into C-F interactions, where the spectrum for **L¹H** is presented as an example in **Figure 3.10**. A quartet was seen at a downfield position of ~147 ppm with a long-range coupling of $^3J_{CF}$ = 1.8 Hz alongside a quartet at ~121 ppm with a $^1J_{CF}$ coupling of 249.0 Hz. These values were consistent with literature reports on trifluoromethoxy systems.[57,58] Previous $^{13}C\{^1H\}$ analysis of **L⁴H** displayed $^3J_{CF}$ couplings of 3.7 and 4.0 Hz and a $^1J_{CF}$ value of 272 Hz.[59] The reduced *J* values in the OCF$_3$ compounds were suggested to be the result of increased donor ability of the oxygen atom, promoting deshielding of the CF$_3$ carbon.[60]

3.3.2: Synthesis and Characterisation of Pt(II) Complexes

The 2-phenylquinoxaline compounds discussed in **Section 3.3.1** were investigated as prospective ligands in the development of a series of neutral, square planar Pt(II) species (**Scheme 3.2**).
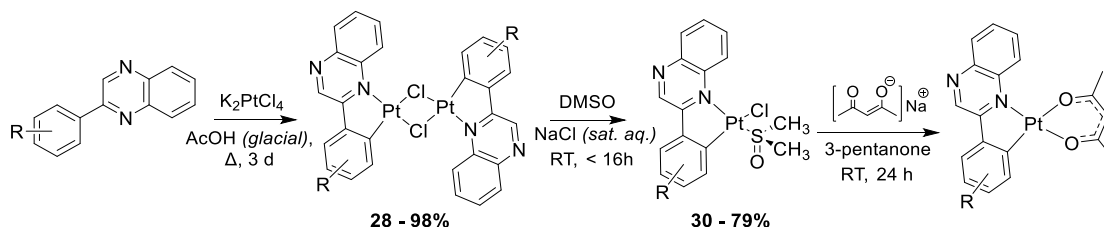
Scheme 3.2: *General synthetic approach for the synthesis of the Pt(II) complexes with the general formula [Pt(C^N)(acac)].*

The adopted methodology involved the synthesis of a dimetallic intermediate with the general formula $[Pt(L^n)(\mu\text{-Cl})]_2$, where potassium tetrachloroplatinate (K_2PtCl_4) was used as the Pt(II) source. This required relatively forceful conditions, where the substrates were dissolved in glacial acetic acid and heated to ~120°C for 3 days.[4] The crude dimeric species were readily isolated as solids by precipitation with water and used in subsequent reactions without further purification or characterisation, where they were split into their monometallic counterparts by dissolving in DMSO and precipitating out with an aqueous solution of brine. This resulted in the replacement of one bridging chloride ligand with DMSO for each platinum centre, ultimately splitting the dimeric species into two equivalents of mononuclear, solvated complex with the general formula $[PtCl(L^n)(DMSO)]$.[61] The enhanced solubility of these intermediates offered a simple approach to removing any elemental Pt^0 nanoparticles that may have formed due to degradation processes during the dimerisation step. These compounds were isolated as brown or orange solids over a large range of experimental yields (30 – 79%), where the synthesis of the OCF_3 variants were more efficient.

The final complexes were formed through reaction of $[PtCl(L^n)(DMSO)]$ with sodium acetylacetonate, the anionic conjugate base form of 2,4-pentanone, which was formed by deprotonation of the diketone using sodium hydroxide. This acetylacetonate species was selected as an appropriate source of acac,

since the negative charge is localised on the binding sites of the compound (*i.e.* the two oxygen atoms).
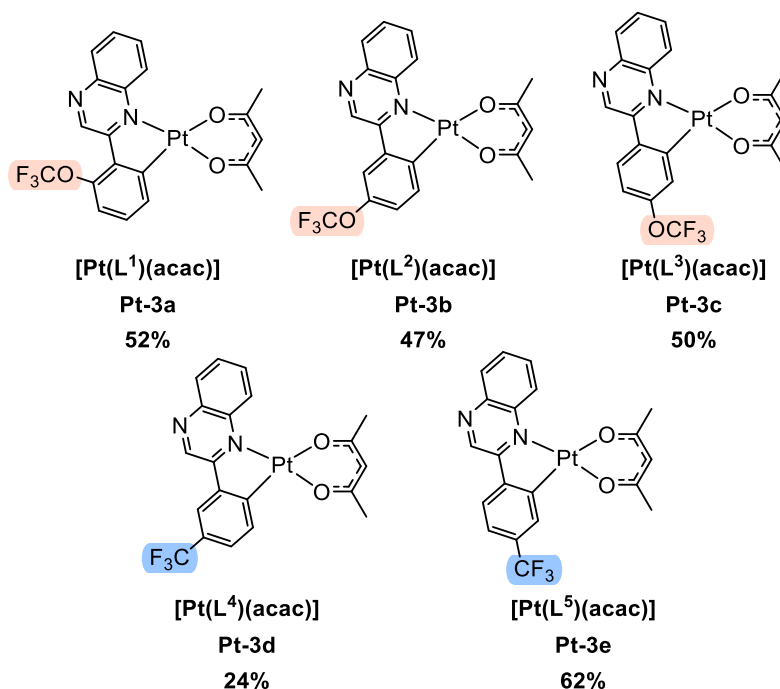
Figure 3.11: *Structures of the neutral, cyclometallated Pt(II) complexes. Experimental yields are displayed below each species.*

Five of the prospective C^N ligands were successfully incorporated into the organometallic species with the general formula **[Pt(Lⁿ)(acac)]** (**Figure 3.11**). The complexes were purified by flash column chromatography, where the products eluted as the first yellow band with DCM on a silica-gel stationary phase and subsequent recrystallisation techniques were required for **Pt-3d** and **Pt-3e**. All neutral Pt(II) complexes were isolated as highly coloured red solids. Interestingly, remarkable solubility was seen in chlorinated solvents along with reasonable solubility in non-polar solvents such as hexane and toluene. This was attributed to the highly polarised functional groups incorporated into the ligands.

Despite numerous efforts, the corresponding complex of **L⁶H** was not isolated. This may be the result of steric interference, where the spacial arrangement of the CF$_3$ group at the *ortho*-position resulted in reduced planarity of the ligand system and a consequent unfavourable geometry for square planar coordination (**Figure 3.12**). Previous work has suggested that the inclusion of CF$_3$ at this position reduces the acidity of phenylboronic acids, due to steric

hindrance.[62] This issue was not encountered with **L¹H**, since the OCF₃ group has been shown to situate in a position orthogonal to the plane of the ring system,[63] in contrast to the in-plane C-C bond for CF₃.[64]
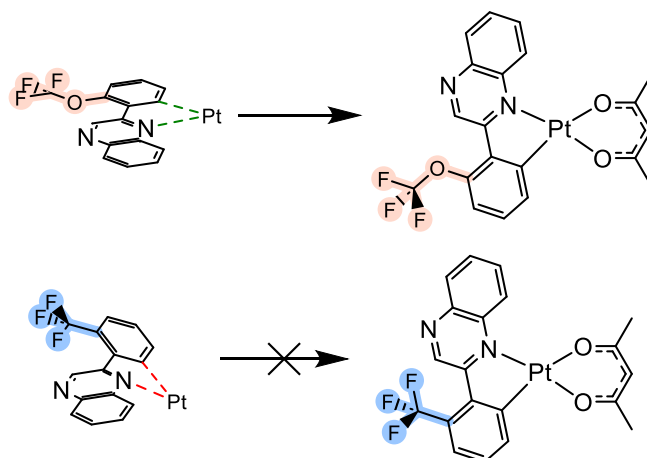
Figure 3.12: *Illustration of the intramolecular steric interference experienced by the ortho-substituted ligand, **L⁶H**, suggested to prevent the formation of the square planar Pt(II) complex.*

Although the Pt(II) species remained as the main investigative source for this study, due to the relatively unexplored area of OCF₃ substituents in organometallic chemistry, synthesis of the analogous Ir(III) species bearing **L¹⁻³H** was undertaken. The properties associated with octahedral, positively charged Ir(III) species have been discussed extensively in the previous chapter, but were investigated in this study as a means of direct comparison to the neutral, square planar Pt(II) compounds. The preparative procedure was similar to that discussed in **Chapter 2** and is shown in **Scheme 3.3**.[65]

L¹H   **[{Ir(L¹)₂(µ-Cl)}₂]**   **[Ir(L¹)₂(bpy)]PF₆**
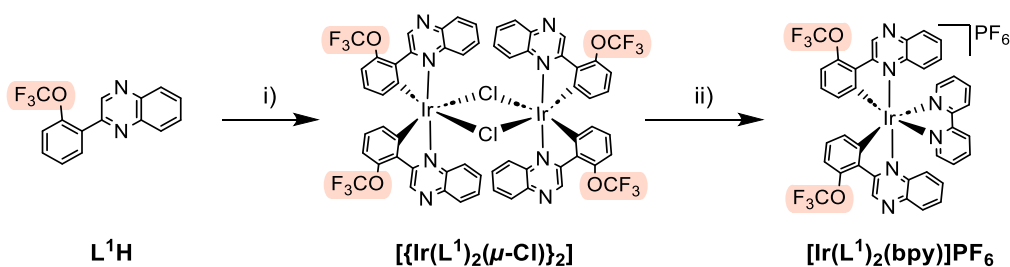
Scheme 3.3: *Synthetic approach to the Ir(III) complexes, where **L¹H** has been used as an example to form **[Ir(L¹)₂(bpy)]PF₆**.[65] i) IrCl₃.xH₂O, 2-methoxyethanol, H₂O (3:1 v/v), 48 h, 150°C; ii) 2,2'-bpy, CHCl₃, 24 h, 70°C.*

The dimers formed in relatively high yields of 79 – 90%, attributed to enhanced solubility of the ligands in the polar solvent mixture. These were split into monometallic cationic complexes by use of 2,2'-bipyridine as the N^N-

coordinating ancillary ligand, as previous chapters have indicated that bpy had very little influence on the excited state properties.[53] Solvent interactions were deemed to be more significant in the **L³** dimeric intermediate due to the highly polarised substituent being directed away from the coordination sphere. Therefore, the splitting reaction was performed in a more polar solvent (2-ethoxyethanol) for the preparation of the complex bearing **L³** ligands, but chloroform was deemed to be suitable for the remaining species.

Purification techniques were analogous to those previously discussed and are discussed in detail within the experimental section of this chapter. The corresponding structures and experimental yields of the three novel Ir(III) complexes are shown in **Figure 3.13**.

[Ir(L¹)₂(bpy)]PF₆
Ir-3a
22%

[Ir(L²)₂(bpy)]PF₆
Ir-3b
18%

[Ir(L³)₂(bpy)]PF₆
Ir-3c
19%
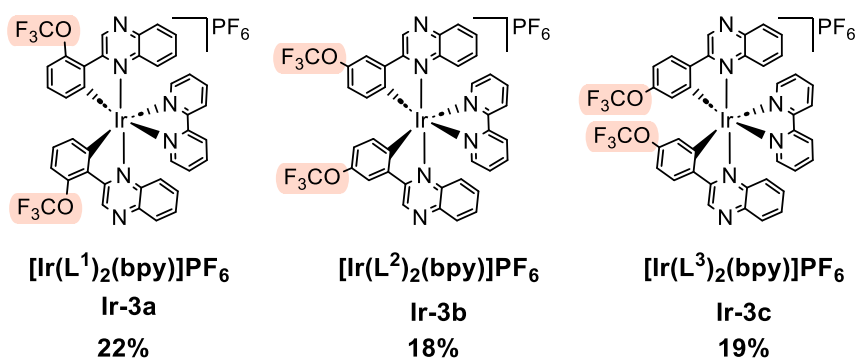
Figure 3.13: Structures of the three novel bis-cyclometallated Ir(III) complexes formed. The experimental yields are indicated below each structure.

All Pt(II) and Ir(III) complexes were fully characterised by various analytical techniques including ¹H, ¹³C{¹H} and ¹⁹F{¹H} NMR spectroscopies alongside IR spectroscopy and HRMS.

¹H NMR spectroscopy data of the complexes displayed drastic deviations from the free ligands upon cyclometallation. An example of this can be seen in **Figure 3.14**, where the spectrum for **L³H** is superimposed with that of the corresponding **[Pt(C^N)(O^O)]** complex, **Pt-3c**.
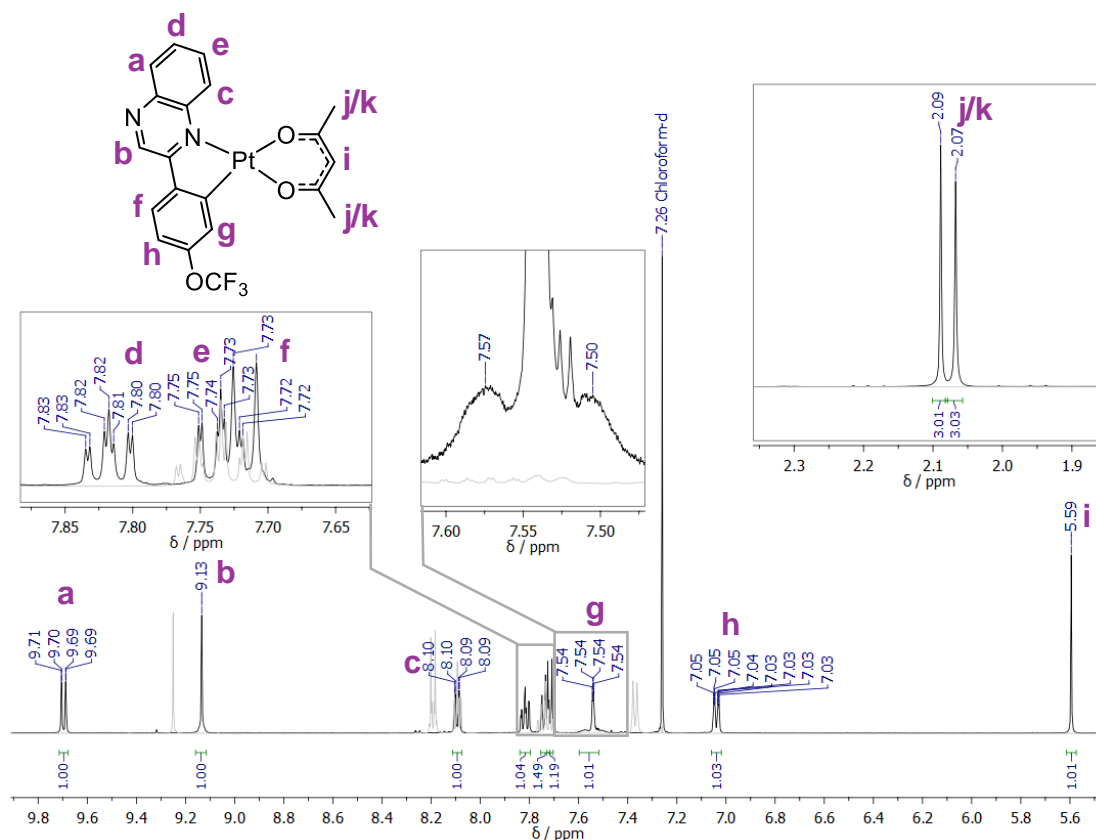
Figure 3.14: *Overlapped ¹H NMR spectra of **L³H** (grey) and the corresponding Pt(II) complex **Pt-3c** (black), both measured in CDCl₃ at 500 MHz. Two regions have been magnified and all positions have been assigned relative to the structure displayed. Inset: The two aliphatic peaks relating to the methyl protons.*

In total, 11 proton environments were assigned and there was no evidence of any remaining **[PtCl(Lⁿ)(DMSO)]** adduct from the previous step. The indicative singlet associated with the pyrazine proton was recorded at 9.13 – 9.73 ppm, where an overall upfield shift was seen in most cases. **Pt-3a** was the only exception to this, where a downfield shift of 0.52 ppm was recorded relative to the equivalent proton at this position on **L¹H**. In most cases, the most downfield resonance recorded at 9.59 – 9.74 ppm was assigned to one of the protons on the benzene sub-unit of the quinoxaline. Peak positions, multiplicity patterns and *J*-coupling values remained consistent throughout, independent of the position of substitution at the phenyl ring ($^3J_{HH}$ = 8.8 – 8.9 Hz, $^4J_{HH}$ = 0.9 – 1.3 Hz and $^5J_{p\text{-}HH}$ = 0.5 Hz). The coupling constants were also comparable with similar quinoxaline-based systems.[53,66] In contrast, **Pt-3a** displayed a deshielded singlet at 9.73 ppm, and the peak affiliated with the benzylic proton (ddd) was seen at a relatively low chemical shift value of 9.59 ppm due to the

proximity of the EWG to the quinoxaline system. In **Pt-3c** (**Figure 3.14**), positions **h** and **g** were assigned as multiplets due to long-range interactions with the fluorine atoms. The loss of symmetry upon cyclometallation brought about an increase in the number of aromatic signals, where a similar effect was seen for the other *para*-substituted compound, **L⁵H**. Assignments of the protons on the phenyl ring were dependent on the position and nature of the EWG.

The presence of the acetylacetonate ligand was verified by the incidence of two methyl resonances within the aliphatic region of the spectra. These remained relatively consistent, exhibited as singlets within a narrow range of 2.07 – 2.11 ppm. Similarly, a singlet at ~5.60 ppm was representative of a methine proton present in the enol form of the ligand,[67] consistent with reports of other β-diketonate Pt(II) complexes.[68]

Interestingly, through-bond interactions between the proton adjacent to the cyclometallated carbon and the NMR-active ^{195}Pt nuclei (I = ½, 34%)[69] were seen in some cases. An example is shown in **Figure 3.14**, where the multiplet ascribed to position **g** at 7.54 ppm exhibited characteristic satellites and $^3J_{\text{H-Pt}}$ couplings were able to be calculated. These were observable in **Pt-3a**, **Pt-3c** and **Pt-3e** and are tabulated below in **Table 3.1**, where the values were within the expected range.[70]

Complex	δ_H / ppm
Pt-3a	7.82 – 7.75 ($^3J_{\text{H-Pt}}$ = 35.2 Hz)
Pt-3c	7.57 – 7.50 ($^3J_{\text{H-Pt}}$ = 34.6 Hz)
Pt-3e	8.03 – 7.94 ($^3J_{\text{H-Pt}}$ = 31.0 Hz)

Table 3.1: Chemical shifts and assigned $^3J_{\text{H-Pt}}$ couplings of the complexes, where observable.

^{1}H NMR data was also collected for the octahedral Ir(III) species, where the spectrum for **Ir-3a** is shown in **Figure 3.15** with clear distinctions from the free ligand (**L¹H**) and corresponding Pt(II) complex (**Pt-3a**). The pyrazine singlet appeared at 10.06 ppm for **Ir-3a** compared with 9.73 ppm for **Pt-3a**. More aromatic signals were seen due to the presence of the bipyridine ancillary ligand, with the previously assigned acac peaks being absent. Upfield-shifted

peaks below 7 ppm were seen due to the enhanced electronic shielding induced by the octahedral geometry and this trend was observed throughout the series.
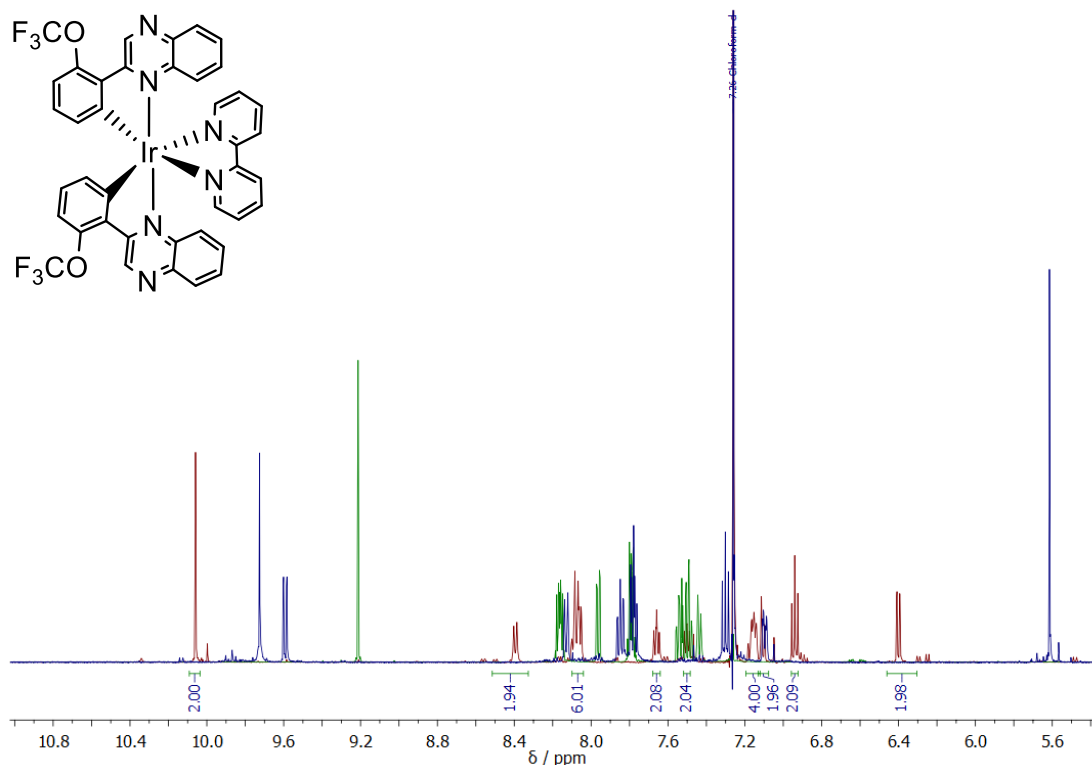
*Figure 3.15: Superimposed ^{1}H NMR spectra of **Ir-3a** (red), **Pt-3a** (blue) and **L^{1}H** (green) in CDCl$_3$ (500 MHz) where the assigned integration values relate to **Ir-3a**.*

$^{13}C\{^{1}H\}$ NMR data is usually difficult to acquire for square planar Pt(II) systems, due to aggregation features and resultant issues regarding solubility.[71] However, this data was collected with relative ease by the inclusion of the polarised substituents on the C^N ligands and resultant solvation effects. All Pt(II) complexes displayed peaks within the expected range for a metal acetylacetonate species. Firstly, chemical shifts at ~186 and ~184 ppm were representative of the carbonyl carbon atoms on the acac ligands, peaks at ~102 ppm were attributed to the methine carbon and two CH$_3$ signals were seen between 27 – 29 ppm.[68,72–74]

Singlet resonances were seen for all complexes and ligands in the $^{19}F\{^{1}H\}$ NMR spectra as a result of the three equivalent fluorine atoms associated with the trifluoromethyl entity. Studies have suggested that direct attachment of the trifluoromethyl substituent polarises the aromatic system, where ring current effects impact the extent of shielding experienced by the ^{19}F nuclei.[75] This was

exemplified in the recorded spectra, where a range of δ_F values were seen (**Table 3.2**). All compounds displayed significantly downfield signals in comparison to directly fluorinated analogues (**Chapter 2**), where the OCF_3 compounds were reported at positions much more downfield than their CF_3 counterparts. Only slight deviations were seen between free ligands and the resultant complexes and closely resembled values for other compounds containing these functionalities.[57,62]

	δ_F / ppm		
	Free Ligand	**Pt Complex**	**Ir complex**
L^1	-57.15	-56.46	-56.50
L^2	-57.64	-57.95	-57.78
L^3	-57.67	-56.93	-57.37
L^4	-62.65	-62.23	-
L^5	-62.74	-63.01	-
L^6	-56.55	-	-

Table 3.2: $^{19}F\{^1H\}$ NMR chemical shift positions for the singlets observed in the spectra for all free ligands and their corresponding organometallic complexes (CDCl$_3$, 376 MHz). PF$_6$ counterion signals are not included for the iridium species.

All final complexes were further characterised by HRMS, where electrospray ionisastion (ES+) was employed to generate either a $[M + H]^+$ or $[M]^+$ molecular ion peak for the platinum and iridium complexes, respectively. These were consistent with the molecular masses of the target compounds in all cases, where structurally isomeric complexes displayed almost identical *m/z* peaks. Parent ion peaks were seen at *m/z* = 584 and 568 for the OCF_3 and CF_3 Pt(II) complexes respectively, whereas *m/z* = 927 was recorded for the OCF_3 Ir(III) complexes. The iridium complexes displayed a characteristic pattern similar to that previously discussed in **Chapter 2**, where the two abundant isotopes were seen. Platinum also exhibited a unique isotopic distribution pattern as a result of its four stable, naturally occurring isotopes with relatively high abundances (**Table 3.3**). This was reflected in the spectrum for **Pt-3a**, where the molecular and adduct ion peaks have been assigned in **Figure 3.16**.

Isotope	Relative Abundance / %
^{194}Pt	32.967
^{195}Pt	33.832
^{196}Pt	25.242
^{198}Pt	7.163

Table 3.3: Relative abundances of the stable, naturally occurring isotopes of Pt.[76]

Greater *m/z* values were seen for most Pt(II) complexes, and were classified as [M + M + H]$^+$ and [M + M – acac]$^+$ adducts attributed with cluster formation. These were consistent with the dimerised species, for example, the [M + H]$^+$ parent ion was measured at *m/z* = 584.0765 for **Pt-3b**, but additional peaks were seen at *m/z* = 1067.1075 and 1167.1697 for the [M + M – acac]$^+$ and [M + M + H]$^+$ respectively.
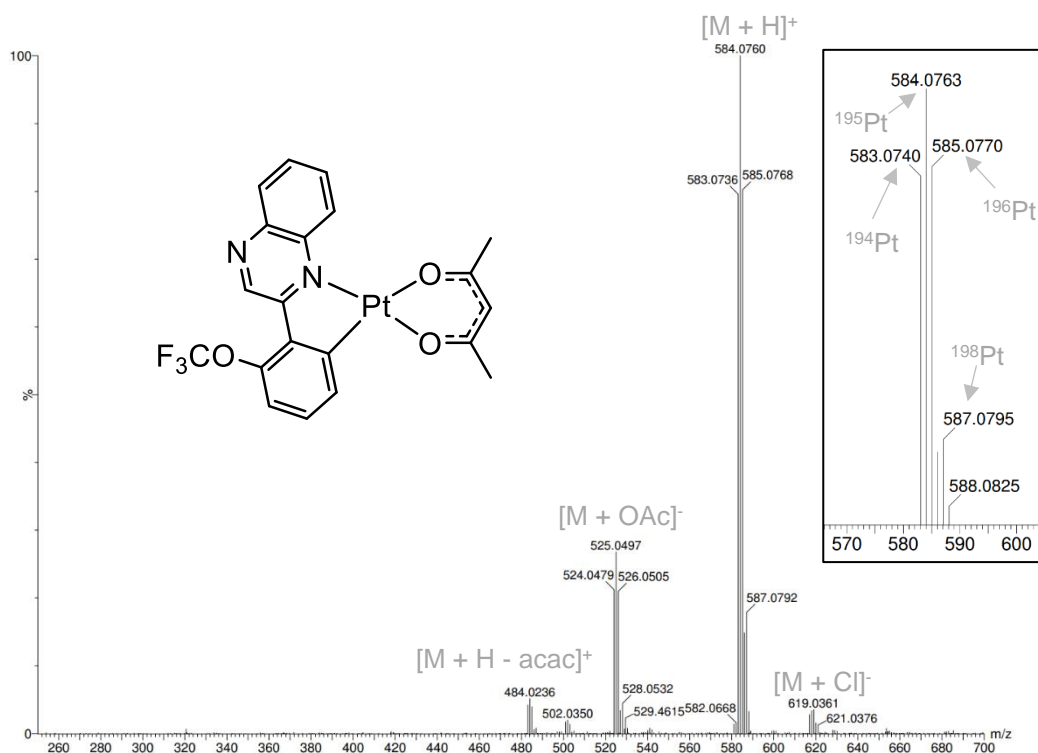
*Figure 3.16: HRMS (ES+) of **Pt-3a**. Inset: Magnified region of the molecular ion peak, [M + H]$^+$, where the isotopic distribution has been assigned to the different Pt isotopes. The mass was calculated for $C_{20}H_{16}F_3N_2O_3{}^{194}Pt$ (m/z = 583.0736).*

119

IR-active functional groups were identified within the complexes. Features at ~1600 cm^{-1} were assigned as carbonyl stretching frequencies, v(C=O), indicative of a coordinated metal-acac species.[77] Acetylacetonate ligands can bind to Pt(II) *via* the central carbon atom, presented as higher energy carbonyl peaks within the range of 1630 – 1680 cm^{-1}. No evidence of this was seen, and the lower energy peaks indicated that the carbonyl groups were interacting directly with the metal center.[68] Strong C-F symmetric and antisymmetric stretching vibrations are often observed within the range of 1100 – 1200 cm^{-1} alongside symmetrical CF$_3$ deformation at ~750 cm^{-1}.[78,79] Despite being present within the fingerprint region, the latter peak was assigned in the spectra between 758 – 770 cm^{-1} for all ligands and complexes. Examples of the IR spectra are shown in **Figure 3.17** for **Pt-3b** and **Pt-3d**.
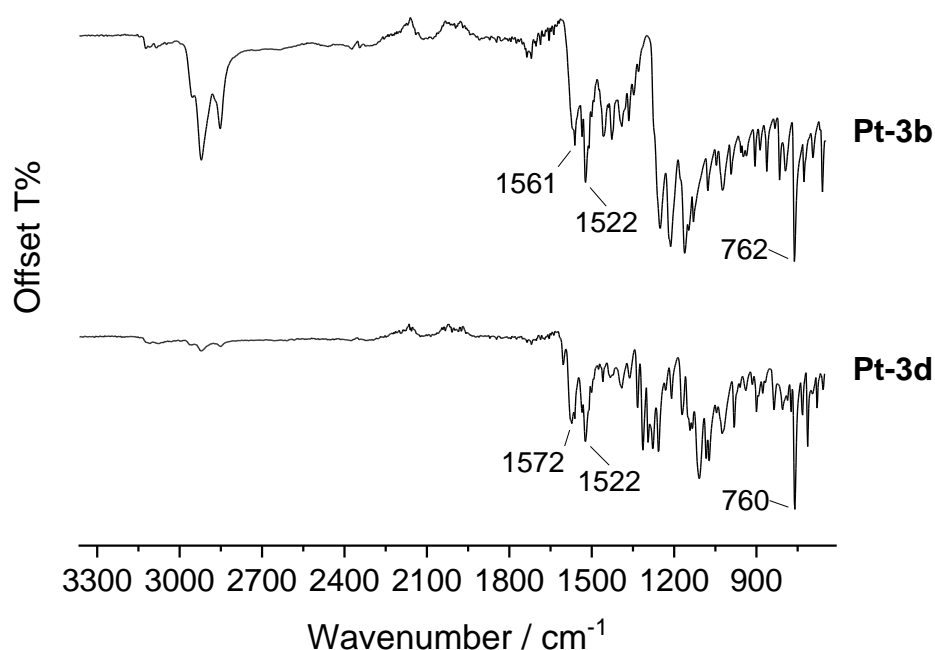
Figure 3.17: *IR spectra for **Pt-3b** and **Pt-3d**, where some characteristic C-F peaks have been assigned.*

3.3.3: X-Ray Crystallography

Single crystals of **Pt-3a**, **Pt-3b** and **Pt-3c** were grown *via* slow evaporation from dichloroethane (DCE), DCM or CHCl₃, producing red-coloured crystals which were blade-shaped for **Pt-3a**, either lath- or needle-shaped for **Pt-3b** and block-shaped for **Pt-3c** (**Figure 3.18**).
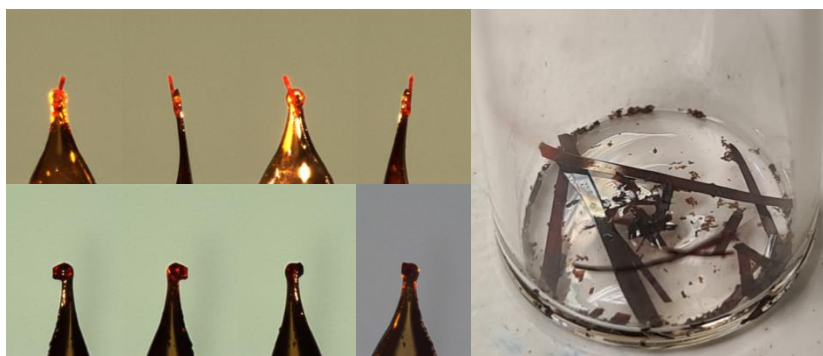
*Figure 3.18: Images of the crystals for **Pt-3b** (top) and **Pt-3c** (bottom) on the diffractometer during XRD measurements.*

The XRD data was once again collected by Dr. Peter Horton at the EPSRC National Crystallography Service at the University of Southampton and confirmed the validity of the theorised structures of the complexes, where cyclometallation was seen *via* one C^N 2-phenylquinoxaline ligand along with direct coordination to the acac through a bidentate O^O coordination mode. The crystal structures are presented below in **Figure 3.19**. All structures displayed an approximate square planar geometry, with a slight distortion induced by the C^N ligand by formation of a 5-membered chelate intermediate.[12]

Two modes of cyclometallation were possible for **Pt-3b**, where metal-carbon bond formation could occur at positions *para-* or *ortho-* relative to the OCF₃ substituent. It was suggested that the former was favourable, avoiding any steric interference as the substituent is directed away from the coordination sphere, and this was confirmed in the crystal structure. The CF₃ sub-unit of the substituent displayed pronounced rotational disorder in **Pt-3b**, where two sets of bond lengths and angles were represented.
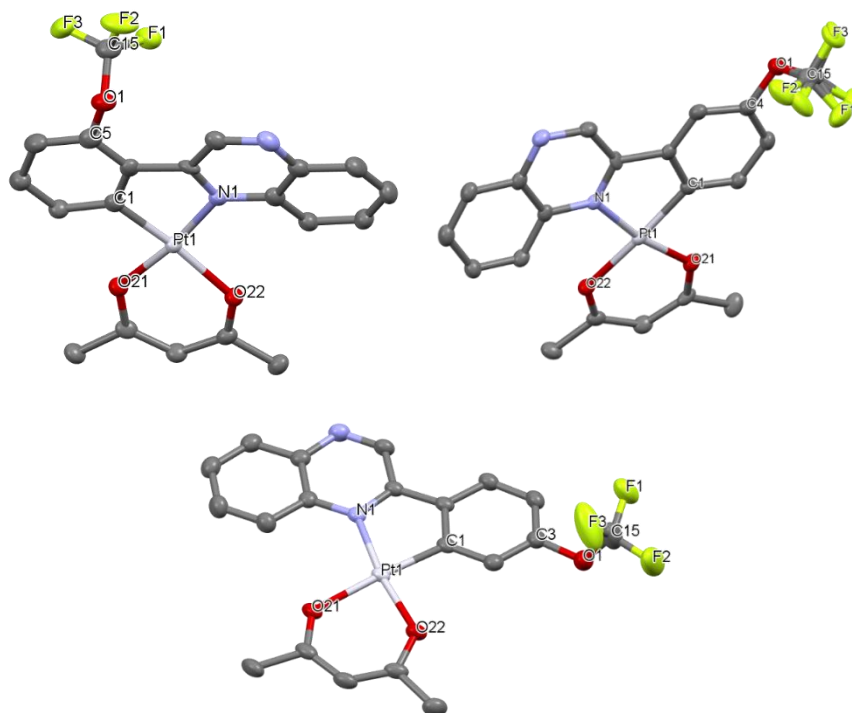
*Figure 3.19: X-ray crystal structures of **Pt-3a** (top left), **Pt-3b** (top right) and **Pt-3c** (bottom), where thermal ellipsoids are drawn at 50%.*

Selected bond lengths and angles are presented in **Table 3.4** and **Table 3.5**, respectively, where values were consistent with similar compounds in the literature.[12,15,19,20,80] Two sets of data were recorded for **Pt-3b**. Initially, measurements were carried out at 200K, due to cracking of the lath-shaped crystals upon cooling to 100K, but the needle-shaped crystals of **Pt-3b** were proven to be more stable at low temperatures, allowing data collection at 100K.

Bond	Length / Å			
	Pt-3a	**Pt-3b**[a]	**Pt-3b**[a,c]	**Pt-3c**
Pt(1)-O(21)	2.000(5)	1.994(3)	1.996(3)	2.094(2)
Pt(1)-O(22)	2.108(5)	2.104(3)	2.103(3)	1.994(2)
Pt(1)-N(1)	2.041(6)	2.044(4)	2.034(3)	2.044(2)
Pt(1)-C(1)	1.967(8)	1.973(4)	1.967(4)	1.965(3)
O(1)-C(X)[b]	1.429(10)	1.416(6)	1.420(5)	1.421(4)
O(1)-C(15)	1.343(10)	1.340(9) / 1.338(14)	1.335(10) / 1.339(14)	1.319(5)

*Table 3.4: Selected bond lengths for the crystal structures of **Pt-3a**, **Pt-3b** and **Pt-3c** at 100K unless otherwise specified. [a] Two bond angles were recorded due to disorder of the OCF₃ in **Pt-3b**; [b] X = 5 for **Pt-3a**, X = 4 for **Pt-3b** and X = 3 for **Pt-3c**; [c] 200K.*

Bonds	Angle / °			Bonds	Pt-3c
	Pt-3a	Pt-3b[a]	Pt-3b[a,c]		
O(21)-Pt(1)-O(22)	88.4(2)	88.97(13)	88.71(12)	O(21)-Pt(1)-O(22)	89.19(8)
O(21)-Pt(1)-N(1)	169.9(2)	169.96(14)	170.10(12)	O(22)-Pt(1)-N(1)	169.27(9)
N(1)-Pt(1)-O(22)	101.1(2)	100.71(14)	100.80(13)	N(1)-Pt(1)-O(21)	100.39(9)
C(1)-Pt(1)-O(21)	89.7(3)	89.05(17)	89.38(16)	C(1)-Pt(1)-O(22)	88.96(10)
C(1)-Pt(1)-O(22)	173.4(2)	173.67(15)	174.00(12)	C(1)-Pt(1)-O(21)	175.94(9)
C(1)-Pt(1)-N(1)	80.5(3)	81.04(17)	80.88(15)	C(1)-Pt(1)-N(1)	81.16(10)
C(15)-O(1)-C(X)[b]	117.6(6)	114.4(6) / 118.9(10)	113.1(6) / 119.7(8)	C(15)-O(1)-C(3)	118.3(3)
F(1)-C(15)-O(1)	113.4(7)	113.5(9) / 111.1(15)	111.5(9) / 113.6(13)	F(1)-C(15)-O(1)	113.4(3)
F(2)-C(15)-F(1)	108.0(7)	107.6(8) / 106.7(14)	108.2(10) / 106.3(14)	F(2)-C(15)-F(1)	107.4(3)
F(2)-C(15)-F(3)	108.2(7)	108.1(11) / 107.2(18)	107.7(11) / 106.3(15)	F(2)-C(15)-F(3)	109.8(4)
F(2)-C(15)-O(1)	107.1(7)	112.5(9) / 113.2(15)	115.3(9) / 110.3(12)	F(2)-C(15)-O(1)	108.8(4)
F(3)-C(15)-F(1)	106.2(7)	107.5(11) / 108.1(17)	106.6(11) / 109.0(17)	F(3)-C(15)-F(1)	104.6(4)
F(3)-C(15)-O(1)	113.7(7)	107.3(10) / 110.3(18)	107.1(11) / 110.9(16)	F(3)-C(15)-O(1)	112.7(3)

*Table 3.5: Selected bond angles from the crystal structures of **Pt-3a**, **Pt-3b** and **Pt-3c**, measured at 100K unless otherwise specified; [a]Two bond angles observed due to disorder of OCF₃ in **Pt-3b**; [b]X = 5 for **Pt-3a**, X = 4 for **Pt-3b**; [c]200K.*

Pt-N bond distances were between 2.034(3) – 2.044(2) Å, comparatively longer than values for 2-benzimidazole (2.000 Å)[5] and 2-(2'-thienyl)pyridyl (1.984 Å)[12] derivatives. The increased Pt-N bond length is in agreement with the more closely related quinoline compounds, where 2.070 Å was measured for a complex containing a 4-methyl-2-(4-(trifluoromethyl)phenyl)quinoline ligand.[81] The length of this bond has been attributed to the weak *trans influence* of the acac oxygen atom directly opposite the Pt-N bond, where **[Pt(ppq)(acac)]** displayed bond lengths of 2.054, 2.114/2.005 and 1.961 Å for Pt-N, Pt-O and Pt-C respectively, resembling the experimental values obtained in this study.[82]

The disparities in the two Pt-O bond lengths were a result of the cyclometallated carbon atom inducing a stronger *trans influence*, extending the length of the Pt-O bond at the *trans*-position, a common feature in *mono* cyclometallated platinum acetylacetonate species.[12,70,83] All experimental bond lengths were within error, suggesting that they were independent of the position of the OCF$_3$ substituent.

Bond angles were also investigated, where C-Pt-N angles were at 80.5(3)° - 81.16(10)° and O-Pt-O angles were between 88.4(2)° – 89.19(8)°. These deviated from the ideal value of 90°, in accordance with the values of comparable species.[19,81]

Bond lengths and angles were also measured for the OCF$_3$ functionality, which was expectedly positioned perpendicular to the plane of the phenyl ring in all cases, exemplified by F$_3$C-O-C$_{Ar}$ bond angles measured at 113.1(6) – 119.7(8)°. This orientation was suggested to be the combined result of the bulkiness of the OCF$_3$ group in addition to hyperconjugation effects, where the lone pairs on the oxygen atom overlapped with antibonding orbitals on the C-F bond ($n_o \rightarrow \sigma^*$). Additionally, torsion angles approaching 90° for C-O-C-C were recorded from the diffraction data, commonly seen for trifluoromethyl ethers adjoined to aromatic systems.[84] These are illustrated in **Figure 3.20** and corresponding values are tabulated in **Table 3.6**.
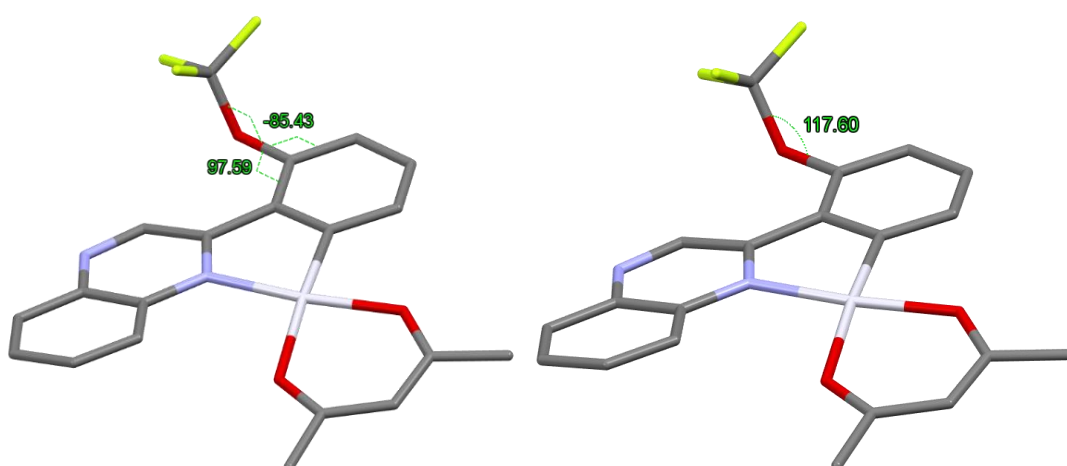
Figure 3.20: *Measured torsion (dihedral) angles for F$_3$**C-O-C$_{Ar}$-C$_{Ar}$** (left) and bond angles for F$_3$**C-O-C$_{Ar}$** (right).*

Torsion Angles / °				F$_3$C-O-C$_{Ar}$ Angle / °			
Pt-3a	**Pt-3b**[a]	**Pt-3b**[a,b]	**Pt-3c**	**Pt-3a**	**Pt-3b**[a]	**Pt-3b**[a,b]	**Pt-3c**
-85.5(9)	-86.1(8)	-93.3(8)	-108.5(4)	117.6(6)	114.4(6)	113.1(6)	118.3(3)
97.5(9)	98.2(8)	90.6(8)	76.7(4)		118.9(10)	119.7(8)	
	-74.4(13)	-107.8(10)					
	109.8(12)	76.1(10)					

Table 3.6: *Torsion angles and angles relative to the OCF$_3$ substituent for **Pt-3a**, **Pt-3b** and **Pt-3c**, measured at 100K unless otherwise specified. [a]Two sets of values were observed due to disorder of OCF$_3$ in **Pt-3b**; [b]200K.*

Pt-Pt and π-π interactions were seen in all cases and distinct bonds between Pt atoms were detected between two molecules in the asymmetric units for **Pt-3a** and **Pt-3b**. These dimerised species were a consequence of the planarity of these complexes, permitting intermolecular contacts and aggregation effects (**Figure 3.21**). Studies on complexes containing bulky O^O ligands suggest that π-π interactions are a prerequisite for the highly ordered packing arrangement, where long Pt-Pt distances (4.92 Å) for **thpyPt(dpm)** resulted in no direct Pt-Pt interactions.[12] However, solid-state Pt-Pt interactions are common in more planar arrangements, where acetylacetonate is employed as the O^O ligand. For example, Velusamy *et al.* reported CF$_3$-substituted 2-phenylquinoline complexes with short Pt-Pt contacts (3.249 Å), where head-to-tail dimer formation was seen.[81] The Pt-Pt distance was comparatively shorter at 3.2041(6) Å for **Pt-3a**.
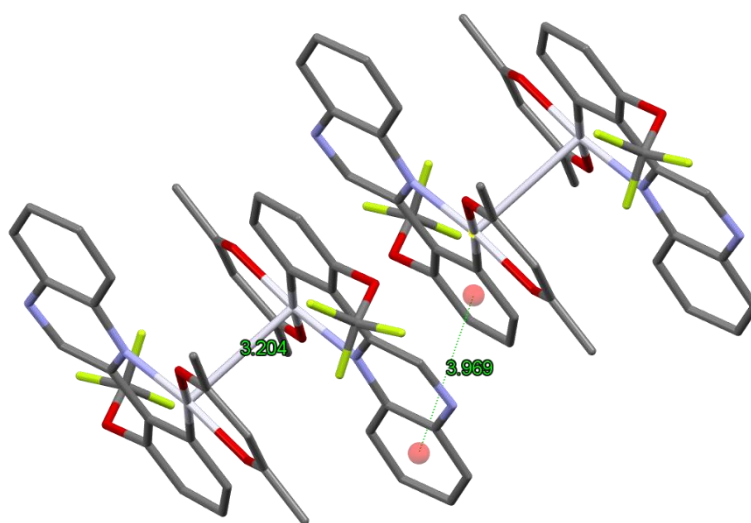
Figure 3.21: *Partial packing arrangement of the crystal structure for **Pt-3a**, where Pt-Pt and π-π (centroid-centroid) interactions are displayed.*

Upon inspection of the packing arrangement of these structures, moderate π-π interactions were seen between two separate dimeric species. These were the result of the observed head-to-tail formation, where the phenyl ring system interacted with the fused benzene system on the quinoxaline in a neighboring molecule (**Figure 3.21**). The distances between these two centroids were measured for all complexes and are reported in **Table 3.7**, where distances were dependent upon the steric impact of the orthogonally positioned OCF_3 group and greatly influenced the packing arrangement. Since these interactions were between adjacent dimers, the pre-arrangement of the asymmetric unit was determined to be the result of the strong intramolecular $dz^2 \rightarrow dz^2$ Pt-Pt interaction (to form d_σ and d_σ* molecular orbitals), rather than the π-π contacts between ligands (**Figure 3.1**).

Interaction	Length / Å			
	Pt-3a	**Pt-3b**	**Pt-3b**[a]	**Pt-3c**
Pt-Pt	3.2041(6)	3.2020(3)	3.2199(3)	3.259[b]
Centroid-Centroid	3.969	3.846	3.869	-
Shift Distance	1.755	1.504	1.541	-

*Table 3.7: XRD data displaying the solid-state interactions observed for **Pt-3a**, **Pt-3b** and **Pt-3c** at 100K unless otherwise specified. [a]200K; [b]Measured by inspection of the packing arrangement.*

The long distance (3.259 Å) between the two metal centres in **Pt-3c** precluded the detection of a Pt-Pt bond, but an interaction was still seen within the ordered packing arrangement (**Figure 3.22**) and allowed this distance to be measured. Although this difference seems insignificant, the reduced metal-metal interaction was supported by empirical evidence, where the sample displayed noticeably weaker emission in the solid state. This was supported by spectroscopic analysis and will be explored in more detail in **Section 3.3.4**. The head-to-tail formation was maintained, but π-π stacking interactions were not observable in **Pt-3c**.
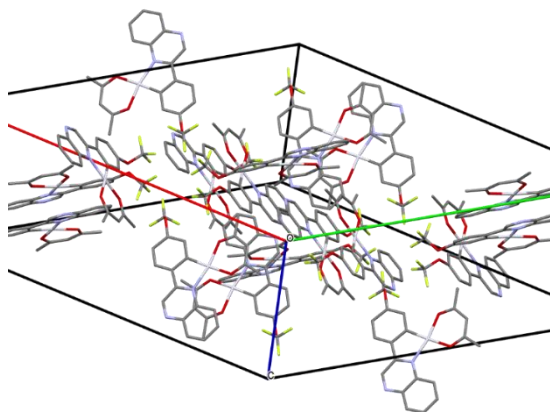
*Figure 3.22: Packing arrangement of **Pt-3c**.*

Shift distances (*i.e.* how far 'shifted' the ligand is on an adjacent monomeric unit) were calculated as 1.755 Å for **Pt-3a** and 1.504 Å for **Pt-3b**, suggesting that electronic repulsion decreased upon OCF$_3$ migrating further away from the metallic core. Similarly, angles between the two planes of the ligand (*i.e.* the phenyl ring and quinoxaline component) showed that the ligands with substituents closest to the centre of the coordination sphere exhibited the most substantial deviation from planarity (**Table 3.8**).

Complex	Angle between two planes of ligand / °
Pt-3a	9.97
Pt-3b	6.71
Pt-3c	1.48
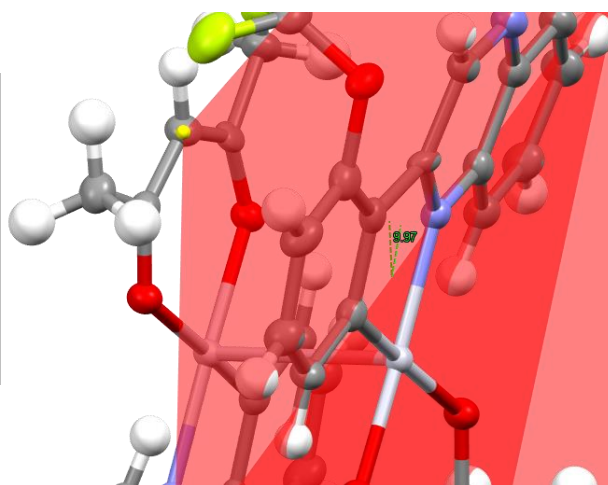
*Table 3.8: Angles between the two planes on the C^N ligand, illustrated in the image (right) for **Pt-3a**.*

3.3.4: Photophysical Properties

UV-vis absorption measurements of the free ligands (**L$^{1-6}$H**) were collected in *ca.* 10^{-5} M aerated chloroform solutions under ambient conditions (**Figure 3.23**). All organic compounds displayed transition bands in the UV range and below 380 nm, where the profiles appeared to be reasonably consistent throughout

the series. **L²⁻⁵H** exhibited peaks within a very narrow range (334 – 336 nm), where the nature of the substituent only influenced the intensity of these bands, and subtle variations were seen for the *ortho*-substituted compounds (**L¹H** and **L⁶H**), where maximum λ_{abs} values were at 326 and 321 nm respectively. All peaks were indicative of spin-allowed $^1(\pi\rightarrow\pi^*)$ transitions from the extended aromatic system consisting of phenyl ring and quinoxaline moieties.
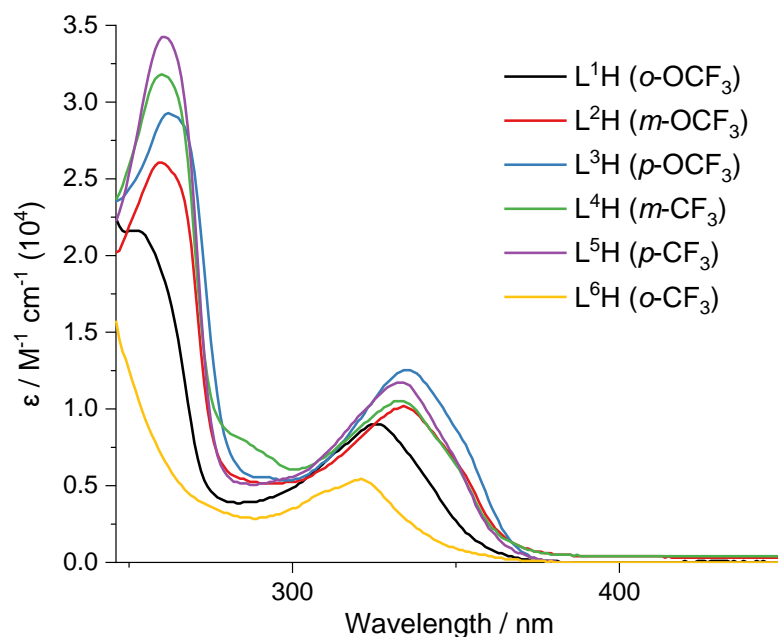
Figure 3.23: *UV-vis absorption spectra of free ligands **L¹⁻⁶H** (CHCl₃, 0.99 × 10⁻⁵ M, RT).*

Steady state emission spectra for the free ligands displayed emission in the visible range with λ_{em} peaks at 402 – 407 nm. Although the peak positions remained relatively consistent, the intensity of emission was noticeably greater for the *meta*-substituted compounds, **L²H** and **L⁴H** (**Figure 3.24**).
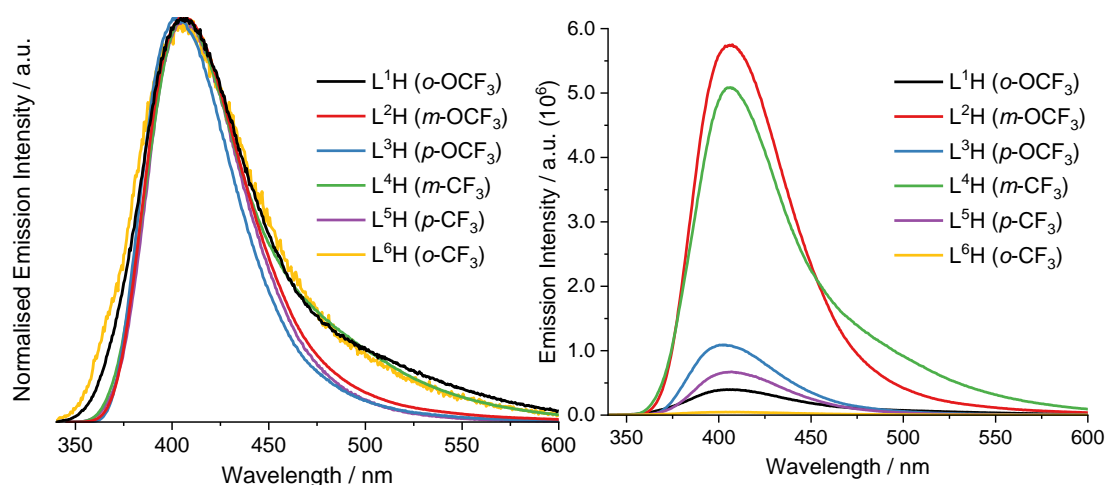
Figure 3.24: *Normalised (left) and relative (right) emission spectra of the free ligands, **L¹⁻⁶H** (CHCl₃, ca. 10⁻⁵ M, RT, λ_{ex} = 330 nm).*

Photophysical properties for the organic species (**Table 3.9**) were consistent with a fluorescence decay pathway and provided insight into the electronic nature of the free ligands. Small Stokes shifts were measured between 66 – 84 nm and fluorescence quantum yields were lowest for the *para*-substituted compounds (**L³H** and **L⁵H**), but all compounds ranged between 1.3 – 3.3%.

Ligand	λ_{abs} ($\varepsilon \times 10^4$ / M^{-1} cm^{-1}) / nm	λ_{em}[a] / nm	Φ_F[b] / %	*Stokes shift* / *nm*
L¹H	252 (2.2), 326 (0.9)	406	2.0	80
L²H	260 (2.6), 334 (1.0)	406	2.0	72
L³H	263 (2.9), 336 (1.3)	402	1.3	66
L⁴H	260 (3.2), 333 (1.1)	406	2.5	73
L⁵H	261 (3.4), 333 (1.2)	407	1.5	74
L⁶H	321 (0.5)	405	3.3	84

Table 3.9: *Photophysical properties of* **L¹⁻⁶H**, *measured in aerated CHCl₃ at room temperature (10^{-5} M).* [a]*λ_{ex} = 330 nm;* [b]*Quinine sulphate in 0.1M H₂SO₄ (Φ = 0.546)* [85] *used as standard for quantum yield determination, λ_{ex} = 350 nm.*

The spectroscopic properties of the corresponding Pt(II) and Ir(III) complexes were also investigated in 10^{-5} M aerated chloroform solutions under ambient conditions, and are discussed in detail below.

The UV-vis absorption spectra for the Pt(II) complexes are displayed in **Figure 3.25** and presented as relatively similar profiles with three distinguishable attributes. The high-energy absorption bands between 250 – 320 nm and 340 – 400 nm revealed ε values of 11000 – 44000 M^{-1} cm^{-1} and 5600 – 16000 M^{-1} cm^{-1}, respectively. These were assigned as ligand-centred $^1(\pi{\rightarrow}\pi^*)$ contributions from the C^N ligands, due to their high intensities and presence in the corresponding free ligand spectra. These peaks became more structured upon coordination accompanied by a small bathochromic shift, which was attributed to perturbation from the metal.[12]
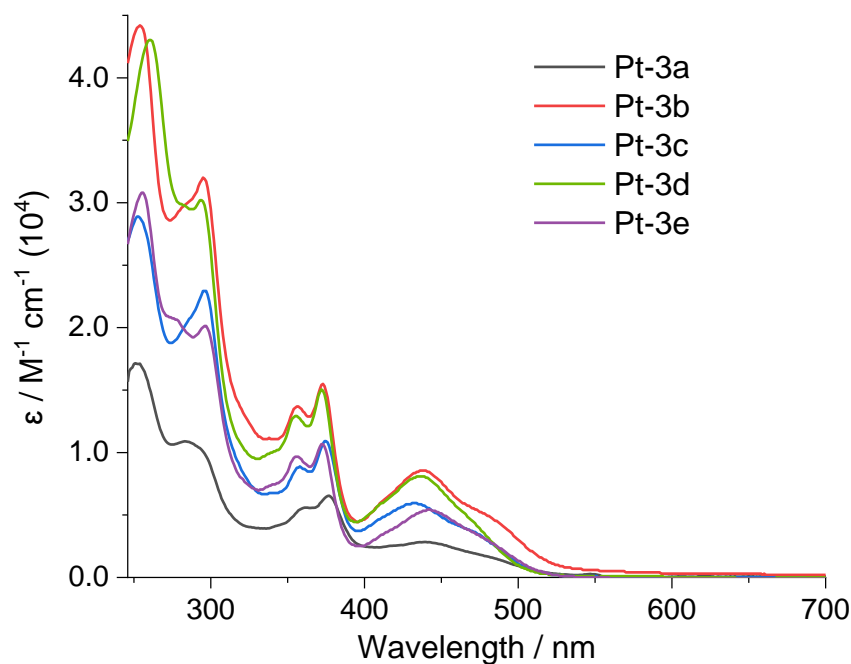
Figure 3.25: *UV-vis absorption spectra for all Pt(II) complexes (CHCl$_3$, 0.99 × 10^{-5} M, RT).*

The low-energy signals within the visible range (>400 nm) were only present in the complexes and were assigned as a mixture of contributions. Large ε values of up to 8600 M^{-1} cm^{-1} for peaks between 400 – 460 nm were indicative of a spin-allowed ^{1}MLCT contribution, where previous studies on **[Pt(ppy)(acac)]** in DCM displayed comparable absorption features.[12] Research has found that strong spin-orbit coupling promotes the efficient mixing of singlet and triplet excited states within these systems, where the low-energy absorption band has been assigned as a transitions consisting of mixed MLCT and intra-ligand (IL) π→π* character.[86,87] A directly comparable system bearing a trifluoromethyl-substituted 2-phenylquinoline C^N ligand displayed a feature at 414 nm in DCM (ε ~6500 M^{-1} cm^{-1}), also assigned as a mixture of MLCT and IL contributions.[19] The significant bathochromic shift in λ_{abs} for this feature for all Pt(II) species in this study was consistent with previous reports on closely-related pyrazine-based cyclometallated analogues, where 2,3-diphenylquinoxaline as the C^N ligand displayed a peak at 446 nm in DCM (ε ~ 6500 M^{-1} cm^{-1}),[23] suggesting that incorporation of a quinoxaline moiety reduces the energy of the π* orbitals. These derivations were in alignment with comparative studies on various analogues of ppy-based systems, where **bzq** (benzo[*h*]quinoline) and **dbq** (dibenzo[*f,h*]-quinoline) have been employed as C^N ligands.[83]

Weak shoulder peaks at >500 nm were assigned as spin-forbidden transitions to ^{3}MLCT states, typical for complexes of this nature where shoulder peaks were recognised at ~488 (ε ~ 3800 M^{-1} cm^{-1}) for quinoxaline species.[23] The spin-forbidden nature of this process is relaxed as a consequence of the heavy platinum atom, which facilitates the direct excitation to a triplet state by efficient spin-orbit coupling.[88]
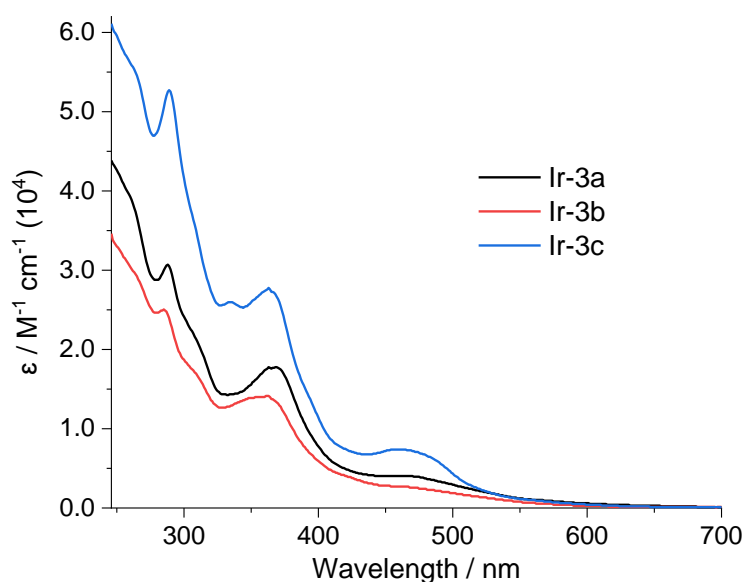
Figure 3.26: *UV-vis absorption spectra for the Ir(III) complexes (CHCl$_3$, RT). Concentrations (in 10^{-5} M) of; 0.99 (**Ir-3a**), 0.75 (**Ir-3b**), 0.99 (**Ir-3c**).*

The absorption profiles of the Ir(III) complexes (**Figure 3.26**) also displayed high-intensity ^{1}IL features below 400 nm, whilst MLCT character was detected at longer wavelengths between 460 – 502 nm (ε < 10000 M^{-1} cm^{-1}). The latter features were comparatively less well-defined than in the equivalent Pt(II) complexes, where only **Ir-3c** displayed a distinguished peak at 468 nm. Once again, broadened ^{3}MLCT features were recognised at the tail-end of the spectra at >500 nm. An overall hypsochromic shift in all absorption bands was seen as the position of the OCF$_3$ substituent was repositioned further away from the coordination sphere, where **Ir-3c** displayed high-intensity bands at shorter wavelengths. Comparison of the absorption profiles for **L^{1}H** and its corresponding Pt(II) and Ir(III) complexes illustrates the key differences discussed above (**Figure 3.27**).
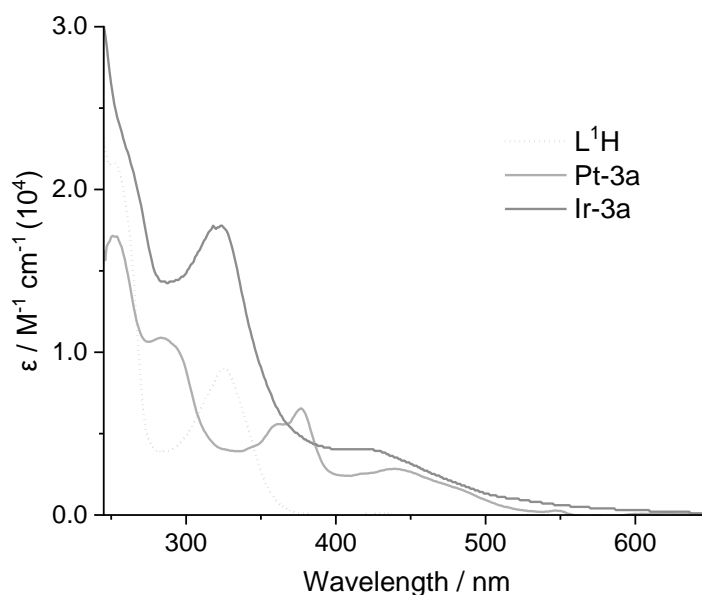
Figure 3.27: *Comparison of UV-vis absorption spectra for **L¹H**, **Pt-3a** and **Ir-3a** in aerated CHCl₃ solutions (ca. 10⁻⁵ M, RT).*

Steady state luminescence measurements were recorded for all complexes in aerated chloroform solutions (*ca.* 10⁻⁵ M). The Pt(II) complexes displayed broad emission features in the orange-to-red region of the visible range upon excitation at 440 nm (**Figure 3.28**), in accordance with the low-energy band in the absorption profiles. These were once again in agreement with analogous species bearing conjugated cyclometallated pyrazine-based ligands.[23] Peak maxima were seen at 604 – 620 nm, where **Pt-3d** displayed the most blue-shifted emission peak and **Pt-3a** was most red-shifted. A characteristic shoulder peak was present in most cases at 655 – 658 nm, remaining relatively consistent across the series.
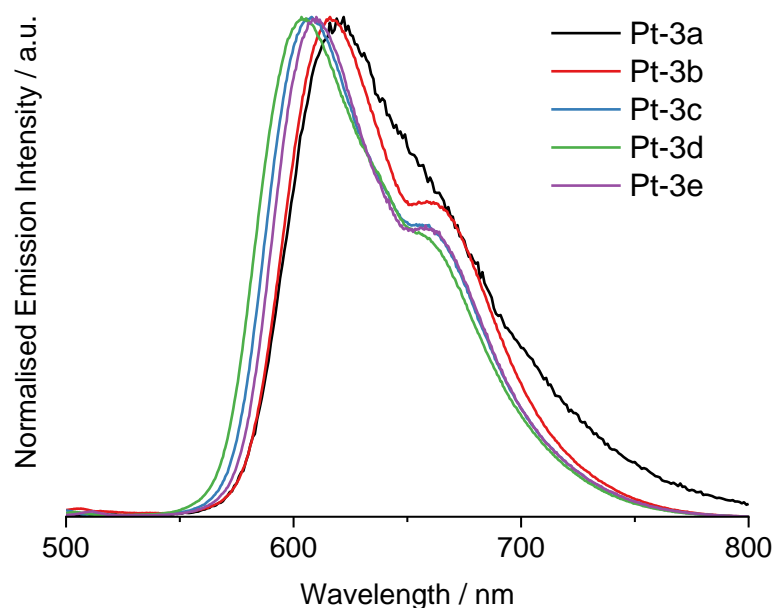
Figure 3.28: *Normalised emission spectra for all Pt(II) complexes with the general formula **[Pt(Lⁿ)(acac)]** in CHCl₃ solutions (10⁻⁵ M) λₑₓ = 440 nm.*

The Ir(III) species showed broad emission features within a similar range, where emission maxima were seen at 591 – 606 nm and shoulder features were at 658 – 660 nm (**Figure 3.29**). **Ir-3b** displayed the most red-shifted λ_{max} whilst the λ_{max} was seen at a shorter wavelength for **Ir-3c**, consistent with the trend in the analogous Pt(II) complexes. Overall, the emission of the Ir(III) complexes were shifted closer towards the orange region of the visible range, and all λ_{em} values were hypsochromically shifted in comparison to their Pt(II) analogues.
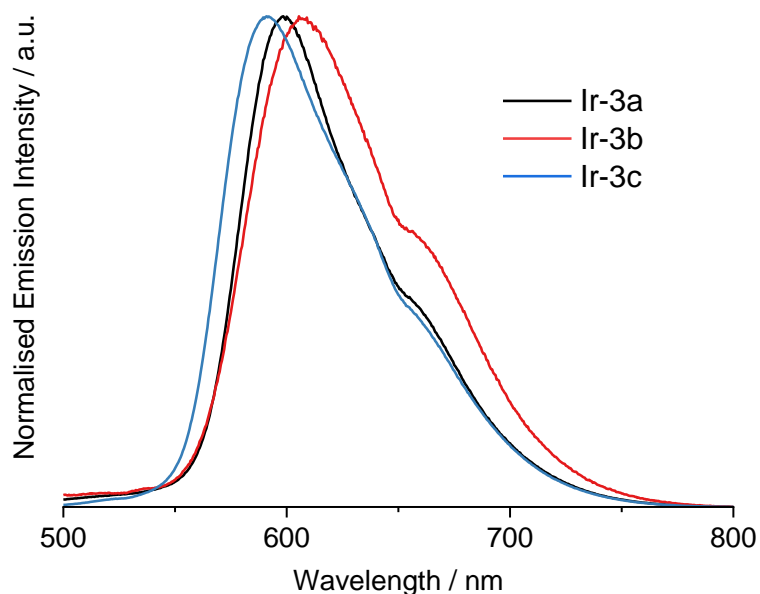
Figure 3.29: *Normalised emission spectra for the Ir(III) complexes with the general formula **[Ir(Lⁿ)₂(bpy)]PF₆** in CHCl₃ solutions (10⁻⁵ M, RT) λₑₓ = 440 nm.*

The overlapped emission spectra for **L³H** and its corresponding organometallic complexes are displayed in **Figure 3.30**, where a drastic shift in λ_{em} can be seen upon coordination. A slight bathochromic shift was seen in all cases when comparing the Pt(II) species with analogous Ir(III) variants, where a shift of 21 nm was seen between **Ir-3a** to **Pt-3a**.
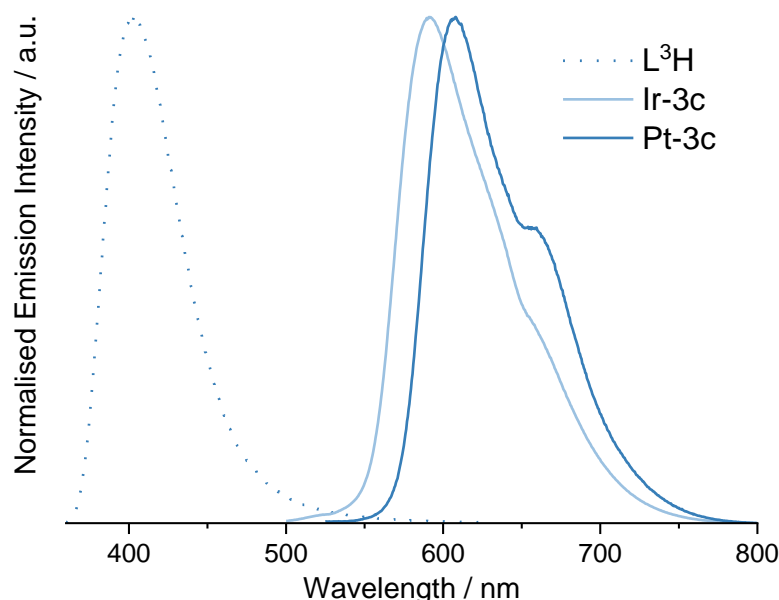
*Figure 3.30: Comparison of normalised emission spectra for **L³H**, **Pt-3c** and **Ir-3c** in aerated CHCl₃ solutions (10⁻⁵ M, RT). λₑₓ = 330 nm for **L¹H**, λₑₓ = 440 nm for **Pt-3c** and Ir-3c.*

The absorption and emission properties are tabulated in **Table 3.10**, where photophysical parameters are summarised. Data recorded in toluene and in degassed solutions were measured by Xiao Xiao and Prof. Jianzhang Zhao of Dalian University of Technology and further information including absorption data in toluene can be found in the published work.[52] Quantum yields of the Pt(II) complexes were measured in aerated chloroform with values of 1.2 – 3.2%. However, significant enhancements were seen in degassed solutions, where values were recorded at 14.4 – 24.8% in toluene and 21.9 – 37.1% for DCM. In all cases, **Pt-3c** displayed the highest value and **Pt-3a** presented the lowest in accordance with the energy gap law which states that higher energy emission results in a reduction of quantum yields. Quantum yields ranged between 5.7 – 10.4% in aerated solutions of chloroform for the Ir(III) complexes and values were consistent with the emission data, where the most blue-shifted complex, **Ir-3c**, displayed a Φ value of 10.4%.

Complex	λ_{abs} / nm ($\varepsilon \times 10^4$ / M^{-1} cm^{-1})	λ_{em}[a] / nm	Φ_P[b] / %	Φ_P[c] / %	τ_{obs}[d] / ns	τ_{obs}[e] / μs	$\Delta\lambda$[f] / nm
Pt-3a	253 (1.7), 284 (1.1), 361 (0.6), 377 (0.7), **439** (0.3), 482 sh (0.2)	620 (*620*)	1.2	*14.4* (*21.9*)	(*267*)	*0.9 (25.3%) 2.2 (74.7%)*	181
Pt-3b	254 (4.4), 295 (3.2), 356 (1.4), 373 (1.6), **438** (0.9), 480 sh (0.5)	615, 657 sh (*611*)	2.4	*21.9* (*32.1*)	323 (*271*)	*1.3 (26.6%) 2.3 (73.4%)*	177
Pt-3c	252 (2.9), 296 (2.3), 358 (0.9), 374 (1.1), **433** (0.6), 473 sh (0.4)	608, 657 sh (*603*)	3.2	*24.8* (*37.1*)	364 (*304*)	*1.5 (34.0%) 2.7 (66.0%)*	175
Pt-3d	260 (4.3), 293 (3.0), 355 (1.3), 372 (1.5), **437** (0.8), 468 sh (0.5)	604, 655 sh (*604*)	2.8	*19.1* (*34.3*)	342 (*500*)	*1.4 (23.4%) 2.6 (76.6%)*	167
Pt-3e	255 (3.1), 297 (2.0), 355 (1.0), 372 (1.1), **442** (0.5), 475 sh (0.3)	610, 658 sh (*607*)	2.1	*14.9* (*27.1*)	270 (*268*)	*1.2 (59.1%) 1.7 (40.9%)*	168
Ir-3a	288 (3.1), 323 (1.8), **460** (0.4), 499 sh (0.3)	599, 658 sh	6.9	-	540	-	139
Ir-3b	285 (2.5), 361 (1.4), **461** (0.3), 500 sh (0.2)	606, 658 sh	5.7	-	348	-	145
Ir-3c	289 (5.3), 363 (2.8), **468** (0.7), 502 sh (0.4)	591, 660 sh	10.4	-	467	-	123

Table 3.10: *Photophysical properties for the complexes in aerated CHCl$_3$ solutions (10^{-5} M, RT) unless otherwise specified. Italicised data was recorded by Xiao Xiao and Prof. Jianzhang Zhao of Dalian University of Technology.* [a]*λ_{ex} = 440 nm, values in parentheses in toluene;* [b]*Quantum yields calculated against known standard* **[Ru(bpy)$_3$](PF$_6$)$_2$**, *Φ_P = 0.016 in MeCN),* [89] *λ_{ex} = 450 nm;* [c]*λ_{ex} = 440 nm in degassed toluene, values in parentheses are in degassed DCM;* [d]*λ_{ex} = 459 nm, values in parentheses in aerated toluene (λ_{ex} = 405 nm), recorded at λ_{em} = 750 nm;* [e]*in degassed toluene (λ_{ex} = 405 nm), relative contributions are shown;* [f]*difference between low-energy absorption band associated with MLCT transition (bold) and λ_{em}.*

Time-resolved luminescence measurements revealed that all Pt(II) complexes displayed lifetimes within the sub-microsecond domain in aerated solutions and were extended to the microsecond region in degassed solutions – consistent with a triplet emissive state due to the spin-forbidden nature of the relaxation process. The differences in these values were related to quenching mechanisms in oxygenated media, where the photochemical generation of $^1O_2$ (where the complexes act as photosensitisers) resulted in rapid quenching of the long-lived triplet excited states of the phosphors. This was supported by quantum yield measurements, which also diminished in aerated solutions. Notably, the Pt(II) complexes displayed no evidence of photobleaching since quantum yield measurements remained consistent over a period of months, demonstrating their photostability. The Ir(III) complexes demonstrated an enhancement in lifetime relative to their Pt(II) analogues, where 364 ns for **Pt-3c** was extended to 467 ns in **Ir-3c**, but all values were still recorded within a sub-microsecond range.

Complex	Φ_Δ / %
Pt-3a	38
Pt-3b	54
Pt-3c	39
Pt-3d	30
Pt-3e	57
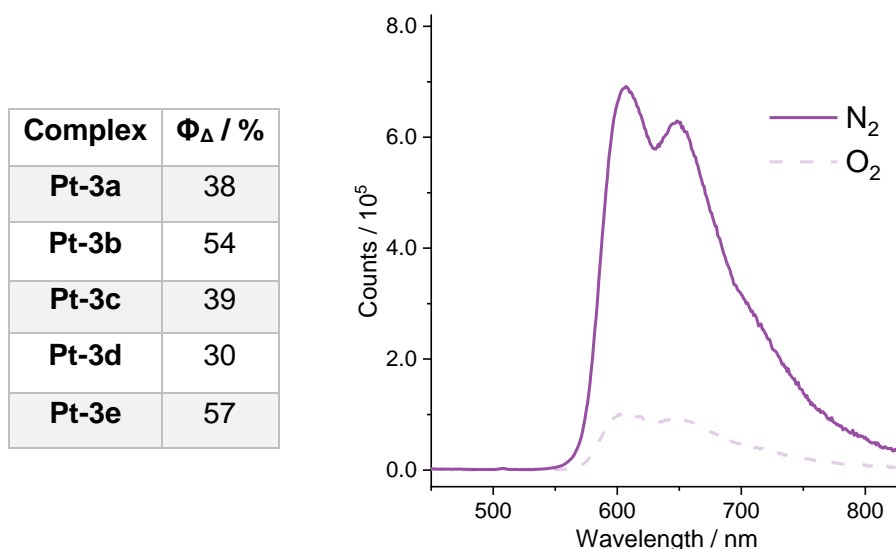
Figure 3.31: *(Left) $^1O_2$ quantum yields of the Pt(II) complexes using **[Ru(bpy)$_3$]$^{2+}$** (Φ_Δ = 0.57 in DCM) as the standard, λ_{ex} = 440 nm. (Right) Phosphorescence emission spectra of **Pt-3e** in degassed (solid) and aerated (dashed) toluene solutions (λ_{ex} = 440 nm, RT, 10^{-5} M). Data obtained by Xiao Xiao of Dalian University of Technology.*

Complexes based upon **[Pt(ppy)(acac)]** are reported to be highly efficient photosensitisers of singlet oxygen.[90,91] This sensitivity to oxygen is clearly demonstrated by comparison of the emission spectra and **Pt-3e** is presented as an example in **Figure 3.31**, where a reduction in emission intensity is seen in

oxygenated solution relative to the degassed sample. Singlet oxygen quantum yield (Φ_Δ) data is also tabulated and exemplifies their potential in oxygen sensing applications, where **Pt-3e** is the most efficient in $^1O_2$ generation.

The unique solvation properties of the Pt(II) complexes enabled spectroscopic measurements to be collected in various solvents. λ_{abs} values were generally consistent throughout, suggesting that the absorption features were not strongly solvatochromic. In contrast, emission properties varied depending on the solvent, where intensities diminished by quenching effects in polar solvents such as acetonitrile. However, the peak positions of the emission bands displayed little solvatochromic behaviour, suggesting minimal change in the dipole moment between the ground state and excited state. An example of this is shown in **Figure 3.32** for **Pt-3c**, but this trend was seen for all five complexes.
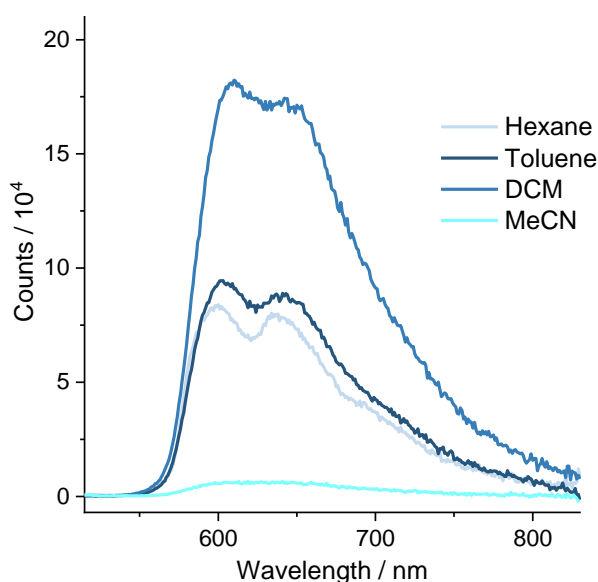
Figure 3.32: *Emission spectra of **Pt-3c** in a variety of aerated solvents, λ_{ex} = 440 nm. Data obtained by Xiao Xiao of Dalian University of Technology.*

Overall, the Pt(II) complexes displayed a relative bathochromic shift in absorption and emission properties accompanied by an enhanced phosphorescent quantum yield when compared to **[Pt(ppy)(acac)]** and **[Pt(pq)(acac)]**.[12,19] Notably, the quinoline analogue of **Pt-3e** displayed λ_{em} at 588 nm and Φ_P = 6% in degassed DCM, suggesting that inclusion of the quinoxaline system results in a significant enhancement of the quantum yield in addition to a bathochromically shifted emission band.[19]

Solid state emission data was also collected for the square planar platinum species to monitor the interactions discussed in **Section 3.3.3** alongside any resultant photophysical effects (**Table 3.11**). Lifetimes were recorded within the sub-microsecond domain, comparable with those seen in aerated solutions.

	Solution[a]		Solid state	
Complex	λ_{em}/ nm[b]	τ_{obs} / ns[c]	λ_{em}/ nm[d]	τ_{obs} / ns[e]
Pt-3a	620	-	678	123
Pt-3b	615, 657 sh	323	680	133
Pt-3c	608, 657 sh	364	630, 660 sh	142
Pt-3d	604, 655 sh	342	677	136
Pt-3e	610, 658 sh	270	679	140

Table 3.11: *Emission data for the Pt(II) complexes. [a]in aerated CHCl₃; [b]λ_{ex} = 440; [c]λ_{ex} = 459 nm, λ_{em} = 620 nm; [d]λ_{ex} = 450 nm; [e]λ_{ex} = 459 nm, λ_{em} = 680 nm*

Most of the solid state emission profiles were bathochromically shifted into the deep-red region compared to the solvated emission (**Figure 3.33**), where λ_{em} values of 677 – 680 nm were seen for **Pt-3a**, **Pt-3b**, **Pt-3d** and **Pt-3e**. Despite the lack of diffusional quenching mechanisms in the solid state, a significant reduction in observed lifetimes was observed compared to the samples in solution and was consistent with the energy gap law. The shifted emission wavelengths were ascribed to aggregation effects, where the bimetallic nature of the compounds (**Section 3.3.3**) may promote MMLCT emission.[15] These have been previously described as $\sigma^*(5d_{z2}/5d_{z2}) \rightarrow \pi^*$ transitions, where shorter Pt-Pt distances reduce the HOMO-LUMO gap and result in a red-shifted emission.[92]

Pt-3c displayed a peak at 630 nm with a distinguishable shoulder feature at 660 nm. This was congruent with the crystal data where a long Pt-Pt distance was measured, suggesting a weak intermolecular interaction. **Pt-3d** and **Pt-3e** displayed similar profiles to their OCF₃ analogues, suggesting that solid-state interactions were significant within these species.
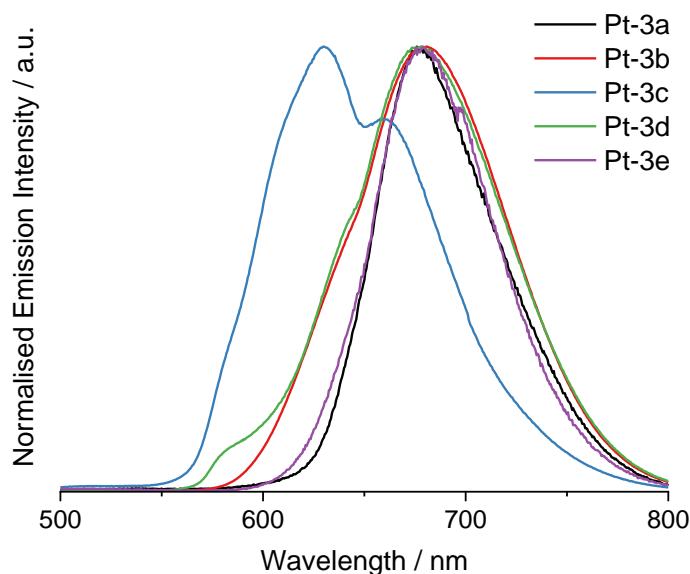
Figure 3.33: *Normalised emission spectra for all Pt(II) complexes (solid), $\lambda_{ex} = 450$ nm.*

3.3.5: Transient Absorption Spectroscopy

Nanosecond time-resolved transient absorption (TA) studies were also carried out by Xiao Xiao (Dalian University of Technology) on the Pt(II) complexes in degassed toluene solutions with a pump wavelength of 355 nm. Three significant features were seen with positive ΔOD values within the range of 300 – 600 nm (**Figure 3.34**). The low-energy band at ~520 nm varied in relative amplitude and broadness between complexes. Kinetic studies demonstrated lifetimes in the range of 0.9 – 2.6 µs, where the decay traces resembled those seen for the time-resolved studies conducted previously in **Section 3.3.4**. These lifetimes were reduced to the sub-microsecond domain upon aeration of the solvent, consistent with previously obtained data on these complexes and indicative of a triplet transient excited state in both instances.
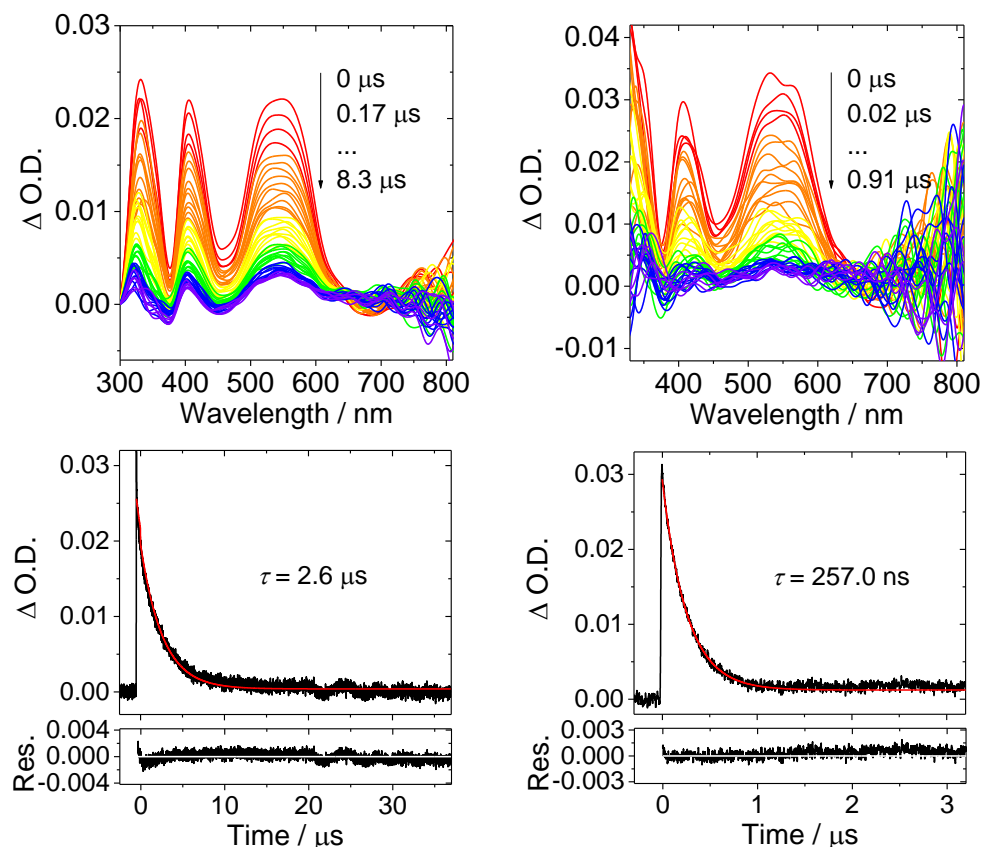
Figure 3.34: *Nanosecond TA spectra of **Pt-3a** in degassed (top, left) and aerated (top, right) toluene solutions (ca. 10^{-5} M, RT), with the corresponding kinetic traces underneath for the feature at 540 nm (λ_{ex} = 355 nm). τ values are also displayed.*

3.3.6: Density Functional Theory & NBO Analysis

DFT studies were performed for the Pt(II) complexes, where geometry optimisation calculations provided insight into the nature of the frontier molecular orbitals and their corresponding energies. In all cases, the theoretical models were based upon an M06 hybrid functional with a 6-31G* basis set and a LANL2DZ basis set for the platinum core. Chloroform solvent correction was applied in accordance with the spectroscopic measurements.

Frontier molecular orbital analysis determined that the HOMO was localised over the Pt atom and the π orbitals on the phenyl ring and acac ligand, whilst the LUMO was shown to mostly reside on the C^N ligand (**Figure 3.35**). This was consistent with previous studies, which have suggested that emission is dominated by LC and MLCT transitions, where the former relates to the C^N ligand as the high energy triplet levels of the acac ligand renders it inaccessible

in ppy-type species.[15] Similarly, theoretical studies for when EWGs were added to the phenyl ring displayed subtle variations in the energies of the HOMOs and LUMOs, depending on the nature and position of the EWG.[93] The calculations were generally consistent with the spectroscopic data of the monomeric species (*i.e.* in dilute solutions), where a reduced HOMO-LUMO energy gap from **Pt-3c** relative to its CF$_3$ analogue **Pt-3e** was represented by red-shifted absorption and emission features.
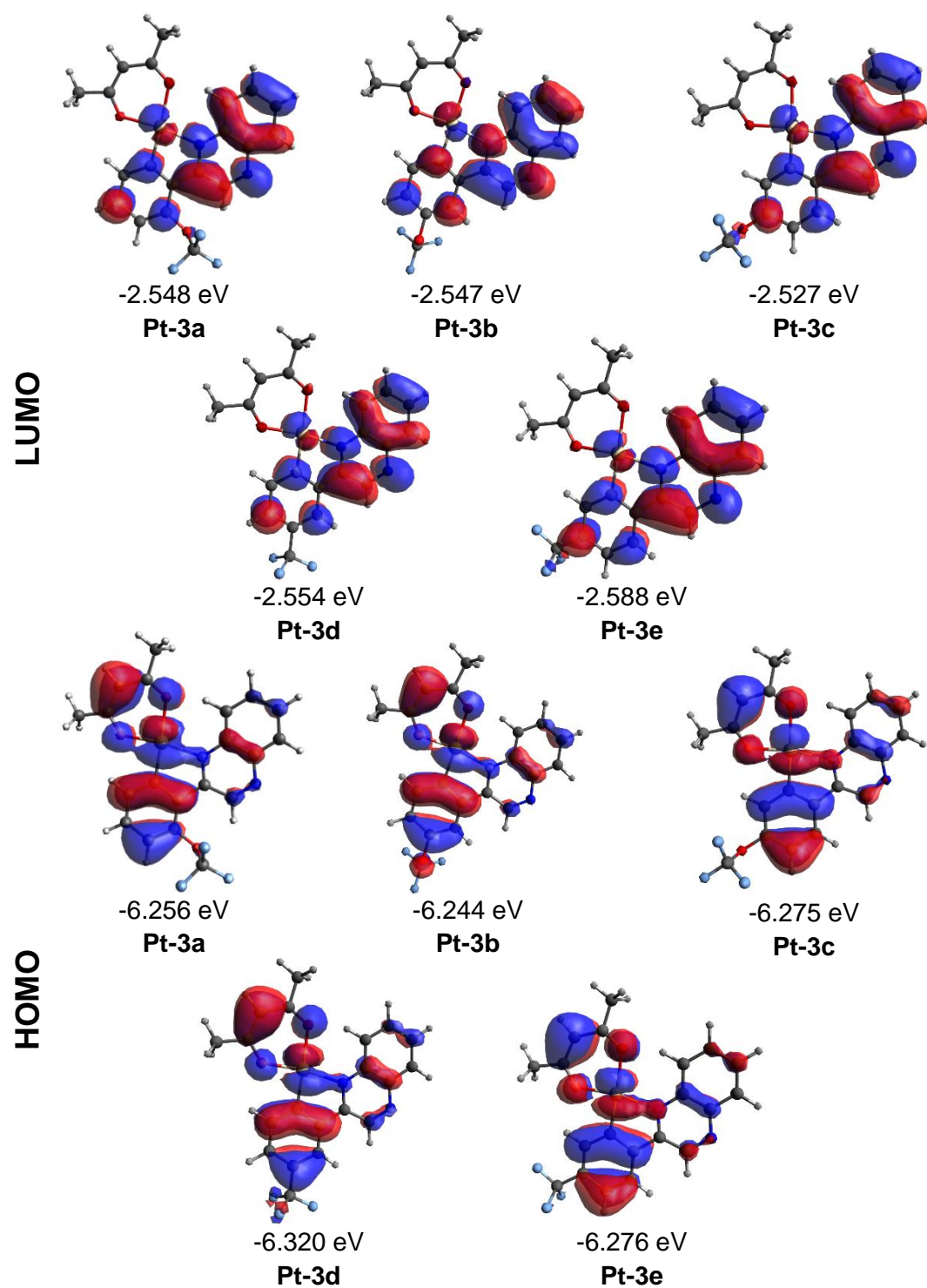
	Pt-3a	Pt-3b	Pt-3c	Pt-3d	Pt-3e
ΔE / eV	3.708	3.697	3.748	3.766	3.688

Figure 3.35: DFT-calculated frontier molecular orbitals and their corresponding energies (M06, 6-31G*/LANL2DZ), isovalues = 0.02. Energy differences (E_{LUMO}-E_{HOMO}) are tabulated below.

Calculations were also performed on the dimerised forms of the species to investigate the solid-state interactions. The dz^2 contribution to the HOMO from each Pt centre can be clearly recognsied by analysis of the frontier MOs (**Figure 3.36**), consistent with a MMLCT-type transition.
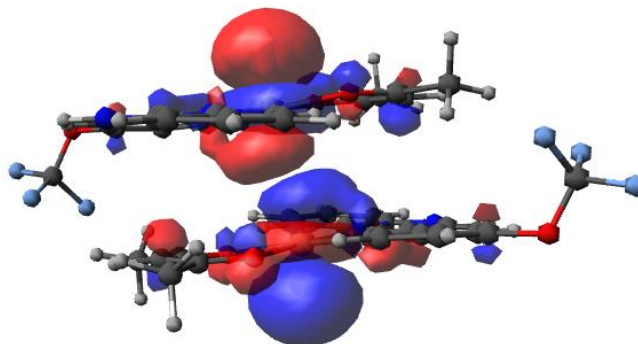
Figure 3.36: Side-on view of the HOMO, where the dz^2 orbitals show a significant contribution.

Natural bond orbital (NBO) studies were undertaken on the DFT-optimised structure (M06 | LANL2DZ/6-31G*) to investigate significant interactions between donor and acceptor Lewis-type NBOs *via* second order perturbation theory analysis. The Pt-Pt bonding interactions were described by bilateral d → $sd^{0.3}$ donor-acceptor interactions, illustrated in **Figure 3.37**.
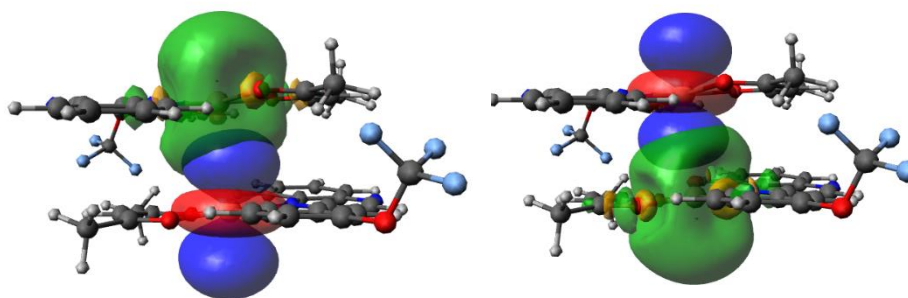
*Figure 3.37: Illustration of the NBO interactions between the two Pt atoms in **Pt-3b** where the donor NBO is coloured in red/blue and the acceptor in green/yellow.*

The OCF_3 substituent was also investigated, where one of the lone pairs on the oxygen were shown to donate to the three σ^*_{CF} orbitals and also directly into the aromatic ring ($n_O \rightarrow \pi^*$), whereas a second lone pair was shown to only interact with two σ^*_{C-F} orbitals. These exhibited sp^2 and p character respectively, and the calculated relative stabilisation energies are shown in **Table 3.12**.

Complex	Relative Stabilisation Energy / kcal/mol		
	$n_O \rightarrow \sigma^*_{C-F}$	$n_O \rightarrow \pi^*$	$n_O \rightarrow \sigma^*_{C-F}$
Pt-3a	1.28, 7.31, 4.09	6.81, 1.49	17.53, 13.81
Pt-3b	7.33, 2.60, 2.46	6.97	17.12, 16.02
Pt-3c	8.24, 2.49, 3.05	1.00, 20.40	14.08, 17.19

*Table 3.12: Calculated NBO interactions within the OCF$_3$ functionality on **Pt-3a**, **Pt-3b** and **Pt-3c**. The stabilisation energies relate to the delocalisation of electrons between donor and acceptor.*

Quantum theory of atoms in molecules (QTAIM) analysis indicated bond critical points between the two Pt centres in the bimetallic DFT-optimised species, supporting the Pt-Pt bonds seen in the XRD data.

3.3.7: Energy Upconversion

Triplet-triplet annihilation energy upconversion (TTA-UC) studies were undertaken by Xiao Xiao (Dalian University of Technology), where the Pt(II) species were studied as photosensitisers and 9,10-diphenylanthracene (DPA) was used as the acceptor (also known as the annihilator) molecule. The energy upconversion emission spectra were measured in degassed DCM and are displayed in **Figure 3.38**, along with images illustrating the process. In all instances, the ^{3}MLCT emission was quenched by the addition of DPA and was indicative of an upconversion process. An λ_{ex} of 473 nm was applied, which is outside the excitation range for DPA. The triplet excited state of DPA lies below that of the Pt(II) complex (~700 nm), ensuring that TTA-UC was responsible for any emission from the acceptor component within the range of 400 – 500 nm. Peaks observed at 410 and 432 nm were therefore associated with DPA emission.[94] Photographs are also shown alongside their respective emission spectra (**Figure 3.38**) to give a visual representation of the process, where high energy light was generated from low energy red or orange light. This was demonstrated further by applying a band-path filter, where the intensity of blue light is greater upon addition of the acceptor. Upon increasing the concentration of DPA, the emission intensity of the corresponding sensitiser was quenched (**Figure 3.39**), confirming the deactivation of the T$_1$ state in the complex.
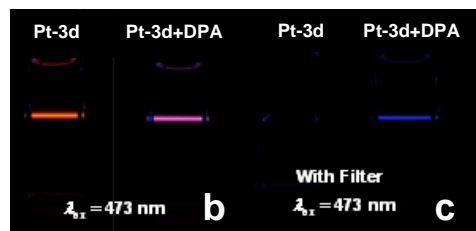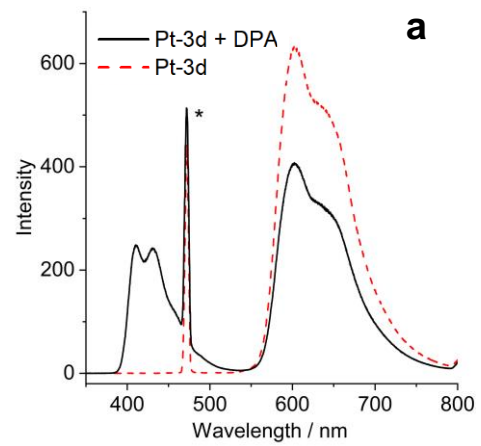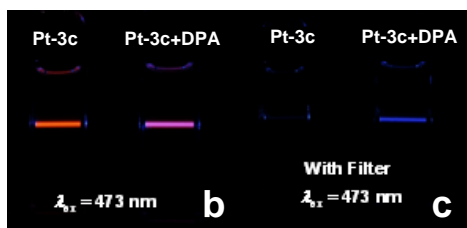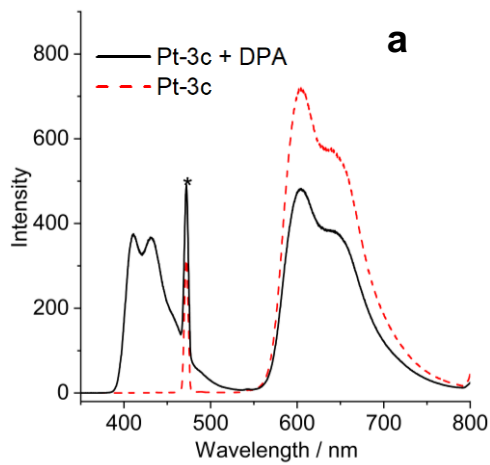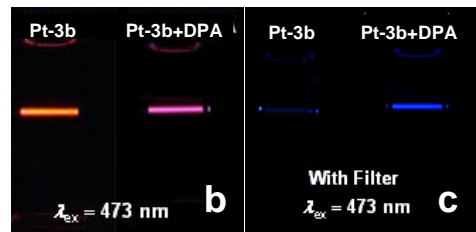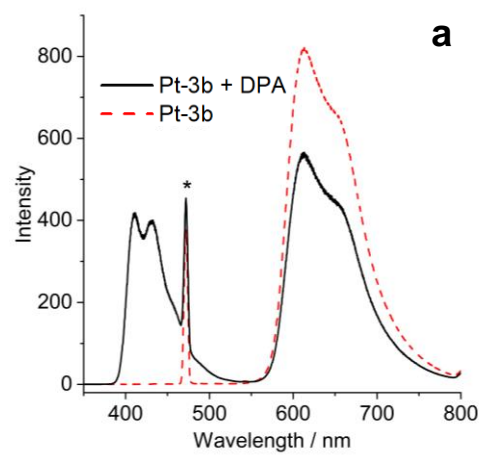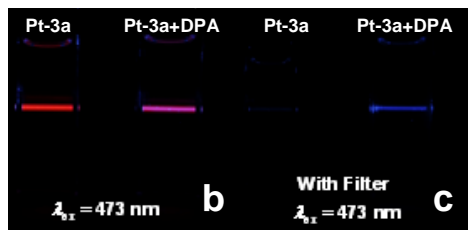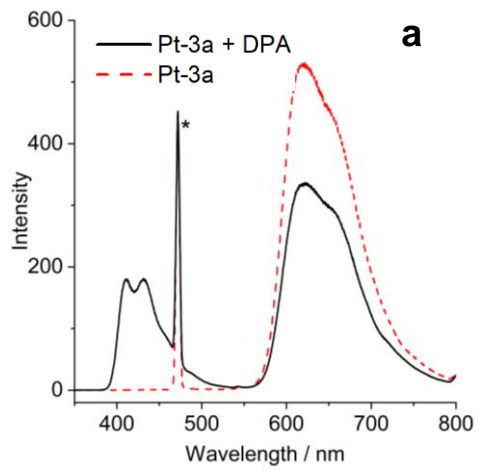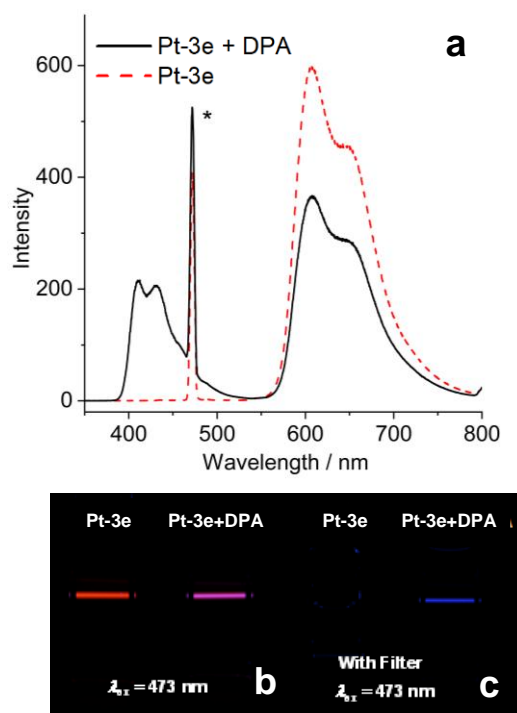
*Figure 3.38: (a) TTA-UC emission spectra for all Pt(II) complexes as photosensitisers and DPA as the acceptor in degassed DCM solutions ([**Pt-3n**] = 1.0 × 10⁻⁵ M, [DPA] = 3.0 × 10⁻⁵ M, RT, λ$_{ex}$ = 473 nm using a CW laser pulse with a power density of 80 mW cm⁻²) *Scattering from the laser; (b) Photographical images of the complexes irradiated alone alongside the upconversion; (c) Photographical images with a band-pass filter applied (transparent in the range of 380 – 520 nm). Data obtained by Xiao Xiao (Dalian University of Technology).*
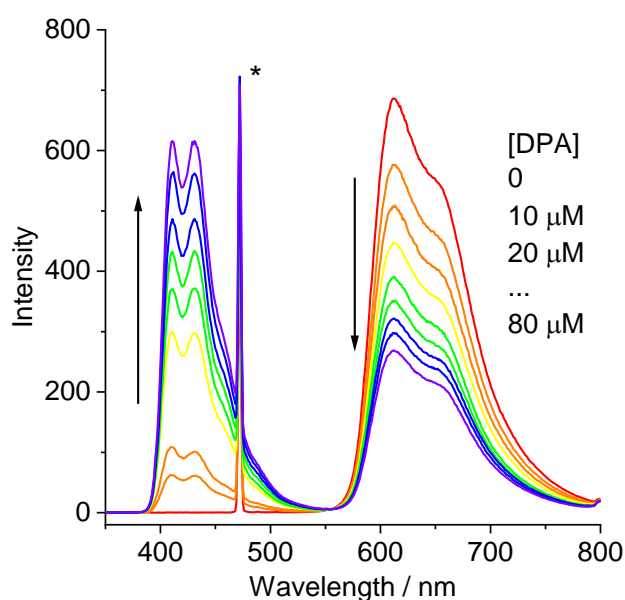
*Figure 3.39: TTA-UC emission spectra for **Pt-3b** at varying concentrations of DPA (λ$_{ex}$ = 473 nm, RT) *Scattering from the laser. Data obtained by Xiao Xiao (Dalian University of Technology).*

Quantum yield data was also collected (**Table 3.13**), where their potential as triplet photosensitisers was eluclidated. **Pt-3c** displayed the highest Φ_{UC} at 14.1%, exemplifying that complexes of this nature could directly compete with previously reported species.[29] In comparison to other Pt(II) photosensitisers for TTA-UC,[31] these complexes displayed relatively short triplet lifetimes, offering scope for short-lived species that may be suitable for thin-film applications.

Complex	λ_{em} [a] / nm	Φ_P [b] / %	Φ_{UC} [c] / %
Pt-3a	623	21.9	5.9
Pt-3b	614	32.1	12.1
Pt-3c	608	37.1	14.1
Pt-3d	606	34.3	9.5
Pt-3e	610	27.1	8.5

***Table 3.13:** Emission and quantum yield data for the Pt(II) complexes measured in degassed DCM (10^{-5} M, RT). [a]Emission maxima, $\lambda_{ex} = 440$ nm; [b]$\lambda_{ex} = 440$ nm; [c] TTA-UC quantum yields using **[Ru(dmb)$_3$]$^{2+}$** ($\Phi_P = 0.073$ in degassed MeCN) as a known standard, $\lambda_{ex} = 473$ nm.*

The trend for TTA-UC performance is reasonably consistent, where the OCF$_3$ analogues were deemed to be more efficient in comparison to their CF$_3$ counterparts and the Φ_{UC} decreased alongside an increase in λ_{em}, rendering **Pt-3a** the least efficient. The position of substitution was therefore proven to impact both the phosphorescence character and energy upconversion efficiencies, impacting their behaviour as photosensitisers.

3.4: Conclusions

The work presented within this chapter explored the design and synthesis of a series of 2-phenylquinoxaline ligands, where changes in substituent positioning around the phenyl ring imparted significant changes to the structural and electronic properties of the resultant cyclometallated Pt(II) complexes. Five novel neutral Pt(II) complexes were developed as deep-red emitters and displayed enhanced solubilities relative to previously studied analogues, due to the incorporation of lipophilic OCF_3 or CF_3 substituents. Corresponding Ir(III) species were developed for the OCF_3 ligands, exemplifying some key differences between neutral, square planar and cationic, octahedral phosphorescent complexes, where the latter has been vastly explored in other chapters within this thesis. Subtle tunability of the photophysical properties of all the complexes was achieved, reliant upon the position and nature of the substituent on the phenyl ring.

Computational analysis explored the electronic effects in more detail, complementing the experimental data in solution whilst offering insight into the emission properties of the samples in the solid state through NBO analysis.

The Pt(II) species offered significant potential as photosensitisers for TTA-UC, where Φ_{UC} values ranged between 5.9 – 14.1% and showed great dependency on the position of the EWG within the ligand. These could compete with analogous Pt(II) species as efficient photosensitisers,[29] whilst providing unique properties such as reduced lifetimes and enhanced solubilities in organic solvents,[31] offering potential in thin-film and solution-based electronic applications.

3.5: Experimental

3.5.1: General Considerations

All commercially available reagents were used without further purification, and all reactions employed vacuum line and Schlenk techniques. ^1H, $^{13}C\{^1H\}$ and $^{19}F\{^1H\}$ NMR spectra were recorded on NMR-FT Bruker 500, 400 and 300 MHz spectrometers in the appropriate solvents (CDCl$_3$, (CD$_3$)$_2$CO, CD$_3$CN or DMSO-d_6), where chemical shift (δ) positions (ppm) were determined relative to TMS and residual solvent peaks[95] through digital locking. High resolution mass spectra were obtained by staff at Cardiff University using a Waters Xevo G2-XS QTof spectrometer, and IR spectra were recorded on a Shimadzu IRAffinty-1 FTIR spectrometer. UV-vis spectroscopy studies were performed on 10^{-5} M solutions using either a Shimadzu UV-1800 or a Perkin Elmer Lamda20 spectrophotometer. The 10^{-5} M samples were prepared by dilution of 10^{-3} M bulk stock solutions. Upon sonication in an ultrasonic bath, the samples were inspected to ensure that solute was fully dissolved. Luminescence data was acquired for CHCl$_3$ solutions of the samples using a JobinYvon-Horiba Fluorolog spectrometer fitted with a JY TBX picosecond single-photon detection module. Time-resolved measurements were recorded using a Nano-LED pulsed laser source configured for 295 or 459 nm output, operating at 1 MHz. Time-resolved measurements were recorded using the JobinYvon-Horiba FluoroHub single photon counting module and the data was resolved using the DAS6 deconvolution software. Further detail on the experimental considerations for TTA-UC and other photophysical measurements can be found in the published work related to this study.[52]

3.5.2: X-Ray Crystallography

Crystals were gown *via* evaporation techniques from concentrated solutions of DCE, DCM or CHCl$_3$. Suitable crystals were mounted on a MITIGEN holder in oil on a Rigaku 007HF diffractometer equipped with HF Varimax confocal mirrors and an AFC11 goniometer and HyPix 6000HE detector for **Pt-3a**, or a Rigaku FRE+ diffractometer equipped with VHF Varimax confocal mirrors and an AFC12 goniometer and HyPix 6000 detector for **Pt-3b** and **Pt-3c**.[96] The

crystals were kept at 100(2)K, apart from one **Pt-3b** sample, which was measured at 200K. Using Olex2,[97] the structures were solved with the ShelXT[98] structure solution program, using the Intrinsic Phasing Solution method. The models were refined with version 2014/7 of ShelXL[99] by use of Least Squares minimisation. All non-H atoms were refined anisotropically and idealised hydrogen atom positions were calculated using the riding hydrogen model.

3.5.3: Preparation of Ligands and Precursors

Synthesis of sodium acetylacetonate

Following an adapted literature method,[100] NaOH (4.00 g, 0.100 mol) in distilled H_2O (5mL) was added to MeOH (20mL) and was then added dropwise to a stirred solution of 2,4-pentanedione (10.0 mL, 0.100 mol), where an off-white precipitate formed. A sealed flask containing the suspension was cooled overnight at ~4°C. The salt was collected by filtration under reduced pressure and washed with ice-cold methanol (2 × 5 mL) to give the product as an off-white solid (12.2 g, 87.1%).

Synthesis of 2-bromo-1-(2-(trifluoromethoxy)phenyl)ethan-1-one

Dioxane dibromide (668 mg, 2.69 mmol) in a solution of 1,4-dioxane and diethyl ether (1:1, 40 mL) was added dropwise to 2'-(trifluoromethoxy)acetophenone (500 mg, 2.45 mmol) in the same solvent mixture whilst stirring under air at room temperature for 2 h. The solution was added to water and extracted with diethyl ether. The combined organic layers were dried over $MgSO_4$ and the solvent was removed *in vacuo* to give the product as a yellow oil (570 mg, 82.2%). ^1H NMR (300 MHz, $CDCl_3$) δ_H = 7.78 (dd, $^3J_{HH}$ = 7.8, $^4J_{HH}$ = 1.7 Hz, 1H), 7.58 (*app.* td, $^3J_{HH}$ = 8.2, $^4J_{HH}$ = 1.7 Hz, 1H), 7.42 – 7.35 (m, 1H), 7.33 (d, $^3J_{HH}$ = 8.3 Hz, 1H), 4.46 (s, 2H) ppm.

Synthesis of 2-bromo-1-(3-(trifluoromethoxy)phenyl)ethan-1-one

Prepared similarly from 3'-(trifluoromethoxy)acetophenone (250 mg, 1.23 mmol) and dioxane dibromide (334 mg, 1.35 mmol) to give the product as a yellow oil (335 mg, 96.7%). ^1H NMR (300 MHz, $CDCl_3$) δ_H = 7.92 (d, $^3J_{HH}$ = 7.7 Hz, 1H), 7.83 (s, 1H), 7.55 (*app.* t, $^3J_{HH}$ = 7.9, 1H), 7.50 – 7.43 (m, 1H), 4.43 (s, 2H) ppm.

Synthesis of 2-bromo-1-(4-(trifluoromethoxy)phenyl)ethan-1-one

Prepared similarly from 4'-(trifluoromethoxy)acetophenone (250 mg, 1.23 mmol) and dioxane dibromide (334 mg, 1.35 mmol) to give the product as yellow crystals (335 mg, 96.5%). ^{1}H NMR (300 MHz, CDCl$_3$) δ_H = 8.09 – 8.01 (m, 2H), 7.32 (d, $^3J_{HH}$ = 8.1 Hz, 2H), 4.42 (s, 2H) ppm. The data was consistent with literature findings.[101]

Synthesis of 2-bromo-1-(3-(trifluoromethyl)phenyl)ethan-1-one

Prepared similarly from 3'-(trifluoromethyl)acetophenone (250 mg, 1.33 mmol) and dioxane dibromide (362 mg, 1.46 mmol) to give the product as a colourless oil (3.08 g, 86.9%). ^{1}H NMR (500 MHz, CDCl$_3$) δ_H = 8.24 (s, 1H), 8.17 (d, $^3J_{HH}$ = 7.8 Hz, 1H), 7.87 (d, $^3J_{HH}$ = 8.2 Hz, 1H), 7.65 (*app.* t, $^3J_{HH}$ = 7.8 Hz, 1H), 4.46 (s, 2H) ppm. The data was consistent with literature findings.[102,103]

Synthesis of 2-bromo-1-(4-(trifluoromethyl)phenyl)ethan-1-one

Prepared similarly from 4'-(trifluoromethyl)acetophenone (250 mg, 1.33 mmol) and dioxane dibromide (362 mg, 1.46 mmol) to give the product as white crystals (311 mg, 87.6%). ^{1}H NMR (500 MHz, CDCl$_3$) δ_H = 8.10 (d, $^3J_{HH}$ = 8.2 Hz, 2H), 7.77 (d, $^3J_{HH}$ = 8.2 Hz, 2H), 4.45 (s, 2H) ppm. The data was consistent with literature findings.[104,105]

Synthesis of 2-bromo-1-(2-(trifluoromethyl)phenyl)ethan-1-one

Prepared similarly from 2'-(trifluoromethyl)acetophenone (1.50 g, 7.97 mmol) and dioxane dibromide (2.17 g, 8.77 mmol) to give the product as a yellow oil (1.95 g, 91.5%). ^{1}H NMR (500 MHz, CDCl$_3$) δ_H = 7.75 (d, $^3J_{HH}$ = 7.1 Hz, 1H), 7.67 – 7.60 (m, 2H), 7.51 (dd, $^3J_{HH}$ = 7.1, $^4J_{HH}$ = 1.2 Hz, 1H), 4.37 (s, 2H) ppm. The data was consistent with literature findings.[105,106]

Synthesis of 2-(2-(trifluoromethoxy)phenyl)quinoxaline *(L^{1}H)*

2-bromo-1-(2-(trifluoromethoxy)phenyl)ethan-1-one (1.30 g, 4.60 mmol) and 1,2-phenylenediamine (547 mg, 5.06 mmol) were heated to reflux in ethanol under air for 24 h. Upon cooling to room temperature, the solvent was removed *in vacuo* and the product was purified by column chromatography (SiO$_2$, DCM), where the product eluted as a yellow band with DCM. The solvent was removed *in vacuo* to give the product as yellow crystals (515 mg, 38.6%). ^{1}H NMR (500 MHz, CDCl$_3$) δ_H = 9.21 (s, 1H), 8.19 – 8.13 (m, 2H), 7.96 (dd, $^3J_{HH}$ = 7.7, $^4J_{HH}$ =

1.8 Hz, 1H), 7.82 – 7.76 (m, 2H), 7.54 (ddd, $^3J_{HH}$ = 8.1, 7.5, $^4J_{HH}$ = 1.9 Hz, 1H), 7.49 (*app.* td, $^3J_{HH}$ = 7.5, $^4J_{HH}$ = 1.3 Hz, 1H), 7.45 – 7.42 (m, 1H) ppm. $^{13}C\{^1H\}$ NMR (126 MHz, CDCl$_3$) δ_C = 150.3, 146.9 (q, $^3J_{CF}$ = 1.8 Hz), 146.0, 142.6, 141.5, 132.3, 131.4, 131.1, 130.4, 130.3, 129.8, 129.4, 127.8, 121.5, 120.5 (q, $^1J_{CF}$ = 259.0 Hz) ppm. $^{19}F\{^1H\}$ NMR (376 MHz, CDCl$_3$) δ_F = −57.15 (s) ppm. HRMS (ES+) found *m/z* 291.0754, calc'd *m/z* 291.0745 for C$_{15}$H$_{10}$F$_3$N$_2$O [M + H]$^+$. UV−vis (CHCl$_3$) λ_{max} (ε × 10^4 / L mol^{-1} cm^{-1}): 252 (2.2), 326 (0.9) nm. FTIR (solid, cm^{-1}) (ATR) v_{max}: 3063, 3038, 1614, 1605, 1584, 1547, 1489, 1450, 1412, 1368, 1314, 1246, 1206, 1194, 1155 (br), 1059, 1032, 959, 924, 874, 818, 799, 758, 687, 629, 610, 569, 559, 530, 486, 469, 432, 409.

Synthesis of 2-(3-(trifluoromethoxy)phenyl)quinoxaline *(L²H)*

Prepared similarly from 2-bromo-1-(3-(trifluoromethoxy)phenyl)ethan-1-one (303 mg, 1.07 mmol) and 1,2-phenylenediamine (127 mg, 1.18 mmol) to give the product as pale yellow crystals (73.3 mg, 23.6%). ^1H NMR (500 MHz, CDCl$_3$) δ_H = 9.31 (s, 1H), 8.19 – 8.12 (m, 2H), 8.13 – 8.10 (m, 2H), 7.84 – 7.74 (m, 2H), 7.59 (*app.* t, $^3J_{HH}$ = 8.2 Hz, 1H), 7.41 – 7.35 (m, 1H) ppm. $^{13}C\{^1H\}$ NMR (126 MHz, CDCl$_3$) δ_C = 150.2, 143.0, 142.3, 142.0, 139.0, 130.7, 130.7, 130.2, 129.9, 129.3, 125.8, 122.6, 120.7 (q, $^1J_{CF}$ = 257.7 Hz), 120.6, 120.3 ppm. $^{19}F\{^1H\}$ NMR (376 MHz, CDCl$_3$) δ_F = −57.64 (s) ppm. HRMS (ES+) found *m/z* 291.0743, calc'd *m/z* 291.0745 for C$_{15}$H$_{10}$F$_3$N$_2$O [M + H]$^+$. UV−vis (CHCl$_3$) λ_{max} (ε × 10^4 / L mol^{-1} cm^{-1}): 260 (2.6), 334 (1.0) nm. FTIR (solid, cm^{-1}) (ATR) v_{max}: 3078, 3061, 3044, 1605, 1589, 1545, 1487, 1447, 1377, 1369, 1317, 1254, 1211, 1182, 1148, 1130, 1059, 999, 968, 937, 905, 878, 827, 802, 789, 764, 694, 685, 635, 611, 584, 563, 527, 484, 440, 407.

Synthesis of 2-(4-(trifluoromethoxy)phenyl)quinoxaline *(L³H)*

Prepared similarly from 2-bromo-1-(4-(trifluoromethoxy)phenyl)ethan-1-one (693 mg, 2.45 mmol) and 1,2-phenylenediamine (291 mg, 2.69 mmol) to give the product as pale yellow crystals (184 mg, 25.9%). ^1H NMR (500 MHz, CDCl$_3$) δ_H = 9.25 (s, 1H), 8.22 – 8.16 (m, 2H), 8.12 – 8.06 (m, 2H), 7.78 – 7.69 (m, 2H), 7.37 (d, $^3J_{HH}$ = 8.0 Hz, 2H) ppm. $^{19}F\{^1H\}$ NMR (376 MHz, CDCl$_3$) δ_F = −57.67 (s) ppm. UV−vis (CHCl$_3$) λ_{max} (ε × 10^4 / L mol^{-1} cm^{-1}): 263 (2.9), 336 (1.3) nm. FTIR (solid, cm^{-1}) (ATR) v_{max}: 3075, 3059, 3044, 1605, 1578, 1560, 1545, 1508, 1491, 1431, 1425, 1312, 1256, 1204, 1161, 1136, 1126, 1042, 1015, 957, 860,

808, 760, 692, 669, 662, 615, 610, 559, 492, 419, 411, 407. The data was consistent with literature findings.[107]

Synthesis of 2-(3-(trifluoromethyl)phenyl)quinoxaline (*L⁴H*)

Prepared similarly from 2-bromo-1-(3-(trifluoromethyl)phenyl)ethan-1-one (3.38 g, 12.6 mmol) and 1,2-phenylenediamine (1.50 g, 13.9 mmol) to give the product as an off-white solid (383 mg, 11.1%). ^{1}H NMR (500 MHz, CDCl$_3$) δ_H = 9.36 (s, 1H), 8.52 (s, 1H), 8.39 (d, $^3J_{HH}$ = 7.9 Hz, 1H), 8.22 – 8.14 (m, 2H), 7.86 – 7.76 (m, 3H), 7.71 (*app.* t, $^3J_{HH}$ = 7.7 Hz, 1H) ppm. ^{19}F{^{1}H} NMR (376 MHz, CDCl$_3$) δ_F = −62.65 (s) ppm. UV−vis (CHCl$_3$) λ_{max} ($\varepsilon \times 10^4$ / L mol^{-1} cm^{-1}): 260 (3.2), 333 (1.1) nm. FTIR (solid, cm^{-1}) (ATR) v_{max}: 1614, 1547, 1483, 1339, 1323, 1308, 1279, 1263, 1231, 1223, 1209, 1159, 1140, 1130, 1111, 1097, 1076, 1057, 1013, 961, 935, 918, 885, 876, 810, 795, 764, 706, 691, 652, 611, 561, 548, 419. The data was consistent with literature findings.[59]

Synthesis of 2-(4-(trifluoromethyl)phenyl)quinoxaline (*L⁵H*)

Prepared similarly from 2-bromo-1-(4-(trifluoromethyl)phenyl)ethan-1-one (3.11 g, 11.6 mmol) and 1,2-phenylenediamine (1.38 g, 12.8 mmol) to give the product as pale yellow crystals (786 mg, 24.6%). ^{1}H NMR (500 MHz, CDCl$_3$) δ_H = 9.35 (s, 1H), 8.33 (d, $^3J_{HH}$ = 8.1 Hz, 2H), 8.20 – 8.13 (m, 2H), 7.83 (d, $^3J_{HH}$ = 8.2 Hz, 2H), 7.85 – 7.78 (m, 2H) ppm. ^{19}F{^{1}H} NMR (376 MHz, CDCl$_3$) δ_F = −62.74 (s) ppm. UV−vis (CHCl$_3$) λ_{max} ($\varepsilon \times 10^4$ / L mol^{-1} cm^{-1}): 261 (3.4), 333 (1.2) nm. FTIR (solid, cm^{-1}) (ATR) v_{max}: 1609, 1545, 1491, 1431, 1325, 1312, 1229, 1209, 1163, 1123, 1109, 1069, 1045, 1011, 957, 928, 876, 853, 839, 962, 762, 743, 700, 669, 598, 586, 546, 488, 417, 407. The data was consistent with literature findings.[107,108]

Synthesis of 2-(2-(trifluoromethyl)phenyl)quinoxaline (*L⁶H*)

Prepared similarly from 2-bromo-1-(2-(trifluoromethyl)phenyl)ethan-1-one (2.18 g, 8.17 mmol) and 1,2-phenylenediamine (972 mg, 8.98 mmol) to give the product as a yellow oil (907 mg, 40.5%). ^{1}H NMR (500 MHz, CDCl$_3$) δ_H = 8.99 (s, 1H), 8.21 – 8.12 (m, 2H), 7.86 (d, $^3J_{HH}$ = 7.8 Hz, 1H), 7.85 – 7.81 (m, 2H), 7.72 (d, $^3J_{HH}$ = 7.6 Hz, 1H), 7.67 – 7.61 (m, 2H) ppm. ^{19}F{^{1}H} NMR (376 MHz, CDCl$_3$) δ_F = −56.55 (s) ppm. UV−vis (CHCl$_3$) λ_{max} ($\varepsilon \times 10^4$ / L mol^{-1} cm^{-1}): 321 (0.5) nm. FTIR (solid, cm^{-1}) (ATR) v_{max}: 3065, 1605, 1582, 1553, 1487, 1449,

1408, 1364, 1310, 1263, 1167, 1109, 1072, 1034, 959, 930, 883, 872, 800, 760, 700, 648, 613, 598, 567, 554, 438, 424, 405. The data was consistent with literature findings.[109]

3.5.4: Preparation of Inorganic Compounds

General synthetic route to the platinum dimers, $[Pt(L^n)(\mu\text{-Cl})]_2$

Based on a modified literature procedure,[23] K_2PtCl_4 (1.0 – 1.5 eq.) in H_2O (<2 mL) was added to a stirring solution of **L^nH** (1.0 eq.) in glacial acetic acid (~10 mL) under an inert N_2 atmosphere. The solution was heated to 130°C for 3 days.[71] Solids precipitated out of solution upon cooling to room temperature, which were filtered under suction and washed with glacial AcOH (<2 mL) and EtOH (<2 mL) to give the dimeric species as brown or dark red solids (28.4 – 98.3%), which were used in subsequent reactions without further purification or characterisation.

General synthetic route towards $[Pt(L^n)(DMSO)Cl]$

Based on a modified literature procedure,[61] **$[Pt(L^n)(\mu\text{-Cl})]_2$** was dissolved in the minimum amount of DMSO (<5 mL) followed by dropwise addition of a saturated aqueous solution of brine (~10 mL). The mixture was stirred for ~16 h under ambient, aerated conditions and the resultant precipitates were filtered under suction and washed with distilled water (2 × ~10 mL). The adducts formed as brown or orange solids (29.8 – 78.7%) and were used in subsequent steps without further purification.

Synthesis of $[Pt(L^1)(acac)]$ *(Pt-3a)*

Based on a modified literature procedure,[87] **$[Pt(L^1)(DMSO)Cl]$** (45.0 mg, 0.075 mmol) was dissolved in 3-pentanone (5 mL) and sodium acetylacetonate (105 mg, 0.753 mmol) was added and the mixture was stirred at room temperature for 24 h under an inert N_2 atmosphere. The solvent was removed *in vacuo* and dissolved in DCM, where excess insoluble salts were removed by filtration under reduced pressure. The solvent was once again removed *in vacuo* to generate the crude product and was purified by column chromatography (SiO_2, DCM), where the compound eluted as the first yellow band to give the product as an orange solid (22.7 mg, 51.6%).^{1}H NMR (500 MHz, $CDCl_3$) δ_H = 9.73 (s, 1H), 9.59 (ddd, $^3J_{HH}$ = 8.9, $^4J_{HH}$ = 1.2, $^5J_{HH}$ = 0.5 Hz, 1H), 8.13 (dd, $^3J_{HH}$ = 8.3,

$^4J_{HH}$ = 1.5 Hz, 1H), 7.85 (ddd, $^3J_{HH}$ = 8.7, 6.9, $^4J_{HH}$ = 1.6 Hz, 1H), 7.82 – 7.75 (m, $^3J_{H\text{-}Pt}$ = 35.2 Hz, 2H), 7.30 (*app.* t, $^3J_{HH}$ = 7.9 Hz, 1H), 7.12 – 7.08 (m, 1H), 5.61 (s, 1H, acac) 2.09 (overlapping s, 6H) ppm. ^{13}C{^{1}H} NMR (126 MHz, CDCl$_3$) δ_C = 186.3, 184.6, 144.7, 144.3, 143.2, 140.3, 131.3, 130.6, 130.2, 129.4, 128.5, 126.5, 120.5, 116.0, 102.2, 28.4, 27.3 ppm. ^{19}F{^{1}H} NMR (376 MHz, CDCl$_3$) δ_F = −56.46 (s) ppm. HRMS (ES+) found *m/z* 583.0736, calc'd *m/z* 583.0740 for C$_{20}$H$_{16}$F$_3$N$_2$O$_3$^{194}Pt [M + H]$^+$. UV−vis (CHCl$_3$) λ_{max} (ε × 10^4 / L mol^{-1} cm^{-1}): 253 (1.7), 284 (1.1), 361 (0.6), 377 (0.7), 439 (0.3), 482 sh (0.2) nm. FTIR (solid, cm^{-1}) (ATR) v_{max}: 2951, 2922, 2852, 1587, 1571, 1560, 1522, 1432, 1387, 1363, 1340, 1319, 1233, 1197, 1156, 1068, 1048, 963, 782, 761, 653, 642, 621.

Synthesis of [Pt(L^2)(acac)] *(Pt-3b)*

Prepared similarly from **[Pt(L^2)(DMSO)Cl]** (84.1 mg, 0.141 mmol) and sodium acetylacetonate (197 mg, 1.41 mmol) to give the product as dark red crystals (38.9 mg, 47.4%). ^{1}H NMR (500 MHz, CDCl$_3$) δ_H = 9.72 (dd, $^3J_{HH}$ = 8.9, $^4J_{HH}$ = 0.9 Hz, 1H), 9.16 (s, 1H), 8.13 (dd, $^3J_{HH}$ = 8.3, $^4J_{HH}$ = 1.4 Hz, 1H), 7.85 (ddd, $^3J_{HH}$ = 8.7, 6.9, $^4J_{HH}$ = 1.6 Hz, 1H), 7.78 (d, $^3J_{HH}$ = 8.5 Hz, 1H), 7.76 (ddd, $^3J_{HH}$ = 8.2, 6.9 $^4J_{HH}$ = 1.2 Hz, 1H), 7.58 – 7.56 (m, 1H), 7.21 – 7.17 (m, 1H), 5.61 (s, 1H, acac), 2.10 (s, 3H), 2.07(s, 3H) ppm. ^{13}C{^{1}H} NMR (126 MHz, CDCl$_3$) δ_C = 186.0, 184.3, 161.8, 146.6, 144.7, 143.7, 143.3, 141.6, 139.8, 131.7, 131.4, 130.1, 129.6, 126.1, 123.3, 117.8, 102.1, 28.5, 27.3 ppm. ^{19}F{^{1}H} NMR (376 MHz, CDCl$_3$) δ_F = −57.95 (s) ppm. HRMS (ES+) found *m/z* 583.0743, calc'd *m/z* 583.0740 for C$_{20}$H$_{16}$F$_3$N$_2$O$_3$^{194}Pt [M + H]$^+$. UV−vis (CHCl$_3$) λ_{max} (ε × 10^4 / L mol^{-1} cm^{-1}): 254 (4.4), 295 (3.2), 356 (1.4), 373 (1.6), 438 (0.9), 480 sh (0.5) nm. FTIR (solid, cm^{-1}) (ATR) v_{max}: 2953, 2921, 2852, 1561, 1535, 1522, 1459, 1427, 1390, 1366, 1252, 1213, 1161, 1129, 1077, 1025, 993, 948, 937, 906, 887, 863, 816, 796, 762, 727, 660.

Synthesis of [Pt(L^3)(acac)] *(Pt-3c)*

Prepared similarly from **[Pt(L^3)(DMSO)Cl]** (98.7 mg, 0.165 mmol) and sodium acetylacetonate (231 mg, 1.65 mmol) to give the product as bright red crystals (47.8 mg, 49.6%). ^{1}H NMR (500 MHz, CDCl$_3$) δ_H = 9.70 (dd, $^3J_{HH}$ = 8.8, $^4J_{HH}$ = 0.8 Hz, 1H), 9.13 (s, 1H), 8.09 (dd, $^3J_{HH}$ = 8.2, $^4J_{HH}$ = 1.3 Hz, 1H), 7.82 (ddd, $^3J_{HH}$ = 8.7, 6.9, $^4J_{HH}$ = 1.6 Hz, 1H), 7.73 (ddd, $^3J_{HH}$ = 8.2, 6.9, $^4J_{HH}$ = 1.3 Hz, 1H), 7.72 (d, $^3J_{HH}$ = 8.6 Hz, 1H), 7.57 − 7.50 (m, $^3J_{H\text{-}Pt}$ = 34.6 Hz, 1H), 7.06 − 7.02

(m, 1H), 5.59 (s, 1H, acac), 2.09 (s, 3H), 2.07 (s, 3H) ppm. ^{13}C{^{1}H} NMR (126 MHz, CDCl$_3$) δ_C = 186.0, 184.4, 161.9, 144.4, 143.4, 143.3, 142.1, 141.9, 131.7, 129.8, 129.6, 126.5, 125.9, 121.2, 116.1, 102.2, 28.4, 27.3 ppm. ^{19}F{^{1}H} NMR (376 MHz, CDCl$_3$) δ_F = −56.93 (s) ppm. HRMS (ES+) found m/z 583.0738, calc'd m/z 583.0740 for C$_{20}$H$_{16}$F$_3$N$_2$O$_3$^{194}Pt [M + H]$^+$. UV−vis (CHCl$_3$) λ_{max} ($\varepsilon \times 10^4$ / L mol^{-1} cm^{-1}): 252 (2.9), 296 (2.3), 358 (0.9), 374 (1.1), 433 (0.6), 473 sh (0.4) nm. FTIR (solid, cm^{-1}) (ATR) v_{max}: 2953, 2921, 2852, 1580, 1561, 1537, 1511, 1459, 1381, 1338, 1254, 1211, 1155, 1137, 1075, 1042, 1029, 1017, 898, 816, 770, 676.

Synthesis of [Pt(L^4)(acac)] *(Pt-3d)*

Prepared similarly from **[Pt(L^4)(DMSO)Cl]** (57.9 mg, 0.100 mmol) and sodium acetylacetonate (139 mg, 0.995 mmol). The product was further purified by recrystallisation from DCM and Et$_2$O, where the solid was filtered under suction to give the pure product as a red solid (13.6 mg, 24.1%). ^{1}H NMR (500 MHz, CDCl$_3$) δ_H = 9.73 (ddd, $^3J_{HH}$ = 8.9, $^4J_{HH}$ = 1.3, $^5J_{HH}$ = 0.5 Hz, 1H), 9.24 (s, 1H), 8.14 (dd, $^3J_{HH}$ = 8.2, $^4J_{HH}$ = 1.3 Hz, 1H), 7.93 – 7.91 (m, 1H), 7.88 (d, $^3J_{HH}$ = 8.1 Hz, 1H), 7.85 (ddd, $^3J_{HH}$ = 8.6, 6.9, $^4J_{HH}$ = 1.6 Hz, 1H), 7.77 (ddd, $^3J_{HH}$ = 8.2, 6.9, $^4J_{HH}$ = 1.3 Hz, 1H), 7.50 – 7.45 (m, 1H), 5.62 (s, 1H, acac), 2.11 (s, 3H), 2.09 (s, 3H) ppm. ^{13}C{^{1}H} NMR (126 MHz, CDCl$_3$) δ_C = 186.2, 184.5, 144.1, 143.8, 141.6, 131.8, 130.7, 130.1, 129.7, 126.4, 126.1, 124.0, 102.2, 28.4, 27.3 ppm. ^{19}F{^{1}H} NMR (376 MHz, CDCl$_3$) δ_F = −62.23 (s) ppm. HRMS (ES+) found m/z 568.0814, calc'd m/z 568.0812 for C$_{20}$H$_{16}$F$_3$N$_2$O$_2$^{195}Pt [M + H]$^+$. UV−vis (CHCl$_3$) λ_{max} ($\varepsilon \times 10^4$ / L mol^{-1} cm^{-1}): 260 (4.3), 293 (3.0), 355 (1.3), 372 (1.5), 437 (0.8), 468 sh (0.5) nm. FTIR (solid, cm^{-1}) (ATR) v_{max}: 1572, 1561, 1536, 1522, 1459, 1433, 1390, 1362, 1332, 1314, 1295, 1278, 1258, 1209, 1170, 1142, 1135, 1109, 1083, 1073, 1025, 982, 900, 837, 805, 773, 760, 732, 714, 680.

Synthesis of [Pt(L^5)(acac)] *(Pt-3e)*

Prepared similarly from **[Pt(L^5)(DMSO)Cl]** (64.0 mg, 0.110 mmol) and sodium acetylacetonate (154 mg, 1.10 mmol). The product was further purified by recrystallisation from DCM and Et$_2$O, where the solid was filtered under suction to give the pure product as a red solid (38.7 mg, 62.0%). ^{1}H NMR (500 MHz, CDCl$_3$) δ_H = 9.74 (dd, $^3J_{HH}$ = 8.9, $^4J_{HH}$ = 1.1 Hz, 1H), 9.22 (s, 1H), 8.13 (dd, $^3J_{HH}$ = 8.2, $^4J_{HH}$ = 1.5 Hz, 1H), 8.03 – 7.94 (m, $^3J_{H\text{-}Pt}$ = 31.0 Hz, 1H), 7.85 (ddd, $^3J_{HH}$

= 8.8, 6.9, $^4J_{HH}$ = 1.6 Hz, 1H), 7.80 – 7.75 (m, 2H), 7.44 – 7.40 (m, 1H), 5.60 (s, 1H, acac), 2.10 (s, 3H), 2.08 (s, 3H) ppm. ^{13}C{^{1}H} NMR (126 MHz, CDCl$_3$) δ_C = 186.1, 184.6, 144.0, 143.4, 141.9, 131.8, 130.3, 129.7, 126.6, 126.2, 124.9, 120.9, 102.2, 28.4, 27.3 ppm. ^{19}F{^{1}H} NMR (376 MHz, CDCl$_3$) δ_F = −63.01 ppm. HRMS (ES+) found m/z 568.0814, calc'd m/z 568.0812 for C$_{20}$H$_{16}$F$_3$N$_2$O$_2$^{195}Pt [M + H]$^+$. UV−vis (CHCl$_3$) λ_{max} ($\varepsilon \times 10^4$ / L mol^{-1} cm^{-1}): 255 (3.1), 297 (2.0), 355 (1.0), 372 (1.1), 442 (0.5), 475 sh (0.3) nm. FTIR (solid, cm^{-1}) (ATR) v_{max}: 1578, 1561, 1542, 1520, 1476, 1461, 1392, 1319, 1276, 1258, 1163, 1153, 1138, 1131, 1112, 1075, 1032, 1017, 911, 820, 775, 760, 714, 671.

General procedure for the synthesis of [(Ir(L^n)$_2$(μ-Cl))$_2$] [110]

IrCl$_3$.xH$_2$O (1.0 eq.) and **L^{n}H** (>2.0 eq.) were dissolved in 2-methoxyethanol and distilled water (3:1, ~20 mL) and the mixture was heated to reflux under an inert N$_2$ atmosphere whilst stirring for 48 h. The reaction mixture was cooled to room temperature, where the crude product precipitated out of solution upon addition of distilled water (~ 30 mL). Solids were removed by filtration under reduced pressure and were washed with water (>10 mL). The crude products were dissolved in dichloromethane and filtered under suction to remove any insoluble side-products. Solvent was removed from the filtrate *in vacuo* to give the products as brown solids (79.2 – 89.9%), which were used in subsequent steps without further purification or characterisation.

Synthesis of [Ir(L^1)$_2$(bpy)][PF$_6$] *(Ir-3a)*

A solution of **[(Ir(L^1)$_2$(μ-Cl))$_2$]** (110 mg, 0.074 mmol) and 2,2'-bipyridine (25.3 mg, 0.162 mmol) in chloroform (10mL) was heated to reflux for 24 h under an inert N$_2$ atmosphere. The reaction mixture was cooled to room temperature and the solvent was removed *in vacuo*. The crude solid was then purified by column chromatography (SiO$_2$), where impurities were initially removed using acetone as the mobile phase, followed by elution of the product as a red band using a solvent mixture of MeCN:H$_2$O:KNO$_3$ (aq. sat.) (14:2:1). The solvent was removed *in vacuo* and the product was left to dry in a heated oven at ~60°C for 16 h to remove any traces of water. The product was dissolved in dichloromethane, and the insoluble salts were filtered off under suction. The solvent was once again removed *in vacuo* and the sample was dissolved in acetonitrile (10 mL), where a saturated aqueous solution of NH$_4$PF$_6$ was added

and the solution was stirred for 15 min to ensure that all of the complex existed purely as a PF_6 salt. The solvent was removed *in vacuo* and then filtered under suction, washing successively with distilled water to remove excess insoluble inorganic salts once again. The crude product was recrystallised from dichloromethane and diethyl ether to give the pure product as a dark red solid (35.3 mg, 22.3%). ^{1}H NMR (500 MHz, CDCl$_3$) δ_H = 10.06 (s, 2H), 8.39 (d, $^3J_{HH}$ = 8.1 Hz, 2H), 8.12 – 8.03 (m, 6H), 7.66 (ddd, $^3J_{HH}$ = 8.2, 6.9, $^4J_{HH}$ = 1.2 Hz, 2H), 7.50 (ddd, $^3J_{HH}$ = 8.2, 6.8, $^4J_{HH}$ = 1.3 Hz, 2H), 7.24 – 7.12 (m, 4H), 7.11 (dd, $^3J_{HH}$ = 8.9, $^4J_{HH}$ = 1.4 Hz, 2H), 6.94 (*app.* t, $^3J_{HH}$ = 7.9 Hz, 2H), 6.40 (dd, $^3J_{HH}$ = 7.7, $^4J_{HH}$ = 1.0 Hz, 2H) ppm. ^{13}C{^{1}H} NMR (126 MHz, CDCl$_3$) δ_C = 159.1, 155.7, 154.0, 148.7, 148.6, 147.1, 145.2, 142.2, 141.5, 141.0, 135.3, 134.6, 133.0, 132.9, 132.8, 131.4, 131.0, 128.5, 126.3, 123.7 ppm. ^{19}F{^{1}H} NMR (376 MHz, CDCl$_3$) δ_F = –56.50 (s), –72.91 (d, $^1J_{PF}$ = 712.6 Hz) ppm. UV−vis (CHCl$_3$) λ_{max} ($\varepsilon \times 10^4$ / L mol^{-1} cm^{-1}): 288 (3.1), 323 (1.8), 460 (0.4), 499 sh (0.3) nm. HRMS (ES+) found *m/z* 927.1494, calc'd *m/z* 927.1494 for C$_{40}$H$_{24}$F$_6$^{193}IrN$_6$O$_2$ [M − PF$_6$]$^+$. FTIR (solid, cm^{-1}) (ATR) ν_{max}: 1585, 1528, 1491, 1468, 1447, 1431, 1242, 1198, 1163, 1045, 835, 760, 735, 650, 635, 555.

Synthesis of [Ir(L^2)$_2$(bpy)][PF$_6$] *(Ir-3b)*

Prepared similarly from **[(Ir(L^2)$_2$(μ-Cl))$_2$]** (69.6 mg, 0.043 mmol) and 2,2'-bipyridine (14.8 mg, 0.095 mmol), where the product formed as a dark orange solid (16.5 mg, 17.8%). ^{1}H NMR (500 MHz, CD$_3$CN) δ_H = 9.63 (s, 2H), 8.26 – 8.22 (m, 2H), 8.13 (d, $^3J_{HH}$ = 8.1 Hz, 2H), 8.05 – 8.02 (m, 4H), 7.98 – 7.94 (m, 2H), 7.62 (ddd, $^3J_{HH}$ = 8.3, 6.9, $^4J_{HH}$ = 1.2 Hz, 2H), 7.51 – 7.47 (m, 4H), 7.16 (ddd, $^3J_{HH}$ = 8.6, 7.0, $^4J_{HH}$ = 1.5 Hz, 2H), 7.05 (ddd, $^3J_{HH}$ = 8.9, $^4J_{HH}$ = 1.3, $^5J_{HF}$ = 0.4 Hz, 2H), 6.55 (d, $^3J_{HH}$ = 8.4 Hz, 2H) ppm. ^{19}F{^{1}H} NMR (376 MHz, CDCl$_3$) δ_F = –57.78 (s), –72.81 (d, $^1J_{PF}$ = 719.7 Hz) ppm. UV−vis (CHCl$_3$) λ_{max} ($\varepsilon \times 10^4$ / L mol^{-1} cm^{-1}): 285 (2.5), 361 (1.4), 461 (0.3), 500 sh (0.2) nm. FTIR (solid, cm^{-1}) (ATR) ν_{max}: 1535, 1472, 1447, 1258, 1213, 1157, 1086, 1013, 837, 795, 764, 691, 635, 557.

Synthesis of [Ir(L^3)$_2$(bpy)][PF$_6$] *(Ir-3c)*

Prepared similarly from **[(Ir(L^3)$_2$(μ-Cl))$_2$]** (129 mg, 0.086 mmol) and 2,2'-bipyridine (29.6 mg, 0.190 mmol), but in 2-ethoxyethanol. The product formed as a bright orange solid (35.2 mg, 19.0%). ^{1}H NMR (500 MHz, CDCl$_3$) δ_H = 9.54

(s, 2H), 8.25 – 8.21 (m, 2H), 8.13 – 8.09 (m, 4H), 7.95 – 7.91 (m, 2H), 7.66 (ddd, $^3J_{HH}$ = 8.1, 6.9, $^4J_{HH}$ = 1.3 Hz, 2H), 7.53 – 7.46 (m, 2H), 7.23 – 7.15 (m, 2H), 7.12 (dd, $^3J_{HH}$ = 8.8, $^4J_{HH}$ = 1.2 Hz, 2H), 6.99 – 6.96 (m, 2H) ppm. ^{13}C{^{1}H} NMR (126 MHz, CDCl$_3$) δ_C = 162.0, 155.9, 153.5, 153.4, 151.4, 147.9, 142.6, 142.6, 141.3, 141.3, 140.7, 133.0, 131.4, 130.9, 129.4, 128.8, 126.0, 124.9, 122.9, 115.7 ppm. ^{19}F{^{1}H} NMR (376 MHz, CDCl$_3$) δ_F = −57.37 (s), −72.44 (d, $^1J_{PF}$ = 713.2 Hz) ppm. UV−vis (CHCl$_3$) λ_{max} (ε × 10^4 / L mol^{-1} cm^{-1}): 289 (5.3), 363 (2.8), 468 (0.7), 502 sh (0.4) nm. HRMS (ES+) found m/z 927.1499, calc'd m/z 927.1494 for C$_{40}$H$_{24}$F$_6$^{193}IrN$_6$O$_2$ [M − PF$_6$]$^+$. FTIR (solid, cm^{-1}) (ATR) v_{max}: 1585, 1531, 1472, 1445, 1242, 1215, 1159, 1132, 1073, 1038, 835, 760, 735, 650, 637, 555.

3.6: References

1   J. Zhou, Y. Kang, L. Chen, H. Wang, J. Liu, S. Zeng and L. Yu, *Front. Pharmacol.*, 2020, **11**, 343.

2   M. Mauro, A. Aliprandi, D. Septiadi, N. S. Kehr and L. De Cola, *Chem. Soc. Rev.*, 2014, **43**, 4144–4166.

3   C. M. Che, S. C. Chan, H. F. Xiang, M. C. W. Chan, Y. Liu and Y. Wang, *Chem. Commun.*, 2004, **4**, 1484–1485.

4   I. R. Laskar, S. F. Hsu and T. M. Chen, *Polyhedron*, 2005, **24**, 881–888.

5   H. Li, J. Ding, Z. Xie, Y. Cheng and L. Wang, *J. Organomet. Chem.*, 2009, **694**, 2777–2785.

6   Z. Li, Y. Han, Z. Gao and F. Wang, *ACS Catal.*, 2017, **7**, 4676–4681.

7   N. M. Shavaleev, H. Adams, J. Best, R. Edge, S. Navaratnam and J. A. Weinstein, *Inorg. Chem.*, 2006, **45**, 9410–9415.

8   V. W. W. Yam, K. H. Y. Chan, K. M. C. Wong and N. Zhu, *Eur. J. Chem.*, 2005, **11**, 4535–4543.

9   Q. Wan, J. Yang, W.-P. To and C.-M. Che, *Proc. Natl. Acad. Sci. U.S.A.*, 2021, **118**, e2019265118.

10   B. Ma, J. Li, P. I. Djurovich, M. Yousufuddin, R. Bau and M. E. Thompson, *J. Am. Chem. Soc.*, 2005, **127**, 28–29.

11   Y. Zhu, K. Luo, L. Zhao, H. Ni and Q. Li, *Dyes Pigments*, 2017, **145**, 144–151.

12   J. Brooks, Y. Babayan, S. Lamansky, P. I. Djurovich, I. Tsyba, R. Bau and M. E. Thompson, *Inorg. Chem.*, 2002, **41**, 3055–3066.

13   H. Tsujimoto, S. Yagi, Y. Honda, H. Terao, T. Maeda, H. Nakazumi and Y. Sakurai, *J. Lumin.*, 2010, **130**, 217–221.

14   S. J. Farley, D. L. Rochester, A. L. Thompson, J. A. K. Howard and J. A. G. Williams, *Inorg. Chem.*, 2005, **44**, 9690–9703.

15   J. Liu, C. J. Yang, Q. Y. Cao, M. Xu, J. Wang, H. N. Peng, W. F. Tan, X. X. Lü and X. C. Gao, *Inorganica Chim. Acta*, 2009, **362**, 575–579.

16   A. Tronnier, N. Nischan, S. Metz, G. Wagenblast, I. Münster and T. Strassner, *Eur. J. Inorg. Chem.*, 2014, **2014**, 256–264.

17   Y. Xing, L. Wang, C. Liu and X. Jin, *Sens. Actuators B: Chem.*, 2020, **304**, 127378.

18   Y. Xing, C. Liu, J. H. Xiu and J. Y. Li, *Inorg. Chem.*, 2015, **54**, 7783–7790.

19   C. Liu, X. Song, Z. Wang and J. Qiu, *Chempluschem*, 2014, **79**, 1472–1481.

20   A. S. Ionkin, W. J. Marshall and Y. Wang, *Organometallics*, 2005, **24**, 619–627.

21   H. S. El–Beshti, Y. Yildizhan, H. Kayi, Y. Cetin, Z. Adigüzel, G. Gungor-Topcu, Z. Gercek and Ş. Özalp-Yaman, *J. Mol. Struct.*, 2022, **1250**, 131928.

22   K. Choroba, B. Machura, A. Szlapa-Kula, J. G. Malecki, L. Raposo, C. Roma-Rodrigues, S. Cordeiro, P. V. Baptista and A. R. Fernandes, *Eur. J. Med. Chem.*, 2021, **218**, 113404.

23   S. Culham, P. H. Lanoë, V. L. Whittle, M. C. Durrant, J. A. G. Williams and V. N. Kozhevnikov, *Inorg. Chem.*, 2013, **52**, 10992–11003.

24   J. Chen and J. X. Zhao, *Sensors (Basel)*, 2012, **12**, 2414.

25   A. Ghazy, M. Safdar, M. Lastusaari, H. Savin and M. Karppinen, *Sol. Energy Mater. Sol. Cells*, 2021, **230**, 111234.

26   J. C. Goldschmidt, S. Fischer, J. C. Goldschmidt and S. Fischer, *Adv. Opt. Mater.*, 2015, **3**, 510–535.

27   L. Huang, W. Wu, Y. Li, K. Huang, L. Zeng, W. Lin and G. Han, *J. Am. Chem. Soc.*, 2020, **142**, 18460–18470.

28   T. N. Singh-Rachford and F. N. Castellano, *Coord. Chem. Rev.*, 2010, **254**, 2560–2573.

29   W. Wu, J. Zhao, H. Guo, J. Sun, S. Ji and Z. Wang, *Eur. J. Chem.*, 2012, **18**, 1961–1968.

30   T. N. Singh-Rachford and F. N. Castellano, *J. Phys. Chem. Lett.*, 2010, **1**, 195–200.

31   W. Wu, D. Huang, X. Yi and J. Zhao, *Dyes Pigments*, 2013, **96**, 220–231.

32   W. Wu, J. Sun, S. Ji, W. Wu, J. Zhao and H. Guo, *Dalton Trans.*, 2011, **40**, 11550–11561.

33   K. Chen, M. Hussain, S. S. Razi, Y. Hou, E. A. Yildiz, J. Zhao, H. G. Yaglioglu and M. Di Donato, *Inorg. Chem.*, 2020, **59**, 14731–14745.

34   T. M. Cooper, D. M. Krein, A. R. Burke, D. G. McLean, J. E. Haley, J. Slagle, J. Monahan and A. Fratini, *J. Phys. Chem. A*, 2012, **116**, 139–149.

35   S. Gharaati, C. Wang, C. Förster, F. Weigert, U. Resch-Genger and K. Heinze, *Eur. J. Chem.*, 2020, **26**, 1003–1007.

36   J. Sun, W. Wu and J. Zhao, *Eur. J. Chem.*, 2012, **18**, 8100–8112.

37   X. Yi, J. Zhao, W. Wu, D. Huang, S. Ji and J. Sun, *Dalton Trans.*, 2012, **41**, 8931–8940.

38   T. N. Singh-Rachford and F. N. Castellano, *Coord. Chem. Rev.*, 2010, **254**, 2560–2573.

39   K. Okumura, K. Mase, N. Yanai and N. Kimizuka, *Eur. J. Chem.*, 2016, **22**, 7721–7726.

40   Y. Y. Cheng, B. Fückel, T. Khoury, R. G. C. R. Clady, M. J. Y. Tayebjee, N. J. Ekins-Daukes, M. J. Crossley and T. W. Schmidt, *J. Phys. Chem. Lett.*, 2010, **1**, 1795–1799.

41   G. Massaro, J. Hernando, D. Ruiz-Molina, C. Roscini and L. Latterini, *Chem. Mater.*, 2016, **28**, 738–745.

42   T. N. Singh-Rachford, A. Haefele, R. Ziessel and F. N. Castellano, *J. Am. Chem. Soc.*, 2008, **130**, 16164–16165.

43   L. Xing, T. Honda, L. Fitz and I. Ojima, in *Fluorine in Life Sciences: Pharmaceuticals, Medicinal Diagnostics, and Agrochemicals Progress in Fluorine Science Series*, Academic Press, 2019, pp. 181–211.

44   M. Schlosser, *Angew. Chem. Int. Ed.*, 2006, **45**, 5432–5446.

45   D. A. Nagib and D. W. C. Macmillan, *Nature 2011 480:7376*, 2011, **480**, 224–228.

46   A. Tlili, F. Toulgoat and T. Billard, *Angew. Chem. Int. Ed.*, 2016, **55**, 11726–11735.

47   D. Gimenez, A. Phelan, C. D. Murphy and S. L. Cobb, *Beilstein J. Org. Chem.*, 2021, **17**, 293.

48   F. R. Leroux, B. Manteau, J. P. Vors and S. Pazenok, *Beilstein J. Org. Chem.*, 2008, **4**, 13.

49   D. Federsel, A. Herrmann, D. Christen, S. Sander, H. Willner and H. Oberhammer, *J. Mol. Struct.*, 2001, **567–568**, 127–136.

50   Y. Xing, C. Liu, X. Song and J. Li, *J. Mater. Chem. C*, 2015, **3**, 2166–2174.

51   N. M. Shavaleev, F. Monti, R. Scopelliti, N. Armaroli, M. Grätzel and M. K. Nazeeruddin, *Organometallics*, 2012, **31**, 6288–6296.

52   S. A. Fitzgerald, X. Xiao, J. Zhao, P. N. Horton, S. J. Coles, R. C. Knighton, B. D. Ward and S. J. A. Pope, *Eur. J. Chem.*, 2022, e202203241.

53   S. A. Fitzgerald, H. Y. Otaif, C. E. Elgar, N. Sawicka, P. N. Horton, S. J. Coles, J. M. Beames and S. J. A. Pope, *Inorg. Chem.*, 2021, **60**, 15467–15484.

54   Q. W. Zhang and J. F. Hartwig, *Chem. Commun.*, 2018, **54**, 10124–10127.

55   W. Q. Xu, X. H. Xu and F. L. Qing, *Chin. J. Chem.*, 2020, **38**, 847–854.

56   A. Abula, Z. Xu, Z. Zhu, C. Peng, Z. Chen, W. Zhu and H. A. Aisa, *J. Chem. Inf. Model.*, 2020, **60**, 6242–6250.

57   A. Adamczyk-Woźniak, J. T. Gozdalik, E. Kaczorowska, K. Durka, D. Wieczorek, D. Zarzeczańska and A. Sporzyński, *Molecules*, 2021, **26**, 2007.

58   T. Schaefer, G. H. Penner, R. Sebastian, J. Peeling and C. Beaulieu, *Can. J. Chem.*, 1991, **69**, 1047–1053.

59   Z. Dong, G. C. Clososki, S. H. Wunderlich, A. Unsinn, J. Li and P. Knochel, *Eur. J. Chem.*, 2009, **15**, 457–468.

60   W. R. Dolbier, in *Guide to Fluorine NMR for Organic Chemists*, John Wiley & Sons, Ltd, 2016, pp. 187–235.

61   N. Godbert, T. Pugliese, I. Aiello, A. Bellusci, A. Crispini and M. Ghedini, *Eur. J. Chem.*, 2007, **2007**, 5105–5111.

62   J. T. Gozdalik, P. H. Marek, I. D. Madura, B. Gierczyk, Ł. Popenda, G. Schroeder, A. Adamczyk-Woźniak and A. Sporzyński, *J. Mol. Struct.*, 2019, **1180**, 237–243.

63   K. N. Lee, J. W. Lee and M. Y. Ngai, *Synlett*, 2016, **27**, 313.

64   N. J. DeWeerd, E. V. Bukovsky, K. P. Castro, I. V. Kuvychko, A. A. Popov, S. H. Strauss and O. V. Boltalina, *J. Fluor. Chem.*, 2019, **221**, 1–7.

65   M. Nonoyama, *Bull. Chem. Soc. Jpn.*, 1974, **47**, 767–768.

66   Y. M. Jing, F. Z. Wang, Y. X. Zheng and J. L. Zuo, *J. Mater. Chem. C*, 2017, **5**, 3714–3724.

67   S. K. Kurapati and S. Pal, *Dalton Trans.*, 2015, **44**, 2401–2408.

68   S. A. De Pascali, P. Papadia, A. Ciccarese, C. Pacifico and F. P. Fanizzi, *Eur. J. Inorg. Chem.*, 2005, **2005**, 788–796.

69   B. M. Still, P. G. A. Kumar, J. R. Aldrich-Wright and W. S. Price, *Chem. Soc. Rev.*, 2007, **36**, 665–686.

70   M. Ghedini, D. Pucci, A. Crispini and G. Barberio, *Organometallics*, 1999, **18**, 2116–2124.

71   I. R. Laskar, S. F. Hsu and T. M. Chen, *Polyhedron*, 2005, **24**, 881–888.

72   J. Y. Cho, B. Domercq, S. Barlow, K. Y. Suponitsky, J. Li, T. v. Timofeeva, S. C. Jones, L. E. Hayden, A. Kimyonok, C. R. South, M. Weck, B. Kippelen and S. R. Marder, *Organometallics*, 2007, **26**, 4816–4829.

73   C. A. Wilkie and D. T. Harworth, *J. Inorg. Nucl. Chem.*, 1978, **40**, 195–197.

74   C. Liu, X. Song, Z. Wang and J. Qiu, *Chempluschem*, 2014, **79**, 1472–1481.

75   D. Gimenez, A. Phelan, C. D. Murphy and S. L. Cobb, *Beilstein J. Org. Chem.*, 2021, **17**, 293.

76   David. R. Lide, *CRC Handbook of Chemistry and Physics*, CRC Press, Boca Raton, FL, 86 edn., 2005.

77   M. K. Raza, K. Mitra, A. Shettar, U. Basu, P. Kondaiah and A. R. Chakravarty, *Dalton Trans.*, 2016, **45**, 13234–13243.

78   M. A. A. Beg and H. C. Clark, *Can. J. Chem.*, 1962, **40**, 393–398.

79   J. D. Brown, R. C. Dobbie and B. P. Straughan, *J. Chem. Soc., Dalton Trans.*, 1973, 1691–1694.

80   O. J. Stacey, J. A. Platts, S. J. Coles, P. N. Horton and S. J. A. Pope, *Inorg. Chem.*, 2015, **54**, 6528–6536.

81   M. Velusamy, C. H. Chen, Y. S. Wen, J. T. Lin, C. C. Lin, C. H. Lai and P. T. Chou, *Organometallics*, 2010, **29**, 3912–3921.

82   H. Li, W. Yuan, X. Wang, H. Zhan, Z. Xie and Y. Cheng, *J. Mater. Chem. C*, 2015, **3**, 2744–2750.

83   A. Bossi, A. F. Rausch, M. J. Leitl, R. Czerwieniec, M. T. Whited, P. I. Djurovich, H. Yersin and M. E. Thompson, *Inorg. Chem.*, 2013, **52**, 12403–12415.

84   H. J. Böhm, D. Banner, S. Bendels, M. Kansy, B. Kuhn, K. Müller, U. Obst-Sander and M. Stahl, *ChemBioChem*, 2004, **5**, 637–643.

85   W. H. Melhuish, *J. Phys. Chem.*, 1961, **65**, 229–235.

86   J. C. H. Chan, W. H. Lam, H. L. Wong, N. Zhu, W. T. Wong and V. W. W. Yam, *J. Am. Chem. Soc.*, 2011, **133**, 12690–12705.

87   D. N. Kozhevnikov, V. N. Kozhevnikov, M. M. Ustinova, A. Santoro, D. W. Bruce, B. Koenig, R. Czerwieniec, T. Fischer, M. Zabel and H. Yersin, *Inorg. Chem.*, 2009, **48**, 4179–4189.

88　S. Develay, O. Blackburn, A. L. Thompson and J. A. G. Williams, *Inorg. Chem.*, 2008, **47**, 11129–11142.

89　K. Suzuki, A. Kobayashi, S. Kaneko, K. Takehira, T. Yoshihara, H. Ishida, Y. Shiina, S. Oishi and S. Tobita, *Phys. Chem. Chem. Phys.*, 2009, **11**, 9850–9860.

90　D. Ashen-Garry and M. Selke, *Photochem. Photobiol.*, 2014, **90**, 257–274.

91　P. I. Djurovich, D. Murphy, M. E. Thompson, B. Hernandez, R. Gao, P. L. Hunt and M. Selke, *Dalton Trans.*, 2007, 3763–3770.

92　P. Pinter, J. Soellner, T. Strassner, P. Pinter, J. Soellner and T. Strassner, *Eur. J. Inorg. Chem.*, 2021, **2021**, 3104–3107.

93　L. Zhang, L. Tian, M. Li, R. He and W. Shen, *Dalton Trans.*, 2014, **43**, 6500–6512.

94　P. Du and R. Eisenberg, *Chem. Sci.*, 2010, **1**, 502.

95　G. R. Fulmer, A. J. M. Miller, N. H. Sherden, H. E. Gottlieb, A. Nudelman, B. M. Stoltz, J. E. Bercaw and K. I. Goldberg, *Organometallics*, 2010, **29**, 2176–2179.

96　S. J. Coles and P. A. Gale, *Chem. Sci.*, 2012, **3**, 683–689.

97　O. V. Dolomanov, L. J. Bourhis, R. J. Gildea, J. A. K. Howard and H. Puschmann, *J. Appl. Crystallogr.*, 2009, **42**, 339–341.

98　G. M. Sheldrick, *Acta Crystallogr. A*, 2015, **71**, 3–8.

99　G. M. Sheldrick, *Acta Crystallogr. C*, 2015, **71**, 3–8.

100　R. G. Charles, *Org. Synth.*, 1959, **39**, 61.

101　S. Mikami, S. Nakamura, T. Ashizawa, I. Nomura, M. Kawasaki, S. Sasaki, H. Oki, H. Kokubo, I. D. Hoffman, H. Zou, N. Uchiyama, K. Nakashima, N. Kamiguchi, H. Imada, N. Suzuki, H. Iwashita and T. Taniguchi, *J. Med. Chem.*, 2017, **60**, 7677–7702.

102　S. A. May, M. D. Johnson, T. M. Braden, J. R. Calvin, B. D. Haeberle, A. R. Jines, R. D. Miller, E. F. Plocharczyk, G. A. Rener, R. N. Richey, C. R. Schmid, R. K. Vaid and H. Yu, *Org. Process Res. Dev.*, 2012, **16**, 982–1002.

103　E. Bellale, M. Naik, V. Vb, A. Ambady, A. Narayan, S. Ravishankar, V. Ramachandran, P. Kaur, R. McLaughlin, J. Whiteaker, S. Morayya, S. Guptha, S. Sharma, A. Raichurkar, D. Awasthy, V. Achar, P. Vachaspati, B. Bandodkar, M. Panda and M. Chatterji, *J. Med. Chem.*, 2014, **57**, 6572–6582.

104   Y. Nishio, K. Yubata, Y. Wakai, K. Notsu, K. Yamamoto, H. Fujiwara and H. Matsubara, *Tetrahedron*, 2019, **75**, 1398–1405.

105   Z. W. Chen, D. N. Ye, M. Ye, Z. G. Zhou, S. H. Li and L. X. Liu, *Tetrahedron Lett.*, 2014, **55**, 1373–1375.

106   K. Lafleur, J. Dong, D. Huang, A. Caflisch and C. Nevado, *J. Med. Chem.*, 2013, **56**, 84–96.

107   X. T. Wang, J. L. Song, M. Zhong, H. J. Kang, H. Xie, T. Che, B. Shu, D. Peng, L. Zhang and S. S. Zhang, *Eur. J. Org. Chem.*, 2020, **2020**, 3635–3639.

108   K. B. Harsha, S. Rangappa, H. D. Preetham, T. R. Swaroop, M. Gilandoust, K. S. Rakesh and K. S. Rangappa, *ChemistrySelect*, 2018, **3**, 5228–5232.

109   K. M. Liu, L. Y. Liao and X. F. Duan, *Chem. Commun.*, 2014, **51**, 1124–1127.

110   M. Nonoyama, *Bull. Chem. Soc. Jpn.*, 1974, **47**, 767–768.

Chapter 4: Thiophene-Quinoxaline Chromophores as Cyclometallating Ligands for Deep Red Emissive Ir(III) Complexes

Chapter 4

4.1: Introduction

In previous chapters, 2-phenylquinoxaline ligands were studied to successfully tune the photophysical and optical properties of the subsequent organometallic complexes. This chapter explores the resultant features of *bis*-cyclometallated Ir(III) complexes when the carbon-metal bond is formed on a thiophene ring.

4.1.1: Thiophene-Based Organic Chromophores

Thiophenes are 5-membered aromatic heterocycles with a resonance energy (121 kJ mol^{-1}) comparable to that of benzene (138 – 151 kJ mol^{-1}).[1] As a result of this pronounced aromatic character, thiophenes have gained vast amounts of interest as D-π-A type organic dyes; both as electron-donating groups,[2] and as π-spacers in such systems.[3] The slight reduction in resonance energy offers its own advantages such as a reduced energy of charge-transfer mechanisms, which is advantageous for the generation of photoactive devices and materials.[4]

Chemical stability, high polarisability and excellent charge-transporting capability are some of the desirable properties that allow thiophenes to be explored in various areas of research. Such areas include the use of thiophenes as conductive backbones for photoactive organic polymers and oligomers.[5] Reports have indicated that significant bathochromic shifts in the emission and absorption bands of oligothiophenes occur as a result of increased chain length, whilst quantum yields and τ_{obs} increase accordingly.[6] In 2002, Seixas de Melo *et al.* concluded that three-ringed systems exclusively containing thiophenes resulted in an enhancement of spin-orbit coupling when compared to furan and pyrrole variants.[7]

Recently, Popczyk *et al.* investigated the tunability of organic chromophores, where thiophenes and benzothiophenes were employed as EDGs (**Table 4.1**).[2] It was concluded that the position of the acceptor group (nitrophenyl or benzonitrile) heavily influenced the photophysical tunability. *Meta*-substituted derivatives displayed moderate charge transfer, whereas *para-* and *ortho-* variations exhibited much stronger charge transfer character. This was observed through bathochromic shifts in λem and λabs in conjunction with peak

broadening. Fluorescence quantum yields and Stokes shift values differed significantly, depending upon the nature of the acceptor.
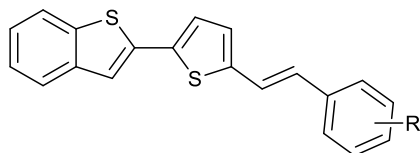
R	λ_{abs}/ nm	λ_{em}/ nm	Φ_F
o-NO$_2$	376	466	$<10^{-2}$
m-NO$_2$	393	447	$<10^{-3}$
p-NO$_2$	424	572	0.15
o-CN	397	480	0.15
m-CN	394	465	0.22
p-CN	404	485	0.18

Table 4.1: *Photophysical properties of chromophores developed by Popczyk et al. in CHCl$_3$ solutions.*[2]

Dye-sensitised solar cells (DSSCs) were first reported in 1991,[8] and are an area of great interest for the development of cost-effective, sustainable devices.[9] Thiophene compounds have been vastly studied in the development of DSSCs because of their appeal as D-π-A chromophores.[3] Here, they are generally incorporated as π-spacers and / or electron-donors.

In 2016, Fernandes developed four novel push-pull type organic dyes,[10] where different electron-rich heterocycles acted simultaneously as donors and π-spacers on a thieno[3,2-b]thiophene backbone, altering the photophysical properties (**Figure 4.1**). The nature of the electron-donating heterocycle heavily impacted the optical properties of the conjugated systems, where the electron-accepting component remained constant. Electronic behaviour of the substituents, conjugation length and planarity of the π-spacers affected the charge separation, and hence the resultant photophysical properties of the corresponding dyes. **4.1d** displayed a red-shift in emission and absorption maxima with a considerably high fluorescence efficiency in comparison to **4.1c**, whilst the observed Stokes shift value (Δλ) also increased upon extension of the chain length. Therefore, the inclusion of an additional thiophene ring bearing a hexyl chain improved the electron-donating ability and the extent of conjugation of the compound, thus increasing solar-cell efficiency.

4.1d
λ_{abs}^{a}: 443 nm
ε: 25666 M^{-1} cm^{-1}
λ_{em}: 527 nm
$\Delta\lambda$: 94 nm
Φ_F: 0.356

4.1a
λ_{abs}^{a}: 398 nm
ε: 24348 M^{-1} cm^{-1}
λ_{em}: 469 nm
$\Delta\lambda$: 71 nm
Φ_F: 0.015

4.1b
λ_{abs}^{a}: 364 nm
ε: 5996 M^{-1} cm^{-1}
λ_{em}: 471 nm
$\Delta\lambda$: 107 nm
Φ_F: 0.021

4.1c
λ_{abs}^{a}: 339 nm
ε: 23315 M^{-1} cm^{-1}
λ_{em}: 476 nm
$\Delta\lambda$: 77 nm
Φ_F: 0.020
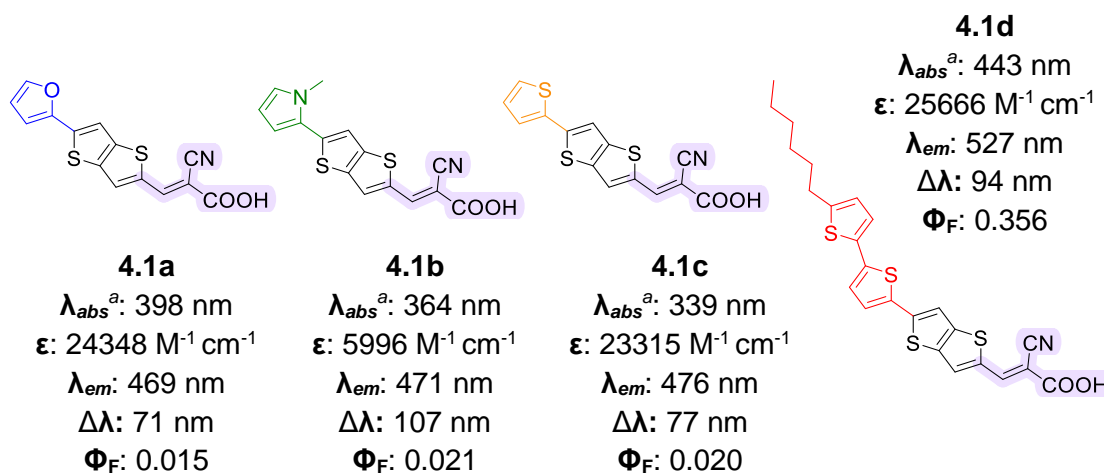
Figure 4.1: *Push-pull type organic chromophores developed by Fernandes.*[10] *The acceptor component is highlighted in purple, and electron-donating heterocycles are indicated by colour. UV-vis and emission spectroscopy data were collected in EtOH* $(10^{-5} M)$*;* *[a]Peak at* λ_{max}*.*

4.1.2: Thiophene-Containing Quinoxalines

There have been numerous reports detailing the unique photophysical properties of combined thiophene and quinoxaline units.[11] In 2019, Mahadik *et al.* studied new D-A type compounds bearing a 2,3-di(thiophen-2-yl)quinoxaline core (**Figure 4.2**).[12] Prominent ICT character was observable in the absorption spectra (390 – 461 nm) as a result of electron transfer between the substituted amines (donor) and the di-thienyl quinoxaline core (acceptor). Here, subtle tunability was achieved by adjusting the nature of the donor.
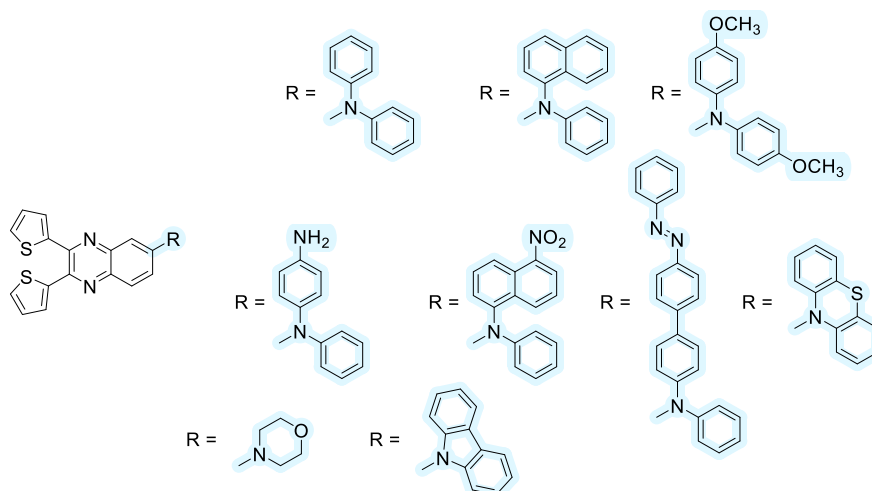
Figure 4.2: *D-A type compounds synthesised by Mahadik,*[12] *based upon 2,3-di(thiophen-2-yl)quinoxaline.*

More recently, Moshkina *et al.* published work on quinoxaline-centred, V-shaped D-π-A-π-D type chromophores, where 1,5-thiophenylene behaved as a π-conjugated spacer and either 6-cyano or 6,7-difluoroquinoxaline functioned as electron-acceptors.[13] Here, notable push-pull character was established as a consequence of efficient ICT, offering vast prospects with substantial colour tunability (**Figure 4.3**). Adjustments in electron-withdrawing strength of the quinoxaline was achievable, thus enhancing the ICT character. This was dependent upon the substitution at the benzene constituent, as a significant bathochromic shift in λ_{abs} and λ_{em} were discovered when a *cyano*- group was incorporated into the quinoxaline backbone. **4.2d** exhibited a high Φ_F value of 10% and a relatively long τ_{obs} of 1.57 ns, especially in comparison to **4.2e** (τ_{obs} = 0.57 ns).
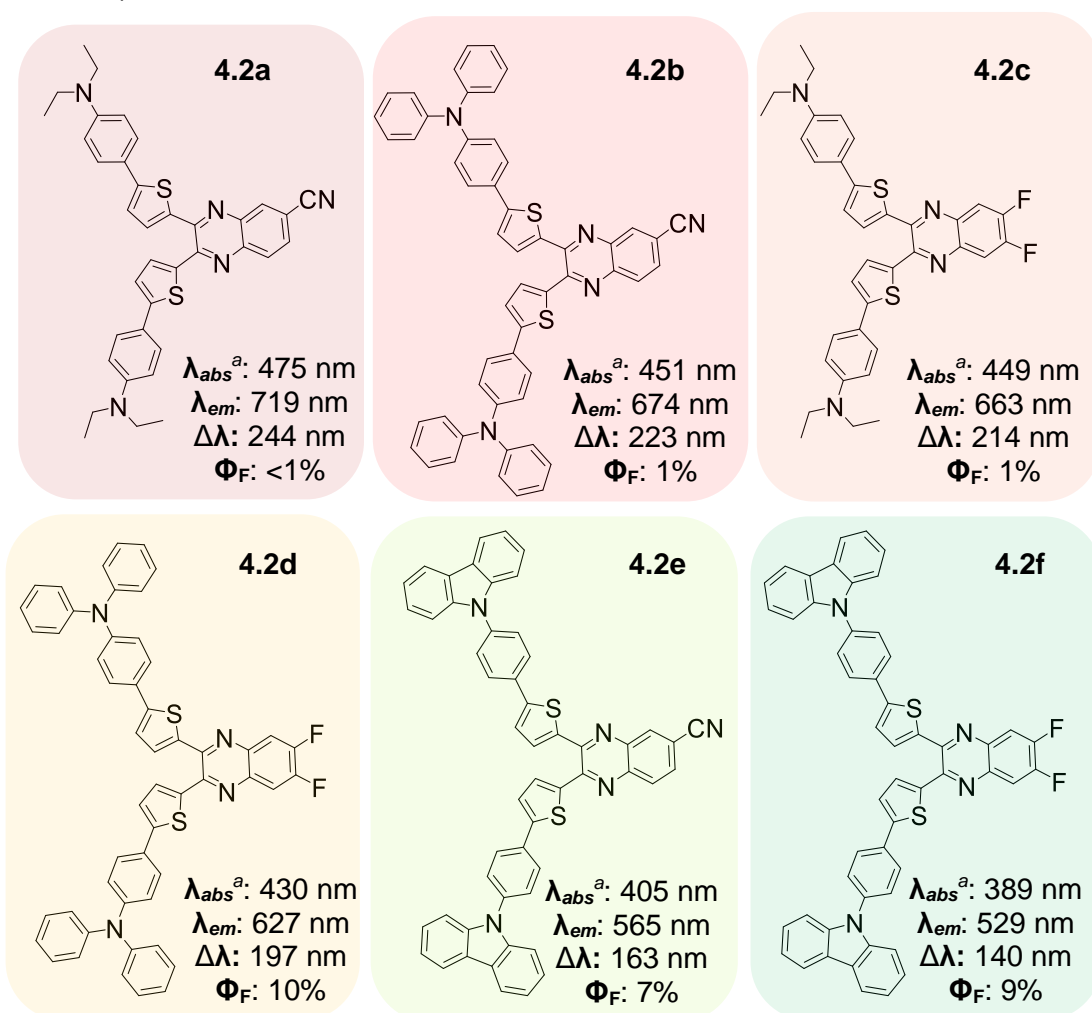
Figure 4.3: *V-shaped push-pull chromophores by Moshkina.*[13] *Absorption and emission data are also shown (THF, 10^{-5} M). ^{a}Peak at λ_{max}.*

4.1.3: Cyclometallated Thiophene Complexes

Organometallic complexes containing a cyclometallated thiophene unit have been reported as early as 1975, where 2-(2'-thienyl)pyridine was used in conjunction with a platinum metal centre as a means to investigate the mode of coordination.[14] In 1979, Nonoyama suggested that iridium complexes bearing a 2-(2-thienyl)pyridine C^N ligand were also attainable, due to the chemical properties of thiophene bearing a close resemblance to benzene and therefore reminiscent of ppy-type systems.[15]

In 2001, Lamansky developed neutral **[Ir(C^N)₂(acac)]** complexes, demonstrating the effect on subsequent photophysical properties upon altering the nature of the C^N ligands. The investigated ligands were based upon phenylpyridine (**Ir-ppy**), thienylpyridine (**Ir-thp**) and benzo-thienylpyridine (**Ir-btp**) (**Figure 4.4**).[16] **Ir-ppy** exhibited a relatively small Stokes shift for the ^{3}MLCT bands (56 nm), whereas **Ir-thp** and **Ir-btp** displayed significantly larger shifts (109 and 117 nm, respectively). This was correlated to the nature of the emissive state, where emission was suggested to occur from a predominantly ^{3}MLCT state for **Ir-ppy**, but from a predominantly ligand-based excited state for **Ir-thp** and **Ir-btp**. This is due to the $^3(\pi\text{-}\pi^*)$ excited state for **Ir-ppy** possessing a higher energy than the ^{3}MLCT level, and *vice-versa* for **Ir-thp**. λ$_{em}$ were significantly longer for **Ir-thp** and **Ir-btp**, along with extended τ_{obs} values. Consequently, these properties allowed the complexes to be considered as desirable candidates for high-efficiency OLEDs.

Ir-ppy
λ$_{abs}$^{a}: 497 nm
λ$_{em}$: 516 nm
Δλ^b: 56 nm
Φ$_F$: 0.34
τ_{obs}: 1.6 µs

Ir-thp
λ$_{abs}$^{a}: 453 nm
λ$_{em}$: 562 nm
Δλ^b: 109 nm
Φ$_F$: 0.12
τ_{obs}: 5.3 µs

Ir-btp
λ$_{abs}$^{a}: 495 nm
λ$_{em}$: 612 nm
Δλ^b: 117 nm
Φ$_F$: 0.21
τ_{obs}: 5.8 µs
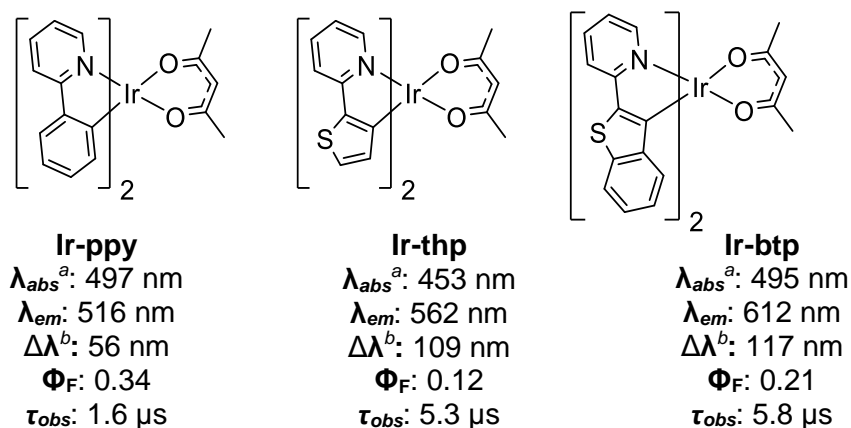
Figure 4.4: *Neutral iridium species developed by Lamansky in 2001.*[16]

Similar motifs have been utilised to achieve tunable emission within the red region of the visible range (**Figure 4.5**).[17] Functionalisation of the cyclometallating ligands has proven to impart significant changes in emission wavelength. More recently, work with *bis*-cyclometallated cationic variants have given rise to efficient deep-red[18] and NIR[19] phosphors, with excellent tunability, where relatively high radiative decay rates (k_r) were achievable.

(btfmp)₂Ir(acac)
λ$_{em}$: 638 nm

(btmp)₂Ir(acac)
λ$_{em}$: 604 nm

(btp)₂Ir(acac)
λ$_{em}$: 613 nm
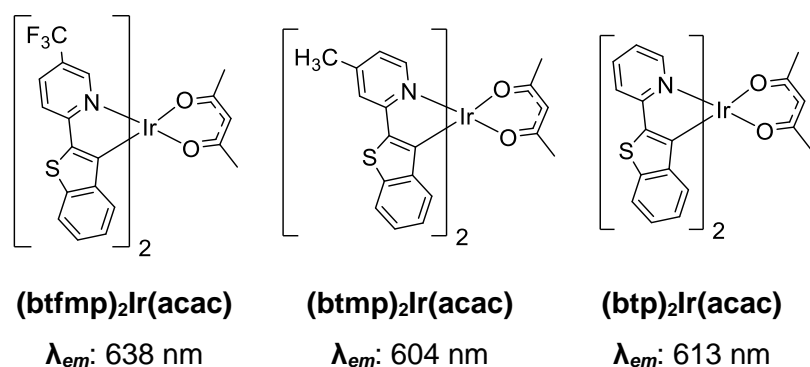
Figure 4.5: Neutral iridium complexes containing 2-benzo[b]thiophen-2-yl-pyridine cyclometallating ligands, reported by Xu et al. in 2007.[17]

Therefore, in addition to their use in OLEDs,[20,21] recent developments have allowed cationic Ir(III) complexes based upon these structural motifs to thrive in other more specialised areas such as photocatalytic H₂ generation,[22,23] electrochemiluminescent materials[24] and biomedical fields.[25] In addition to pyridine-type N-donors, systems containing other heterocycles based upon quinoline or quinazoline have been formed and have been proven to display desirable properties for development of high efficiency PhOLED dopants and in the field of photovoltaics (**Figure 4.6**).[26–28]

λ$_{em}$: 611 nm
Φ$_P$: 0.55

λ$_{em}$: 602 nm
Φ$_P$: 0.15 (0.12)^a

λ$_{em}$: 693 nm
Φ$_P$: 0.6 × 10^{-3}
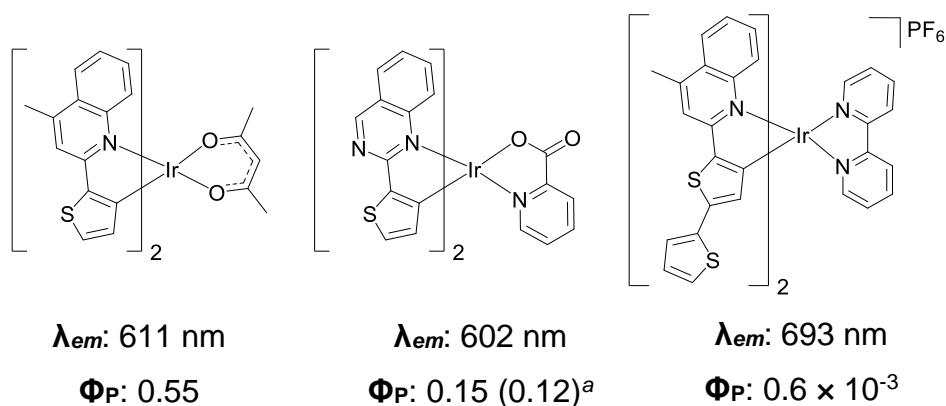
Figure 4.6: Examples of some Ir(III) species with thiophene systems as the point of C-M bond formation and quinoline or quinazoline at the N-coordination site. Measurements were in degassed DCM solutions; ^{a}aerated DCM.

4.2: Aims

The work undertaken in this chapter explores the synthesis and characterisation of eleven potential cyclometallating ligands based upon a 2-thienyl quinoxaline core, along with their corresponding Ir(III) complexes. Eight of these *bis*-cyclometallated iridium complexes were successfully isolated. With each ligand possessing unique structural characteristics, the photophysical properties of both the chromophores and subsequent complexes were monitored and compared.

With the overall aim of synthesising relatively efficient deep-red emitting complexes, the scope for tunability within this region was examined. The emission and absorption properties of all compounds were monitored in relation to the position and nature of substitution, extent of conjugation and point of attachment of the thiophene ring to the quinoxaline. The coordination mode for all complexes was also determined. **L^{11}H** and **Ir-4h** were synthesised and characterised by Ellie Payce.

4.3: Results and Discussion

4.3.1: Synthesis of Ligands and Complexes

A series of eleven substituted 2-thienyl quinoxaline chromophores were synthesised, each incorporating different features and functionalities. All compounds were successfully isolated, with a broad range of experimental yields between 16 – 73%. The general synthesis comprised of two stages, analogous to those described in previous chapters.[29]
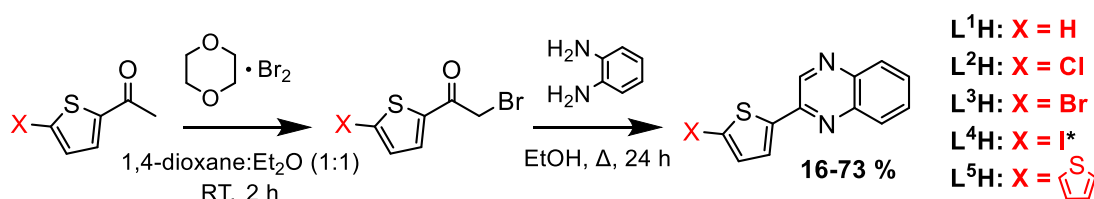
Scheme 4.1: *General synthetic approach for the preparation of L$^{1-5}$H.*
*The bromination step for **L^{4}H** was performed in glacial AcOH overnight.*[35]

Firstly, **L$^{1-5}$H** were synthesised according to the route shown in **Scheme 4.1**. These compounds varied in substitution at the 5-position of the thienyl component, where **L^{1}H** was formed as the unsubstituted analogue. **L$^{2-4}$H** contained a halogen atom at the C5 position, whereas **L^{5}H** involved an extension of the π-conjugated system by incorporation of a 2,2'-bithiophene unit. Two of the compounds, **L^{4}H** and **L^{5}H**, are novel species and were characterised as such.

Ethanol was selected as a suitable solvent for the condensation step in most cases. This was because it is a volatile and relatively 'green' solvent,[30] permitting a facile work-up as most pure compounds precipitated out of solution upon cooling. Although the obtained yields were modest, there was no requirement for a precious metal catalyst.[31] However, it was later discovered that a much more efficient method could be used for this step and was employed in the repeated formation of **L^{1}H** for the sake of comparison (**Scheme 4.2**).[32] Here, the experimental yield was double of that observed in ethanol and therefore, this approach should be considered in future work relating to these compounds to maximise efficiency.
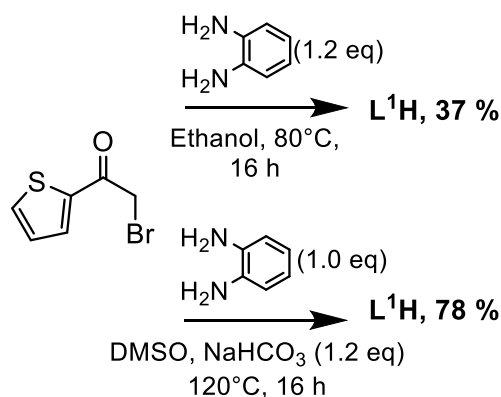
Scheme 4.2: *Comparison of the two synthetic routes to L^{1}H.*

Following the general route (**Scheme 4.1**) for **L^{4}H** led to the formation of various products for the bromination stage, detectable by NMR studies. Although the major product was the desired mono-brominated species (63%), di-bromination (*via* a second α-halogenation) had occurred at much more considerable quantities than previously detected, whilst the 2-acetylthiophene starting material was still observable. This indicated that the 2-acetyl-5-iodothiophene starting material possessed a higher degree of chemical reactivity and was suggested to be due to its photochemical activity and resultant light-sensitivity.[33,34] Therefore, deviations in the synthetic methodology were implemented for the formation of this compound, where glacial acetic acid was used as a solvent and the mixture was stirred for a longer period in the absence of light.[35]

L$^{6-9}$H were also formed *via* the same synthetic procedure (**Scheme 4.3**). Here, substitution was applied on the quinoxaline backbone instead of the thienyl unit by use of a disubstituted *o*-phenylenediamine or 2,3-diaminonaphthalene, offering an additional point of functionalisation to be monitored.
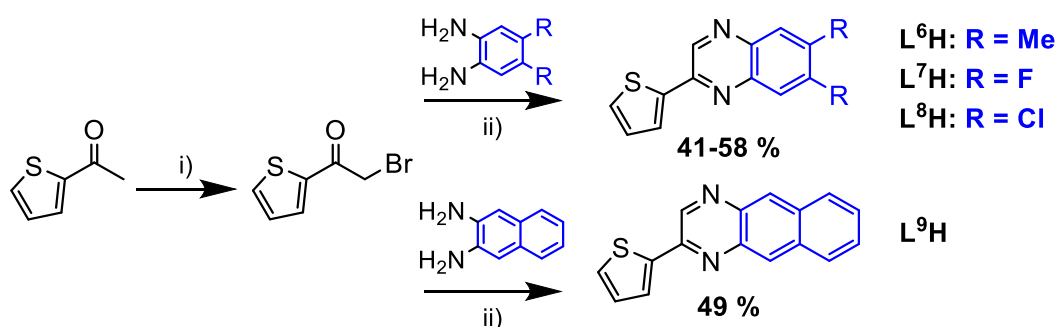
Scheme 4.3: *General synthetic approach for the preparation of L$^{6-9}$H. i) Dioxane dibromide, 1,4-dioxane/Et$_2$O (1:1), RT, 2h; ii) EtOH, 80°C, 24 h.*
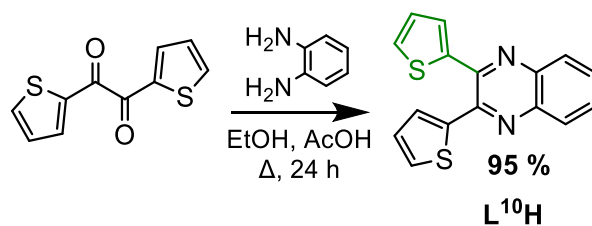
*Scheme 4.4: Synthetic approach for the preparation of **L¹⁰H**.*

L¹⁰H was synthesised through a modified literature procedure from the β-diketone starting material (**Scheme 4.4**).[36,37] Here, the reagents were once again dissolved in ethanol, but with a catalytic amount of acetic acid. The principle was to examine any differences in ICT character by the inclusion of two thienyl donor sub-units.

Finally, 2-(thiophen-3-yl)quinoxaline (**L¹¹H**) was formed to observe any changes in electronic behaviour as a result of structural isomerism (relative to **L¹H**), where the point of attachment was at the C3 position. This was synthesised by Ellie Payce, where a similar synthetic pathway was undertaken but with more forceful conditions for the bromination reaction (**Scheme 4.5**). The reduced reactivity of this isomer was a consequence of fewer resonance structures being available for the enol form of the compound. Therefore, the brominating agent was added to the mixture at elevated temperatures and the combined solution was stirred for a longer period.
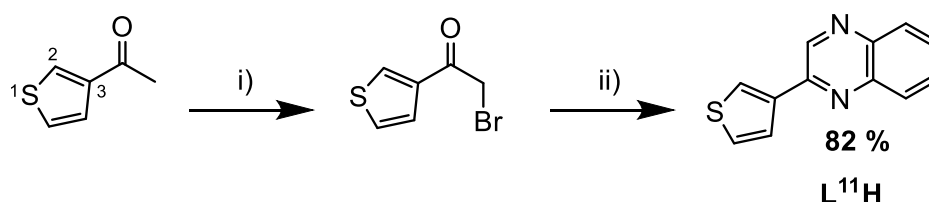
*Scheme 4.5: Synthesis of **L¹¹H**. Atom numbers are labelled on the starting material to indicate the C3 point of attachment; i) dioxane dibromide, 1,4-dioxane/Et₂O (1:1), 70°C, 24 h; ii) 1,2-phenylenediamine, EtOH, 80°C, 24 h.*

L¹⁻¹¹H were investigated as cyclometallating ligands for Ir(III) *via* the formation of the corresponding chloro-bridged iridium dimers (**Scheme 4.6**). These were formed similarly to those mentioned in previous chapters, where stoichiometric quantities of the free ligand, **LⁿH**, and IrCl₃.xH₂O were added to 2-methoxyethanol and heated to reflux for 48 hours.[38]
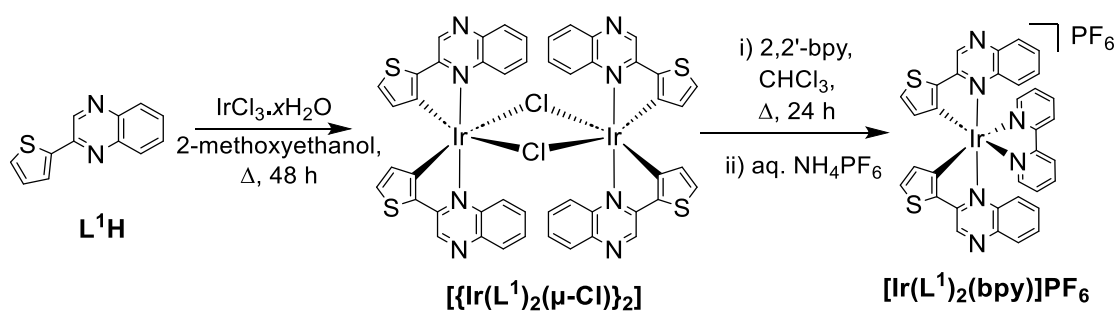
Scheme 4.6: *General synthetic approach for the preparation of [Ir(L¹)₂(bpy)]PF₆.*

Subsequently, the dimeric species were cleaved into their monomeric, cationic counterparts by refluxing a solution of the dimer with the selected ancillary ligand (2,2'-bipyridine). For most complexes, the splitting reaction was carried out in chloroform due to enhanced solubility over alcoholic glycol ethers. Despite the intrinsically reduced boiling point of chloroform (61°C) compared to 2-(m)ethoxyethanol (124 – 135°C), the observed yields were not adversely impacted. Studies have shown that high yields are obtainable under mild conditions, where >70% conversion can be achieved after a 19-hour reflux in DCM:MeOH (5:1) at 40°C.[39]

Attempts to isolate the corresponding iridium complexes from the halogenated thiophene ligands ($L^{2-4}H$) were deemed to be unsuccessful. However, the remaining ligands were more prosperous and led to the isolation of pure complexes. These were purified by means of column chromatography, where the stationary phase was silica gel and the eluent was acetone followed by a solvent mixture of $CH_3CN:H_2O:KNO_3$ (*sat. aq.*) in a ratio of 14:2:1, in which the products eluted as red or orange bands. A counterion exchange was performed, where the unfavourable chloride counterion was exchanged with the less polar PF_6 anion, enhancing solubility in organic solvents. Finally, recrystallisation from DCM and Et_2O was carried out, generating the final complexes, **[Ir(Lⁿ)₂(bpy)]PF₆** (**Ir-4a** – **Ir-4h**) in high purities (**Figure 4.7**).

Comparable to the free ligands, a wide range of yields were observed for the final complexes (14 – 78%), suggesting that the efficiency of the cyclometallation step varied depending on the ligand.
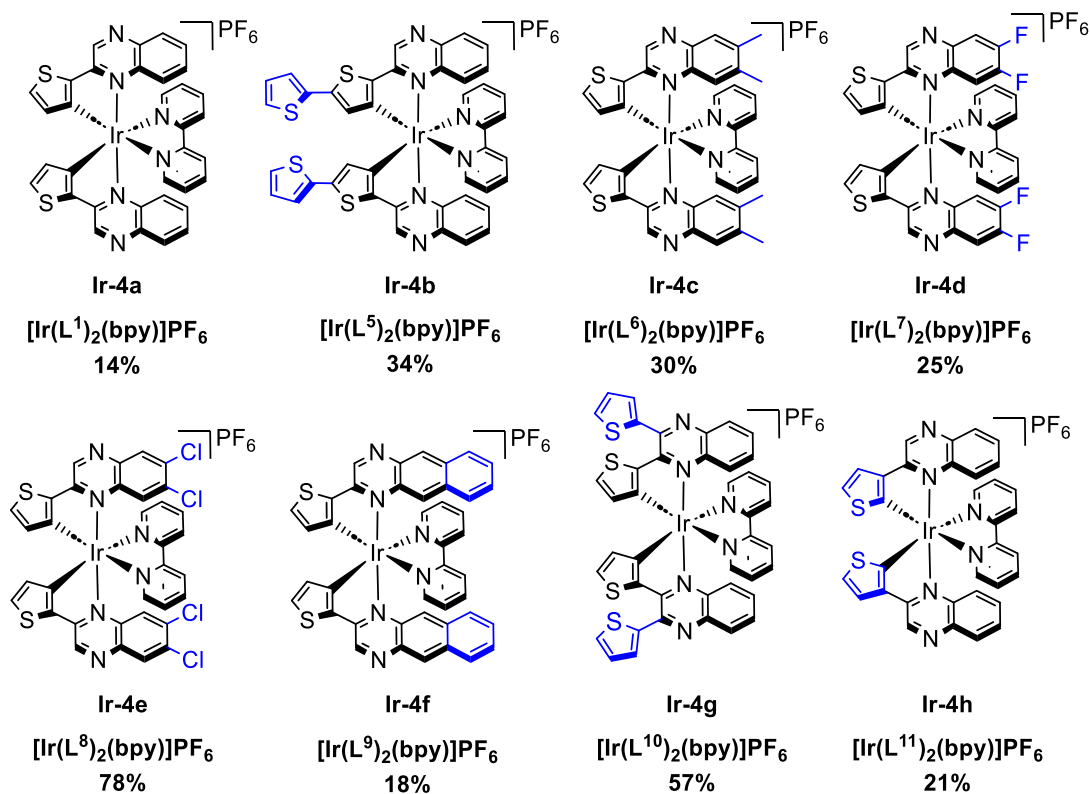
Figure 4.7: *Structures and experimental yields of the successfully isolated Ir(III) complexes. All functional deviations from **Ir-4a** are displayed in blue.*

4.3.2: Characterisation of Ligands and Complexes

All novel compounds were fully characterised by ^{1}H, ^{13}C{^{1}H} and ^{19}F{^{1}H} NMR, IR spectroscopies, and HRMS. Photophysical data was obtained through UV-vis absorption, steady-state and time-resolved luminescence spectroscopies.

The stacked ^{1}H NMR spectra of **L$^{1-4}$H** are presented in **Figure 4.8**. An indicative singlet peak was observed at between 9.15 – 9.24 ppm for these compounds, corresponding to the uncoupled, deshielded proton on the pyrazine segment of the quinoxaline. Similar peaks are observed for all the free ligands except for **L^{10}H**, as this proton is replaced by a secondary thiophene unit. Two multiplets between 8.10 – 7.99 ppm for **L$^{1-4}$H** were related to the two pairs of protons on the quinoxaline moiety. These were recorded as multiplets rather than resolved peaks due to the asymmetric nature of the molecules, resulting in two similar, yet chemically unique overlapping peaks. Relative disparities in electronic effects were observed in **L$^{1-4}$H**, depending on the nature of the substituent at the C5 position of the thiophene ring. As electronegativity decreases down the

group 17 elements,[40] the chemical shift values for the two doublets on the thiophene ring differ more drastically as the halogen atom becomes larger.
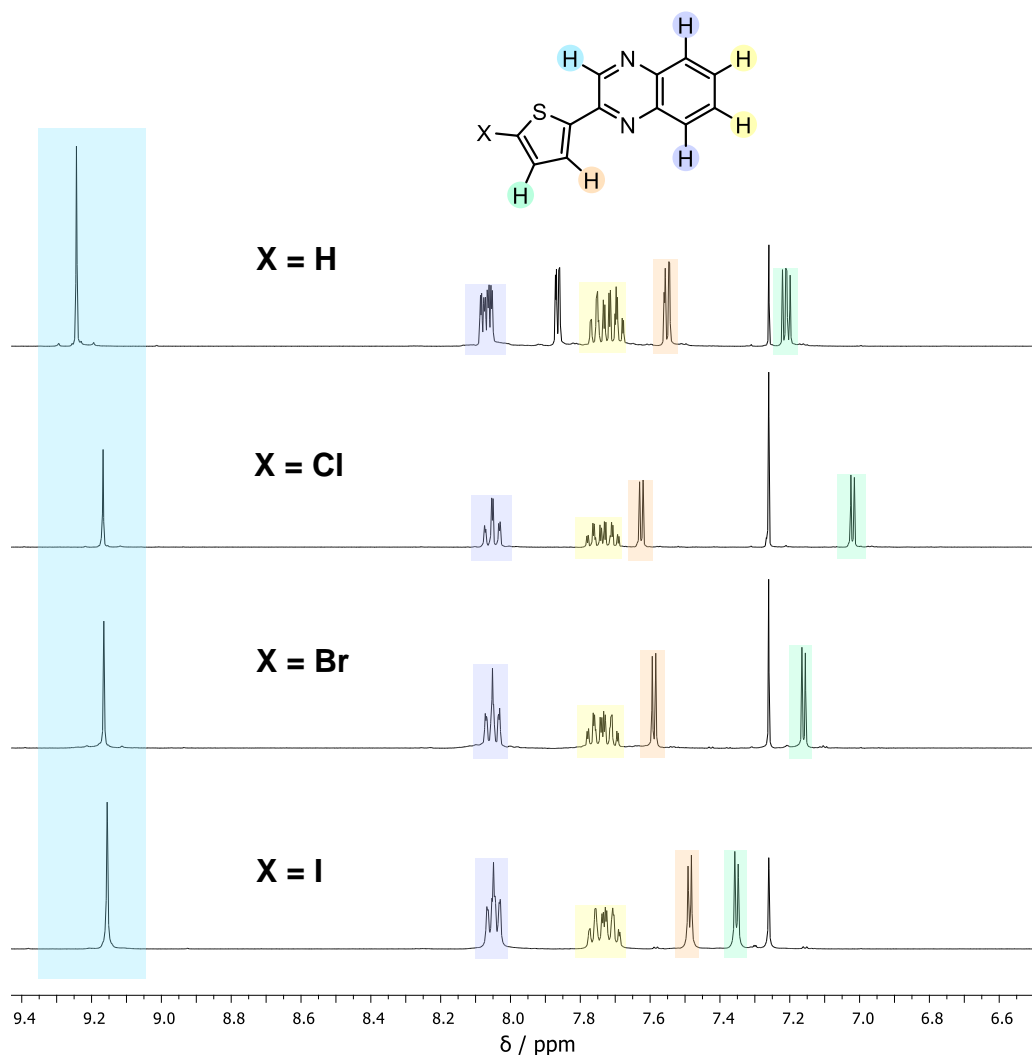
Figure 4.8: *Stacked* ^1H *NMR spectra of* ***L$^{1-4}$H***, *400 MHz, CDCl$_3$.*

The superimposed ^{1}H NMR spectra for **L^{1}H** and **Ir-4a** are shown in **Figure 4.9**, where the displayed relative intensities correspond to the complex, and each proton environment is assigned. The proposed coordination mode is also shown, where cyclometallation occurs at the C3 (β) position relative to the sulphur atom. This was supported by the presence of two doublets with $^3J_{HH}$ values of 4.7 Hz, which were consistent with previous studies on similar systems,[41] where the formation of a stable 5-membered chelate intermediate was expected. The ^{1}H NMR spectra of all complexes show that only one species is present in each case, with no indication of the formation of geometric isomers. The doublet at 7.54 ppm was assigned to position **g** on **Ir-4a** as the relative electronegativity[40] of the sulphur atom permitted the withdrawal of electron

density from the adjacent proton at C5, resulting in a downfield peak position. This peak was displayed as a doublet of doublets (dd) at 7.86 ppm in the free ligand spectrum, with a $^3J_{HH}$ value of 3.7 Hz and a $^4J_{HH}$ of 1.1 Hz. The other doublet was seen at 6.24 ppm – a significant upfield chemical shift value in comparison to the free ligand (where this peak was present at 7.21 ppm) and was suggested to be a consequence of the fixed orientation of the cyclometallating ligands, allowing them to interact with each other whilst shielding this proton from the effects of the external magnetic field.
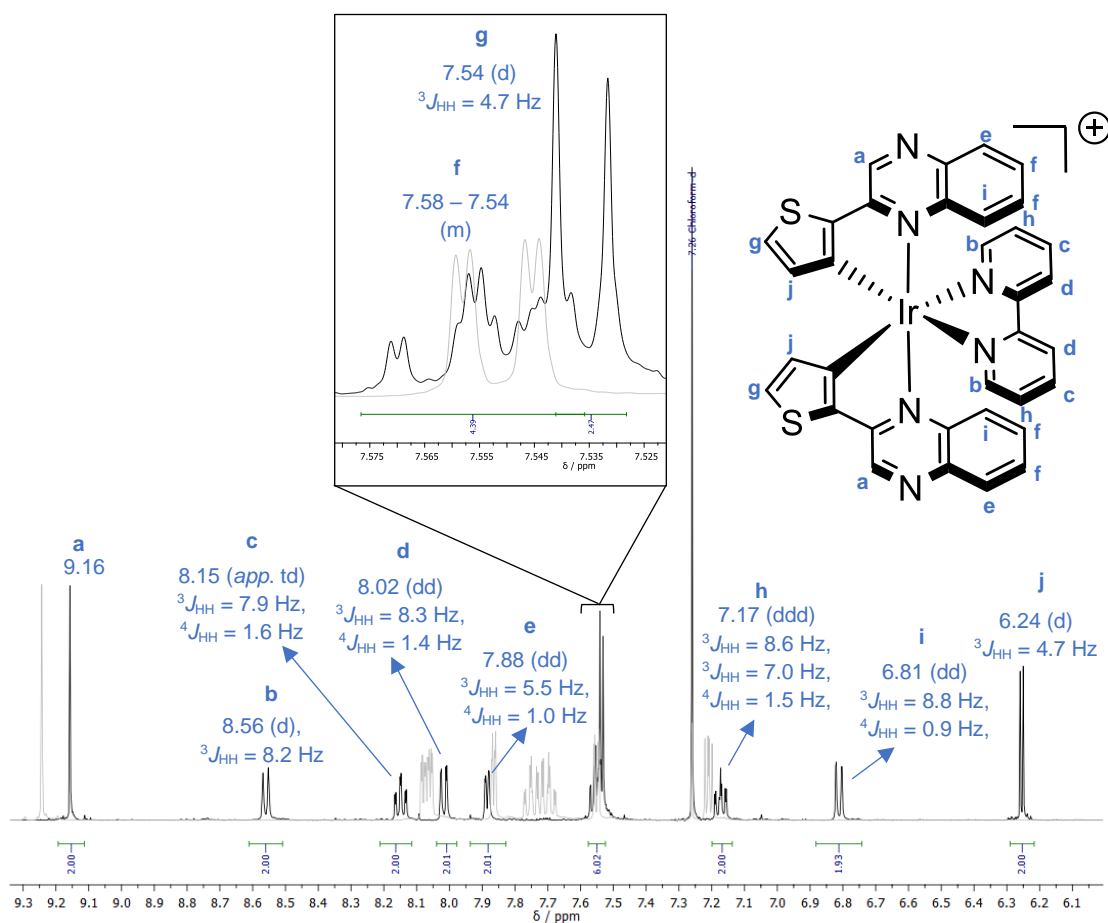
Figure 4.9: *Overlapped ^1H NMR spectra of the unsubstituted free ligand,* ***L^{1}H*** *(grey, 400 MHz), and the corresponding Ir(III) complex* ***Ir-4a*** *(black, 500 MHz) in CDCl$_3$.*

A doublet of doublets at 6.81 ppm was attributed to one of the protons on the benzene unit of the quinoxaline moiety (**i**). This became far more chemically inequivalent to **e** upon complexation, as the fixed orientation of the ligand means that the proton interacts with the π-system on the bipyridine ancillary ligand. The proposed octahedral geometry is displayed alongside the resultant interaction between the ligands in **Figure 4.10**.
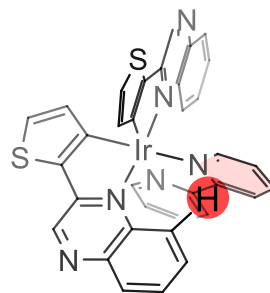
*Figure 4.10: Three-dimensional representation of **Ir-4a**.*
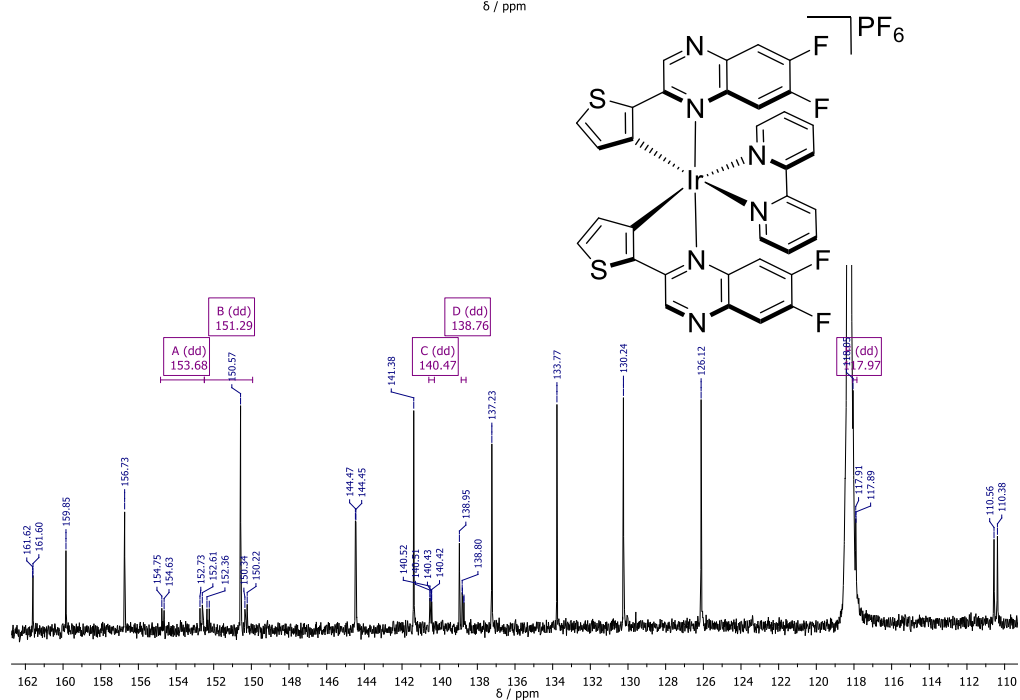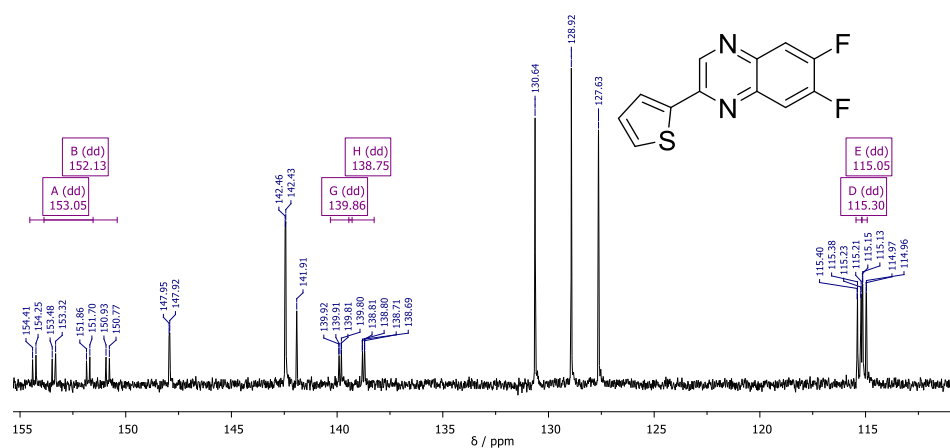
Figure 4.11: $^{13}C\{^{1}H\}$ *NMR spectra of **L⁷H**, CDCl₃, 101 MHz (above) and **Ir-4d**, CD₃CN, 126 MHz (below).*

For **L⁷H** and **Ir-4d**, NMR-active ^{19}F nuclei allowed H-F and C-F coupling constants to be determined. The $^{13}C\{^{1}H\}$ NMR spectra for these compounds are displayed in **Figure 4.11**, where six doublets of doublets are seen in the spectrum for the free ligand, whilst five are visible in the corresponding complex. The peak at 118 ppm for **Ir-4d** was coincident with the residual solvent peak from CD_3CN. Deconvolution techniques were applied to assign the multiplicity and coupling constant for this peak and in doing so, it matched the free ligand values. It was believed that the remaining doublet of doublets coincided with the solvent peak and was unable to be resolved. However, it can be assumed that the coupling constant would be identical to the peak observed at 118 ppm, as this was exemplified in the spectrum for **L⁷H**.

Chemical shift positions (**δc**) and coupling constants ($^{X}J_{CF}$) of the doublet of doublet peaks are displayed in **Table 4.2**, along with their assignments. The C-F couplings were consistent with literature values,[42] offering insight into the relative peak positions and which carbon atom they could be assigned to. The carbon atoms directly attached to the highly electronegative fluorine atoms are heavily deshielded, resulting in a prominent downfield chemical shift (151.3 – 153.7 ppm). The large coupling constant of 253.4 – 256.6 Hz was in agreement with this assignment, as it falls within the accepted range of a $^{1}J_{CF}$ coupling.[42] The peaks at 138.8 – 140.5 ppm were relatively downfield, owing to the electron-withdrawing nature of the pyrazine ring. Only slight variations were perceived between the free ligand and the complex, but it is not possible to attribute this exclusively to the effect of complexation, as the solvent environment and strength of magnetic field were inconsistent.
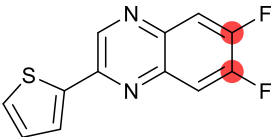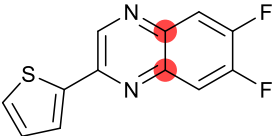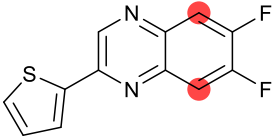
Assignment	δ_C / ppm	
	Free Ligand[a]	**Complex**[b]
(structure)	152.9: $^1J_{CF}$ = 256.6 Hz $^2J_{CF}$ = 16.1 Hz	153.7: $^1J_{CF}$ = 255.0 Hz $^2J_{CF}$ = 15.4 Hz
	151.9: $^1J_{CF}$ = 256.0 Hz $^2J_{CF}$ = 16.0 Hz	151.3: $^1J_{CF}$ = 253.4 Hz $^2J_{CF}$ = 15.4 Hz
(structure)	139.7: $^3J_{CF}$ = 11.1 Hz $^4J_{CF}$ = 1.2 Hz	140.5: $^2J_{CF}$ = 10.4 Hz $^3J_{CF}$ = 1.2 Hz
	138.6: $^3J_{CF}$ = 10.6 Hz $^4J_{CF}$ = 1.1 Hz	138.8: $^2J_{CF}$ = 10.5 Hz $^3J_{CF}$ = 1.4 Hz
(structure)	115.1: $^2J_{CF}$ = 17.5 Hz $^3J_{CF}$ = 1.9 Hz	118.0: $^2J_{CF}$ = 17.9 Hz $^3J_{CF}$ = 2.1 Hz
	114.9: $^2J_{CF}$ = 17.5 Hz $^3J_{CF}$ = 1.6 Hz	

*Table 4.2: Peak positions and coupling constants for all doublets of doublets in the $^{13}C\{^1H\}$ NMR spectra of **L⁷H** and **Ir-4d**. [a]CDCl₃, 101 MHz; [b]CD₃CN, 126 MHz.*

$^{19}F\{^1H\}$ NMR spectra were also measured for all complexes to confirm that all compounds existed as a PF₆ salt. A doublet was present between –73.1 and –71.6 ppm for all species, with a $^1J_{PF}$ coupling in the range of 706 – 713 Hz. This was reinforced by IR spectroscopy data by the presence of a sharp band at ~833 cm⁻¹ – appertaining to the vibrational frequency of the v(P-F) stretching mode. $^{19}F\{^1H\}$ NMR data collected for **L⁷H** and **Ir-4d** showed an additional two doublets and are shown relative to the free ligand in **Table 4.3**. The J_{FF} values were consistent with experimental values for 1,2-difluorobenzene.[43]

δ_F / ppm	
Free Ligand	**Complex**
–129.3 (d, $^3J_{FF}$ = 21.1 Hz)	–123.59 (d, $^3J_{FF}$ = 22.2 Hz)
–130.9 (d, $^3J_{FF}$ = 21.4 Hz)	–130.41 (d, $^3J_{FF}$ = 22.2 Hz)

*Table 4.3: $^{19}F\{^1H\}$ NMR data collected for the fluorinated compounds **L⁷H** and **Ir-4d** (excluding the PF₆ doublet), CDCl₃, 376 MHz.*
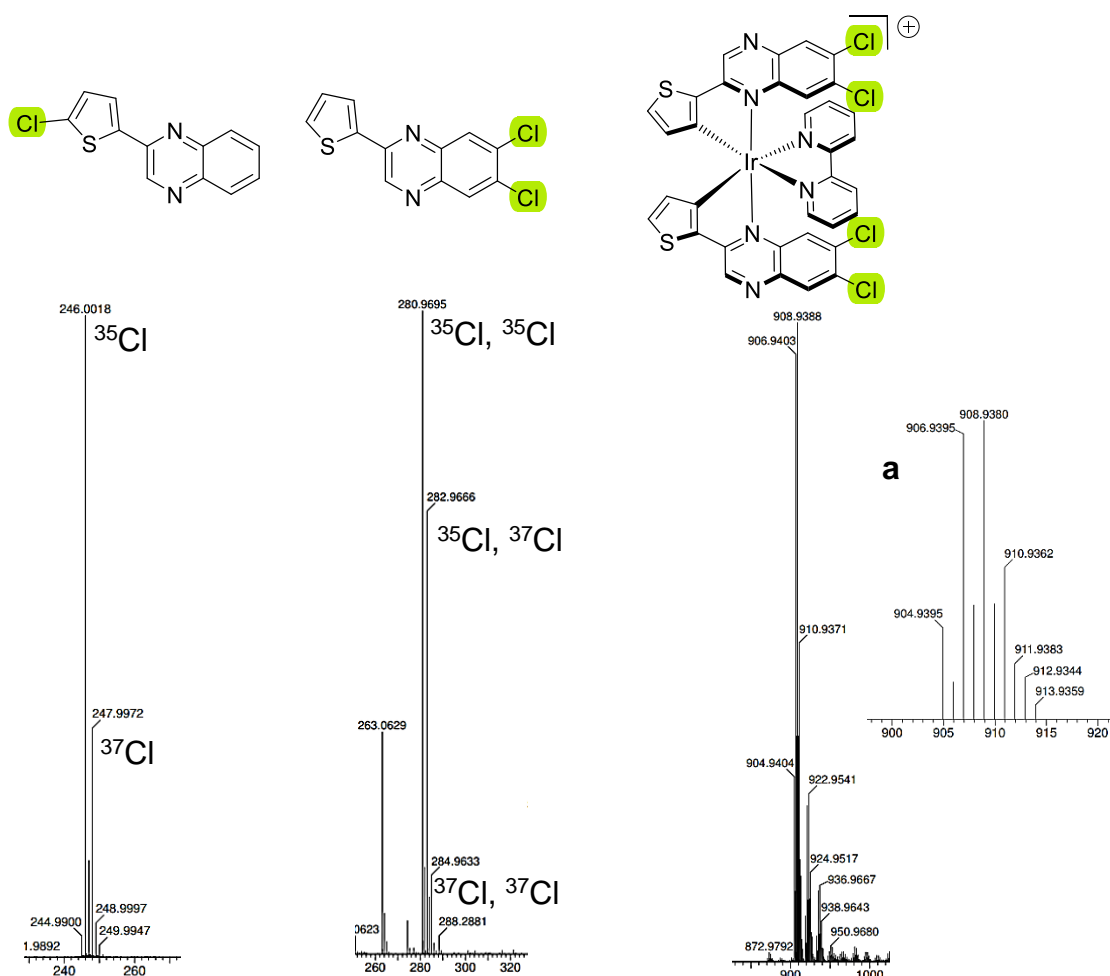
Figure 4.12: *HRMS data for the chlorinated compounds (EI for L²H, ES+ for L⁸H and Ir-4e) where corresponding structures are placed above. ᵃMagnified section of the Ir-4e spectrum, displaying the two unique sets of peaks.*

HRMS spectra for the chlorinated compounds (**L²H**, **L⁸H** and **Ir-4e**) are shown in **Figure 4.12**. Electrospray ionisation (ES+) techniques were employed for the larger molecules **L⁸H** and **Ir-4e**, generating [M + H]⁺ and [M]⁺ molecular ion peaks, respectively. Electron impact ionisation (EI+) was used for **L²H**, also generating an [M]⁺ parent ion. Various combinations of the two stable and abundant isotopes of chlorine (^{35}Cl and ^{37}Cl) gave rise to distinct sets of peaks. **L²H** contains only one chlorine atom, so there are only two peaks – the largest (m/z = 246) corresponded to the more abundant ^{35}Cl isotope (rel. abundance of 75.78%), and the reduced intensity peak (m/z = 248) represented the heavier ^{37}Cl isotope (rel. abundance of 24.22%).[44] For **L⁸H**, there are three possibilities – the largest peak (m/z 281) is present for when both atoms exist as the ^{35}Cl isotope, the second peak (m/z 283) represented a combination of one ^{35}Cl and one ^{37}Cl atom in the structure, and the smallest peak (m/z 285) was seen for

when both atoms were present as the less-abundant [37]Cl isotope. The mass spectrum for the complex is far more complicated, as iridium also exists as two abundant isotopes – [191]Ir (37.3%) and [193]Ir (62.7%).[44] Therefore, there are two sets of peaks, each with five potential combinations of isotopes of Cl. The relative magnitudes of the two peaks seen for the parent ion for all complexes were similar, where the iridium isotopes are observed for all other complexes – for example, **Ir-4a** displayed peaks at *m/z* = 769 ([191]Ir) and 771 ([193]Ir).

4.3.3: X-Ray Crystallographic Data

Single crystal XRD data was collected for **Ir-4c**, supporting the theorised structure of the complex and suggested site of cyclometallation (**Figure 4.13**). Red, block-shaped crystals were grown from a solution of DCM and diethyl ether and were analysed by Dr. Peter N Horton of the UK National Crystallography Service at the University of Southampton.
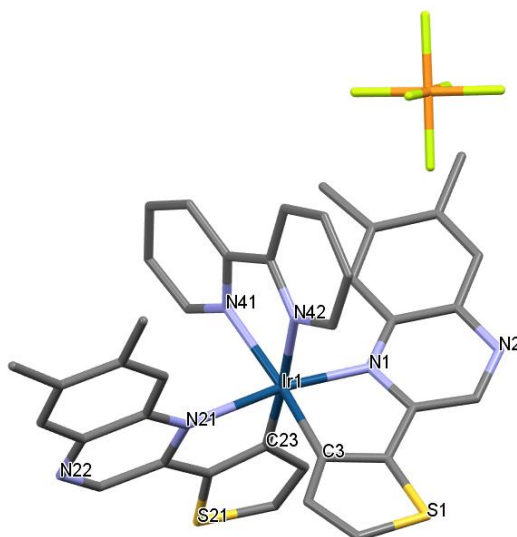
Figure 4.13: XRD Crystal structure of Ir-4c.

Bond	Length / Å
Ir(1)-N(1)	1.979(16)
Ir(1)-N(21)	2.204(14)
Ir(1)-N(41)	2.141(3)
Ir(1)-N(42)	2.145(4)
Ir(1)-C(3)	1.979(15)
Ir(1)-C(23)	2.013(14)

Table 4.4: Selected bond lengths for Ir-4c.

Bonds	Angle / °
N(1)-Ir(1)-N(41)	105.0(5)
N(1)-Ir(1)-N(42)	87.6(6)
N(21)-Ir(1)-N(1)	168.6(7)
N(21)-Ir(1)-N(41)	80.3(4)
N(21)-Ir(1)-N(42)	103.6(3)
N(42)-Ir(1)-N(41)	76.53(13)
C(3)-Ir(1)-N(1)	84.2(7)
C(3)-Ir(1)-N(21)	92.3(7)
C(3)-Ir(1)-N(41)	166.9(7)
C(3)-Ir(1)-N(42)	94.9(8)
C(23)-Ir(1)-N(1)	93.2(7)
C(23)-Ir(1)-N(21)	75.9(5)
C(23)-Ir(1)-N(41)	98.6(4)
C(23)-Ir(1)-N(42)	175.1(4)
C(23)-Ir(1)-C(3)	90.0(9)

*Table 4.5: Selected bond angles for **Ir-4c**.*

Some selected bond lengths are shown in **Table 4.4**, whilst selected bond angles are displayed in **Table 4.5**. These values were consistent with analogous systems such as **[Ir(thpy)$_2$(bpy)]PF$_6$**,[24] since cyclometallation occurred at the C3 position of the thiophene ring and exhibited an overall distorted octahedral geometry. Once again, the complex displayed a *cis*-C,C and *trans*-N,N configuration. Interestingly, the C-Ir-C bond angle was almost exactly 90° due to reduced steric repulsion between the C^N ligands upon inclusion of a 5-membered ring, as opposed to a 6-membered ring system.

4.3.4: Photophysical Properties

The UV-vis absorption profiles of **L$^{1\text{-}11}$H** in *ca.* 10^{-5} M aerated acetonitrile solutions are shown in **Figure 4.14**. All ligands displayed absorption features within the UV range, with some entering the visible range. Despite the possibility for n→π* absorption bands to appear, all transitions shown can be attributed to π→π* features due to their high molar absorptivity values. Previous reports on 2-([2-2'-bithiophen]-5-yl)quinoline suggests that low-energy π→π* singlet

states can possess some n→π* character, and depending on the energy difference between such states, efficient mixing can be achieved.[45] However, a high intensity, broadened peak prevented the resolution of these peaks.
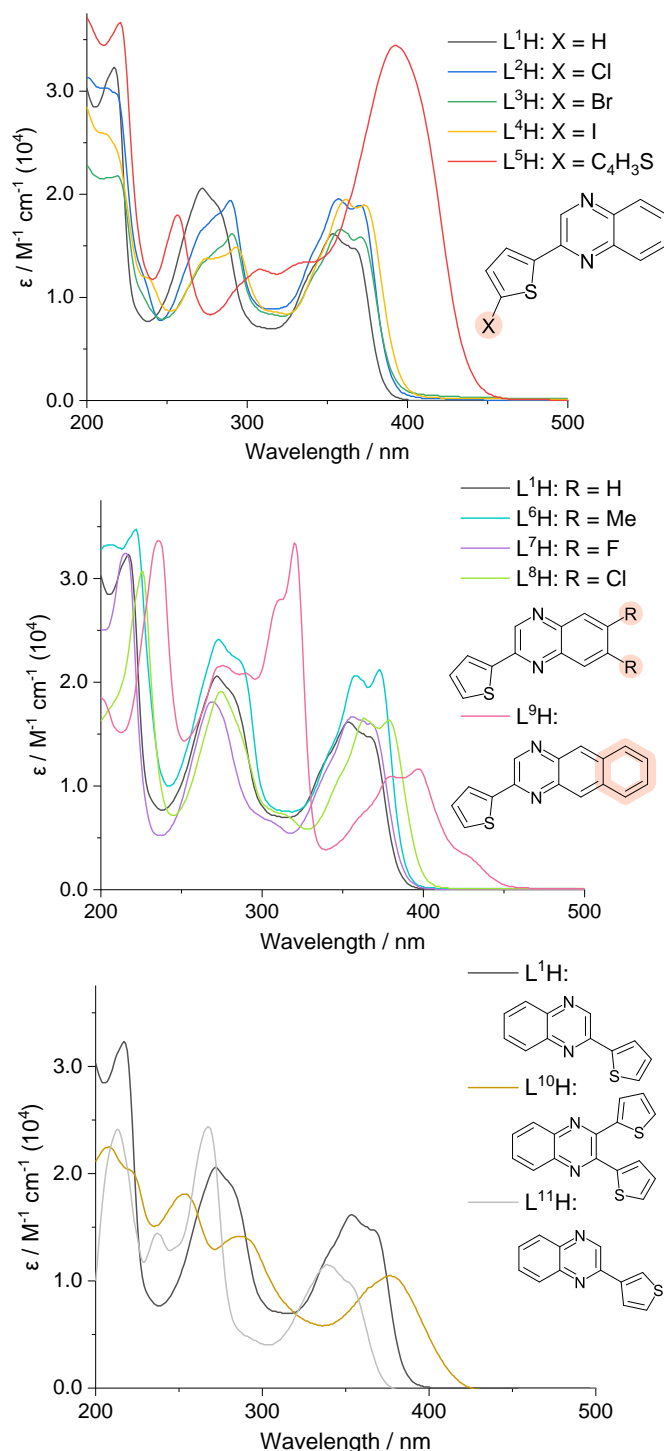
Figure 4.14: *UV-vis absorption spectra of* **L**$^{1-11}$**H** *(MeCN, 0.99 × 10^{-5} M, RT).*

The measured spectra demonstrated that the position and nature of the substituent greatly influenced the absorption properties of the compounds. Substitution of the thiophene subunit with a halogen atom (**L$^{2-4}$H**) or di-substitution of the quinoxaline backbone (**L$^{6-8}$H**) exhibited subtle changes in peak maxima. Fluctuations in ε values were also seen for all compounds, indicating that the probability of the transition greatly varied upon functionalisation. Comparisons between the two isomeric compounds (**L^{1}H** and **L^{11}H**) provided insight into the relative electronics, where a hypsochromic shift in λ_{max} was observed for the 3-substituted analogue in comparison with the 2-substituted compound. This offered insight into the importance of the linkage between the thiophene and quinoxaline, specifically in terms of the electronic properties. The longest λ_{max} was seen for **L^{9}H** (396 nm), where an additional ring system was fused to the quinoxaline backbone, compared to 353 nm for the unsubstituted compound. This peak was of relatively low intensity compared to the higher energy peak at 320 nm. However, a high intensity peak (ε = 3.4 × 10^4 M^{-1} cm^{-1}) at 392 nm was seen for **L^{5}H**, where the thienyl moiety incorporated another thiophene ring and thus extended the π-conjugated system. The intensity of this peak was attributed to the increased probability of a π→π* transition. In comparison, when a thiophene ring was added to the pyrazine sub-unit (**L^{10}H**), a lower ε value (1.0 × 10^4 M^{-1} cm^{-1}) at λ_{max} 378 nm was recorded. By altering the functionality at one end of the molecule, the overall absorption properties were influenced, as these types of compounds have an inbuilt donor-acceptor system. Previous studies have shown that charge transfer is observed from the thiophene ring donors to the quinoxaline acceptors,[12] therefore owing to the observation of lower energy absorption bands.[46]

All organic compounds were further analysed by steady state luminescence spectroscopy (**Figure 4.15**). The relative intensities and positions of the lowest energy peaks in the absorption profiles gives some indication of the magnitude of the HOMO-LUMO gap, which is reflected in the emission spectra.
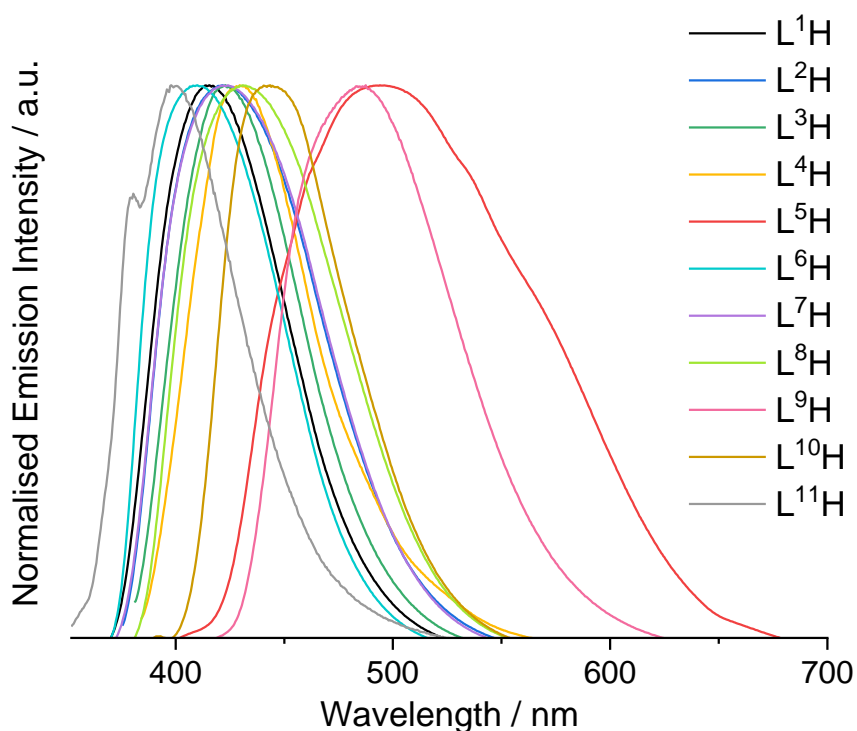
Figure 4.15: *Normalised steady-state emission spectra for all free ligands, **L$^{1-11}$H**, in aerated MeCN (10^{-5} M, RT, λ_{ex} = 350 nm).*

All compounds emitted light in the visible range between 410 – 491 nm from a $^1(\pi\rightarrow\pi^*)$ excited state. The observed trend was proportional to that seen in the corresponding absorption profiles, specifically for the lowest energy bands. The ligands with the longest λ_{max} value in the absorption profiles, **L^{5}H** and **L^{9}H**, displayed emission bands at 491 and 488 nm respectively. Notably, added conjugation resulted in longer λ_{em}, but **L^{5}H** displayed a much broader profile in comparison to **L^{9}H** since the absorption maxima at lower energy was of much higher intensity. Subtle tunability was achieved by altering the substituents at the thiophene ring or the quinoxaline – for example, the iodine-substituted ligand was red-shifted by 8 nm compared to the chlorine analogue, consistent with previous findings.[47] Quinoxaline functionalisation displayed more significant differences, where the dimethyl-substituted analogue showed a hypsochromic shift in emission (λ_{em} = 410 nm) when compared to the dichloro compound (λ_{em} = 431 nm). This suggested that the electronic nature of substituents at these positions resulted in deviations in emission properties from the original structure, offering more scope for tunability within a specific range.

L^{11}H was the most blue-shifted compound with emission at 401 nm, also displaying a shoulder peak – this was 15 nm blue-shifted when compared to **L^{1}H**, suggesting that the point of attachment also played a vital role in the electronic nature of the compounds.

Ligand	λ_{abs} / nm	λ_{em} / nm[a]	Φ_F[b]	τ_{obs} / ns[c]	$\Delta\lambda$ / nm[d]
L^{1}H	217, 272, 353, 368	416	0.035	0.59	56
L^{2}H	214, 289, 357, 369	422	0.050	0.60	59
L^{3}H	219, 290, 357, 370	423	0.036	0.46	60
L^{4}H	213, 275, 292, 361, 373	430	0.017	0.26	63
L^{5}H	221, 256, 307, 335, 392	491	0.264	2.68	99
L^{6}H	222, 273, 357, 373	410	0.047	0.24	45
L^{7}H	215, 268, 355, 367	424	0.058	0.54	63
L^{8}H	226, 274, 363, 378	431	0.060	0.71	61
L^{9}H	235, 275, 311, 320, 379, 396, 426	488	0.036	1.30	92
L^{10}H[d]	208, 252, 286, 378	444	0.190	0.26	66
L^{11}H	213, 237, 267, 339, 351	401	0.010	-	62

Table 4.6: *Photophysical properties of the free ligands, **L$^{1-11}$H**, in aerated MeCN solutions at room temperature (10^{-5} M). ^{a} λ_{ex} = 350-400 nm, relative to unique absorption spectra; ^{b} Quinine sulphate in 0.1M H$_2$SO$_4$ (Φ = 0.546)[48] used as standard for quantum yield determination, λ_{ex} = 350 nm. ^{c}Observed lifetimes, λ_{ex} = 295nm. ^{d}Stokes' shift; ^{e}Values are similar to previously reported data.[36,49]*

The photophysical properties of **L$^{1-11}$H** are tabulated in **Table 4.6**. All ligands expectedly displayed fluorescence lifetimes in the nanosecond domain, with the compounds containing an extended π-system exceeding 1 ns (**L^{5}H** and **L^{9}H**). Interestingly, observed lifetimes and quantum yields were reduced upon descending down the group for the halogenated compounds. This was

theorised to be the result of enhanced non-radiative processes, which in turn competes with fluorescence (radiative) decay. Previous studies have indicated that this is possible due to the presence of a heavy halogen atom. Further work must be undertaken to prove this in more detail (by direct measurement of the triplet state) but was not explored further in this study.
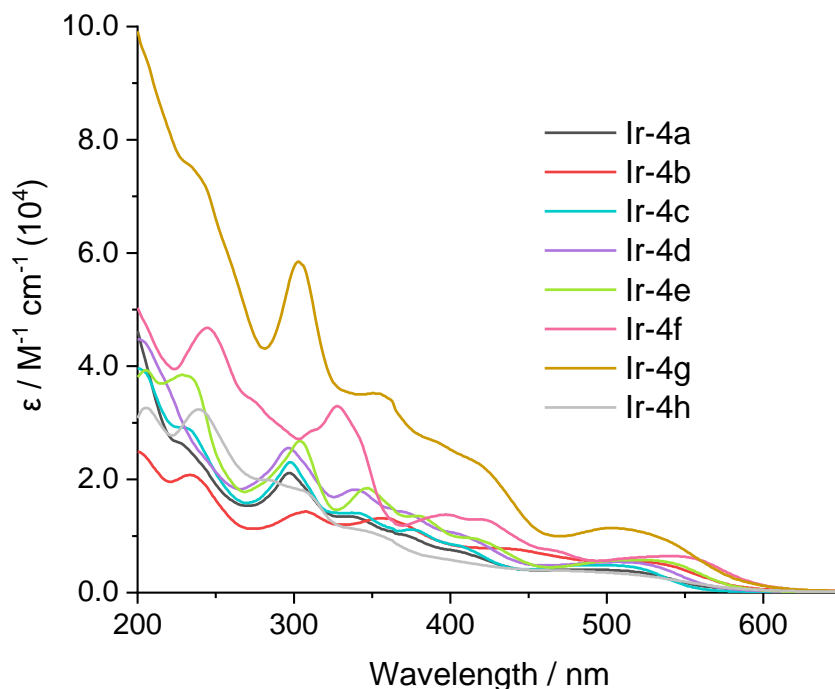
Figure 4.16: *UV-vis absorption spectra of the isolated cationic iridium complexes, [Ir(Lⁿ)₂(bpy)]PF₆ (MeCN, 0.99 × 10⁻⁵ M, RT).*

UV-vis absorption data for the complexes were also recorded in 10^{-5} M aerated acetonitrile solutions (**Figure 4.16**). All complexes absorbed light throughout the UV range as well as the visible range, with absorption bands spanning a large range of wavelengths. The peaks centred below 450 nm can be assigned to ligand-centred $^1(\pi \rightarrow \pi^*)$ transitions, due to relatively high molar extinction coefficients, similar to those seen for the free ligands. Characteristic broad peaks were seen within the range of 475 – 545 nm with relatively high ε values between 3900 and 11400 M^{-1} cm^{-1}. These peaks were attributed to spin-allowed ^{1}MLCT absorption features, but previous reports have shown that $^3(\pi \rightarrow \pi^*)$ transitions are also possible.[50] Weak spin-forbidden ^{3}MLCT bands are expected to be present due to efficient mixing as a result enhanced ISC due to the central iridium atom. However, it is not possible to resolve these two peaks due to the low intensity of the triplet band. The positions of the MLCT bands are relative to the nature of the cyclometallated ligands, where the most red-shifted assigned

[1]MLCT band was observed for **Ir-4f** (λ_{max} = 545 nm), with **Ir-4h** displaying the shortest wavelength peak (λ_{max} = 475 nm). Anderson *et al.* investigated Ru(II) complexes incorporating dpb (2,3-*bis*(2-pyridyl)benzoquinoxaline) ligands that alter the high energy MLCT states to produce compounds that absorb throughout the entirety of the visible range.[51] Low-lying π* states assist in the bathochromic shift in absorption wavelength, and the UV-vis spectra of the Ru(II) complexes displayed peaks that were attributed to the dpb moiety in MeCN at room temperature which approximates to that observed for **Ir-4f**.

Comparisons between the absorption profiles associated with the free ligands and their corresponding complexes provided insight into the effect on electronic behaviour upon complexation. An example is shown in **Figure 4.17**, where **L⁹H** and the corresponding complex (**Ir-4f**) are shown, where enhancements in ε values are observed and characteristic MLCT features were recognised.
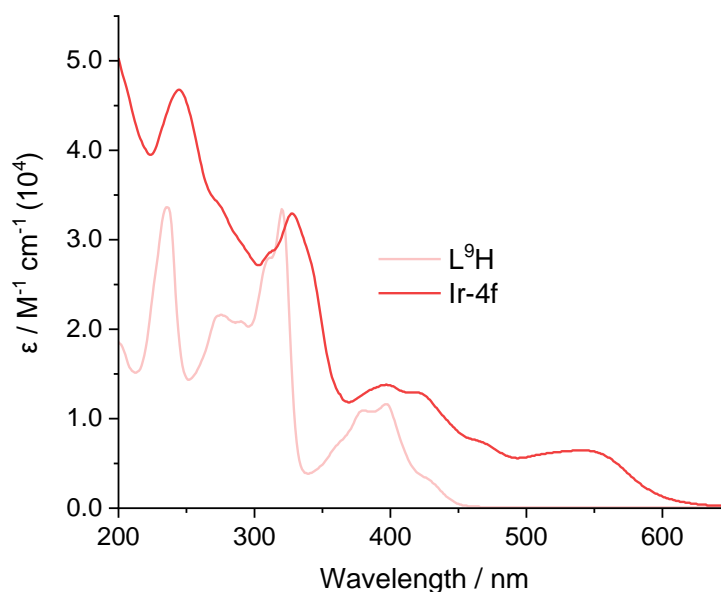
Figure 4.17: *Comparison of UV-vis spectra of **L⁹H** and **Ir-4f**. (MeCN, 0.99 × 10⁻⁵ M, RT).*

Steady state emission data was collected for all isolated iridium complexes (**Figure 4.18**). All complexes were shown to be deep-red emitters, with two approaching the NIR region. The complexes with the longest λ_{em} were **Ir-4b** (751 nm) and **Ir-4f** (749 nm). More subtle tunability over a range of 20 nm was seen between 665 and 685 nm, where the methylated quinoxaline ligand (**Ir-4c**) was the most blue-shifted and the complex containing two separate thiophene rings on the pyrazine ring (**Ir-4g**) was red-shifted.
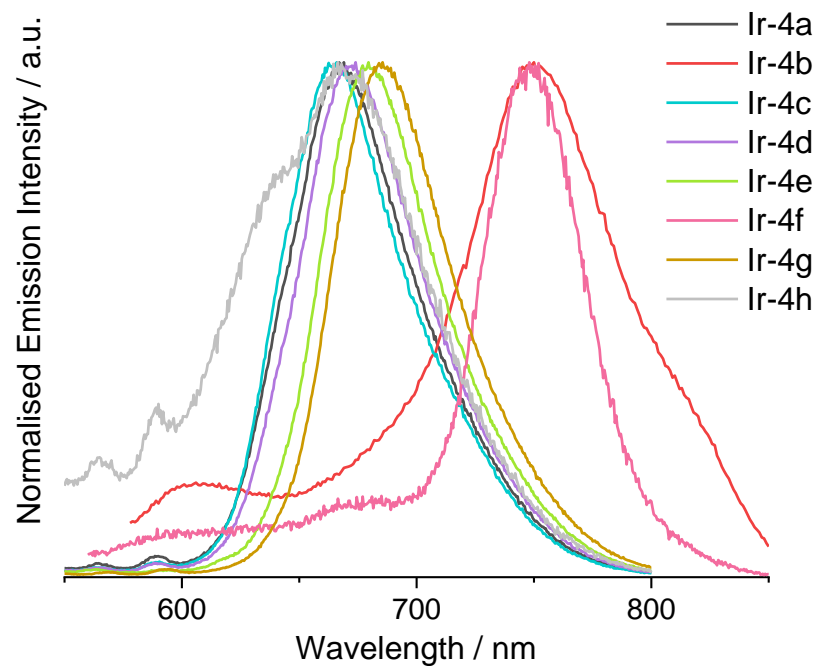
Figure 4.18: *Normalised emission profiles of all isolated complexes, where λ$_{ex}$ = λ$_{max}$ nm from the respective absorption spectra. Measured in aerated MeCN (10^{-5} M, RT),*
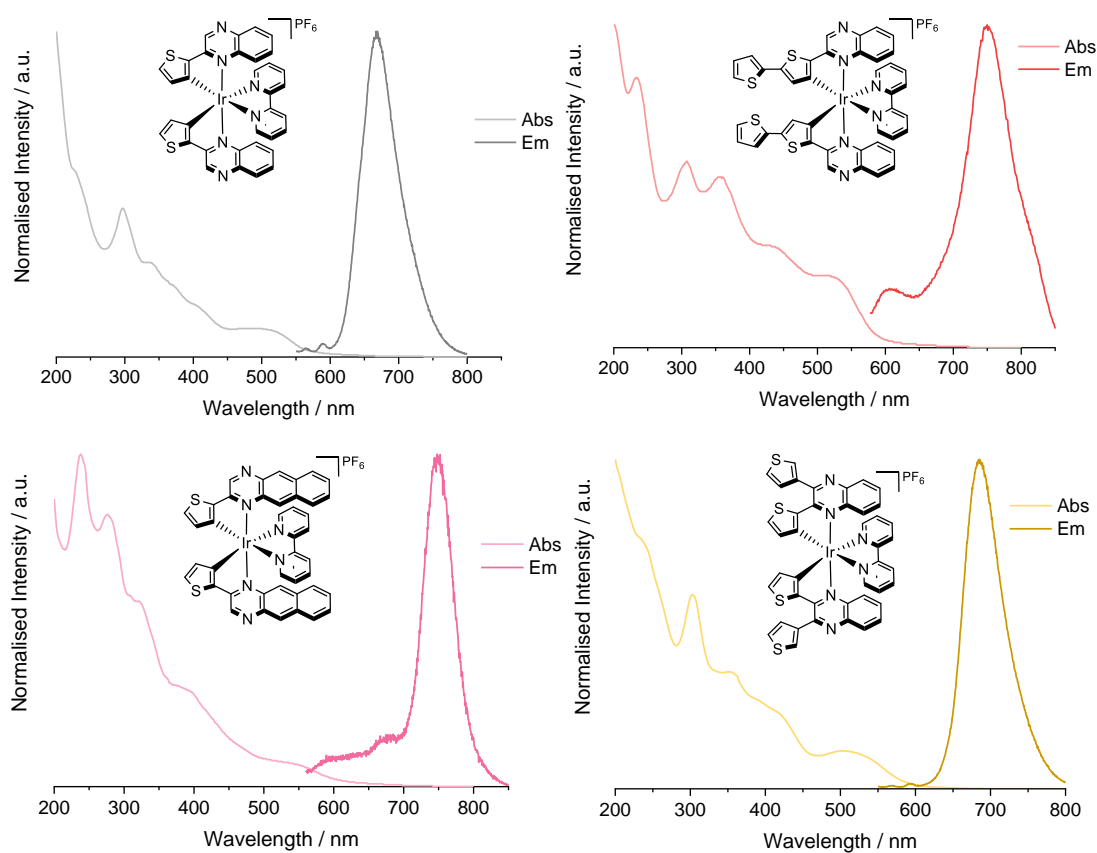
Figure 4.19: *Normalised absorption and emission spectra for selected complexes, demonstrating the Stokes' shifts.*

Figure 4.19 shows the absorption and emission profiles of some selected complexes, **Ir-4a**, **Ir4b**, **Ir4f** and **Ir4g**, demonstrating the magnitude of the observed Stokes' shifts. The largest shift was seen for **Ir-4b**, with a value of 219 nm. These shifts were characteristic of phosphorescent decay, as energy is lost *via* the enhancement of the ISC process.

The photophysical data of the iridium complexes is shown in **Table 4.7**. Emission was proposed to be from a ^{3}MLCT excited state due to efficient ISC from the ^{1}MLCT energy level and was reflected in the time-resolved luminescence measurements, where single exponential decay profiles were seen. All complexes displayed a significant enhancement in observed lifetimes compared to the free ligands, with lifetimes in the range of 95 – 241 ns. This was expected since the change in electron spin allows the electrons to remain in the excited state for a longer time period, in accordance with the spin-forbidden nature of the decay process. The longest lifetime was observed for **Ir-4d**, and **Ir-4f** displayed the shortest, which was attributed to the reduced radiative decay rate (k_r), where rapid depopulation of the excited state leads to shorter lifetimes.

Quantum yield values were measured for each of the complexes, using **[Ru(bpy)₃](PF₆)₂** in aerated acetonitrile solution as a standard (Φ = 0.016),[52] where calculated quantum yield values ranged between 0.26% and 0.57%. Red-shifted photoluminescence quantum yields diminished as a result of non-radiative decay pathways (such as internal conversion) dominating.[53] This value could not be determined for **Ir-4f**, as emission was very weak at λ_{ex} = 450 nm. Additionally, the value of **Ir-4b** is representative of the overall photoluminescence quantum yield, due to dual-emission being observed at shorter excitation wavelengths, where ligand-centred fluorescence can also be seen. In addition to the inherent issues arising from the reduced energy gap, NIR and deep-red shifted standards for quantum yield determination remain scarce, hence their discovery is an active area of research.[54] As a result, efficient deep-red and NIR transition metal-based phosphors remain as a challenge within this field, and since the emission peaks presented are within the deep-red region for these complexes, the limited efficiency is consistent with the literature.[55]

Complex	λ_{abs} / nm	λ_{em}/ nm[a]	λ_{em} 77K / nm[b]	Φ_P[c] (10⁻³)	τ_{obs}/ ns[d]	Stokes shift / nm	k_r / s⁻¹ (10⁴)	k_{nr} / s⁻¹ (10⁶)
Ir-4a	227, 297, 338, 371, 406, 485	668	648, 704 sh	4.0	192	183	2.08	5.19
Ir-4b	233, 307, 358, 441, 532	751	741, 734 sh,	3.1*	141	157	2.20	7.07
Ir-4c	228, 297, 337, 372, 406, 493	665	644, 669 sh, 705	5.7	203	172	2.81	4.90
Ir-4d	296, 337, 368, 406, 512	672	651, 705 sh	5.2	241	160	2.16	4.13
Ir-4e	205, 228, 303, 347, 375, 417, 525	680	664, 717 sh	5.1	209	155	2.44	4.76
Ir-4f	244, 327, 312, 397, 421, 545	749	739, 659	0.1[e]	95	204	-	-
Ir-4g	238, 303, 355, 425, 503	685	679, 737 sh	2.6	151	182	1.72	6.61
Ir-4h	205, 239, 284, 307, 348, 475	670	630, 668 sh	5.2	117	195	4.44	8.50

Table 4.7: *Photophysical properties of the complexes in aerated MeCN (10⁻⁵ M, RT). [a]λ_{ex} = 475 – 545 nm, relative to unique low-energy bands in the absorption spectra (bold λ_{abs} values); [b]77K measurements in 3:1 EtOH:MeOH glass; [c]**[Ru(bpy)₃](PF₆)₂** in MeCN (Φ = 0.016)[52] used as standard for quantum yield determination, λ_{ex} = 450 nm; [d]λ_{ex} = 295nm or 456 nm. [e]Emission was too weak to detect. * **Ir-4b**: At λ_{ex} = 450 nm, there may be some ligand-centred emission.*

Low temperature (77 K) emission spectra were collected for all iridium complexes in EtOH/MeOH glass (3:1). Some of these are shown in **Figure 4.20**. Data was collected for the same solutions at ambient temperature to draw direct comparisons, ensuring that temperature was the only variable to be considered. For all complexes, the relative intensities of the low energy ³MLCT emission peaks exhibit a remarkable increase in emission intensity, therefore displaying enhanced phosphorescence efficiency. A hypsochromic shift in emission wavelength was also presented, with structural features appearing to be more prominent due to enhanced vibronic coupling. These features are attributed to

the reduction in thermal deactivation pathways, where even the ligand-centred triplet state can be accessed at low temperatures. Shoulder peaks can be observed for all complexes, suggesting that phosphorescence occurs from a mixture of ^{3}MLCT and $^3\pi$-π* states.[56,57] This was particularly prevalent in **Ir-4f**, indicating that the ligand-centred states greatly contributed to the emission.
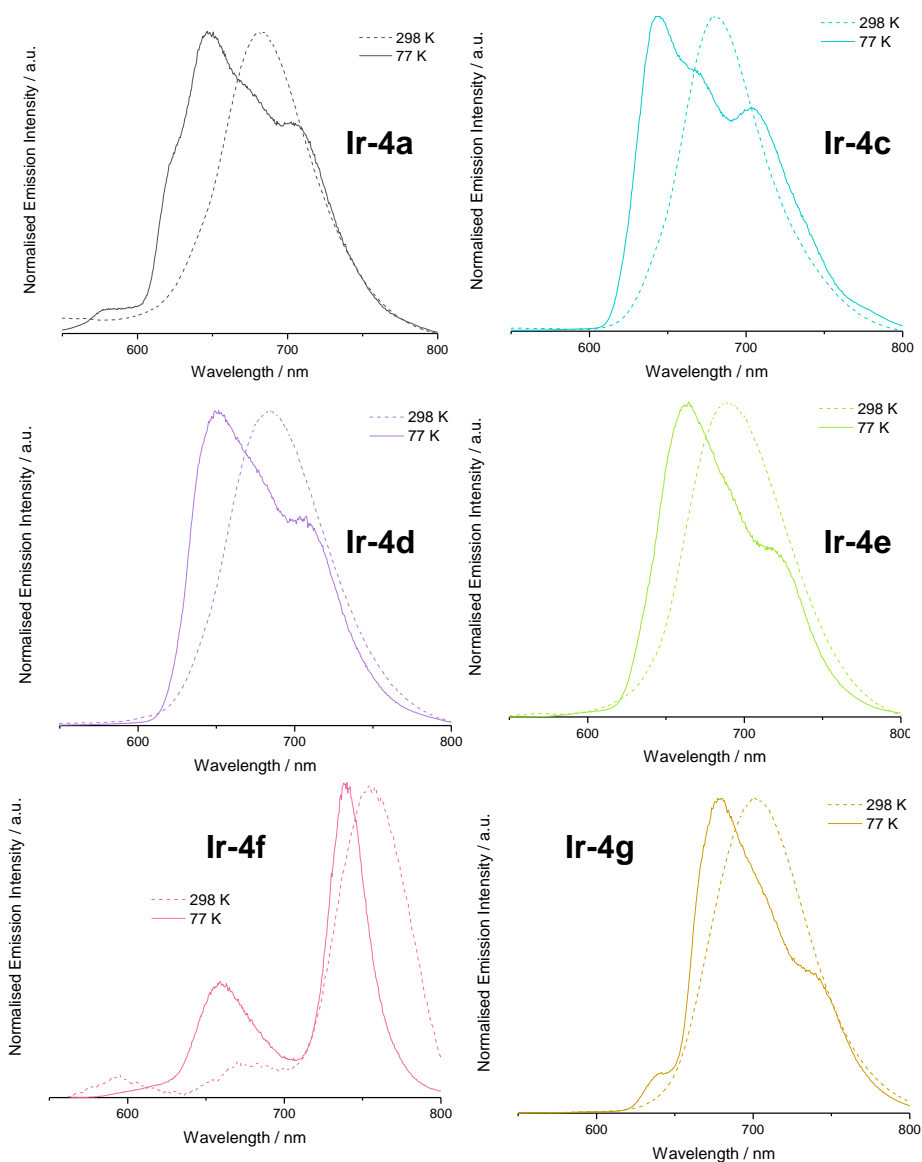
Figure 4.20: *Normalised room temperature (298 K, dashed lines) and low temperature (77 K, solid lines) emission spectra for some complexes in EtOH:MeOH glass (3:1). λ_{ex} = λ_{max} (from absorption spectra).*

4.3.5: Solvatochromic Studies

Emission and absorption spectra of the unsubstituted complex, **Ir-4a**, were measured in various solvents to observe solvatochromic effects. Thiophenes

have been proven to display interesting solvatochromic behaviour due to the intramolecular charge transfer mechanisms observed in D-π-A systems.[58] By selecting solvents that span a range of polarities, changes in the UV-vis and emission spectra were measured. The UV-vis absorption spectra for **Ir-4a** remained relatively consistent throughout, and there appeared to be no correlation with regards to polarity of the solvent and peak positions. This is common, since absorption spectra are less responsive to differences in solvent polarity than luminescence studies, due to the very short timescale in which absorption occurs.[58]

However, solvatochromic behaviour was much more noticeable in the emission spectra of **Ir-4a** (**Figure 4.21**). This was expected, since molecules in the excited state interact with the solvent environment to a higher degree, where excited states may be stabilised by polar solvents due to a larger dipole moment when compared with the ground state.[59] Positive solvatochromism was observed, as peaks shifted to a higher λ_{em} upon increasing polarity of the solvent. Resultantly, an increase in the rate of non-radiative decay pathways such as internal conversion occurs due to the reduced energy gap, resulting in the most red-shifted peak (in methanol) displaying a low-intensity feature.[60] The peak for the compound in the most polar solvent (MeOH) was present at a wavelength 25 nm longer (686 nm) than the peak in the relatively apolar solvent (toluene) (661 nm).
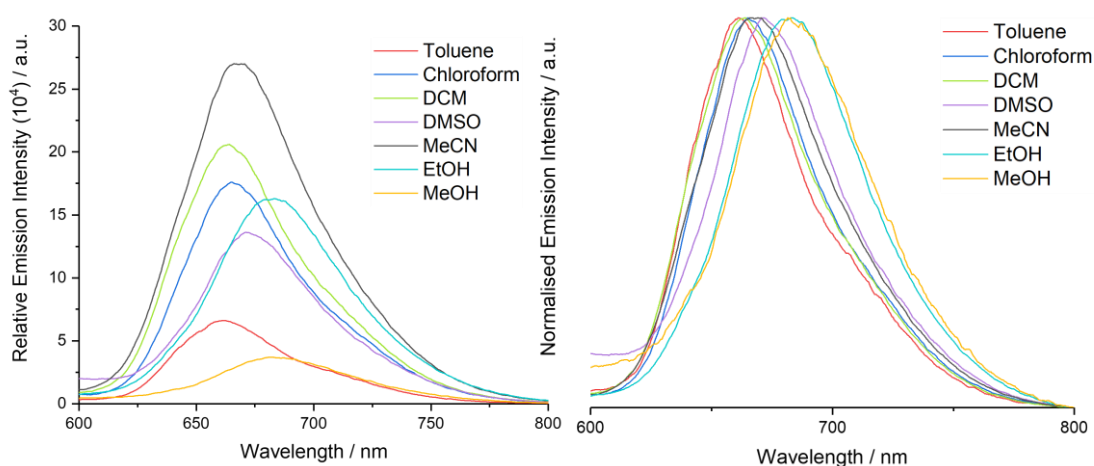
Figure 4.21: *Relative emission spectra (left) and normalised emission spectra (right) of **Ir-4a** in various solvents. λ_{ex} = 485 nm, 10^{-5}M.*

4.4: Conclusions

This chapter of work sought out to design and synthesise *bis*-cylometallated cationic iridium complexes as potential deep-red phosphors. In total, eight complexes were successfully isolated, all employing thienyl-quinoxaline cyclometallating ligands. Photophysical measurements showed that subtle tunability was achieved by altering the type of substituent on the quinoxaline backbone. More prominent tunability was feasible, accessing the deep-red region by increasing conjugation on the ligands, where emission up to 751 nm was achieved. The emissive state was not purely ^{3}MLCT in character by observations from the low temperature emission spectra, indicating a high degree of mixing between excited states.

4.5: Experimental

4.5.1: General Considerations

All commercially available reagents were used without further purification, and all reactions employed vacuum line and Schlenk techniques. ^{1}H, ^{13}C{^{1}H} and ^{19}F{^{1}H} NMR spectra were recorded on NMR-FT Bruker 500, 400 and 300 MHz spectrometers in the appropriate solvents (CDCl$_3$, (CD$_3$)$_2$CO, CD$_3$CN or DMSO-d_6), where chemical shift (δ) positions (ppm) were determined relative to TMS and residual solvent peaks[61] through digital locking. High resolution mass spectra were obtained by staff at Cardiff University using a Waters Xevo G2-XS QTof spectrometer, and IR spectra were recorded on a Shimadzu IRAffinty-1 FTIR spectrometer. UV-vis spectroscopy studies were performed on 10^{-5} M MeCN solutions a Shimadzu UV-1800 spectrophotometer. The 10^{-5} M samples were prepared by dilution of 10^{-3} M bulk stock solutions. Upon sonication in an ultrasonic bath, the samples were inspected to ensure that solute was fully dissolved. Luminescence data was acquired for MeCN solutions of the samples using a JobinYvon-Horiba Fluorolog spectrometer fitted with a JY TBX picosecond single-photon detection module. Time-resolved measurements were recorded using a Nano-LED pulsed laser source configured for 295 or 459 nm output, operating at 1 MHz. Time-resolved measurements were recorded using the JobinYvon-Horiba FluoroHub single photon counting module and the data was resolved using the DAS6 deconvolution software.

4.5.2: X-Ray Crystallography

Crystals of **Ir-4c** were grown from a mixture of DCM and Et$_2$O. Suitable crystals were mounted on a MITIGEN holder in oil on a Rigaku FRE+ diffractometer equipped with VHF Varimax confocal mirrors and an AFC12 goniometer and HyPix 6000 detector.[62] The crystals were kept at 100(2)K. Using Olex2,[63] the structure was solved with the ShelXT[64] structure solution program, using the Intrinsic Phasing Solution method. The models were refined with version 2018/2 of ShelXL[65] by use of Least Squares minimisation. All non-H atoms were refined anisotropically and idealised hydrogen atom positions were calculated using the riding hydrogen model.

4.5.3: Preparation of Organic Ligands and Precursors

Synthesis of 2-bromo-1-(thiophen-2-yl)ethan-1-one

A simple bromination reaction took place, where dioxane dibromide (1.10 g, 8.05mmol) in a solution of 1,4-dioxane and diethyl ether (1:1, 40 mL) was added dropwise to 2-acetyl thiophene (0.92 g, 7.31 mmol) in the same solvent mixture over 2 h whilst stirring under air at room temperature. The solution was added to water and extracted with diethyl ether. The combined organic layers were dried over $MgSO_4$, and the solvent was removed *in vacuo* to yield a brown/yellow oil (1.49 g, 99.3%). ^{1}H NMR (400 MHz, $CDCl_3$) δ_H = 7.80 (dd, $^3J_{HH}$ = 3.8, $^4J_{HH}$ = 1.1 Hz, 1H), 7.71 (dd, $^3J_{HH}$ = 5.0, $^4J_{HH}$ = 1.1 Hz, 1H), 7.16 (dd, $^3J_{HH}$ = 4.9, 3.9 Hz, 1H), 4.36 (s, 2H) ppm. The data is consistent with literature findings.[66]

Synthesis of 2-bromo-1-(5-bromothiophen-2-yl)ethan-1-one

Prepared similarly from 2-acetyl-5-bromothiophene (1.08 g, 5.28 mmol) and dioxane dibromide (1.43 g, 5.81 mmol) to give the product as an off-white solid (1.39 g, 92.6%). ^{1}H NMR (400 MHz, $CDCl_3$) δ_H = 7.55 (d, $^3J_{HH}$ = 4.1 Hz, 1H), 7.14 (d, $^3J_{HH}$ = 4.1 Hz, 1H), 4.28 (s, 2H) ppm.

Synthesis of 2-bromo-1-(5-chlorothiophen-2-yl)ethan-1-one

Prepared similarly from 2-acetyl-5-chlorothiophene (1.01 g, 6.26 mmol) and dioxane dibromide (1.71 g, 6.89 mmol) to give the product as an off-white solid (1.06 g, 70.7%). ^{1}H NMR (400 MHz, $CDCl_3$) δ_H = 7.60 (d, $^3J_{HH}$ = 4.1 Hz, 1H), 7.00 (d, $^3J_{HH}$ = 4.1 Hz, 1H), 4.28 (s, 2H) ppm.

Synthesis of 2-bromo-1-(5-iodothiophen-2-yl)ethan-1-one

A modified bromination method was adopted, where 2-acetyl-5-iodothiophene (1.00 g, 3.97 mmol) was dissolved in glacial acetic acid (15 mL) and dioxane dibromide (0.984 g, 3.97 mmol) in acetic acid (6 mL) was added dropwise. The mixture was stirred at room temperature under an inert nitrogen atmosphere in the absence of light for 24 h. The solvent was removed *in vacuo*, ensuring that the temperature remained under 40°C. The residue was dissolved in dichloromethane and washed with saturated aqueous $NaHCO_3$, water and saturated aqueous NaCl. The combined organic layers were dried over $MgSO_4$, then the solvent was removed *in vacuo* to give the product as a brown solid

(1.23 g, 93.3%). ^{1}H NMR (500 MHz, CDCl$_3$) δ_H = 7.42 (d, $^3J_{HH}$ = 4.0 Hz, 1H), 7.34 (d, $^3J_{HH}$ = 4.0 Hz, 1H), 4.28 (s, 2H) ppm. ^{13}C{^{1}H} NMR (126 MHz, CDCl$_3$) δ_C = 183.1, 146.6, 138.5, 134.4, 87.4, 30.2 ppm. HRMS (EI+): found m/z 329.8209, calc'd m/z 329.8211 for C$_6$H$_4$OSBr^{127}I. FTIR (solid, cm^{-1}) (ATR) v_{max}: 3084, 3073, 2996, 2949, 1663, 1638, 1510, 1396, 1389, 1312, 1271, 1215, 1192, 1146, 1067, 1034, 1015, 959, 924, 903, 870, 795, 762, 739, 679, 662, 638, 603, 596, 573, 540, 474, 444, 415.

Synthesis of 1-([2,2'-bithiophen]-5-yl)-2-bromoethan-1-one

Prepared similarly to 2-bromo-1-(thiophen-2-yl)ethan-1-one from 5-acetyl-2,2'-bithienyl (122 mg, 0.585 mmol) and dioxane dibromide (174 mg, 0.702 mmol) to give the crude product. The pure product was obtained by column chromatography (SiO$_2$) where the band eluted with 99:1 DCM:MeOH to give the product as a dark yellow solid (118 mg, 70.0%). ^{1}H NMR (400 MHz, CDCl$_3$) δ_H = 7.70 (d, $^3J_{HH}$ = 4.0 Hz, 1H), 7.37 – 7.34 (m, 2H), 7.20 (d, $^3J_{HH}$ = 4.0 Hz, 1H), 7.07 (dd, $^3J_{HH}$ = 5.0, 3.7 Hz, 1H), 4.34 (s, 2H) ppm. ^{13}C{^{1}H} NMR (101 MHz, CDCl$_3$) δ_C = 184.2, 147.5, 138.6, 136.1, 134.6, 128.5, 127.2, 126.3, 124.5, 30.2 ppm. HRMS (CI): found m/z 285.9115, calc'd m/z 285.91162 for C$_{10}$H$_7$O^{79}Br^{32}S$_2$ [M]$^+$. FTIR (solid, cm^{-1}) (ATR) v_{max}: 3084, 3034, 2922, 2853, 1665, 1639, 1504, 1443, 1422, 1358, 1310, 1273, 1204, 1192, 1159, 1115, 1065, 1051, 1034, 972, 934, 887, 839, 799, 750, 741, 702, 640, 610, 592, 542, 488, 446.

Synthesis of 2-bromo-1-(thiophen-3-yl)ethan-1-one

The brominated compound was prepared *via* a modified synthetic method. 3-acetylthiophene (804 mg, 6.372 mmol) in a solution of 1,4-dioxane and diethyl ether (1:1, 40 mL) was heated to 70°C under an inert nitrogen atmosphere whilst stirring. Dioxane dibromide (1.73 g, 7.01 mmol) in the same solvent mixture (40 mL) was added dropwise over 2 h. The reaction mixture was heated to reflux for a further 24 h. The mixture was monitored by thin-layer chromatography (DCM, SiO$_2$). Upon cooling to room temperature, the mixture was washed with distilled water (30 mL) and extracted with diethyl ether (3 × 25 mL). The combined organic layers were dried over MgSO$_4$ and the solvent was removed *in vacuo* giving rise to the crude product. Purification took place by column chromatography (DCM → DCM:MeOH, 9:1) where the pure product was obtained as an off-white crystalline solid (752 mg, 57.5%). ^{1}H NMR (400 MHz,

CDCl$_3$) δ_H = 8.18 (dd, $^4J_{HH}$ = 2.9, 1.3 Hz, 1H), 7.58 (dd, $^3J_{HH}$ = 5.1, $^4J_{HH}$ = 1.3 Hz, 1H), 7.36 (dd, $^3J_{HH}$ = 5.1, $^4J_{HH}$ =2.9 Hz, 1H), 4.34 (s, 2H). ^{13}C{^{1}H} NMR (101 MHz, CDCl$_3$) δ_C = 185.7, 138.9, 133.9, 127.4, 127.0, 31.7 ppm. The data was consistent with literature findings.[67]

Synthesis of 2-(thiophen-2-yl)quinoxaline *(L^{1}H)*

2-bromo-1-(thiophen-2-yl)ethan-1-one (1.49 g, 7.26 mmol) and 1,2-phenylenediamine (0.86 g, 7.99 mmol) were heated to reflux in ethanol (10 mL) for 24 h under an inert nitrogen atmosphere. The formation of a precipitate took place upon cooling the mixture to room temperature, and the resultant suspension was filtered under reduced pressure. This was washed with a small amount of cold ethanol to give the product as an orange solid (0.33 g, 21.6%). ^{1}H NMR (400 MHz, CDCl$_3$) δ_H = 9.24 (s, 1H), 8.09 – 8.04 (m, 2H), 7.86 (dd, $^3J_{HH}$ = 3.7, $^4J_{HH}$ = 1.1 Hz, 1H), 7.77 – 7.67 (m, 2H), 7.55 (dd, $^3J_{HH}$ = 5.0, $^4J_{HH}$ = 1.1 Hz, 1H), 7.21 (dd, $^3J_{HH}$ = 5.0, 3.7 Hz, 1H) ppm. ^{13}C{^{1}H} NMR (101 MHz, CDCl$_3$) δ_C = 147.5, 142.4, 142.3, 142.2, 141.5, 130.6, 130.0, 129.4, 129.3, 129.3, 128.6, 127.1 ppm. HRMS (EI+): found *m/z* 212.0411, calc'd *m/z* 212.0408 for C$_{12}$H$_8$N$_2$S [M]$^+$. UV-vis (MeCN) λ_{max} ($\varepsilon \times 10^4$ / L mol^{-1} cm^{-1}): 217 (3.2), 272 (2.1), 353 (1.6), 368 (1.5) nm. FTIR (solid, cm^{-1}) (ATR) v_{max}: 3121, 3059, 2363, 2330, 1734, 1545, 1491, 1427, 1319, 1238, 1207, 1134, 1125, 1074, 1053, 997, 941, 926, 866, 851, 758, 721, 677, 613, 583, 567, 542, 471, 419, 407. The data was consistent with literature findings.[68,69]

Synthesis of 2-(5-chlorothiophen-2-yl)quinoxaline *(L^{2}H)*

Prepared similarly from 2-bromo-1-(5-chlorothiophen-2-yl)ethan-1-one (976 mg, 4.07 mmol) and 1,2-phenylenediamine (485 mg, 4.48 mmol) to give the product as an orange solid (164 mg, 16.3%). ^{1}H NMR (400 MHz, CDCl$_3$) δ_H = 9.17 (s, 1H), 8.10 – 7.99 (m, 2H), 7.79 – 7.67 (m, 2H), 7.63 (d, $^3J_{HH}$ = 4.0 Hz, 1H), 7.02 (d, $^3J_{HH}$ = 4.0 Hz, 1H) ppm. ^{13}C{^{1}H} NMR (101 MHz, CDCl$_3$) δ_C = 146.7, 142.2, 141.6, 141.3, 141.2, 135.2, 130.8, 129.6, 129.3, 129.2, 127.8, 126.3 ppm. HRMS (EI+): found *m/z* 246.0018, calc'd *m/z* 246.0018 for C$_{12}$H$_7$ClN$_2$S [M]$^+$. UV-vis (MeCN) λ_{max} ($\varepsilon \times 10^4$ / L mol^{-1} cm^{-1}): 214 (3.0), 289 (1.9) 357 (2.0), 369 (1.9) nm. FTIR (solid, cm^{-1}) (ATR) v_{max}: 3098, 3077, 3007, 2369, 2345, 2322, 1751, 1611, 1547, 1487, 1466, 1431, 1364, 1348, 1323,

1312, 1300, 1225, 1213, 1198, 1123, 1082, 1022, 966, 935, 908, 856, 799, 768, 754, 675, 669, 615, 588, 567, 536, 482, 467, 455, 413.

Synthesis of 2-(5-bromothiophen-2-yl)quinoxaline *(L³H)*

Prepared similarly from 2-bromo-1-(5-bromothiophen-2-yl)ethan-1-one (1.37 g, 4.81 mmol) and 1,2-phenylenediamine (0.57 g, 5.29 mmol) to give the product as a brown crystalline solid (0.52 g, 37.4%). ^{1}H NMR (400 MHz, CDCl$_3$) δ_H = 9.15 (s, 1H), 8.09 – 7.99 (m, 2H), 7.79 – 7.66 (m, 2H), 7.57 (d, $^3J_{HH}$ = 3.9 Hz, 1H), 7.15 (d, $^3J_{HH}$ = 3.9 Hz, 1H) ppm. ^{13}C{^{1}H} NMR (101 MHz, CDCl$_3$) δ_C = 146.6, 144.1, 142.2, 141.6, 141.3, 131.5, 130.8, 129.6, 129.3, 129.2, 127.0, 117.9 ppm. HRMS (ES+): found *m/z* 290.9599, calc'd *m/z* 290.9592 for C$_{12}$H$_8$BrN$_2$S [M + H]$^+$. UV-vis (MeCN) λ_{max} ($\epsilon \times 10^4$ / L mol^{-1} cm^{-1}): 219 (2.2), 290 (1.6), 357 (1.7), 370 (1.6) nm. FTIR (solid, cm^{-1}) (ATR) v_{max}: 3310, 3084, 3073, 2997, 2949, 1661, 1510, 1389, 1312, 1287, 1215, 1190, 1146, 1067, 959, 924, 903, 870, 795, 762, 739, 662, 638, 573, 540.

Synthesis of 2-(5-iodothiophen-2-yl)quinoxaline *(L⁴H)*

Prepared similarly from 2-bromo-1-(5-iodothiophen-2-yl)ethan-1-one (1.22 g, 3.69 mmol) and 1,2-phenylenediamine (399 mg, 3.69 mmol) to give the product as an off-white solid (540 mg, 43.3%). ^{1}H NMR (400 MHz, CDCl$_3$) δ_H = 9.16 (s, 1H), 8.10 – 8.00 (m, 2H), 7.79 – 7.67 (m, 2H), 7.49 (d, $^3J_{HH}$ = 3.9 Hz, 1H), 7.35 (d, $^3J_{HH}$ = 3.9 Hz, 1H) ppm. ^{13}C{^{1}H} NMR (126 MHz, CDCl$_3$) δ_C = 148.4, 146.4, 142.2, 141.6, 141.5, 138.5, 130.8, 129.6, 129.3, 129.3, 128.0, 79.8 ppm. HRMS (ES+): found *m/z* 338.9456, calc'd *m/z* 338.9453 for C$_{12}$H$_8$^{127}IN$_2$S [M + H]$^+$. UV-vis (MeCN) λ_{max} ($\epsilon \times 10^4$ / L mol^{-1} cm^{-1}): 213 (2.6), 275 (1.4), 292 (1.5), 361 (1.9), 373 (1.9) nm. FTIR (solid, cm^{-1}) (ATR) v_{max}: 3080, 3048, 3013, 1609, 1572, 1545, 1491, 1420, 1402, 1323, 1312, 1292, 1225, 1200, 1128, 1063, 1018, 999, 951, 932, 910, 881, 874, 856, 802, 797, 783, 768, 756, 739, 673, 613, 573, 538, 490, 469, 411.

Synthesis of 2-([2,2'-bithiophen]-5-yl)quinoxaline *(L⁵H)*

Prepared similarly from 1-([2,2'-bithiophen]-5-yl)-2-bromoethan-1-one (112 mg, 0.388 mmol) and 1,2-phenylenediamine (50.3 mg, 0.465 mmol) to give the product as a yellow solid (83.2 mg, 72.5%). ^{1}H NMR (500 MHz, CDCl$_3$) δ_H = 9.22 (s, 1H), 8.11 – 8.05 (m, 2H), 7.78 (d, $^3J_{HH}$ = 3.8 Hz, 1H), 7.78 – 7.73 (m,

1H), 7.70 (ddd, $^3J_{HH}$ = 8.4, 6.9, $^4J_{HH}$ = 1.4 Hz, 1H), 7.34 (dd, $^3J_{HH}$ = 3.6, $^4J_{HH}$ = 1.1 Hz, 1H), 7.30 (dd, $^3J_{HH}$ = 5.1, $^4J_{HH}$ = 1.1 Hz, 1H), 7.27 (d, $^3J_{HH}$ = 3.9 Hz, 1H), 7.08 (dd, $^3J_{HH}$ = 5.1, 3.6 Hz, 1H) ppm. $^{13}C\{^1H\}$ NMR (126 MHz, CDCl$_3$) δ_C = 147.3, 142.3, 142.1, 141.7, 141.1, 140.6, 137.1, 130.8, 129.4, 129.2, 129.1, 128.3, 128.0, 125.7, 125.0, 124.9 ppm. HRMS (ES+): found *m/z* 295.0358, calc'd *m/z* 295.0364 for $C_{16}H_{11}N_2S_2$ [M + H]$^+$. UV-vis (MeCN) λ_{max} ($\varepsilon \times 10^4$ / L mol^{-1} cm^{-1}): 221 (3.7), 256 (1.8), 307 (1.3), 335 (1.3), 392 (3.4) nm. FTIR (solid, cm^{-1}) (ATR) v_{max} / cm^{-1}: 3100, 3082, 3063, 3046, 2918, 2849, 1609, 1571, 1553, 1537, 1514, 1489, 1468, 1445, 1423, 1341, 1317, 1227, 1202, 1132, 1119, 1070, 1053, 1013, 999, 949, 939, 930, 887, 858, 837, 812, 791, 783, 752, 681, 675, 611, 569, 550, 480, 455, 407.

Synthesis of 6,7-dimethyl-2-(thiophen-2-yl)quinoxaline (*L^{6}H*)

Prepared similarly from 2-bromo-1-(thiophen-2-yl)ethan-1-one (500 mg, 2.44 mmol) and 4,5-dimethyl-*o*-phenylenediamine (365 mg, 2.68 mmol) to give the product as a yellow solid (270 mg, 46.1%). ^1H NMR (400 MHz, CDCl$_3$) δ_H = 9.14 (s, 1H), 7.83 (s, 1H), 7.81 (dd, $^3J_{HH}$ = 3.7, $^4J_{HH}$ = 1.0 Hz, 1H), 7.79 (s, 1H), 7.51 (dd, $^3J_{HH}$ = 5.0, $^4J_{HH}$ = 1.0 Hz, 1H), 7.19 (dd, $^3J_{HH}$ = 5.0, 3.7 Hz, 1H), 2.48 (s, 6H) ppm. $^{13}C\{^1H\}$ NMR (101 MHz, CDCl$_3$) δ_C = 146.7, 142.8, 141.2, 141.1, 141.1, 140.4, 139.9, 129.3, 128.5, 128.3, 126.4, 20.5, 20.4 ppm. UV-vis (MeCN) λ_{max} ($\varepsilon \times 10^4$ / L mol^{-1} cm^{-1}): 222 (3.5), 273 (2.4), 357 (2.1), 373 (2.1) nm. FTIR (solid, cm^{-1}) (ATR) v_{max}: 3069, 3034, 1541, 1487, 1422, 1317, 1213, 1082, 1067, 1024, 1005, 930, 872, 847, 704, 638, 621, 494, 428. The data was consistent with literature findings.[70,71]

Synthesis of 6,7-difluoro-2-(thiophen-2-yl)quinoxaline (*L^{7}H*)

Prepared similarly from 2-bromo-1-(thiophen-2-yl)ethan-1-one (250 mg, 1.22 mmol) and 4,5-difluoro-*o*-phenylenediamine (193 mg, 1.34 mmol) to give the product as an off-white solid (176 mg, 57.9%). ^1H NMR (400 MHz, CDCl$_3$) δ_H = 9.20 (s, 1H), 7.86 (dd, $^3J_{HH}$ = 3.7, $^4J_{HH}$ = 1.1 Hz, 1H), 7.82 (dd, $^3J_{HF}$ = 8.4, $^4J_{HF}$ = 1.9 Hz, 1H), 7.80 (dd, $^3J_{HF}$ = 8.3, $^4J_{HF}$ = 1.6 Hz, 1H), 7.57 (dd, $^3J_{HH}$ = 5.0, $^4J_{HH}$ = 1.1 Hz, 1H), 7.21 (dd, $^3J_{HH}$ = 5.0, 3.7 Hz, 1H) ppm. $^{13}C\{^1H\}$ NMR (101 MHz, CDCl$_3$) δ_C = 152.9 (dd, $^1J_{CF}$ = 256.6, $^2J_{CF}$ = 16.1 Hz), 151.9 (dd, $^1J_{CF}$ = 256.0, $^2J_{CF}$ = 16.0 Hz), 147.7, 142.2, 141.7, 139.7 (dd, $^3J_{CF}$ = 11.1, $^4J_{CF}$ = 1.2 Hz), 138.6 (dd, $^3J_{CF}$ = 10.6, $^4J_{CF}$ = 1.1 Hz), 130.4, 128.7, 127.4, 115.1 (dd, $^2J_{CF}$ =

17.5, $^3J_{CF}$ = 1.9 Hz), 114.9 (dd, $^2J_{CF}$ = 17.5, $^3J_{CF}$ = 1.6 Hz) ppm. $^{19}F\{^1H\}$ NMR (376 MHz, CDCl$_3$) δ_F = −129.3 (d, $^3J_{FF}$ = 21.1 Hz), −130.9 (d, $^3J_{FF}$ = 21.4 Hz).[72] HRMS (ES+): found m/z 249.0293, calc'd m/z 249.0298 for C$_{12}$H$_7$N$_2$F$_2$S [M + H]$^+$. UV-vis (MeCN) λ_{max} ($\varepsilon \times 10^4$ / L mol^{-1} cm^{-1}): 215 (3.2), 268 (1.8), 355 (1.7), 367 (1.6) nm. FTIR (solid, cm^{-1}) (ATR) v_{max}: 3117, 3024, 1803, 1626, 1547, 1499, 1418, 1358, 1335, 1314, 1233, 1223, 1209, 1165, 1124, 1119, 1051, 999, 934, 920, 907, 864, 849, 833, 756, 731, 706, 646, 619, 611, 567, 486, 444.

Synthesis of 6,7-dichloro-2-(thiophen-2-yl)quinoxaline (*L^{8}H*)

Prepared similarly from 2-bromo-1-(thiophen-2-yl)ethan-1-one (250 mg, 1.22 mmol) and 4,5-dichloro-*o*-phenylenediamine (237 mg, 1.34 mmol) to give the product as an off-white solid (140 mg, 40.8%). ^{1}H NMR (400 MHz, CDCl$_3$) δ_H = 9.20 (s, 1H), 8.19 (s, 1H), 8.17 (s, 1H), 7.87 (dd, $^3J_{HH}$ = 3.8, $^4J_{HH}$ = 1.0 Hz, 1H), 7.59 (dd, $^3J_{HH}$ = 5.0, $^4J_{HH}$ = 1.1 Hz, 1H), 7.22 (dd, $^3J_{HH}$ = 5.0, 3.8 Hz, 1H) ppm. $^{13}C\{^1H\}$ NMR (101 MHz, CDCl$_3$) δ_C = 148.4, 143.2, 141.7, 141.1, 140.1, 135.2, 133.7, 130.9, 129.9, 129.8, 128.8, 127.9 ppm. HRMS (ES+): found m/z 280.9695, calc'd m/z 280.9707 for C$_{12}$H$_7$N$_2$SCl$_2$ [M + H]$^+$. UV-vis (MeCN) λ_{max} ($\varepsilon \times 10^4$ / L mol^{-1} cm^{-1}): 226 (3.1), 274 (1.9), 363 (1.7), 378 (1.6) nm.

Synthesis of 2-(thiophen-2-yl)benzo[*g*]quinoxaline (*L^{9}H*)

Prepared similarly from 2-bromo-1-(thiophen-2-yl)ethan-1-one (250 mg, 1.22 mmol) and 2,3-diaminonaphthalene (212 mg, 1.34 mmol), but instead of filtering the pure product, the yield was maximised by removing the solvent *in vacuo* to obtain the crude product. This was then purified by column chromatography (SiO$_2$, DCM), where the product eluted as an orange band. The solvent was removed *in vacuo* to give the product as an orange solid (158 mg, 49.4%). ^{1}H NMR (400 MHz, CDCl$_3$) δ_H = 9.31 (s, 1H), 8.64 (s, 1H), 8.63 (s, 1H), 8.11 (dd, $^3J_{HH}$ = 4.6, $^4J_{HH}$ = 0.9 Hz, 1H), 8.09 (dd, $^3J_{HH}$ = 4.6, $^4J_{HH}$ = 0.9 Hz, 1H), 7.93 (dd, $^3J_{HH}$ = 3.7, $^4J_{HH}$ = 1.1 Hz, 1H), 7.60 (dd, $^3J_{HH}$ = 5.1, $^4J_{HH}$ = 1.1 Hz, 1H), 7.59 – 7.56 (m, 2H), 7.25 (dd, $^3J_{HH}$ = 5.0, 3.8 Hz, 1H) ppm. $^{13}C\{^1H\}$ NMR (101 MHz, CDCl$_3$) δ_C = 147.5, 143.6, 142.8, 138.7, 138.1, 134.5, 133.6, 130.5, 128.7, 128.7, 128.5, 127.8, 127.7, 127.5, 127.1, 126.8 ppm. HRMS (ES+): found m/z 263.0632, calc'd m/z 263.0643 for C$_{16}$H$_{11}$N$_2$S [M + H]$^+$. UV-vis (MeCN) λ_{max} ($\varepsilon \times 10^4$ / L mol^{-1} cm^{-1}): 235 (3.4), 275 (2.2), 311 (2.8), 320 (3.3), 379 (1.1), 396 (1.2), 426 (0.3) nm. FTIR (solid, cm^{-1}) (ATR) v_{max}: 3049, 2955, 2924, 2853,

1719, 1570, 1553, 1526, 1456, 1425, 1408, 1360, 1339, 1317, 1304, 1271, 1260, 1244, 1223, 1171, 1163, 1113, 1080, 1063, 995, 933, 912, 874, 849, 743, 700, 637, 608, 573, 561, 492, 469, 424.

Synthesis of 2,3-di(thiophen-2-yl)quinoxaline *(L¹⁰H)*

2,2'-thenil (100 mg, 0.450 mmol) and 1,2-phenylenediamine (53.5 mg, 0.495 mmol) were dissolved in ethanol (15 mL). A catalytic amount of acetic acid (0.5 mL) was added and the reaction mixture was heated to reflux and stirred for 24 h under an inert nitrogen atmosphere. Upon cooling to room temperature, the solvent was removed *in vacuo*, and the crude product was dissolved in dichloromethane and washed with 0.1M HCl (2 × 10 mL). The combined organic layers were dried over MgSO$_4$ and the solvent was removed *in vacuo* to give the product as a pale yellow crystalline solid (125 mg, 94.5%). ^{1}H NMR (400 MHz, CDCl$_3$) δ_H = 8.08 (dd, $^3J_{HH}$ = 6.3, $^4J_{HH}$ = 3.5 Hz, 1H), 7.72 (dd, $^3J_{HH}$ = 6.4, $^4J_{HH}$ = 3.4 Hz, 1H), 7.50 (dd, $^3J_{HH}$ = 5.0, $^4J_{HH}$ = 0.8 Hz, 1H), 7.26 (d, $^3J_{HH}$ = 3.7 Hz, 1H), 7.05 (dd, $^3J_{HH}$ = 4.8, 3.9 Hz, 1H) ppm. UV-vis (MeCN) λ_{max} (ε × 10^4 / L mol^{-1} cm^{-1}): 208 (2.3), 252 (1.8), 286 (1.4), 378 (1.0) nm. The data was consistent with literature findings.[73]

Synthesis of 2-(thiophen-3-yl)quinoxaline *(L¹¹H)*

The ligand was prepared similarly to **L¹H** (initial method) with slight modifications, where 2-bromo-1-(thiophen-3-yl)ethan-1-one (728 mg, 3.55 mmol) and 1,2-phenylenediamine (406 mg, 3.76 mmol) were dissolved in ethanol (40 mL) and heated to reflux under an inert nitrogen atmosphere for 24 h. The mixture was cooled to room temperature and the crude product was extracted with DCM (3 × 20 mL) and washed with distilled water (30 mL). The combined organic layers were dried over MgSO$_4$ and the solvent was removed *in vacuo*. Purification took place using column chromatography (DCM → DCM:MeOH 9:1, SiO$_2$) to obtain the pure product as a dark brown solid (619 mg, 82.1%). ^{1}H NMR (400 MHz, CDCl$_3$) δ_H = 9.24 (s, 1H), 8.16 (dd, $^4J_{HH}$ = 2.9, 1.3 Hz, 1H), 8.09 (ddd, $^3J_{HH}$ = 5.8, 5.4, $^4J_{HH}$ = 1.6 Hz, 2H), 7.92 (dd, $^3J_{HH}$ = 5.1, $^4J_{HH}$ = 1.3 Hz, 1H), 7.69 – 7.80 (m, 2H), 7.50 (dd, $^3J_{HH}$ = 5.1, $^4J_{HH}$ = 2.9 Hz, 1H) ppm. ^{13}C{^{1}H} NMR (126 MHz, CDCl$_3$) δ_C = 148.0, 143.3, 142.3, 141.3, 139.5, 130.4, 129.4, 129.3, 129.1, 127.2, 126.5, 126.0 ppm. UV-vis (MeCN) λ_{max} (ε ×

10^4 / L mol^{-1} cm^{-1}): 213 (2.4), 237 (1.4), 267 (2.4), 339 (1.2), 351 (1.0) nm. The data was consistent with literature findings.[74]

4.5.4: Preparation of Inorganic Complexes

General procedure for the synthesis of $[(Ir(L^n)_2(\mu\text{-}Cl))_2]$

The chloride-bridged dimer intermediates were synthesised according to the Nonoyama route.[75] IrCl$_3$.xH$_2$O (1.0 eq.) and the free ligand, **L^{n}H** (2.0 eq.) were dissolved in 2-methoxyethanol and distilled water (3:1, 10 – 20 mL) and the mixture was heated to reflux under an inert nitrogen atmosphere whilst stirring for 48 h. The reaction mixture was then cooled to room temperature, and precipitates formed upon the addition of distilled water (20 – 30 mL). The solids were collected by filtration under reduced pressure and washed with water (5 – 10 mL). The crude product was dissolved in dichloromethane and filtered under suction to remove any insoluble side-products, the solvent was removed *in vacuo* to give the products as brown/red solids (37.4 – 91.4%), which were used in subsequent steps without further purification or characterisation.

Synthesis of $[Ir(L^1)_2(bpy)][PF_6]$ *(Ir-4a)*

$[(Ir(L^1)_2(\mu\text{-}Cl))_2]$ (52.6 mg, 0.405 mmol) and 2,2'-bipyridine (14.5 mg, 0.930 mmol) were dissolved in chloroform (10 mL) and the solution was heated to reflux for 24 h under an inert nitrogen atmosphere. The reaction mixture was cooled to room temperature and the solvent was removed *in vacuo*. The crude solid was then purified by column chromatography (MeCN:H$_2$O:KNO$_3$ (aq. sat.) (14:2:1), SiO$_2$), where the red band was collected. The solvent was removed *in vacuo* and the product was left to dry in a heated oven at ~60°C for 16 h. The product was dissolved in acetonitrile, and the insoluble salts were filtered off under suction. A saturated aqueous solution of NH$_4$PF$_6$ was added to the filtrate and stirred for 15 min to ensure that all of the complex existed purely as a PF$_6$ salt. The solvent was removed *in vacuo*, and the solid was washed with distilled water to, once again, remove excess insoluble inorganic salts. The crude product was recrystallised from dichloromethane and diethyl ether to give the pure product as a red solid (10.2 mg, 13.9%). ^{1}H NMR (500 MHz, CDCl$_3$) δ_H = 9.16 (s, 2H), 8.56 (d, $^3J_{HH}$ = 8.2 Hz, 2H), 8.15 (*app.* td, $^3J_{HH}$ = 8.0, $^4J_{HH}$ = 1.6 Hz, 2H), 8.02 (dd, $^3J_{HH}$ = 8.3, $^4J_{HH}$ = 1.4 Hz, 2H), 7.88 (dd, $^3J_{HH}$ = 5.5, $^4J_{HH}$ = 0.9 Hz,

2H), 7.58 – 7.54 (m, 4H), 7.54 (d, $^3J_{HH}$ = 4.7 Hz, 2H), 7.17 (ddd, $^3J_{HH}$ = 8.6, 7.0, $^4J_{HH}$ = 1.5 Hz, 2H), 6.81 (dd, $^3J_{HH}$ = 8.8, $^4J_{HH}$ = 0.8 Hz, 2H), 6.24 (dd, $^3J_{HH}$ = 11.2, 5.0 Hz, 2H) ppm. $^{13}C\{^1H\}$ NMR (126 MHz, CDCl$_3$) δ$_C$ = 160.2, 158.6, 156.2, 148.7, 142.2, 141.9, 141.2, 140.8, 137.9, 135.2, 132.9, 132.8, 131.2, 129.2, 128.7, 125.9, 121.8 ppm. $^{19}F\{^1H\}$ NMR (376 MHz, CDCl$_3$) δ$_F$ = −73.06 (d, $^1J_{PF}$ = 710.4 Hz) ppm. HRMS (ES+): found *m/z* 769.0957, calc'd *m/z* 769.0953 for C$_{34}$H$_{22}$N$_6$S$_2$^{191}Ir [M − PF$_6$]$^+$. UV-vis (MeCN) λ$_{max}$ (ε × 10^4 / L mol^{-1} cm^{-1}): 227 (2.6), 297 (2.1), 338 (1.3), 371 (1.0), 406 (0.7), 485 (0.4) nm. FTIR (solid, cm$^{−1}$) (ATR) *v*$_{max}$: 2959, 2922, 2853, 1537, 1499, 1447, 1429, 1389, 1260, 1061, 1018, 881, 839, 795, 756, 733, 633, 500.

Synthesis of [Ir(L^5)$_2$(bpy)][PF$_6$] *(Ir-4b)*

Prepared similarly from **[(Ir(L^5)$_2$(*μ*-Cl))$_2$]** (20.7 mg, 0.013 mmol) and 2,2'-bipyridine (4.57 mg, 0.029 mmol) to give the product as a red solid (9.4 mg, 34.2%). ^{1}H NMR (500 MHz, CDCl$_3$) δ$_H$ = 9.10 (s, 2H), 8.58 (d, $^3J_{HH}$ = 8.1 Hz, 2H), 8.17 (*app.* td, $^3J_{HH}$ = 8.1, $^4J_{HH}$ =1.6 Hz, 2H), 8.07 (dd, $^3J_{HH}$ = 5.5, $^4J_{HH}$ = 0.9 Hz, 2H), 8.02 (dd, $^3J_{HH}$ = 8.2, $^4J_{HH}$ = 1.4 Hz, 2H), 7.60 – 7.50 (m, 4H), 7.25 (dd, $^3J_{HH}$ = 5.1 $^4J_{HH}$ = 1.1 Hz, 2H), 7.21 (dd, $^3J_{HH}$ = 3.7, $^4J_{HH}$ = 1.1 Hz, 2H), 7.15 (ddd, $^3J_{HH}$ = 8.6, 7.1, $^4J_{HH}$ = 1.5 Hz, 2H), 6.99 (dd, $^3J_{HH}$ = 5.1, 3.7 Hz, 2H), 6.77 (d, $^3J_{HH}$ = 8.1 Hz, 2H), 6.32 (s, 2H) ppm. HRMS (ES+): found *m/z* 935.0718, calc'd *m/z* 935.0731 for C$_{42}$H$_{26}$N$_6$S$_4$^{193}Ir [M − PF$_6$]$^+$. UV-vis (MeCN) λ$_{max}$ (ε × 10^4 / L mol^{-1} cm^{-1}): 233 (2.1), 307 (1.4), 358 (1.3), 438 (0.8), 515 (0.6) nm. FTIR (solid, cm$^{−1}$) (ATR) *v*$_{max}$: 2961, 2849, 1701, 1533, 1499, 1439, 1387, 1260, 1084, 1015, 837, 797, 775, 700, 557, 474.

Synthesis of [Ir(L^6)$_2$(bpy)][PF$_6$] *(Ir-4c)*

Prepared similarly from **[(Ir(L^6)$_2$(*μ*-Cl))$_2$]** (67.0 mg, 0.052 mmol) and 2,2'-bipyridine (18.5 mg, 0.119 mmol) to give the product as a red solid (15.2 mg, 30.2%). ^{1}H NMR (500 MHz, CDCl$_3$) δ$_H$ = 9.05 (s, 2H), 8.66 (d, $^3J_{HH}$ = 8.1 Hz, 2H), 8.17 (*app.* td, $^3J_{HH}$ = 8.0, $^4J_{HH}$ = 1.4 Hz, 2H), 7.92 (dd, $^3J_{HH}$ = 5.3, $^4J_{HH}$ = 0.7 Hz, 2H), 7.75 (s, 1H), 7.57 – 7.51 (m, 2H), 7.47 (d, $^3J_{HH}$ = 4.7 Hz, 2H), 6.54 (s, 2H), 6.23 (d, $^3J_{HH}$ = 4.7 Hz, 2H), 2.32 (s, 6H), 1.80 (s, 6H) ppm. $^{13}C\{^1H\}$ NMR (126 MHz, CDCl$_3$) δ$_C$ = 159.1, 157.1, 156.3, 148.9, 143.8, 141.1, 140.9, 140.5, 139.9, 139.7, 137.8, 134.0, 132.7, 130.2, 128.4, 125.9, 121.7, 20.6, 19.7 ppm. $^{19}F\{^1H\}$ NMR (376 MHz, CDCl$_3$) δ$_F$ = −73.03 (d, $^1J_{PF}$ = 712.0 Hz) ppm. HRMS

(ES+): found m/z 825.1589, calc'd m/z 825.1579 for $C_{38}H_{30}N_6S_2{}^{191}Ir$ [M − PF$_6$]$^+$. UV-vis (MeCN) λ_{max} ($\varepsilon \times 10^4$ / L mol^{-1} cm^{-1}): 229 (2.9), 298 (2.3), 342 (1.4), 375 (1.1), 406 (0.8), 496 (0.5) nm. FTIR (solid, cm^{-1}) (ATR) v_{max}: 3094, 2959, 2920, 2853, 1703, 1603, 1524, 1495, 1447, 1404, 1339, 1260, 1219, 1092, 1057, 1018, 833, 795, 767, 733, 662, 555, 465, 457, 419.

Synthesis of [Ir(L⁷)₂(bpy)][PF₆] *(Ir-4d)*

Prepared similarly from **[(Ir(L⁷)₂(*µ*-Cl))₂]** (70.0 mg, 0.048 mmol) and 2,2'-bipyridine (17.4 mg, 0.112 mmol) to give the product as a red solid (24.3 mg, 25.3%). ^{1}H NMR (500 MHz, CD$_3$CN) δ_H = 9.24 (s, 2H), 8.38 (d, $^3J_{HH}$ = 8.2 Hz, 2H), 8.12 (*app.* td, $^3J_{HH}$ = 7.9, $^4J_{HH}$ = 1.5 Hz, 2H), 7.96 (dd, $^3J_{HH}$ = 5.5, $^4J_{HH}$ = 0.9 Hz, 2H), 7.90 (dd, $^3J_{HF}$ = 10.5, $^4J_{HF}$ = 8.4 Hz, 2H), 7.72 (d, $^3J_{HH}$ = 4.8 Hz, 2H), 7.62 (ddd, $^3J_{HH}$ = 7.6, 5.6, $^4J_{HH}$ = 1.2 Hz, 2H), 6.62 (dd, $^3J_{HF}$ = 12.5, $^4J_{HF}$ = 7.8 Hz, 2H), 6.43 (d, $^3J_{HH}$ = 4.8 Hz, 2H) ppm. ^{19}F{^{1}H} NMR (376 MHz, CDCl$_3$) δ_F = −73.02 (d, $^1J_{PF}$ = 713.2 Hz), −123.59 (d, $^3J_{FF}$ = 22.2 Hz), −130.41 (d, $^3J_{FF}$ = 22.2 Hz) ppm. ^{13}C{^{1}H} NMR (126 MHz, CD$_3$CN) δ_C = 161.6, 159.9, 156.7, 153.7 (dd, $^1J_{CF}$ = 255.0, $^2J_{CF}$ = 15.4 Hz), 151.3 (dd, $^1J_{CF}$ = 253.4, $^2J_{CF}$ =15.4 Hz), 150.6, 144.5, 141.4, 140.5 (dd, $^3J_{CF}$ = 10.4, $^4J_{CF}$ = 1.2 Hz), 139.0, 138.8 (dd, $^3J_{CF}$ = 10.5, $^4J_{CF}$ = 1.4 Hz), 137.2, 133.8, 130.2, 126.1, 118.0 (dd, $^2J_{CF}$ = 17.9, $^3J_{CF}$ = 2.1 Hz) 110.5 (d, $^2J_{CF}$ = 22.8 Hz) ppm. HRMS (ES+): found m/z 843.0607, calc'd m/z 843.0600 for $C_{34}H_{18}N_6F_4S_2{}^{193}Ir$ [M − PF$_6$]$^+$. UV-vis (MeCN) λ_{max} ($\varepsilon \times 10^4$ / L mol^{-1} cm^{-1}): 297 (2.6), 340 (1.8), 369 (1.4), 404 (1.0), 509 (0.5) nm. FTIR (solid, cm^{-1}) (ATR) v_{max}: 3073, 2920, 2849, 1539, 1506, 1445, 1404, 1246, 1051, 835, 764, 733, 723, 613, 555, 509, 471.

Synthesis of [Ir(L⁸)₂(bpy)][PF₆] *(Ir-4e)*

Prepared similarly from **[(Ir(L⁸)₂(*µ*-Cl))₂]** (48.3 mg, 0.031 mmol) and 2,2'-bipyridine (11.0 mg, 0.070 mmol) to give the product as a red solid (25.2 mg, 78.0%). ^{1}H NMR (500 MHz, CDCl$_3$) δ_H = 9.14 (s, 2H), 8.66 (d, $^3J_{HH}$ = 8.2 Hz, 2H), 8.24 (*app.* td, $^3J_{HH}$ = 8.0, $^4J_{HH}$ = 1.6 Hz, 2H), 8.12 (s, 2H), 7.85 (dd, $^3J_{HH}$ = 5.6, $^4J_{HH}$ = 0.9 Hz, 2H), 7.68 − 7.64 (m, 2H), 7.65 (d, $^3J_{HH}$ = 4.8 Hz, 2H), 6.85 (s, 2H), 6.28 (d, $^3J_{HH}$ = 4.7 Hz, 2H) ppm. ^{13}C{^{1}H} NMR (126 MHz, CD$_3$CN) δ_C = 162.2, 161.4, 156.7, 150.8, 145.5, 141.8, 141.6, 140.5, 139.0, 138.2, 136.5, 133.9, 132.8, 132.0, 130.4, 126.1, 124.4 ppm. ^{19}F{^{1}H} NMR (376 MHz, CDCl$_3$) δ_F = −73.11 (d, $^1J_{PF}$ = 713.0 Hz) ppm. HRMS (ES+): found m/z 904.9404, calc'd

m/z 904.9394 for $C_{34}H_{18}N_6S_2{}^{35}Cl_4{}^{191}Ir$ [M – PF_6]$^+$. UV-vis (MeCN) λ_{max} ($\varepsilon \times 10^4$ / L mol^{-1} cm^{-1}): 205 (3.9), 228 (3.8), 303 (2.7), 347 (1.8), 379 (1.4), 416 (0.9), 523 (0.6) nm. FTIR (solid, cm^{-1}) (ATR) v_{max}: 3084, 2918, 2849, 1701, 1599, 1566, 1522, 1477, 1443, 1396, 1184, 1152, 1115, 1065, 833, 766, 691, 650, 555, 430, 420.

Synthesis of [Ir(L⁹)₂(bpy)][PF₆] *(Ir-4f)*

Prepared similarly from **[(Ir(L⁹)₂(*μ*-Cl))₂]** (77.4 mg, 0.052 mmol) and 2,2'-bipyridine (17.7 mg, 0.114 mmol) to give the product as a dark red solid (19.1 mg, 18.2%). ^{1}H NMR (500 MHz, CD$_3$CN) δ_H = 9.29 (s, 2H), 8.60 (s, 2H), 8.25 (d, $^3J_{HH}$ = 8.0 Hz, 2H), 8.18 (d, $^3J_{HH}$ = 4.7 Hz, 2H), 8.11 (*app.* t, $^3J_{HH}$ = 7.2 Hz, 2H), 8.04 (d, $^3J_{HH}$ = 8.4 Hz, 2H), 7.76 – 7.70 (m, 2H), 7.69 (d, $^3J_{HH}$ = 4.7 Hz, 2H), 7.56 – 7.46 (m, 2H), 7.46 – 7.38 (m, 2H), 7.37 (s, 2H), 6.96 (d, $^3J_{HH}$ = 8.4 Hz, 2H), 6.50 (d, $^3J_{HH}$ = 4.7 Hz, 2H) ppm. ^{13}C{^{1}H} NMR (126 MHz, CD$_3$CN) δ_C = 162.5, 162.0, 156.7, 151.1, 145.1, 141.3, 139.9, 139.2, 138.5, 137.7, 135.0, 134.2, 133.2, 130.5, 130.1, 129.3, 129.1, 128.2, 128.0, 125.6, 121.0 ppm. ^{19}F{^{1}H} NMR (376 MHz, CD$_3$CN) δ_F = −72.97 (d, $^1J_{PF}$ = 706.1 Hz) ppm. HRMS (ES+): found *m/z* 871.1296, calc'd *m/z* 871.1290 for $C_{42}H_{26}N_6S_2{}^{193}Ir$ [M – PF_6]$^+$. UV-vis (MeCN) λ_{max} ($\varepsilon \times 10^4$ / L mol^{-1} cm^{-1}): 244 (4.7), 312 (2.9), 327 (3.3), 397 (1.4), 420 (1.3), 545 (0.6) nm. FTIR (solid, cm^{-1}) (ATR) v_{max}: 3096, 3055, 2916, 2849, 1705, 1601, 1557, 1479, 1456, 1443, 1427, 1375, 1344, 1323, 1314, 1184, 1163, 1152, 1138, 1119, 1053, 833, 766, 743, 733, 660, 555, 469, 444, 420.

Synthesis of [Ir(L¹⁰)₂(bpy)][PF₆] *(Ir-4g)*

Prepared similarly from **[(Ir(L¹⁰)₂(*μ*-Cl))₂]** (74.2 mg, 0.050 mmol) and 2,2'-bipyridine (19.0 mg, 0.105 mmol) to give the product as a dark red solid (55.8 mg, 56.7%). ^{1}H NMR (500 MHz, CDCl$_3$) δ_H = 8.55 (d, $^3J_{HH}$ = 7.6 Hz, 2H), 8.20 (*app.* t, $^3J_{HH}$ = 7.4 Hz, 2H), 8.16 (d, $^3J_{HH}$ = 5.2 Hz, 2H), 7.98 (dd, $^3J_{HH}$ = 8.3, $^4J_{HH}$ = 1.1 Hz, 2H), 7.72 (dd, $^3J_{HH}$ = 5.1, $^4J_{HH}$ = 1.1 Hz, 2H), 7.70 – 7.64 (m, 2H), 7.62 (dd, $^3J_{HH}$ = 3.6, $^4J_{HH}$ = 1.1 Hz, 2H), 7.54 (ddd, $^3J_{HH}$ = 8.1, 7.0, $^4J_{HH}$ = 1.0 Hz, 2H), 7.31 (dd, $^3J_{HH}$ = 5.1, 3.6 Hz, 2H), 7.30 (d, $^3J_{HH}$ = 4.9 Hz, 2H), 7.14 (ddd, $^3J_{HH}$ = 8.4, 7.0, $^4J_{HH}$ = 1.3 Hz, 2H), 6.97 (d, $^3J_{HH}$ = 8.5 Hz, 2H), 6.20 (d, $^3J_{HH}$ = 4.9 Hz, 2H) ppm. ^{13}C{^{1}H} NMR (126 MHz, CDCl$_3$) δ_C = 160.7, 160.3, 156.1, 148.2, 146.7, 141.3, 141.2, 139.7, 138.5, 137.4, 135.8, 132.5, 132.3, 131.0, 130.9,

129.7, 129.5, 128.6, 127.7, 125.7, 122.2 ppm. $^{19}F\{^1H\}$ NMR (376 MHz, CDCl$_3$) δ_F = −73.05 (d, $^1J_{PF}$ = 712.6 Hz) ppm. HRMS (ES+): found m/z 933.0696, calc'd m/z 933.0708 for C$_{42}$H$_{26}$N$_6$S$_4$^{191}Ir [M − PF$_6$]$^+$. UV-vis (MeCN) λ_{max} ($\varepsilon \times 10^4$ / L mol^{-1} cm^{-1}): 238 (7.4), 303 (5.8), 355 (3.5), 425 (2.1), 507 (1.1) nm. FTIR (solid, cm^{-1}) (ATR) ν_{max}: 3094, 3061, 2918, 1603, 1506, 1483, 1472, 1441, 1429, 1416, 1300, 1323, 1231, 1144, 1130, 1076, 1051, 1032, 833, 762, 721, 637, 584, 555, 498, 457, 426, 420, 417.

Synthesis of [Ir(L^{11})$_2$(bpy)][PF$_6$] *(Ir-4h)*

The complex was prepared *via* an adapted method, where 2-ethoxyethanol (20 mL) was used as the solvent. **[(Ir(L^{11})$_2$(μ-Cl))$_2$]** (44.0 mg, 0.034 mmol) and 2,2'-bipyridine (11.2 mg, 0.071 mmol) were used, to give the product as a red solid (13.0 mg, 20.9%). ^1H NMR (500 MHz, (CD$_3$)$_2$CO) δ_H = 9.60 (s, 2H), 8.73 (d, $^3J_{HH}$ = 8.2 Hz, 2H), 8.32 (dd, $^3J_{HH}$ = 8.0, $^4J_{HH}$ = 1.5 Hz, 2H), 8.21 (ddd, $^3J_{HH}$ = 5.7, $^4J_{HH}$ = 1.5, 0.5 Hz, 2H), 8.04 (dd, $^3J_{HH}$ = 8.3, $^4J_{HH}$ = 1.4 Hz, 2H), 8.03 (d, $^3J_{HH}$ = 5.2 Hz, 2H), 7.84 (m, 2H), 7.65 (m, 2H), 7.49 (d, $^3J_{HH}$ = 5.2 Hz, 2H), 7.29 (m, 2H), 7.04 (dd, $^3J_{HH}$ = 8.9, $^4J_{HH}$ = 0.9 Hz, 2H) ppm. $^{19}F\{^1H\}$ NMR (376 MHz, (CD$_3$)$_2$CO) δ_F = −72.52 (d, $^1J_{PF}$ = 707.4 Hz). HRMS (ES+): found m/z 771.0980, calc'd m/z 771.0977 for C$_{34}$H$_{22}$N$_6$S$_2$Ir [M − PF$_6$]$^+$. UV-vis (MeCN) λ_{max} ($\varepsilon \times 10^4$ / L mol^{-1} cm^{-1}): 205 (3.3), 239 (3.2), 284 (2.0), 307 (1.8), 348 (1.1), 475 (0.4) nm. FTIR (solid, cm^{-1}) (ATR) ν_{max}: 3353, 1605, 1534, 1507, 1471, 1447, 1428, 1383, 1314, 1295, 1208, 1070, 1023, 980, 914, 833, 756, 729, 630, 621, 555.

4.6: References

1   M. Loudon, *Organic Chemistry*, Roberts & Company Publishers, Greenwood Village, Co, 5th edn., 2009.

2   A. Popczyk, Y. Cheret, A. Grabarz, P. Hanczyc, P. Fita, A. El-Ghayoury, L. Sznitko, J. Mysliwiec and B. Sahraoui, *New J. Chem.*, 2019, **43**, 6728–6736.

3   K. S. Keremane, I. M. Abdellah, P. Naik, A. El-Shafei and A. V. Adhikari, *Phys. Chem. Chem. Phys.*, 2020, **22**, 23169–23184.

4   W. Sharmoukh, J. Cong, B. A. Ali, N. K. Allam and L. Kloo, *ACS Omega*, 2020, **5**, 16856–16864.

5   J. S. De Melo, H. D. Burrows, M. Svensson, M. R. Andersson and A. P. Monkman, *J. Chem. Phys.*, 2003, **118**, 1550.

6   M. D'Auria, in *Advances in Heterocyclic Chemistry*, Academic Press, 2011, vol. 104, pp. 127–390.

7   J. Seixas De Melo, F. Elisei and R. S. Becker, *J. Chem. Phys.*, 2002, **117**, 4428–4435.

8   B. O'Regan and M. Grätzel, *Nature*, 1991, **353**, 737–740.

9   N. Mariotti, M. Bonomo, L. Fagiolari, N. Barbero, C. Gerbaldi, F. Bella and C. Barolo, *Green Chem.*, 2020, **22**, 7168–7218.

10   S. S. M. Fernandes, M. C. R. Castro, I. Mesquita, L. Andrade, A. Mendes and M. M. M. Raposo, *Dyes Pigments*, 2017, **136**, 46–53.

11   G. Angulo, J. Dobkowski, A. Kapturkiewicz and K. Maclolek, *J. Photochem. Photobiol. A: Chem.*, 2010, **213**, 101–106.

12   S. S. Mahadik, S. Chacko and R. M. Kamble, *ChemistrySelect*, 2019, **4**, 10021–10032.

13   T. N. Moshkina, E. V. Nosova, A. E. Kopotilova, B. Ośmiałowski, A. I. Reguant, P. A. Slepukhin, G. N. Lipunova, O. S. Taniya, A. A. Kalinichev and V. N. Charushin, *Dyes Pigments*, 2022, **204**, 110434.

14   T. J. Giordano and P. G. Rasmussen, *Inorg. Chem.*, 1975, **14**, 1628–1634.

15   M. Nonoyama, *Bull. Chem. Soc. Jpn.*, 1979, **52**, 3749–3750.

16   S. Lamansky, P. Djurovich, D. Murphy, F. Abdel-Razzaq, H.-E. Lee, C. Adachi, P. E. Burrows, S. R. Forrest and M. E. Thompson, *J. Am. Chem. Soc.*, 2001, **123**, 4304–4312.

17   M. L. Xu, G. Y. Wang, R. Zhou, Z. W. An, Q. Zhou and W. L. Li, *Inorganica Chim. Acta*, 2007, **360**, 3149–3154.

18   P.-N. Lai, C. H. Brysacz, K. Alam, N. A. Ayoub, T. G. Gray, J. Bao and T. S. Teets, *J. Am. Chem. Soc.*, 2018, **140**, 14.

19   P. N. Lai, S. Yoon and T. S. Teets, *Chem. Commun.*, 2020, **56**, 8754–8757.

20   A. Liang, M. Luo, Y. Liu, H. Wang, Z. Wang, X. Zheng, T. Cao, D. Liu, Y. Zhang and F. Huang, *Dyes Pigments*, 2018, **159**, 637–645.

21   W. Cho, G. Sarada, H. Lee, M. Song, Y. S. Gal, Y. Lee and S. H. Jin, *Dyes Pigments*, 2017, **136**, 390–397.

22   S. C. Yiu, P. Y. Ho, Y. Y. Kwok, X. He, Y. Wang, W. H. Yu, C. L. Ho and S. Huang, *Eur. J. Chem.*, 2022, **28**, e202104575.

23   S. Y. Takizawa, S. Katoh, A. Okazawa, N. Ikuta, S. Matsushima, F. Zeng and S. Murata, *Inorg. Chem.*, 2021, **60**, 4891–4903.

24   M. Bandini, M. Bianchi, G. Valenti, F. Piccinelli, F. Paolucci, M. Monari, A. Umani-Ronchi and M. Marcaccio, *Inorg. Chem.*, 2010, **49**, 1439–1448.

25   Y. Park, G. S. Lee, H.-R. Choi, Y. Jeon, S. Y. Jeong, B. Noh, K.-C. Park, Y.-H. Kim and K.-C. Choi, *Adv. Photonics Res.*, 2021, **2**, 2100121.

26   C. H. Fan, P. Sun, T. H. Su and C. H. Cheng, *Adv. Mater.*, 2011, **23**, 2981–2985.

27   Q. Mei, J. Weng, Z. Xu, B. Tong, Q. Hua, Y. Shi, J. Song and W. Huang, *RSC Adv.*, 2015, **5**, 97841–97848.

28   G. Szafraniec-Gorol, A. Słodek, M. Filapek, B. Boharewicz, A. Iwan, M. Jaworska, L. Zur, M. Sołtys, J. Pisarska, I. Grudzka-Flak, S. Czajkowska, M. Sojka, W. Danikiewicz and S. Krompiec, *Mater. Chem. Phys.*, 2015, **162**, 498–508.

29   S. A. Fitzgerald, H. Y. Otaif, C. E. Elgar, N. Sawicka, P. N. Horton, S. J. Coles, J. M. Beames and S. J. A. Pope, *Inorg. Chem.*, 2021, **60**, 15467–15484.

30   C. Capello, U. Fischer and K. Hungerbühler, *Green Chem.*, 2007, **9**, 927–934.

31   X. T. Wang, J. L. Song, M. Zhong, H. J. Kang, H. Xie, T. Che, B. Shu, D. Peng, L. Zhang and S. S. Zhang, *Eur. J. Org. Chem.*, 2020, **2020**, 3635–3639.

32   D. Lu, Q. Xiang, L. Zhou and Q. Zeng, *Asian J. Chem.*, 2015, **27**, 2639–2641.

33   M. D'Auria, G. Piancatelli and T. Ferri, *J. Org. Chem.*, 1990, **55**, 4019–4025.

34   M. D'auria, R. Ferri, G. Poggi, G. Mauriello and R. Racioppi, *Eur. J. Org. Chem.*, 2000, **2000**, 1653–1659.

35   US Pat. 7 858 785 B2, 2010.

36   V. Lukeš, M. Breza, D. Végh, P. Hrdlovič, J. Krajèovič and V. Laurinc, *Synth. Met.*, 2001, **124**, 279–286.

37   W.-X. Guo, H.-L. Jin, J.-X. Chen, F. C. Ding and H.-Y. Wu, *J. Braz. Chem. Soc.*, 2009, **20**, 1674–1679.

38   M. Nonoyama, *Bull. Chem. Soc. Jpn.*, 1974, **47**, 767–768.

39   A. K. Pal, D. B. Cordes, A. M. Z. Slawin, C. Momblona, E. Ortí, I. D. W. Samuel, H. J. Bolink and E. Zysman-Colman, *Inorg. Chem.*, 2016, **55**, 10361–10376.

40   A. L. Allred, *J. Inorg. Nucl. Chem.*, 1961, **17**, 215–221.

41   A. M. Bünzli, H. J. Bolink, E. C. Constable, C. E. Housecroft, J. M. Junquera-Hernández, M. Neuburger, E. Ortí, A. Pertegás, J. J. Serrano-Pérez, D. Tordera and J. A. Zampese, *Dalton Trans.*, 2013, **43**, 738–750.

42   F. J. Weigert and J. D. Roberts, *J. Am. Chem. Soc.*, 1971, **93**, 2361–2369.

43   N. Castillo, C. F. Matta and R. J. Boyd, *J. Chem. Inf. Model.*, 2005, **45**, 354–359.

44   David. R. Lide, *CRC Handbook of Chemistry and Physics*, CRC Press, Boca Raton, FL, 86 edn., 2005.

45   R. E. Atkinson and P. R. H. Speakman, *J. Chem. Soc. B*, 1971, 2077–2081.

46   J. Moussa, T. Cheminel, G. R. Freeman, L. M. Chamoreau, J. A. G. Williams and H. Amouri, *Dalton Trans.*, 2014, **43**, 8162–8165.

47   M. Hemgesberg, D. M. Ohlmann, Y. Schmitt, M. R. Wolfe, M. K. Müller, B. Erb, Y. Sun, L. J. Gooßen, M. Gerhards and W. R. Thiel, *Eur. J. Org. Chem.*, 2012, **2012**, 2142–2151.

48   W. H. Melhuish, *J. Phys. Chem.*, 1961, **65**, 229–235.

49   G. Angulo, J. Dobkowski, A. Kapturkiewicz and K. Maclolek, *J. Photochem. Photobiol. A: Chem.*, 2010, **213**, 101–106.

50   J. Qiao, L. Duan, L. Tang, L. He, L. Wang and Y. Qiu, *J. Mater. Chem.*, 2009, **19**, 6573–6580.

51   P. A. Anderson, F. R. Keene, T. J. Meyer, J. A. Moss, G. F. Strouse and J. A. Treadway, *J. Chem. Soc., Dalton Trans.*, 2002, 3820–3831.

52   K. Suzuki, A. Kobayashi, S. Kaneko, K. Takehira, T. Yoshihara, H. Ishida, Y. Shiina, S. Oishi and S. Tobita, *Phys. Chem. Chem. Phys.*, 2009, **11**, 9850–9860.

53   C. Erker and T. Basché, *J. Am. Chem. Soc.*, 2022, **144**, 14053–14056.

54   A. M. Brouwer, *Pure Appl. Chem.*, 2011, **83**, 2213–2228.

55   Y. X. Liu, R. H. Yi, C. H. Lin, Z. P. Yang, C. W. Lu and H. C. Su, *J. Mater. Chem. C*, 2020, **8**, 14378–14385.

56   A. Tsuboyama, H. Iwawaki, M. Furugori, T. Mukaide, J. Kamatani, S. Igawa, T. Moriyama, S. Miura, T. Takiguchi, S. Okada, M. Hoshino and K. Ueno, *J. Am. Chem. Soc.*, 2003, **125**, 12971–12979.

57   Y. Sun, X. Yang, Z. Feng, B. Liu, D. Zhong, J. Zhang, G. Zhou and Z. Wu, *ACS Appl. Mater. Interfaces*, 2019, **11**, 26152–26164.

58   A. Popczyk, Y. Cheret, A. El-Ghayoury, B. Sahraoui and J. Mysliwiec, *Dyes Pigments*, 2020, **177**, 108300.

59   J. R. Lakowicz, *Principles of fluorescence spectroscopy*, Springer, 2006.

60   M. J. Wildervanck, R. Hecht and A. Nowak-Król, *Molecules*, 2022, **27**, 5510.

61   G. R. Fulmer, A. J. M. Miller, N. H. Sherden, H. E. Gottlieb, A. Nudelman, B. M. Stoltz, J. E. Bercaw and K. I. Goldberg, *Organometallics*, 2010, **29**, 2176–2179.

62   S. J. Coles and P. A. Gale, *Chem. Sci.*, 2012, **3**, 683–689.

63   O. V. Dolomanov, L. J. Bourhis, R. J. Gildea, J. A. K. Howard and H. Puschmann, *J. Appl. Crystallogr.*, 2009, **42**, 339–341.

64   G. M. Sheldrick, *Acta Crystallogr. A*, 2015, **71**, 3–8.

65   G. M. Sheldrick, *Acta Crystallogr. C*, 2015, **71**, 3–8.

66   G. Gudipudi, S. R. Sagurthi, S. Perugu, G. Achaiah and G. L. D. Krupadanam, *RSC Adv.*, 2014, **4**, 56489–56501.

67   M. Ye, Y. Wen, H. Li, Y. Fu and Q. Wang, *Tetrahedron Lett.*, 2016, **57**, 4983–4986.

68   K. B. Harsha and K. S. Rangappa, *RSC Adv.*, 2016, **6**, 57154–57162.

69   K. B. Harsha, S. Rangappa, H. D. Preetham, T. R. Swaroop, M. Gilandoust, K. S. Rakesh and K. S. Rangappa, *ChemistrySelect*, 2018, **3**, 5228–5232.

70   Y. Zhang, M. Luo, Y. Li, H. Wang, X. Ren and C. Qi, *Mol. Divers.*, 2018, **22**, 183–189.

71   S. Uçar and A. Daştan, *J. Org. Chem.*, 2020, **85**, 15502–15513.

72   NMR Spectroscopy: ^{19}F NMR Coupling Constants, https://organicchemistrydata.org/hansreich/resources/nmr/?index=nmr_index%2F19F_coupling, (accessed 16 September 2022).

73   F. Amaya-García, M. Caldera, A. Koren, S. Kubicek, J. Menche and M. M. Unterlass, *ChemSusChem*, 2021, **14**, 1853–1863.

74   Y. Yang, F. Ni, W. M. Shu and A. X. Wu, *Eur. J. Chem.*, 2014, **20**, 11776–11782.

75   M. Nonoyama, *Bull. Chem. Soc. Jpn.*, 1974, **47**, 767–768.

Chapter 5: Development of Ir(III) Polychromorphores with Pendant Naphthalimide Units

Chapter 5

5.1: Introduction

As previously discussed, the emissive state of Ir(III) complexes heavily relies upon the nature of the ligands surrounding the metallic core. The work presented in this chapter investigates the excited state properties of complexes containing pendant naphthalimide-based chromophores covalently attached to the ligands in *bis*-cyclometallated **[Ir(C^N)$_2$(N^N)]$^+$** type complexes.

5.1.1: Naphthalimides

Fluorescent compounds derived from 1,8-naphthalimide (NI) are commonly explored due to their stability, high fluorescence quantum yields and excellent electron-transporting properties.[1] The general structure of 1,8-naphthalimide consists of a cyclic imide attached to an extended π-conjugated system in the form of a naphthalene ring, resulting in planarity of the molecule (**Figure 5.1**).
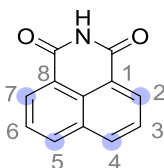
Figure 5.1: Chemical structure of 1,8-naphthalimide.

Electronic behaviour is attributed to the strong electron-withdrawing capability of the imide, which has been explored in the development of red-to-orange thermally activated delayed fluorescence (TADF) emitters for use in OLED development.[2,3] The unique structural and electronic properties of NI derivatives have permitted their use as fluorescent probes,[4,5] fluorescent brightening agents (FBAs) in materials,[6] and as anticancer agents and DNA intercalators.[7,8]

5.1.2: Altering the Electronic Nature of Naphthalimides

Functionalisation of the NI unit can impart significant changes to the electronic nature of the resultant compound. This is dependent on the relative positioning of electron-donating and electron-withdrawing components, where the latter is usually the imide constituent positioned at the C1 and C8 position of the naphthalene system. Electron density is significantly reduced at the C2, C4, C5 and C7 positions, rationalised by the corresponding resonance structures (**Figure 5.2**).
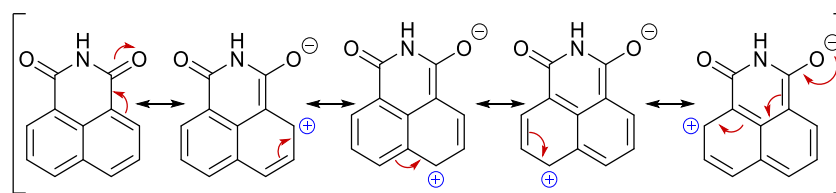
Figure 5.2: *Resonance structures of 1,8-naphthalimide, illustrating the electron-deficient carbon positions.*

Attachment of an electron-donating group at one of these positions allows intramolecular charge transfer (ICT) mechanisms to occur, permitting enhanced absorption features within the visible range. This is the result of efficient electronic delocalisation between the EWG and EDG, initiating a push-pull (D-π-A) type system. Therefore, the position of functionalisation and electronic nature of the substituent has a profound effect on the photophysical properties of the species.[9] In 1990, Alexiou reported that the presence of an amino, alkylamino or alkoxy group, either on the backbone or directly on the nitrogen atom of the NI system, imparted a substantial influence on the electronic properties of the resultant compounds (**Figure 5.3**).[10] Upon incorporation of these substituents, charge-transfer absorption features appeared at ~450 nm and emission bands were recorded up to 560 nm, with quantum yields of up to 0.81. This was attributed to the optimal donor properties of the substituents.
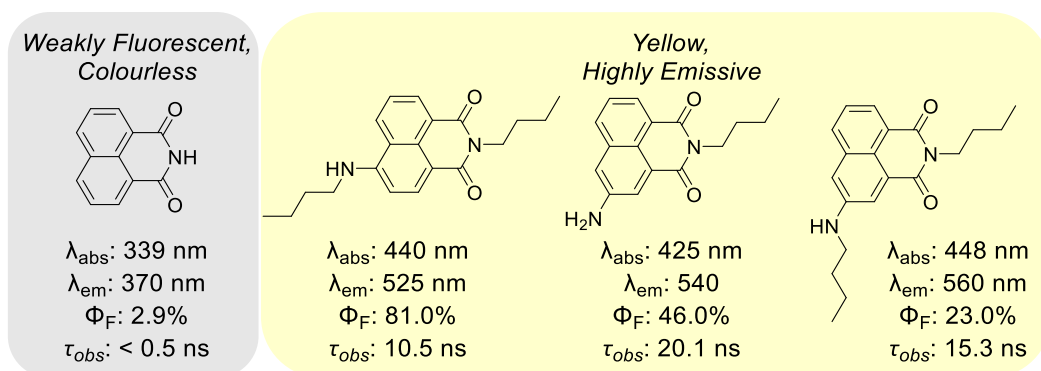
Figure 5.3: *Substituted 1,8-naphthalimide derivatives developed by Alexiou et al. in 1990.[10] Photophysical measurements were recorded in absolute EtOH.*

The use of NI as a π-acceptor has been sufficiently recognised when electron-donors have been introduced in the form of cyclic secondary amines such as morpholine or piperidine at the C4 position. Positive solvatochromism is often depicted in these systems, exemplifying the ICT process from the lone pair on the nitrogen to the NI unit.[11–13] Additionally, extension of the π-conjugated

naphthalene backbone has been explored in the development of NIR fluorescent dyes with low-energy absorption features.[14,15]

In 2006, Ding *et al.* produced a series of NI-based compounds containing an azole as an electron-transporting component.[16] An electron-donating substituent in the form of piperidine, morpholine or dimethylamine was incorporated at the 4-position of the NI backbone and their electronic properties were directly compared (**Table 5.1**). Whilst the absorption and emission signals showed little variation, the morpholine variants exemplified an enhancement of quantum yields relative to their dimethylamine counterparts, whilst presenting longer lifetimes than the piperidine-substituted species.
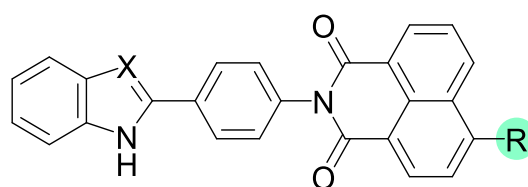
X: N-H, S, O

R	λ_{abs} / nm	λ_{em} / nm	Φ_F	τ_{obs} / ns
	302 – 307, 411 – 412	512 – 513	0.48 – 0.54	7.56 – 7.65
	302 – 307, 411 – 414	518 – 521	0.71 – 0.80	10.48 – 10.83
	302 – 309, 390 – 392	511 – 513	0.71 – 0.75	11.48 – 12.00

Table 5.1: *Photophysical data for the NI-substituted benzoazole compounds, developed by Ding, in CHCl₃.*[16]

5.1.3: Naphthalimides in Bioimaging Applications

As previously stated, morpholine substituents can be used to initiate charge-transfer processes, but it is also used as a lysosome-targeting fragment. The acidity of these organelles permits the diffusion of morpholine variants through the membrane, allowing these species to be useful as probes for intracellular pH detection when combined with an efficient chromophore.[17,18] Many

commercial lysosome-targeting probes (LysoSensor™) feature morpholine separated from a chromophore by an alkyl spacer, where fluorescence is enhanced in acidic media by the inhibition of PET (photoinduced electron transfer), a photoquenching process (**Figure 5.4**). Recently, Biswas *et al.* developed a series of pH-tolerant lysotrackers, where a morpholine substituent was separated from the NI unit through alkyl spacers of various lengths. The chain length between the donor (morpholine) and acceptor (NI) were altered and strong fluorescence was maintained in basic conditions through minimised PET.[12]
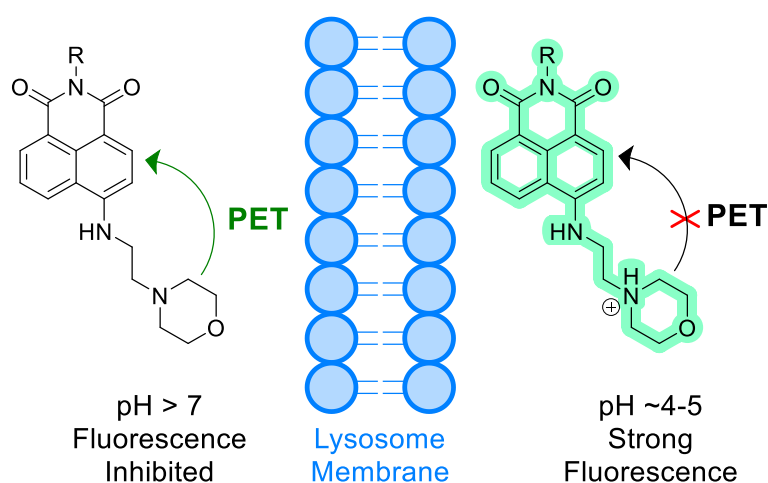
Figure 5.4: PET-induced fluorescence quenching for lysosome-targeting intracellular pH detection.[18]

DND-167, developed by de Silva *et al.* in 1985, contained anthracene as an electron-accepting moiety.[19] However, anthracene displays absorption and emission at short wavelengths, undesirable for biological imaging due to the increased possibility of autofluorescence. Therefore, the commercial probes **DND-189** and **DND-153** were developed (**Figure 5.5**), which utilised NI cores.[20]

Blue (DND-167)
pKa: 5.1
Φ_F: 0.80 (pH: 3.0)
λ_{abs}: 373 nm
λ_{em}: 425 nm

Green (DND-189)
pKa: 5.2
Φ_F: 0.48 (pH: 4.4)
λ_{abs}: 443 nm
λ_{em}: 505 nm

Green (DND-153)
pKa: 7.5
Φ_F: 0.48 (pH: 4.0)
λ_{abs}: 442 nm
λ_{em}: 505 nm
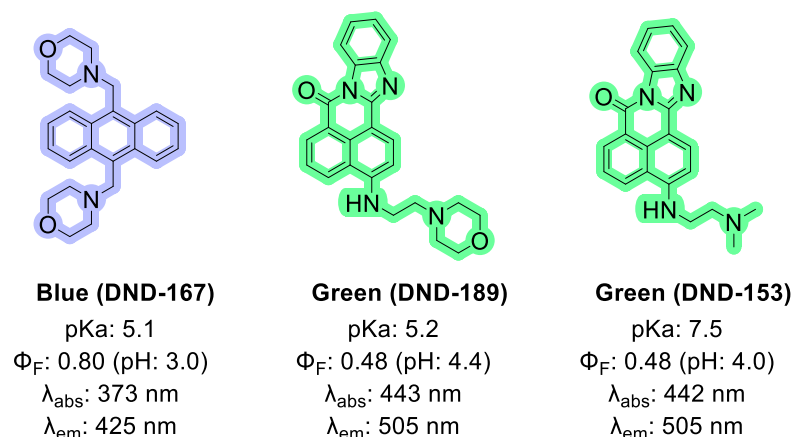
Figure 5.5: *Chemical structures and photophysical properties of some commercial lysosome-targeting probes in acidic environments.*[20]

This concept and NI-based structural motif has been explored in applications such as monitoring nitric oxide in lysosomes,[21] Pd[0] detection,[22] chemosensors for cellular CO detection,[23] and H_2S detection within cells.[24] Other fluorescence-quenching transfer mechanisms such as twisted internal charge transfer (TITC) have also been explored.[25]

NI-derived species have also gained traction as DNA intercalators with potential anticancer properties. Such examples include amonafide[26] and azonafide,[27] alongside fused heterocyclic variants developed by Braña, where enhanced cytotoxicity and efficient DNA-binding was achieved (**Figure 5.6**).[28] By utilising the electronic nature of the NI core, hybrid molecules have been developed as dual anticancer and fluorescence imaging agents.[29]

Amonafide   Azonafide   *Braña, 2003*
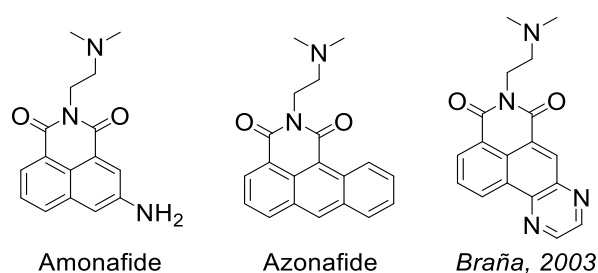
Figure 5.6: *NI-based compounds explored as anti-cancer compounds.*[26–28]

5.1.4: Naphthalimides in Organometallic Chemistry

Low-energy triplet ligand-centred excited states (^{3}LC) can become accessible by attachment of an elaborate π-conjugated system, where efficient mixing with the ^{3}MLCT state can occur as a result of their comparable relative energies.[30]

In 2011, Yarnell *et al.* reported that ^{3}MLCT emission lifetimes in a series of Re(I) complexes were enhanced by ~3000 times when a piperidine-substituted NI unit was attached to a 1,10-phenanthroline ligand at room temperature.[31] This was suggested to be the result of a thermal equilibrium between the ^{3}MLCT and ^{3}LC states. By accessing the organic triplet state, the longest excited-state lifetime of a Re(I) complex at room temperature (651 µs) at the time was reported, where the unsubstituted analogue presented a lifetime of ~200 ns. Upon excitation of the ^{1}LC state, rapid Förster resonance energy transfer (FRET) to the ^{1}MLCT state located at the Re(I) complex was deemed to take place, followed by rapid ISC to the ^{3}MLCT level. Energy transfer from the ^{3}MLCT state to the NI-confined ^{3}LC energy level occurred within the nanosecond timescale (~15 ns) *via* triplet-triplet energy transfer (TTET), displaying a phenomenon referred to as "ping-pong" energy transfer. This process is outlined in **Figure 5.7**.
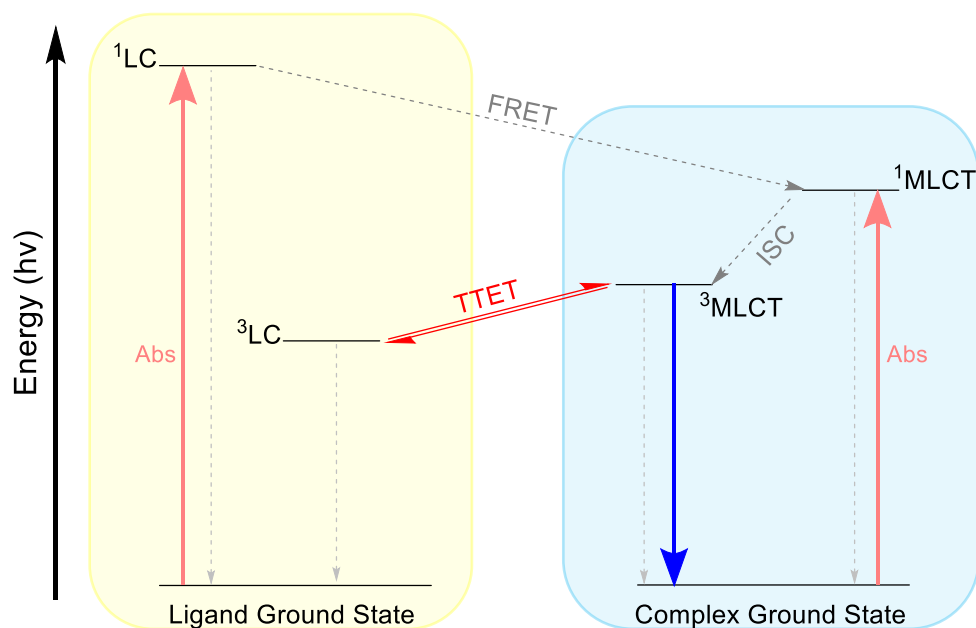
Figure 5.7: Energy level diagram for the "ping-pong" energy transfer process responsible for prolonged excited-state lifetimes in the Re(I) series developed by Yarnell et al. at room temperature.[31] Solid lines represent radiative transitions and dotted lines represent non-radiative transitions.

It was determined that luminescence occurred from the ^{3}MLCT state through thermal activation, where rapid reverse TTET was permitted by the closeness in energy of the two triplet states and was responsible for the significant enhancement in luminescence lifetime. These two equilibrated states became

isolated at low temperatures (77 K), where the low-energy, long-lived emission was assigned to radiative decay from the ^{3}LC state.

R =	H					
$T_{obs}{}^a$	176 ns	14.5 µs	56.6 µs	54.7 µs	*<15 ns** (116 µs)	*<15 ns** (136 µs)

Table 5.2: *Series of long-lived Re(I) bichromophores developed by Yarnell et al. in 2019.[32] Average measured lifetimes in deaerated MeCN are also displayed. *Transient absorption measurements were carried out to investigate decay from the ^{3}NI state (average lifetimes are in parentheses).*

In 2019, this work was developed by synthesising a range of weakly fluorescent prospective NI-based ligands for Re(I) complexes.[32] The aforementioned thermal equilibrium was investigated relative to synthetic modulation of the NI unit, where most of the complexes displayed this type of energy transfer mechanism alongside significant enhancement of lifetimes compared to the unsubstituted complex (**Table 5.2**). Modulation of the triplet-triplet energy gap heavily impacted the luminescent lifetimes of the species, where greater energy difference prevented the repopulation of the shorter-lived ^{3}MLCT state (*i.e.* breaking the thermal equilibrium), promoting deactivation from the ^{3}LC level. Through transient-absorption measurements, these lifetimes were determined to be 116 µs and 136 µs for when R = thiobenzene and piperidine, respectively, consistent with the long-lived nature of an organic triplet excited state.

A *bis*-cyclometallated Ir(III) species, bearing two phenylpyridine ligands and an NI-functionalised phenanthroline derivative as the N^N ancillary ligand, was also investigated.[33] Once again, the unique photophysical properties observed for the polychromophoric species were attributed to a thermal equilibrium between the low-lying ^{3}LC and ^{3}MLCT excited states, which were isolated due to the lack of interaction between the pendant NI unit and the iridium centre. A broad absorption profile spanning the visible range was accompanied by an exceedingly long excited state lifetime of 8.8 ms, increasing by four orders of magnitude relative to the model complex, **[Ir(ppy)$_2$(phen)]PF$_6$**. The emission properties remained fairly consistent, offering a route to lifetime extension whilst retaining the emission properties. The structure and photophysical parameters are displayed in **Figure 5.8** alongside the unsubstituted species for comparison. This concept has been explored in several applications, such as the development of long-lived photosensitisers for TTA-UC,[34–36] solar energy conversion[37] and DNA photocleavage.[38]

[Ir(phen)(ppy)$_2$]PF$_6$
λ_{abs}: 379 nm
ε: 6940 M^{-1} cm^{-1}
λ_{em}: 592 (507) nm
τ_{obs}: 821 ns (6.33 µs)
Φ_P: 0.40

[Ir(PNI-phen)(ppy)$_2$]PF$_6$
λ_{abs}: 404 nm
ε: 17200 M^{-1} cm^{-1}
λ_{em}: 593 (507, 606) nm
τ_{obs}: 8.8 ms (5.3 µs, 242 ms)
Φ_P: 0.13
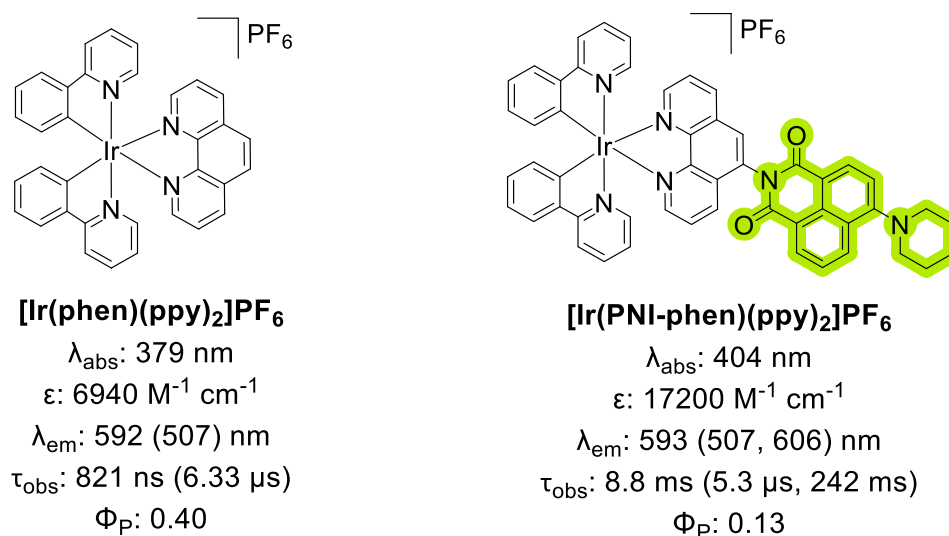
Figure 5.8: *Photophysical properties of the bichromophore developed by Yarnell et al. (right),[33] compared with the model complex **[Ir(phen)(ppy)$_2$]PF$_6$** (left) in degassed THF solutions at RT. Values in parentheses measured at 77 K in 2-methyl-THF.*

Early work by Tyson in 2001 suggested that the enhancement in lifetimes was dependent on the number of PNI-type chromophores in a Ru(II) octahedral system, where the observed lifetimes increased significantly from **[Ru(bpy)$_2$(PNI-phen)]$^{2+}$** to **[Ru(PNI-phen)$_3$]$^{2+}$** in a range of solvents.[39] This was

suggested to be due to the incorporation of additional PNI units driving the equilibrium towards the ^{3}LC excited state, whilst increasing the energy gap between the ^{3}MLCT and ^{3}PNI states to directly impact their relative populations.

Direct cyclometallation to an NI unit itself has shown deep red ^{3}LC emission.[40,41] However, NI appendages that are isolated from the metallic core have been scarcely recognised on C^N ligands, as focus has remained predominantly on the functionalisation of N^N-type ancillary ligands. In 2012, a neutral, *tris*-cyclometallated Ir(III) complex was developed by Sun *et al.*, which displayed a TTA-UC quantum yield (Φ_{UC}) of 14.4%.[34] The corresponding cationic *bis*-cyclometallated species with modification at the bipyridine ancillary ligand exhibited longer triplet state lifetimes (**Figure 5.9**). The enhanced Φ_{UC} of the neutral complex was attributed to the strong absorption properties of the complex in conjunction with the long-lived excited state.

9.30 µs (313.7 ns)   16.45 µs (387.3 ns)
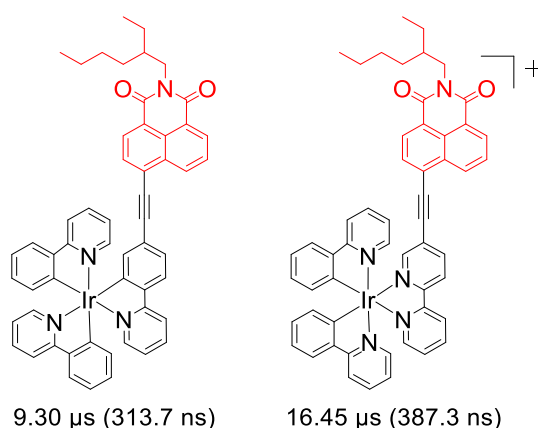
Figure 5.9: *Long-lived triplet photosensitisers developed by Sun.[34] Triplet excited state lifetimes in degassed toluene are displayed below the corresponding structures. Values in parentheses are in aerated toluene.*

5.2: Aims

Previous chapters have demonstrated that emission from *bis*-cyclometallated Ir(III) species with phenylpyridine-type C^N ligands tend to be dominated by mixed MLCT/LC excited states.[42] The work undertaken in this chapter explores the subsequent impact on the photophysical properties upon incorporating different NI-based chromophores into the backbone of either the ancillary (N^N = 1,10-phenanthroline) or cyclometallated (C^N = 2-phenylquinoxaline) ligands, and were directly compared to the model complex, **[Ir(pqx)$_2$(phen)]$^+$**.

It was hypothesised that thermal equilibrium of the ^{3}LC and ^{3}MLCT excited states could occur, resulting in long-lived excited states at room temperature alongside enhanced absorption properties within the visible range. Synthetic modification of the NI unit was therefore undertaken to adjust the energy of the ^{3}LC level through either enhanced electronic delocalisation or extension of the π-conjugated system. Since these NI systems were localised at the extremities of the metal complexes, the separation of these states was explored through low temperature steady state emission measurements in conjunction with time-resolved luminescence studies.

Very few examples of NI units being incorporated into cyclometallating ligands have been reported. To the best of our knowledge, this is the first report of NI components being covalently bound to the backbone of ppy-based ligands in a **[Ir(ppy)$_2$(N^N)]$^+$** type system.

5.3: Results and Discussion

5.3.1: Synthesis and ^{1}H NMR Spectroscopy of Ligands

In this study, a multitude of organic chromophores were developed as prospective ligands for organometallic iridium species. Firstly, a series based upon 1,10-phenanthroline was synthesised as potential N^N-coordinating ligands, where a 1,8-naphthalimide (NI) analogue was incorporated into the backbone of the ring system. In all cases, commercially available 1,10-phenanthrolin-5-amine was used as the precursor, where the primary amine permitted direct integration of the NI unit *via* condensation with an acid anhydride in glacial acetic acid for 16 – 24 hours (**Scheme 5.1**).
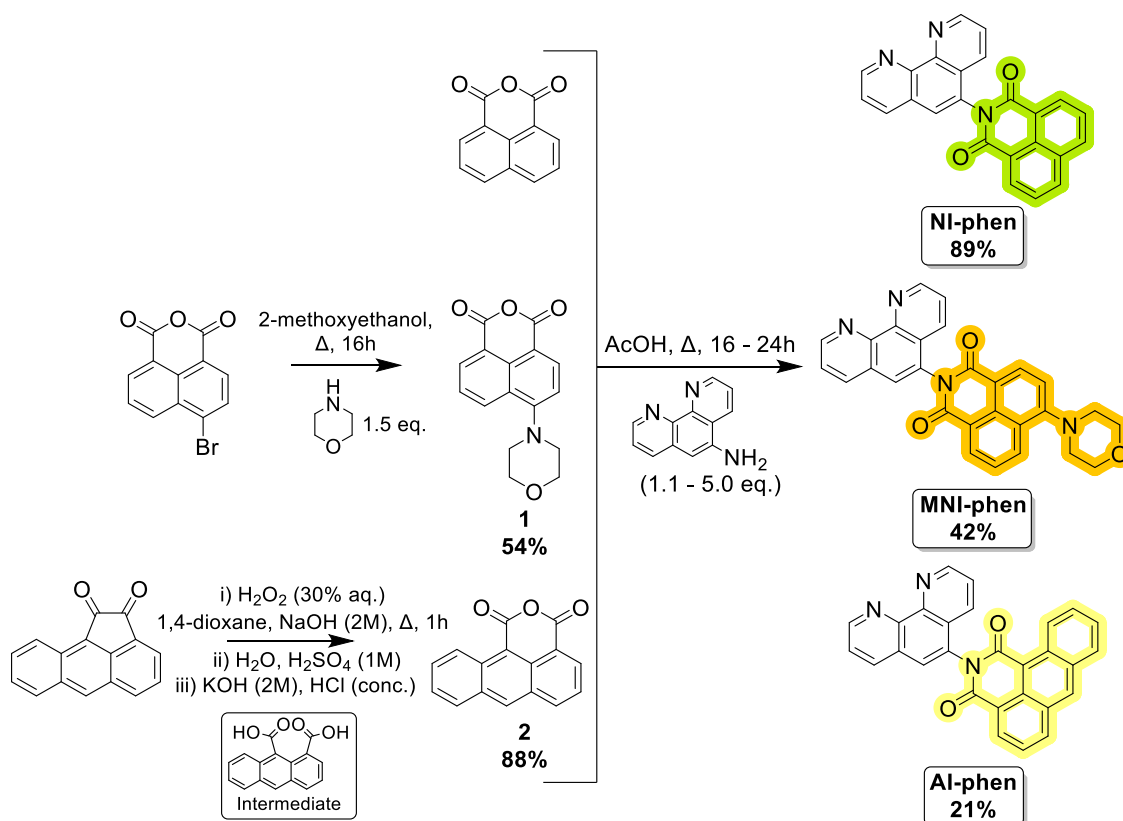
Scheme 5.1: *General synthesis of the NI-substituted phenanthroline ligands.*

Commercially available 1,8-naphthalic anhydride was used to develop the unsubstituted variant, **NI-phen**, with a high synthetic yield of 89%. The remaining ligands required preliminary formation of the anhydride precursors according to the preparative procedures illustrated in **Scheme 5.1**. Morpholine was introduced to the naphthalene backbone through nucleophilic aromatic

substitution of 4-bromo-1,8-naphthalic anhydride, where bromide acted as a favourable leaving group in the presence of excess morpholine in 2-methoxyethanol at reflux, forming intermediate **1**.[43,44] The tricyclic anhydride **2** was synthesised from aceanthrenequinone, where the addition of 30% aqueous H_2O_2 under basic conditions at reflux in 1,4-dioxane promoted ring-opening *via* oxidation to form a dicarboxylic intermediate. Subsequent ring-closure occurred upon dehydration of the carboxyl groups, observable by a distinct colour change from pale yellow to bright orange.[15,27] Imide formation was less efficient for the functionalised anhydrides, with overall yields of 42% and 21% for **MNI-phen** and **AI-phen** respectively. This was suggested to be due to the relative solubilities and reactivities of the anhydride precursors, where the additional π-conjugation in **2** resulted in enhanced stability of the anhydride.
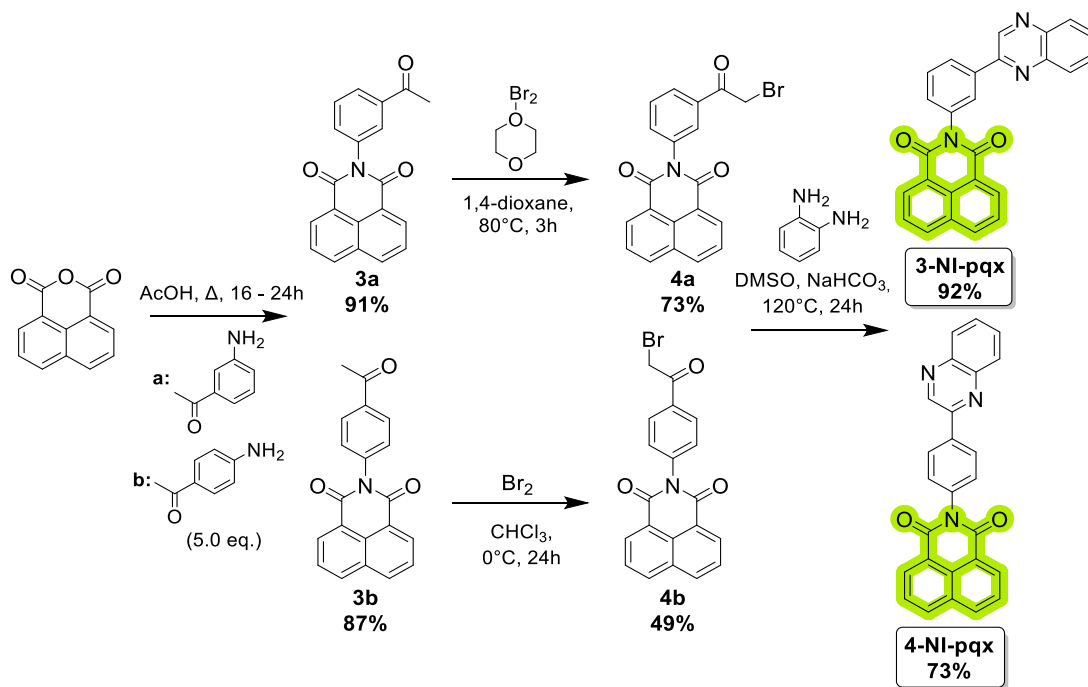
*Scheme 5.2: General synthesis of **3-NI-pqx** and **4-NI-pqx**.*

A second series of ligands was synthesised based upon 2-phenylquinoxaline (**pqx**), for use as potential C^N ligands. These were developed through a multistep synthesis and contained NI units that were functionalised similarly to those described above. The NI unit was situated at either the 3- or 4- position of the phenyl ring (relative to the quinoxaline), to compare electronic and steric influences on the resultant chemical and photophysical properties of the final species. The synthetic procedures of the unsubstituted analogues, **3-NI-pqx** and **4-NI-pqx** are illustrated in **Scheme 5.2**.

Once again, the imides were formed through condensation of an acid anhydride with a primary amine through a nucleophilic acyl substitution reaction, and the proposed mechanistic route is displayed in **Scheme 5.3**. Excess amine was necessary due to the reduced nucleophilicity of aromatic primary amines through mesomeric effects,[45] whilst increasing the pH of solution to prevent deactivation through protonation.
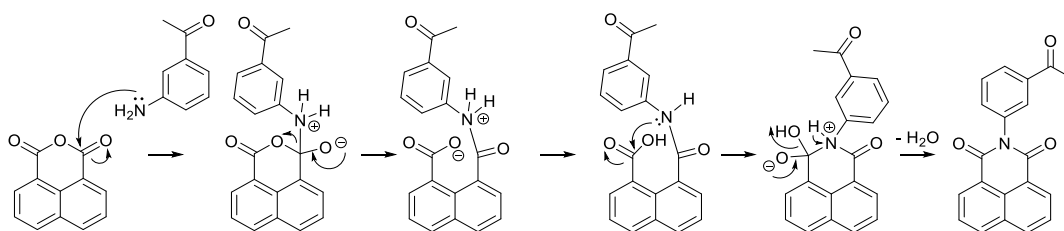
Scheme 5.3: *Proposed mechanism for the nucleophilic acyl substitution reaction of the anhydride to generate the naphthalimide intermediate* ***3a***.[46]

The acetyl functionality was then utilised as the basis for the development of the quinoxaline system through a brominated intermediate (**Scheme 5.2**).[42] The experimental method towards quinoxalines reported in previous chapters was deemed to be undesirable for a multistep synthesis due to relatively poor overall efficiencies, where the benchmark compound, 2-phenylquinoxaline (**pqx**), formed with a yield of 49%. Additionally, the limited solubilities of the highly planar, polycyclic systems made it necessary to seek alternative methods. The bromination step required only subtle modification, where alternative solvents were used, and heat was applied to the system to solubilise the NI starting material. However, an entirely new approach was adopted for the quinoxaline formation, based upon findings by Lu *et al.* in 2015.[47] In this study, yields of up to 99% were attainable for the title compound, **pqx**, without the need for further purification using the optimised method. This method involved dissolving stoichiometric quantities of the brominated precursor, 1,2-phenylenediamine and a slight excess (1.2 eq.) of $NaHCO_3$ in DMSO and heating to 120°C overnight. It was postulated that using $NaHCO_3$ as a deacidification reagent would remove HBr as it formed, driving the reaction forward to generate the quinoxaline product. This approach resulted in an extreme enhancement of experimental yields. No further purification was required in the cases of **3-NI-pqx** and **4-NI-pqx** since the pure products precipitated out of solution, owing to

the increased conversion. This prevented the need for time-consuming purification methods such as column chromatography, which was a prerequisite for the previous methodology. Therefore, this approach must be considered for any future work relating to phenylquinoxaline species.

Following the same preparative procedure, **3-MNI-pqx** and **4-MNI-pqx** were synthesised, where a morpholine ring was incorporated into the NI system at the 4-position, directly comparable with **MNI-phen** (**Scheme 5.4**).
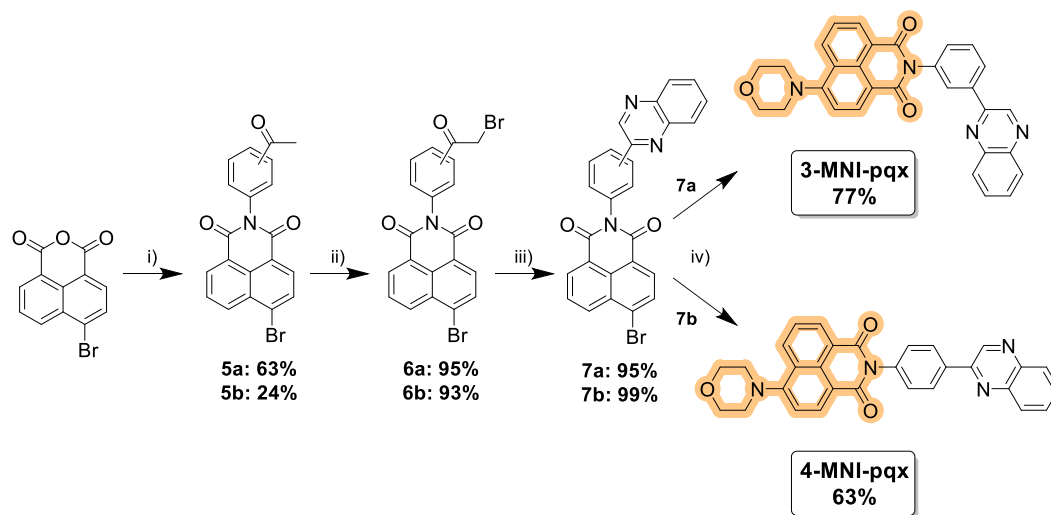
Scheme 5.4: *General synthesis of 3-MNI-pqx and 4-MNI-pqx; i) 3-aminoacetophenone (a) or 4-aminoacetophenone (b) (5.0 eq.), glacial AcOH, reflux, 24h; ii) DDB, 1,4-dioxane, 80°C, 3h; iii) 1,2-phenylenediamine, NaHCO₃ (1.2 eq.), DMSO, 120°C, 24h; iv) morpholine (5.0 eq.), 2-methoxyethanol, reflux, 16-24h.*

Initially, precursor **1** was employed as the anhydride source for both ligands, but issues arose as a mixture of products were formed during the bromination step, detected by TLC and ^{1}H NMR spectroscopy. Therefore, 4-bromo-1,8-naphthalic anhydride was used, where the bromine functionality was maintained until after the formation of the quinoxaline. In doing so, a much higher conversion was achieved and purification through chromatographic techniques were deemed to be successful. The nucleophilic aromatic substitution step was performed similarly to **1**, but a larger excess of morpholine was added to ensure maximum yield due to the poorer solubility of **7a** and **7b**.

Challenges arose in the attempted syntheses of **3-AI-pqx** and **4-AI-pqx**, mostly attributed to the additional fused aromatic ring in the delocalised backbone. The limited solubility of **2** in various solvents (alongside diminished electrophilicity)

led to issues in the initial substitution step. The imides formed in extremely poor yields *via* the previously discussed methodology – unfavourable for a multi-step synthesis. Therefore, an alternative approach was adopted to combat these issues (**Scheme 5.5**) and the preparation of **8a** and **8b** is detailed below.
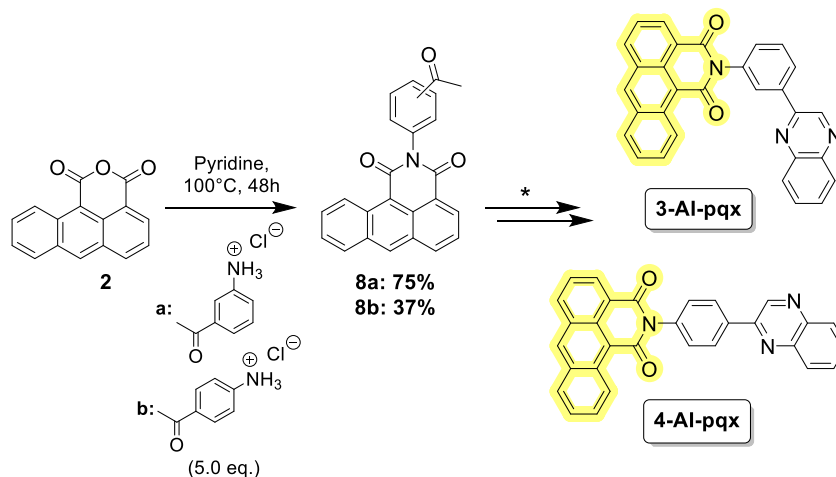
Scheme 5.5: *General synthesis of **8a** and **8b**. *Attempted synthesis of **3-Al-pqx** and **4-Al-pqx** through similar preparative procedures as those previously discussed.*

Firstly, 6M HCl was added dropwise to a stirred suspension of the aryl amine in distilled water until a homogenous solution ensued (pH ~1 – 2), suggesting that the amine was predominantly in its water-soluble hydrochloride salt form (**a** or **b**). Nucleophilicity of the amine is impeded in this form due to the nitrogen lone pair being inaccessible, but liberation of the free amine occurs upon addition of a base, promoting a reaction with the anhydride *in situ* (optimum pH ~5.5).[48] Therefore, the hydrochloride salt form was added dropwise to a stirred solution of **2** dissolved in pyridine, and the resultant mixture was heated to 100°C for 48 hours under an inert N_2 atmosphere.[49] Upon cooling, the mixture was poured into 1M HCl, where the crude product precipitated out of solution. TLC (SiO_2, DCM) analysis confirmed that the crude sample consisted of only two species – product and anhydride starting material (**2**) – whilst ^{1}H NMR spectroscopy data indicated that ~75% conversion was achieved for **8a**. The two species were readily separated through column chromatography (SiO_2) where **2** was removed with DCM, whilst the product eluted with DCM:MeOH (9:1) as the mobile phase. Therefore, this method displayed a vast improvement in both efficiency and ease of purification, offering significant potential for future studies.
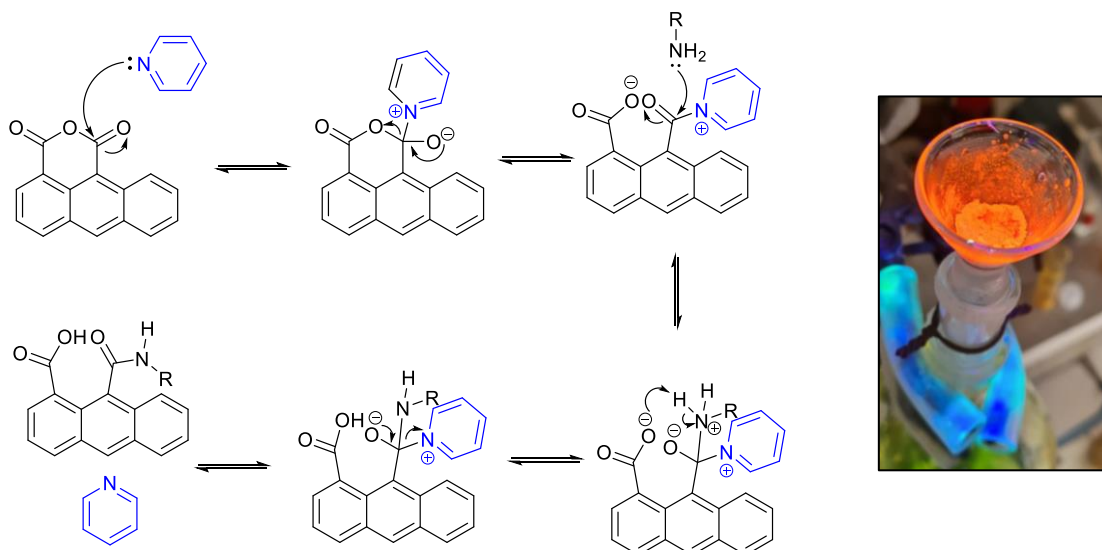
Scheme 5.6: *Proposed mechanism for the first pyridine-assisted nucleophilic acyl substitution (ring opening).[50] A subsequent intramolecular nucleophilic attack leads to ring closure and the generation of intermediate **8a** (photographed).*

The nitrogen lone pair on anilinic (*i.e.* primary aromatic) amines is delocalised within the ring current, diminishing its nucleophilicity. This can be enhanced by use of aromatic heterocycles such as pyridine or DMAP, where the lone pair can attack a carbonyl to form an acyl pyridinium intermediate. This essentially 'activates' the anhydride by promoting nucleophilic attack from the amine, where pyridine/DMAP acts as a favourable leaving group and therefore exhibits catalytic behaviour.[50] This process is illustrated in **Scheme 5.6**, displaying the first of two nucleophilic acyl substitutions involved in the formation of the imide. As opposed to precursor **2**, crude sample of **8a** displayed remarkable solid-state fluorescence under UV light irradiation (*ca.* 395 nm) due to extension of the π-conjugated system and delocalisation across the phenyl ring.

For all 2-phenylquinoxaline-based ligands, substitution at the 4-position of the phenyl ring resulted in poorer yields. This was suggested to be an effect of enhanced planarity, where the precursors displayed noticeably reduced solubilities in most solvents.

^{1}H NMR spectra were measured for all the isolated ligands and precursors. The phenanthroline-based series were characterised in line with previous assignments of 1,10-phenanthroline,[51] and the ^{1}H NMR spectrum of **NI-phen** is shown in **Figure 5.10**. Although this species has been previously synthesised,[32,37] its exploration in iridium chemistry remains unknown. A plane of symmetry exists down the centre of the NI unit due to rotational freedom of the C-N bond, demonstrated by three sets of signals (each corresponding to two equivalent protons) in the resultant spectrum.
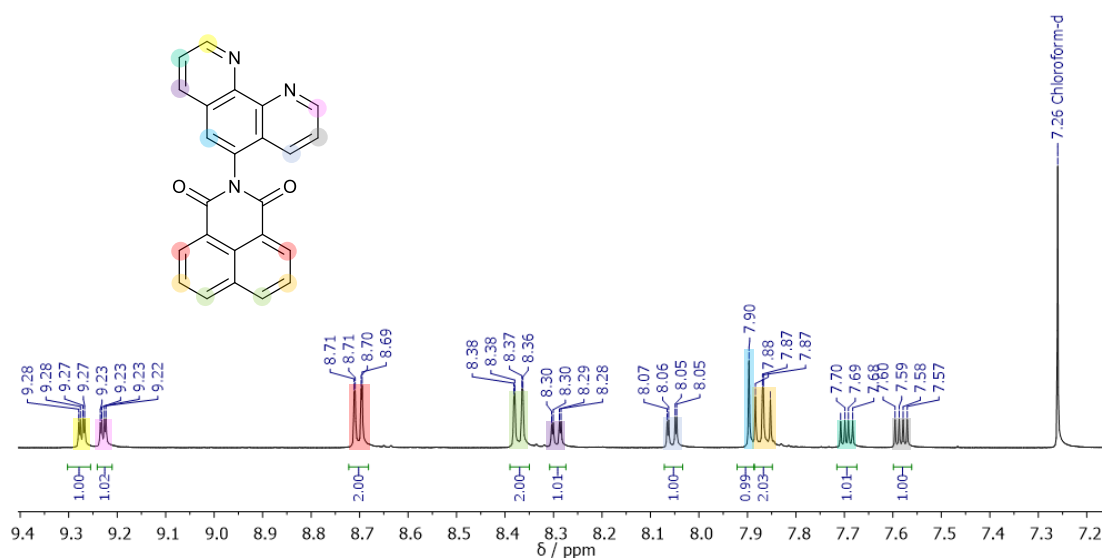
Figure 5.10: *^{1}H NMR spectrum of **NI-phen** (CDCl₃, 500 MHz), fully assigned in accordance with the chemical structure displayed above.*

This was directly compared with the modified variants, **MNI-phen** and **AI-phen**, where the overlaid spectra are displayed in **Figure 5.11**. Although the phenanthroline peaks remained reasonably consistent, the initial symmetry of the NI unit was lost upon functionalisation, resulting in all aromatic NI peaks becoming chemically unique.
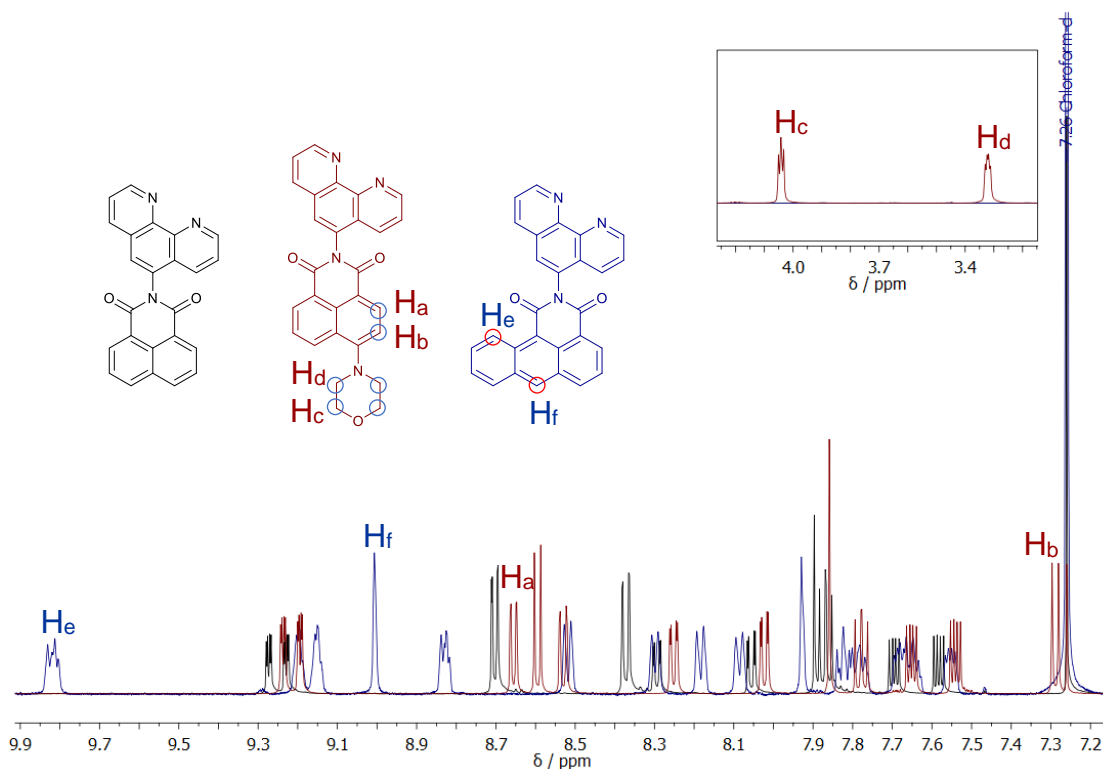
*Figure 5.11: Overlapping ^1H NMR spectra of **NI-phen** (black), **MNI-phen** (red) and **AI-phen** (blue) (CDCl₃, 500 MHz). Inset: Aliphatic region. Some selected protons have been assigned and are discussed in the main text.*

The three doublets of doublets seen in **NI-phen** become two doublets at 8.60 and 7.29 ppm in **MNI-phen** (**H$_a$** and **H$_b$**, respectively). The latter experienced a substantial upfield shift due to the presence of an adjacent electron-donating morpholine substituent, where the nitrogen is electron deficient as a result of withdrawal from the oxygen atom. Two aliphatic multiplets (**Figure 5.11**, inset) were characteristic of the eight protons at the saturated morpholine ring, where the downfield signal at 4.08 – 4.01 ppm represented the four protons on either side of the highly-electronegative oxygen atom (**H$_c$**). Both peaks were broadened due to the conformational rearrangement of the morpholine ring system, where a preference for the *gauche* conformation leads to a *pseudo*-triplet type signal being displayed.[52] **AI-phen** exhibited a characteristic doublet of doublets at ~9.9 ppm, representative of the deshielded proton closest to the imide on the additional ring system (**H$_e$**). Peaks representing the anthracene component broadened at higher concentrations as a consequence of aggregation and limited solubility. A singlet at ~9.0 ppm was indicative of the proton at the centre of the anthracene system (**H$_f$**) as it does not experience any through-bond coupling.

Stacked ^{1}H NMR spectra for the isomeric ligands **3-NI-pqx** and **4-NI-pqx** are displayed in **Figure 5.12**. The NI and quinoxaline peaks remained fairly consistent, but the phenylic protons differed significantly depending upon the position of substitution. In **4-NI-pqx**, *para*-positioning of the quinoxaline relative to NI generated a plane of symmetry within the phenyl ring, represented by two signals corresponding to two equivalent nuclei. This symmetry was lost in **3-NI-pqx** and the peaks became more distinct, where four unique environments were observed.
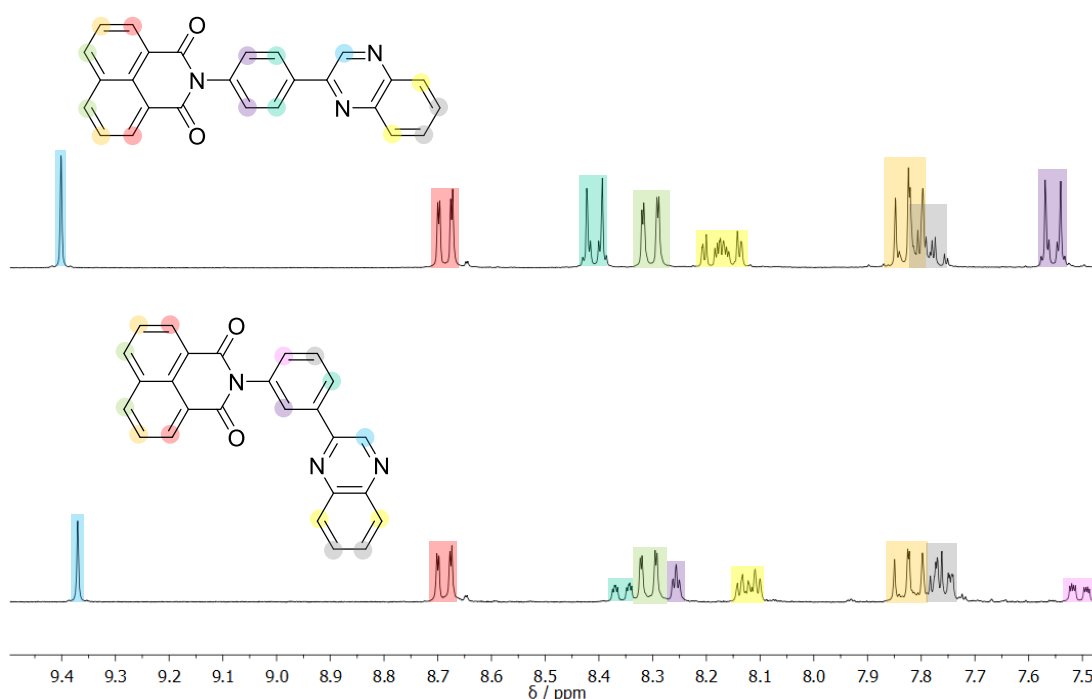
Figure 5.12: *Stacked ^{1}H NMR spectra of **4-NI-pqx** (top) and **3-NI-pqx** (bottom) in CDCl₃ (300 MHz), assigned in accordance with the displayed chemical structures.*

5.3.2: Synthesis and ^{1}H NMR Spectroscopy of Complexes

The 1,10-phenanthroline-based compounds (**NI-phen**, **MNI-phen** and **AI-phen**) were investigated as N^N-coordinating ancillary ligands on *bis*-cyclometallated Ir(III) species, where the cyclometallating ligands were 2-phenylquinoxaline (**pqx**). These were studied alongside a model complex bearing an unsubstituted 1,10-phenanthroline N^N ligand to investigate the impact of incorporating NI fluorophores into the backbone of the ligand.
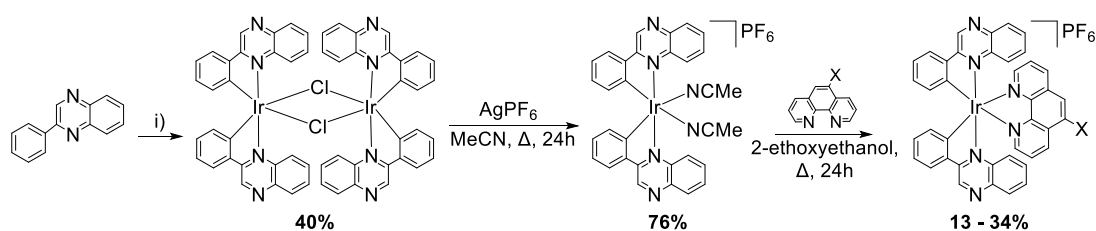
Scheme 5.7: *Synthesis of the Ir(III) complexes, where the ancillary ligand was used as the point of functionalisation; i) IrCl₃.xH₂O, 2-ethoxyethanol (3:1 v/v with H₂O), reflux, 48 h.*[53]

The dimeric species were prepared in accordance with methods described in previous chapters.[53] An alternative approach was used to isolate the final complexes, where a solvated intermediate was formed by splitting the dimer in a heated solution of acetonitrile with two equivalents of silver hexafluorophosphate in the dark overnight.[54] AgCl formed as a by-product and confirmed that the splitting had taken place. The advantage of this method was that a whole series of complexes could be synthesised from one intermediate, where the acetonitrile ligands were considerably more labile than the bridging chloride ligands in the dimer. The *bis*-acetonitrile complex was purified by recrystallisation from DCM and Et₂O, promoting a higher efficiency for the incorporation of the N^N ligand. This final step involved heating the solvated species and the N^N ligand in 2-ethoxyethanol to generate the crude complexes, which were purified by column chromatography using silica gel as the stationary phase and a mixture of DCM/MeOH (95:5) as the eluent, followed by recrystallisation from DCM and Et₂O where necessary. The overall procedure is illustrated in **Scheme 5.7**.
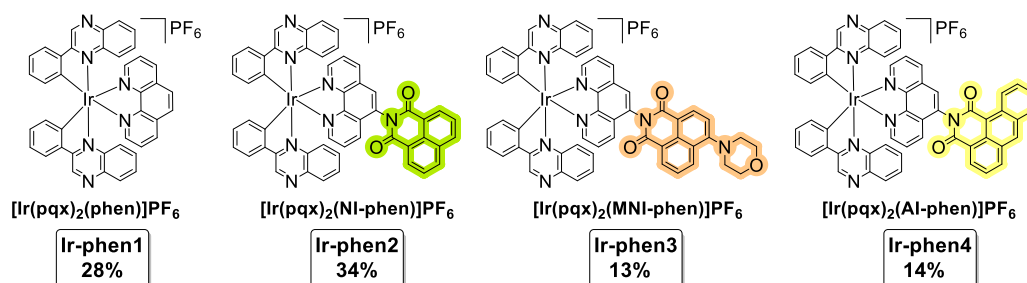
Figure 5.13: *Structures and synthetic yields of the phenanthroline-functionalised iridium complexes including the control complex (**Ir-phen1**).*

Four Ir(III) complexes were formed through this route, each containing a variation of phenanthroline as the N^N ligand (**Figure 5.13**). These were formed in yields between 13 – 34%, with **Ir-phen2** displaying the highest efficiency. The poor yields of **Ir-phen3** and **Ir-phen4** were attributed to the steric bulkiness of the connected functionalised NI fluorophore, where a single-bond attachment to the phenanthroline ligand promoted steric and electronic repulsion with the iridium species, subsequently inhibiting coordination in solution.
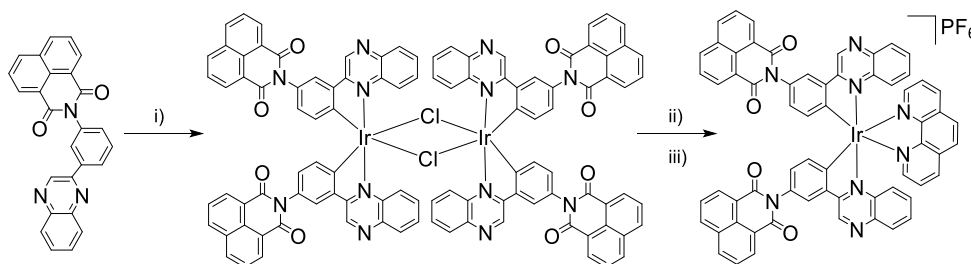
*Scheme 5.8: Synthesis of **Ir-pqx1**, where the cyclometallated ligands were used as the point of functionalisation; i) IrCl₃.xH₂O, 2-ethoxyethanol (3:1 v/v with H₂O), reflux, 48h,[53] ii) 1,10-phenanthroline, 2-ethoxyethanol, reflux, 24h; iii) NH₄PF₆ (aq.), MeCN.*

The phenylquinoxaline ligands were also explored as a point of attachment for the NI unit, where the chromophores were covalently bound to the two C^N ligands. 1,10-phenanthroline was used as the N^N ancillary ligand in most cases, allowing direct comparisons with the **Ir-phen** species, but 2,2'-bipyridine was also briefly investigated. The complexes were synthesised similarly to the experimental procedure outlined above, but directly from their corresponding dimeric intermediates. The synthetic route is shown in **Scheme 5.8**, where the formation of the complex bearing **3-NI-pqx** ligands is presented as an example. The structures of the complexes are displayed in **Figure 5.14**. Five of the complexes were successfully isolated whilst only crude sample of **Ir-pqx6** was obtained. The synthetic yields of the unsubstituted variants were modest, within the range of 10 – 20%, whilst **Ir-pqx5** was generated with a good synthetic yield of 73%, potentially due to the enhanced solubility as a result of the morpholine substituent external to the coordination sphere.
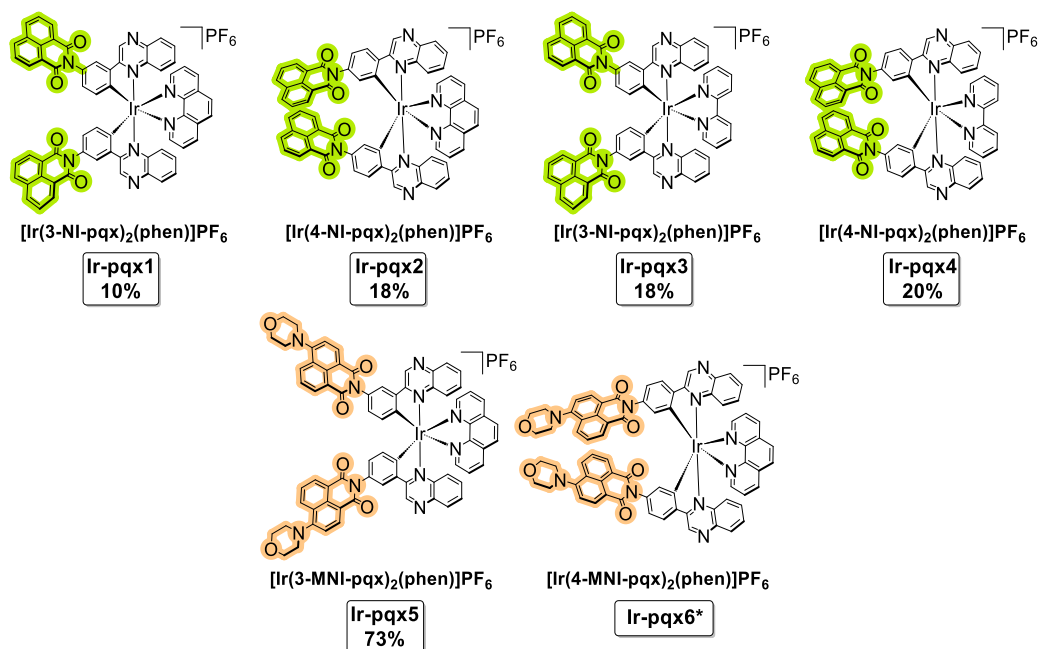
Figure 5.14: *Structures and synthetic yields of the phenylquinoxaline-functionalised iridium complexes. ***Ir-pqx6** was not isolated.*

Purification involved column chromatography using a silica gel stationary phase and acetone as the initial mobile phase, where the desired complex remained immobile. Upon removal of these impurities, a solvent mixture of acetonitrile, distilled water and saturated aqueous KNO_3 solution (14:2:1) was employed as the mobile phase, where the complex eluted from the column. Upon drying and filtering off any excess salts, a counterion exchange was carried out using saturated NH_4PF_6 solution to ensure that the complex existed as a PF_6 salt. Further purification using chromatographic and/or recrystallisation techniques were necessary. In some cases, a DCM/MeOH (~9:1) solvent mixture was employed as the mobile phase, followed by recrystallisation from DCM and Et_2O. The complexes bearing **NI-pqx** ligands formed with relative ease, whilst purification of the **MNI-pqx** complexes were much more scrupulous.

Upon coordination, all isolated complexes displayed significant changes in the ^{1}H NMR spectra relative to the free ligands. An example is shown in **Figure 5.15**, where the ^{1}H NMR spectra of **MNI-phen** and **Ir-phen3** are compared.
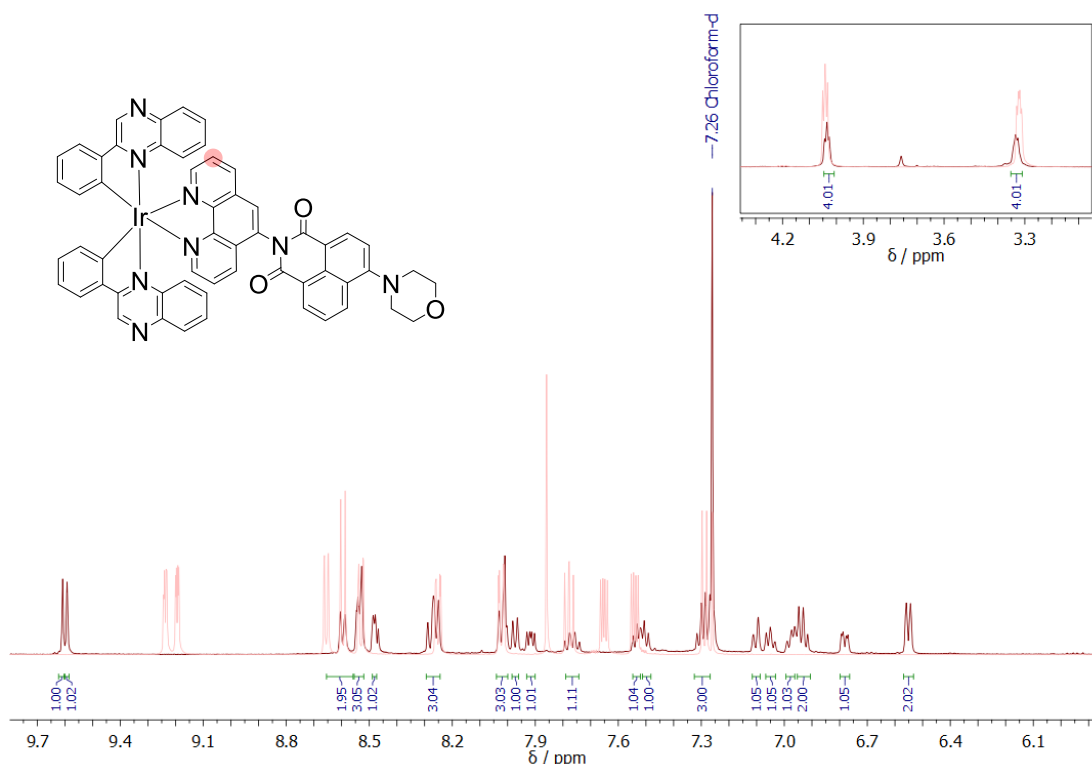
*Figure 5.15: Overlaid ^{1}H NMR spectra of **Ir-phen3** (dark red) and the corresponding free ligand, **MNI-phen** (red) in CDCl$_3$ (500 MHz). Integrals shown correspond to **Ir-phen3**. Inset: aliphatic region.*

The spectra for **Ir-phen2**, **Ir-phen3** and **Ir-phen4** were difficult to fully assign since the complexes were asymmetrical. This led to two sets of peaks with very similar chemical shift values being observed for the two C^N ligands, where two unique singlets at 9.61 and 9.59 ppm were recorded for the deshielded pyrazine protons in **Ir-phen3** (**Figure 5.15**). The sums of the integrals were consistent with the number of protons in the theorised structures and there was no direct overlap with the corresponding free ligand spectra. Therefore, it was concluded that the complexes were isolated as one species in each case. Some peaks were able to be assigned to the N^N ligand for **Ir-phen3**, further confirming coordination had ensued. For example, the proton located at the position highlighted in **Figure 5.15** shifted from 7.65 ppm in the free ligand to 7.92 ppm in the complex, recognised by its unique *J*-coupling value of $^3J_{HH} = 5.1$ Hz, which was consistent with other phenanthroline-coordinated iridium species.[55]
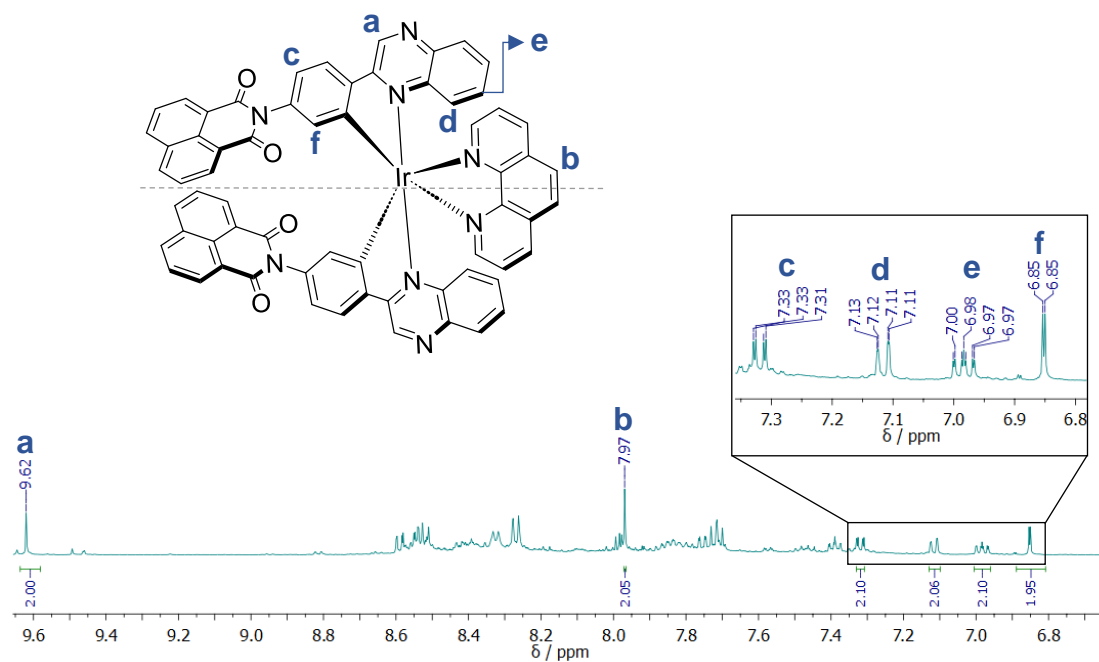
Figure 5.16: *¹H NMR spectrum of **Ir-pqx2**, where some selected peaks are assigned (CD₃CN, 500 MHz).*

In contrast to the first set of complexes, the C^N-functionalised variants were suggested to possess C_2 symmetry, resulting in a single set of peaks being observed in the ¹H NMR spectra. In **Ir-pqx2** (**Figure 5.16**), the singlet at 9.62 ppm corresponded to the indicative pyrazine singlet. When the integral of this peak was normalised to represent two protons, the total sum of integrals was in alignment with the number of protons in the suggested chemical structure. These complexes displayed relatively broad NMR signals due to two large pendant NI units increasing the molecular size, limiting the solubility. However, indicative peaks were recognised and assigned according to the free ligands. A singlet at 7.97 ppm was ascribed to the central position (**b**) on the phenanthroline ligand, with no observable coupling with the adjacent proton by virtue of their chemical equivalence. This further supported the hypothesised plane of symmetry present in the structure. The most upfield peak position was a doublet at 6.85 ppm with a $^4J_{HH}$ coupling of 1.9 Hz, assigned to the position directly adjacent to the site of cyclometallation (**f**), exhibiting through-bond coupling with the proton at position **c**.

5.3.3: Further Characterisation of Ligands and Complexes

$^{13}C\{^1H\}$ NMR spectroscopy data for all NI-containing free ligands exhibited downfield peaks between 163.5 and 168.1 ppm. These were representative of the two C=O carbons at the lactam ring, where rotational freedom of the unsubstituted NI units resulted in only one signal being displayed. These values are presented in **Table 5.3**, alongside data for the corresponding complexes.
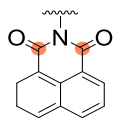
Ligand	δ_C (C=O)	Complex	δ_C (C=O)
NI-phen	164.5	Ir-phen2	*
MNI-phen	164.8, 164.2	Ir-phen3	164.0, 163.5
AI-phen	165.7, 164.2	Ir-phen4	*
3-NI-pqx	163.8	Ir-pqx1	165.3^a
		Ir-pqx3	166.8
4-NI-pqx	164.4	Ir-pqx2	164.7, 163.9^a
		Ir-pqx4	166.0^b
3-MNI-pqx	168.1, 164.2	Ir-pqx5	165.7, 164.3^b
4-MNI-pqx	164.2, 163.5	Ir-pqx6	Not isolated

*Table 5.3: $^{13}C\{^1H\}$ NMR carbonyl peak positions (highlighted in the above chemical structure) of the isolated NI-containing free ligands and complexes in CDCl$_3$ at 126 MHz, unless otherwise stated; ^{a}in CD$_3$CN; ^{b}in (CD$_3$)$_2$CO. *Not determined.*

The morpholine-substituted ligands demonstrated additional chemical shifts at ~156 ppm in the ^{13}C NMR spectra, representative of the carbon directly bonded to the nitrogen atom of the morpholine.[13]

$^{19}F\{^1H\}$ NMR data confirmed the presence of the PF$_6$ counterion in the final iridium species at ~ −70 ppm ($^1J_{PF}$ ~ 710 Hz). This was supported by IR spectroscopic studies, where strong P-F stretching modes were recognised at ~830 cm^{-1}.[56]

Two characteristic carbonyl stretches, v(C=O), were observed in the IR spectra for the free ligands between 1692 – 1709 and 1651 – 1666 cm^{-1}, and were representative of symmetric and asymmetric stretching vibrations, respectively.[57] These are typically observed at higher wavenumbers for acid anhydrides,[58] observable in precursor **1** at 1744 and 1719 cm^{-1}. The incorporation of a nitrogen atom upon formation of the imide significantly alters the vibrational behaviour, offering a simple approach to product determination.

An additional C-N-C stretch was seen at 1350 – 1370 cm^{-1} in the free ligands, consistent with the formation of the cyclic imide.[59] An example is shown below for **3-NI-pqx** (**Figure 5.17**).
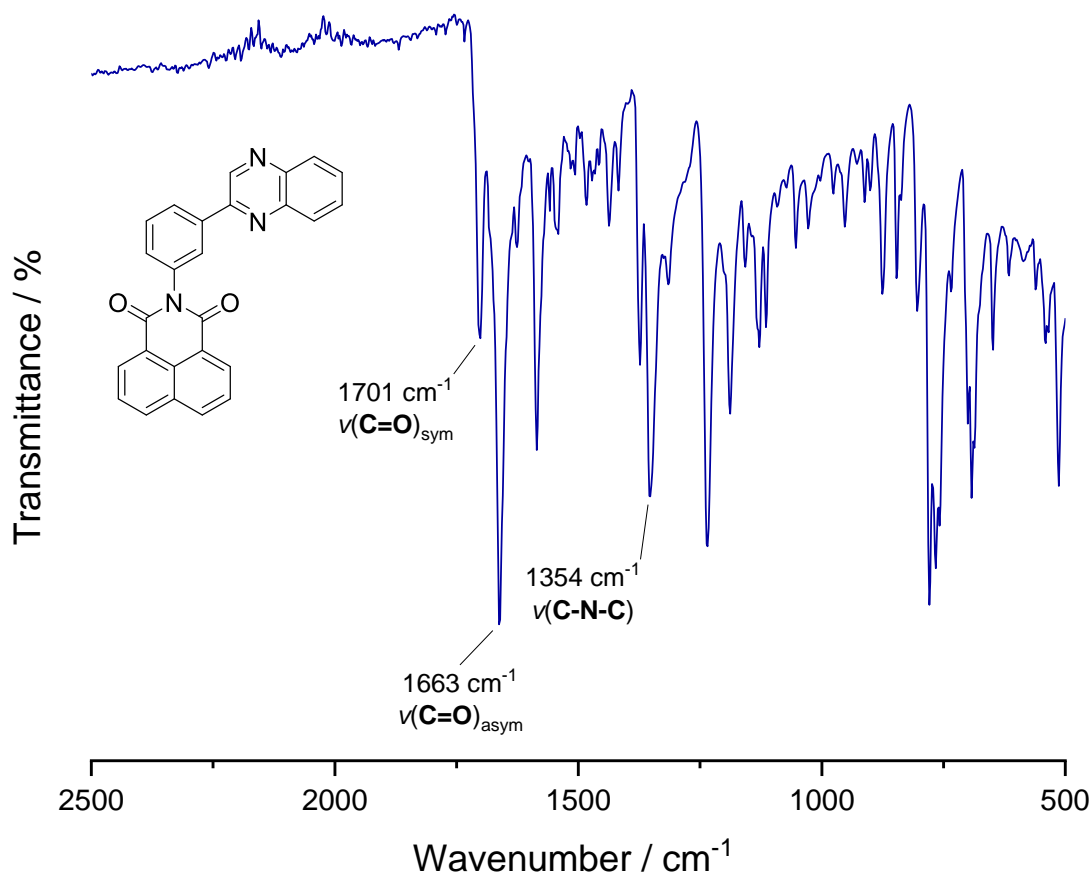
Figure 5.17: *FT-IR spectrum for **3-NI-pqx**, with some assigned characteristic peaks associated with the naphthalimide.*

Strong aromatic vibrations were assigned within the fingerprint region, with aromatic C-H stretches exceeding 3000 cm^{-1}. These features were particularly prevalent for **Al-phen**, which contained an extended fused ring system within the NI-type unit.

High-resolution mass spectrometry was performed for the isolated ligands and complexes, where electrospray ionisation techniques were employed. In most cases, experimental values were within error of the calculated masses of the theorised structures. An example of a spectrum for a ligand and its corresponding complex are displayed in **Figure 5.18**.
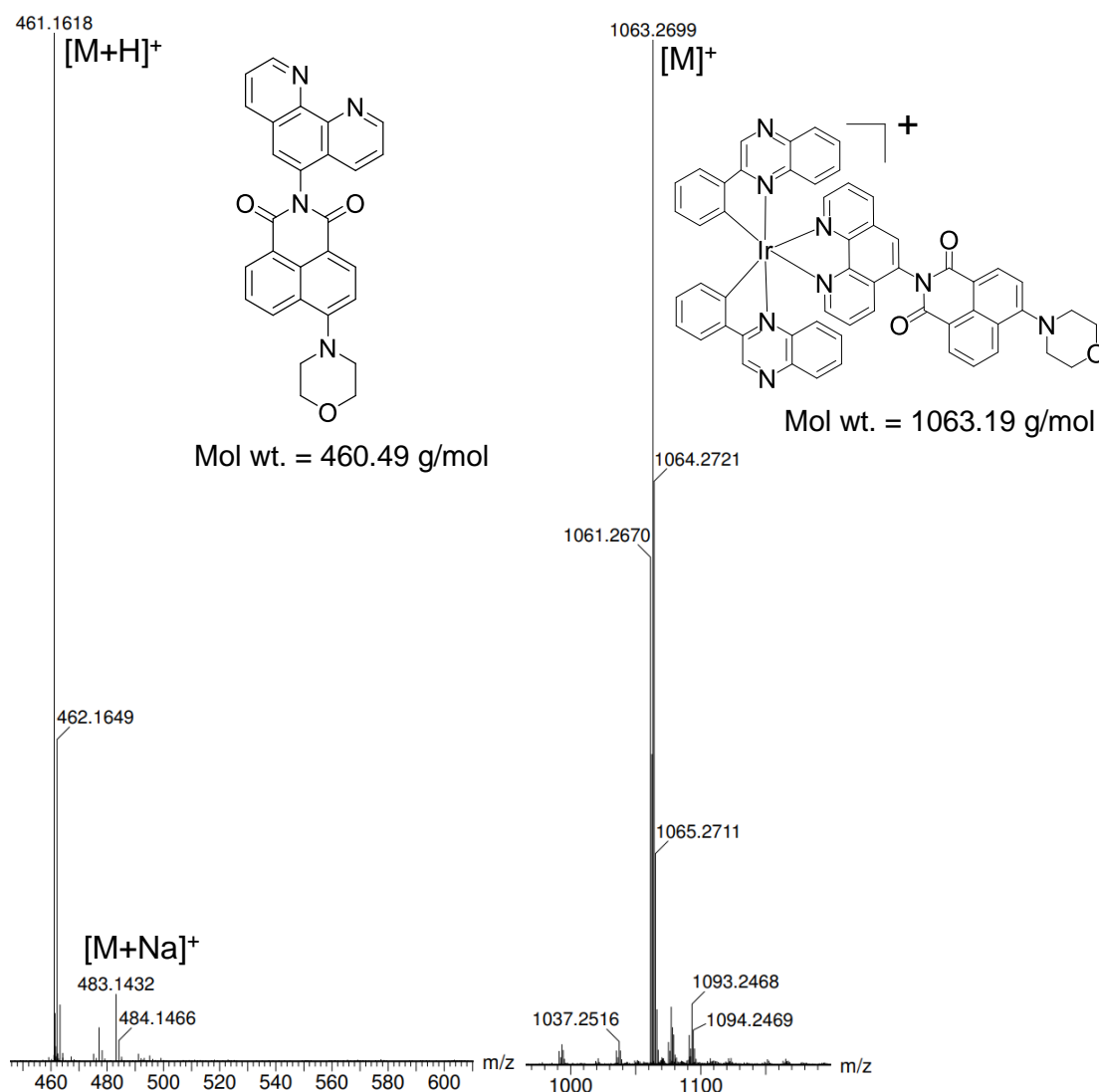
*Figure 5.18: HRMS (ES+) of **MNI-phen** and **Ir-phen3**, where the parent ion peaks are in alignment with the molecular weight of the structures.*

5.3.4: Photophysical Properties of Ligands

UV-vis absorption measurements were carried out on the phenanthroline-based ligands in *ca.* 10^{-5} M aerated acetonitrile at room temperature (**Figure 5.19**). All compounds displayed two high-intensity absorption bands within the UV range at ~230 nm and ~263 nm, in alignment with the characteristic peaks for 1,10-phenanthroline (**phen**). These were assigned as spin-allowed $^1(\pi\rightarrow\pi^*)$ transitions by virtue of the polycyclic nature of the compounds, with high ε values up to ~90000 $M^{-1}cm^{-1}$.
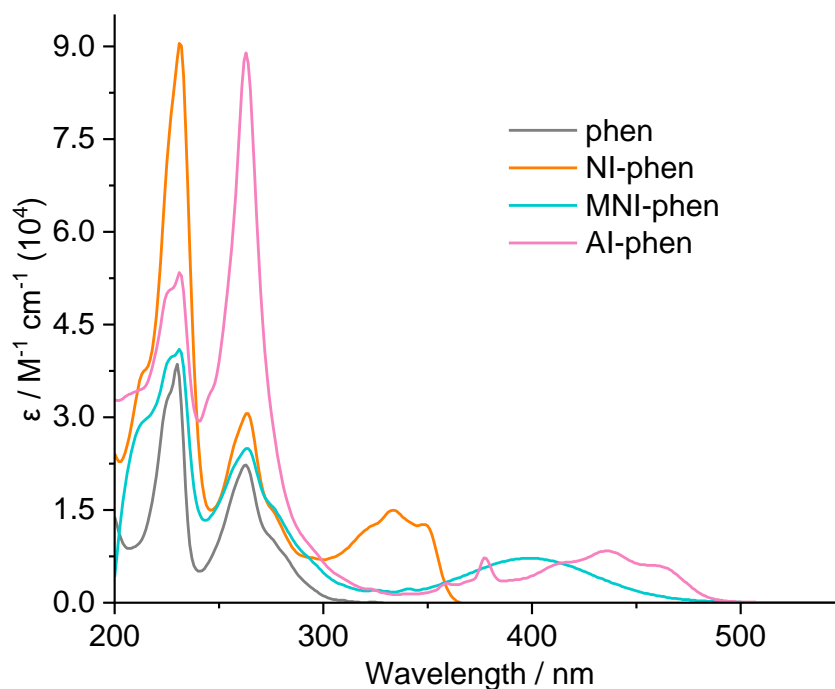
Figure 5.19: *UV-vis absorption spectra of the N^N-coordinating free ligands (MeCN, RT). Concentrations (in 10^{-5} M) of; 1.00 (**phen**), 0.99 (**NI-phen, MNI-phen, AI-phen**).*

Upon inclusion of an unsubstituted NI unit (**NI-phen**), mildly vibronically structured features arose between 322 – 349 nm ($\varepsilon \sim 12000 - 15000$ M^{-1} cm^{-1}). These were assigned as $^1(\pi\rightarrow\pi^*)$ transitions localised on the NI unit, closely resembling the profile for 1,8-naphthalimide.[10,60] This band experienced a significant bathochromic shift into the visible range (401 nm, $\varepsilon \sim 7200$ M^{-1} cm^{-1}) upon insertion of a morpholine unit (**MNI-phen**), suggesting stabilisation of the excited state. In conjunction with band broadening and a reduced intensity, this was evidence of an intramolecular charge-transfer (ICT) excited state displaying symmetry-forbidden n$\rightarrow\pi^*$ character. This was a consequence of introducing morpholine as an electron-donor to the 4-position,[61] where n corresponds to the nitrogen lone pair.[39,62,63] Extending the π-conjugated system on the backbone of the imide (**AI-phen**) also resulted in a significant bathochromic shift towards the visible region ($\lambda_{abs} = 415 - 461$ nm, $\varepsilon \sim 6000 - 8300$ M^{-1} cm^{-1}), where weak vibronic structure was maintained. This was the result of an efficient donor-acceptor interaction between the anthracene unit and the imide,[64] formally assigned as $^1(\pi\rightarrow\pi^*)$.[49] A sharp peak at 377 nm was consistent with similar variants in the literature.[49,65] Notably, peak positions remained unaltered when measured in CHCl$_3$ solutions of the same concentration, suggesting the ground state was not sensitive to solvent environment.
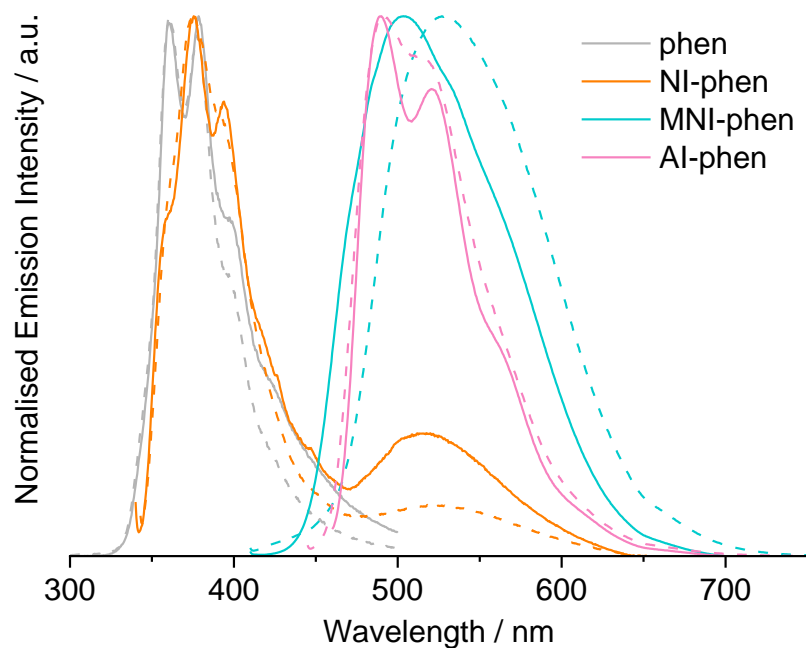
Figure 5.20: *Normalised fluorescence spectra of the phenanthroline ligands in CHCl$_3$ (solid) and MeCN (dashed) solutions (ca. 10^{-5}M) at RT. $\lambda_{ex} = 265 – 450$ nm, where the lowest-energy absorption band was used as the λ_{ex}.*

Steady-state luminescence measurements were recorded in 10^{-5} M solutions of acetonitrile and chloroform for the phenanthroline-based ligands (**Figure 5.20**). The excitation wavelength used in each case was the low-energy peak maxima in the corresponding absorption spectra. **MNI-phen** and **AI-phen** were highly emissive, with bands in the visible range between 490 and 528 nm in acetonitrile. **NI-phen** exhibited dual-emission with highly structured phenanthroline-localised bands seen at <450 nm alongside a broad peak centred at 523 nm, where the latter displayed solvent-dependence relative to emission intensity. In both solvents, **MNI-phen** presented a single broad, featureless emission signal in accordance with the low-energy absorption peak, whilst a bathochromic shift of 24 nm occurred upon increasing solvent polarity. **AI-phen** presented a structured emission profile in chloroform, a consequence of the enhanced vibronic structure associated with the rigid anthracene moiety.[65]

UV-vis absorption measurements were also performed on the phenylquinoxaline cyclometallating ligands and 2-phenylquinoxaline (**pqx**) in *ca.* 10^{-5} M chloroform solutions (**Figure 5.21**). The spectra closely resembled that of the previously discussed phenanthroline series, where intense peaks

with $\pi \rightarrow \pi^*$ character were prevalent within the UV range whilst some compounds displayed absorption features in the visible region. Signals at 336 and 351 nm ($\varepsilon \sim 19000 - 16000$ M^{-1} cm^{-1}, respectively) for **3-NI-pqx** were consistent with 1,8-naphthalimide and its derivatives,[61] but also overlapped with **pqx** absorption bands. A broad feature at ~400 nm was apparent in the morpholine analogues, once again consistent with an ICT state.[39,63] Although peak positions remained consistent, the 4-substituted variants (**Figure 5.21**, dotted lines) displayed higher intensity absorption bands than their 3-substituted counterparts. This difference was attributed to relative planarity of the systems and was most apparent in the **MNI**-containing compounds. Enhanced electronic delocalisation within the highly planar compound **4-MNI-pqx** enabled the ICT process, thereby increasing the molar absorptivity by almost four-fold relative to **3-NI-pqx**.
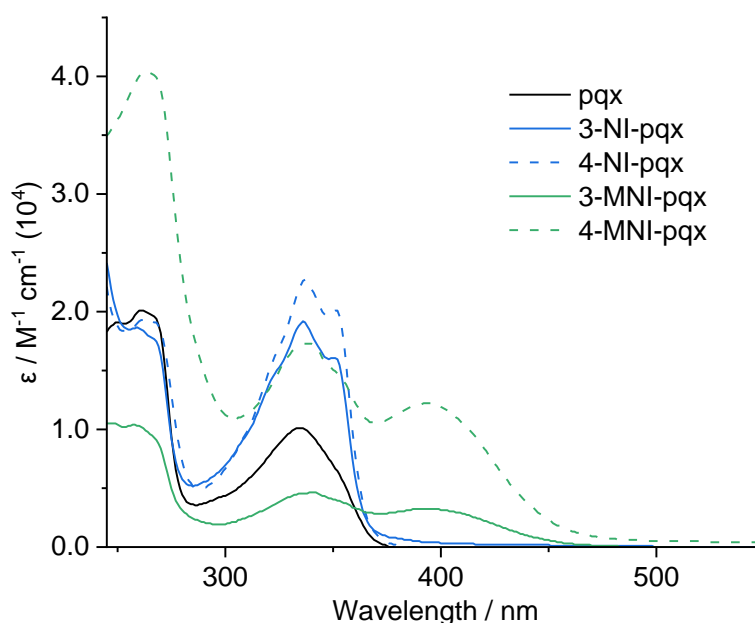
Figure 5.21: *UV-vis absorption spectra of the 3-substituted (solid) and 4-substituted (dashed) C^N-coordinating free ligands (CHCl$_3$, 0.99 × 10^{-5}M, RT).*

Steady-state emission data of the C^N ligands were collected in dilute chloroform solutions and presented peak maxima spanning across a large range of 402 – 518 nm. All functionalised variants displayed longer emission wavelengths relative to **pqx** (**Figure 5.22**). A broadened peak with a similar λ_{max} value to **pqx** was seen for **3-NI-pqx**, whereas **4-NI-pqx** displayed two components and enhanced broadening at longer wavelengths. It was suggested that this was due to conformational rearrangement permitting

enhanced electronic delocalisation in the planarised variants. **3-MNI-pqx** and **4-MNI-pqx** demonstrated substantial bathochromic shifts in λ_{em}, where broad emission features within the visible range were observed with little variation between the two isomers. This was in alignment with the suggested ICT character of the emissive state.
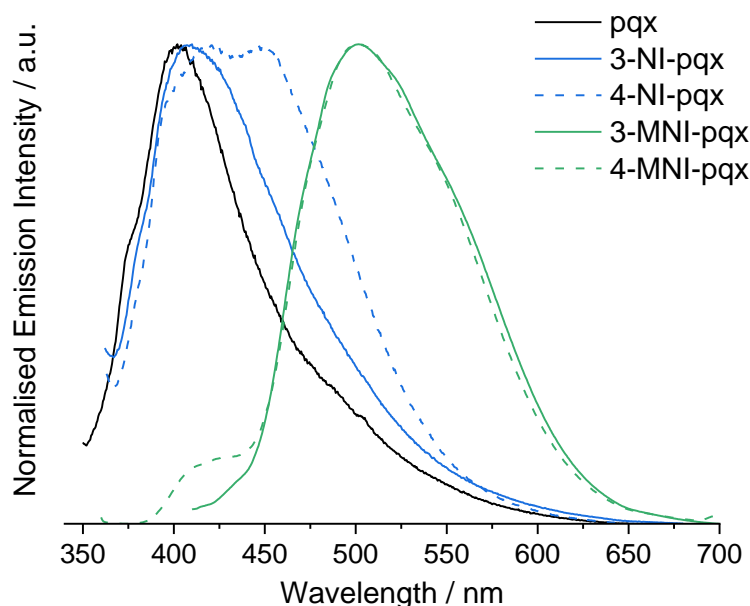
Figure 5.22: *Normalised fluorescence spectra of the phenylquinoxaline ligands in CHCl$_3$ (10^{-5}M, RT). λ_{ex} = 335 – 400 nm, targeting the lowest-energy absorption band.*

Only slight bathochromic shifts of 10 and 17 nm for the emission maxima were measured for **3-NI-pqx** and **4-NI-pqx** (respectively), relative to **pqx**. In contrast, a significant bathochromic shift of 145 nm was measured for the low-energy emission band for **NI-phen**, relative to **phen**. All functionalised analogues presented much more red-shifted emission bands relative to their corresponding model compounds.

Photophysical data are shown in **Table 5.4** for the phenanthroline ligands and in **Table 5.5** for the phenylquinoxaline compounds. In general, the incorporation of unsubstituted NI was deemed to have minimal impact on the electronic properties at room temperature, where quantum yields remained low (Φ_F < 3.7%). Calculated Φ_F values increased drastically upon incorporation of a morpholine unit, reminiscent of a charge-transfer species where Φ_F was 38.8% and 61.5% for **MNI-phen** and **4-MNI-pqx**, respectively.

Ligand	λ_{abs} / nm	λ_{em} / nm[a]	λ_{em} / nm (77K)[a,b]	Φ_{em} / %[c]	τ_{obs} / ns[d]	τ_{obs} / ns[e]	$\Delta\lambda$ / nm[f]
phen	230, **263**	360, **378**, 397 sh *(360, 378, 398 sh)*	-	-	< 1.0[67]	-	97
NI-phen	231, 263, 322, **333**, 349	375, 393, **523** *(375, 394, 520)*	**542**, 588, 641	2.4	1.2 (6%) 8.7 (94%)	8.3	42
MNI-phen	231, 264, **401**	**528** *(504)*	474, **562**	38.8	2.4 (83%) 6.8 (17%)	3.1	127
AI-phen	231, 263, 377, 415, **435**, 461	**490**, 515 sh *(490, 521, 564 sh)*	488, 521, 556 sh	94.4	4.0 (4%) 13.7 (96%)	13.3	55

***Table 5.4:** Photophysical properties of the phenanthroline-based free ligands, measured in aerated MeCN at room temperature (ca. 10^{-5} M), values in parentheses in ca. 10^{-5} M CHCl$_3$ solutions (λ_{max} in bold). $^a\lambda_{ex}$ = max λ_{abs} value; ^{b}in DCM/MeOH glass (1:1) λ_{ex} = 350 nm, unless otherwise specified; ^{c}using known standard, quinine sulphate in 0.1M H$_2$SO4 (Φ = 0.546 at λ_{ex} = 350);[66] $^d\lambda_{ex}$ = 295 nm, measured at λ_{em} indicated in bold, relative contributions of τ_1 and τ_2 in parentheses; ^{e}average lifetime; $^f\lambda_{em} - \lambda_{abs}$ for peak maxima.*

Time-resolved luminescence measurements were carried out in aerated solutions of acetonitrile or chloroform, where the NI derivatives displayed slight enhancement relative to their respective ligand scaffold (**phen** and **pqx**). Inclusion of an NI unit produced bi-exponential decay profiles in all cases, where the short-lived minor component contributions were negligible in **NI-phen**, **AI-phen** and the **MNI-pqx** compounds. In general, all observed lifetimes were indicative of a singlet emissive state (*i.e.* fluorescence), with averaged lifetimes between 3.1 and 13.3 ns for the **phen**-type ligands, and 0.9 – 7.6 ns for the **pqx**-type variants. Average lifetimes were extremely short for the **NI-pqx** analogues (τ_{obs} < 1.1 ns), whereas the lifetime of **NI-phen** was slightly longer (τ_{obs} = 8.3 ns). The exceedingly short lifetime of the **NI-pqx** ligands were consistent with previous reports on N-phenyl NI systems where the short-lived nature of the excited state has been attributed to rapid internal conversion,

which was also responsible for reduced quantum yields.[68] However, the **MNI-pqx** compounds displayed longer average lifetimes than **MNI-phen**, with a maximum value of 7.6 ns for **3-MNI-pqx**. All lifetimes were within the nanosecond region, consistent with a singlet emissive (*i.e.* a fluorescence decay pathway) state at room temperature. Additionally, measurements of the **NI-phen** species were recorded in both chloroform and acetonitrile, but only slight deviations between them were recognised.

Ligand	λ_{abs}/ nm	λ_{em} / nm[a]	λ_{em} / nm (77K)[e]	Φ_{em} / %[f]	τ_{obs} / ns[g]	τ_{av} / ns[h]	$\Delta\lambda$ / nm[i]
pqx	261, 334	402[b] (377)[b]	385, 502, 536	3.2 (2.7)	< 1.0	-	68
3-NI-pqx	260, 336, 351	**410**	**540**, 587, 638	3.7	0.5 (65%) 2.3 (35%)	1.1	59
4-NI-pqx	264, 337, 351	**419**, 449	**542**, 588, 640	3.5	0.3 (58%) 1.8 (42%)	0.9	68
3-MNI-pqx	260, 340, 398	**502**	**592**[c]	*	2.2 (6%) 7.9 (94%)	7.6	104
4-MNI-pqx	264, 338, 396	**501**	**583**[c]	61.5	2.5 (4%) 7.5 (96%)	7.3	105

*Table 5.5: Photophysical properties of the quinoxaline-based free ligands, measured in aerated CHCl$_3$ (ca. 10^{-5} M, RT), values in parentheses in ca. 10^{-5} M MeCN solutions (λ_{max} in bold). [a]λ_{ex} = 350 nm, unless otherwise specified; [b]λ_{ex} = 335 nm; [c]λ_{ex} = 400 nm; [d]λ_{ex} = 450 nm; [e]in DCM/MeOH glass (1:1) λ_{ex} = 350 nm, unless otherwise specified; [f]using known standard, quinine sulphate in 0.1M H$_2$SO$_4$ (Φ = 0.546 at λ_{ex} = 350)[66] samples in CHCl$_3$ or MeCN; [g]λ_{ex} = 295 nm, measured at λ_{em} in bold, relative contributions of τ_1 and τ_2 in parentheses; [h]average lifetime; [i]$\lambda_{em} - \lambda_{abs}$ for peak maxima. *Quantum yield was not able to be calculated due to poor solubility.*

Stokes' shifts were calculated by the difference between peak maxima in the absorption and emission spectra. Overall, these values were greater for the 4-substituted analogues relative to their 3-substituted counterparts, suggesting that the excited states of the former were of lower energy. The **NI-pqx** compounds displayed the smallest Stokes' shifts (42 – 68 nm) whereas the **MNI** variants presented large shifts exceeding 100 nm – indicative of enhanced ICT character by the reduced energy of the ICT excited state.

Low temperature (77 K) total emission spectra were collected for all ligand species in an attempt to investigate possible phosphorescence contributions from an organic triplet excited state. In some cases, the steady-state emission profiles exhibited a significant red-shift and enhanced vibronic coupling upon cooling, giving rise to three highly structured features. It appeared that the triplet state localised at the naphthalimide unit (^{3}NI) became accessible at low temperatures. **Figure 5.23** compares the spectra of three different NI-containing species, where the highly structured spectral features at 540 – 640 nm are closely comparable and must belong to the NI component. These features are also consistent with previous reports on similar 1,8-napthalimide systems.[69,70]
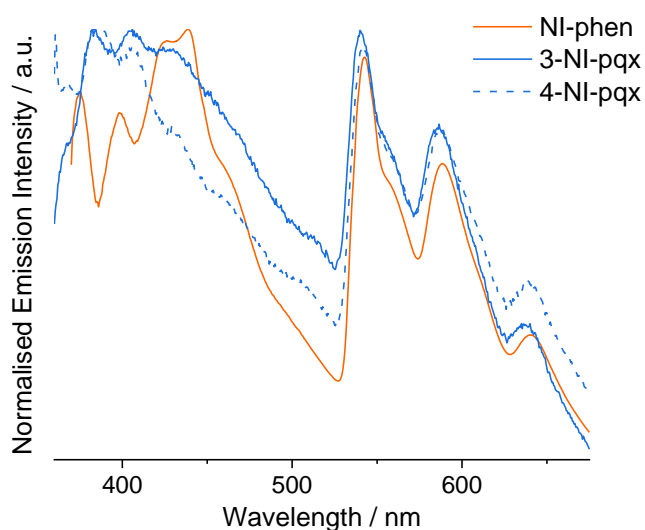
Figure 5.23: *Normalised emission spectra of the NI-containing free ligands, where phosphorescence from ^{3}NI becomes observable alongside fluorescence.*

5.3.5: Photophysical Properties of Complexes

UV-vis absorption spectra were collected for all Ir(III) species in *ca.* 10^{-5} M chloroform or acetonitrile solutions, depending on their relative solubilities (**Figure 5.24** and **Figure 5.25**). Highly structured, ^{1}LC transitions were observed below 400 nm, assigned by their presence in the corresponding free ligand spectra. The complexes also displayed additional broadened features up to ~600 nm, representing 5d→π* ^{1}MLCT and ^{3}MLCT contributions. These were expectedly very weak and were consistent with an analogous Re(I) series.[32]
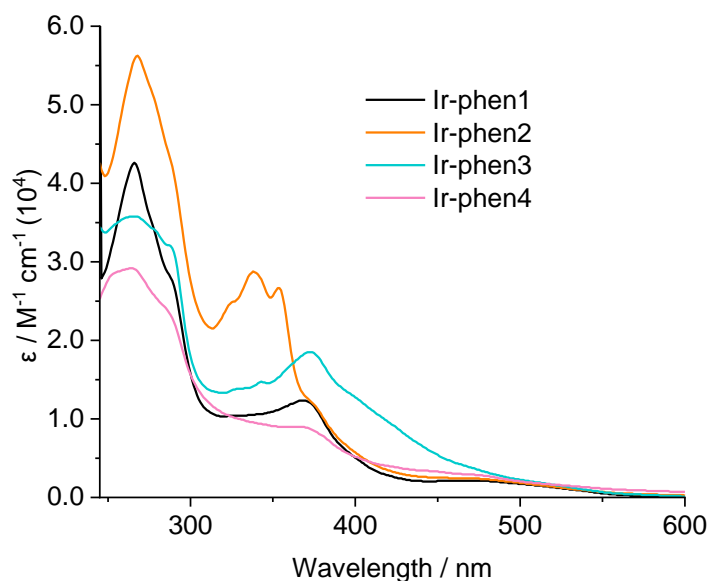
Figure 5.24: *UV-vis absorption spectra of the phenanthroline-substituted complexes and the control complex, **Ir-phen1** (CHCl₃, 0.99 × 10⁻⁵M, RT).*

All spectra resembled that of **Ir-phen1** with additional ligand-centred transitions at 336 – 352 nm in most cases, associated with the appendaged NI units. These bands were more prevalent in the modified **pqx** complexes, where two equivalents of chromophore were incorporated into the structure. Interestingly, these bands, along with the assigned MLCT absorption features, were of greater intensity when the N^N ligand was 1,10-phenanthroline rather than 2,2'-bipyridine, with little variation in λ_{abs}. This suggested that the ancillary ligand influenced the absorption properties of the complex but did not directly impact the HOMO-LUMO energy gap. Absorption features were also intensified in the complexes with 4-substituted **pqx** ligands (**Figure 5.25**, dashed line), relative to their isomeric forms. Ligand-centred ICT features overlapped with the assigned MLCT bands in the **MNI**-containing complexes, giving rise to an extremely broadened, structureless feature – clearly seen in the absorption profile of **Ir-phen3**. Measurements of **Ir-pqx5** and **Ir-pqx6** were carried out in acetonitrile, due to limited solubilities in chloroform. Therefore, physical properties of the complexes were largely affected by the position at which the chromophore was attached.
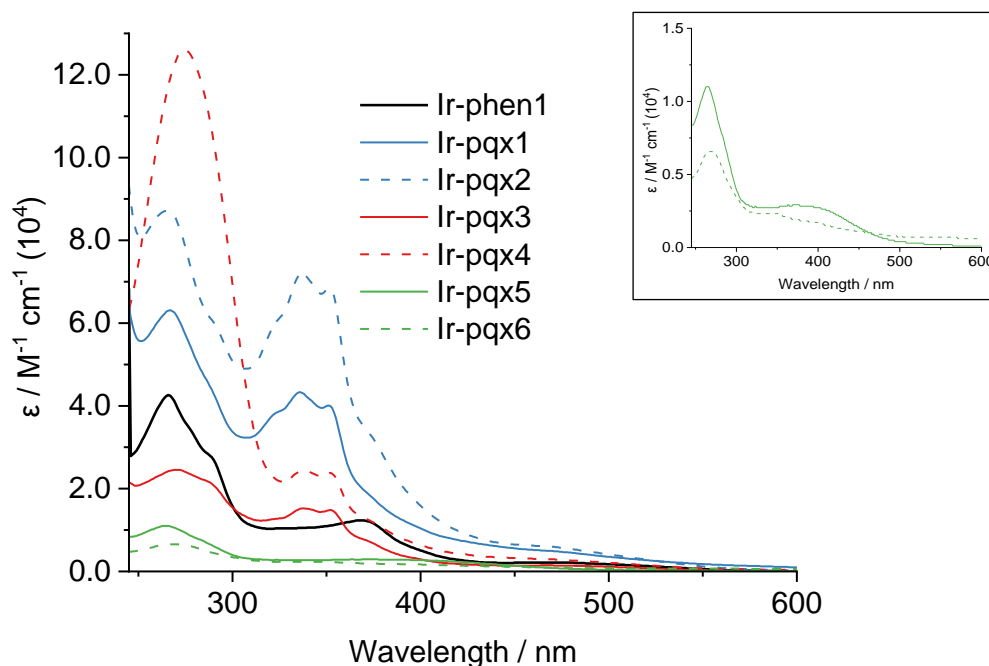
Figure 5.25: *UV-vis absorption spectra of the 3-(solid) and 4-(dashed) substituted 2-phenylquinoxaline complexes (CHCl$_3$, 0.99 × 10^{-5} M, RT).* ***Ir-pqx5*** *and* ***Ir-pqx6*** *(inset: magnified) were recorded in MeCN (0.99 × 10^{-5}M, RT).*
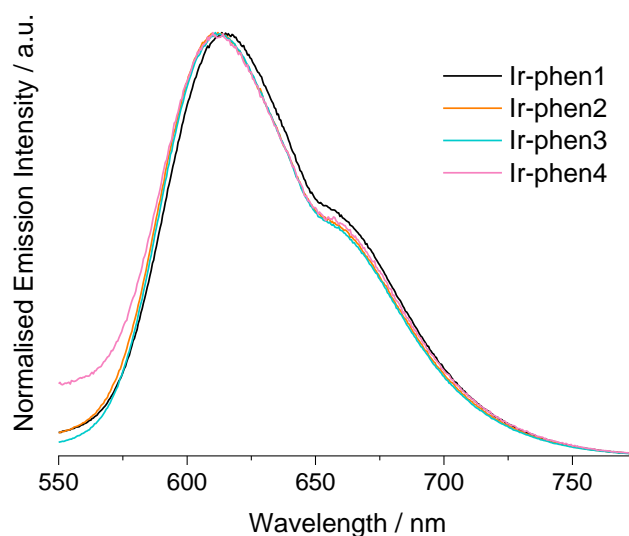
Figure 5.26: *Normalised emission spectra of the phenanthroline-substituted complexes in ca. 10^{-5}M CHCl$_3$ solutions at RT, λ$_{ex}$ = 500 nm.*

Steady-state luminescence measurements were also recorded for all Ir(III) species. The spectra for the series of complexes containing functionalised N^N ancillary ligands are shown in **Figure 5.26**, where broad emission profiles were exhibited within the orange-to-red region of the visible range using λ$_{ex}$ = 500 nm. Peak maxima were recorded at almost identical positions, with only a small hypsochromic shift of ~3-4 nm upon incorporation of an NI unit – characteristic

shoulder peaks were also seen in all instances. This suggested that the emission wavelength was not largely affected by the nature of the ancillary ligands.

Due to the significant ICT character observed in the morpholine-containing free ligands, the absorption and emission properties of **Ir-phen3** were studied in various solvents in order to observe the solvatochromic behaviour of the resultant complex. The UV-vis spectra remained fairly consistent, with only slight variations in the peak at ~370 – 375 nm with no discernible changes to the assigned MLCT absorption feature. In contrast, the emission properties showed great dependence on the nature of the solvent (**Figure 5.27**), where emission maxima were seen within the range of 606 – 637 with shoulder features observed up to 660 nm. The complex exhibited positive solvatochromism, where a bathochromic shift in λ_{em} was seen upon increasing solvent polarity, indicative of a polar excited state which became stabilised in polar solvents. Notably, the shoulder peaks became much more pronounced in polar solvents, where it displayed almost equal intensity to the highest intensity peak in methanol.
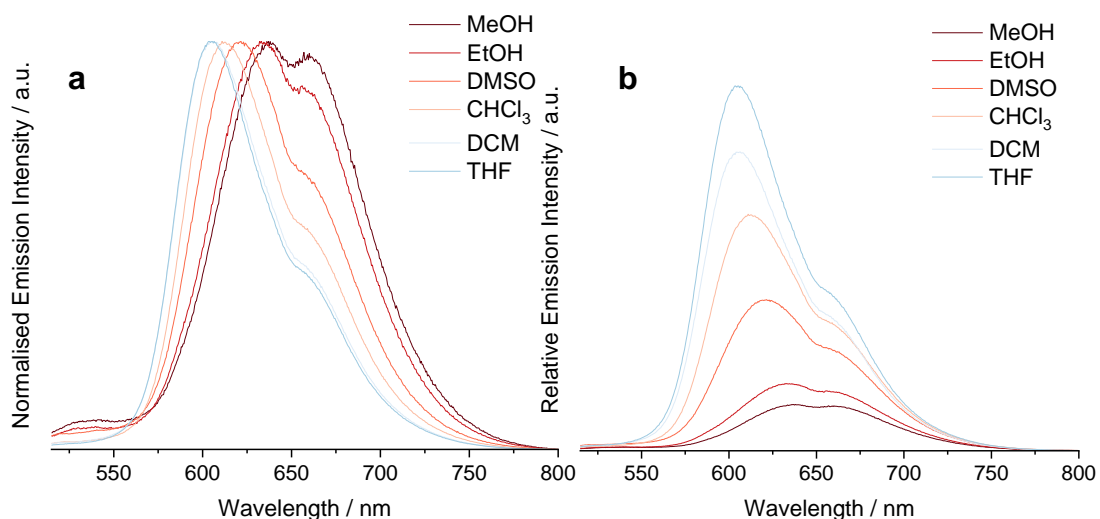
Figure 5.27: *Normalised (left) and relative (right) emission spectra of **Ir-phen3** in various solvents (0.99 × 10⁻⁵M, RT) λ_{ex} = 500 nm.*

Steady-state emission spectra for the series of complexes where substitution occurred at the C^N ligands are displayed in **Figure 5.28** and **Figure 5.29**. The broad emission profiles closely resembled those seen for the substituted N^N

ligands, with peak maxima between 605 – 615 nm alongside shoulder peaks using $\lambda_{ex} = 500 - 520$ nm.
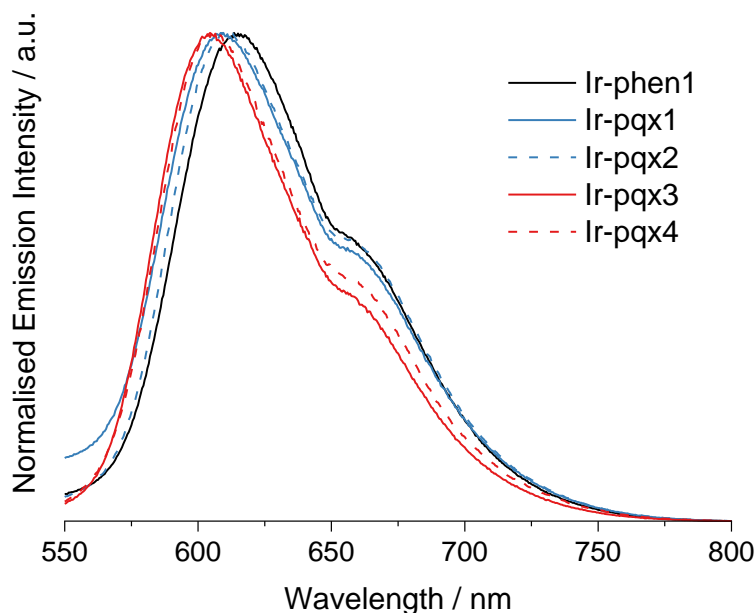
Figure 5.28: *Normalised emission spectra of the complexes containing **NI-pqx** C^N ligands in CHCl$_3$ (ca. 10^{-5}M, RT), $\lambda_{ex} = 500$ nm.*

Upon changing the N^N ligand from 1,10-phenanthroline to 2,2'-bipyridine, a slight hypsochromic shift was observed alongside a reduced intensity of the shoulder feature. However, differences were minimal and peak maxima positions once again displayed little dependence on the nature of the surrounding ligands.

Dual emission was recognised at $\lambda_{ex} = 450$ nm in some cases, where the shorter wavelength peak likely originated from a ligand-centred excited state. An example is shown in **Figure 5.30**, where the high-energy peak for **Ir-phen4** is in alignment with the emission of **Al-phen**. Here, fluorescence from the NI chromophore was observed alongside phosphorescence, causing a reduction in intensity of the MLCT-type emission. This was attributed to the overlap of LC and MLCT contributions in the absorption spectrum at ~450 nm. A similar effect was seen for the **MNI-pqx** complexes (**Ir-pqx5** and **Ir-pqx6**) where the intense ligand-centred fluorescence peak overlapped with the assigned ^{3}MLCT emission. Whilst ligand-centred emission dominated at shorter wavelengths, the assigned MLCT feature was distinguishable when $\lambda_{ex} > 500$ nm (**Figure 5.31**). Notably, these features also became isolated at low temperatures.
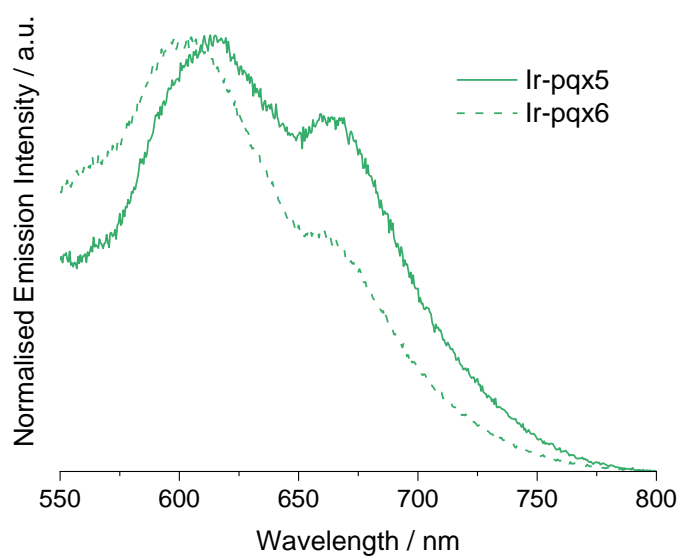
Figure 5.29: *Normalised emission spectra of the complexes containing **MNI-pqx** C^N ligands in MeCN (ca. 10^{-5}M, RT), λ_{ex} = 520 nm.*
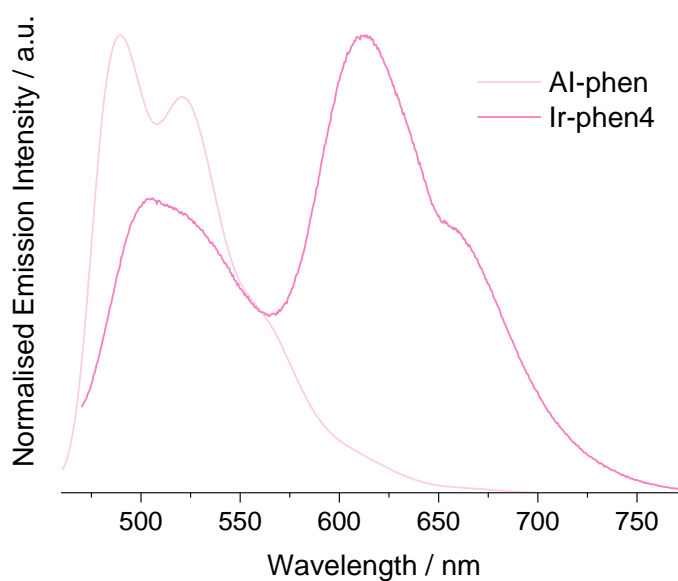
Figure 5.30: *Normalised emission spectra of **Ir-phen4** and **Al-phen** in CHCl₃ (ca. 10^{-5}M), λ_{ex} = 450 nm.*
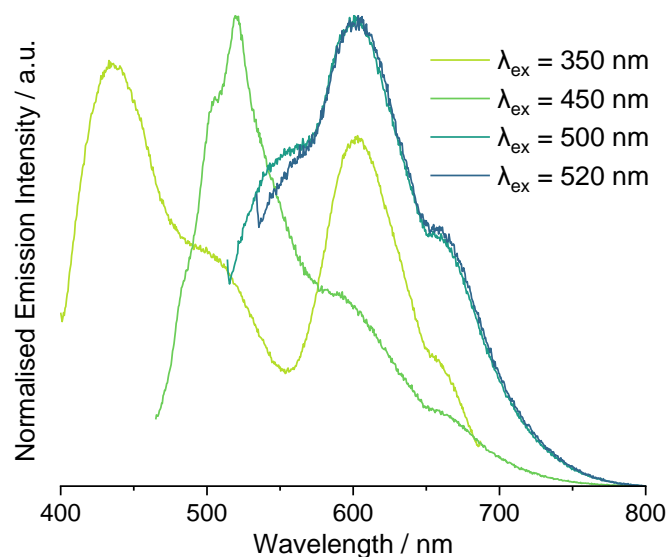
Figure 5.31: *Normalised emission spectra of **Ir-pqx6** recorded using different excitation wavelengths (MeCN, ca. 10^{-5}M, RT).*

Complex	λ_{abs}/ nm	λ_{em} / nm[a]	λ_{em} / nm (77K)[a,b]	Φ_{PL}/ %[e]	τ_{obs} / ns[f]	τ_{obs} / µs[g]
Ir-phen1	266, 289, 368, 480, 525 sh	**616**, 658 sh	**598**, 659 sh	7.7	492	2.02
Ir-phen2	268, 338, 353, 475, 524 sh	**612**, 657 sh	**598**, 651 sh	5.9	599	4.77
Ir-phen3	265, 288, 372, 424, 472, 518, 547 sh	**613**, 659 sh	**599**, 649 sh[c] 606, 657 sh[d]	9.1	438	1.22
Ir-phen4	263, 287, 369, 444, 518 sh	**612**, 657 sh	**599**, 639 sh, 657 sh[c] **606**, 657 sh[d]	1.6	417	2.15

Table 5.6: *Photophysical properties of the **Ir-phen** complexes measured in aerated CHCl$_3$ (ca. 10^{-5} M, RT) unless otherwise specified (λ_{max} in bold text). [a]λ_{ex} = 500 nm; [b]in DCM/MeOH glass (1:1); [c]λ_{ex} = 520 nm; [d]λ_{ex} = 550 nm; [e]using known standard, [e]**[Ru(bpy)$_3$](PF$_6$)$_2$** in MeCN (Φ = 0.016 at λ_{ex} = 450 nm)[71] used as a standard for quantum yield determination; [f]λ_{ex} = 295 nm, measured at λ_{em} indicated in bold; [g]λ_{ex} = 295 nm, measured at λ_{em} indicated in bold, degassed CHCl$_3$.*

Complex	λ_{abs} / nm	λ_{em} / nm[b]	λ_{em} / nm (77K)[d]	Φ_{PL} / %[e]	τ_{obs} / ns[f]	τ_{obs} / μs[g]
Ir-pqx1	266, 336, 351, 463, 529 sh	609, 657 sh	590, 629 sh[c]	3.0	592	2.21
Ir-pqx2	265, 337, 351, 468, 525 sh	612, 657 sh	595, 638 sh[c]	4.9	562	3.01
Ir-pqx3	269, 337, 352, 431, 490 sh	605, 657 sh	583, 624 sh	10.0	700	2.26
Ir-pqx4	274, 336, 352, 432, 494 sh	606, 660 sh	586, 628 sh	7.6	632	4.91
Ir-pqx5	227, 265, 378, 438 sh[a]	615, 663 sh [a,c]	603, 655 sh	-	397	3.73
Ir-pqx6*	229, 267, 347, 443 sh[a]	603, 658 sh[a,c]	620, 659 sh	-	-	-

*Table 5.7: Photophysical properties of the **Ir-pqx** complexes measured in aerated CHCl₃ at room temperature (ca. 10⁻⁵ M) unless otherwise specified (λ_{max} in bold). [a]in aerated MeCN (ca. 10⁻⁵ M); [b]λ_{ex} = 500 nm, unless otherwise specified; [c]λ_{ex} = 520 nm; [d]in DCM/MeOH glass (1:1); [e]using known standard, **[Ru(bpy)₃](PF₆)₂** in MeCN (Φ = 0.016 at λ_{ex} = 450 nm) [71] for quantum yield determination; [f]λ_{ex} = 295 nm, measured at λ_{em} indicated in bold; [g]λ_{ex} = 295 nm, measured at λ_{em} indicated in bold, degassed CHCl₃. ***Ir-pqx6** was crude sample.*

The photophysical properties for the complexes are displayed in **Table 5.6** and **Table 5.7**. Although there was little variation in emission wavelength, the nature of the ligand had a profound impact on other properties, namely the photoluminescence lifetimes and absorption features. Φ_{PL} values were calculated using the proposed ³MLCT emission band at longer wavelengths to specifically target the phosphorescence decay pathway, since LC emission directly competes with this process. Values were calculated up to 10.0% for **Ir-pqx3**, with **Ir-phen4** displaying the lowest value of 1.6% – consistent with the significant dual-emission exhibited at the excitation wavelength used. The large quantum yields of some species were accounted for by the absence of any significant dual-emission at this particular λ_{ex}, where phosphorescence was the dominant radiative decay pathway. There was no clear trend in quantum yields with regard to the chemical structures, but an enhancement was recognised upon replacing a phenanthroline N^N ligand with bipyridine in the **Nl-pqx**

species. At λ_{ex} = 450 nm, the luminescence spectra for **Ir-pqx5** and **Ir-pqx6** were dominated by ligand-centred emission; therefore, accurate phosphorescent quantum yields could not be determined for these complexes.

Time-resolved measurements were performed for the complexes and displayed significant enhancements in luminescence lifetimes in aerated solutions, relative to the free ligands. Mono-exponential decay was measured in all cases when targeting the long-wavelength emission band. The longest lifetime for the **Ir-phen** series was recorded as 599 ns for **Ir-phen2**, whereas lifetimes of the **Ir-pqx** species in oxygenated media were generally longer with a maximum value of 700 ns for **Ir-pqx3**. This supported previous studies, where excited state lifetimes were sensitive to the number of chromophores attached to the species, offering tunability of the triplet-triplet equilibrium.[39] The data was consistent with emission from a low-lying triplet state, where lifetimes increased significantly upon complexation due to the spin-forbidden nature of the relaxation pathway.

Ir-phen2 exhibited a significantly longer lifetime than **Ir-phen1**, possibly indicative of a TTET mechanism. However, measurements in degassed solutions were essential to validate this assumption. In the absence of molecular oxygen, the lifetime of **Ir-phen2** was enhanced to 4.77 µs, over twice as long as the lifetime of **Ir-phen1** (2.02 µs) in degassed solvent. For **Ir-phen3** and **Ir-phen4**, no observable delayed luminescence was seen as the lifetimes were comparable to the model complex in both aerated and degassed solutions.

Lifetimes of the **Ir-pqx** complexes were also measured in degassed solutions, where a significant enhancement in τ_{obs} (relative to **Ir-phen1**) was recognised upon incorporation of an NI unit at the 4-position (relative to the quinoxaline). Interestingly, **Ir-pqx4** displayed the longest-lived excited state with τ_{obs} = 4.91 µs in degassed solvent, exhibiting luminescence that was over twice as long-lived as its isomeric form (**Ir-pqx3**). An overall enhancement was also recognised when N^N was **bpy** as opposed to **phen**. Interestingly, although the complex containing the MNI-substituted ancillary ligand displayed a shorter lifetime than the model complex, the complex with MNI-substituted C^N ligands presented an enhancement, where τ_{obs} was ~1.71 µs longer than for **Ir-phen1**.

Low temperature (77 K) steady-state luminescence measurements were carried out to gain insight into the accessibility of the ^{3}NI state. It was hypothesised that if a thermal equilibrium existed between the ^{3}MLCT and ^{3}NI energy levels, it would become restricted at low temperatures and the two decay pathways would become independent.[39] A hypsochromic shift in emission wavelength, probably due to rigidochromism, of the ^{3}MLCT peak was seen, accompanied by an enhancement in vibronic structure upon cooling (**Figure 5.32** and **Figure 5.33**).
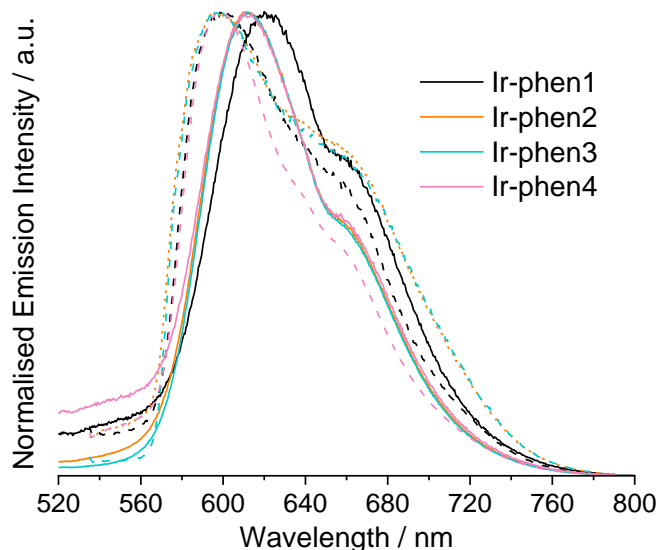
Figure 5.32: *Normalised emission profiles for the phenanthroline-functionalised Ir(III) species at at 77 K (dashed lines, DCM/MeOH 1:1 glass) and 298 K (solid lines, CHCl$_3$) (λ_{ex} = 500 – 520 nm).*
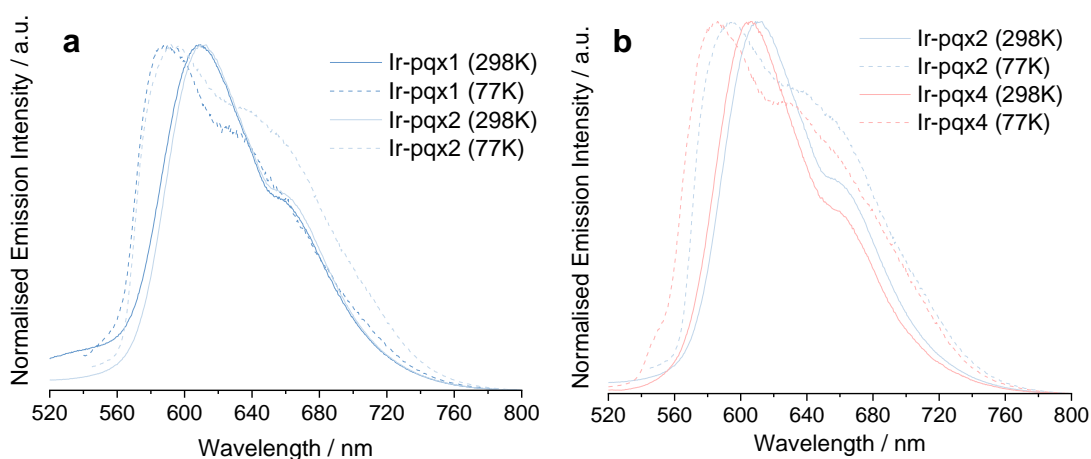
Figure 5.33: *(a) Normalised emission spectra of **Ir-pqx1** and **Ir-pqx2** at 298 K (CHCl$_3$, λ_{ex} = 500 nm) (solid) and 77 K (DCM/MeOH 1:1 glass, λ_{ex} = 525 nm) (dashed). (b) Normalised emission spectra of **Ir-pqx2** and **Ir-pqx4** at 298 K (CHCl$_3$, λ_{ex} = 500 nm) (solid) and 77 K (DCM/MeOH 1:1 glass, λ_{ex} = 490 nm) (dashed).*

5.4: Conclusions

This chapter focused on the design, synthesis and characterisation of two series of ligands with chromophores containing modified NI units. The photophysical properties of the resultant novel complexes were investigated, where the impact of the site of attachment of the NI unit (either through an N^N ligand based upon 1,10-phenanthroline or a C^N ligand based upon 2-phenylquinoxaline) at the extremities of the complex were investigated, and directly compared to the model complex **Ir-phen1**.

Low temperature photoluminescence measurements suggested that the triplet state of the NI unit was accessible in the free ligands, suggesting that some TTET could be occurring upon complexation. This was supported by the significantly enhanced luminescence lifetimes at room temperature, especially noticeable in degassed solutions when lifetimes up to 4.77 and 4.91 µs were measured for the ancillary and cyclometallating ligands containing unmodified NI units, respectively. It was shown that structural modification had less significant impact on the lifetime of the excited state and was more reminiscent of emission from an isolated ^{3}MLCT state. Additionally, broad absorption features were widespread across the visible range up to ~600 nm, consisting of many individual features.

5.5: Experimental

5.5.1: General Considerations

All commercially available reagents were used without further purification, and all reactions employed vacuum line and Schlenk techniques. ^{1}H, ^{13}C{^{1}H} and ^{19}F{^{1}H} NMR spectra were recorded on NMR-FT Bruker 500, 400 and 300 MHz spectrometers in the appropriate solvents (CDCl$_3$, (CD$_3$)$_2$CO, CD$_3$CN or DMSO-d_6), where chemical shift (δ) positions (ppm) were determined relative to TMS and residual solvent peaks[72] through digital locking. High resolution mass spectra were obtained by staff at Cardiff University using a Waters Xevo G2-XS QTof spectrometer, and IR spectra were recorded on a Shimadzu IRAffinty-1 FTIR spectrometer. UV-vis spectroscopy studies were performed on 10^{-5} M CHCl$_3$ or MeCN solutions using a Shimadzu UV-1800 spectrophotometer. The 10^{-5} M samples were prepared by dilution of 10^{-3} M bulk stock solutions. Upon sonication in an ultrasonic bath, the samples were inspected to ensure that solute was fully dissolved. Luminescence data was acquired for 10^{-5} M CHCl$_3$ or MeCN solutions of the samples using a JobinYvon-Horiba Fluorolog spectrometer fitted with a JY TBX picosecond single-photon detection module. Time-resolved measurements were recorded using a Nano-LED pulsed laser source configured for 295 or 459 nm output, operating at 1 MHz. Time-resolved measurements were recorded using the JobinYvon-Horiba FluoroHub single photon counting module and the data was resolved using the DAS6 deconvolution software.

5.5.2: Preparation of Organic Precursors and Ligands

Synthesis of 6-morpholino-1H,3H-benzo[*de*]isochromene-1,3-dione *(1)*
Following an adapted literature method,[43] 4-bromo-1,8-naphthalic anhydride (750 mg, 2.71 mmol) and morpholine (354 mg, 4.06 mmol) were dissolved in 2-methoxyethanol (30 mL) and the solution was heated to reflux under an inert N$_2$ atmosphere for 12 h. The solution was cooled to room temperature and the solvent was removed *in vacuo* to give the crude product, which was purified by column chromatography (SiO$_2$, DCM), where the pure product eluted as the first band and the solvent was removed *in vacuo* to give a dark yellow solid (411 mg,

53.6%). ^{1}H NMR (300 MHz, (CD$_3$)$_2$CO) δ_H = 8.60 (dd, $^3J_{HH}$ = 8.5, $^4J_{HH}$ = 1.1 Hz, 1H), 8.48 (dd, $^3J_{HH}$ = 7.3, $^4J_{HH}$ = 1.1 Hz, 1H), 8.42 (d, $^3J_{HH}$ = 8.1 Hz, 1H), 7.80 (dd, $^3J_{HH}$ = 8.5, 7.3 Hz, 1H), 7.37 (d, $^3J_{HH}$ = 8.2 Hz, 1H), 3.95 – 3.89 (m, 4H), 3.32 – 3.25 (m, 4H) ppm. FTIR (solid, cm^{-1}) (ATR) v_{max}: 2955, 2853, 1744, 1719, 1584, 1570, 1518, 1454, 1433, 1396, 1375, 1327, 1300, 1236, 1211, 1117, 1088, 1009, 991, 916, 864, 849, 835, 785, 758, 729, 665, 652, 588, 573, 492, 455. The data was consistent with literature findings.[73,74]

Synthesis of 1H,3H-dibenzo[*de,h*]isochromene-1,3-dione *(2)*

To a stirred solution of aceanthrequinone (1.79 g, 0.772 mmol) in 1,4-dioxane (40 mL) and 2M NaOH (12 mL), aqueous H$_2$O$_2$ (30%, 9 mL) was added dropwise. The mixture was then heated to reflux for 1 hour. Upon addition of distilled water (40 mL) and 1M H$_2$SO$_4$ (80 mL), a yellow solid precipitated out of solution and the suspension was allowed to stand at room temperature overnight. The resultant mixture was filtered under suction to give rise to an orange solid, which was subsequently dissolved in a minimal volume of 2M KOH and the insoluble solids were removed *via* filtration under gravity. HCl (conc.) was added dropwise to the filtrate to initiate precipitation of the product, which was isolated by vacuum filtration and washed sequentially with distilled water (~15 mL) to give rise to the pure product as a bright orange solid (1.69 g, 88.2%). ^{1}H NMR (300 MHz, CDCl$_3$) δ_H = 9.76 (dd, $^3J_{HH}$ = 9.1, $^4J_{HH}$ = 0.7 Hz, 1H), 8.98 (s, 1H), 8.79 (dd, $^3J_{HH}$ = 7.1, $^4J_{HH}$ = 1.2 Hz, 1H), 8.52 – 8.47 (m, 1H), 8.20 (dd, $^3J_{HH}$ = 8.4, 0.6 Hz, 1H), 7.94 (ddd, $^3J_{HH}$ = 9.1, 6.7, $^4J_{HH}$ = 1.4 Hz, 1H), 7.81 (dd, $^3J_{HH}$ = 8.4, 7.0 Hz, 1H), 7.76 – 7.70 (m, 1H) ppm. The data was consistent with literature findings.[15]

Synthesis of 2-(1,10-phenanthrolin-5-yl)-1H-benzo[*de*]isoquinoline-1,3-(2H)-dione *(NI-phen)*

1,8-naphthalic anhydride (100 mg, 0.505 mmol) and 5-aminophenanthroline (345 mg, 1.77 mmol) were dissolved in glacial acetic acid (10 mL). The solution was heated to reflux for 24 hours. Upon cooling to room temperature, distilled water (50 mL) was added, and the resultant precipitate was filtered under reduced pressure, washing the solid sequentially with distilled water (~20 mL) to give rise to the pure product as an off-white crystalline solid (168 mg, 88.8%). ^{1}H NMR (500 MHz, CDCl$_3$) δ_H = 9.27 (dd, $^3J_{HH}$ = 4.4, $^4J_{HH}$ = 1.7 Hz, 1H), 9.23

(dd, $^3J_{HH}$ = 4.3, $^4J_{HH}$ = 1.6 Hz, 1H), 8.70 (dd, $^3J_{HH}$ = 7.3, $^3J_{HH}$ = 1.1 Hz, 2H), 8.37 (dd, $^3J_{HH}$ = 8.4, $^4J_{HH}$ = 1.0 Hz, 2H), 8.29 (dd, $^3J_{HH}$ = 8.1, $^4J_{HH}$ = 1.7 Hz, 1H), 8.06 (dd, $^3J_{HH}$ = 8.3, $^4J_{HH}$ = 1.7 Hz, 1H), 7.90 (s, 1H), 7.87 (dd, $^3J_{HH}$ = 8.2, 7.3 Hz, 2H), 7.70 (dd, $^3J_{HH}$ = 8.0, 4.4 Hz, 1H), 7.58 (dd, $^3J_{HH}$ = 8.3, 4.3 Hz, 1H) ppm. ^{13}C{^{1}H} NMR (126 MHz, CDCl$_3$) δ_C = 164.5, 151.2, 150.7, 135.1, 132.3, 132.1, 131.3, 131.2, 129.0, 128.2, 127.7, 127.4, 123.7, 123.6, 122.6 ppm. UV−vis (MeCN) λ_{max} ($\varepsilon \times 10^4$ / L mol^{-1} cm^{-1}): 231 (9.0), 263 (3.1), 332 (1.2), 333 (1.5), 349 (1.3) nm. FTIR (solid, cm^{-1}) (ATR) v_{max}: 3053, 1709, 1663, 1585, 1510, 1418, 1373, 1350, 1234, 1186, 1022, 880, 847, 804, 779, 739, 702, 625, 604, 528, 509, 469. The data was consistent with literature findings.[32]

Synthesis of 6-morpholino-2-(1,10-phenanthrolin-5-yl)-1H-benzo[*de*]iso-quinoline-1,3(2H)-dione *(MNI-phen)*

The compound was prepared from a modified literature preparation,[32] where **1** (217 mg, 0.766 mmol) and 5-aminophenanthroline (165 mg, 0.843 mmol) in glacial acetic acid (6 mL) were added to a 75 mL pressure vessel and heated to 145°C (~2 bar) for 24 hours. Upon cooling to room temperature, distilled water (5 mL) was added, where the resultant precipitate was filtered under reduced pressure and washed with distilled water (20 mL). The solid was dried overnight in an oven (~60°C) and then purified by column chromatography (SiO$_2$, DCM/MeOH) where the pure product eluted as a yellow band with 9:1 DCM/MeOH as the eluent. The solvent was removed *in vacuo* and the solid was dried to generate the pure product as a yellow solid (149 mg, 42.3%). ^{1}H NMR (500 MHz, CDCl$_3$) δ_H = 9.24 (dd, $^3J_{HH}$ = 4.4, $^4J_{HH}$ = 1.6 Hz, 1H), 9.19 (dd, $^3J_{HH}$ = 4.3, $^4J_{HH}$ = 1.6 Hz, 1H), 8.66 (dd, $^3J_{HH}$ = 7.2, $^4J_{HH}$ = 0.9 Hz, 1H), 8.60 (d, $^3J_{HH}$ = 8.0 Hz, 1H), 8.53 (dd, $^3J_{HH}$ = 8.5, $^4J_{HH}$ = 1.0 Hz, 1H), 8.25 (dd, $^3J_{HH}$ = 8.1, $^4J_{HH}$ = 1.6 Hz, 1H), 8.02 (dd, $^3J_{HH}$ = 8.3, $^4J_{HH}$ = 1.6 Hz, 1H), 7.86 (s, 1H), 7.78 (dd, $^3J_{HH}$ = 8.4, 7.3 Hz, 1H), 7.65 (dd, $^3J_{HH}$ = 8.0, 4.4 Hz, 1H), 7.54 (dd, $^3J_{HH}$ = 8.3, 4.3 Hz, 1H), 7.29 (d, $^3J_{HH}$ = 8.1 Hz, 1H), 4.08 − 4.01 (m, 4H), 3.36 − 3.28 (m, 4H) ppm. ^{13}C{^{1}H} NMR (126 MHz, CDCl$_3$) δ_C = 164.8, 164.2, 156.7, 151.2, 150.7, 136.6, 133.6, 132.2, 131.3, 131.2, 131.2, 130.8, 128.1, 127.6, 126.6, 126.4, 126.3, 123.6, 123.5, 123.2, 116.8, 115.3, 67.1, 53.6 ppm. HRMS (ES+): *m/z* calc'd 461.1614 for C$_{28}$H$_{21}$N$_4$O$_3$; found 461.1618 [M + H]$^+$. UV−vis (MeCN) λ_{max} ($\varepsilon \times 10^4$ / L mol^{-1} cm^{-1}): 231 (4.1), 264 (2.5), 401 (0.7) nm. FTIR (solid,

cm^{-1}) (ATR) v_{max}: 3343 (br), 3065, 2972, 2849, 2818, 1701, 1655, 1585, 1578, 1508, 1422, 1364, 1227, 1190, 1155, 1111, 997, 924, 887, 756, 739, 710, 494, 469, 457.

Synthesis of 2-(1,10-phenanthrolin-5-yl)-1H-dibenzo[*de,h*]isoquinoline-1,3(2H)-dione *(Al-phen)*

1 (132 mg, 0.532 mmol) and 5-aminophenanthroline (519 mg, 2.66 mmol) were dissolved in glacial acetic acid (30 mL) and heated to reflux for 48 hours. Upon cooling to room temperature, distilled water (~40 mL) was added, and the resultant precipitate was filtered under reduced pressure, washing the solid sequentially with distilled water (~20 mL). The solid was dried overnight in an oven (~60°C) and then purified by column chromatography (SiO$_2$, DCM/MeOH), where the starting material eluted with pure DCM and the product with DCM/MeOH (9:1). The solvent was removed *in vacuo* and the solid was dried to generate the pure product as an orange solid (46.7 mg, 20.6%). ^{1}H NMR (500 MHz, CDCl$_3$) δ_H = 9.91 (d, $^3J_{HH}$ = 9.0 Hz, 1H), 9.29 (dd, $^3J_{HH}$ = 4.4, $^4J_{HH}$ = 1.7 Hz, 1H), 9.24 (dd, $^3J_{HH}$ = 4.3, $^4J_{HH}$ = 1.6 Hz, 1H), 9.04 (s, 1H), 8.89 (dd, $^3J_{HH}$ = 7.0, $^4J_{HH}$ = 1.2 Hz, 1H), 8.55 (dd, $^3J_{HH}$ = 8.4, $^4J_{HH}$ = 1.0 Hz, 1H), 8.32 (dd, $^3J_{HH}$ = 8.0, $^4J_{HH}$ = 1.7 Hz, 1H), 8.23 (d, $^3J_{HH}$ = 8.3 Hz, 1H), 8.12 (dd, $^3J_{HH}$ = 8.3, $^4J_{HH}$ = 1.6 Hz, 1H), 7.96 (s, 1H), 7.87 (dd, $^3J_{HH}$ = 8.4, 7.1 Hz, 1H), 7.83 (ddd, $^3J_{HH}$ = 9.3, 6.6, $^4J_{HH}$ = 1.4 Hz, 1H), 7.72 – 7.69 (m, 2H), 7.58 (dd, $^3J_{HH}$ = 8.4, 4.2 Hz, 1H) ppm. ^{13}C{^{1}H} NMR (126 MHz, CDCl$_3$) δ_C = 165.7, 164.2, 151.2, 150.7, 137.8, 136.7, 136.4, 134.8, 134.3, 132.3, 130.1, 129.7, 129.3, 128.2, 127.6, 127.1, 126.9, 126.8, 126.5, 125.9, 125.7, 125.4, 123.6, 123.5, 122.6 ppm. HRMS (ES+): *m/z* calc'd 426.1243 for C$_{28}$H$_{16}$N$_3$O$_2$; found 426.1246 [M + H]$^+$. UV−vis (MeCN) λ_{max} ($\varepsilon \times 10^4$ / L mol^{-1} cm^{-1}): 231 (5.3), 263 (8.9), 377 (0.7), 415 (0.6), 435 (0.8), 461 (0.6) nm. FTIR (solid, cm^{-1}) (ATR) v_{max}: 3335 (br), 2918, 2851, 1692, 1651, 1562, 1531, 1420, 1389, 1369, 1323, 1242, 1209, 1196, 1146, 878, 839, 793, 739, 698, 619, 602, 521, 430.

Synthesis of 2-(3-acetylphenyl)-1H-benzo[*de*]isoquinoline-1,3(2H)-dione *(3a)*

Following a modified literature procedure,[3] 1,8-naphthalic anhydride (371 mg, 1.87 mmol) and 3-aminoacetophenone (1.27 g, 9.36 mmol) were dissolved in glacial acetic acid (10 mL) and heated to reflux for 24 hours. Upon cooling to

room temperature, distilled water (15 mL) was added to initiate the formation of a precipitate, which was filtered under reduced pressure and washed with distilled water (10 mL) to generate the product as an off-white solid (539 mg, 91.4%). ^{1}H NMR (300 MHz, CDCl$_3$) δ_H = 8.66 (dd, $^3J_{HH}$ = 7.3, $^4J_{HH}$ = 1.1 Hz, 2H), 8.30 (dd, $^3J_{HH}$ = 8.4, $^4J_{HH}$ = 1.1 Hz, 2H), 8.09 (ddd, $^3J_{HH}$ = 7.8, $^4J_{HH}$ = 1.7, 1.2 Hz, 1H), 7.93 (ddd, $^4J_{HH}$ = 2.2, 1.7, $^5J_{HH}$ = 0.6 Hz, 1H), 7.82 (dd, $^3J_{HH}$ = 8.2, 7.3 Hz, 2H), 7.67 (*app.* td, $^3J_{HH}$ = 7.8, $^4J_{HH}$ = 0.6 Hz, 1H), 7.54 (ddd, $^3J_{HH}$ = 7.9, $^4J_{HH}$ = 2.1, 1.2 Hz, 1H), 2.63 (s, 3H) ppm. FTIR (solid, cm^{-1}) (ATR) v_{max}: 3078, 3048, 1707, 1665, 1584, 1429, 1371, 1348, 1279, 1236, 1192, 1182, 1155, 1026, 1003, 962, 932, 885, 843, 808, 773, 729, 702, 687, 648, 598, 513. The data was consistent with literature findings.[75]

Synthesis of 2-(4-acetylphenyl)-1H-benzo[*de*]isoquinoline-1,3(2H)-dione (3b)

Prepared similarly from 1,8-naphthalic anhydride (408 mg, 1.65 mmol) and 4-aminoacetophenone (1.11 g, 8.23 mmol). Purification was achieved by column chromatography (DCM, Al$_2$O$_3$) to generate the product as an off-white crystalline solid (564.1 mg, 86.9%). ^{1}H NMR (300 MHz, CDCl$_3$) δ_H = 8.66 (dd, $^3J_{HH}$ = 7.3, $^4J_{HH}$ = 1.1 Hz, 2H), 8.30 (dd, $^3J_{HH}$ = 8.4, $^4J_{HH}$ = 1.0 Hz, 2H), 8.18 – 8.12 (m, 2H), 7.82 (dd, $^3J_{HH}$ = 8.2, 7.3 Hz, 2H), 7.48 – 7.42 (m, 2H), 2.67 (s, 3H) ppm. ^{13}C{^{1}H} NMR (126 MHz, CDCl$_3$) δ_C = 197.4, 164.3, 139.9, 137.3, 134.7, 132.0, 129.6, 129.4, 128.7, 127.3, 122.7, 26.9 ppm. FTIR (solid, cm^{-1}) (ATR) v_{max}: 3061, 1699, 1678, 1661, 1584, 1506, 1435, 1410, 1371, 1348, 1294, 1234, 1184, 1109, 1024, 1016, 961, 947, 901, 831, 781, 718, 689, 596, 577, 544, 498, 478. The data was consistent with literature findings.[76]

Synthesis of 2-(3-acetylphenyl)-6-bromo-1H-benzo[*de*]isoquinoline-1,3-(2H)-dione (5a)

Prepared similarly from 4-bromo-1,8-naphthalic anhydride (258 mg, 0.931 mmol) and 3-aminoacetophenone (1.26 g, 9.31 mmol) in glacial acetic acid (10 mL). Purification was achieved by recrystallisation from glacial acetic acid to give the pure product as a pale yellow crystalline solid (230 mg, 62.7%). ^{1}H NMR (500 MHz, CDCl$_3$) δ_H = 8.71 (dd, $^3J_{HH}$ = 7.3, $^4J_{HH}$ = 0.9 Hz, 1H), 8.67 (dd, $^3J_{HH}$ = 8.5, $^4J_{HH}$ = 0.9 Hz, 1H), 8.47 (d, $^3J_{HH}$ = 7.8 Hz, 1H), 8.10 (d, $^3J_{HH}$ = 7.8 Hz, 1H), 8.10 – 8.07 (m, 1H), 7.94 – 7.92 (m, 1H), 7.91 (dd, $^3J_{HH}$ = 7.2, 6.1 Hz,

1H), 7.67 (*app.* t, $^3J_{HH}$ = 7.8 Hz, 1H), 7.53 (ddd, $^3J_{HH}$ = 7.8, $^4J_{HH}$ = 2.2, 1.2 Hz, 1H), 2.63 (s, 3H) ppm. $^{13}C\{^1H\}$ NMR (126 MHz, CDCl$_3$) δ$_C$ = 197.0, 163.9, 163.8, 138.6, 135.7, 134.1, 133.5, 132.8, 131.9, 131.5, 131.2, 131.0, 129.9, 129.5, 129.0, 128.9, 128.4, 123.2, 122.3, 26.8 ppm. FTIR (solid, cm^{-1}) (ATR) ν$_{max}$: 3088, 3067, 1711, 1692, 1657, 1585, 1568, 1364, 1344, 1277, 1233, 1188, 1126, 972, 961, 802, 781, 727, 689, 594, 521.

Synthesis of 2-(4-acetylphenyl)-6-bromo-1H-benzo[*de*]isoquinoline-1,3-(2H)-dione *(5b)*

Prepared similarly from 4-bromo-1,8-naphthalic anhydride (539 mg, 1.95 mmol) and 4-aminoacetophenone (2.63 g, 19.5 mmol) in glacial acetic acid (15 mL). Purification was achieved by recrystallisation from glacial acetic acid to give the pure product as an off-white solid (186 mg, 24.3%). ^1H NMR (300 MHz, CDCl$_3$) δ$_H$ = 8.72 (dd, $^3J_{HH}$ = 7.3, $^4J_{HH}$ = 1.2, 1H), 8.67 (dd, $^3J_{HH}$ = 8.6, $^4J_{HH}$ = 1.2 Hz, 1H), 8.47 (d, $^3J_{HH}$ = 7.9 Hz, 1H), 8.20 − 8.13 (m, 2H), 8.11 (d, $^3J_{HH}$ = 7.9 Hz, 1H), 7.91 (dd, $^3J_{HH}$ = 8.6, 7.3 Hz, 1H), 7.49 − 7.40 (m, 2H), 2.68 (s, 3H) ppm. $^{13}C\{^1H\}$ NMR (126 MHz, CDCl$_3$) δ$_C$ = 197.3, 163.7, 163.7, 139.5, 137.4, 134.1, 132.8, 131.9, 131.5, 131.2, 131.1, 129.6, 129.6, 129.3, 128.4, 123.1, 122.2, 26.9 ppm. FTIR (solid, cm^{-1}) (ATR) ν$_{max}$: 1670, 1587, 1528, 1406, 1358, 1317, 1263, 1234, 1182, 1016, 966, 854, 837, 822, 779, 721, 619, 594, 505, 480.

Synthesis of 2-(3-acetylphenyl)-1H-dibenzo[*de,h*]isoquinoline-1,3(2H)-dione *(8a)*

The product was prepared through a modified literature procedure,[48] where **2** (51.5 mg, 0.207 mmol) was dissolved in pyridine (0.5 mL) and 3-aminoacetophenone (27.2 mg, 0.201 mmol) in 6M HCl was added dropwise to the solution whilst stirring. The mixture was heated to 100°C for 48 hours. Upon cooling to room temperature, the mixture was poured into 1M HCl (5 mL), where the resultant precipitate was filtered and washed successively with distilled water (5 mL). The product was purified by column chromatography (SiO$_2$, DCM/MeOH), where the starting material eluted with pure DCM and the product with DCM/MeOH (9:1). The solvent was removed *in vacuo* and the solid was dried to generate the pure product as a bright orange solid (54.7 mg, 74.9%). ^1H NMR (500 MHz, CDCl$_3$) δ$_H$ = 9.93 (ddd, $^3J_{HH}$ = 9.2, $^4J_{HH}$ = 2.0, $^5J_{HH}$ = 1.0 Hz, 1H), 8.94 (s, 1H), 8.83 (dd, $^3J_{HH}$ = 7.0, $^4J_{HH}$ = 1.2 Hz, 1H), 8.46 (dd, $^3J_{HH}$ = 8.4,

$^4J_{HH}$ = 0.8 Hz, 1H), 8.17 (d, $^3J_{HH}$ = 8.4, 1H), 8.12 (ddd, $^3J_{HH}$ = 7.9, $^4J_{HH}$ = 1.7, 1.2 Hz, 1H), 8.00 (*app.* t, $^4J_{HH}$ = 1.7 Hz, 1H), 7.82 (ddd, $^3J_{HH}$ = 9.2, 6.6, $^4J_{HH}$ = 1.4 Hz, 1H), 7.80 (dd, $^3J_{HH}$ = 8.4, 7.0 Hz, 1H), 7.71 (app. t, $^3J_{HH}$ = 7.8 Hz, 1H), 7.67 (ddd, $^3J_{HH}$ = 8.4, 6.6, $^4J_{HH}$ = 1.1 Hz, 1H), 7.61 (ddd, $^3J_{HH}$ = 7.8, $^4J_{HH}$ = 2.0, 1.1 Hz, 1H), 2.65 (s, 3H) ppm. $^{13}C\{^1H\}$ NMR (126 MHz, CDCl$_3$) δ_C = 197.2, 165.6, 164.1, 138.6, 137.4, 136.8, 136.0, 134.4, 134.1, 133.8, 132.7, 132.0, 130.0, 129.9, 129.2, 129.2, 129.2, 128.6, 126.9, 126.9, 125.7, 122.7, 115.3, 26.8 ppm. FTIR (solid, cm^{-1}) (ATR) v_{max}: 3069, 3044, 1686, 1676, 1647, 1560, 1530, 1429, 1395, 1360, 1325, 1271, 1213, 1142, 1080, 1053, 1022, 959, 876, 793, 750, 735, 719, 708, 685, 604, 559, 486, 430.

Synthesis of 2-(4-acetylphenyl)-1H-dibenzo[*de,h*]isoquinoline-1,3(2H)-dione (8b)

Prepared similarly from **2** (102 mg, 0.413 mmol) and 4-aminoacetophenone (54.1 mg, 0.401 mmol) to give the product as an orange solid (54.8 mg, 37.4%). ^1H NMR (500 MHz, CDCl$_3$) δ_H = 9.93 (dd, $^3J_{HH}$ = 9.2, $^4J_{HH}$ = 1.0 Hz, 1H), 8.96 (s, 1H), 8.84 (dd, $^3J_{HH}$ = 7.0, $^4J_{HH}$ = 1.3 Hz, 1H), 8.47 (dd, $^3J_{HH}$ = 8.3, $^4J_{HH}$ = 1.2 Hz, 1H), 8.20 (d, $^3J_{HH}$ = 8.2, 2H), 8.18 – 8.17 (m, 1H), 7.84 (ddd, $^3J_{HH}$ = 9.2, 6.5, $^4J_{HH}$ = 1.4 Hz, 1H), 7.81 (dd, $^3J_{HH}$ = 8.4, 7.0 Hz, 1H), 7.67 (ddd, $^3J_{HH}$ = 8.5, 6.6, $^4J_{HH}$ = 1.1 Hz, 1H), 7.52 (d, $^3J_{HH}$ = 8.2, 2H), 2.69 (s, 3H) ppm. $^{13}C\{^1H\}$ NMR (126 MHz, CDCl$_3$) δ_C = 197.4, 165.5, 163.9, 137.2, 136.8, 134.3, 132.7, 132.7, 132.6, 132.6, 129.4, 129.2, 129.2, 129.0, 129.0, 128.9, 128.9, 127.5, 126.4, 125.1, 124.9, 124.4, 122.7, 26.4 ppm. FTIR (solid, cm^{-1}) (ATR) v_{max}: 3067, 1680, 1647, 1601, 1560, 1530, 1431, 1393, 1366, 1321, 1261, 1207, 1148, 1053, 959, 901, 862, 831, 789, 748, 733, 712, 621, 594, 482, 455, 440.

Synthesis of 2-bromo-1-phenylethan-1-one

Following an adapted literature method,[42] acetophenone (2.18 g, 18.1 mmol) was dissolved in 1,4-dioxane and diethyl ether (1:1, 40 mL) and DDB (4.95 g, 20.0 mmol) in the same solvent mixture (40 mL) was added dropwise. The solution was stirred for 2 hours at room temperature and the product was extracted into Et$_2$O and washed with distilled water (2 × 30 mL). The combined organic layers were dried over MgSO$_4$ and the solvent was removed *in vacuo* and oven-dried (~60°C) to give the product as a yellow oil (3.37 g, 93.1%). ^1H NMR (300 MHz, CDCl$_3$) δ_H = 8.02 – 7.97 (m, 2H), 7.65 – 7.58 (m 1H), 7.54 –

7.47 (m, 2H), 4.47 (s, 2H) ppm. The data was consistent with literature findings.[77]

Synthesis of 2-(3-(2-bromoacetyl)phenyl)-1H-benzo[*de*]isoquinoline-1,3-(2H)-dione *(4a)*

3a (1.42 g, 4.51 mmol) was dissolved in 1,4-dioxane (20 mL) and was heated to 80°C until fully dissolved, DDB (1.23 g, 4.96 mmol) in 1,4-dioxane (20 mL) was added dropwise and the solution was stirred for 3 hours under an inert N_2 atmosphere whilst the temperature was maintained at ~80°C. The solution was then cooled to room temperature and stirred under N_2 overnight. Half of the solvent was removed *in vacuo* and the solution was washed incrementally with distilled water (2 × ~20 mL) and extracted into DCM. The combined organic layers were dried over $MgSO_4$ and filtered, where the solvent was removed *in vacuo* to give rise to the product as an off-white solid (1.30 g, 72.9%). ^{1}H NMR (500 MHz, $CDCl_3$) δ_H = 8.66 (dd, $^3J_{HH}$ = 7.2, $^4J_{HH}$ = 1.0 Hz, 2H), 8.31 (dd, $^3J_{HH}$ = 8.3, $^4J_{HH}$ = 0.9 Hz, 2H), 8.12 (ddd, $^3J_{HH}$ = 7.8, $^4J_{HH}$ = 1.7, 1.2 Hz, 1H), 7.97 (*app.* t, $^4J_{HH}$ = 1.9 Hz, 1H), 7.82 (dd, $^3J_{HH}$ = 8.3, 7.2 Hz, 2H), 7.69 (*app.* t, $^3J_{HH}$ = 7.9 Hz, 1H), 7.59 (ddd, $^3J_{HH}$ = 7.9, $^4J_{HH}$ = 2.1, 1.1 Hz, 1H), 4.48 (s, 2H) ppm. ^{13}C{^{1}H} NMR (126 MHz, $CDCl_3$) δ_C = 191.2, 163.7, 136.8, 134.8, 134.6, 131.5, 130.8, 129.5, 129.4, 129.0, 128.9, 127.9, 127.3, 122.6, 34.0 ppm. FTIR (solid, cm^{-1}) (ATR) v_{max}: 2990, 2941, 1701, 1655, 1584, 1433, 1377, 3158, 1236, 1204, 1188, 1177, 1001, 885, 864, 847, 800, 779, 700, 681, 654, 633, 540, 515, 488, 436.

Synthesis of 6-bromo-2-(3-(2-bromoacetyl)phenyl)-1H-benzo[*de*]iso-quinoline-1,3(2H)-dione *(6a)*

Prepared similarly from **5a** (155 mg, 0.392 mmol) and DDB (107 mg, 0.431 mmol) in 1,4-dioxane (20 mL) to give the product as a pale yellow solid (181 mg, 95.0%). ^{1}H NMR (500 MHz, $CDCl_3$) δ_H = 8.69 (dd, $^3J_{HH}$ = 7.3, $^4J_{HH}$ = 1.0 Hz, 1H), 8.64 (dd, $^3J_{HH}$ = 8.5, $^4J_{HH}$ = 1.0 Hz, 1H), 8.44 (d, $^3J_{HH}$ = 7.8 Hz, 1H), 8.13 – 8.09 (m, 1H), 8.08 (d, $^3J_{HH}$ = 7.9 Hz, 1H), 7.96 (*app.* t, $^4J_{HH}$ = 1.8 Hz, 1H), 7.89 (dd, $^3J_{HH}$ = 8.5, 7.3 Hz, 1H), 7.69 (*app.* t, $^3J_{HH}$ = 7.8 Hz, 1H), 7.57 (ddd, $^3J_{HH}$ = 7.9, $^4J_{HH}$ = 2.1, 1.1 Hz, 1H), 4.47 (s, 2H) ppm. ^{13}C{^{1}H} NMR (101 MHz, $CDCl_3$) δ_C = 190.3, 163.7, 136.0, 135.4, 134.4, 134.2, 132.8, 131.9, 131.5, 131.0, 130.1, 129.6, 129.4, 128.4, 123.1, 122.2, 31.0 ppm. FTIR (solid, cm^{-1}) (ATR) v_{max}:

3092, 3069, 1701, 1680, 1663, 1584, 1570, 1504, 1485, 1429, 1402, 1364, 1344, 1296, 1287, 1234, 1190, 1121, 1030, 972, 889, 874, 858, 816, 779, 748, 725, 679, 656, 623, 519, 498, 420.

Synthesis of 6-bromo-2-(4-(2-bromoacetyl)phenyl)-1H-benzo[*de*]isoquinoline-1,3(2H)-dione *(6b)*

Following the general procedure from **5b** (163 mg, 0.414 mmol) and DDB (113 mg, 0.455 mmol) in 1,4-dioxane (30 mL) to give the product as an off-white solid (182 mg, 92.9%). ^{1}H NMR (500 MHz, CDCl$_3$) δ_H = 8.71 (dd, $^3J_{HH}$ = 7.3, $^4J_{HH}$ = 1.1 Hz, 1H), 8.67 (dd, $^3J_{HH}$ = 8.5, $^4J_{HH}$ = 1.1 Hz, 1H), 8.46 (d, $^3J_{HH}$ = 7.9 Hz, 1H), 8.18 (d, $^3J_{HH}$ = 8.4 Hz, 2H), 8.10 (d, $^3J_{HH}$ = 7.9 Hz, 1H), 7.91 (dd, $^3J_{HH}$ = 8.5, 7.3 Hz, 1H), 7.47 (d, $^3J_{HH}$ = 8.4 Hz, 2H), 4.50 (s, 2H) ppm. ^{13}C{^{1}H} NMR (126 MHz, CDCl$_3$) δ_C = 190.5, 163.6, 133.5, 132.6, 132.2, 131.4, 131.3, 130.4, 130.4, 130.3, 130.3, 129.6, 129.5, 129.1, 127.8, 123.0, 122.2, 30.9 ppm. FTIR (solid, cm^{-1}) (ATR) ν_{max}: 3067, 1709, 1659, 1585, 1566, 1504, 1460, 1427, 1398, 1366, 1279, 1236, 1190, 1132, 1013, 966, 907, 856, 829, 781, 745, 727, 606, 573, 548, 528, 474, 428.

Synthesis of 2-(4-(2-bromoacetyl)phenyl)-1H-benzo[*de*]isoquinoline-1,3-(2H)-dione *(4b)*

Following an adapted literature method,[78] **3b** (1.90 g, 6.01 mmol) was dissolved in CHCl$_3$ (50 mL) and Br$_2$ (0.34 mL, 6.61 mmol) was added dropwise to the solution at 0°C. The solution was stirred under an inert N$_2$ atmosphere for 24 hours and a colour change from orange to yellow was observed. The resultant solution was washed with distilled water (2 × 30 mL) and the combined organic layers were dried over MgSO$_4$. The solvent was removed *in vacuo* and the crude product was purified by column chromatography (SiO$_2$, DCM/MeOH), where the product eluted with 9:1 DCM/MeOH. The solvent was once again removed *in vacuo* and any residual solvent was left to evaporate, generating the pure product as an off-white solid (1.17 g, 49.3%). ^{1}H NMR (300 MHz, CDCl$_3$) δ_H = 8.66 (dd, $^3J_{HH}$ = 7.3, $^4J_{HH}$ = 1.0 Hz, 2H), 8.31 (dd, $^3J_{HH}$ = 8.3, $^4J_{HH}$ = 0.9 Hz, 2H), 8.19 (d, $^3J_{HH}$ = 8.6 Hz, 2H), 7.82 (dd, $^3J_{HH}$ = 8.3, 7.2 Hz, 2H), 7.49 (d, $^3J_{HH}$ = 8.6 Hz, 2H), 4.51 (s, 2H) ppm. ^{13}C{^{1}H} NMR (101 MHz, DMSO-d_6) δ_C = 191.2, 163.6, 141.0, 134.6, 133.8, 131.5, 130.8, 129.9, 129.4, 127.9, 127.3, 122.5, 34.4 ppm. FTIR (solid, cm^{-1}) (ATR) ν_{max}: 3069, 2988, 2938, 1713, 1655, 1585,

1512, 1435, 1375, 1354, 1283, 1233,1186, 1111, 1016, 993, 901, 839, 820, 779, 723, 708, 563, 544, 528, 471, 424. The data was consistent with literature findings.[76]

Synthesis of 2-phenylquinoxaline *(pqx)*

2-bromo-1-phenylethan-1-one (1.61 g, 8.07 mmol) and 1,2-phenylenediamine (1.05 g, 9.68 mmol) were dissolved in ethanol (10 mL) and the solution was heated to reflux for 24 hours. Upon cooling to room temperature, distilled water (10 mL) was added, and the resultant precipitate was filtered under reduced pressure to generate the product as a light brown solid (818 mg, 49.1%). ^{1}H NMR (300 MHz, CDCl$_3$) δ_H = 9.31 (s, 1H), 8.27 – 8.06 (m, 4H), 7.82 – 7.68 (m, 2H), 7.61 – 7.47 (m, 3H) ppm. UV−vis (CHCl$_3$) λ_{max} ($\varepsilon \times 10^4$ / L mol^{-1} cm^{-1}): 261 (2.0), 334 (1.0) nm. FTIR (solid, cm^{-1}) (ATR) v_{max}: 3059, 3022, 1543, 1487, 1445, 1371, 1312, 1300, 1227, 1207, 1126, 1076, 1047, 1028, 1007, 955, 918, 764, 748, 687, 669, 608, 550, 455. The data was consistent with literature findings.[79]

Synthesis of 2-(3-(quinoxalin-2-yl)phenyl)-1H-benzo[*de*]isoquinoline-1,3-(2H)-dione *(3-Nl-pqx)*

Following an adapted literature method,[47] **4a** (139 mg, 0.352 mmol), 1,2-phenylenediamine (38.1 mg, 0.352 mmol) and NaHCO$_3$ (35.5 mg, 0.423 mmol) were dissolved in DMSO (15 mL) and heated to 120°C under air for 24 hours. Upon cooling to room temperature, distilled water (20 mL) was added to the mixture and the resultant precipitate was filtered under reduced pressure, where the crude solid was washed sequentially with distilled water (10 mL) and oven-dried (60°C), generating the pure product as a pale brown solid (131 mg, 92.3%). ^{1}H NMR (300 MHz, CDCl$_3$) δ_H = 9.37 (s, 1H), 8.69 (dd, $^3J_{HH}$ = 7.3, $^4J_{HH}$ = 1.1 Hz, 2H), 8.36 (ddd, $^3J_{HH}$ = 7.9, $^4J_{HH}$ = 1.7, 1.1 Hz, 1H), 8.31 (dd, $^3J_{HH}$ = 8.4, $^4J_{HH}$ = 1.1 Hz, 2H), 8.26 (*app.* t, $^4J_{HH}$ = 1.7 Hz, 1H), 8.15 – 8.09 (m, 2H), 7.82 (dd, $^3J_{HH}$ = 8.3, 7.3 Hz, 2H), 7.79 – 7.76 (m, 2H), 7.75 – 7.74 (m, 1H), 7.51 (ddd, $^3J_{HH}$ = 7.9, $^4J_{HH}$ = 2.0, 1.0 Hz, 1H) ppm. ^{13}C{^{1}H} NMR (126 MHz, DMSO-d_6) δ_C = 163.8, 150.2, 143.7, 141.4, 141.2, 137.1, 137.0, 134.6, 134.5, 131.5, 131.3, 130.8, 130.8, 130.1, 129.8, 129.2, 128.9, 128.2, 127.9, 127.3, 127.3, 122.7 ppm. HRMS (ES+): *m/z* calc'd 402.1243 for C$_{26}$H$_{16}$N$_3$O$_2$; found 402.1241 [M + H]$^+$. UV−vis (CHCl$_3$) λ_{max} ($\varepsilon \times 10^4$ / L mol^{-1} cm^{-1}): 260 (1.9), 336 (1.9), 351

(1.6) nm. FTIR (solid, cm⁻¹) (ATR) v_{max}: 3055, 3015, 1701, 1663, 1585, 1437, 1373, 1354, 1234, 1188, 1128, 1115, 1053, 953, 876, 847, 804, 779, 767, 692, 648, 540, 513, 446.

Synthesis of 2-(4-(quinoxalin-2-yl)phenyl)-1H-benzo[*de*]isoquinoline-1,3-(2H)-dione *(4-NI-pqx)*

Prepared similarly from **4b** (123 mg, 0.313 mmol), 1,2-phenylenediamine (33.8 mg, 0.313 mmol) and NaHCO₃ (31.5 mg, 0.375 mmol) to give rise to the pure product as a pale brown solid (91.3 mg, 72.8%). ¹H NMR (300 MHz, CDCl₃) δ_H = 9.40 (s, 1H), 8.69 (dd, $^3J_{HH}$ = 7.3, $^4J_{HH}$ = 1.1 Hz, 2H), 8.41 (d, $^3J_{HH}$ = 8.7 Hz, 2H), 8.30 (dd, $^3J_{HH}$ = 8.4, $^4J_{HH}$ = 1.1 Hz, 2H), 8.21 − 8.12 (m, 2H), 7.87 − 7.77 (m, 4H), 7.61 − 7.51 (m, 2H). ¹³C{¹H} NMR (126 MHz, CDCl₃) δ_C = 164.4, 142.7, 134.0, 132.0, 131.3, 131.2, 130.4, 130.4, 129.3, 129.3, 129.2, 128.7, 128.1, 128.1, 127.9, 126.6, 125.3, 122.9 ppm. HRMS (ES+): *m/z* calc'd 402.1243 for $C_{26}H_{16}N_3O_2$; found 402.1244 [M + H]⁺. UV−vis (CHCl₃) λ_{max} ($\varepsilon \times 10^4$ / L mol⁻¹ cm⁻¹): 264 (1.9), 337 (2.3), 351 (2.0) nm. FTIR (solid, cm⁻¹) (ATR) v_{max}: 3065, 1703, 1666, 1585, 1545, 1516, 1489, 1427, 1373, 1346, 1314, 1236, 1182, 1151, 1047, 1022, 955, 895, 839, 777, 756, 692, 561, 542, 503.

Synthesis of 6-bromo-2-(3-(quinoxalin-2-yl)phenyl)-1H-benzo[*de*]-iso-quinoline-1,3(2H)-dione *(7a)*

Prepared similarly from **6a** (158 mg, 0.334 mmol), 1,2-phenylenediamine (36.1 mg, 0.334 mmol) and NaHCO₃ (33.7 mg, 0.401 mmol) to give the product as a pale yellow solid (152 mg, 94.7%). ¹H NMR (400 MHz, DMSO-d_6) δ_H = 9.63 (s, 1H), 8.68 − 8.63 (m, 2H), 8.50 − 8.47 (m, 1H), 8.43 (*app.* t, $^4J_{HH}$ = 1.9 Hz, 1H), 8.41 (d, $^3J_{HH}$ = 7.8 Hz, 1H), 8.31 (d, $^3J_{HH}$ = 7.9 Hz, 1H), 8.17 − 8.13 (m, 2H), 8.08 (dd, $^3J_{HH}$ = 8.5, 7.5 Hz, 1H), 7.91 − 7.86 (m, 2H), 7.81 − 7.76 (m, 1H), 7.67 − 7.62 (m, 1H) ppm. ¹³C NMR (126 MHz, DMSO-d_6) δ_C = 158.3, 149.5, 143.6, 142.0, 136.1, 135.3, 131.7, 131.5, 130.8, 130.1, 129.6, 129.2, 129.2, 129.1, 129.0, 129.0, 128.9, 128.1, 127.4, 127.0, 126.7, 123.1 ppm. FTIR (solid, cm⁻¹) (ATR) v_{max}: 1709, 1663, 1585, 1570, 1547, 1364, 1344, 1315, 1233, 1190, 1128, 1053, 961, 881, 853, 783, 758, 729, 691, 615, 561, 519, 447, 424.

Synthesis of 6-bromo-2-(4-(quinoxalin-2-yl)phenyl)-1H-benzo[*de*]iso-quinoline-1,3(2H)-dione *(7b)*

Prepared similarly from **6b** (164 mg, 0.346 mmol), 1,2-phenylenediamine (37.4 mg, 0.346 mmol) and $NaHCO_3$ (34.8 mg, 0.415 mmol) to give the product as an off-white solid (164 mg, 98.7%). ^1H NMR (400 MHz, DMSO-d_6) δ_H = 9.69 (s, 1H), 8.73 – 8.61 (m, 2H), 8.53 – 8.47 (m, 2H), 8.40 (d, $^3J_{HH}$ = 7.7 Hz, 1H), 8.30 (d, $^3J_{HH}$ = 7.7 Hz, 1H), 8.22 – 8.14 (m, 2H), 8.07 (*app.* t, $^3J_{HH}$ = 7.9 Hz, 1H), 7.94 – 7.87 (m, 2H), 7.66 (d, $^3J_{HH}$ = 7.8 Hz, 2H) ppm. $^{13}C\{^1H\}$ NMR (126 MHz, DMSO-d_6) δ_C = 163.2, 150.6, 143.9, 141.5, 141.2, 137.9, 136.1, 132.9, 131.7, 131.5, 131.1, 130.8, 130.1, 129.9, 129.3, 129.0, 128.9, 128.9, 128.1, 128.1 ppm. FTIR (solid, cm^{-1}) (ATR) v_{max}: 1707, 1668, 1589, 1572, 1362, 1344, 1234, 1128, 1049, 959, 835, 777, 754, 747, 559, 457, 426.

Synthesis of 6-morpholino-2-(3-(quinoxalin-2-yl)phenyl)-1H-benzo[*de*]iso-quinoline-1,3(2H)-dione *(3-MNI-pqx)*

Following an adapted literature method,[43] **7a** (147 mg, 0.305 mmol) and morpholine (0.132 mL, 1.53 mmol) in 2-methoxyethanol (8 mL) were heated to reflux for 16 hours under an inert N_2 atmosphere. Precipitation occurred upon cooling to room temperature, and the resultant suspension was filtered under reduced pressure and washed with *n*-hexane (10 mL). The crude product was purified by column chromatography (SiO_2, DCM/MeOH), where the product eluted with 95:5 DCM/MeOH and the solvent was removed *in vacuo* to give the product as a yellow solid (114 mg, 76.8%). ^1H NMR (300 MHz, CDCl$_3$) δ_H = 9.37 (s, 1H), 8.67 (dd, $^3J_{HH}$ = 7.3, $^4J_{HH}$ = 1.2 Hz, 1H), 8.61 (d, $^3J_{HH}$ = 8.1 Hz, 1H), 8.51 (dd, $^3J_{HH}$ = 8.5, $^4J_{HH}$ = 1.2 Hz, 1H), 8.35 (ddd, $^3J_{HH}$ = 7.9, $^4J_{HH}$ = 1.7, 1.1 Hz, 1H), 8.23 (*app.* t, $^4J_{HH}$ = 1.8 Hz, 1H), 8.15 – 8.10 (m, 2H), 7.81 – 7.72 (m, 4H), 7.49 (ddd, $^3J_{HH}$ = 7.9, $^4J_{HH}$ = 2.1, 1.1 Hz, 1H), 7.29 (d, $^3J_{HH}$ = 8.1 Hz, 1H), 4.09 – 4.02 (m, 4H), 3.36 – 3.29 (m, 4H) ppm. $^{13}C\{^1H\}$ NMR (126 MHz, CDCl$_3$) δ_C = 173.5, 168.1, 164.2, 156.2, 149.9, 143.1, 142.4, 138.1, 133.2, 131.8, 131.3, 130.7, 130.5, 130.4, 130.2, 129.8, 129.2, 128.1, 127.6, 126.4, 126.1, 115.2, 67.1, 53.6 ppm. HRMS (ES+): *m/z* calc'd 487.1770 for $C_{30}H_{23}N_4O_3$; found 487.1775 [M + H]$^+$. UV−vis (CHCl$_3$) λ_{max} ($\varepsilon \times 10^4$ / L mol^{-1} cm^{-1}): 260 (1.0), 340 (0.5), 398 (0.3) nm. FTIR (solid, cm^{-1}) (ATR) v_{max}: 3067, 2959, 2920, 2855,

1701, 1655, 1585, 1452, 1364, 1231, 1186, 1113, 1070, 1051, 1007, 837, 785, 756, 692, 557, 447.

Synthesis of 8-morpholino-2-(4-(quinoxalin-2-yl)phenyl)-1H-dibenzo-[*de,h*]isoquinoline-1,3(2H)-dione *(4-MNI-pqx)*

Prepared similarly from **7b** (151 mg, 0.315 mmol) and morpholine (0.136 mL, 1.57 mmol) to give the product as an orange solid (97.0 mg, 63.4%). ^{1}H NMR (300 MHz, CDCl$_3$) δ_H = 9.40 (s, 1H), 8.67 (dd, $^3J_{HH}$ = 7.3, $^4J_{HH}$ = 1.2 Hz, 1H), 8.61 (d, $^3J_{HH}$ = 8.1 Hz, 1H), 8.50 (dd, $^3J_{HH}$ = 8.5, $^4J_{HH}$ = 1.2 Hz, 1H), 8.40 (d, $^3J_{HH}$ = 8.7 Hz, 2H), 8.22 – 8.13 (m, 2H), 7.85 – 7.74 (m, 3H), 7.54 (d, $^3J_{HH}$ = 8.7 Hz, 2H), 7.29 (d, $^3J_{HH}$ = 8.1 Hz, 1H), 4.09 – 4.00 (m, 4H), 3.35 – 3.27 (m, 4H) ppm. ^{13}C{^{1}H} NMR (126 MHz, CDCl$_3$) δ_C = 171.1, 164.2, 163.5, 156.3, 155.4, 143.4, 142.5, 138.3, 137.2, 136.0, 133.2, 131.9, 130.5, 129.9, 129.9, 129.8, 129.3, 128.8, 128.7, 126.1, 124.8, 124.2, 123.5, 115.2, 67.1, 53.6 ppm. HRMS (ES+): *m/z* calc'd 487.1770 for C$_{30}$H$_{23}$N$_4$O$_3$; found 487.1770 [M + H]$^+$. UV−vis (CHCl$_3$) λ_{max} ($\varepsilon \times 10^4$ / L mol^{-1} cm^{-1}): 264 (4.0), 338 (1.7), 396 (1.2) nm. FTIR (solid, cm^{-1}) (ATR) v_{max}: 3061, 2857, 2833, 1697, 1659, 1653, 1589, 1580, 1547, 1373, 1364, 1240, 1229, 1194, 1111, 1049, 1003, 959, 930, 837, 785, 758, 725, 611, 559, 497, 417.

5.5.3: Preparation of Inorganic Complexes

Synthesis of [Ir(pqx)$_2$(CH$_3$CN)$_2$]PF$_6$

Prepared according to an adapted literature procedure,[54] where [(Ir(pqx)$_2$(μ-Cl))$_2$] (483 mg, 0.378 mmol) and AgPF$_6$ (191 mg, 0.756 mmol) were added to acetonitrile (20 mL) and heated to reflux in the absence of light for 16 hours under an inert N$_2$ atmosphere. The solution was cooled to room temperature, filtered through celite, and washed with acetonitrile, where the solvent was removed from the filtrate *in vacuo* and the complex was purified by recrystallisation from DCM/Et$_2$O to give the pure product as a dark brown crystalline solid (479 mg, 76.3%). FTIR (solid, cm^{-1}) (ATR) v_{max}: 3059, 2972, 2922, 2870, 1578, 1535, 1491, 1449, 1292, 1130, 1061 (br), 1026, 837, 758, 694, 557, 490.

Synthesis of [Ir(pqx)₂(phen)]PF₆ *(Ir-phen1)*

[Ir(pqx)₂(CH₃CN)₂]PF₆ (145 mg, 0.175 mmol) and 1,10-phenanthroline (34.6 mg, 0.192 mmol) were dissolved in 2-ethoxyethanol (15 mL) and the solution was heated to reflux for 24 hours under an inert N_2 atmosphere. Upon cooling to room temperature, the solvent was removed *in vacuo* and the crude product was purified by column chromatography (SiO_2), where the product eluted with DCM/MeOH (95:5) as the eluent and then recrystallised from DCM/Et₂O to give the pure product as a red solid (45.6 mg, 28.1%). ¹H NMR (500 MHz, CDCl₃) δ_H = 9.54 (s, 2H), 9.13 – 9.06 (m, 2H), 8.61 – 8.53 (m, 2H), 8.37 (d, $^3J_{HH}$ = 5.2 Hz, 2H), 8.24 (d, $^3J_{HH}$ = 7.6 Hz, 2H), 8.03 – 7.96 (m, 2H), 7.93 – 7.86 (m, 4H), 7.42 – 7.38 (m, 2H), 6.91 – 6.83 (m, 6H), 6.48 (dd, $^3J_{HH}$ = 7.7, $^4J_{HH}$ = 1.2 Hz, 2H) ppm. ¹³C{¹H} NMR (126 MHz, (CD₃)₂CO) δ_C = 150.7, 144.9, 144.7, 143.2, 142.1, 140.3, 135.7, 132.8, 132.3, 132.1, 131.5, 130.7, 129.4, 129.3, 128.4, 124.6, 124.3 ppm. ¹⁹F{¹H} NMR (376 MHz, (CD₃)₂CO) δ_F = −76.62 (d, $^1J_{PF}$ = 708.2 Hz) ppm. HRMS (ES+): *m/z* calc'd 783.1848 for $C_{40}H_{26}N_6Ir$; found 783.1857 [M − PF₆]⁺. UV−vis (CHCl₃) λ_{max} ($\varepsilon \times 10^4$ / L mol⁻¹ cm⁻¹): 266 (4.3), 289 (2.8), 368 (1.2), 480 (0.2), 525 sh (0.1) nm. FTIR (solid, cm⁻¹) (ATR) v_{max}: 2924, 2853, 1597, 1580, 1530, 1452, 1429, 1339, 1256, 1146, 1126, 1099, 1070, 1040, 831, 766, 718, 635, 555, 463, 428.

Synthesis of [Ir(pqx)₂(NI-phen)]PF₆ *(Ir-phen2)*

Prepared similarly from [Ir(pqx)₂(CH₃CN)₂]PF₆ (111 mg, 0.134 mmol) and **NI-phen** (50.3 mg, 0.134 mmol) to give the product as a red crystalline solid (51.1 mg, 34.0%). ¹H NMR (500 MHz, CDCl₃) δ_H = 9.63 – 9.57 (m, 1H), 9.27 (dd, $^3J_{HH}$ = 4.4, $^4J_{HH}$ = 1.6 Hz, 1H), 9.23 (dd, $^3J_{HH}$ = 4.3, $^4J_{HH}$ = 1.6 Hz, 1H), 8.71 (s, 1H), 8.70 (s, 1H), 8.38 (d, $^4J_{HH}$ = 1.0 Hz, 1H), 8.36 (d, $^4J_{HH}$ = 1.1 Hz, 1H), 8.30 (dd, $^3J_{HH}$ = 8.1, $^4J_{HH}$ = 1.4 Hz, 1H), 8.27 – 8.23 (m, 1H), 8.13 – 7.96 (m, 5H), 7.90 – 7.85 (m, 5H), 7.72 – 7.68 (m, 2H), 7.60 – 7.56 (m, 2H), 7.54 – 7.51 (m, 1H), 7.46 (d, $^3J_{HH}$ = 7.7 Hz, 1H), 7.33 – 7.28 (m, 1H), 7.14 – 7.06 (m, 1H), 7.00 – 6.91 (m, 2H), 6.78 (d, $^3J_{HH}$ = 8.7 Hz, 1H), 6.55 (dd, $^3J_{HH}$ = 7.8, $^4J_{HH}$ = 4.1 Hz, 1H) ppm. ¹⁹F{¹H} NMR (376 MHz, CDCl₃) δ_F = −67.52 (d, $^1J_{PF}$ = 709.8 Hz) ppm. HRMS (ES+): *m/z* calc'd 978.2168 for $C_{52}H_{31}N_7O_2Ir$; found 978.2173 [M − PF₆]⁺. UV−vis (CHCl₃) λ_{max} ($\varepsilon \times 10^4$ / L mol⁻¹ cm⁻¹): 268 (5.6), 338 (2.9), 353 (2.7), 475 (0.2), 524 sh (0.1) nm. FTIR (solid, cm⁻¹) (ATR) v_{max}: 3057, 2970, 2870, 1707,

1668, 1585, 1530, 1429, 1371, 1346, 1234, 1186, 1055 (br), 880, 847, 779, 764, 741, 702, 519, 457, 436, 417.

Synthesis of [Ir(pqx)$_2$(MNI-phen)]PF$_6$ *(Ir-phen3)*

Prepared similarly from [Ir(pqx)$_2$(CH$_3$CN)$_2$]PF$_6$ (155 mg, 0.187 mmol) and **MNI-phen** (86.0 mg, 0.187 mmol) to give the product as a red crystalline solid (28.7 mg, 12.7%). ^{1}H NMR (500 MHz, CDCl$_3$) δ_H = 9.61 (s, 1H), 9.59 (s, 1H), 8.60 (d, $^3J_{HH}$ = 8.2 Hz, 2H), 8.56 – 8.52 (m, 3H), 8.50 – 8.46 (m, 1H), 8.29 – 8.24 (m, 3H), 8.04 – 7.98 (m, 3H), 7.97 (d, $^3J_{HH}$ = 8.1 Hz, 1H), 7.92 (dd, $^3J_{HH}$ = 8.5, 5.1 Hz, 1H), 7.80 – 7.73 (m, 1H), 7.53 (*app.* t, $^3J_{HH}$ = 7.8 Hz, 1H), 7.53 – 7.48 (m, 1H), 7.32 – 7.27 (m, 3H), 7.12 – 7.08 (m, 1H), 7.05 (*app.* t, $^3J_{HH}$ = 7.9 Hz, 1H), 6.97 (dd, $^3J_{HH}$ = 7.2, 5.4 Hz, 1H), 6.96 – 6.90 (m, 2H), 6.80 – 6.77 (m, 1H), 6.55 (dd, $^3J_{HH}$ = 7.7, $^4J_{HH}$ = 1.6 Hz, 2H), 4.06 – 4.01 (m, 4H), 3.35 – 3.31 (m, 4H) ppm. ^{13}C{^{1}H} NMR (126 MHz, CDCl$_3$) δ_C = 164.4, 164.0, 163.5, 149.7, 149.7, 149.5, 148.4, 147.6, 146.7, 146.7, 144.8, 143.2, 143.1, 142.8, 142.3, 141.1, 140.0, 139.9, 134.9, 134.8, 134.0, 133.9, 133.6, 132.5, 132.4, 132.2, 131.2, 131.1, 130.3, 130.3, 129.5, 128.2, 128.1, 127.6, 126.5, 126.2, 124.3, 123.2, 122.7, 122.5, 121.7, 115.3, 67.0, 53.6 ppm. ^{19}F{^{1}H} NMR (376 MHz, CDCl$_3$) δ_F = −73.07 (d, $^1J_{PF}$ = 712.6 Hz) ppm. HRMS (ES+): *m/z* calc'd 1063.2696 for C$_{56}$H$_{38}$N$_8$O$_3$Ir; found 1063.2699 [M − PF$_6$]$^+$. UV−vis (CHCl$_3$) λ_{max} (ε × 10^4 / L mol^{-1} cm^{-1}): 265 (3.6), 288 (3.2), 372 (1.8), 424 (0.9), 472 (0.4), 518 (0.2), 547 sh (0.1) nm. FTIR (solid, cm^{-1}) (ATR) ν_{max}: 3057, 2961, 2926, 2853, 1701, 1663, 1580, 1530, 1452, 1427, 1358, 1339, 1231, 1128, 1115, 1070, 1040, 999, 835, 760, 727, 712, 635, 555, 492, 473.

Synthesis of [Ir(pqx)$_2$(AI-phen)]PF$_6$ *(Ir-phen4)*

Prepared similarly from [Ir(pqx)$_2$(CH$_3$CN)$_2$]PF$_6$ (52.1 mg, 0.063 mmol) and **AI-phen** (26.7 mg, 0.063 mmol) to give the product as a brown solid (10.5 mg, 14.3%). ^{1}H NMR (500 MHz, CDCl$_3$) δ_H = 9.61 (s, 1H), 9.53 (s, 1H), 8.99 (dd, $^3J_{HH}$ = 8.5, $^4J_{HH}$ = 0.9 Hz, 1H), 8.82 (s, 1H), 8.49 (s, 1H), 8.37 – 8.34 (m, 1H), 8.26 – 8.23 (m, 3H), 8.20 (d, $^3J_{HH}$ = 7.3 Hz, 1H), 8.03 (d, $^3J_{HH}$ = 8.4 Hz, 1H), 7.95 – 7.92 (m, 2H), 7.72 (dd, $^3J_{HH}$ = 8.1, 5.1 Hz, 1H), 7.51 – 7.44 (m, 6H), 7.31 – 7.27 (m, 2H), 6.99 (d, $^3J_{HH}$ = 8.9 Hz, 2H), 6.95 – 6.92 (m, 4H), 6.71 (d, $^3J_{HH}$ = 8.9 Hz, 1H), 6.55 (d, $^3J_{HH}$ = 7.3 Hz, 2H), 6.51 (d, $^3J_{HH}$ = 7.9 Hz, 2H) ppm. ^{19}F{^{1}H} NMR (376 MHz, CDCl$_3$) δ_F = −72.31 (d, $^1J_{PF}$ = 714.4 Hz) ppm. UV−vis (CHCl$_3$)

λ_{max} ($\varepsilon \times 10^4$ / L mol^{-1} cm^{-1}): 263 (2.9), 287 (2.4), 369 (0.9), 444 (0.3), 518 sh (0.2) nm. FTIR (solid, cm^{-1}) (ATR) v_{max}: 3060, 2965, 2924, 2860, 1695, 1653, 1582, 1531, 1454, 1429, 1339, 1273, 1252, 1211, 1107, 1072, 1042, 837, 762, 739, 698, 555, 420.

General synthesis of Ir(III) dimers, [(Ir(C^N)$_2$(μ-Cl))$_2$]

Prepared according to an adapted literature procedure,[53] IrCl$_3$.xH$_2$O (2.0 eq.) in 2-ethoxyethanol and distilled water (3:1, v/v) was stirred at 60°C under an inert N$_2$ atmosphere for 30 minutes until fully dissolved. Free ligand (4.0 – 4.5 eq.) in 2-ethoxyethanol was added to the stirred solution and the mixture was heated to reflux for 48 hours. Upon cooling to room temperature, distilled water was added, and the resultant precipitate was filtered under reduced pressure and washed with distilled water and a small amount of Et$_2$O. The product was filtered through with DCM, removing any insoluble impurities. The solvent was removed *in vacuo* and the solid was oven-dried (~60°C) to generate the dimers as brown solids (39.9 – 85.6%), which were used in subsequent steps without further purification.

Synthesis of [Ir(3-NI-pqx)$_2$(phen)]PF$_6$ *(Ir-pqx1)*

[(Ir(3-NI-pqx)$_2$(μ-Cl))$_2$] (181 mg, 0.088 mmol) and 1,10-phenanthroline (34.8 mg, 0.193 mmol) were dissolved in 2-ethoxyethanol (10 mL) and the solution was heated to reflux for 24 hours under an inert N$_2$ atmosphere. Upon cooling to room temperature, saturated aqueous NH$_4$PF$_6$ solution (~2mL) was added, and the solution was stirred for 15 minutes. The crude product precipitated out of solution upon the addition of distilled water (10 mL) and the suspension was filtered under reduced pressure and washed with distilled water and Et$_2$O. The solid was washed through with DCM to remove any excess inorganic salts and the solvent was removed *in vacuo* to isolate the crude product, which was purified by column chromatography (SiO$_2$), where the product eluted with DCM/MeOH (9:1) as the eluent and then recrystallised from DCM/Et$_2$O to give the pure product as a dark brown crystalline solid (21.9 mg, 9.6%). ^{1}H NMR (500 MHz, CDCl$_3$) δ_H = 9.53 (s, 1H), 9.38 (s, 1H), 8.71 – 8.67 (m, 6H), 8.55 (dd, $^3J_{HH}$ = 5.1, $^4J_{HH}$ = 1.3 Hz, 1H), 8.36 (d, $^3J_{HH}$ = 7.9 Hz, 1H), 8.34 – 8.30 (m, 6H), 8.25 (*app.* t, $^4J_{HH}$ = 1.8 Hz, 2H), 8.22 (d, $^4J_{HH}$ = 2.0 Hz, 1H), 8.15 – 8.11 (m, 3H), 8.00 – 7.96 (m, 2H), 7.87 – 7.81 (m, 7H), 7.50 (dd, $^3J_{HH}$ = 8.4, $^4J_{HH}$ = 1.5 Hz,

2H), 6.99 – 6.93 (m, 2H), 6.76 (d, $^3J_{HH}$ = 8.0 Hz, 1H) ppm. $^{13}C\{^1H\}$ NMR (126 MHz, CD$_3$CN) δ_C = 165.3, 152.6, 152.5, 152.1, 151.1, 151.0, 150.7, 150.3, 149.1, 147.8, 147.4, 145.6, 144.7, 144.6, 142.0, 140.5, 140.1, 136.0, 135.5, 135.5, 131.9, 131.9, 131.3, 131.0, 128.2, 128.1, 123.8 ppm. $^{19}F\{^1H\}$ NMR (376 MHz, CD$_3$CN) δ_F = −72.91 (d, $^1J_{PF}$ = 706.0 Hz) ppm. HRMS (ES+): m/z calc'd 1173.2489 for C$_{64}$H$_{36}$N$_8$O$_4$Ir; found 1173.2507 [M − PF$_6$]$^+$. UV−vis (CHCl$_3$) λ_{max} (ε × 10^4 / L mol^{-1} cm^{-1}): 266 (6.3), 336 (4.3), 351 (4.0), 463 (0.5), 529 (0.2) nm. FTIR (solid, cm^{-1}) (ATR) v_{max}: 3059, 2859, 1701, 1655, 1624, 1585, 1533, 1431, 1375, 1348, 1236, 1188, 1128, 1115, 835, 777, 718, 702, 555, 513.

Synthesis of [Ir(4-NI-pqx)₂(phen)]PF₆ *(Ir-pqx2)*

Prepared similarly from [(Ir(4-NI-pqx)$_2$(μ-Cl))$_2$] (99.8 mg, 0.049 mmol) and 1,10-phenanthroline (19.2 mg, 0.107 mmol) to give the product as an orange solid (23.5 mg, 18.4%). ^1H NMR (500 MHz, CD$_3$CN) δ_H = 9.62 (s, 2H), 8.59 (dd, $^3J_{HH}$ = 8.3, $^4J_{HH}$ = 1.4 Hz, 2H), 8.54 (dd, $^3J_{HH}$ = 5.2, $^4J_{HH}$ = 1.4 Hz, 2H), 8.52 (d, $^3J_{HH}$ = 8.4 Hz, 2H), 8.35 – 8.31 (m, 4H), 8.27 (dd, $^3J_{HH}$ = 8.3, $^4J_{HH}$ = 0.9 Hz, 4H), 7.98 (dd, $^3J_{HH}$ = 8.2, 5.2 Hz, 2H), 7.97 (s, 2H), 7.76 (dd, $^3J_{HH}$ = 8.5, $^4J_{HH}$ = 1.5 Hz, 2H), 7.72 (dd, $^3J_{HH}$ = 8.3, 7.3 Hz, 4H), 7.39 (ddd, $^3J_{HH}$ = 8.3, 7.0, $^4J_{HH}$ = 1.2 Hz, 2H), 7.32 (dd, $^3J_{HH}$ = 8.3, $^4J_{HH}$ = 1.9 Hz, 2H), 7.12 (dd, $^3J_{HH}$ = 8.8, $^4J_{HH}$ = 0.8 Hz, 2H), 6.98 (ddd, $^3J_{HH}$ = 8.7, 7.0, $^4J_{HH}$ = 1.5 Hz, 2H), 6.85 (d, $^4J_{HH}$ = 1.9 Hz, 2H) ppm. $^{13}C\{^1H\}$ NMR (126 MHz, CD$_3$CN) δ_C = 164.7, 163.9, 152.7, 150.2, 147.4, 144.8, 144.7, 144.4, 143.2, 142.1, 140.2, 139.7, 136.4, 135.2, 132.5, 132.1, 131.9, 131.8, 131.5, 131.0, 130.7, 130.3, 129.9, 129.6, 128.9, 128.9, 128.1, 128.1, 128.1, 127.9, 125.4, 124.4, 123.6 ppm. $^{19}F\{^1H\}$ NMR (376 MHz, CD$_3$CN) δ_F = −72.89 (d, $^1J_{PF}$ = 706.5 Hz) ppm. HRMS (ES+): m/z calc'd 1173.2489 for C$_{64}$H$_{36}$N$_8$O$_4$Ir; found 1173.2495 [M − PF$_6$]$^+$. UV−vis (CHCl$_3$) λ_{max} (ε × 10^4 / L mol^{-1} cm^{-1}): 265 (8.7), 337 (7.2), 351 (6.9), 468 (0.6), 525 sh (0.3) nm. FTIR (solid, cm^{-1}) (ATR) v_{max}: 3061, 2961, 2922, 1701, 1663, 1584, 1530, 1508, 1431, 1373, 1348, 1236, 1188, 837, 777, 719, 698, 638, 557, 517.

Synthesis of [Ir(3-NI-pqx)₂(bpy)]PF₆ *(Ir-pqx3)*

Prepared similarly from [(Ir(3-NI-pqx)$_2$(μ-Cl))$_2$] (45.0 mg, 0.022 mmol) and 2,2'-bipyridyl (7.5 mg, 0.048 mmol). The crude product was purified by an alternative method, where column chromatography (SiO$_2$) was carried out using acetone as the mobile phase to remove impurities, followed by elution of the product as

a red band using a solvent mixture of MeCN:H$_2$O:KNO$_3$ (aq. sat.) (14:2:1). The solvent was removed *in vacuo* and the product was left to dry in a heated oven at ~60°C for 16 h to remove any traces of water. The solid was dissolved in DCM, and the insoluble salts were filtered off under suction. The solvent was once again removed *in vacuo* and dissolved in acetonitrile (10 mL), where a saturated aqueous solution of NH$_4$PF$_6$ was added and stirred for 15 min to ensure that all of the complex existed purely as a PF$_6$ salt. The solvent was removed *in vacuo* and then filtered under suction, washing successively with distilled water to remove excess insoluble inorganic salts once again. The crude product was recrystallised from DCM and Et$_2$O to give the pure product as an orange solid (10.2 mg, 18.0%). ^{1}H NMR (500 MHz, CDCl$_3$) δ_H = 9.50 (s, 2H), 8.67 (dd, $^3J_{HH}$ = 7.3, $^4J_{HH}$ = 1.1 Hz, 4H), 8.57 (dd, $^3J_{HH}$ = 8.5, $^4J_{HH}$ = 0.8 Hz, 2H), 8.32 (dd, $^3J_{HH}$ = 8.3, $^4J_{HH}$ = 1.0 Hz, 4H), 8.18 – 8.13 (m, 6H), 8.09 (dd, $^3J_{HH}$ = 8.4, $^4J_{HH}$ = 1.4 Hz, 2H), 7.85 (d, $^3J_{HH}$ = 7.5 Hz, 2H), 7.83 (d, $^3J_{HH}$ = 7.4 Hz, 2H), 7.67 (ddd, $^3J_{HH}$ = 8.4, 7.0, $^4J_{HH}$ = 1.3 Hz, 2H), 7.56 (ddd, $^3J_{HH}$ = 7.3, 5.7, $^4J_{HH}$ = 1.1 Hz, 2H), 7.24 – 7.22 (m, 2H), 7.12 (dd, $^3J_{HH}$ = 8.9, $^4J_{HH}$ = 0.9 Hz, 2H), 6.90 (dd, $^3J_{HH}$ = 8.1, $^4J_{HH}$ = 2.1 Hz, 2H), 6.66 (d, $^3J_{HH}$ = 8.1 Hz, 2H) ppm. ^{13}C{^{1}H} NMR (101 MHz, CDCl$_3$) δ_C = 166.8, 162.3, 161.9, 155.0, 153.1, 151.3, 149.3, 142.3, 139.7, 137.6, 136.4, 134.1, 133.1, 131.1, 131.0, 130.9, 128.5, 127.2, 124.5, 123.8, 122.9, 122.6, 117.6, 114.9 ppm. ^{19}F{^{1}H} NMR (376 MHz, CDCl$_3$) δ_F = −73.10 (d, $^1J_{PF}$ = 712.6 Hz) ppm. HRMS (ES+): *m/z* calc'd 1149.2489 for C$_{62}$H$_{36}$N$_8$O$_4$Ir; found 1149.2506 [M − PF$_6$]$^+$. UV−vis (CHCl$_3$) λ_{max} (ε × 10^4 / L mol^{-1} cm^{-1}): 269 (2.5), 337 (1.5), 352 (1.5), 431 (0.2), 490 sh (0.1) nm. FTIR (solid, cm^{-1}) (ATR) v_{max}: 2924, 2859, 1699, 1661, 1587, 1454, 1435, 1377, 1356, 1238, 1182, 1072, 839, 779, 766, 741, 731, 557, 469, 461, 440.

Synthesis of [Ir(4-NI-pqx)$_2$(bpy)]PF$_6$ *(Ir-pqx4)*
Prepared similarly from [(Ir(4-NI-pqx)$_2$(μ-Cl))$_2$] (96.7 mg, 0.047 mmol) and 2,2'-bipyridyl (15.6 mg, 0.100 mmol) to give the product as an orange solid (24.8 mg, 20.4%). ^{1}H NMR (500 MHz, (CD$_3$)$_2$CO) δ_H = 9.79 (s, 2H), 8.62 (d, $^3J_{HH}$ = 8.6 Hz, 2H), 8.54 (d, $^3J_{HH}$ = 8.2 Hz, 2H), 8.39 (d, $^4J_{HH}$ = 1.0 Hz, 2H), 8.38 – 8.35 (m, 8H), 8.23 (*app.* td, $^3J_{HH}$ = 7.9, $^4J_{HH}$ = 1.6 Hz, 2H), 7.89 (dd, $^3J_{HH}$ = 8.5, $^4J_{HH}$ = 1.3 Hz, 2H), 7.88 – 7.85 (m, 2H), 7.81 (d, $^3J_{HH}$ = 8.4, 2H), 7.80 (d, $^3J_{HH}$ = 8.0, 2H) 7.62 (ddd, $^3J_{HH}$ = 8.4, 7.2, $^4J_{HH}$ = 1.4 Hz, 2H), 7.42 (dd, $^3J_{HH}$ = 8.7, $^4J_{HH}$ =

1.0 Hz, 2H), 7.39 (dd, $^3J_{HH}$ = 8.3, $^4J_{HH}$ = 1.9 Hz, 2H), 7.32 (ddd, $^3J_{HH}$ = 8.9, 7.0, $^4J_{HH}$ = 1.5 Hz, 2H), 6.96 (d, $^4J_{HH}$ = 1.9 Hz, 2H) ppm. $^{13}C\{^1H\}$ NMR (126 MHz, (CD$_3$)$_2$CO) δ_C = 166.0, 164.7, 161.3, 160.4, 159.0, 157.9, 157.8, 153.6, 153.2, 149.2, 147.7, 144.6, 144.3, 140.0, 136.6, 135.1, 134.0, 132.8, 132.5, 131.5, 130.9, 130.7, 130.0, 130.0, 129.6, 128.0 ppm. HRMS (ES+): *m/z* calc'd 1149.2489 for C$_{62}$H$_{36}$N$_8$O$_4$Ir; found 1149.2509 [M − PF$_6$]$^+$. UV−vis (CHCl$_3$) λ_{max} ($\varepsilon \times 10^4$ / L mol^{-1} cm^{-1}): 274 (12.6), 336 (2.4), 352 (2.4), 432 (0.4), 494 sh (0.2) nm. FTIR (solid, cm^{-1}) (ATR) ν_{max}: 3069, 2924, 2851, 1701, 1663, 1584, 1533, 1437, 1375, 1348, 1236, 1188, 837, 773, 764, 698, 638, 557, 442.

Synthesis of [Ir(3-MNI-pqx)$_2$(phen)]PF$_6$ *(Ir-pqx5)*

Prepared similarly from [(Ir(3-MNI-pqx)$_2$(μ-Cl))$_2$] (70.5 mg, 0.029 mmol) and 1,10-phenanthroline (11.7 mg, 0.065 mmol) to give the pure product as a red-orange solid (64.1 mg, 73.3%). ^1H NMR (500 MHz, (CD$_3$)$_2$CO) δ_H = 9.54 (s, 2H), 8.92 (dd, $^3J_{HH}$ = 8.2, $^4J_{HH}$ = 1.4 Hz, 2H), 8.77 (dd, $^3J_{HH}$ = 8.2, $^4J_{HH}$ = 1.3 Hz, 2H), 8.64 (dd, $^3J_{HH}$ = 8.2, $^4J_{HH}$ = 1.3 Hz, 2H), 8.56 − 8.52 (m, 2H), 8.51 − 8.48 (m, 2H), 8.37 (s, 2H), 8.33 (s, 2H), 8.09 − 8.05 (m, 4H), 7.99 (dd, $^3J_{HH}$ = 5.3, $^4J_{HH}$ = 1.2 Hz, 2H), 7.94 − 7.90 (m, 4H), 7.76 − 7.73 (m, 6H), 7.42 (d, $^3J_{HH}$ = 7.8 Hz, 2H), 4.09 − 3.87 (m, 8H), 3.37 − 3.22 (m, 8H) ppm. $^{13}C\{^1H\}$ NMR (126 MHz, (CD$_3$)$_2$CO) δ_c = 175.4, 165.7, 164.3, 158.3, 157.9, 152.8, 143.7, 143.0, 142.6, 135.5, 133.4, 131.8, 130.7, 130.1, 129.8, 129.6, 129.0, 125.7, 124.6, 124.0, 118.1, 117.7, 116.9, 115.6, 114.9, 114.7, 112.5, 111.9, 110.8, 110.4, 110.3, 75.9, 68.8 ppm. $^{19}F\{^1H\}$ NMR (376 MHz, (CD$_3$)$_2$CO) δ_F = −72.52 (d, $^1J_{PF}$ = 707.4 Hz) ppm. HRMS (ES+): *m/z* calc'd 1343.3544 for C$_{72}$H$_{50}$N$_{10}$O$_6$^{193}Ir; found 1343.3608 [M − PF$_6$]$^+$. UV−vis (MeCN) λ_{max} ($\varepsilon \times 10^4$ / L mol^{-1} cm^{-1}): 227 (1.6), 265 (1.1), 378 (0.3), 438 sh (0.2) nm. FTIR (solid, cm^{-1}) (ATR) ν_{max}: 3323, 1695, 1651, 1584, 1423, 1364, 1238, 1196, 1109, 824, 781, 555.

5.6: References

1   S. Kagatikar and D. Sunil, *J. Mater. Sci.*, 2022, **57**, 105–139.

2   W. Zeng and C. Yang, in *Thermally Activated Delayed Fluorescence Organic Light-Emitting Diodes (TADF-OLEDs)*, Woodhead Publishing, 2022, pp. 193–234.

3   B. Wang, Y. Zheng, T. Wang, D. Ma and Q. Wang, *Org. Electron.*, 2021, **88**, 106012.

4   G. He, C. Liu, X. Liu, Q. Wang, A. Fan, S. Wang and X. Qian, *PLoS One*, 2017, **12**, e0186994.

5   G. Saito, D. Velluto and M. Resmini, *R. Soc. Open Sci.*, 2018, **5**, 172137–172137.

6   I. Grabtchev and T. Philipova, *Dyes Pigments*, 1995, **27**, 321–325.

7   S. Banerjee, E. B. Veale, C. M. Phelan, S. A. Murphy, G. M. Tocci, L. J. Gillespie, D. O. Frimannsson, J. M. Kelly and T. Gunnlaugsson, *Chem. Soc. Rev.*, 2013, **42**, 1601–1618.

8   M. Verma, V. Luxami and K. Paul, *Eur. J. Med. Chem.*, 2013, **68**, 352–360.

9   P. A. Panchenko, Y. V. Fedorov, O. A. Fedorova and G. Jonusauskas, *Dyes Pigments*, 2013, **98**, 347–357.

10   M. S. Alexiou, V. Tychopoulos, S. Ghorbanian, J. H. P. Tyman, R. G. Brown and P. I. Brittain, *J. Chem. Soc., Perkin Trans. 2*, 1990, 837–842.

11   Z. Ou, Z. Li, Y. Gao, W. Xing, H. Jia, H. Zhang and N. Yi, *J. Mol. Struct.*, 2019, **1185**, 27–37.

12   S. Biswas, T. Dutta, A. Silswal, R. Bhowal, D. Chopra and A. L. Koner, *Chem. Sci.*, 2021, **12**, 9630–9644.

13   R. Tigoianu, A. Airinei, E. Georgescu, A. Nicolescu, F. Georgescu, D. L. Isac, C. Deleanu and F. Oancea, *Int. J. Mol. Sci.*, 2022, **23**, 2760.

14   J. H. Yao, C. Chi, J. Wu and K. P. Loh, *Eur. J. Chem.*, 2009, **15**, 9299–9302.

15   H. Langhals, G. Schönmann and K. Polborn, *Eur. J. Chem.*, 2008, **14**, 5290–5303.

16   G. Ding, Z. Xu, G. Zhong, S. Jing, F. Li and W. Zhu, *Res. Chem. Intermed.*, 2008, **34**, 299–308.

17 C. L. Andrew, A. R. Klemm and J. B. Lloyd, *Biochim. Biophys. Acta - Biomembr.*, 1997, **1330**, 71–82.

18 B. Dong, X. Song, C. Wang, X. Kong, Y. Tang and W. Lin, *Anal. Chem.*, 2016, **88**, 4085–4091.

19 A. P. de Silva and R. A. D. D. Rupasinghe, *J. Chem. Soc., Chem. Commun.*, 1985, 1669–1670.

20 J. Han and K. Burgess, *Chem. Rev.*, 2010, **110**, 2709–2728.

21 H. Yu, Y. Xiao and L. Jin, *J. Am. Chem. Soc.*, 2012, **134**, 17486–17489.

22 Z. Xie, Y. Zhou, M. Fu, L. Ni, Y. Tong, Y. Yu, N. Li, Z. Yang, Q. Zhu and J. Wang, *Talanta*, 2021, **231**, 122365.

23 B. Das, S. Lohar, A. Patra, E. Ahmmed, S. K. Mandal, J. N. Bhakta, K. Dhara and P. Chattopadhyay, *New J. Chem.*, 2018, **42**, 13497–13502.

24 Z. Wu, D. Liang and X. Tang, *Anal. Chem.*, 2016, **88**, 9213–9218.

25 Y. Ke, J. Cao, J. Gong and N. Fu, *Sens. Actuators B: Chem.*, 2022, **352**, 131015.

26 G. Kornek, M. Raderer, D. Depisch, K. Haider, B. Fazeny, C. Dittrich and W. Scheithauer, *Eur. J. Cancer*, 1994, **30**, 398–400.

27 S. M. Sami, R. T. Dorr, D. S. Alberts and W. A. Remers, *J. Med. Chem.*, 1993, **36**, 765–770.

28 M. F. Braña, M. Cacho, A. Ramos, M. T. Domínguez, J. M. Pozuelo, C. Abradelo, M. F. Rey-Stolle, M. Yuste, C. Carrasco and C. Bailly, *Org. Biomol. Chem.*, 2003, **1**, 648–654.

29 A. D. Johnson, R. Zammit, J. Vella, M. Valentino, J. A. Buhagiar and D. C. Magri, *Bioorg. Chem.*, 2019, **93**, 103287.

30 J. M. Favale, C. E. Hauke, E. O. Danilov, J. E. Yarnell and F. N. Castellano, *Dalton Trans.*, 2020, **49**, 9995–10002.

31 J. E. Yarnell, J. C. Deaton, C. E. McCusker and F. N. Castellano, *Inorg. Chem.*, 2011, **50**, 7820–7830.

32 J. E. Yarnell, K. A. Wells, J. R. Palmer, J. M. Breaux and F. N. Castellano, *J. Phys. Chem. B*, 2019, **123**, 7611–7627.

33 J. E. Yarnell, C. E. McCusker, A. J. Leeds, J. M. Breaux and F. N. Castellano, *Eur. J. Inorg. Chem.*, 2016, **2016**, 1808–1818.

34 J. Sun, W. Wu and J. Zhao, *Eur. J. Chem.*, 2012, **18**, 8100–8112.

35 Y. Liu, W. Wu, J. Zhao, X. Zhang and H. Guo, *Dalton Trans.*, 2011, **40**, 9085–9089.

36   L. Ma, H. Guo, Q. Li, S. Guo and J. Zhao, *Dalton Trans.*, 2012, **41**, 10680–10689.

37   Y. Yang, F. Doettinger, C. Kleeberg, W. Frey, M. Karnahl and S. Tschierlei, *Front. Chem.*, 2022, **10**, 673.

38   G. J. Ryan, S. Quinn and T. Gunnlaugsson, *Inorg. Chem.*, 2008, **47**, 401–403.

39   D. S. Tyson, C. R. Luman, X. Zhou and F. N. Castellano, *Inorg. Chem.*, 2001, **40**, 4063–4071.

40   P. H. Lanoë, J. Chan, G. Gontard, F. Monti, N. Armaroli, A. Barbieri and H. Amouri, *Eur. J. Inorg. Chem.*, 2016, **2016**, 1631–1634.

41   P. H. Lanoë, J. Chan, A. Groué, G. Gontard, A. Jutand, M. N. Rager, N. Armaroli, F. Monti, A. Barbieri and H. Amouri, *Dalton Trans.*, 2018, **47**, 3440–3451.

42   S. A. Fitzgerald, H. Y. Otaif, C. E. Elgar, N. Sawicka, P. N. Horton, S. J. Coles, J. M. Beames and S. J. A. Pope, *Inorg. Chem.*, 2021, **60**, 15467–15484.

43   M. Zhou, X. Xiao, Z. Cong, Y. Wu, W. Zhang, P. Ma, S. Chen, H. Zhang, D. Zhang, D. Zhang, X. Luan, Y. Mai, R. Liu, M. Zhou, X. Xiao, Z. Cong, Y. Wu, W. Zhang, P. Ma, S. Chen, H. Zhang, D. Zhang, R. Liu, X. Luan and Y. Mai, *Angew. Chem. Int. Ed.*, 2020, **59**, 7240–7244.

44   T. Konstantinova, R. Lazarova, A. Venkova and V. Vassileva, *Polym. Degrad. Stab.*, 2004, **84**, 405–409.

45   W. A. Henderson and C. J. Schultz, *J. Org. Chem.*, 1962, **27**, 4643–4646.

46   S. Rouhani, K. Gharanjig and M. H. Nezhad, *Green Chem. Lett. Rev.*, 2014, **7**, 174–178.

47   D. Lu, Q. Xiang, L. Zhou and Q. Zeng, *Asian J. Chem.*, 2015, **27**, 2639–2641.

48   S. Naik, G. Bhattacharjya, V. R. Kavala and B. K. Patel, *Arkivoc*, 2004, 55–63.

49   M. Ikbal, R. Banerjee, S. Atta, D. Dhara, A. Anoop and N. D. P. Singh, *J. Org. Chem.*, 2012, **77**, 10557–10567.

50   J. Clayden, N. Greeves and S. Warren, *Organic Chemistry*, OUP Oxford, United States, 2nd edn., 2012.

51   F. Najóczki, M. Szabó, N. Lihi, A. Udvardy and I. Fábián, *Molecules*, 2021, **26**, 3632.

52   H. Reich, Hans Reich's Collection. NMR Spectroscopy., https://organicchemistrydata.netlify.app/hansreich/resources/nmr/?page=05-hmr-15-aabb/, (accessed 19 January 2023).

53   M. Nonoyama, *Bull. Chem. Soc. Jpn.*, 1974, **47**, 767–768.

54   L. M. Groves, C. Schotten, J. Beames, J. A. Platts, S. J. Coles, P. N. Horton, D. L. Browne and S. J. A. Pope, *Eur. J. Chem.*, 2017, **23**, 9407–9418.

55   X. Liu, M. Shao, C. Liang, J. Guo, G. Wang, X. A. Yuan, Z. Jing, L. Tian and Z. Liu, *ChemBioChem*, 2021, **22**, 557–564.

56   D. Lin-Vien, N. B. Colthup, W. G. Fateley and J. G. Grasselli, in *The Handbook of Infrared and Raman Characteristic Frequencies of Organic Molecules*, Elsevier, 1991, pp. 263–276.

57   W. Grzesiak and B. Brycki, *Molecules*, 2012, **17**, 12427–12448.

58   R. Aroca, S. Corrent and J. R. Menendez, *Vib. Spectrosc.*, 1997, **13**, 221–226.

59   I. Grabchev, V. Bojinov and C. Petkov, *Chem. Heterocycl. Compd.*, 2003, **39**, 179–183.

60   Z. Szakács, M. Bojtár, D. Hessz, S. Rousseva, I. Bitter, L. Drahos, M. Hilbers, H. Zhang, M. Kállay and M. Kubinyi, *New J. Chem.*, 2019, **43**, 6666–6674.

61   P. Kucheryavy, G. Li, S. Vyas, C. Hadad and K. D. Glusac, *J. Phys. Chem. A*, 2009, **113**, 6453–6461.

62   Z. Szakács, S. Rousseva, M. Bojtár, D. Hessz, I. Bitter, M. Kállay, M. Hilbers, H. Zhang and M. Kubinyi, *Phys. Chem. Chem. Phys.*, 2018, **20**, 10155–10164.

63   E. E. Langdon-Jones, C. F. Williams, A. J. Hayes, D. Lloyd, S. J. Coles, P. N. Horton, L. M. Groves and S. J. A. Pope, *Eur. J. Inorg. Chem.*, 2017, **2017**, 5279–5287.

64   J. Yin, K. Zhang, C. Jiao, J. Li, C. Chi and J. Wu, *Tetrahedron Lett.*, 2010, **51**, 6313–6315.

65   E. E. Langdon-Jones, A. B. Jones, C. F. Williams, A. J. Hayes, D. Lloyd, H. J. Mottram and S. J. A. Pope, *Eur. J. Inorg. Chem.*, 2017, **2017**, 759–766.

66   W. H. Melhuish, *J. Phys. Chem.*, 1961, **65**, 229–235.

67   N. Armaroli, L. De Cola, V. Balzani, J. P. Sauvage, C. O. Dietrich-Buchecker and J. M. Kern, *J. Chem. Soc., Faraday Trans.*, 1992, **88**, 553–556.

68   A. Demeter, T. Berces, L. Biczok, V. Wintgens, P. Valat and J. Kossanyi, *J. Phys. Chem.*, 1996, **100**, 2001–2011.

69   B. Ventura, A. Bertocco, D. Braga, L. Catalano, S. D'Agostino, F. Grepioni and P. Taddei, *J. Phys. Chem. C*, 2014, **118**, 18646–18658.

70   D. Kolosov, V. Adamovich, P. Djurovich, M. E. Thompson and C. Adachi, *J. Am. Chem. Soc.*, 2002, **124**, 9945–9954.

71   K. Suzuki, A. Kobayashi, S. Kaneko, K. Takehira, T. Yoshihara, H. Ishida, Y. Shiina, S. Oishi and S. Tobita, *Phys. Chem. Chem. Phys.*, 2009, **11**, 9850–9860.

72   G. R. Fulmer, A. J. M. Miller, N. H. Sherden, H. E. Gottlieb, A. Nudelman, B. M. Stoltz, J. E. Bercaw and K. I. Goldberg, *Organometallics*, 2010, **29**, 2176–2179.

73   Y.-L. Liu, A.-X. Feng and M.-S. Yuan, *Spectrochim. Acta A Mol. Biomol. Spectrosc.*, 2021, **256**, 119720.

74   J. Wu, T. Yi, T. Shu, M. Yu, Z. Zhou, M. Xu, Y. Zhou, H. Zhang, J. Han, F. Li and C. Huang, *Angew. Chem. Int. Ed.*, 2008, **47**, 1063–1067.

75   W. Huang, B. Chen and G. Zhang, *Eur. J. Chem.*, 2019, **25**, 12497–12501.

76   A. J. Taylor, E. S. Davies, J. A. Weinstein, I. V. Sazanovich, O. V. Bouganov, S. A. Tikhomirov, M. Towrie, J. McMaster and C. D. Garner, *Inorg. Chem.*, 2012, **51**, 13181–13194.

77   J. Hou, Z. Li, X. D. Jia and Z. Q. Liu, *Synth. Commun.*, 2014, **44**, 181–187.

78   J. Li, P. Zhang, M. Jiang, H. Yang, Y. Zhao and H. Fu, *Org. Lett.*, 2017, **19**, 1994–1997.

79   K. Gopalaiah, A. Saini, S. N. Chandrudu, D. C. Rao, H. Yadav and B. Kumar, *Org. Biomol. Chem.*, 2017, **15**, 2259–2268.

Chapter 6: Exploration of Pyrene Cyclometallation in a Novel Ligand

6.1: Introduction

The previous chapter explored the use of 1,8-naphthalimide derivatives as pendant organic chromophores to alter the photophysical properties of the resultant iridium complexes. This chapter explores the impact of direct cyclometallation to the extended delocalised π-system of pyrene.

6.1.1: Pyrene as a Photoactive Species

Pyrene is a polycyclic aromatic hydrocarbon (PAH) comprising of four fused benzene rings to form an electron-rich, highly planar delocalised system containing carbons of mainly sp²-hybridised character.[1] It exhibits unique excited state properties by virtue of intermolecular π-π aggregation features, where excited state dimers (excimers) are formed in solid state and in concentrated solutions (**Figure 6.1**). These features can either reduce the intensity of luminescence through *aggregation-induced quenching* (ACQ)[2] or enhance it through *aggregation-induced emission* (AIE), where the latter displays weak fluorescence in dilute solutions due to intramolecular motion.[3] Pyrene is an exception to the *mirror image rule* for fluorophores since highly structured emission is exhibited with significant vibronic character at ~375 – 410 nm in dilute solutions, whereas broad emission becomes prevalent at ~460 nm upon increasing the concentration.[4] These are indicative of monomer and excimer emission, respectively.[5]
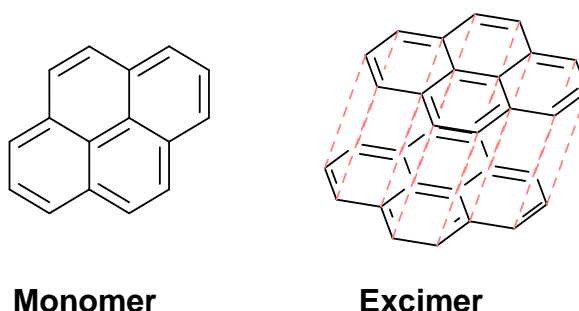
Monomer　　　　　　**Excimer**

Figure 6.1: *Pyrene as a monomer and resultant excimer formation by π-π stacking interactions (dotted lines).*

Pyrene analogues are extremely sensitive to their environment and the distinctive emission properties associated with monomer and excimer are considered to be favourable in many applications. These have been harnessed

in pyrene-based ratiometric probes to investigate DNA sequences,[6] protein conformation,[4] pH,[7] dynamic behaviour of lipid membranes[8] and for metal ion detection.[9,10] One example of a probe presenting AIE character is 2-(pyren-1-yl)pyridine, which has been explored as a sensor for H^+, Al^{3+} and picric acid detection, where short π-π contacts prevented intramolecular rotation of the pyridyl moieties in the solid state, precluding non-radiative deactivation.[11] Here, it was also recognised that these compounds could be utilised as ligands in Ir(III) species for enhanced photophysical character.

Preventing close π-π contacts between pyrene systems usually involves the introduction of bulky substituents[12] or by imparting a twisted molecular conformation,[13] allowing pyrene derivatives to be explored as efficient deep-blue organic luminophores. The unique features of pyrene offer significant scope for optical properties, where generation of efficient white,[14] pure blue,[15] and NIR[16] emission have been achieved. Additionally, due to the electron-rich nature of the pyrene system, ICT mechanisms can arise, offering more potential for probing applications.[17]

6.1.2: Pyrene in Organometallic Chemistry

Pyrene has been explored in inorganic photochemistry by introducing pyrene-containing ligands into a metal coordination complex. In 1992, the first report of rapid intramolecular TTET being observed in a bichromophoric species involved a Ru(II) polypyridine complex with a pendant pyrene component, where it was discovered that the lowest-lying ^{3}IL level was isoenergetic to the ^{3}MLCT state.[18] It was later discovered by Wilson *et al.* that the relative energies of these states resulted in excitation residing predominantly at the pyrene moiety.[19] Interestingly, naphthalene and anthracene analogues showed pure ^{3}MLCT and ^{3}IL character respectively, with no evidence of TTET, whilst the two states could only be separated at low temperatures in the pyrene species.[20] Emission was indistinguishable from **[Ru(bpy)₃]²⁺**, but a significant enhancement in lifetime was measured (from 720 ns to 5.23 µs).

Tyson *et al.* demonstrated that a significant enhancement in lifetime could be achieved by increasing the number of pyrene units incorporated into the structure. This was exemplified by values of 2.96 µs to 9.00 µs for one and three

pyrene-substituted dmb (4,4'-dimethyl-2,2'-bipyridine) ligands, respectively, with little deviation in other properties (**Figure 6.2**).[21] This enhancement in lifetime was associated with an increase in K_{eq} (the equilibrium constant associated with the two excited states), where the excited-state equilibrium is driven towards the [3]IL state when additional pyrene units were attached to the other ligands. Therefore, through incorporating multiple triplet acceptors, luminescence lifetimes can be extended.

Ru-6a

λ_{abs}: 343,[a] 459[b] nm

λ_{em}: 621 nm

τ: 2.96 µs

Φ: 0.065

Ru-6b

λ_{abs}: 343,[a] 460[b] nm

λ_{em}: 617 nm

τ: 9.00 µs

Φ: 0.064
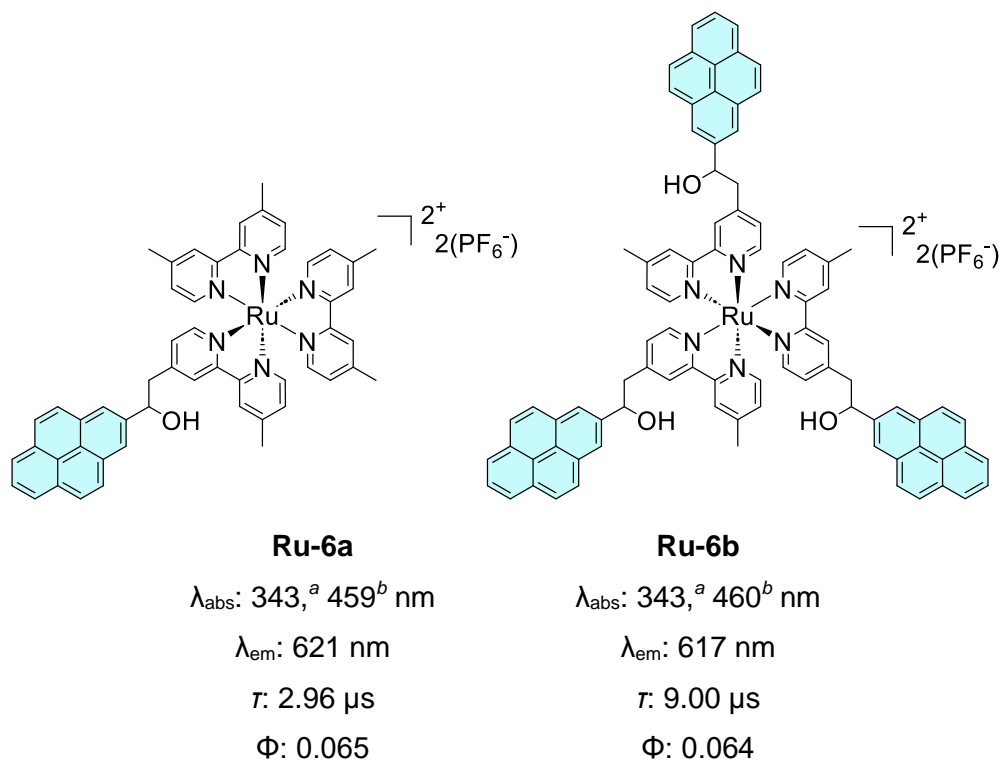
Figure 6.2: Ru(II) complexes studied by Tyson in degassed MeCN; [a]pyrene-based absorption; [b]Ru-based absorption.[21]

Pyrene-functionalised ancillary ligands have also been used to initiate the TTET process in iridium species, where extended lifetimes can be achieved by population of the low-lying triplet pyrene state.[22,23] In 2016, Lu *et al.* reported a series of extremely efficient Ir(III) complexes with enhanced triplet lifetimes (τ_T) as photosensitisers for TTA-UC. Strong absorption was seen across the visible range and Φ_{UC} values up to 31.6% were recorded.[24] Two of these complexes are shown in **Figure 6.3**, where the shortening of τ_T is noticeable upon addition of a second pyrene unit to the phenanthroline backbone.

Ir-6a

λ_{abs}: 440 nm

ε: 3.07 M^{-1}cm^{-1}

λ_{em}: 672, 747 nm

τ_T: 157.2 μs

Φ_{UC}: 30.2%

Ir-6b

λ_{abs}: 481 nm

ε: 5.24 M^{-1}cm^{-1}

λ_{em}: 682, 757 nm

τ_T: 85.8 μs

Φ_{UC}: 31.6%
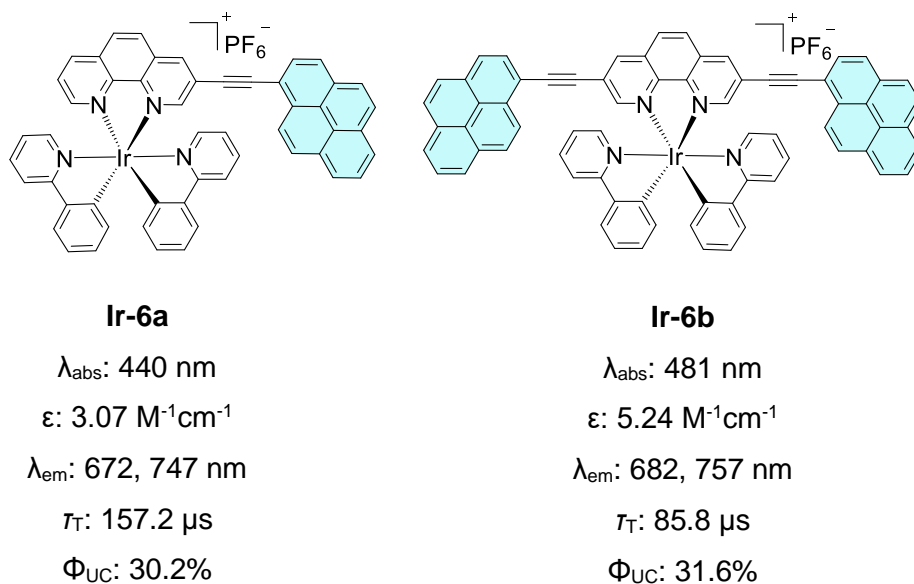
Figure 6.3: Ir(III) complexes as highly efficient photosensitisers for TTA-UC, measured in degassed DCM solutions.[24]

Although less commonly explored, this concept has also been extended to functionalised C^N ligands. Recently, complexes with cyclometallating ligands based upon methylated phenylquinoxalines were developed, where a pyrene system was covalently bound to the quinoxaline component.[25] Deep-red emission was achieved from an emissive state that was determined to be of ^{3}MLCT/^{3}ILCT character.

Direct cyclometallation to an efficient organic chromophore can offer advantages in photophysical behaviour such as high absorption within the visible range and enhanced quantum yields.[26] An early report of direct C-M bond formation at a pyrene unit was reported by Williams in 2006, where NIR emission at 720 nm was measured.[27] This displayed a significant bathochromic shift of ~100 nm in λ_{em} relative to the model complex **[Ir(piq)₂(acac)]** (λ_{em} = 622 nm).[28] In 2012, Hallett reported a species where cyclometallation occurred at the C10 position of the pyrenyl system, displaying an unusual chelating mode through a 6-membered metallacycle (**Figure 6.4**).[29] It was theorised that the driving force was a pre-arrangement of C^N ligands prior to complexation, due to short π-π contacts on the pyrene components in conjunction with bulky alkyl chains at the imidazole, preventing co-planarity. Although MLCT features were assigned in the absorption spectra and broadened red-shifted emission profiles were seen relative to the free ligands, the emission properties were attributed

to monomer-type fluorescence from the pyrene systems due to short lifetimes (<5 ns). However, τ_T values up to 15.0 µs in deoxygenated solutions were reported, displaying a significant enhancement relative to **[Ir(ppy)$_2$(bpy)]$^+$** (0.34 µs). The T_1 state was determined to be localised at the pyrene system and the study offered scope for efficient $^1O_2$ generation for applications in PDT (Φ_Δ up to 0.70).

	R = ^{n}Bu	R =
	Ir-6c	**Ir-6d**
	λ_{abs}: 423 nm	λ_{abs}: 425 nm
	λ_{em}: 435 nm	λ_{em}: 407 nm
	τ_T: 13.3 µs	τ_T: 3.9 µs
	Φ_Δ: 0.86	Φ_Δ: 0.80
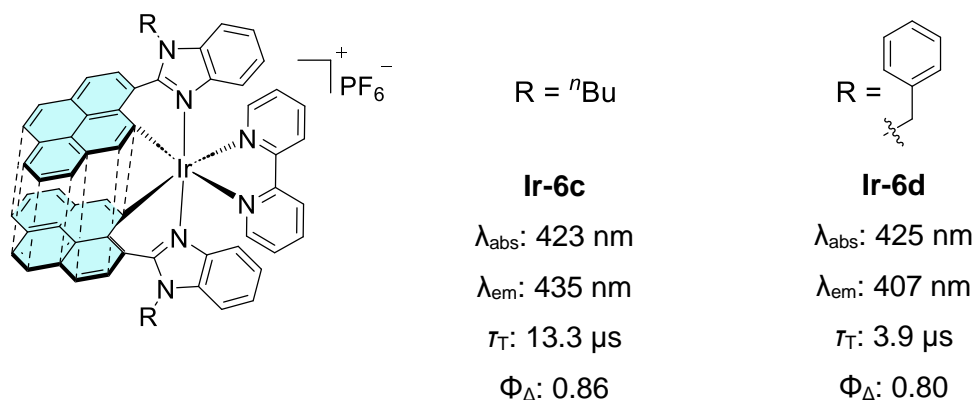
Figure 6.4: Cycloiridiated complexes by Hallett, where intramolecular π-π contacts facilitate the formation of a 6-membered metallacycle. Measurements were in degassed DCM solutions. [29]

In 2013, Edkins *et al.* formed two neutral isomeric Ir(III) species that were cyclometallated at either the C1 or C2 position of a pyrene system in 1- or 2-(2'-pyridyl)pyrene.[30] Significant differences in photophysical attributes were recognised (**Figure 6.5**), where the emissive state was concluded to be exclusively pyrene-localised ^{3}LC-type for **[Ir(1-pypyr)$_2$(acac)]**, whilst **[Ir(2-pypyr)$_2$(acac)]** possessed mixed ^{3}LC/^{3}ILCT character with enhanced vibronic structure in the emission spectrum. The reduced Φ_{PL} for **[Ir(1-pypyr)$_2$(acac)]** was attributed to the conformational arrangement and subsequent positioning of orbitals, where non-radiative decay processes dominated.
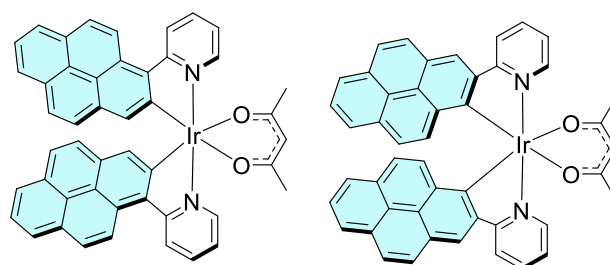
Ir(1-pypyr)₂(acac)

λ_{abs}: 519 nm

λ_{em}: 680 nm

τ: 2.7 µs

Φ: 5.6 × 10⁻³

Ir(2-pypyr)₂(acac)

λ_{abs}: 493 nm

λ_{em}: 626 nm

τ: 37.0 µs

Φ: 0.063

Figure 6.5: Isomeric Ir(III) complexes developed by Edkins et al.,[30] photophysical properties were measured in degassed DCM solutions.

Direct cyclometallation to pyrene has also been explored specifically for deep-red and NIR emission in the development of PLEDs (polymer light emitting diodes) and two recent examples are displayed in **Figure 6.6**.[31,32]
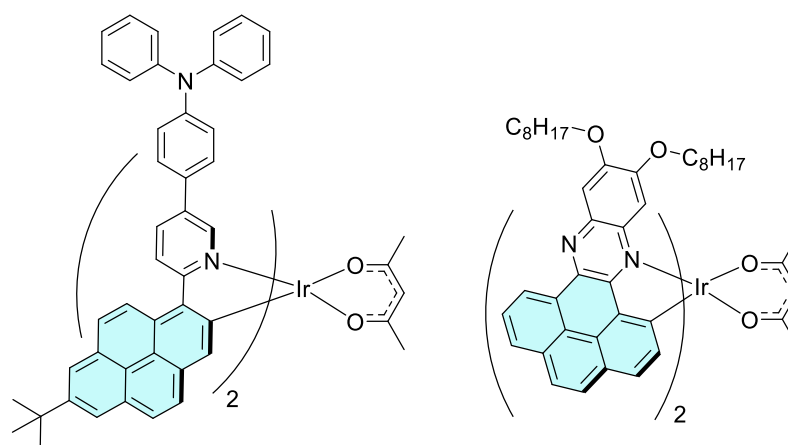
[(t-BuPyrPyTPA)₂Ir(acac)]

λ_{abs}: 525 nm

ε: 4.05 M⁻¹cm⁻¹

λ_{em}: 697 nm

τ: 0.66 µs

Φ: 0.019

[(PPz-11,12-DO)₂Ir(acac)]

λ_{abs}: 608 nm

ε: 0.9 M⁻¹cm⁻¹

λ_{em}: 732 nm

τ: 0.60 µs

Φ: 0.13

Figure 6.6: Examples of NIR emitters as dopants for PLED fabrication. Measurements in degassed DCM solutions.[31,32]

6.2: Aims

Although iridium complexes containing pendant pyrene chromophores exist in the literature, reports of direct cyclometallation to its π-conjugated system are generally limited. The aim of the work presented in this chapter is to investigate the synthesis and spectroscopic properties of **2-(pyren-1-yl)quinoxaline** and its corresponding cationic iridium(III) complex with the general formula **[Ir(C^N)$_2$(bpy)]PF$_6$**. With a specific interest in the photophysical effects of direct cyclometallation to the polycyclic system, comparisons were made to previous analogues which have primarily focused on pyridine or imidazole *N*-donors.[29,30]

6.3: Results and Discussion

6.3.1: Synthesis of Ligand and Complex

The proposed ligand consisted of pyrene covalently bound *via* the C1 position to a quinoxaline moiety. By use of analogous methods detailed in **Chapter 5**, **pyr-qx** was synthesised from commercially available 1-acetylpyrene (**Scheme 6.1**). The crude product was deemed to be >98% pure by analysis with the only contaminant being 1-acetylpyrene, but scrupulous purification was required to obtain spectroscopically pure compound. This was necessary since 1-acetylpyrene also exhibits strong luminescence even at low concentrations.[33]
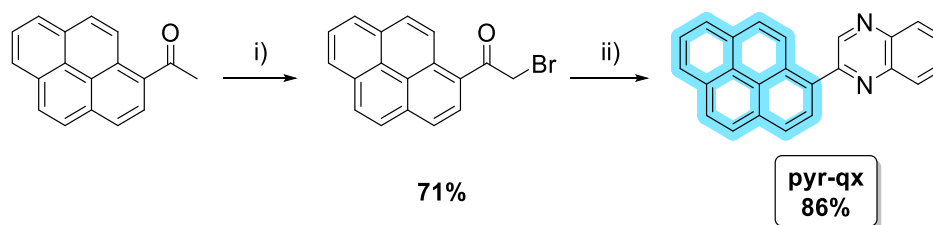
Scheme 6.1: *Synthesis of* **pyr-qx**; *i) DDB, 1,4-dioxane/Et$_2$O (1:1), RT, 2h; ii) 1,2-phenylenediamine, NaHCO$_3$ (1.2 eq.), DMSO, 120°C, 24h.*

Through the same experimental procedure outlined in previous chapters, **pyr-qx** was investigated as a C^N ligand where the point of cyclometallation was expected to be at a carbon atom on the pyrene moiety (**Scheme 6.2**).
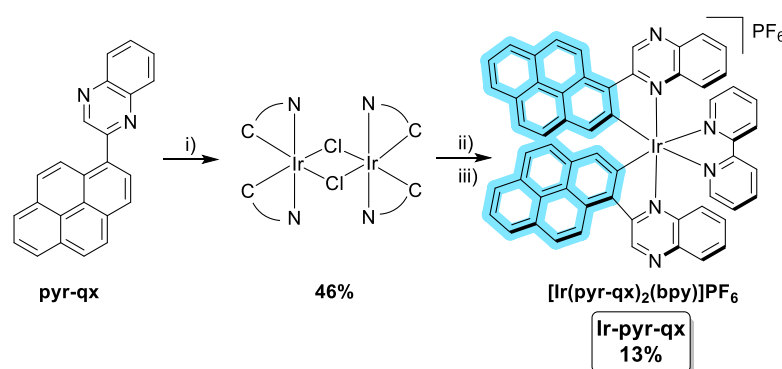
Scheme 6.2: *Synthesis, chemical structure, and experimental yield of* **Ir-pyr-qx**; *i) IrCl$_3$.xH$_2$O, 2-ethoxyethanol, 48h; ii) 2,2'-bipyridyl, 2-ethoxyethanol, reflux, 24h; iii) NH$_4$PF$_6$ (aq.).*

The complex was purified by column chromatography using a mixture of DCM/MeOH as the mobile phase and silica gel as the stationary phase. Polarity of the solvent mixture was increased incrementally, and the product eluted as a dark red band with a mixture of approximately 9:1 DCM/MeOH. Residual impurities were present according to TLC analysis, which were successfully isolated from the product by recrystallisation techniques (DCM, Et$_2$O) to give the product as a dark brown solid in a relatively poor yield (~13%). However, it is worth noting that the presence of product was indicated in other fractions, but co-elution made it difficult to isolate the complex from impurities.

Five-membered chelating modes are most common for Ir(III) species since they are entropically favoured. Studies have indicated that C-M bond formation occurs at the C2 position when there are no steric limitations on the *N*-coordinating component of the ligand.[30] Therefore, the proposed structure of **Ir-pyr-qx** was assumed to be consistent with the most common chelating mode of Ir(III) species and is displayed in **Scheme 6.2**.

6.3.2: Characterisation of Ligand and Complex

^{1}H NMR spectra for **pyr-qx** and **Ir-pyr-qx** are displayed in **Figure 6.7**. The spectrum for **pyr-qx** was consistent with previous assignments of pyrene-based compounds, where a cluster of peaks appeared within the aromatic region between 8.15 – 8.37 ppm.[34] Integrals were in alignment with the chemical structure of the ligand, whilst bearing similarities to 2-(pyren-1-yl)pyridine.[11] A singlet at 9.33 ppm was representative of the pyrazine proton within the quinoxaline moiety, which became vastly deshielded to 10.14 ppm upon complexation to form **Ir-pyr-qx**. The downfield position was correlated to the fixed orientation, preventing interaction with the adjacent π-system on pyrene. The sum of integrals was calculated to be 34 when this singlet was normalised to 2 protons, consistent with the theorised structure of **Ir-pyr-pqx**, and the presence of one set of peaks in the spectrum suggested that it adopted a symmetrical trans-*N,N* octahedral geometry, typical for Ir(III) species containing two equivalent C^N ligands and one symmetrical ancillary ligand.[35] A singlet at 7.37 ppm was also assigned for the proton directly adjacent to the site of cyclometallation on pyrene.
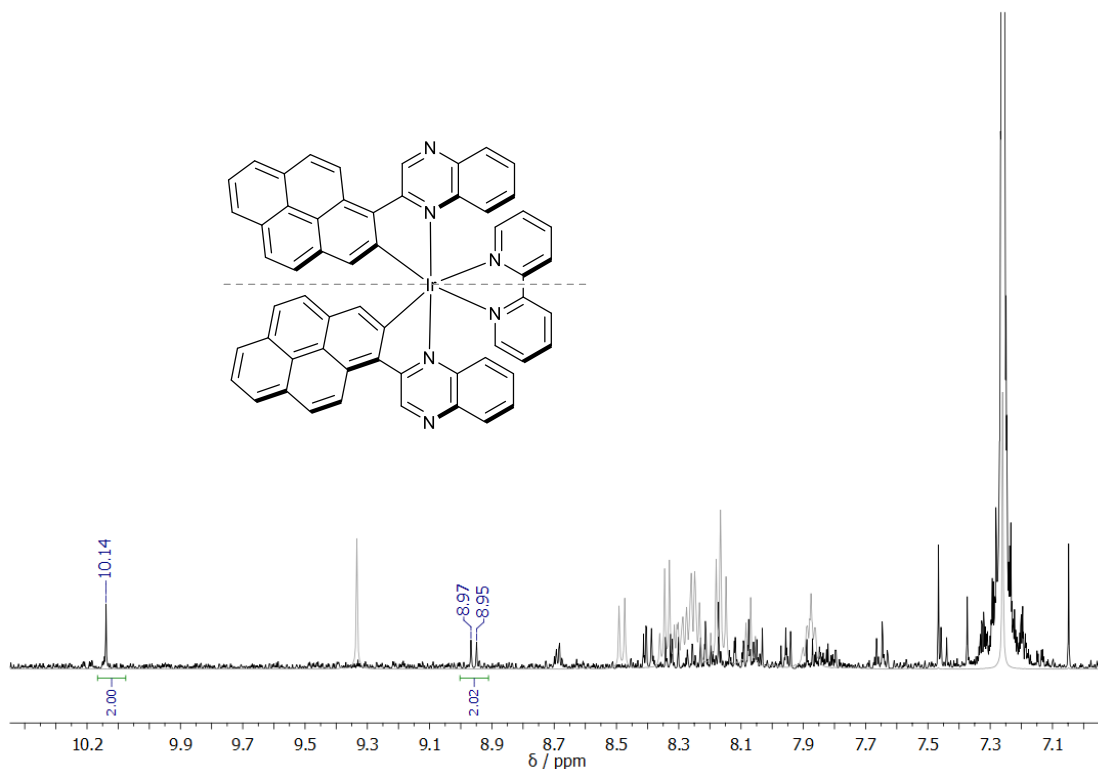
*Figure 6.7: Overlaid ^1H NMR spectra of **Ir-pyr-qx** (black) and **pyr-qx** (grey), both in CDCl$_3$, 500 MHz.*

$^{13}C\{^1H\}$ NMR spectroscopy data was also collected for **pyr-qx** and **Ir-pyr-qx** and some assignments are shown in **Figure 6.8**. Peaks at 154.8 and 147.2 ppm in **pyr-qx** were assigned to the deshielded carbon atoms directly adjacent to the imine nitrogens on the quinoxaline. Downfield signals at 155.8 and 148.9 ppm for the complex were tentatively assigned as the C2 and C6 position on the ancillary bipyridine ligand, whilst the peak at 145.8 ppm was ascribed to the unsubstituted carbon on the pyrazine component. The data was generally consistent with other reports on cyclometallated pyrene complexes.[29,30,32]
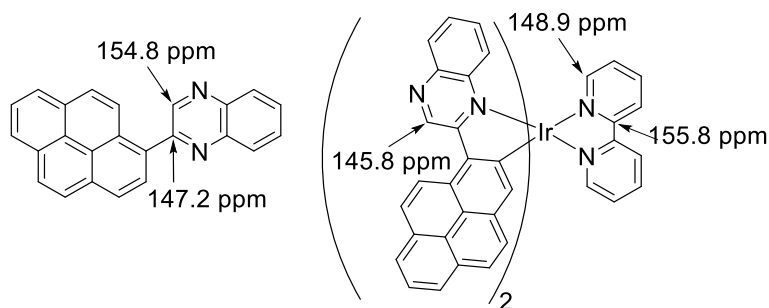
*Figure 6.8: Some assignments made for **pyr-qx** and **Ir-pyr-qx** in their respective $^{13}C\{^1H\}$ NMR spectra (CDCl$_3$, 126 MHz).*

FTIR spectroscopy measurements gave rise to characteristic C-H stretches up to 3036 and 3312 cm^{-1} for the ligand and complex, respectively.[36] High-intensity signals below 1000 cm^{-1} were assigned to out-of-plane deformations,[37] apart from a PF$_6$ peak at 835 cm^{-1} for **Ir-pyr-qx**.

High-resolution mass spectrometry (ES+) was performed on the ligand and complex, to generate data that was consistent with the respective molecular masses. The molecular ion peak for **Ir-pyr-qx** is shown in **Figure 6.9**, where the experimental value (1007.2479) closely resembled the calculated mass (1007.2474).

Ir-pyr-qx

Molecular Weight: 1007.17 g/mol
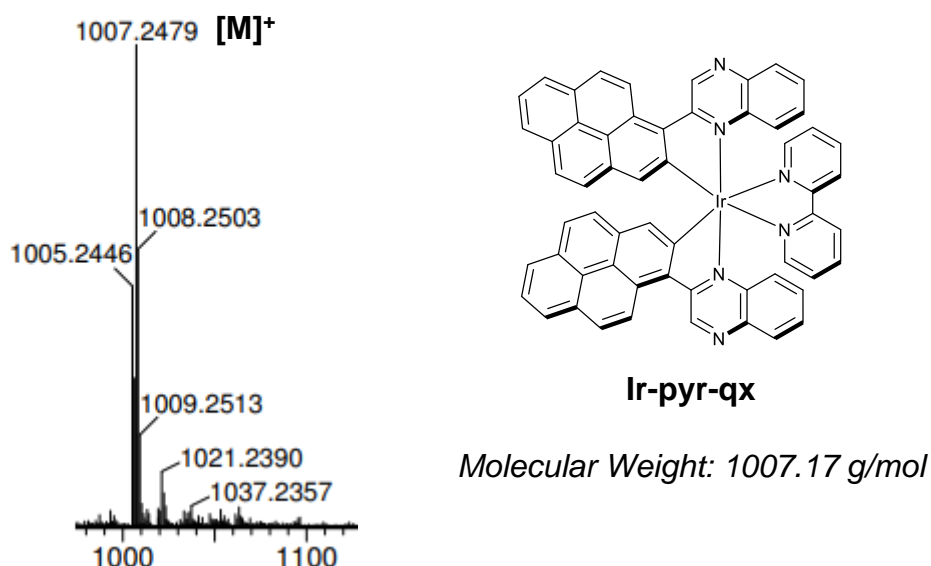
*Figure 6.9: Section of the HRMS (ES+) of **Ir-pyr-qx**, where the M+ peak is assigned.*

Although cyclometallation at C2 was hypothesised, the 6-membered chelate isomer was considered to be possible through Ir-C bond formation at C10.[29] However, due to the limiting solubility of the complex, detailed analysis through X-ray crystallography was not possible and further studies must be implemented for unequivocal structural determination.

6.3.3: Photophysical Properties

Pyr-qx displayed an absorption profile consisting of significant π→π* character alongside a high-intensity structureless feature at ~390 nm (**Figure 6.10a**).[11] The absence of the latter peak in the absorption profile for 2-phenylquinoxaline

(**pqx**) (**Table 6.1**), and unsubstituted pyrene (336 nm)[38] suggested that significant electronic mixing occurred between the two chromophores, leading to a bathochromically-shifted feature. This peak was characteristic for substitution at the C1 position due to pronounced orbital contributions.[39]
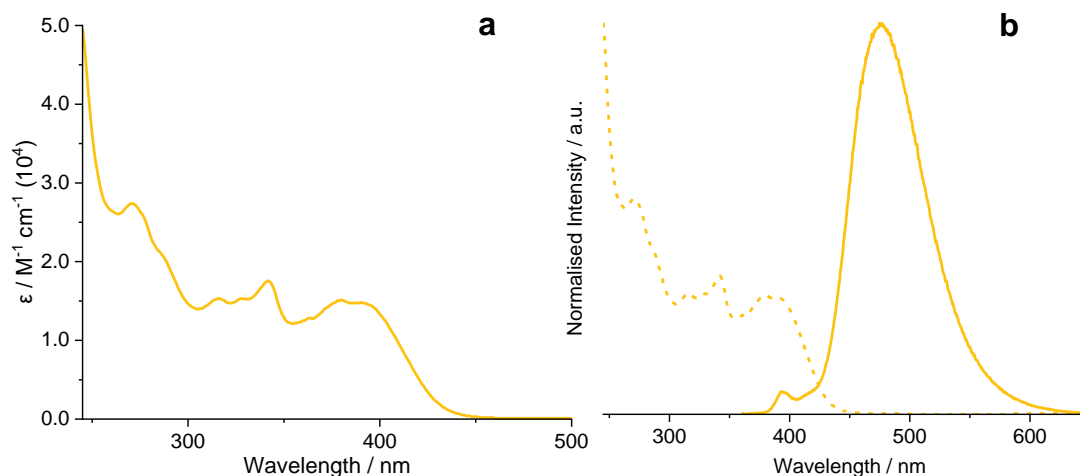
Figure 6.10: *UV-vis absorption (**a**) and normalised absorption (dashed) and emission (λ_{ex} = 350 nm, solid line) spectra (**b**) of **pyr-qx** in aerated CHCl₃ (RT, 0.99 × 10⁻⁵M).*

A broad emission peak was seen at 474 nm for **pyr-qx** in 0.99 × 10⁻⁵ M CHCl₃ solution (**Figure 6.10b**), consistent with analogous systems.[30] This may be indicative of excimer emission ascribed to the stacking of the pyrene component, suggesting that π-π interactions were significant at this concentration.[4,40]

Compound	λ_{abs} / nm	λ_{em} / nm	λ_{em} (77K)[c] / nm	Φ_F / %[d]	τ_{obs} / ns[e]	$\Delta\lambda$ / nm[f]
pqx[a]	261, 334	402 (377)	385, 502, 536	3.2 (2.7)	< 1.0	68
pyr-qx[b]	271, 316, 342, 380, 390	474 (498)	460	53.9 (37.4)	1.1 (2.3)	84

Table 6.1: *Photophysical properties of 2-phenylquinoxaline (**pqx**) and the free ligand **pyr-qx** in aerated CHCl₃ at room temperature (ca. 10⁻⁵ M), values in parentheses are in ca. 10⁻⁵ M MeCN solutions. [a]λ_{ex} = 334 nm; [b]λ_{ex}= 350 nm; [c]in DCM/MeOH glass (1:1); [d]using known standard, quinine sulphate in 0.1M H₂SO₄ (Φ = 0.546 at λ_{ex} = 350),[41] samples in CHCl₃ or MeCN; [e]λ_{ex}= 295 nm, measured at λ_{em}; [f]λ_{em} − λ_{abs} for peak maxima (Stokes shift).*

Photophysical properties were measured (**Table 6.1**) and directly compared with **pqx** to monitor the effects upon incorporation of a pyrene component in place of a phenyl ring. Emission maxima were recorded at longer λ_{em} relative to **pqx**, where a shift of 72 nm and 121 nm in chloroform and acetonitrile (respectively) were measured for **pyr-qx**. An enhancement in Stokes shift and Φ_F was also recognised upon incorporation of a pyrene unit.

Emission data of **pyr-qx** was collected at various concentrations in chloroform to study the aggregation effects in solution (**Figure 6.11**). A single broad feature at ~475 nm was seen at high concentrations and narrowed upon dilution alongside the generation of a sharp signal at ~395 nm. These were attributed to excimer and monomer emission respectively.[42] The ratios of the relative emission intensities (I_{exc}/I_{mono}) at particular dilutions decayed exponentially, levelling off at reduced concentrations (<0.33 mM). This suggested that monomeric emission only became significant when [**pyr-qx**] < 0.25 mM, due to increased spatial separation reducing the intramolecular π-π stacking arrangements. Emission intensity generally increased in line with the concentration until maximum intensity was reached at ~0.11mM. Subsequently, aggregation-induced quenching was recognised upon increasing the concentration past this point by a diminution of intensity.[43] This is demonstrated in **Figure 6.11d**, where emission intensity of the assigned excimer feature at 475 nm diminishes upon increasing concentration past 0.25 mM.
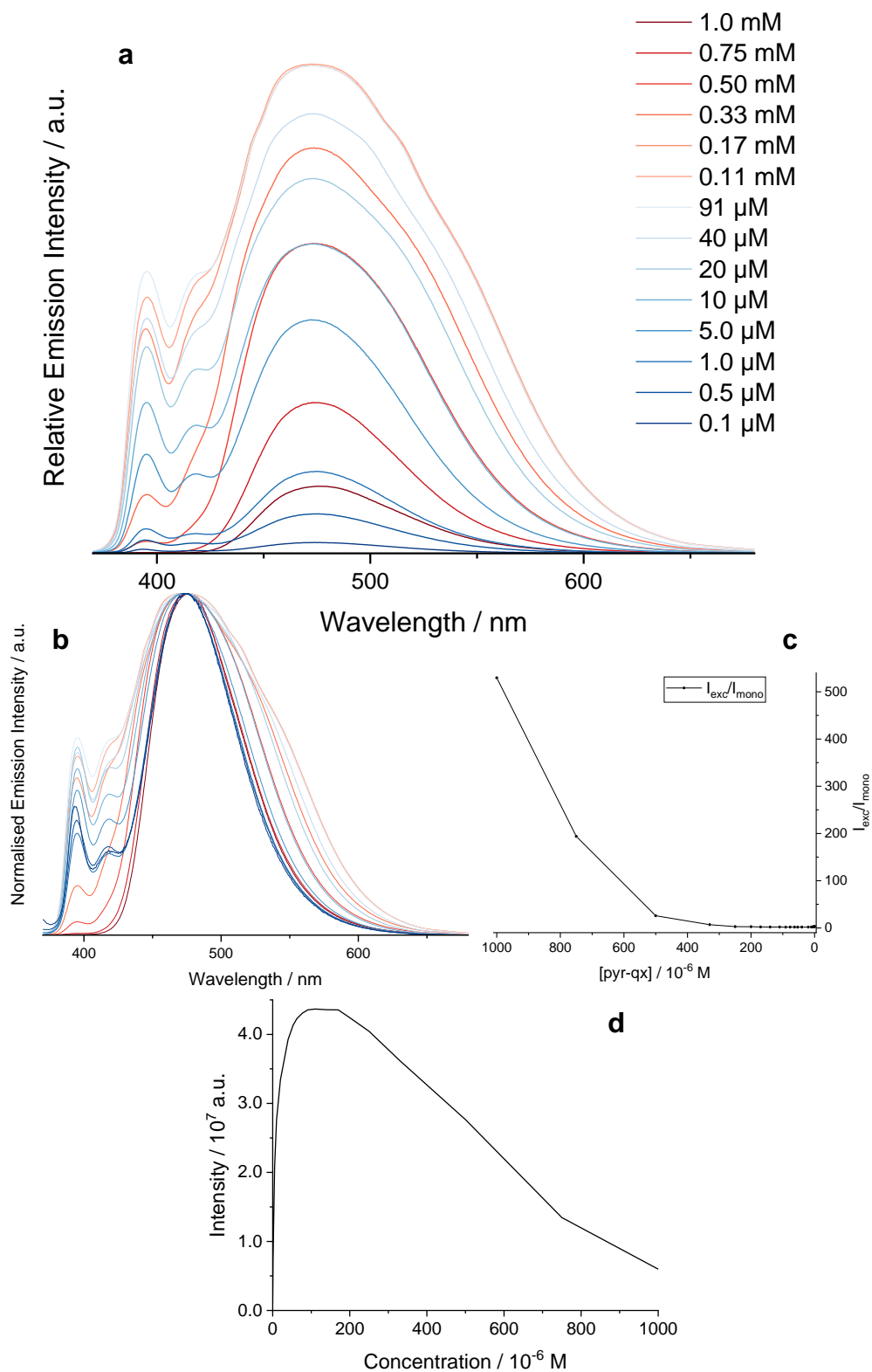
*Figure 6.11: Emission spectra of **pyr-qx** recorded in CHCl₃ at various concentrations (λ_{ex} = 340 nm). (**a**) Relative emission spectra. (**b**) Normalised emission spectra. (**c**) Ratio of emission intensities for monomer emission peak (395 nm) and excimer emission (475 nm) as a function of concentration. (**d**) Emission intensity at 475 nm as a function of concentration, demonstrating excimer formation.*

The UV-vis absorption spectrum for **Ir-pyr-qx** in chloroform is shown in **Figure 6.12** alongside that of **pyr-qx**, exposing discernible differences in absorption behaviour upon cyclometallation. Ligand-centred $^1(\pi \rightarrow \pi^*)$ features were noted within the UV range, due to their resemblance to signals at the same positions in the free ligand. A broad, featureless peak arose at ~450 nm, tailing off at wavelengths exceeding 600 nm. This was indicative of ^{1}MLCT and ^{3}MLCT/^{3}ILCT character (respectively) and was validated by the lack of absorption features measured at >400 nm in **pyr-qx**. The broad nature of the peak suggested that multiple contributions were present, in accordance with studies correlating absorption features at ~525 nm ($\varepsilon \sim 10^4$ M^{-1} cm^{-1}) to mixed ^{1}LC/^{3}LC features at the pyrene system.[32]
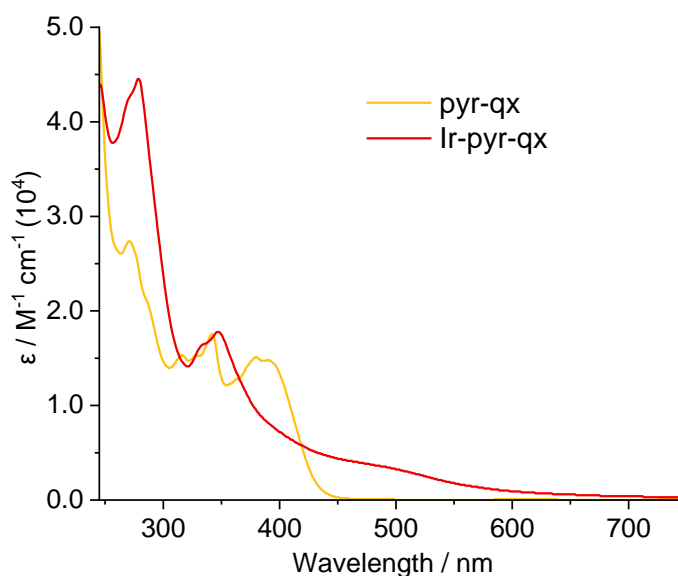
*Figure 6.12: UV-vis absorption spectra of **pyr-qx** (dashed) and its corresponding Ir(III) complex, **Ir-pyr-qx** (solid), both measured in CHCl$_3$ (RT, 0.99 × 10^{-5}M).*

The emission properties of **Ir-pyr-qx** in chloroform (*ca.* 10^{-5}M) were explored at room temperature at various excitation wavelengths (**Figure 6.13**). At $\lambda_{ex} = 350$ nm, highly structured features dominated at 395 and 415 nm and were congruent with the emission profile of pyrene.[4,5] This differed from that of **pyr-qx**, which displayed a broadened peak at 474 nm with very little pyrene character, suggesting that pyrene-localised fluorescence was significant in **Ir-pyr-qx** and became isolated upon complexation. Broad features of lower intensity were recognised at longer wavelengths and were isolated at $\lambda_{ex} = 450$ and 500 nm. These were centred at 516 and 547 nm, respectively, where

disparities in position were speculated to be the result of reduced electronic mixing at longer λ_{ex}. Although these were red-shifted relative to the free ligand, λ_{em} were still shorter than that of **[Ir(ppy)₂(bpy)]PF₆** (585 and 595 nm in MeCN and DCM, respectively).[44,45] Peak maxima and overall spectral appearance remained consistent in both chloroform and acetonitrile, suggesting that emission was independent of solvent polarity and was therefore suggested to display LC character.[30] This differed from the model complex **[Ir(ppy)₂(bpy)]⁺**, which displays solvent-dependent λ_{em} due to primarily ^{3}MLCT excited state properties. [31,46]
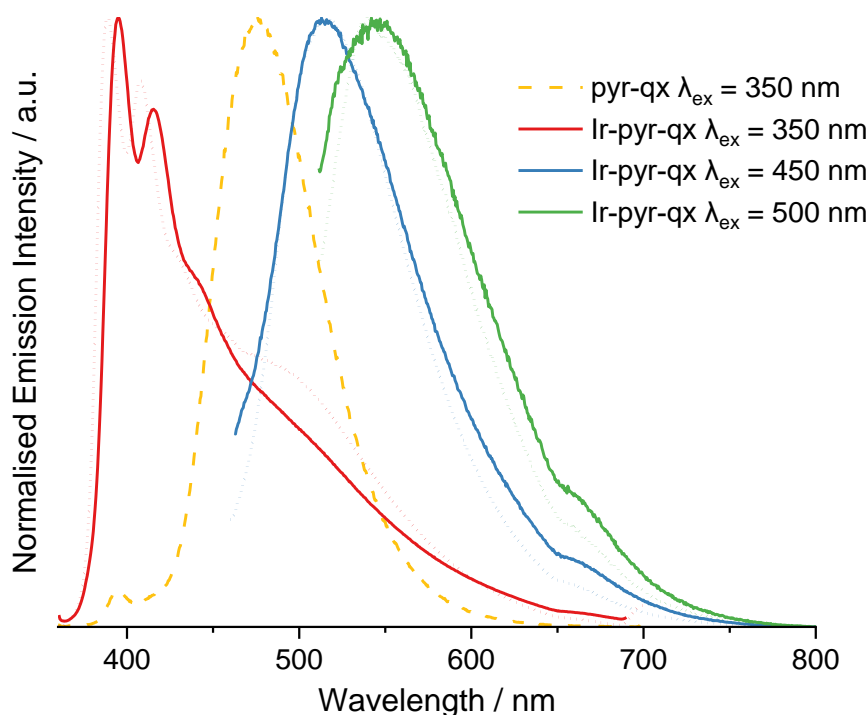
*Figure 6.13: Emission profile of **Ir-pyr-qx** at room temperature in CHCl₃ (solid lines) and MeCN (dotted lines), measured at various λ_{ex}. The free ligand spectrum in CHCl₃ is also included (dashed line).*

Low temperature (77 K) emission data was collected for the ligand and complex in a rigid matrix of 1:1 DCM/MeOH glass, where enhanced vibronic character was generally recognised (**Figure 6.14**). In the free ligand spectrum and when $\lambda_{ex} < 500$ nm for the complex, emission maxima experienced a hypsochromic, thermally induced Stokes shift, consistent with a charge transfer species. However, distinguishable features were recognised at 605 and 662 nm in all cases and were able to be isolated at $\lambda_{ex} = 550$ nm, where the structured nature of the peaks were established. These signals were absent in the free ligand

spectrum in addition to the corresponding room temperature emission profiles and their position remained constant regardless of λ_{ex}. Therefore, these were suggested to possess [3]LC character from the pyrene moiety, which can be accessed at low temperature.[32,47]
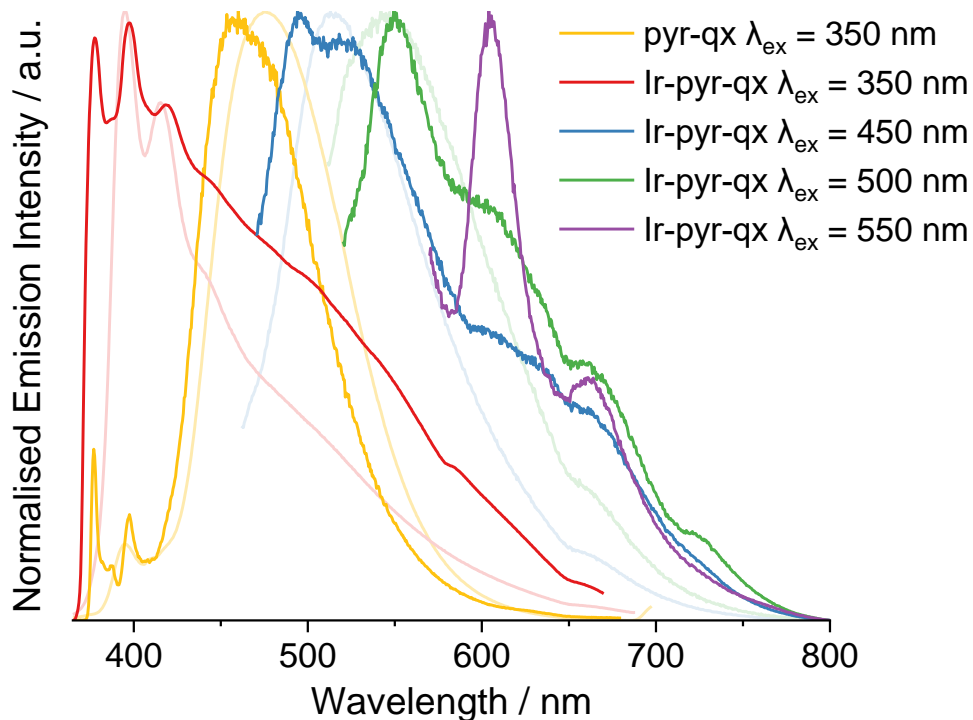
Figure 6.14: *Normalised emission spectra for **Ir-pyr-qx** and **pyr-qx** at 77 K in DCM/MeOH (1:1) glass. Room temperature spectra are also shown in light colours.*

λ_{abs} / nm	λ_{em} / nm	λ_{em} / nm (77 K)[b,c]	Φ_{PL} / %[d]	τ_{obs} / ns[e]
269, 278, 333, 347, 491, 559 sh	516, 662 sh[a] (518, 662 sh)[a] 547, 662 sh[b] (545, 662 sh)[b]	551, 605, 662, 726	1.5	2.9 (61.5%), 9.8 (38.5%)

Table 6.2: *Photophysical properties of **Ir-pyr-qx** measured in aerated CHCl₃ (ca. 10⁻⁵ M) at room temperature, values in parentheses in ca. 10⁻⁵ M MeCN. ᵃλₑₓ = 450 nm; ᵇλₑₓ = 500 nm; ᶜin DCM/MeOH glass (1:1); ᵈusing known standard, **[Ru(bpy)₃](PF₆)₂** in MeCN (Φ = 0.016 at λₑₓ = 450 nm),[48] samples in CHCl₃; ᵉλₑₓ = 295 nm, λₑₘ = 550 nm, relative contributions of τ₁ and τ₂ in parentheses.*

Photophysical properties of **Ir-pyr-qx** are presented in **Table 6.2**. Luminescence was associated with a fluorescence decay pathway at room temperature due to short lifetimes (<10 ns) being measured for all emission bands. This was in agreement with the complexes described by Hallett, where emission was measured from a low-lying pyrene-localised singlet excited state under ambient conditions.[29] It was concluded that the excited state was sensitive to quenching by molecular oxygen and triplet emission could originate from a potentially long-lived excited state. However, emission was too weak in degassed solvent and therefore, time-resolved measurements were not able to be recorded to confirm this hypothesis. Triplet excited state lifetimes must be calculated from transient absorption measurements to determine the excited state behaviour and if any phosphorescence occurs.

6.4: Conclusions

This chapter explored the preparation and photophysical properties of a novel pyrene-based ligand system. Aggregation features were monitored spectroscopically, where both AIE and ACQ were recognised.

Synthesis of a corresponding iridium(III) species was undertaken, where experimental observations were compared directly to analogous systems in the literature. Although crystallographic data could not be obtained (due to limited solubility) for absolute structural determination, the data aligned with previous analogues. It was suggested that the complex adopted the conventional geometry containing a 5-membered metallacycle. Preliminary photophysical measurements were carried out, where short-lived luminescence was measured at room temperature. This was tentatively assigned as ligand-centred fluorescence from the pyrene moiety, due to characteristically short lifetimes (<10 ns).

At 77 K, some evidence was seen for ^{3}LC emission at $\lambda_{ex} > 450$ nm, but transient absorption measurements must be conducted to confirm this by determination of the triplet excited state lifetimes. Additionally, deoxygenated samples must be analysed since the pyrene triplet manifold is highly sensitive to quenching by molecular oxygen.

6.5: Experimental

6.5.1: General Considerations

All commercially available reagents were used without further purification, and all reactions employed vacuum line and Schlenk techniques. ^{1}H, ^{13}C{^{1}H} and ^{19}F{^{1}H} NMR spectra were recorded on NMR-FT Bruker 500, 400 and 300 MHz spectrometers in the appropriate solvents (CDCl$_3$, (CD$_3$)$_2$CO, CD$_3$CN or DMSO-d_6), where chemical shift (δ) positions (ppm) were determined relative to TMS and residual solvent peaks[49] through digital locking. High resolution mass spectra were obtained by staff at Cardiff University using a Waters Xevo G2-XS QTof spectrometer, and IR spectra were recorded on a Shimadzu IRAffinty-1 FTIR spectrometer. UV-vis spectroscopy studies were performed on 10^{-5} M CHCl$_3$ or MeCN solutions using a Shimadzu UV-1800 spectrophotometer. The 10^{-5} M samples were prepared by dilution of 10^{-3} M bulk stock solutions. Upon sonication in an ultrasonic bath, the samples were inspected to ensure that solute was fully dissolved. Luminescence data was acquired for 10^{-5} M CHCl$_3$ or MeCN solutions of the samples using a JobinYvon-Horiba Fluorolog spectrometer fitted with a JY TBX picosecond single-photon detection module. Time-resolved measurements were recorded using a Nano-LED pulsed laser source configured for 295 or 459 nm output, operating at 1 MHz. Time-resolved measurements were recorded using the JobinYvon-Horiba FluoroHub single photon counting module and the data was resolved using the DAS6 deconvolution software.

6.5.2: Preparation of the Organic Precursor and Ligand

Synthesis of 2-bromo-1-(pyren-1-yl)ethan-1-one

Following an adapted literature method,[50] 1-acetylpyrene (196 mg, 0.801 mmol) was dissolved in 1,4-dioxane and diethyl ether (1:1, 40 mL) and dioxane dibromide (219 mg, 0.882 mmol) in the same solvent mixture (40 mL) was added dropwise. The solution was stirred for 2 hours at room temperature and the product was extracted into Et$_2$O and washed with distilled water (2 × 30 mL). The combined organic fractions were dried over MgSO$_4$ and the solvent was removed *in vacuo*. Purification was carried out by recrystallisation from

DCM/cyclohexane to give the pure product as yellow crystals (187 mg, 70.6%). ^{1}H NMR (300 MHz, CDCl$_3$) δ_H = 8.99 (d, $^3J_{HH}$ = 9.5 Hz, 1H), 8.37 (d, $^3J_{HH}$ = 8.1 Hz, 1H), 8.31 – 8.25 (m, 3H), 8.23 – 8.17 (m, 2H), 8.12 – 8.06 (m, 2H), 4.74 (s, 2H) ppm. The data was consistent with literature findings.[51]

Synthesis of 2-(pyren-1-yl)quinoxaline *(pyr-qx)*

Following an adapted literature method,[52] 2-bromo-1-(pyren-1-yl)ethan-1-one (179 mg, 0.554 mmol), 1,2-phenylenediamine (59.9 mg, 0.554 mmol) and NaHCO$_3$ (55.8 mg, 0.665 mmol) were dissolved in DMSO (15 mL) and heated to 120°C under air for 24 hours. Upon cooling to room temperature, distilled water (20 mL) was added to the mixture and the resultant precipitate was filtered under reduced pressure, where the crude solid was washed sequentially with distilled water (10 mL) and oven-dried (60°C). The crude product was purified by column chromatography (SiO$_2$) where the starting material eluted with DCM/hexane (9:1) and the pure product eluted with DCM. The solvent was removed *in vacuo* to give the product as a yellow solid (157 mg, 86.0%). ^{1}H NMR (500 MHz, CDCl$_3$) δ_H = 9.33 (s, 1H), 8.48 (d, $^3J_{HH}$ = 9.2 Hz, 1H), 8.37 – 8.31 (m, 2H), 8.32 – 8.23 (m, 4H), 8.20 – 8.15 (m, 3H), 8.07 (*app.* t, $^3J_{HH}$ = 7.6 Hz, 1H), 7.91 – 7.84 (m, 2H) ppm. ^{13}C{^{1}H} NMR (126 MHz, CDCl$_3$) δ_H = 154.8, 147.3, 142.6, 141.4, 132.4, 132.2, 131.5, 131.0, 130.6, 130.1, 129.9, 129.5, 129.3, 129.1, 128.8, 128.1, 127.5, 126.5, 126.0, 125.7, 125.3, 125.2, 124.8, 124.3 ppm. HRMS (ES+): *m/z* calc'd 331.1235 for C$_{24}$H$_{15}$N$_2$; found 331.1235 [M + H]$^+$. UV−vis (CHCl$_3$) λ_{max} ($\varepsilon \times 10^4$ / L mol^{-1} cm^{-1}): 271 (2.7), 316 (1.5), 342 (1.8), 380 (1.5), 390 (1.5) nm. FTIR (solid, cm^{-1}) (ATR) v_{max}: 3036, 1549, 1535, 1483, 1402, 1273, 1179, 1124, 1115, 1072, 1026, 957, 930, 856, 841, 829, 764, 719, 691, 623, 604, 546, 532, 500, 457, 420.

6.5.3: Preparation of Inorganic Complexes

General synthesis of [(Ir(C^N)$_2$(μ-Cl))$_2$]

Prepared according to an adapted literature procedure,[53] IrCl$_3$.xH$_2$O (77.4 mg, 0.259 mmol) in 2-ethoxyethanol and distilled water (3:1, v/v, 10 mL) was stirred at 60°C under an inert N$_2$ atmosphere for 30 minutes until fully dissolved. **Pyr-qx** (180.0 mg, 0.545 mmol) in 2-ethoxyethanol (5 mL) was added to the stirred solution and the mixture was heated to reflux for 48 hours. Upon cooling to room

temperature, distilled water was added, and the resultant precipitate was filtered under reduced pressure and washed with distilled water and a small amount of Et_2O. The product was filtered through with DCM, removing any insoluble impurities. The solvent was removed *in vacuo* and the solid was oven-dried (~60°C) to generate the dimer as a brown solid (106 mg, 46.1%) which was used in the subsequent step without further purification.

Synthesis of [Ir(pyr-qx)₂(bpy)]PF₆ *(Ir-pyr-qx)*

[(Ir(pyr-qx)$_2$(μ-Cl))$_2$] (95.0 mg, 0.054 mmol) and 2,2'-bipyridyl (18.4 mg, 0.118 mmol) were dissolved in 2-ethoxyethanol (10 mL) and the solution was heated to reflux for 24 hours under an inert N_2 atmosphere. Upon cooling to room temperature, saturated aqueous NH_4PF_6 solution (~2 mL) was added, and the solution was stirred for 15 minutes. The crude product precipitated out of solution upon the addition of distilled water (10 mL) and the suspension was filtered under reduced pressure and washed with distilled water and Et_2O. The solid was washed through with DCM to remove any excess inorganic salts and the solvent was removed *in vacuo* to isolate the crude product, which was purified by column chromatography (SiO_2), where the product eluted with DCM/MeOH (9:1) as the eluent and then recrystallised from DCM/Et_2O to give the product as a dark brown solid (15.7 mg, 12.7%). ^{1}H NMR (500 MHz, CDCl$_3$) δ_H = 10.14 (s, 2H), 8.96 (d, $^3J_{HH}$ = 9.0 Hz, 2H), 8.70 – 8.67 (m, 2H), 8.42 – 8.38 (m, 2H), 8.35 – 8.30 (m, 2H), 8.28 – 8.23 (m, 2H), 8.22 – 8.17 (m, 4H), 8.13 – 8.08 (m, 2H), 8.08 – 8.03 (m, 4H), 7.98 – 7.94 (m, 2H), 7.89 – 7.78 (m, 6H), 7.64 (dd, $^3J_{HH}$ = 8.1, $^4J_{HH}$ = 1.0 Hz, 2H), 7.37 (s, 2H) ppm. ^{13}C{^{1}H} NMR (126 MHz, CDCl$_3$) δ_C = 155.8, 148.9, 145.8, 144.4, 141.5, 137.3, 131.8, 131.5, 131.2, 130.8, 130.4, 129.5, 126.0, 125.9, 125.0, 124.9, 123.0, 120.5, 117.8, 115.7 ppm. ^{19}F{^{1}H} NMR (376 MHz, CDCl$_3$) δ_F = −72.81 (d, $^1J_{PF}$ = 692.6 Hz) ppm. HRMS (ES+): *m/z* calc'd 1007.2474 for $C_{58}H_{34}N_6Ir$; found 1007.2479 [M − PF$_6$]$^+$. UV−vis (CHCl$_3$) λ_{max} ($\varepsilon \times 10^4$ / L mol^{-1} cm^{-1}): 269 (4.2), 278 (4.5), 333 (1.6), 347 (1.8), 491 (0.4), 559 sh (0.2) nm. FTIR (solid, cm^{-1}) (ATR) v_{max}: 3312, 2918, 2851, 2050, 1605, 1584, 1530, 1450, 1425, 1377, 1314, 1246, 1177, 1161, 1111, 1072, 1032, 835, 766, 727, 555.

6.6: References

1   S. R. D. George, T. D. H. Frith, D. S. Thomas and J. B. Harper, *Org. Biomol. Chem.*, 2015, **13**, 9035–9041.

2   Z. Q. Liang, Y. X. Li, J. X. Yang, Y. Ren and X. T. Tao, *Tetrahedron Lett.*, 2011, **52**, 1329–1333.

3   Y. Li, W. Huang, J. Yong, S. Huang, Y. Li, Y. Liu and D. Wu, *New J. Chem.*, 2018, **42**, 12644–12648.

4   G. K. Bains, S. H. Kim, E. J. Sorin and V. Narayanaswami, *Biochemistry*, 2012, **51**, 6207–6219.

5   J. R. Lakowicz, *Principles of fluorescence spectroscopy*, Springer, New York, 3rd edn., 2006.

6   P. Conlon, C. J. Yang, Y. Wu, Y. Chen, K. Martinez, Y. Kim, N. Stevens, A. A. Marti, S. Jockusch, N. J. Turro and W. Tan, *J. Am. Chem. Soc.*, 2008, **130**, 336–342.

7   T. Liu, Z. Huang, R. Feng, Z. Ou, S. Wang, L. Yang and L. J. Ma, *Dyes Pigments*, 2020, **174**, 108102.

8   R. L. Melnick, H. C. Haspel, M. Goldenberg, L. M. Greenbaum and S. Weinstein, *Biophys. J.*, 1981, **34**, 499–515.

9   M. Zhao, Z. Deng, J. Tang, X. Zhou, Z. Chen, X. Li, L. Yang and L. J. Ma, *Analyst*, 2016, **141**, 2308–2312.

10   Y.-S. Wu, C.-Y. Li, Y.-F. Li, D. Li and Z. Li, *Sens. Actuators B: Chem.*, 2016, **222**, 1226–1232.

11   V. Kachwal, P. Alam, H. R. Yadav, S. S. Pasha, A. Roy Choudhury and I. R. Laskar, *New J. Chem.*, 2018, **42**, 1133–1140.

12   X. Feng, J. Y. Hu, F. Iwanaga, N. Seto, C. Redshaw, M. R. J. Elsegood and T. Yamato, *Org. Lett.*, 2013, **15**, 1318–1321.

13   H. Guo, X. Song, X. Wang, Y. Liu, C. Redshaw and X. Feng, *ChemistrySelect*, 2022, **7**, e202202208.

14   H. Aggarwal, R. Kumar and A. Srivastava, *Chem. Commun.*, 2018, **54**, 11479–11482.

15   T. P. D. De Silva, S. G. Youm, F. R. Fronczek, G. Sahasrabudhe, E. E. Nesterov and I. M. Warner, *Molecules*, 2021, **26**, 6523.

16   J. Merz, M. Dietz, Y. Vonhausen, F. Wöber, A. Friedrich, D. Sieh, I. Krummenacher, H. Braunschweig, M. Moos, M. Holzapfel, C. Lambert and T. B. Marder, *Chem. Eur. J.*, 2020, **26**, 438–453.

17   J. Chao, X. Wang, Y. Liu, Y. Zhang, F. Huo, C. Yin, M. Zhao, J. Sun and M. Xu, *Sens. Actuators B: Chem.*, 2018, **272**, 195–202.

18   W. E. Ford and M. A. J. Rodgers, *J. Phys. Chem.*, 1992, **96**, 2917–2920.

19   G. J. Wilson, W. H. F. Sasse and A. W. H. Mau, *Chem. Phys. Lett.*, 1996, **250**, 583–588.

20   G. J. Wilson, A. Launikonis, W. H. F. Sasse and A. W. H. Mau, *J. Phys. Chem. A*, 1997, **101**, 4860–4866.

21   D. S. Tyson and F. N. Castellano, *J. Phys. Chem. A*, 1999, **103**, 10955–10960.

22   F. Spaenig, J. H. Olivier, V. Prusakova, P. Retailleau, R. Ziessel and F. N. Castellano, *Inorg. Chem.*, 2011, **50**, 10859–10871.

23   A. J. Howarth, D. L. Davies, F. Lelj, M. O. Wolf and B. O. Patrick, *Inorg. Chem.*, 2014, **53**, 11882–11889.

24   Y. Lu, J. Wang, N. McGoldrick, X. Cui, J. Zhao, C. Caverly, B. Twamley, G. M. Ó Máille, B. Irwin, R. Conway-Kenny and S. M. Draper, *Angew. Chem. Int. Ed.*, 2016, **55**, 14688–14692.

25   Z. Hao, K. Zhang, P. Wang, X. Lu, Z. Lu, W. Zhu and Y. Liu, *Inorg. Chem.*, 2020, **59**, 332–342.

26   J. E. Yarnell, P. De La Torre and F. N. Castellano, *Eur. J. Inorg. Chem.*, 2017, **2017**, 5238–5245.

27   E. L. Williams, J. Li and G. E. Jabbour, *Appl. Phys. Lett.*, 2006, **89**, 083506.

28   Y. Zhang and J. Qiao, *iScience*, 2021, **24**, 102858.

29   A. J. Hallett, N. White, W. Wu, X. Cui, P. N. Horton, S. J. Coles, J. Zhao and S. J. A. Pope, *Chem. Commun.*, 2012, **48**, 10838–10840.

30   R. M. Edkins, K. Fucke, M. J. G. Peach, A. G. Crawford, T. B. Marder and A. Beeby, *Inorg. Chem.*, 2013, **52**, 9842–9860.

31   C. You, D. Liu, F. Meng, Y. Wang, J. Yu, S. Wang, S. Su and W. Zhu, *J. Mater. Chem. C*, 2019, **7**, 10961–10971.

32   Y. Liu, Z. Hao, F. Meng, P. Wang, L. Yang, Y. Wang, Y. Pei and S. Su, *Chem. Phys. Lett.*, 2018, **699**, 99–106.

33   A. Jana, S. Atta, S. K. Sarkar and N. D. P. Singh, *Tetrahedron*, 2010, **66**, 9798–9807.

34   N. P. E. Barry and B. Therrien, in *Organic Nanoreactors: From Molecular to Supramolecular Organic Compounds*, Academic Press, 2016, pp. 421–461.

35   A. S. Ionkin, W. J. Marshall and B. M. Fish, *Organometallics*, 2006, **25**, 1461–1471.

36   P. E. Hansen, A. Berg, L. C. Eriksson, B. Olsson and T. Lave, *Acta Chem. Scand.*, 1981, **35b**, 131–137.

37   S. Califano and G. Abbondanza, *J. Chem. Phys.*, 1963, **39**, 1016.

38   J. Y. Hu, H. Hiyoshi, J. H. Do and T. Yamato, *J. Chem. Res.*, 2010, 278–282.

39   A. G. Crawford, A. D. Dwyer, Z. Liu, A. Steffen, A. Beeby, L. O. Pålsson, D. J. Tozer and T. B. Marder, *J. Am. Chem. Soc.*, 2011, **133**, 13349–13362.

40   Bernard. Valeur and M. Nuno. Berberan-Santos, *Molecular Fluorescence : Principles and Applications*, Wiley-VCH, Weinheim, 2nd edn., 2013.

41   W. H. Melhuish, *J. Phys. Chem.*, 1961, **65**, 229–235.

42   M. Szadkowska-Nicze, M. Wolszczak, J. Kroh and J. Mayer, *J. Photochem. Photobiol. A: Chem.*, 1993, **75**, 125–129.

43   C. Z. Wang, Y. Noda, C. Wu, X. Feng, P. Venkatesan, H. Cong, M. R. J. Elsegood, T. G. Warwick, S. J. Teat, C. Redshaw and T. Yamato, *Asian J. Org. Chem.*, 2018, **7**, 444–450.

44   R. D. Costa, E. Ortí, H. J. Bolink, S. Graber, S. Schaffner, M. Neuburger, C. E. Housecroft and E. C. Constable, *Adv. Funct. Mater.*, 2009, **19**, 3456–3463.

45   R. D. Costa, F. Monti, G. Accorsi, A. Barbieri, H. J. Bolink, E. Ortí and N. Armaroli, *Inorg. Chem.*, 2011, **50**, 7229–7238.

46   S. H. Wu, J. W. Ling, S. H. Lai, M. J. Huang, C. H. Cheng and I. C. Chen, *J. Phys. Chem. A*, 2010, **114**, 10339–10344.

47   L. Ma, H. Guo, Q. Li, S. Guo and J. Zhao, *Dalton Trans.*, 2012, **41**, 10680–10689.

48   K. Suzuki, A. Kobayashi, S. Kaneko, K. Takehira, T. Yoshihara, H. Ishida, Y. Shiina, S. Oishi and S. Tobita, *Phys. Chem. Chem. Phys.*, 2009, **11**, 9850–9860.

49   G. R. Fulmer, A. J. M. Miller, N. H. Sherden, H. E. Gottlieb, A. Nudelman, B. M. Stoltz, J. E. Bercaw and K. I. Goldberg, *Organometallics*, 2010, **29**, 2176–2179.

50   S. A. Fitzgerald, H. Y. Otaif, C. E. Elgar, N. Sawicka, P. N. Horton, S. J. Coles, J. M. Beames and S. J. A. Pope, *Inorg. Chem.*, 2021, **60**, 15467–15484.

51   N. El Guesmi, E. M. Hussein, B. H. Asghar, R. J. Obaid, R. S. Jassas, A. Alharbi, H. M. Altass, I. I. Althagafi, M. Morad, Z. Moussa and S. A. Ahmed, *Arab. J. Chem.*, 2020, **13**, 3702–3713.

52   D. Lu, Q. Xiang, L. Zhou and Q. Zeng, *Asian J. Chem.*, 2015, **27**, 2639–2641.

53   M. Nonoyama, *Bull. Chem. Soc. Jpn.*, 1974, **47**, 767–768.

Chapter 7: Summary and Future Work

7.1: Summary

The work presented in this thesis primarily studied the design, synthesis, characterisation, and spectroscopic properties of a variety of organic compounds based upon 2-phenylquinoxaline and their subsequent utilisation as cyclometallating ligand systems in photoactive metallic complexes.

Chapter 2 explored tunability of emission wavelength within the yellow, orange and deep-red regions of the visible range by altering the 2-phenylquinoxaline C^N ligand in a cationic *bis*-cyclometallated Ir(III) system. By simple synthetic modifications, a significant degree of control was achieved, where phosphorescence was tuned between 579 – 655 nm.

Upon recognising the benefits of incorporating a 2-phenylquinoxaline core as the basis of the C^N ligand to achieve efficient deep-red emission, Chapter 3 focused on the development of neutral, square planar Pt(II) species containing one C^N ligand once again based upon 2-phenylquinoxaline. The ligands differed by the position and nature of a long-range electron-withdrawing substituent, imparting significant changes to the electronic and structural behaviour of the complexes whilst enhancing solubilities to overcome issues that are generally experienced with complexes of this nature. The species were also proven to be effective photosensitisers in triplet-triplet annihilation energy upconversion studies.

Chapter 4 also explored the synthesis and characterisation of Ir(III) complexes, analogous to those presented in Chapter 2. However, the phenyl ring was replaced with a thiophene system, where deep-red emission up to 751 nm was achieved by extending the π-conjugation at the thiophene unit.

Two series of ligands were developed in Chapter 5, where modified 1,8-naphthalimide systems were covalently bound to either 1,10-phenanthroline or 2-phenylquinoxaline, whilst being spatially separated from the metal core. Some evidence of triplet-triplet energy transfer was recognised by means of low temperature steady-state luminescence measurements and time-resolved luminescence data. Lifetimes of up to 700 ns were measured in aerated solutions, whilst deoxygenated samples presented extended lifetimes up to 4.91

μs and all samples displayed enhanced low-energy absorption features up to ~600 nm.

Chapter 6 briefly explored the development of a novel pyrene-based ligand system and its corresponding cationic, *bis*-cyclometallated Ir(III) complex, where some evidence was seen for triplet ligand-centred emission.

7.2: Future Work

In general, future work involving the development of ligand systems based upon a 2-phenylquinoxaline backbone should consider employment of the method detailed in Chapter 5 and Chapter 6 for more efficient conversion.

7.2.1: Thiophene Cyclometallating Ligands on Pt(II)

The findings in Chapter 3 illustrated that emission can occur from a bimolecular excited state, whilst TTA-UC was reasonably efficient for a deep-red emitting Pt(II) complex in solution. Exploration into Pt(II) complexes bearing ligands that were reported in Chapter 4 (**Figure 7.1**) could lead to the formation of photosensitisers with the capability to harness low-energy light. This could be particularly advantageous for applications in solar cell technology and in bioimaging, where there are practical advantages in terms of conversion efficiency and deep skin penetration, respectively. Similarly, the findings on solubility enhancement could be incorporated into the design of such complexes, where fluorination could be implemented either *via* the quinoxaline backbone or through the O^O ligand.
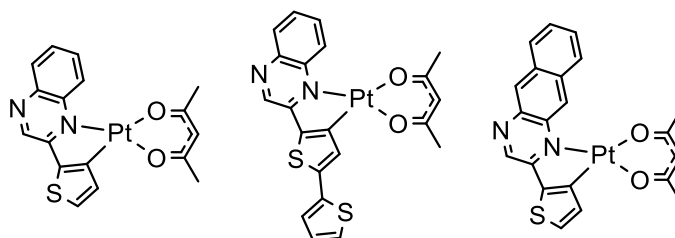

Figure 7.1: *Potential Pt(II) analogues for the thienyl-quinoxaline ligands, directly comparable with the Ir(III) complexes reported in Chapter 4. Two of the most viable candidates for low energy absorption are displayed, along with the unsubstituted model complex.*

7.2.2: Development of AI-pqx Ligands

The initial step in the formation of the anthracene-containing C^N ligands for Chapter 5 has been described and is relatively efficient. Therefore, refinement of the following steps could lead to the formation of 2-(3-(quinoxalin-2-yl)phenyl)-1H-dibenzo[de,h]isoquinoline-1,3(2H)-dione (**3-AI-pqx**) and 2-(4-(quinoxalin-2-yl)phenyl)-1H-dibenzo[de,h]isoquinoline-1,3(2H)-dione (**4-AI-pqx**) as ligand systems. The corresponding complexes are shown in **Figure 7.2**, and would inevitably offer more insight into the impact of adding a modified naphthalimide unit into the backbone of C^N ligands, a previously unexplored area. The complexes presented in Chapter 5 would also benefit from further photophysical analysis in the form of transient absorption measurements to explore the nature of the excited state processes and kinetic behaviour in more detail. This would provide more detail around excited state properties of the cyclometallated complexes and could potentially offer insight into the development of species for applications in biological imaging and diagnostic applications, where the nature of a pendant organic chromophore can significantly impact the interplay across and between excited states, whilst the highly planarised pendant unit could act as a DNA-targeting fragment through intercalation.
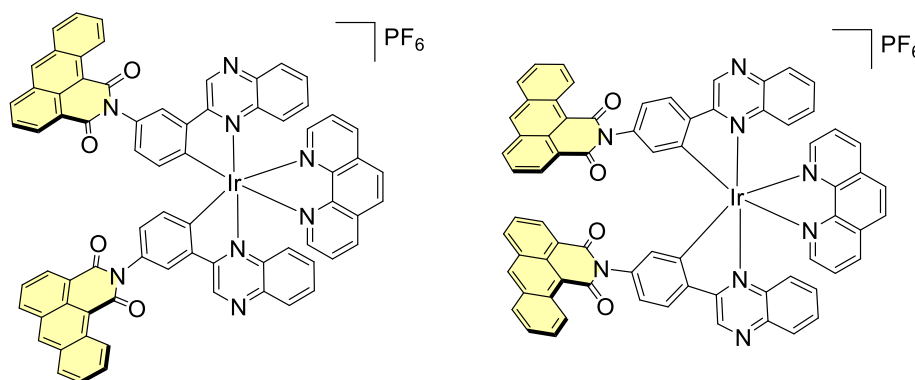

Figure 7.2: *Prospective Ir(III) complexes incorporating **AI-pqx** ligands, which contain a pendant anthracene-based naphthalimide unit.*

7.2.3: Ligand Design to Alter Physical Properties

Chapter 6 detailed the synthesis and characterisation of an iridium complex directly cyclometallated to a pyrene system. Although it was hypothesised that

this bond formation occurred at the C2 position to generate a 5-membered metallacycle, crystallographic data must be obtained to conclude that this is the case, since C-M bond formation is also possible at the C10 position. Previous chapters have demonstrated that solubility can be significantly enhanced by incorporation of lipophilic, fluorinated substituents – therefore, exploration into functionalised ancillary ligands or substitution at the quinoxaline backbone could alleviate issues experienced throughout this study with respect to solubility, for absolute structural determination. Further spectroscopic analysis such as transient absorption measurements and time-resolved luminescence data recorded for degassed solutions of the complex would be beneficial in determining the nature of the excited state and general photophysical properties of the complex.

Additionally, it may be interesting to investigate the **pqx**-functionalised complexes from Chapter 5 in more detail, where other ancillary ligands could be employed to enhance water solubility. The bipyridine analogues were proven to display favourable properties over the phen ligand (λ_{abs} up to 494 nm and τ_{obs} up to 4.91 µs in deoxygenated solution), therefore, by adding a hydrophilic component to the bipyridine, the complexes may have applications in biological applications. For example, ethylene glycols (such as tetraethylene glycol, TEG), can be incorporated into the bipyridine ancillary ligand to improve water-solubility (**Figure 7.3**), offering great potential as luminescent probes and in chemiluminescence.
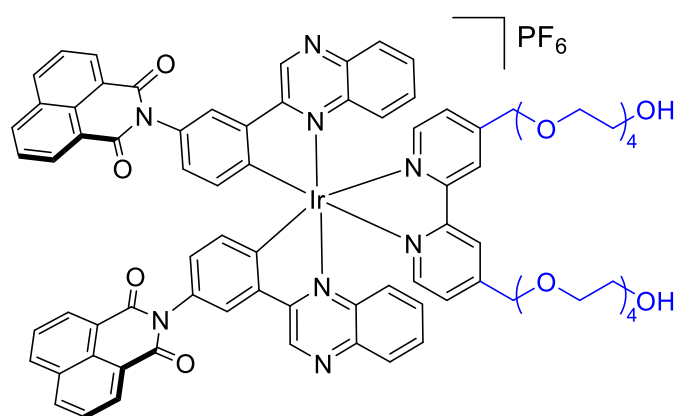

Figure 7.3: Ir-pqx3 from Chapter 5, but with tetraethylene glycol (TEG) groups attached to the 4 positions of the pyridine rings to enhance water solubility.